UNIVERSITY OF OKLAHOMA

GRADUATE COLLEGE

ANALYSIS OF MELT BLOWING DIES USING COMPUTATIONAL FLUID DYNAMICS

A DISSERTATION

SUBMITTED TO THE GRADUATE FACULTY

in partial fulfillment of the requirements for the

degree of

Doctor of Philosophy

By

HOLLY MARIE KRUTKA
Norman, OK
2007

Downloaded from SHAREOK. Persistent Handle URL: https://hdl.handle.net/11244/1313

UMI Number: 3294670

UMI®

UMI Microform 3294670

Copyright 2008 by ProQuest Information and Learning Company.

All rights reserved. This microform edition is protected against unauthorized copying under Title 17, United States Code.

ProQuest Information and Learning Company
300 North Zeeb Road
P.O. Box 1346
Ann Arbor, MI 48106-1346

ANALYSIS OF MELT BLOWING DIES USING COMPUTATIONAL FLUID DYNAMICS

A DISSERTATION APPROVED FOR THE
SCHOOL OF CHEMICAL, BIOLOGICAL AND MATERIALS ENGINEERING

BY

_____
Dimitrios Papavassiliou (chair)

_____
Robert Shambaugh (co-chair)

_____
Lance Lobban

_____
Ramkumar Parthasarathy

_____
Amy Cerato

© Copyright by HOLLY MARIE KRUTKA 2007
All Rights Reserved.

ACKNOWLEDGEMENTS

I would like to thank the following individuals:

Dr. Papavassiliou for being my chair, friend, and mentor. I couldn't have asked for a better advisor, and you have taught me more about science and life than I ever expected or imagined possible.

Dr. Shambaugh for being my co-chair and sharing your passion for polymers. Thank you for your endless supply of jokes.

Dr. Lobban for being on my committee, for being a great instructor, and for being a smiling face with an open door. You are one of the reasons I have been so happy at OU for so many years.

Dr. Parthasarathy for being on my committee and for being one of the best teachers I have ever met. Your dedication to your students is amazing.

Dr. Cerato for being on my committee and for being an inspiring friend. I would not be the same without you in my life.

Phuong Le, I couldn't asked for a better office partner, or cooking buddy. Thank you for your friendship and sharing your culture with me.

Vishnu Marla and Eric Moore for helping me understand how to be a great graduate student. You were both an inspiration.

Courtney Green for being a wonderful friend and workout buddy. You support and understanding helped me more than you know over the last few years.

April and Daniel, my siblings, for always being there for me and pushing me to be the best through your own accomplishments.

Donna Krutka and Mark Self, my step parents, for their support and acceptance.

My parents, who encouraged me from my birth. I never heard the word "can't" from you. Every extra hour you put in loving me, teaching me, and pushing me has made me who I am today. Thank you so much.

My husband, Mark Watkins, you are my best friend, biggest supporter, and the love of my life. I could never have done this without you. Thank you for everything, this is dedicated to you.

TABLE OF CONTENTS

ACKNOWLEDGEMENTS iv
LIST OF TABLES viii
LIST OF ILLUSTRATIONS x
ABSTRACT xix
CHAPTER 1: INTRODUCTION 1
1.1 Melt Blowing 1
1.2 Using Computational Fluid Dynamics to Study Melt Blowing 2
1.3 Modeling of Turbulent Jets 4
1.3.1 The k-ε Model 6
1.3.2 The Reynolds Stress Model 8
1.3.3 Energy Equation 9
1.4 Computational Domain 10
1.4.1 Grid Generation 10
1.4.2 Boundary Conditions 11
1.5 Motivation 14
1.6 Nomenclature 15
1.7 References 16
CHAPTER 2: SLOT MELT BLOWING DIES 23
2.1 Introduction to Slot Dies 23
2.1.1 Planar Jet Literature Review 24
2.1.2 Slot Die Geometries 26
2.1.3 Computational Domain 28
2.1.4 Grid for Blunt Dies and Sharp Flush Dies 29
2.1.4 Grid for Inset and Outset Sharp Dies 30
2.2 Isothermal CFD Results 31
2.2.1 Comparison to Experiments for Flush Blunt and Sharp Dies 31
2.2.2 Blunt Die Results for Positions Close to the Die Face 35
2.2.3 Effect of Changing Jet Angle on Flush Blunt and Sharp Dies 37
2.2.4 Comparison to Experiments for Inset and Outset Dies 42
2.2.5 Effect on Mean Velocity of Changing the Nose Piece Placement for Sharp Dies 43
2.2.6 Effect on Fluctuating Velocity Field of Changing the Nose Piece Placement for Sharp Dies 48
2.3 Comparison of Slot Dies Using New Scales 53
2.3.1 Introduction of a New Length Scale 53
2.3.2 Flush Blunt and Sharp Dies 54
2.3.3 Inset and Outset Sharp Dies 55
2.4 Non-Isothermal Slot Die Simulations 57
2.4.1 Comparison to Experiments 58
2.4.2 Non-isothermal Simulation Results 60
2.5 Conclusions 60
2.7 Nomenclature 64
2.8 References 65
CHAPTER 3: MULTIHOLE MELT BLOWING DIES 155
3.1 Introduction to Multihole Dies 155

3.1.1 Round and Annular Jet Literature Review 156
3.1.2 Computational Domain 159
3.1.3 Grid for Multihole Dies 161
3.1.4 Multihole Geometries 162
3.2 Isothermal CFD Results 162
3.2.1 Comparison to Experiments 163
3.2.2 Comparison between a Schwarz Die and a Single Annular Die 165
3.2.3 Qualitative Flow Field Description 167
3.2.4 Comparison between Different Multihole Geometries 168
3.3 Non-Isothermal Simulation Results 174
3.3.1 Comparison to Experiments 175
3.3.2 Comparison between a Schwarz Die and a Single Annular Die 176
3.3.3 Comparison between Different Multihole Geometries 177
3.4 Conclusions 184
3.5 Nomenclature 186
3.6 References 188
CHAPTER 4: SWIRL MELT BLOWING DIE 245
4.1 Introduction to Swirl Melt Blowing Dies 245
4.1.1 Literature Review 245
4.1.2 Swirl Die Geometry 246
4.2 Experimental Setup 247
4.3 CFD Simulations 248
4.3.1 Computational Domain 249
4.3.2 Grid for Swirl Dies 249
4.3.3 Turbulence Modeling 250
4.3.4 Comparison to Experiments 251
4.3.5 Comparison to Theory 252
4.3.6 Angular Velocity 253
4.4 Conclusions 254
4.5 Nomenclature 254
4.6 References 255
CHAPTER 5: EFFECT OF A FIBER ON AIR FLOW 270
5.1 Introduction 270
5.1.1 Literature Review 270
5.2 Effect of Fiber on Air Flow for an Annular Die 273
5.2.1 Air and Polymer Flow Rates for Simulations 274
5.2.2 Computational Domain 274
5.2.3 Grid Generation 276
5.2.4 Incorporation of Fibers in the Simulation 279
5.2.5 Turbulence Modeling 280
5.2.6 Effects of the Polymer on the Mean Flow Field 281
5.2.7 Fluctuating Velocity Field 285
5.2.8 Stresses on the Fiber Edge 288
5.2.9 Jet Spreading Rate 289
5.3 Effect of Fiber on Air Flow for a Slot Melt Blowing Die 290
5.3.1 Computational Domain 290

5.3.2 Grid Generation 291
5.3.3 Turbulence Modeling 294
5.3.4 Results from the Rheological Model 295
5.3.5 Effects of the Polymer on the Mean Flow Field 296
5.3.6 Fluctuating Flow Field 300
5.3.7 Stress on Fiber Edge 301
5.3.8 Jet Spreading Rate 303
5.3.9 Temperature Field 304
5.4 Conclusions 305
5.5 Nomenclature 307
5.6 References 309
CHAPTER 6: CONCLUSIONS 357
6.1 Conclusions 357
6.2 Major Contributions 360
6.3 Recommended Future Work 361
6.4 Nomenclature 362
6.5 References 362

LIST OF TABLES

CHAPTER 2
Table 2-1. Simulation parameters for the numerical experiments for blunt and flush dies. The computational time designated as P-IV refers to a 1.7 GHz Pentium IV computer and the computational time designated as 2P-II refers to a dual 800MHz Pentium III computer.
Table 2-2. Summary of the problem configuration and the computational requirements for each numerical experiment for the simulation of the inset and outset sharp dies.
Table 2-3. Results of regression analysis for the dual jet problem with Equation 2-2.
Table 2-4. Coefficients in Equation (2-7) for the inset and outset die configurations examined in this work.
Table 2-5. Calculated coefficients for Equation (2-14)
Table 2-6. Number of Cells, Number of Iterations, and Approximate Running Time
Table 2-7. Root Mean Squared (RMS) Error for Velocity and Temperature for Pr_t = 0.30, 0.35, and 0.40
Table 2-8. Reynolds stress model parameters available in the Fluent™ software, and modifications made to agree with the experimental results

CHAPTER 3
Table 3-1. Grid Independence Time Requirements
Table 3-2. Multihole Die Geometries
Table 3-3. Centerline Velocity Decay Equation Constants (see Equation 3-6)
Table 3-4. Empirical Constants for Equation 3-9

CHAPTER 4
Table 4-1: List of models and the modifications made to simulate the swirl die air flow.
Table 4-2: Values of C_m

CHAPTER 5
Table 5-1: Polymer Flow Rates and Initial Air Velocities Used in the Annular Jet Simulations
Table 5-2: Grid and Computational Requirements for the Simulations in Figure 5-4
Table 5-3: Velocity Decay Constants when V_{jo} is used to Nondimensionalize the Velocity (as Defined in Equation 5-3)
Table 5-4: Velocity Decay Constants when $V_{az\text{-}max}$ is used to Nondimensionalize (as defined in Equation 5-3)
Table 5-5: Percent Difference Between Calculated Drag Force and Value from Simulations
Table 5-6: β Values for Calculated Drag Force To Be Within 1% of the Simulation Results
Table 5-7: Spreading Rate Constants for Equation 5-8
Table 5-8: Polymer Flow Rates and Initial Air Velocities Used in the Slot Jet Simulations
Table 5-9: Simulation Grid and the Computational Requirements for the Simulations Shown in Figure 5-20
Table 5-10: Velocity Decay Constants for $y = 0$, $x = x_{max}$ starting at $z > 10$mm

Table 5-11: Wall Shear Stress Deviation
Table 5-12: Comparison of Calculated Drag Force and Simulation Results
Table 5-13: Spreading Rates for $z \geq 30$ mm
Table 5-14: Excess Temperature Decay Constants for at $z \geq 5$ mm

LIST OF ILLUSTRATIONS

CHAPTER 1

Figure 1-1. Cross Section of Melt Blowing Process Using an Annular Air Jet
Figure 1-2. Exxon slot melt blowing die with partial cutout
Figure 1-3. Bottom view of a Schwarz multihole die
Figure 1-4. Swirl melt blowing die

CHAPTER 2

Figure 2-1. Exxon slot melt blowing die with partial cutout
Figure 2-2. Cross Section of Exxon slot melt blowing die
Figure 2-3. Bottom View of Exxon slot melt blowing die
Figure 2-4. Cross section of a sharp slot melt blowing die
Figure 2-5. Cross section of an inset sharp slot die
Figure 2-6. Cross section of an outset sharp slot die
Figure 2-7a. Computational domain for blunt dies and sharp flush dies
Figure 2-7b. Grid close to the inlet
Figure 2-8. Comparison of simulated centerline velocity for blunt die configurations and different grid refinements
Figure 2-9. Computational domain and grid refinements regions used for inset and outset sharp dies.
Figure 2-10. Turbulence intensity and velocity decay for different grid resolutions for inset die with $a = -b_o/2$.
Figure 2-11. Dimensionless z-velocity along the centerline for different turbulence models with the experimental results of TS for a 70° sharp die.
Figure 2-12a. Dimensionless velocity decay along the line of symmetry resulting from the simulation, the empirical decay equations of HS, and the laboratory results for a 60° blunt die geometry. The low V_{jo} is 17.3 m/s and the high V_{jo} is 34.6 m/s.
Figure 2-12b. Dimensionless velocity decay along the line of symmetry resulting from the simulation, the empirical decay equations of TS, and the laboratory results for a 70° sharp die geometry. The low V_{jo} is 17.3 m/s and the high V_{jo} is 34.6 m/s.
Figure 2-13a. Dimensionless velocity close to the die face; experimental measurements and CFD results for the 60° blunt die geometry.
Figure 2-13b. Dimensionless velocity to the die face; experimental measurements and CFD results for the 70° sharp die geometry.
Figure 2-14. Dimensionless velocity profiles within the self-similar region below the die.
Figure 2-15a. Typical total velocity magnitude (i.e. $|V|$) contours for the flow field resulting from the simulation. The case depicted here is for a 60° blunt die with V_{jo} = 17.3 m/s, RSM, and second-order discretization for the whole computational domain.
Figure 2-15b. Typical total velocity magnitude (i.e. $|V|$) contours for the flow field resulting from the simulation. The case depicted here is for a 60° blunt die with V_{jo} = 17.3 m/s, RSM, and second-order discretization; this contour plot is close to the die face.
Figure 2-16. Velocity vector field close to the 60° blunt die face. An area of flow recirculation is seen between the two converging jets. The Figure 2-shows an area below the die face that is 8.8 mm wide by 5.3 mm high.

Figure 2-17a. Mean dimensionless velocity along the centerline for different die angles for blunt die configurations.
Figure 2-17b. Mean dimensionless velocity along the centerline for different die angles for sharp die configurations.
Figure 2-18a. Dimensionless turbulence intensity along the centerline for different die angles for blunt die geometries.
Figure 2-18b. Dimensionless turbulence intensity along the centerline for different die angles for sharp die geometries.
Figure 2-19a. Dimensionless Reynolds stress along the centerline for different die angles for blunt die geometries.
Figure 2-19b. Dimensionless Reynolds stress along the centerline for different die angles for sharp die geometries.
Figure 2-20a. Dimensionless turbulent kinetic energy along the centerline for different die angles for blunt die geometries.
Figure 2-20b. Dimensionless turbulent kinetic energy along the centerline for different die angles for sharp die geometries.
Figure 2-21a. Dimensionless turbulence dissipation rate along the centerline for different die angles for blunt die geometries.
Figure 2-21b. Dimensionless turbulence dissipation rate along the centerline for different die angles for sharp die geometries.
Figure 2-22a. Contours of the Reynolds stress in the flow field close to the die surface for the 60° blunt die with V_{jo} = 17.3 m/s.
Figure 2-22b. Contours of the Reynolds stress in the flow field close to the die surface for the 60° sharp die with V_{jo} = 17.3 m/s.
Figure 2-23a. Contours of the turbulence intensity in the flow field close to the die surface for a 60° blunt die with V_{jo} = 17.3 m/s.
Figure 2-23b. Contours of the turbulence intensity in the flow field close to the die surface for a 60° sharp die with V_{jo} = 17.3 m/s.
Figure 2-24a. Comparison of CFD results with experiments for dimensionless mean velocity close to the die face.
Figure 2-24b. Comparison of CFD results with experiments for the dimensionless mean velocity farther from the die face. The equation $V_o/V_{jo} = 3.66(z/h)^{-0.558}$ is the least squares fit of the experimental data to a power law equation.
Figure 2-25a. Dimensionless mean centerline velocity for the simulated inset dies.
Figure 2-25b. Dimensionless mean centerline velocity for the simulated outset dies.
Figure 2-25c. Maximum mean centerline velocity as a function of the die configuration (R = 0.99998 for the equation shown on the graph).
Figure 2-26a. Dimensionless velocity profiles within the self-similar region (z = 50 mm) for the simulated inset dies and the experimental TS flush die.
Figure 2-26b. Dimensionless velocity profiles within the self-similar region (z = 50 mm) for the simulated outset dies and the experimental TS flush die.
Figure 2-27a. Contour plot of the mean z-velocity below the die face for an inset die with $a = -b_o/2$.
Figure 2-27b. Contour plot of the mean z-velocity below the die face for an outset die with $a = b_o/2$.
Figure 2-28a. Turbulence intensity along the centerline for inset dies.

Figure 2-28b. Turbulence intensity along the centerline for outset dies.
Figure 2-28c. Maximum turbulence intensity as a function of the die configuration (R = 0.99894 for the equation shown on the graph).
Figure 2-29a. Contour plots of the turbulence intensity below the die face for an inset die with $a = -b_o/2$.
Figure 2-29b. Contour plots of the turbulence intensity below the die face for an outset die with $a = b_o/2$.
Figure 2-30a. Dimensionless Reynolds stress profiles across the centerline for inset dies.
Figure 2-30b. Dimensionless Reynolds stress profiles across the centerline for outset dies.
Figure 2-30c. Maximum Reynolds stress as a function of the die configuration (R = 0.99894 for the equation shown on the graph).
Figure 2-31a. Contour plots of the Reynolds stress below the die face for and inset die with $a = -b_o/2$.
Figure 2-31b. Contour plots of the Reynolds stress below the die face for and outset die with $a = b_o/2$.
Figure 2-32a. Dimensionless turbulence kinetic energy profiles across the centerline for inset dies.
Figure 2-32b. Dimensionless turbulence kinetic energy profiles across the centerline for outset dies.
Figure 2-32c. Maximum turbulence kinetic energy as a function of the configuration (R = 0.99647 for the equation shown on the graph).
Figure 2-33a. Contour plots of the turbulent kinetic energy below the die face for and inset die with $a = -b_o/2$.
Figure 2-33b. Contour plots of the turbulent kinetic energy below the die face for and outset die with $a = b_o/2$.
Figure 2-34a. Dimensionless turbulence dissipation rate profiles along across the centerline for inset dies.
Figure 2-34b. Dimensionless turbulence dissipation rate profiles along across the centerline for outset dies.
Figure 2-34c. Maximum turbulence dissipation rate as a function of the die configuration (R = 0.99825 for the equation shown on the graph).
Figure 2-35a. Prediction of dimensionless mean centerline velocity for blunt flush dies ($R^2 = 0.9953$ for the velocity decay equation shown on the graph).
Figure 2-35b. Prediction of dimensionless mean centerline velocity for sharp flush dies ($R^2 = 0.9819$ for the velocity decay equation shown on the graph).
Figure 2-36. Relationship between zmax and q for the blunt flush dies ($R^2 = 0.9618$ for the curve fit shown on the graph) and sharp dies ($R^2 = 0.9932$ for the curve fit shown on the graph).
Figure 2-37. Maximum mean centerline velocity as a function of the slot angle of flush blunt dies ($R^2 = 0.9801$ for the equation shown on the graph) and flush sharp dies ($R^2 = 0.9920$ for the equation shown on the graph).
Figure 2-38a. Turbulence intensity along the centerline for blunt flush dies.
Figure 2-38b. Turbulence intensity along the centerline for sharp flush dies.
Figure 2-39a. Prediction of dimensionless mean centerline velocity for inset dies ($R^2 = 0.9795$ for the velocity decay equation shown on the graph).

Figure 2-39b. Prediction of dimensionless mean centerline velocity for outset dies ($R^2 = 0.9896$ for the velocity decay equation shown on the graph).
Figure 2-40a. Relationship between z_{max} and $(2+a)/d$ for inset dies ($R^2 = 0.9847$ for the curve fit shown on the graph).
Figure 2-40b. Relationship between z_{max} and $(2+a)/d$ for outset dies ($R^2 = 0.9982$ for the curve fit shown on the graph).
Figure 2-41. Maximum mean centerline velocity as a function of the die configuration for inset, flush, and outset sharp dies ($R^2 = 0.9994$ for the equation shown on the graph).
Figure 2-42a. Turbulence intensity along the centerline for inset dies.
Figure 2-42b. Turbulence intensity along the centerline for outset dies.
Figure 2-43. Comparison of dimensionless centerline velocity profiles for isothermal and non-isothermal cases. These simulations were conducted for a 60° blunt die.
Figure 2-44. Comparison of simulated centerline velocity to experimental data throughout computational domain for 60° blunt die for simulations with different Pr_t values. $\Theta_{jo} = 100$ K for both the simulations and experimental data. The curves shown are simulations run with $V_{jo} = 23.2$ m/s.
Figure 2-45a. Comparison of simulated centerline temperature decay to an experimental correlation for 60° blunt die for $0.20 \leq Pr_t \leq 0.40$. The simulations were performed with $\Theta_{jo} = 100$K for both the simulations and the experimental fit. The curves shown are the simulations with $V_{jo} = 23.2$.
Figure 2-45b. Comparison of simulated centerline temperature decay to an experimental correlation for 60° blunt die for $0.50 \leq Pr_t \leq 0.85$. The simulations were performed with $\Theta_{jo} = 100$K for both the simulations and the experimental fit. The curves shown are the simulations with $V_{jo} = 23.2$.
Figure 2-46. Dimensionless centerline velocity as a function of distance below the die face. The simulated curves and the experimental curves are shown for a 60° blunt die with $Pr_t = 0.30$.
Figure 2-47. Dimensionless centerline temperature as a function of distance below the die face. The simulated curves and the experimental curves are shown for a 60° blunt die with $Pr_t = 0.30$.
Figure 2-48a. Dimensionless temperature decay for blunt and sharp 45° and 50° dies. The general correlation fitting all temperature decays is $\Theta_o/\Theta_{jo} = 0.0074^* (z/z_{max})^{-0.5537}$ with an $R^2 = 0.9831$. The simulations were run for a die with $Pr_t = 0.30$, $\Theta_{jo} = 100$ K, and $V_{jo} = 23.2$ m/s.
Figure 2-48b. Dimensionless temperature decay for blunt and sharp 60° and 70° dies. The general correlation fitting all temperature decays is $\Theta_o/\Theta_{jo} = 0.0074^* (z/z_{max})^{-0.5537}$ with an $R^2 = 0.9831$. The simulations were run for a die with $Pr_t = 0.30$, $\Theta_{jo} = 100$ K, and $V_{jo} = 23.2$ m/s.

CHAPTER 3

Figure 3-5a. View of the face of the Schwarz melt blowing die. Each black circle represents a capillary/air jet configuration. The Schwarz die has an array of 165 jets in 55 rows (the die in the figure has been reduced in size for purposes of illustration.) The *z*-direction is perpendicular to the plane of the die face, and the origin is at the center orifice.

Figure 3-1b. View of the face of the Schwarz melt blowing die. This view shows only 9 holes; the full die has 165 jets in three columns (see Figure 3-1a). The origin of the coordinate system is at the center of the center hole. The *z*-direction is perpendicular to the plane of the die face.
Figure 3-2a. Geometry of the side view of the entire computational domain used in the simulations (shown at the n used in the simulations (shown at the $y = 0$ plane).
Figure 3-2b. A close up of the view of the jet shown surrounded by the dashed lines in Figure 3-2a.
Figure 3-3a. Dimensionless *z*-velocity at $x = 0$ and $y = 0$ for simulations run under the same conditions, but with different grid refinement.
Figure 3-3b. Centerline excess temperature at *z*-velocity at $x = 0$ and $y = 0$ for simulations run under the same conditions, but with different grid refinement.
Figure 3-4. Entrainment coefficient for Case 4 compared with the experimentally determined coefficient from MS.
Figure 3-5. The profiles of z-velocity at $y = 0$ and different *z* positions below the die. The simulations for Case 4 are compared to the experimental data of MS. Also on the figure is the exponential fit equation proposed by MS.
Figure 3-6a. The *z*-velocity profile at a position of $z = 1.27$ mm below the die for the Case 4 simulation.
Figure 3-6b. The *z*-velocity profile at a position of $z = 1.27$ mm below the die for the MS experimental data.
Figure 3-7a. The *z*-velocity profile at a position of $z = 7.62$ mm below the die for the Case 4 simulation.
Figure 3-7b. The *z*-velocity profile at a position of $z = 7.62$ mm below the die for the MS experimental data.
Figure 3-8a. Comparison between the Case 4 and predicted axial velocity profile for the centerline of the center jet. The predictions, which are based on the work of MS, are a derivation of the work of Baron and Alexander (1951).
Figure 3-8b. Comparison between the Case 4 and predicted axial velocity profile for the centerline of the outside jet. The predictions, which are based on the work of MS, are a derivation of the work of Baron and Alexander (1951).
Figure 3-9. A comparison of the jet centerline velocity profile at $x = 0$ and $y = 0$ for a simulated single annular jet with the center and outer jet profiles in the simulated Case 4.
Figure 3-10. A qualitative diagram of the flow zones created by multiple jets. This diagram shows a side view (*x*-*z* plane) of the flow from two annular jets in a Schwarz die configuration. At the top of the figure is an outside jet, while a center jet is located at the bottom of the figure. This diagram was adapted from Moore et al. (2004) and Lai and Nasr (1998).
Figure 3-11a. The dimensionless *z*-velocity, for all six simulations for the centerline of the center jet where $x = 0$ and $y = 0$**.**
Figure 3-11b. The dimensionless *z*-velocity, for all six simulations compared for a line halfway between the center and outside jets where $y = 0$ and $x = h_e/2$**.**
Figure 3-11c. The dimensionless *z*-velocity, for all six simulations, compared for the centerline of the outside jet where $y = 0$ and $x = h_e$**.**
Figure 3-12a. Simulation velocity decay at $x = 0$ and $y = 0$ compared with the correlation for Case 1. The correlation is equation 3-6 with the constants listed in Table 3-3.

Figure 3-12b. Simulation velocity decay at $x = 0$ and $y = 0$ compared with the correlation for Case 4. The correlation is equation 3-6 with the constants listed in Table 3-3.
Figure 3-12c. Simulation velocity decay at $x = 0$ and $y = 0$ compared with the correlation for Case 6. The correlation is equation 3-6 with the constants listed in Table 3-3.
Figure 3-13a. Comparison of the z-velocity profiles of all simulations at $z = 2$ mm. All profiles are shown for the $y = 0$ plane.
Figure 3-13b. Comparison of the z-velocity profiles of all simulations at and $z = 5$ mm. All profiles are shown for the $y = 0$ plane.
Figure 3-13c. Comparison of the z-velocity profiles of all simulations at $z = 10$ mm. All profiles are shown for the $y = 0$ plane.
Figure 3-13d. Comparison of the z-velocity profiles of all simulations at $z = 20$ mm. All profiles are shown for the $y = 0$ plane.
Figure 3-14a. Contour plot of z-velocity for Case 1. All contours are shown for the $y = 0$ plane.
Figure 3-14b. Contour plot of z-velocity for Case 4. All contours are shown for the $y = 0$ plane.
Figure 3-14c. Contour plot of z-velocity for Case 6. All contours are shown for the $y = 0$ plane.
Figure 3-15. Center jet centerline turbulence intensity for all simulations.
Figure 3-16. The location of z_{merge} as a function of h_h for all cases.
Figure 3-17. The spreading rate of the center jets in the multi-hole die as a function of h_h.
Figure 3-18. The centerline excess temperature decay from Case 4 simulation compared with the experimental data of MS2.
Figure 3-19. Comparison of Case 4 and MS2 excess temperature profiles on the $y = 0$ plane.
Figure 3-20a. Excess temperature profile at a position of $z = 2.54$ mm below the die for Case 4.
Figure 3-20b. Excess temperature profile at a position of $z = 2.54$ mm below the die for the averaged MS2 experiments.
Figure 3-21a. Comparison of the temperature profiles at a position of $z = 5.08$ mm below the die for Case 4.
Figure 3-21b. Comparison of the temperature profiles at a position of $z = 5.08$ mm below the die for the averaged MS2 experiments.
Figure 3-22. Comparison between the centerline temperature profiles for a single annular jet and the center and outside jet from Case 4.
Figure 3-23a. Comparison of temperature profiles of all simulations at the centerline of the center jet.
Figure 3-23b. Comparison of temperature profiles of all simulations at a line halfway between the center and outside jets.
Figure 3-23c. Comparison of temperature profiles of all simulations at the centerline of the outside jet.
Figure 3-24a. Comparison of empirical predictive correlation to the simulation results of the temperature decay for Case 1. The correlation is given by equation 3-9 with the corresponding constants given in Table 3-4.

Figure 3-24b. Comparison of empirical predictive correlation to the simulation results of the temperature decay for Case 4. The correlation is given by equation 3-9 with the corresponding constants given in Table 3-4.
Figure 3-24c. Comparison of empirical predictive correlation to the simulation results of the temperature decay for Case 6. The correlation is given by equation 3-9 with the corresponding constants given in Table 3-4.
Figure 3-25a. Comparison of the temperature profiles of all simulations at $z = 0.5$ mm. These profiles are for the $y = 0$ plane.
Figure 3-25b. Comparison of the temperature profiles of all simulations at $z = 2$ mm. These profiles are for the $y = 0$ plane.
Figure 3-25c. Comparison of the temperature profiles of all simulations at $z = 10$ mm. These profiles are for the $y = 0$ plane.
Figure 3-26a. Contour plot of excess temperature for Case 1. These contours are for the $y = 0$ plane.
Figure 3-26b. Contour plot of excess temperature for Case 4. These contours are for the $y = 0$ plane.
Figure 3-26c. Contour plot of excess temperature for Case 6. These contours are for the $y = 0$ plane.
Figure 3-27. Position along the z-axis at which the temperature maximums of the two jets merge. The fit for these points is given by equation 3-10.
Figure 3-28. The temperature spreading rate of the jets versus h_h. The fit for these points is given by equation 3-11.

CHAPTER 4
Figure 4-1a. Cross section of a swirl nozzle.
Figure 4-1b. Bottom view of a swirl melt blowing die.
Figure 4-2. Molten polymer from a swirl die. This picture was taken by Marla et al. (2006) using high speed photography.
Figure 4-3. Experimental setup for measurement of air flow. Figure adapted from Moore (2004).
Figure 4-4. Experimental measurements of z-velocity on centerline.
Figure 4-5a. The computational domain at $\theta = 0^{\circ}$. The letters A, B, and C designate the different areas of grid refinement.
Figure 4-5b. Top view of the die face in the computational domain, both tetrahedral and hexahedral cells are used in this domain.
Figure 4-6. Comparison of centerline velocity for different grid refinements.
Figure 4-7. Comparison of the z-velocity on the centerline as predicted by different turbulence models. Table 4-1 contains the list of all models and modifications for simulations of the swirl melt blowing die.
Figure 4-8a. Comparison of simulations with different turbulence models to experimental measurements.
Figure 4-8b. Comparison of the centerline velocity from three simulations with different turbulence model and/or parameters and experimental results. V_{max} and z_{max} are used to non-dimensionalize velocity and z-position, respectively.
Figure 4-9. Contours of θ-velocity at $\theta = 30^{\circ}$ and at $\theta = 0^{\circ}$ (the periodic boundary). This figure is for $z \leq 10$ mm.

CHAPTER 5

Figure 5-1. Cross-sectional view of an annular melt-blowing die.
Figure 5-2. Computational domain and grid refinement regions. In section A, the outermost region, the length of the sides of the quadrilateral cells is 0.1 mm. Sections B, C_1 and C_2, and D have, respectively, cell sides of 0.05, 0.025, and 0.0125 mm. The curved left side of the domain corresponds to the surface of the polymer fiber.
Figure 5-3a. The fiber radius as a function of position below the die. The fiber radius establishes the left boundary of the computational domain seen in Figure 5-2. The horizontal solid line designates the radius of a cylinder with diameter equal to 5 mm and constant velocity V_{fz} = 5 m/s.
Figure 5-3b. The fiber radius as a function of position below the die. The horizontal solid line designates the velocity of a cylinder with diameter equal to 5 mm and constant velocity V_{fz} = 5 m/s.
Figure 5-3c. The fiber velocity for Case 4 compared with the axial air velocity at r = 0.4 mm for Case 1 and Case 4.
Figure 5-4. The dimensionless axial velocity and turbulence intensity for simulations run under the same (case 4) conditions but with different grid refinements.
Figure 5-5. Comparison of axial velocity at r = 0.4 mm for cases 1 and 4 and a cylinder with a radius of 0.25 mm. Case 4 is based on the model by Marla and Shambaugh (2003).
Figure 5-6a. Axial velocity vector plot in the recirculation area for case 1.
Figure 5-6b. Axial velocity vector plot in the recirculation area for case 4.
Figure 5-7. Comparison of the position of maximum axial velocity for cases 1 and 4.
Figure 5-8. Comparison of axial velocity at r = 0.4 mm for all simulations.
Figure 5-9a. Comparison of axial velocity decay at r = 0.4 mm. V_{jo} was used to nondimensionalize V_{az}. The fit for case 1 is $V_{az}/V_{jo} = 4.176*(z/D_o)^{-0.953}$ (R^2 = 0.996), the fit for the case 2, 3, and 4 simulations is $V_{az}/V_{jo} = 3.288*(z/D_o)^{-0.902}$ (R^2 = 0.998), and the fit for case 6 is $V_{az}/V_{jo} = 1.536*(z/D_o)^{-0.801}$ (R^2 = 0.999).
Figure 5-9b. Comparison of axial velocity decay at r = 0.4 mm. $V_{az\text{-}max}$, rather than V_{jo}, was used to nondimensionalize the ordinate. The fit for the simulations without polymer is $V_{az}/V_{az\text{-}max} = 3.115*(z/D_o)^{-0.922}$ (R^2 = 0.985), the fit for the simulations that include the polymer is $V_{az}/V_{az\text{-}max} = 3.579*(z/D_o)^{-0.902}$ (R^2 = 0.984).
Figure 5-10. Comparison of the entrainment coefficients for cases 1 and 4.
Figure 5-11. Comparison of the turbulence intensity of cases 1-6 at r = 0.4 mm.
Figure 5-12a. The axial velocity contour plots showing the z = 1.6 mm line for case 1.
Figure 5-12b. The axial velocity contour plots showing the z = 1.6 mm line for case 4.
Figure 5-13a. The turbulence intensity profiles for all simulations. The profiles are for z = 1.6 mm.
Figure 5-13b. A comparison at z = 1.6 mm between the turbulence intensity and the axial velocity for case 4.
Figure 5-14. Comparison of $\overline{uw}$ Reynolds stresses of cases 1-6 at r = 0.4 mm.
Figure 5-15. Comparison of turbulence kinetic energy of cases 1-6 at r = 0.4 mm.
Figure 5-16. Comparison of turbulence dissipation rate of cases 1-6 at r = 0.4 mm.
Figure 5-17. Wall shear stress comparison at the polymer edge for cases 2,3,4, and 6.
Figure 5-18. Spreading rate comparison for cases 1-6.

Figure 5-19a. Geometry for an Exxon slot melt blowing die from a cross-sectional view.
Figure 5-19b. The computational domain used in the simulations.
Figure 5-19c. A close up of the area of interest, including the boundary conditions.
Figure 5-20. Centerline velocity at $y = L_c/2$ for different grid resolutions. These simulations all correspond to $V_{jo} = 33.7$ m/s, $m_f = 0.55$ g/min.
Figure 5-21a. The predictions of the rheological model for fiber radii.
Figure 5-21b. The predictions of the rheological model for fiber z-velocity.
Figure 5-22. The location of the maximum air velocity at different z-positions for cases A, D, E and F on the $y = 0$ plane. Also included are the fiber radii for cases D, E and F.
Figure 5-23. Dimensionless velocity for the centerline of case A and at $y = L_c/2$ and $y = 0$ for case D.
Figure 5-24. Contour plots of z-velocity for case D at $z = 1$, 2.5, 5, and 10 mm below the die face.
Figure 5-25a. Dimensionless centerline velocity for all cases at $y = L_c/2$.
Figure 5-25b. Dimensionless centerline velocity for all cases at $y = 0$, $x = x_{max}$. The $R^2 = 0.9835$ for the fit shown on the figure.
Figure 5-26a. Turbulence intensity as a percentage of V_{jo} on the centerline at $y = L_c/2$ for all cases.
Figure 5-26b. Contour plots of turbulence intensity as a percentage of V_{jo} at xy-planes located at $z = 1.2$ mm and $z = 10$ mm for cases A and F.
Figure 5-27. The dimensionless turbulence dissipation rate for all cases on the centerline at $y = L_c/2$.
Figure 5-28. The averaged wall shear stress on the fiber edge for cases B-G.
Figure 5-29a. The excess temperature decay on the centerline at $y = L_c/2$ for all cases.
Figure 5-29b. Contour plot of the excess temperature for case F at $z = 1$ mm and $z = 2.5$ mm.

ABSTRACT

Computational Fluid Dynamics (CFD) was used to study the air flow from different types of melt blowing dies. Specifically, the types of dies studied include Exxon slot dies, Schwarz multihole dies, and swirl dies. For the slot dies, the Reynolds Stress Model with modifications matched the experimentally measured velocity profiles. After the experimental measurements were matched, the RSM was used to study the effect of changing the angle between the air jets and the die face. Simulations were completed for melt blowing dies that have not been tested experimentally. Decreasing this angle changed the centerline velocity profile. For sharp slot dies, the effect of the nose piece placement was also examined. The more inset above the die face the nose piece, the higher the maximum centerline air velocity. However, the centerline turbulence intensity also increased. Non-isothermal simulations were run for all slot die geometries to study the effect of the jet geometry on the temperature profiles. The Schwarz melt blowing die was also examined. The k-ε turbulence model was used to simulate the air flow from this die. The spacing between the annular jets was changed, and the effect of the jet spacing on the centerline velocity, temperature decay, and turbulence was studied. Finally, the isothermal air flow from a swirl melt blowing die was measured experimentally and simulated using CFD.

For a single annular jet and the blunt slot die, a previously developed rheological model was used to predict the fiber diameter, velocity, and temperature. Then, these were used to set boundary conditions in simulations to study the effect of the fiber on the air profiles. Close to the fiber edge, the interactions between the air and fiber are important.

CHAPTER 1: INTRODUCTION

1.1 Melt Blowing

Melt blowing is a process used to convert polymer pellets into long, thin fibers. The goal of melt blowing is that these fibers have a certain diameter, usually between 1-100 μm, and are uniform in size. First, the polymer pellets are melted, and then forced through a small capillary. Then, high-velocity gas streams (usually heated) impinge upon the molten strands of polymer to produce the fine filaments (Shambaugh, 1988). The fibers are attenuated in a matter of microseconds, as they cool. Finally, they are collected on a collection screen, where they form a non-woven mat. The fibers that are produced in this manner are used for filters, insulating materials, geotextiles, medical gowns, and numerous other applications. Figure 1-1 shows a cross section of the melt blowing process when an annular air jet surrounds the polymer capillary (Marla, 2005).

The air flow characteristics are important for the melt blowing process. The air is responsible for creating a strong drag force on the surface of the molten polymer, which is the cause of the fiber attenuation. There are several different jet configurations that have been developed for melt blowing dies that are currently being used industrially. Although the jet geometry is significantly different in the different die designs, they all accomplish the same goal of creating a high drag force on a molten polymer fiber. The types of dies discussed in this work include the common Exxon melt blowing die (composed of two converging planar jets), the multihole Schwarz die (composed of several annular air jets with concentric polymer capillaries), and the swirl die (six round jets surrounding a polymer capillary). Figures 1-2, 1-3, and 1-4 show the Exxon, Schwarz, and swirl melt blowing dies, respectively (Buntin et al., 1974; Schwarz, 1983;

Zieker et al., 1988). Each of these melt blowing die types are discussed in detail in their corresponding chapters.

1.2 Using Computational Fluid Dynamics to Study Melt Blowing

The air flow from melt-blowing nozzles has been studied experimentally. Harpham and Shambaugh (1996, 1997) and Tate and Shambaugh (1998) measured the flow and temperature fields from different slot melt blowing dies. Mohammed and Shambaugh (1993, 1994) experimentally tested the Schwarz die, while Uyttendaele and Shambaugh (1989) as well as Majumdar and Shambaugh (1991) measured the air and temperature field from a single annular jet. In the laboratory, a cylindrical-impact Pitot tube is often used to measure average 1-D velocities at different distances from the die. Other techniques, such as laser Doppler velocimetry (LDV) and hot wire anemometry, can provide one, two, or three components of the velocity field, but these techniques present difficulties in making measurements very close to the die, and seeding is usually required (for LDV). In any case, apart from the difficulty of making measurements for all components of the velocity field and in the region very close to the die, experiments require an intense time commitment, especially when testing alternative equipment designs.

With the development of faster and more powerful computers, Computational Fluid Dynamics (CFD) has emerged as a promising tool in the study of the melt blowing process. The use of CFD can reproduce the air flow field observed in the laboratory in a fraction of the time necessary to design and run experiments. Several commercial packages are available for use; Fluent^{TM} is a finite volume CFD software that is used for this study. One advantage of using CFD to examine melt blowing is the ability to

compare different die designs, while avoiding the cost of building the dies and running experimental tests. In addition, simulations allow for close examination of important areas in the flow field that are difficult to measure experimentally. As mentioned above, with a Pitot tube (or with the other experimental techniques listed) it is difficult to obtain velocity data very close to the die, but simulations have no such restrictions. Furthermore, quantities other than the average velocity in the streamwise direction can be calculated, which is important in the evaluation of new die designs.

Several different computers were used in the computational work presented herein. For the two dimensional simulations, a dual Pentium Xeon PC was adequate. However, as the geometries became three dimensional and much more complex, the use of supercomputing was imperative. Simulations were run remotely on a cluster of Linux dual Pentium 4 Xeon 64 processors. Simulation time varied from a few hours to over a week, depending on the complexity of the computational domain, grid resolution, turbulence modeling, and required convergence criteria.

The steps for completing a simulation of the air flow during the melt blowing process were generally the same, regardless of the jet geometry. First, a computational domain was created, based on the experimental setup. Then, this computational domain was filled with a mesh. The boundary conditions were set, and then the mesh was imported into Fluent^{TM}, and the grid was checked, scaled to the appropriate dimensions, and smoothed if necessary. Next, the turbulence model was specified. The turbulence models will be discussed in detail in following section. After a turbulence model was chosen, the boundary conditions were set. For instance, the mass flow rate of the air through the jet was specified. If the simulation was not isothermal, then the temperature

of the inlet and recirculation air was set. Next, the discretization scheme was chosen. Either first or second order upwind schemes were used in all the simulations discussed in this work. As simulations ran, the residuals of all the equations were calculated and reported. Before beginning each simulation, convergence criteria was determined and specified. The last step before beginning the simulation was initialization. Although initializing did not affect the final solution, choosing a good starting point for the simulation significantly decreased the number of iterations to reach convergence. When all the residuals were less than the given convergence values, the simulation was concluded.

Although using CFD to simulate the air from melt blowing dies is a relatively new field, a short literature review is in order. Chen et al. (2004) used CFD to compare different Exxon slot melt blowing dies. Specifically, the steady flow field was simulated using the non-transient k-ε model. The jet width and jet angle were varied for a limited number of cases and the air profiles from theses different cases were compared. In addition, Mukhopadhyay et al. (2001) used CFD to simulate the time dependent air flow from an Exxon die. Although this work showed the turbulent eddies generated by the two converging jets in the slot die, it reported little quantitative information and did not compare any results to experimental measurements.

1.3 Modeling of Turbulent Jets

The air jets in all simulations discussed in this work have a Reynolds number in the range of 2700 – 7600; this Reynolds number is based on the air speed in the jets and the slot width (Exxon dies), hydraulic diameter (annular jets in multihole Schwarz dies), and air jet diameter (swirl dies). Using computers to simulate turbulent flow presents

challenges. Since turbulent flow has a very large range of scales, some fluctuations may be on the same scale as the flow geometry, while others are several orders of magnitude smaller. Although Direct Numerical Simulations (DNS) have a high level of accuracy, they are computationally expensive for high Reynolds number turbulent flows (Pope, 2000). A computationally cheaper method to simulate turbulent flows is to use the Reynolds-Averaged Navier Stokes (RANS) equations to model the turbulence. In RANS simulations, the velocity field is separated into the average velocity and the fluctuations, and the mean quantities are modeled. For the simulations in this research, the steady (not time dependent) values of the mean flow are modeled and examined. For all the RANS models described in the following sections, the continuity equation as well as the momentum equations are also solved. The RANS continuity and momentum equations are given in equations 1-1 and 1-2, respectively.

$$\frac{\partial \rho}{\partial t} + \frac{\partial}{\partial x_i}\left(\rho U_i\right) = 0 \tag{1-1}$$

$$\begin{aligned} &\frac{\partial}{\partial t}\left(\rho U_i\right) + \frac{\partial}{\partial x_j}\left(\rho U_i U_j\right) = -\frac{\partial p}{\partial x_i} \\ &+ \frac{\partial}{\partial x_j}\left[\mu\left(\frac{\partial U_i}{\partial x_j} + \frac{\partial U_j}{\partial x_i} - \frac{2}{3}\delta_{ij}\frac{\partial U_l}{\partial x_l}\right)\right] + \frac{\partial}{\partial x_j}\left(-\rho\overline{u}_i\overline{u}_j\right) \end{aligned} \tag{1-2}$$

Fluent™ offers the capability of using several different turbulence models. The standard *k*-ε model, the realizable *k*-ε model, and the Reynolds stress model (RSM) are discussed in this research. A great deal of detail about each particular model formulation and implementation can be found in the Fluent™ user's guide (2007). Here, we provide only the basic background information and equations of these models.

1.3.1 The *k*-ε Model

The first model that was tested was the standard *k*-ε model. The standard *k*-ε model is a semiempirical model based on model transport equations for the turbulent kinetic energy, *k*, and the kinetic energy's dissipation rate, ε. The model transport equation for *k* is derived from the exact momentum equation, whereas the model transport equation for ε is obtained using physical reasoning and bears little resemblance to its mathematically exact counterpart (Pope, 2000; Launder, 1972). In the derivation of the *k*-ε model, it is assumed that the flow is fully turbulent and that the effects of molecular viscosity are negligible. The equations that describe the model are as follows (Fluent™, 2007):

$$\frac{\partial}{\partial t}(\rho k)+\frac{\partial}{\partial x_i}(\rho k u_i)=\frac{\partial}{\partial x_i}\left[\left(\mu+\frac{\mu_t}{\sigma_k}\right)\frac{\partial k}{\partial x_i}\right]+G_k-\rho\varepsilon \tag{1-3}$$

and

$$\frac{\partial}{\partial t}(\rho \varepsilon)+\frac{\partial}{\partial x_i}(\rho \varepsilon u_i)=\frac{\partial}{\partial x_i}\left[\left(\mu+\frac{\mu_t}{\sigma_\varepsilon}\right)\frac{\partial \varepsilon}{\partial x_i}\right]+C_{\varepsilon 1}\frac{\varepsilon}{k}G_k-C_{\varepsilon 2}\rho\frac{\varepsilon^2}{k} \tag{1-4}$$

The summation convention is used in the above equations. In these equations, G_k represents the generation of turbulent kinetic energy due to the mean velocity gradients, and G_k is calculated as

$$G_k=-\rho\overline{u_i u_j}\frac{\partial U_j}{\partial x_i} \tag{1-5}$$

$C_{\varepsilon 1}$ and $C_{\varepsilon 2}$ are constants, and σ_k and σ_ε are the turbulent Prandtl numbers for *k* and ε, respectively. The turbulent viscosity μ_t is computed by combining *k* and ε as follows:

$$\mu_t=\rho C_\mu\frac{k^2}{\varepsilon} \tag{1-6}$$

The default values of the constants are $C_{\varepsilon 1}$ = 1.44, $C_{\varepsilon 2}$=1.92, C_μ= 0.09, σ_k = 1.0, and σ_ε = 1.3 (Fluent™, 2007).

It is known that the standard *k*-ε model produces nonphysical results when the rate of strain is rather large. In these cases, the "realizable" *k*-ε model can be used. This model involves a C_μ that varies and a new equation for the calculation of the dissipation rate that is different than the standard *k*-ε model equation (eq. 1-4).

For the realizable *k*-ε model, the equation that describes the turbulent kinetic energy transport is the same as that for the standard *k*-ε model (eq. 1-3). The equation that describes the dissipation rate for the realizable *k*-ε model is

$$\frac{\partial}{\partial t}(\rho\varepsilon)+\frac{\partial}{\partial x_j}(\rho\varepsilon u_j)=\frac{\partial}{\partial x_i}\left[\left(\mu+\frac{\mu_t}{\sigma_\varepsilon}\right)\frac{\partial\varepsilon}{\partial x_i}\right]+\rho C_1 S\varepsilon-\rho C_2\rho\frac{\varepsilon^2}{k+\sqrt{\nu\varepsilon}} \qquad (1\text{-}7)$$

where

$$C_1=\max\left[0.43,\frac{\eta}{\eta+5}\right] \qquad (1\text{-}8)$$

and $\eta = Sk/\varepsilon$ and S is the mean rate of strain tensor ($S=\sqrt{2S_{ij}S_{ji}}$, $S_{ij}=\frac{1}{2}\left(\frac{\partial U_i}{\partial x_j}+\frac{\partial U_j}{\partial x_i}\right)$). This model is also found to resolve the "round-jet anomaly", i.e., it predicts the spreading rate for axisymmetric jets as well as that for planar jets, in contrast to the standard *k*-ε model which fails to predict the spreading rate for an axisymmetric jet (Shih et al., 1995).

The eddy viscosity in the realizable *k*-ε model is predicted with equation 1-6, however C_μ changes as a function of the mean strain and rotation rates, the angular

velocity of the system rotation, and the turbulence fields (k and ε). The default values of the constants of the realizable k-ε model are: $C_{\varepsilon 1} = 1.44$, $C_2 = 1.9$, $\sigma_k = 1.0$, and $\sigma_\varepsilon = 1.2$.

1.3.2 The Reynolds Stress Model

A more sophisticated model for turbulent flow simulations is the Reynolds Stress Model (RSM), which is based on the solution of equations for the individual Reynolds stresses. The individual Reynolds stresses are used to obtain closure of the Reynolds averaged momentum equations. The transport equations for the Reynolds stresses result from the Reynolds averaging of the momentum equation multiplied by a velocity fluctuation, and thus they are exact. These equations have the following form:

$$\frac{\partial}{\partial t}\left(\rho\overline{u_i u_j}\right)+\frac{\partial}{\partial x_k}(\rho U_k \overline{u_i u_j}) = -\frac{\partial}{\partial x_k}\left[\rho\overline{u_i u_j u_k} + \overline{p(\delta_{kj}u_i + \delta_{ik}u_j)}\right]+$$
$$\frac{\partial}{\partial x_k}\left[\mu\frac{\partial}{\partial x_k}(\overline{u_i u_j})\right] - \rho\left(\overline{u_i u_k}\frac{\partial U_j}{\partial x_k}+\overline{u_j u_k}\frac{\partial U_i}{\partial x_k}\right) - G_{ij} + \overline{p\left(\frac{\partial u_i}{\partial x_j}+\frac{\partial u_j}{\partial x_i}\right)} \qquad (1\text{-}9)$$
$$-2\mu\overline{\frac{\partial u_i}{\partial x_k}\frac{\partial u_j}{\partial x_k}}$$

Of these terms, the molecular diffusion term (second term in the RHS of the above equation), the pressure-strain term (fourth term in the RHS of the above equation) and the dissipation term (the fifth term in the above equation) have to be modeled.

The dissipation rate is modeled with an equation that is the same as the dissipation rate equation for the standard k-ε model (eq. 1-4). The suggested values of the constants are $C_{\varepsilon 1} = 1.44$, $C_{\varepsilon 2} = 1.92$, and $\sigma_\varepsilon = 1.0$, as recommended by Fluent™ (2007).

1.3.3 Energy Equation

High temperatures are used during the melt blowing process to melt the polymer pellets. In addition, the die and the air are also heated. For this reason, it is not only important to study the isothermal air flow, but also the temperature field generated by different melt blowing dies. The thermal energy equation must be considered for the nonisothermal examples that were examined. The following equation is the energy equation solved in conjunction with the *k*-ε or RSM model for the case of no heat source due to chemical reactions (Fluent™, 2007):

$$\frac{\partial}{\partial t}(\rho E)+\frac{\partial}{\partial x_i}\left[u_i(\rho E+p)\right]=\frac{\partial}{\partial x_i}\left[\left(k_c+\frac{c_p\,\mu_t}{\mathrm{Pr}_t}\right)\frac{\partial T}{\partial x_i}+u_j\left(\tau_{ij}\right)_{eff}\right] \qquad (1\text{-}10)$$

For compressible, nonisothermal simulations, the parameters used to describe the thermophysical properties of the fluid in CFD are different than the parameters used to simulate the isothermal cases.

For the nonisothermal cases (and cases with higher Mach number), the density of the air was calculated using the ideal gas law. The *k*-ε standard, *k*-ε realizable, and RSM turbulence models do not completely capture compressibility because the fluctuations of density are not included in the constitutive equations. Therefore, throughout this research the assumption is made that the compressibility under the simulation conditions is small enough that it does not significantly affect the flow. For most of the simulations discussed in this dissertation, the Mach number is very low. However, for a few simulations, the Mach number of the simulations is approaching 0.3, which is close to the limit of applicability for the *k*-ε and RSM turbulence models. The thermal compressibility, c_p, and viscosity were calculated using the kinetic theory.

In order to expedite the simulations, the flow field was first allowed to converge for a non-compressible, isothermal case. After the residuals of all the equations reached the specified convergence criteria, if the temperature field was of interest, the energy equation was enabled, and the flow was made compressible. Then, the simulation was run until all the residuals of the equations were lower than the convergence criteria again.

1.4 Computational Domain

Before simulations were begun, an appropriate computational domain was established. Since the geometry of the melt blowing die is known, the computational domain was usually based on this experimental setup. The domain needed to be large enough to encompass all the regions of interest, but small enough to minimize the computational time requirements. The first challenge was to recognize whether the domain could be approximated as two dimensional. Then, the geometry was evaluated to determine if symmetry was present, so that symmetrical boundary conditions could be employed and the computational domain size could be substantially reduced. Similarly, for some cases, using periodic boundary conditions accurately represented the flow of interest, but also reduced the size of the domain. The computational domain was created using the software package Gambit. After the computational domain was established, it was filled with a grid, and the appropriate boundary conditions were set.

1.4.1 Grid Generation

Fluent^{TM} uses a finite volume approximation to find a solution to fluid flow conditions. Therefore, before calculations begin computational domains are divided into small volumes. According to Fluent^{TM}, when the faces (2D) or volumes (3D) are created,

aspect ratios above 5:1 should be avoided (Fluent™, 2007). Highly skewed or stretched cells can compromise the solution as well as reduce the stability of the simulation. In 2D, all cells used were quadrilateral. In 3D, the cells were either hexahedral or tetrahedral.

Tetrahedral cells were useful in areas of the domain where round jets or curved surfaces were present. For each of the grid cells, Fluent™ calculated all the equations for the simulation and reported a residual for each of these equations. Often, in the regions of highest velocity, turbulence, temperature, and interest the grid resolution was made finer to increase accuracy. Then, the computational domain was exported as a mesh, which is a Fluent™ readable file. Each die type required a different grid; the details of these grids will be discussed in the chapters that correspond with each die configuration.

1.4.2 Boundary Conditions

After the computational domain and grid were established, the boundary conditions for the simulation were set. Although the different melt blowing die geometries required different computational domains, the boundary conditions were similar for the different cases. The boundary conditions used in all the simulations in this work include velocity inlet, mass flow inlet, pressure outlet, symmetry, axis, periodic, and walls.

In the melt blowing process, air flows through a single jet or through multiple jets. The flow rate of this air is closely controlled because of the important relationship between the air flow and the fiber dimensions, production rate, and quality. The following two boundary conditions were used to describe the air flow at the top of the jet, where it entered the computational domain:

(a) For simulations where compressibility was negligible (isothermal and low Mach number), the velocity inlet boundary condition was used for the jet. The velocity of the air flow was input into Fluent, and the velocity in the cell neighboring the boundary was computed as follows (Fluent™, 2007):

$$m = \int \rho \vec{v} \cdot d\vec{A} \tag{1-11}$$

where m is the mass flow rate of the air, ρ is the density, $\vec{v}$ is the velocity normal to the surface of the cell, and $d\vec{A}$ is surface area on the side of the cell where the air is entering.

(b) When the conditions are such that the compressibility of the air is not negligible, the mass flow rate boundary condition was used. Instead of defining the velocity, the mass flow rate of the air is set. When the mass flow rate is input into Fluent™, the program converts it into a uniform mass flux by dividing it by the total inlet area (Fluent™, 2007).

The bottom and the side of the computational domain were designated as pressure outlets. Physically, they represent the boundary between the area under the melt blowing die being simulated, and the room where the melt blowing die is used. Since melt blowing is performed in a room that is at ambient conditions, the gauge pressure of the pressure outlet boundaries was set at 0 Pa. Pressure outlets are appropriate boundary conditions because they allow for recirculation and entrainment of air characterized by turbulent jets (Fluent™, 2007; Pope, 2000).

Using symmetry as a boundary condition can reduce the size of the computational domain, which also reduces the computational time required to finish the simulation. This boundary condition can be used when the flow is expected to have mirror symmetry

along a line (2D) or a plane (3D). Similarly, when a computational domain is axisymmetric the simulation is designated as axisymmetric along the axis of symmetry.

Periodic boundary conditions can be used when the melt blowing die consists of repeated, similar geometric patterns. Since the simulations were often compared to experiments where the end effects were not measured, the periodic boundary condition was used to study the air flow near the center of melt blowing dies. In 2D simulations of air from a melt blowing die, periodicity is not applicable, so this boundary was only specified in 3D simulations. For the periodic boundary condition to be used, the grid must be exactly the same on the two periodic boundaries.

The wall boundary condition is used for the die face, and the simulations when a polymer fiber was included. The wall boundary condition uses the no-slip assumption. The shear stress and heat transfer between a wall and the fluid are dependent on the simulated flow conditions (Fluent^{TM}, 2007). For most simulations discussed in this work, the effect of the walls on the simulation results were not of great interest. However, when a moving polymer fiber is included in the simulations, these interactions are more important. In these cases, the Enhanced Wall Functions option was used for the boundary condition. In high Reynolds number flows, when the k-ε and RSM models are used, the boundary layer is usually not resolved (Fluent^{TM}, 2007). Since the boundary layer is not an area of high interest, the simulations discussed in this work did not have grids where the boundary layer was resolved. For standard wall conditions, the log law is used to predict the change in momentum due to the wall (Pope, 2000; Fluent^{TM}, 2007). For the k-ε and RSM turbulence models, the boundary condition for the turbulent kinetic energy, k, equation is as follows (Fluent^{TM}, 2007):

$$\frac{\partial k}{\partial n} = 0 \tag{1-12}$$

where n is the direction normal to the wall boundary. The production of k, G_k, and the dissipation of k, ε, are assumed to be equal at the cells next to the wall boundary. This assumption is called the local equilibrium hypothesis (Fluent™, 2007).

The Enhanced Wall Functions were used for wall boundary conditions for the limited cases where the effect of the wall on the flow field is expected to be significant. These cases include all the fiber inclusive simulations. The Enhanced Wall Functions blend a laminar, which changes linearly, near wall flow with the turbulent log law flow (Fluent™, 2007). The ratio of combination of the laminar and turbulent flow laws are determined by distance from the wall.

1.5 Motivation

Melt blown fibers are becoming ever increasingly used in every walk of life. Producing these fibers requires large amounts of energy. However, it has been shown that only a small amount of the air flow actually is used to attenuate the fiber (Shambaugh, 1988). Although a great deal of experimental work has been completed to increase understanding of the melt blowing process, CFD is a powerful new tool being utilized by researchers in this field.

There are four main objectives associated with this research. They are as follows:

1. Use CFD to accurately reproduce the experimentally measured velocity and temperature fields of air from plane and annular jets associated with melt blowing dies. This includes a rigorous examination of grid characteristics, convergence criteria, and turbulence model parameters.

2. Use the conditions that successfully reproduced experimental data to simulate melt blowing dies that have not been tested experimentally. Compare the velocity and temperature fields of the different dies to more fully understand the effects of die geometry on the melt blowing process.

3. Investigate complex multiple jet flow fields and jet-fiber interactions.

4. Use the simulation results to make predictive correlations about flow field.

The air and fiber velocity are of great interest in melt blowing. In this flow, the vast majority of the velocity is in the *z*-direction, which is also the most important component because it is responsible for the attenuating drag force. Throughout this work, if the component of the velocity is not specified, then the velocity being discussed is the *z*-velocity.

1.6 Nomenclature

C_1	parameter for the *k*-ε model
C_2	parameter for the *k*-ε realizable model
$C_{\varepsilon 1}$	parameter for the *k*-ε model
$C_{\varepsilon 2}$	parameter for the *k*-ε model
C_μ	parameter for the *k*-ε model
E	energy, J
$d\vec{A}$	cross-sectional area of cell
G_k	production of turbulent kinetic energy
k	turbulent kinetic energy ($1/2 u_i u_i$)
k_c	thermal conductivity, J/(m·s·K)

m	mass flow rate, kg/s
n	direction normal to cell boundary
p	pressure (Pa)
Pr_t	turbulent Prandtl number
t	time
T	Temperature, K
u_i	velocity fluctuation in the ith direction
U_i	mean velocity in the ith direction
$\vec{v}$	velocity normal to cell face, m/s
x, y, z	spatial coordinates

Greek Characters

δ_{ij}	Kroeneker delta
ε	dissipation rate of turbulent kinetic energy, m^2/s^3
η	parameter for the realizable k-ε model
μ	viscosity, kg/(m·s)
μ_t	turbulent viscosity, kg/(m·s)
ν	kinematic viscosity m^2/s
ρ	density, kg/m^3
σ_k	turbulent Prandtl number for kinetic energy
σ_ε	turbulent Prandtl number for dissipation
$(\tau_{ij})_{\text{eff}}$	i,jth component of the effective deviatoric stress tensor, Pa

1.7 References

Buntin, R. R.; Keller, J. P.; Harding, J. W.; Nonwoven Mats by Melt Blowing. U.S. Patent 3,849,241, Nov. 19, 1974.

Chen, T.; Xinhou, W.; Huang, X. Modeling Air-Jet Flow Field of a Dual Slot Die in the Melt Blowing Nonwoven Process, *Textile Res. J.*, **2004**, *74*(11), 1018-1024.

Fluent User's Guide; Fluent Inc.: Lebanon, NH, 2007.

Harpham, A. S.; Shambaugh, R. L Flow Field of Practical Dual Rectangular Jets. *Ind. Eng. Chem. Res.* **1996**, *35*, 3776-3781.

Harpham, A.S.; Shambaugh, R.L Velocity and Temperature Fields of Dual Rectangular Jets. *Ind. Eng. Chem. Res.*, **1997**, *36*, 3937-3943.

Launder, B. E.; Spalding, D. B. *Lectures in Mathematical Models of Turbulence*; Academic Press: London, England, 1972.

Majumdar, B.; Shambaugh, R. L. Velocity and Temperature Fields of Annular Jets. *Ind. Eng. Chem. Res.* **1991**, *30*, 1300-1306.

Marla, V. T. Anaylsis of the Formation of Solid and Hollow Fibers in the Melt Blowing Process: Experiments and Modeling. Ph.D. Thesis, University of Oklahoma, Norman, OK, 2005.

Mohammed, A.; Shambaugh, R. L. Three-Dimensional Flow Field of a Rectangular Array of Practical Air Jets. *Ind. Eng. Chem. Res.* **1993**, *32*, 976-980.

Moore, E.M., Shambaugh, R.L., Papavassiliou, D.V. Analysis of Isothermal Annular Jets: Comparison of Computational Fluid Dynamics and Experimental Data, *Journal of Applied Polymer Science*, **2004**, *94*, 909-922.

Mukhopadhyay, A.; Prasad, R.O.S.; Grald, J.; Sun, J. Performance Analysis of Melt-Blown Dies Using Computational Fluid Dynamics, International Nonwovens Technology Conference, September 5-7, 2001, Baltimore, MA.

Pope, S. B. *Turbulent Flows*; Cambridge University Press: Cambridge, U.K., 2000; pp 134-135.

Shambaugh, R. L. A Macroscopic View of the Melt Blowing Process for Producing Microfibers. *Ind. Eng. Chem. Res.* **1988**, *27*(12), 2363-2372.

Schwarz, E. C. A. Apparatus and Process for Melt-Blowing a Fiberforming Thermoplastic Polymer and Product Produced Thereby. U.S. Patent 4,380,570, 1983.

Shih, T.-H.; Liou, W. W.; Shabbir, A.; Zhu, J. A New k-ε Eddy-Viscosity Model for High Reynolds Number Turbulent Flows Model Development and Validation. *Comput. Fluids* **1995**, *24* (3), 227-238.

Tate, B. D.; Shambaugh, R. L. Modified Dual Rectangular Jets for Fiber Production. *Ind. Eng. Chem. Res.* **1998**, *37*, 3772-3779.

Uyttendaele, M. A.; Shambaugh, R. L. The Flow Field of Annular Jets at Moderate Reynolds Numbers. *Ind. Eng. Chem. Res.* **1989**, *28*, 1735.

Zieker, R. A.; Boger, B. B.; Smyrna, L. Adhesive Spray Gun and Nozzle Attachment. U.S. Patent 4,785,966, November 22, 1988.

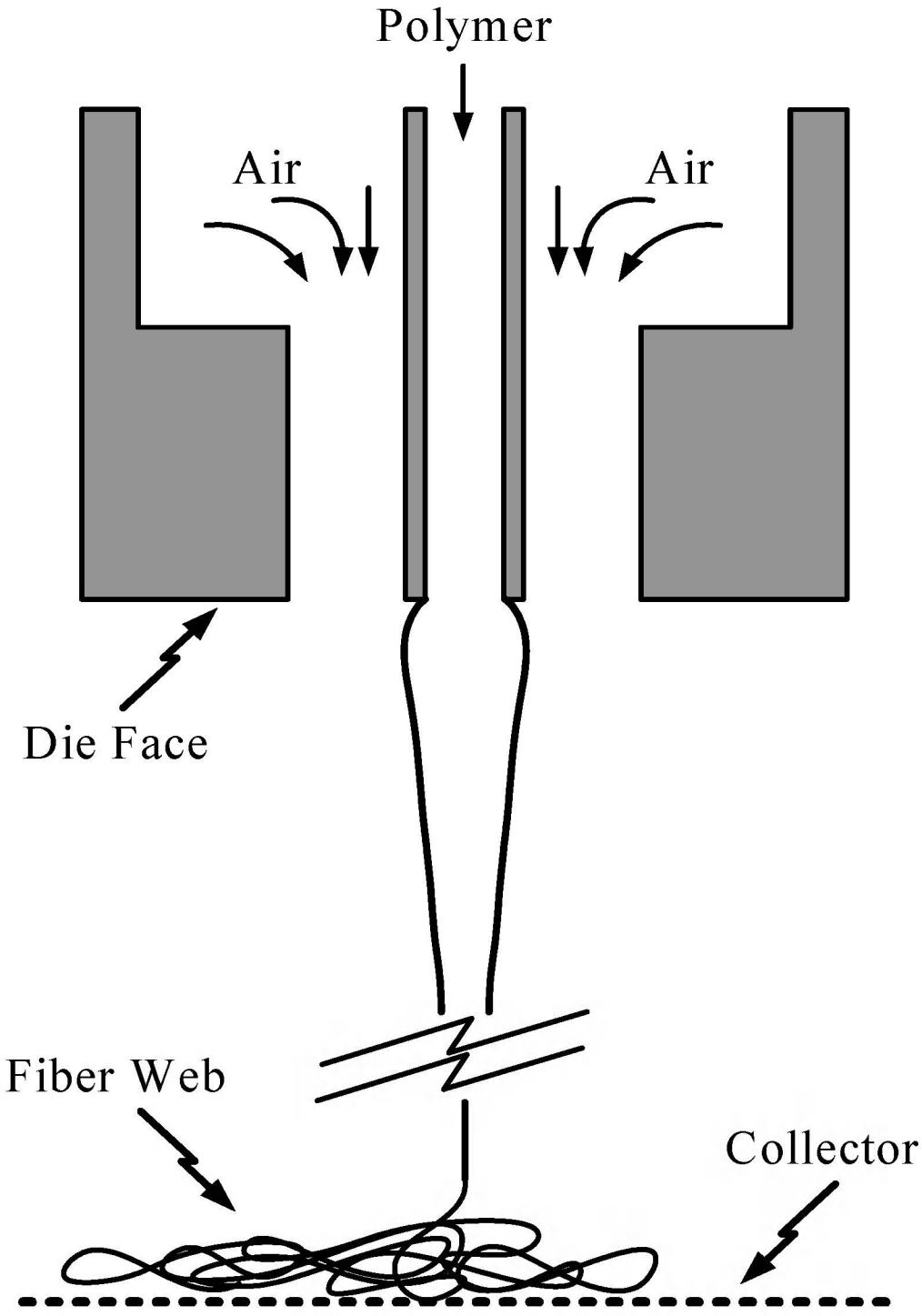

Figure 1-1. Cross Section of Melt Blowing Process Using an Annular Air Jet (Marla, 2005)

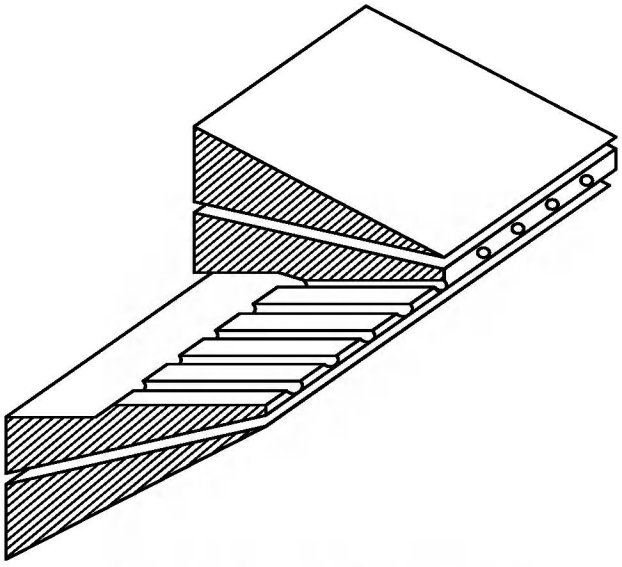

Figure 1-2. Exxon slot melt blowing die with partial cutout

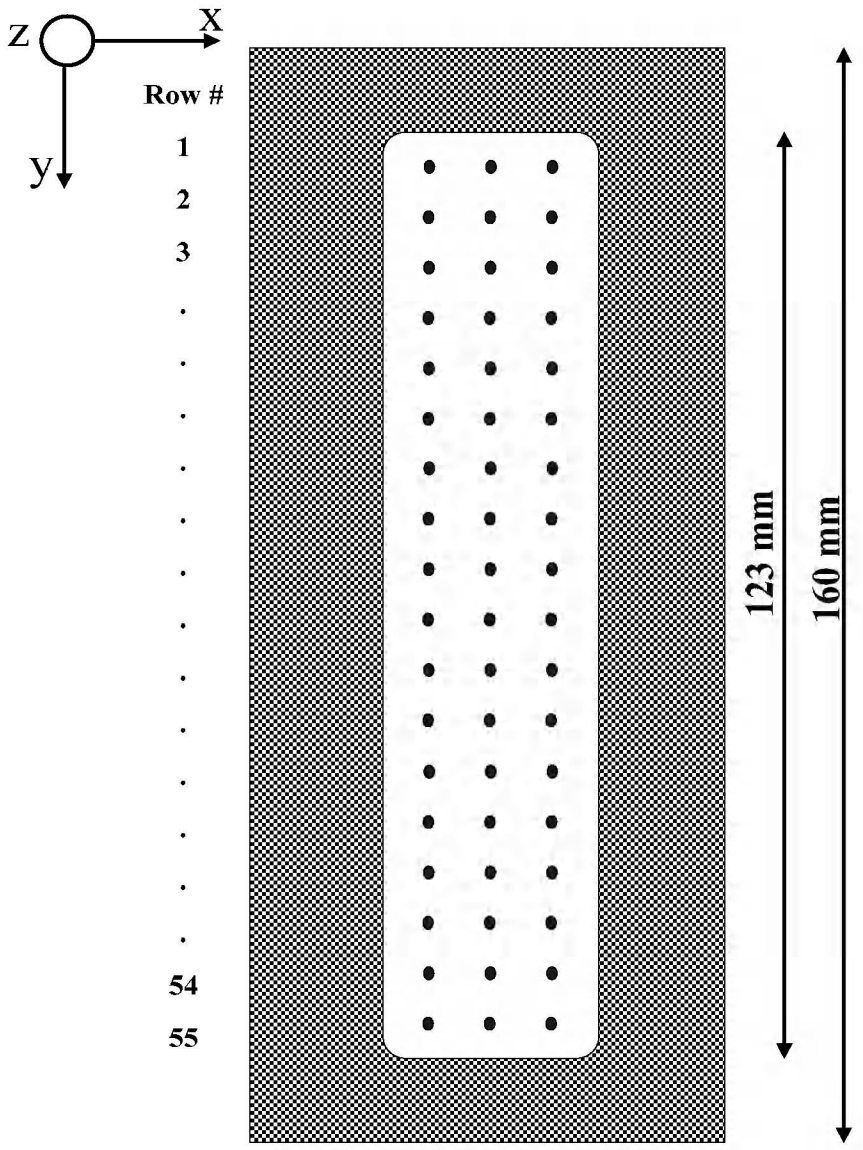

Figure 1-3. Bottom view of a Schwarz multihole die

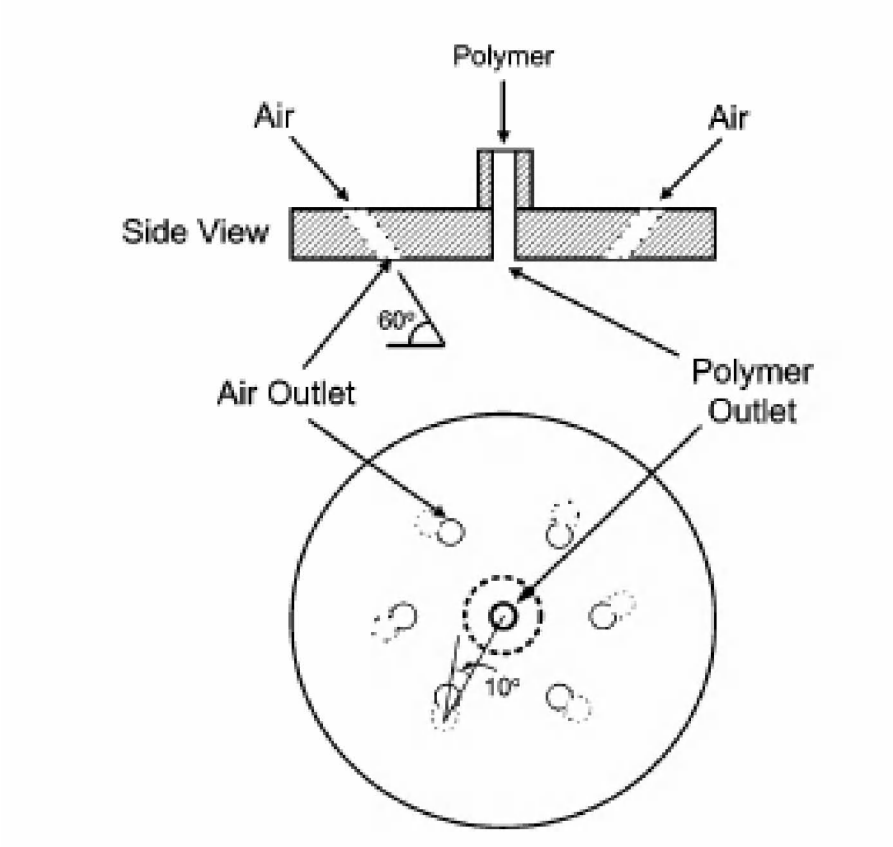

Figure 1-4. Swirl melt blowing die

CHAPTER 2: SLOT MELT BLOWING DIES

Contents of this chapter have been reproduced from the following sources:

Krutka, H. M.; Shambaugh, R. L.; Papavassiliou, D. V. Analysis of a Melt-Blowing Die: Comparison of CFD and Experiment. *Ind. Eng. Chem. Res.* **2002**, *41*(20), 5125-5138. Copyright 2002 Am. Chem. Soc.

Krutka, H. M.; Shambaugh, R. L.; Papavassiliou, D. V. Effects of die geometry on the flow field of the melt blowing process, *Ind. Eng. Chem. Res.*, **2003**, *42*(22), 5541-5553. Copyright 2003 Am. Chem. Soc.

Krutka, H. M.; Shambaugh, R. L.; Papavassiliou, D. V. Effects of Temperature and Geometry on the Flow Field of the Melt Blowing Process, *Ind. Eng. Chem. Res.*, **2004**, *43*(15), 4199-4210. Copyright 2004 Am. Chem. Soc.

Krutka, H. M.; Shambaugh, R. L.; Papavassiliou, D. V. Using Computational Fluid Dynamics To Simulate Flow Fields from Various Melt Blowing Dies, *International Nonwovens Journal*, **2005**, *14*(1), 2-8. Copyright 2005 Am. Chem. Soc.

2.1 Introduction to Slot Dies

The origin of melt blowing can be traced back to filter work completed by Wente at the Naval Research Laboratory in the mid-twentieth century (1954, 1956). The goal of this research was to create fibers with a diameter on the order of 5 μm. Exxon began its own research, based on the findings of Wente, in the 1960s (Shambaugh, 1988). Researchers at Exxon developed a melt blowing die that was able to increase production rates over the die designed by Wente. This new die used two planar air jets to create high drag forces on a molten polymer stream (Buntin et al., 1974). Figure 2-1 illustrates a typical Exxon slot melt blowing die with a partial cutout. The round tubes seen in the cutout are the polymer capillaries, through which molten polymer is forced by an extruder. The two slot jets are set at an angle so that the air streams are converging. These air streams are used to create a strong attenuating force on the surface of the fiber. Although this was the initial design of the Exxon slot melt blowing die, several variations

have been made to this geometry, and the most prominent of these geometries will be described in detail in the following sections. The Exxon slot design is the most commonly used configuration by melt blown product manufacturers (Shambaugh, 1988).

2.1.1 Planar Jet Literature Review

Due to their importance in numerous applications, planar jets have been researched in depth. Statistically planar, or rectangular, jets are two dimensional. One characteristic of planar jets that has been documented is their self similar structure that has been recorded beyond 30 slot widths away from the jet (Bradbury, 1965). For self similarity, the velocity should be nondimensionalized using the inlet jet velocity, V_{jo}, and position must be nondimensionalized using $x_{1/2}$, which is the distance from the centerline where the velocity is equal to half of the centerline velocity (Pope, 2000). The concept of self similarity allows for the velocity profiles to be predicted. For instance, the centerline decay is related to $z^{-1/2}$, where z is the flow direction. Both Bradbury (1965) and Heskestad (1965) used hot wire anemometry to measure the velocity and turbulence profiles from a turbulent planar jet. Planar jets have been measured to have a constant spreading rate. The position of $x_{1/2}$ is related to the distance from the jet using the following equation (Pope, 2000):

$$\frac{dx_{1/2}}{dz} = S \tag{2-1}$$

The spreading rate constant, S, has a value of 0.1.

Although the mean profiles of turbulent jets are predictable in the self similar region, turbulence is random by nature. Grinstein (2001) used CFD, specifically Large Eddy Simulations (LES), to examine the vortex structures present in the turbulent flow

field generated by rectangular jets. Further work quantified the error involved in using LES to study the turbulent eddies from a planar jet (Ribault et al., 1999). Later, the same group tested the ability of LES to simulate the passive scalar development from a planar jet (Ribault et al., 2001). Most of these studies were focused on the flow properties far from the jet, but Stanley et al.(2000) used DNS to examine the effect of the velocity profile in the jet on the flow patterns further downstream. It was determined that the effect of higher turbulence in the jet does affect the flow field close to the jet, but has negligible impact in the self similar region.

Findings reported above have been directed toward single planar jets, while slot melt blowing dies use dual converging jets. Multiple planar jets have many other applications, and therefore, much research has been completed in the effort to more fully understand the interactions between such jets. Hot wire anemometry has been used to measure the mean velocity from multiple planar jets. Although these jets are initially discrete, at further distances away from the jet outlets, the maxima merge together until the profiles of the individual jets are indistinguishable (Krothapalli et al., 1980). When the flow field of two non-equal planar jets is measured, the axis of the initially weaker jet is pulled towards the stronger jet (Elbanna and Sabbaggh, 1987).

Lai et al. (1998) used three different turbulence models, including the k-ε and RSM, to simulate the flow profiles generated by two parallel jets. The effect of the domain size, grid refinement, and discretization schemes were all examined. A recirculation area was predicted qualitatively. When compared with experiments, RSM and k-ε turbulence models were able to accurately predict the merging and combined points of parallel jets, but underpredicted the jet spreading rate (Anderson and Spall,

2001). In the near field of to two parallel jets, an analytical solution was developed to predict the flow, although it does not perform well in the self similar region (Wang et al., 2001).

Both experimental and computational research has been completed for alternative setups for planar jets. For instance, the k-ε model was used to simulate a turbulent planar jet in a cross flow; the simulation results agreed well with experiments (Kalita et al., 2002). Dejoan et al. (2005) used LES to simulate a turbulent plane wall jet; good agreement with experiments was obtained the self similar region. Impinging slot jets were studied both experimentally (Narayanan et al., 2004) and computationally (Voke et al., 1995).

Through an extensive literature review, much evidence has been presented concerning the ability of CFD to accurately simulate plane jets in several different configurations. The goal of the present work is to apply this ability to study the air flow fields generated by Exxon slot melt blowing dies; which offers significant time and financial savings, as well as offers unique insights when compared to experimental techniques.

2.1.2 Slot Die Geometries

Figure 2-1 shows a typical Exxon slot die with a cutout so that the polymer capillaries are visible. Because the slot length of the actual die might be 1 m or more, the die is effectively "infinite" in length, and the die can be modeled as a 2-D jet. This 2-D approximation was used by Harpham and Shambaugh (1996) and Tate and Shambaugh (1997) (henceforth in this chapter, these contributions will be referred to as HS and TS,

respectively). These researchers took velocity measurements in a plane that bisected the center of their experimental dies (end effects were negligible in this center plane).

Figure 2-2 shows a cross section of the type of die used by HS. This die is referred to as a blunt die, because the nose piece has a flat section. Figure 2-3 is a bottom view of this die. TS experimented with both a blunt-type die and a sharp die (see Figure 2-4), which has no flat section on the nose piece. In the simulations discussed in this work, the same die configurations were used for computational studies as were tested experimentally by HS and TS. This choice facilitated direct comparisons of the simulation results with the experimental measurements of HS and TS.

For the simulation, as with the HS and TS experiments, the slot widths of the die were set equal at b = 0.65 mm, and each slot had a length l = 74.6 mm. The distance between the outer edges of the slots was h = 3.32 mm for the blunt die (Figure 2-2) and h = 1.3 mm for the sharp die (Figure 2-4). The coordinate system for the experiments and the simulations is also shown in Figures 2-2, 2-3, and 2-4. The origin of the system is at the center of the face of the die. The y direction is along the axes of the nose piece and the slots, the x direction is transverse to the major axis of the slots, and the z direction is the direction of the flow under the die. The aspect ratio l/b is 114.77, which is much larger than the aspect ratio of 50 recommended for statistically two-dimensional plane jets that are free of end effects at the center of the nozzle, on the $y = 0$ plane (Pope, 2000). Figure 2-4 shows the configuration for the flush sharp-die experiments, which were executed with the same nozzle dimensions as for the blunt die (except that $f = 0$). The sharp die in Figure 2-4 is flush because the nose piece (where the two jets meet) is at the die face ($z = 0$).

Several variations of the sharp die are used in industrial melt-blowing. The *inset die* is characterized by a nose piece that is recessed above the die face. Figure 2-5 shows the geometry of a standard inset die. Observe that, unlike the situation with the sharp flush die (Fig. 2-4), in the inset die the slot face width b_o is not equal to the distance b (which equals h/2). The *outset die* is another modification of the sharp die. The outset die consists of a nose piece that extends below the die face; see Figure 2-6.

One of the objectives of this research was to simulate the air flow from melt blowing die configurations that had not been tested experimentally. For both the blunt and flush sharp slot dies, the angle between the jet and the die face, θ, was changed. The jet angles simulated were 45°, 50°, 60°, and 70°. Table 2-1 lists the simulations completed for the flush blunt and sharp dies. For both the inset and the outset sharp dies, the jet angle θ was kept constant at 60° while the nose piece placement, a, was varied. Table 2-2 lists the inset and outset sharp die simulations completed. The effect of all these geometrical alterations will be explored in later sections.

2.1.3 Computational Domain

The computational domain was based upon the experimental setup of HS and TS in order to reproduce the laboratory results. Therefore, computational domains based on Figures 2-2, 2-4, 2-5, and 2-6 were used. The presence of the polymer and the polymer capillary were neglected, as was the case in the HS study. Symmetry considerations led to the reduction of the size of the computational domain. The experiments provided the average mean z-velocity profile at stationary state. In this framework, the velocity field is symmetric about the $x = 0$ plane, and the simulation was completed in 2D in the zx plane. Since this allows the size of the computational domain to be cut in half, the computation

time is reduced by a factor of two. Figure 2-7a presents the computational domain used in the simulations. A closer view of the inlet jet is given in Figure 2-7b, with the grid included. The dimensions of the computational domain are L_z =100 mm (not including the height of the jet) and L_x = 30 mm. For the case shown in Figure 2-7a, the angle between the jet and the top wall is 60°, and the jet has a height of 5 mm. The difference between the computational domain for the blunt and sharp dies is only related to the jet configuration.

2.1.4 Grid for Blunt Dies and Sharp Flush Dies

After the computational domain size was designated, the grid was generated. Due to the rectangular shape of the computational domain, it was convenient to use a structured grid with quadrilateral cells. The basic grid was created in Gambit™. Then the grid resolution was increased in the area of most interest using Fluent™. The area of most interest is the region where the convergence of the two air streams occurs. Therefore, the grid resolution has been increased starting at the line of symmetry to 4 mm in the *x*-direction, and from the bottom of the die down to 30 mm in the *z*-direction through the computational domain, including the jet. A close view of the increased grid resolution can be seen in Figure 2-7b. The effects of changing grid resolution were examined by running numerical experiments at three mesh sizes. Runs were made with meshes containing 200,348 cells, 235,994 cells, and 271,994 cells. The mesh for the lowest-resolution run was created in Gambit. This mesh was not refined in the region close to the inlet jet. Each cell was 122.5 μm by 122.5 μm. This Gambit mesh had a total of 200,348 quadrilateral cells. The test with the highest resolution utilized a region of refined resolution similar to that seen in Figure 2-7b. For this case, the width of the

refined region was increased to 60 mm below the die face. The velocity decay along the line of symmetry for these meshes is presented in Figure 2-8. For all the blunt die and flush sharp dies simulations, the number of grid cells and computational time for convergence are given in Table 2-1.

2.1.4 Grid for Inset and Outset Sharp Dies

For the sharp die cases with inset or outset geometries, the grid resolution of the flush dies was improved upon. Four regions of grid refinement were adopted in order to reduce computational time relative to the flush runs that utilized only two grid refinement regions. For the inset and outset cases, the inner most region the length of the sides of the quadrilateral cells was 0.05 mm. Outside this region, there was a second section where the grid resolution was larger and the length of the sides of the quadrilateral cells was 0.1 mm. The next (third) level of grid resolution was in the area farther from the line of symmetry; this level consisted of quadrilateral cells with sides of 0.2 mm. Finally, in the fourth section of the computational domain (farthest from the die), the length of the sides of the cells was 0.4 mm. Figure 2-9 shows the four different regions of grid refinement and the regions' dimensions. Figure 2-10 compares the turbulence intensity and the mean velocity decay results for a die with a recess of a = -0.325 mm for different grid resolutions. The grid resolution designated as fine is the one used by for the flush dies. The two simulations show excellent agreement. Therefore, the coarse grid was used for our subsequent calculations in order to minimize computational effort. (An even coarser grid was tested, but was not used because the simulated results did not match the results shown in Fig. 2-10.) The total number of cells in the coarse computational domains for the different inset and outset dies was approximately 113,000, which reduced the number

of grid cells to less than half of those used in for the blunt and sharp flush dies. The exact number of quadrilateral cells, the necessary number of iterations to reach convergence, and the required CPU time for the inset and outset simulations are given in Table 2-2.

2.2 Isothermal CFD Results

Although the literature review showed the ability of CFD to accurately model several different turbulent jet configurations, the exact jet geometry present in melt blowing has not been previously compared to experiments. Since one of the objectives of this research is to simulate the air flow field from melt blowing dies that have not been measured experimentally, it is important to ensure that the simulations successfully predict the flow field. Therefore, the available experimental measurements have been compared to the simulation results. In agreement with the experiments, it was found that the flow field exhibits the following three zones of development for the blunt dies: (a) a region in which the flow field from each jet is not strongly affected by the other jet, (b) the merging region, where the two jets are merging into one, and (c) the self-similar region, where the flow field is similar to that resulting from a single jet. For the sharp dies, only the last two regions were observed. More quantitative comparisons between experiments and simulations are discussed in the subsequent sections.

2.2.1 Comparison to Experiments for Flush Blunt and Sharp Dies

The air flow rate, at standard conditions of 21 °C and 1 atm pressure, was 1.67×10^{-3} m^3/s. For the dimensions described above, a 60° slot produces a calculated average (nominal) discharge velocity of V_{jo} = 17.3 m/s. The corresponding Reynolds number, based on the slot width, is Re = 3800. Because HS and TS also conducted

experiments with air flow rates twice as high (V_{jo} = 34.6 m/s, Re = 7600), corresponding simulations were also conduced with this higher flow rate.

A single-plane jet is statistically two-dimensional. The plane $x = 0$ has statistical symmetry; this symmetry can be utilized in a numerical simulation by implementing a two-dimensional model. It has been found experimentally and computationally that the mean velocity and the Reynolds stresses for a plane jet become self-similar beyond z/b = 40 (see section 2.1.1). For this self-similar determination, the velocities and Reynolds stresses are scaled with the mean centerline velocity in the z direction, V_o [$V_o = V(0,0,z)$], and with the distance from the centerline at which the mean velocity is half of its maximum, $x_{1/2}$ [defined as the point at which $1/2V_o = V(x_{1/2},0,z)$]. Experimental studies of the problem of two converging similar-plane jets at 60° by HS have shown that the flow field downstream from the die nozzle becomes self-similar when $z/h > 1.7$ (using V_o and $x_{1/2}$ for the velocity and length scale, respectively). Similar results have been obtained for the 60° and 70° sharp jets by TS.

Simulations with different turbulence models were completed and were compared to experimental measurements in order to determine the most appropriate model for the case of two converging jets. When the default values for the turbulence model constants were used, the simulation results agreed qualitatively with the experimental results, but not quantitatively. Figure 2-11 shows the centerline velocity decay for the case of a 70° sharp die configuration compared to the experimental measurements of TS. The velocity decay for a two-dimensional jet can be described by the relation,

$$V_o = c_1 V_{jo} z^{-1/2} \qquad (2\text{-}2)$$

where c_1 is an empirical constant. The above equation should also hold for the dual-jet velocity field at intermediate to long distances away from the die surface. For a 70° sharp slot die, TS experimentally determined the following correlation:

$$V_o = 3.09 * V_{jo} z^{-0.635} \qquad (2\text{-}3)$$

The first observation about Figure 2-11 is that the use of a third-order discretization scheme (QUICK) does not improve the simulation results compared to a second order scheme. All three models demonstrate an exponential decay that is close to the theoretically expected value of 1/2 (as in eq 2-1). Regression gives the following exponents: RSM, -0.5931; standard k-ε, -0.4984; realizable k-ε, -0.5073. The corresponding c_1 values are, respectively, 3.8967, 2.8427, and 3.1257. Although the RSM exponent is farthest from the theoretical value, the RSM exponent is closest to the exponent in the experimentally determined correlation (-0.635). However, TS found that $c_1 = 3.09$, a value that is closer to the c_1 values for the other two models.

For the case of the blunt die data, both the standard k-ε model and the realizable k-ε model proved to be inaccurate. After further testing, the RSM was able to reproduce the blunt-die system with the most success. To achieve quantitative as well as qualitative agreement with the experimental measurements, the values of the constants associated with the dissipation equation had to be changed to $C_{\varepsilon 1} = 1.24$ and $C_{\varepsilon 2} = 2.05$. This change of constants also improved the fit of the simulation for the sharp dies. Figure 2-12a shows simulation and experimental results for the 60° blunt die for two values of V_{jo}. Figure 2-12b shows similar results for 60° and 70° sharp dies (compare with Figure 2-11). Figure 2-12a shows the velocity decay along the line of symmetry. The figure presents the simulation results for the RSM model with $C_{\varepsilon 1} = 1.24$ and $C_{\varepsilon 2} = 2.05$ for both

V_{jo} = 17.3 m/s (low velocity) and V_{jo} = 34.6 m/s (high velocity). Figure 2-12a also shows the experimental data for the 60° blunt die. The experiments of HS suggested that the velocity decay away from the die surface can be described by the equation

$$V_o/V_{jo} = 1.4(z/h)^{-0.61} \qquad (2\text{-}4)$$

which is similar to equation 2-1. Equation 2-3 is also shown in Figure 2-12a. Figure 2-12b presents the simulation results, using the same conditions as stated above, for the 70° sharp die and the 60° sharp die; the experimental results of TS; and the best-fit equation suggested by TS for the case of the 70° sharp die. For both Figures 2-12a and 12b, there is excellent agreement between the laboratory data, the best-fit equations, and the CFD results.

The method for selecting the best values $C_{\varepsilon 1}$ = 1.24 and $C_{\varepsilon 2}$ = 2.05 is essentially a calibration procedure that can be assisted by general considerations regarding the physical meaning of the model parameters. For example, the simulations in Figure 2-11 have lower mean velocities than the experiments close to the die face. To reduce the dissipation of the turbulent kinetic energy, and thus increase the mean velocity, the second term on the RHS of equation 1-4 (i.e., $C_{\varepsilon 1}\varepsilon/kG_k$) has to become smaller and the third term on the RHS of equation 1-4 has to become larger (in absolute value). Therefore, $C_{\varepsilon 1}$ has to decrease from the default value, and $C_{\varepsilon 2}$ has to increase from the default value. As a result, the mean velocity becomes higher close to the die face, and the mean velocity slope downstream from the maximum also becomes higher. In this way, G_k increases downstream from the maximum, indicating that turbulent kinetic energy production is higher downstream from the maximum mean velocity, which, in turn,

results in a decrease of the mean velocity away of the die face relative to the mean velocity when the default parameter values are used.

During the initial iterations of the simulation, when the solution was very far from the converged solution, a first-order discretization scheme was used. After the residual converged to order 10^{-3}, the discretization was changed to a second-order upwind scheme. The motive behind this change is that the first-order scheme is faster and can be used early in the simulation. However, the second-order upwind discretization scheme is more accurate. Therefore, as the simulation nears the final solution, the second-order scheme must be used, although it requires more computational time. Finally, it was determined that the convergence criterion for successful description of the flow field of the dual rectangular jets is to obtain residuals that are less than 10^{-5}.

Equations 2-1, 2-2, and 2-3 agree on the form of the decay of the centerline velocity for dual rectangular jets. For several different cases, CFD and experimental values of c_1 and the exponent are compared in Table 2-3. Using the altered turbulence model parameters, good agreement is achieved between CFD and experiments.

2.2.2 Blunt Die Results for Positions Close to the Die Face

The velocity flow field at distances close to the die is compared to the laboratory data in Figure 2-13a and 2-13b for the cases of a 60° blunt die and a 70° sharp die, respectively. The agreement between the data and the CFD results is qualitatively very good. The experiments show that, within the first zone of the flow-field development, the two jets are closer together (i.e., merge more rapidly) than what the simulation predicts. The experiments demonstrated that convergence is completed by $z \approx 5$ mm below the die, and the CFD simulations agreed with this result. Another point to note is

that, at very low z values, there is a difference between the simulation and the laboratory data regarding the minimum velocity at the line of symmetry for the blunt die. This difference might be attributed to the experimental difficulty of measuring the air flow with the Pitot tube very close to the die surface. Furthermore, as discussed below, the velocity field very close to the die surface exhibits an area of flow recirculation that results in negative velocities in the z direction. This recirculation occurs over a distance scale that is too small for the Pitot tube to measure properly.

Figure 2-14 shows the flow field at large distances (z = 10 - 50 mm) below the die face. The flow field becomes self-similar at medium to large distances downstream from the die face, when the velocity is made dimensionless with V_o and the length is made dimensionless with $x_{1/2}$. Figure 2-14 presents the CFD results for the 60° blunt die. The figure also shows the following empirical equation used by HS:

$$V/V_o = \exp\left[-0.6749\left(x/x_{1/2}\right)^2\left(1+0.027\left(x/x_{1/2}\right)^4\right)\right] \qquad (2\text{-}5)$$

This equation is based on a form developed by Bradbury (1965). A simpler equation that was also used by HS is

$$V/V_o = \exp\left[-0.693\left(x/x_{1/2}\right)^2\right] \qquad (2\text{-}6)$$

This simpler form has also been used in other cases, such as slot jets (Rajaratnam, 1976) single-hole jets (Obot et al.,, 1984; Obot et al., 1986), annular jets (Uyttendaele, 1989; Majumadar, 1991) and multihole jet arrays (Mohammed, 1993). This simpler equation is also shown in Figure 2-14. The CFD data show very good agreement with equations 2-5 and 2-6 (and, hence, with the experimental data) and demonstrate the self-similarity of the flow field.

Figure 2-15 displays contours of a velocity field below a 60° blunt die. These contours result from the simulation using the RSM model and the best parameters and procedures described above. Figure 2-15a shows the velocity field over large distances from the air slots of the die. As expected, at large distances (both large x and large z) the velocity becomes very small. Figure 2-15b shows the velocity field closer to the air slots. Figure 2-16 shows the velocity vector field, with velocity arrows, at positions close to the air slots. The size of the arrows represents the magnitude of the velocity. Most of the "action" occurs within a few millimeters of the air slots. The two separate jets impact each other and combine at a position about 3 mm below the die face. Note the two recirculation areas that occur in a triangular space located within a few millimeters of the center of the die. A behavior like this should be expected on the basis of continuity. The simulation results in Figure 2-16 reveal information that is difficult to obtain in the laboratory and is quite important for the melt blowing process. Specifically, the polymer fiber in the region very close to the die surface is subjected to air velocities that push it back toward the die. Also, the forces, and thus the rate of strain, might change dramatically over short distances along the axis of the polymer fiber.

2.2.3 Effect of Changing Jet Angle on Flush Blunt and Sharp Dies

One of the motivations of using CFD to investigate the flow field below a dual jet is to test new jet geometries without the time and financial commitment of actually manufacturing these structures. Several different jet shapes have been used in the industry, but there are limitless possibilities of geometries that could be tested. An obvious issue is the effect of jet angle on the flow field. Changing the angle of the jet

with respect to the die face is expected to change the flow field throughout the entire computational domain.

To investigate the effect of changing the angle on the flow field, several tests were run for different jet geometries. Table 2-1 presents a summary of the simulation parameters and the computational time needed to complete these runs. These simulations were completed at standard temperature and pressure, and all simulations had the same air mass flow rate of 100 slpm. The second-order RSM turbulence model with the modified parameters was used in all of these runs. The air-flow mean velocity through the inlet jet was the same for all of the blunt die runs and for all of the sharp die runs. Figure 2-17a and b provides a comparison of the dimensionless velocities V_o/V_{jo} along the jet centerline for the blunt die and the sharp die, respectively. The nominal velocity V_{jo} is used to make the velocity dimensionless, and the distance h is used to make the distance from the die face dimensionless. For both the blunt and the sharp dies, the maximum velocity is reached closer to the die face (i.e., at smaller z) for smaller angles. This is expected behavior, because the two air streams meet sooner for smaller angles. For the blunt die (Figure 2-17a), the range of the maximum velocity is $1.02 < V_o/V_{jo} < 1.42$. For the sharp die (Figure 2-17b), the range of the maximum air velocity is $1.36 < V_o/V_{jo} < 1.85$. For both blunt and sharp dies, the smaller die angles give higher dimensionless air velocities. For melt blowing, the maximum air velocity is quite important. However, it is also useful to have high air velocity over a large range of z values, i.e., the integral of the velocity versus z curve should be as large as possible. High air velocity leads to high drag on the polymer filament, which results in rapid attenuation of fibers during melt

blowing. Although the 60° die geometry is common in industry, our CFD results suggest that other geometries should be tested in the laboratory.

To choose the best die configuration, other criteria might also be important. In general, it is desirable to have a smooth air flow around the location of the polymer fiber, i.e., near the centerline of the dual jet. Strong velocity fluctuations can cause the fiber to bend, twist, or move relative to the centerline. The result might be the sticking of the bent fiber to the die (or to adjacent fibers), a highly undesirable event. The simulation can provide the information related to the turbulence (such as the turbulence intensity or turbulent kinetic energy) that is needed to assess whether a die configuration is desirable or not regarding this criterion. Figures 2-18a and b presents the dimensionless turbulence intensity along the centerline for different die angles. The turbulence intensity is a measure of the relative strength of the velocity fluctuations. In general, it is expected that the fluctuating velocity field will become stronger as the converging jet angle becomes smaller. This observation makes sense intuitively: higher turbulent fluctuations are expected when the two air jets are tending toward a "head-on" collision. At the limit of a 0° angle, the two jets would collide head-on, in which case the turbulence at the point of convergence would be very strong, as all of the kinetic energy associated with the jets would be immediately transferred to the fluctuations. For Figure 2-18a, the blunt-die case, the positions of maximum turbulence occur earlier (at about half the corresponding z values) than the positions of maximum velocity; compare Figure 2-17a. Also, the turbulence intensity starts at 0. This is expected because the two jets do not impact each other until they reach a z/h value of about 1 (see Figure 2-16).

For the sharp die case (Figure 2-18b), the shape of the turbulence intensity curves is different from that for the blunt case. For each curve, the turbulence intensity rises extremely rapidly to a maximum value for $z/h << 1$; this maximum represents the high turbulence at the sharp tip of the die. Each curve then goes through a minimum, rises to a local maximum, and then falls off as z increases further. The minima correspond with the maximum velocities shown in Figure 2-17b. This is expected because the production of turbulence (term G_k, see eq. 1-7) is almost 0 when the mean velocity slope is almost 0. The curves then rise to local maxima because the slope of the mean velocity increases.

The dimensionless Reynolds stress profile along the centerline for different jet angles is shown in Figure 2-19a and b. As the die angle increases, the location of the maximum Reynolds stress moves farther downstream from the die surface for both types of dies. The difference in the profiles between the blunt and sharp dies is very pronounced. This difference is related to the fact that the Reynolds stress changes sign as the slope of the mean velocity changes sign (i.e., negative Reynolds stress is associated with increasing mean velocity, and positive Reynolds stress is associated with decreasing mean velocity). Hence, if we observe the centerline velocity in Figure 2-16, we see that, because of recirculation, the centerline velocity has both negative and positive values for the range $0 \leq z/h \leq 1$. This is the same z/h range for which Figure 2-19a exhibits negative Reynolds stresses. For the sharp die (Figure 2-19b), the Reynolds stresses start out negative because the mean velocity has a positive slope right at the tip of the die, and it reaches maximum positive values at $z/h \approx 3\text{-}4$ because the mean velocity exhibits the maximum negative slope at this location (see Figure 2-17b).

The turbulent kinetic energy (TKE) is plotted in Figure 2-20a and b for the blunt and sharp dies, respectively. The TKE is made dimensionless by dividing by V_{jo}^2. For the blunt die (Figure 2-20a), the TKE rises to a maximum in the region between the two jets. For larger die angles, the maximum occurs at larger z/h values, and the maximum is lower. This behavior makes physical sense, because the impact of the jets is farther from the die face for a larger angle, and the impact is more "gentle" (less turbulence) when the angle is larger. The TKE curves also exhibit local maxima for z/h values ranging between 1.5 and 3. For the sharp-die case (Figure 2-20b), turbulence is produced just beyond the tip of the die (see the local maximum at $z/h \approx 0$); this turbulence corresponds to the physical impact of the two jets. Also note that, for the sharp die, the TKE exhibits a second maximum at $z/h \approx 6$.

The turbulence dissipation rate is plotted in Figure 2-21a and b for the blunt and sharp dies, respectively. The dissipation rate is made dimensionless by dividing by V_{jo}^3/h. For the blunt dies (Figure 2-21a), the dissipation rates reach maximum values in the region between the jets. For the sharp dies (Figure 2-21b), the dissipation rates are maximum very near the die tip. Also observe that the sharp-die curves exhibit local maxima at about $z/h \approx 5$.

Figure 2-22a and b presents contour plots of the Reynolds stress close to the die surface for the 60° blunt die and the 60° sharp die, respectively. The maximum Reynolds stress is not located on the centerline; instead, there are two local maxima (these are negative maxima) at the location where the two air jets converge (see points labeled A in Figure 2-22). Farther downstream, within the self-similar zone of flow development, the Reynolds stress changes sign and exhibits two maxima in the region next to the

converged jet (see points labeled B in Figure 2-22). Locations of high Reynolds stresses are usually associated with the production of TKE. Figure 2-22a shows that maximum turbulence is produced at the outer edges of the triangular region mentioned in the discussion of Figure 2-16 (i.e., slightly closer to the centerline than the maximum jet velocities shown in Figure 2-16); see points A in Figure 2-22a. As shown in Figure 2-22b (for the sharp die), the locations of maximum turbulence (see points A in Figure 2-22b) differ only slightly from the locations of maximum air velocity.

Figure 2-23a and b presents contour plots of the turbulence intensity close to the die surface for the 60° blunt and 60° sharp dies, respectively. For both the blunt and the sharp dies, the maximum of the intensity is located at the centerline at the point at which the two jets are converging. Beyond that point, the turbulent fluctuations start to decay.

2.2.4 Comparison to Experiments for Inset and Outset Dies

Sharp melt blowing dies have several different possible configurations. The effect of changing the nose piece placement (either above, flush, or outset with respect to the die face) was investigated. Figure 2-4 show the cross section for a flush sharp die. Figure 2-5 is the cross section for an inset die. Since $z = 0$ is at the die face, the nose piece placement, a, for inset dies is a negative value. Figure 2-6 is the cross section for an outset die, which has a nose piece that extends below the die face, and therefore, the value of a is positive for outset sharp dies.

Although extensive laboratory tests have been conducted by TS for an inset die with a recession of $a = -b_o/2 = -0.325$ mm, the effect of other magnitudes of this recession has not been investigated. In the present study, inset dies with the following recess values have been simulated: $a = -b_o/4$, $-b_o/2$, $-b_o$, and $-5b_o/4$, where $b_o = 0.65$ mm. The data of

TS for the case of an inset die with a recession of -0.325 mm have been used to validate the current simulations of an inset die. Both the experimentally tested flow fields of TS and the present simulations neglect the presence of the polymer fiber along the line of symmetry.

Similar to their work with the inset die, TS conducted measurements for an outset die with a nose piece that extended 0.325 mm below the die face. In the present work with CFD, outset dies were examined with the following nose piece extensions below the die face: a = $b_o/4$, $b_o/2$, b_o, $5b_o/4$, and $3b_o/2$ (where b_o = 0.65 mm).

Figure 2-24a presents the dimensionless mean z-velocity, V_o/V_{jo}, along the line of symmetry, where V_o is the mean z-velocity at x = 0 and V_{jo} is the nominal discharge velocity. The simulation and laboratory results close to the die face are presented for the case of an inset die with a recession of $-b_o/2$ = -0.325 mm. Figure 2-24b compares the experimental and simulated dimensionless centerline velocity decay farther from the die face. Good agreement is observed in the flow field both close to and far from the die face. The exponential fit to the experimentally recorded velocity decay is (TS):

$$V_o/V_{jo}=3.66*(z/h)^{-0.558} \qquad (2\text{-}6)$$

while the exponential fit from the present CFD results is

$$V_o/V_{jo}=4.39*(z/h)^{-0.637}. \qquad (2\text{-}7)$$

2.2.5 Effect on Mean Velocity of Changing the Nose Piece Placement for Sharp Dies

Table 2-2 lists the simulations completed for the different inset and outset dies configurations. The number of cells for each simulation, the number of iterations, and the CPU time required are all given. The simulated flow fields from all of the different

inset and outset dies were generated using the same volumetric flow rate as in TS, which is 100 L/min. The slot width d was 0.563 mm for all simulations. The air moving through the jets was set at a temperature of 21°C and 1 atm; these were the conditions used by TS. Even though the air flow in the melt blowing process is not isothermal, the understanding and modeling of the air flow in isothermal conditions is of significant scientific value, since there are no theoretical results available for the case of two converging plane jets. (Also, as shown by the experimental results of HS, the flow patterns of nonisothermal converging jets are a natural extension of the patterns for isothermal converging jets.) The z-component of the air velocity at the jet inlet was set at 17.3 m/s (this is the nominal discharge velocity V_{jo}). To compare the flow fields created by various inset and outset jets, the same model parameters were used. Since the model parameters previously determined when studying the flush blunt and sharp dies lead to accurate simulation of the inset die air flow, these parameters were used for the simulations of all die geometries.

For different inset dies Figure 2-25a shows how the nose piece recession (inset) affects the dimensionless centerline velocity. Increasing the nose piece recession clearly leads to an increase in the maximum centerline velocity; the velocity at the highest recession ($a = -5b_o/4$) is triple the velocity for a flush die ($a = 0$). This result is expected, because increasing the amount of recession of the nose piece leads to a smaller inlet jet width b. Since the same rate of volumetric air flow must pass through a smaller opening, the mean velocity increases.

For the outset die, the centerline velocity is related to the extension of the nose piece below the die face. Figure 2-25b compares this centerline velocity for five different

outset dies. The maximum centerline velocity is found to decrease as the nose piece extends beyond the die face. However, as a comparison of Figure 2-25a with 2-25b shows, the quantitative change in the velocity profiles is less for the case of outset versus inset. Besides the obvious differences at the velocity maxima, all along the velocity profiles there are large differences between the centerline velocities for different inset dies. In contrast, the outset dies have very similar centerline velocity profiles—except for the (relatively small) profile differences at positions near the velocity maximums. A further generalization, for both Figures 2-25a and 2-25b, is that the effect of moving the nose piece decreases as the nose piece moves in the positive *z*-direction.

Figure 2-25c shows how level of die inset or outset correlates with the maximum centerline velocity. To better compare with a "standard" flush die, the maximum velocity along the line of symmetry has been divided by the maximum centerline velocity achieved by the flush die. The abscissa in Figure 2-25c is the dimensionless recession of the nose piece, *a*/d. Figure 2-25c illustrates a significant decrease in the maximum of the mean centerline velocity as the nose piece is moved in the positive *z*-direction. Also shown on Figure 2-25c is the following empirical equation that was fit to the data:

$$\frac{\left(V_o/V_{jo}\right)_{\max}}{\left(V_o/V_{jo}\right)_{\max-flush}} = 0.79013 + 1.7615\left(\frac{a}{d} + 2.3523\right)^{-2.5383} \qquad (2\text{-}8)$$

This equation is an excellent fit (R = 0.99998). Since the nominal velocity V_{jo} is constant for all the simulations, the left side of Equation 2-8 could also be written as simply $(V_o)_{max}/(V_o)_{max\text{-}flush}$. Equation 2-8 is useful for predicting maximum velocities for inset

and outset values that were not considered in the simulations (and the experiments of TS).

For positions away from the die face, the CFD data for the velocity decay of the two converging jets can be correlated with the following relation that is similar to the one used for a plane 2-D jet (Schlichting, 1987 and Uyttendaele and Shambaugh, 1989) (also see equations 2-6 and 2-7 in the previous subsection):

$$(V_o/V_{jo}) = c_1(z/d)^m \qquad (2\text{-}9)$$

The length scale used here is the distance d instead of h that was used in Equations 2-6 and 2-7, because d (as well as b_o) is common for all types of dies, while h changes. Table 2-4 presents empirical fits of the coefficients c_1 and m for the different dies examined here. The exponent has values between -0.6195 and -0.6533; these are different from the exponent of -0.5 suggested for a single two-dimensional turbulent jet (Schlichting, 1987). For the range of inset dies (from the lowest a until a = 0), the parameter c_1 decreases from about 8.5 to 5.5. Then, as a is increased further into the range of the outset dies, the parameter c_1 stays essentially constant. This behavior parallels what was discussed above for inset versus outset dies: more change occurs for the inset than for the outset die (e.g., see Figure 2-25c). Heskestad (1965) and Gutmark and Wygnanski (1976) found experimentally that the mean velocity and the Reynolds stresses for a plane jet become self-similar beyond $z/b_o = 40$. In this region, they scaled the velocities and the Reynolds stresses with V_o, and they scaled the distances with $x_{1/2}$. Figure 2-26a shows the simulated dimensionless mean velocity of the different inset dies at z = 50 mm (z/b_o = 76.92, a position well below the die face). Also shown on Figure 2-26a is the following

correlation used by TS that accurately represents their experimentally determined mean velocity at distances well below the die face:

$$\frac{V}{V_o} = \exp\left[-0.6749\left(x/x_{1/2}\right)^2\left(1+0.027\left(x/x_{1/2}\right)^4\right)\right] \qquad (2\text{-}10)$$

TS found that Equation 2-10 well-fit their data taken for the flush geometry (they did not take corresponding data for inset or outset dies). Equation 2-10 was originally developed by Bradbury (1965) for rectangular jets. Figure 2-26a shows that the level of nose piece recession plays a very small role in the simulated flow field far from the die, since all the inset dies have very similar mean velocities at the 50 mm distance. In addition, V/V_o for the inset dies at z = 50 mm shows excellent agreement with the experimental V/V_o for the flush die at this distance from the die face.

Similarly, Figure 2-26b compares the simulated mean velocity of the different outset dies at z = 50 mm to the experimental results represented by Equation 2-9. As with the inset dies, the simulated flow fields for the different outset dies are very close to the flow field obtained experimentally by TS at long distances from the die face.

As described earlier, Figures 2-25 and 2-26 demonstrate that the flow field resulting from the two converging plane jets exhibits a region of development that depends on the configuration of the die face, followed by a region of self-similarity in which the flow field does not "remember" its origin and behaves like the flow field from a plane jet. The effect of the placement of the nose piece below or above the die face is minimal at a distance far from the die. Figures 2-27a and b illustrate this transition. Figures 2-27a and b present, respectively, the simulated contour plots of the mean z-velocity for inset and outset dies with, respectively, a = $-b_o/2$ and a = $b_o/2$. Though the

flow fields are quite different near the die face, the similarity in the velocity field away from the die face is evident. At these large distances from the die face, mean velocity decay can be easily determined from Equation 2-9 used in conjunction with Table 2-4. For "a" values not given in the table, interpolation/extrapolation can be used.

2.2.6 Effect on Fluctuating Velocity Field of Changing the Nose Piece Placement for Sharp Dies

In addition to the velocity maximum achieved by different dies, the fluctuating velocity field must also be considered for the optimization of die performance. Figure 2-28a compares the turbulence intensity, q, along the line of symmetry for the different inset dies. The turbulence intensity is a measure of the relative strength of the velocity fluctuations. The maximum turbulence intensity increases as the amount of recession above the die face increases, and it exhibits two local maxima: one at the die face ($z = 0$), and one at a location downstream from the die face. The turbulence in the flow field increases as the air moves through the region where the two jets meet. At the first part of this region of intersection (right at the die face), the air flow is forced to accelerate as the air streams mix and move through a smaller space, which increases the turbulence intensity and results in the first observed intensity maximum. After the fluid exits the constriction at the die face, the turbulence intensity starts to decrease, and the intensity shows a local minimum at a location that corresponds to the location at which the mean velocity exhibits its maximum. After this minimum, the intensity increases again, because the turbulence production, which is proportional to the slope of the mean velocity, increases. The maximum turbulence intensity exhibited by the die with an inset

of $5b_o/4$ (= 0.8125 mm) is significantly higher than the maximum turbulence intensities caused by the lower inset settings.

As the nose piece extends below the die face for the outset dies, the difference between the turbulence intensity profiles for different outset dies decreases. Figure 2-28b shows the turbulence intensity for the centerline of the different outset die flow fields. The average outset die intensity is an order of magnitude less than the average intensity for the inset dies of Figure 2-28a (note that the ordinate scale on Figure 2-28a is logarithmic). Similar to the case with the centerline velocities, there is little difference between the turbulence intensity in the flow fields from the dies with outsets of $a = 5b_o/4$ and $a = 3b_o/2$. As shown in Figure 2-28c, movement of the nose piece downward in the positive z-direction decreases the centerline velocity. Figure 2-28c illustrates how the centerline turbulence intensity also decreases when the nose piece is moved in the positive z-direction. As was the case for the velocity profile, the turbulence intensity of the flow tends to a common profile as the nose piece is moved away from inset positions to outset positions. The correlation obtained for the maximum turbulence intensity as a function of the position of the die nose piece is

$$\frac{q_{\max}}{q_{\max-flush}} = 0.80824 + 2.6842\left(\frac{a}{d} + 2.1659\right)^{-3.1618} \qquad (2\text{-}11)$$

As can be seen in Figure 2-28c, for the simulations at large outset, there are negligible differences in the turbulence intensity maxima along the line of symmetry.

Figures 2-29a and b present contour plots of the turbulence intensity for the inset and outset dies with, respectively, $a = -b_o/2$ and $a = b_o/2$. The fluctuations are strong as

the two jets converge (points A), and also at the locations where the mean velocity increases or decreases at a high rate (i.e., high mean velocity slope, points B).

The dimensionless Reynolds stress profile along the line of symmetry is shown in Figures 2-30a and 2-30b for the different die geometries. Figure 2-30a shows the centerline profile of the Reynolds stresses for the different inset dies. The difference between these profiles is much more pronounced for the dies with insets of $5b_o/4$ and b_o. However, the dies with insets of $b_o/2$ and $b_o/4$ are very similar. This difference is related to the fact that the Reynolds stress changes sign as the slope of the mean velocity changes sign (i.e., negative Reynolds stress is associated with increasing mean velocity, and positive Reynolds stress is associated with decreasing mean velocity). Hence, if we observe the centerline velocity in Figure 2-25a, we see that, because of the constriction of the jets at high recess levels, the centerline velocity increases dramatically before the air crosses the die face. The centerline Reynolds stress profiles become much more similar as the nose piece moves in the outset position (Figure 2-30b). Close to the die, the Reynolds stresses profiles have different magnitudes, although they have similar shapes. However, the outset Reynolds stress profiles become identical farther from the die face.

Figure 2-30c is a plot of the centerline Reynolds stress (RS) maximum for both the inset and outset dies. The maximum in the Reynolds Stress decreases as the nose piece is moved downward in the *z*-direction. The location of the maximum Reynolds stress is of interest, because this location is closely associated with area of the flow where turbulence is produced. The relationship between the Reynolds stress and the placement of the die nose piece is found to be

$$\frac{\left(\overline{uw}/V_{jo}^2\right)_{\max}}{\left(\overline{uw}/V_{jo}^2\right)_{\max-flush}} = 0.61019 + 0.95139\left(\frac{a}{d} + 1.9212\right)^{-3.2662} \qquad (2\text{-}12)$$

Figures 2-31a and b present contour plots of nondimensionalized $\overline{uw}$ (i.e., the Reynolds stress divided by the density of the fluid) for inset and outset dies with, respectively, a = -b_o/2 and a = b_o/2. The maximum Reynolds stress is not located on the centerline; instead, there are two local maxima (these are negative maxima) near the location where the two air jets converge (see points labeled A in Figure 2-31). Farther downstream, within the self-similar zone of flow development, the Reynolds stress changes sign and exhibits two maxima in the region next to the converged jet (see points labeled B in Figure 2-31). Figure 2-31a shows that maximum turbulence is produced right at the location where the two jets are merging (i.e., just before and during the flow of the air stream through the constricting die face); see points A in Figure 2-31a. As shown in Figure 2-31b (for the outset die), the locations of maximum turbulence production (see points A in Figure 2-31b) are slightly below the nose piece.

Figure 2-32a demonstrates the relationship between nose piece recession and turbulent kinetic energy, k, for different inset dies. The k is nondimensionalized by dividing by the square of the nominal velocity. The turbulent kinetic energy increases significantly as the amount of recession above the die face is increased. However, as the nose piece approaches the die face, the effect of changing the recession decreases. The reason for the appearance of two local maxima along the k profile is the same as the reason for the appearance of two local maxima for the turbulence intensity profiles, i.e., the locations of maxima correspond to locations of maximum mean velocity slopes, and the locations of minima correspond to locations of mean velocity maxima, or plateaus.

Figure 2-32b shows the centerline turbulent kinetic energy for the different outset dies. As with the inset dies, the effect of increasing z diminishes for larger values of z. However, the range of k for the outset dies is much smaller than for the inset dies. In addition, the outset dies exhibit a much smaller maximum k than their inset counterparts.

The maximum turbulent kinetic energies achieved by the dies are compared in Figure 2-32c. The maximum k achieved along the centerline decreases as the die nose piece is moved downward in the z-direction. In fact, the difference between the magnitudes of the turbulent kinetic energies for the outset dies is negligible. The curve fit for the relationship between k maximum and nose piece placement is as follows:

$$\frac{\left(\mathrm{k}/V_{jo}\right)_{\max}}{\left(\mathrm{k}/V_{jo}\right)_{\max-flush}} = 0.79985 + 2.748\left(\frac{a}{d} + 2.1929\right)^{-3.2712}. \qquad (2\text{-}13)$$

Figures 2-33a and b present contour plots of k for the inset and outset dies with, respectively, a = -b_o/2 and a = b_o/2. One can expect high levels of turbulent kinetic energy in locations that are close to areas that exhibit high Reynolds stresses (since the production of turbulent kinetic energy is the product of the Reynolds stress and the mean velocity slope). A local maximum in the turbulent kinetic energy occurs at the merging location of the converging jets (see points A in Figure 2-33), which is the area between the location of the two maxima in the Reynolds stresses. The maxima in the turbulent energy are represented by points B in Figure 2-33, which correspond to areas of high Reynolds stress.

The rate of the dissipation of the turbulent kinetic energy can be examined for the different dies. Figure 2-34a shows the centerline turbulence dissipation rate for the different inset dies. The magnitude of the turbulence dissipation rate for the die with an

inset of $5b_o/4$ is significantly higher close to the die. However, the turbulence dissipation rate profiles are very similar farther from the die face. Figure 2-34b compares the dissipation rate profiles for the outset dies. The magnitude and shape of these profiles are similar throughout the computational domain, and are indistinguishable after $z/d = 30$.

Figure 2-34c shows the maximum turbulence dissipation rate for the different inset and outset dies. As expected, the dies that exhibit the largest turbulence intensity also exhibit the largest turbulence dissipation rate. As an example of this, compare the turbulence intensity for a die with an inset recess of $5b_o/4$ (see Figure 2-28a) with the dissipation rate at this recess value (in Figure 2-34c). Clearly, as the nose piece is moved in the positive z-direction, the turbulence dissipation rate profiles become more similar. This is exhibited in Figure 2-34c wherein the magnitude of the maximums for the different dies are extremely similar, except for inset values of $a = -b_o$ and $a = -5b_o/2$ (which correspond to placement of the nose piece well above the die face). The relationship between turbulence dissipation rate maximum and placement of the nose piece can be correlated as follows:

$$\frac{\left(\varepsilon d/V_{jo}^3\right)_{\max}}{\left(\varepsilon d/V_{jo}^3\right)_{\max-flush}} = 0.81443 + 0.97901\left(\frac{a}{d} + 1.9336\right)^{-3.8472} \qquad (2\text{-}14)$$

2.3 Comparison of Slot Dies Using New Scales

2.3.1 Introduction of a New Length Scale

Changing the geometry of the different flush dies (by varying the angle θ) changed the flow field that was generated. Similarly, for the nose piece placement, a, for inset and outset dies changed the flow field. Specifically, the flow field characteristics that were examined were the centerline turbulence and velocity profiles. In experimental

papers HS and TS, the distance in the *z*-direction was made dimensionless using *h* for the blunt and flush sharp dies, while d was used to nondimensionlaize the z-direction for the inset and outset sharp dies. However, *h* and d can be replaced with the quantity z_{max}. This parameter z_{max} is defined as the point along the centerline at which the dimensionless *z*-velocity reaches a maximum value. Correspondingly, the *z*-velocity can be non-dimensionalized using the maximum dimensionless centerline velocity, $(V_o/V_{jo})_{z=zmax}$, which by definition occurs at the location of z_{max}.

2.3.2 Flush Blunt and Sharp Dies

Figure 2-35a shows the dimensionless centerline velocity for blunt dies with various die angles. The ordinate of this graph has values of the dimensionless centerline velocity divided by the maximum dimensionless centerline velocity. Likewise, the abscissa values are made dimensionless by dividing by z_{max}. This nondimensionalization procedure produces four centerline velocity profiles that are almost coincident. Therefore, using z_{max} as a length scale is appropriate. Essentially, one curve fit can be used to describe the centerline velocity decay of a blunt die with any angle in the range considered on Figure 2-35a. Similarly, Figure 2-35b shows the dimensionless centerline velocity for the (flush) sharp dies with four different angles. Again, using z_{max} to make the length scale dimensionless allows for one curve to be used to fit the centerline velocity decay of all four flush dies.

Using Figures 2-35a and b, the centerline velocity decay for different types of dies can be estimated without experimentally or computationally testing the die. To use these different plots, however, z_{max} must be known. This need is filled by Figure 2-36, which gives a correlation for the blunt and sharp flush dies that allows z_{max} to be calculated

when the die angle is known. Therefore, for a wide range of die angles, both z_{max} and centerline velocity decay can be estimated without testing of the die.

Although the centerline velocity decay is important to the attenuation of the fiber when the dies are used to extrude polymers, the maximum air velocity must also be considered. A greater centerline velocity maximum can lead to more drag force and therefore a higher rate of polymer production. As a function of die angle, Figure 2-37 compares the maximum velocity achieved by the blunt and sharp flush dies. This plot demonstrates that the maximum velocity along the centerline is increased as the angle between the walls of the jet and the face plates is increased.

While the centerline velocity is extremely important for polymer production, the turbulence along the centerline must also be considered, because strong turbulent velocity fluctuations can cause the polymer fibers to break off and/or stick to the die face. To quantify this effect, the centerline turbulence intensities of the different dies have been compared. In the experiments and simulation results discussed in previous sections, the centerline turbulence intensities were compared by using h as the length scale. However, as was discussed above, z_{max} can also be used as the length scale. Figure 2-38a compares the centerline turbulence intensities of the different blunt dies. Although decreasing the angle increases the velocity, it also increases the turbulence intensity. A similar trend is shown in Figure 2-38b, which compares the centerline turbulence intensities of the different sharp dies. Again, the turbulence intensity increases as the angle θ is decreased.

2.3.3 Inset and Outset Sharp Dies

For the inset and outset dies, plots can be constructed that are similar to the plots in Figures 2-35a and 2-35b. For the case of sharp inset dies, Figure 2-39a compares the

centerline velocity divided by the maximum centerline velocity versus the nondimensional distance from the die face. Again, the use of z_{max} as a length scale makes the velocity profiles nearly coincident: one curve can describe all four of the simulated inset dies. Figure 2-39b shows a similar set of profiles for a range of outset dies. These profiles are also coincident. All of the blunt and sharp dies, including inset, flush, and outset, have centerline velocity profiles that can be described by the following curve fit:

$$\frac{\left(V_o / V_{jo}\right)}{\left(V_o / V_{jo}\right)_{z=z\max}} = e * \left(z / z_{\max}\right)^{-f} \qquad (2\text{-}15)$$

The constants e and f for each of the different types of dies are given in Table 2-5.

For different inset dies, Figure 2-40a relates the nose placement to the position of z_{max}. For outset dies, Figure 2-40b relates the nose piece placement to z_{max}. Thus, for a wide range of nose placements in a sharp die, z_{max} and the centerline velocity decay can be estimated quickly and efficiently.

Figure 2-41 shows the maximum centerline velocity achieved by the different sharp dies. A single curve fit successfully describes the inset, flush, and outset sharp dies. As placement of the nose piece is moved in the positive z-direction, the maximum centerline velocity decreases until it reaches a plateau. Several of the outset dies have similar centerline velocity maximums.

The centerline turbulence intensity can also be compared for the different sharp dies. Figure 2-42a compares the centerline turbulence intensity for the inset dies. As the nose piece is moved in the negative z-direction (i.e, the nose piece is recessed farther above the die face), the turbulence intensity along the centerline increases. Once again, a tradeoff is experienced between increasing centerline velocity and increasing centerline

turbulence intensity. Figure 2-42b compares the centerline turbulence intensity for the different outset dies. Similar to the inset dies, as the nose piece is moved in the positive z-direction, the centerline turbulence intensity is decreased. However, the difference in the flow fields between the different inset dies is much larger than the difference in the flow fields of the outset dies. As the nose piece is moved in the positive z-direction, the turbulence intensity decreases and then plateaus (see Figure 2-28c).

2.4 Non-Isothermal Slot Die Simulations

Based on the experimental setup, all slot die simulations discussed previously were performed under isothermal conditions. However, melt blowing is not an isothermal process. Therefore, the temperature field is also of interest. Simulations were conducted for the flush blunt and sharp slot dies. Table 2-7 gives the tie type, number of cells, number of iterations necessary until convergence is achieved, and computational time for the non-isothermal simulations. The effect of the angle on the temperature field was examined. Figure 2-43 is a comparison of the dimensionless centerline velocity for two 60° blunt die simulations. One simulation was run under isothermal conditions, while the other was run under non-isothermal conditions that are within the range used for melt blowing. There is little difference between the simulation results for the flow field, especially in the area of most interest, close to the die face. Therefore, only the temperature field will be discussed for the non-isothermal cases. The extensive discussion in the previous sections concerning the flow field can be used to determine the velocity profiles of both isothermal and non-isothermal cases.

The excess temperature, Θ, is the temperature of the air above ambient conditions. Θ_{jo} is the temperature above ambient conditions of the air in the jet. For all simulations,

the ambient temperature of the air is 294 K, or 21 °C. Harpham and Shambaugh (1997) (referred to as HS2 for the remainder of the chapter) measured the flow and temperature fields from flush blunt and sharp melt blowing dies.

2.4.1 Comparison to Experiments

For the isothermal simulations, the CFD parameters were established to accurately model the experimentally measured flow fields. However, with the addition of the energy equation and the compressible flow conditions, these parameters had to be reevaluated. The constant default value for the turbulent Prandtl number, Pr_t (see Equation 1-10), was also reevaluated because the default value resulted in a simulation where the temperature decayed more slowly than experimentally observed. The Pr_t also affects the Reynolds stress production term due to buoyancy (G_{ij} in Equation 1-10). The turbulent Prandtl number represents the dispersion of momentum due to turbulence relative to the dispersion of heat. Therefore, in order to increase heat dispersion, Pr_t had to be adjusted to a lower value. A number of different Pr_t values were tested in the range 0.20 to 0.85 (the default value of Pr_t is 0.85). A comparison of the velocity decay found for simulations with different Pr_t values is given in Figure 2-44. In addition, the comparison of the centerline temperature decay for simulations using different Pr_t values is shown in Figures 45a and 45b. In Figures 2-44, 2-45a, and 2-45b, the curves shown are simulations run with a nominal discharge velocity of V_{jo} = 23.2 m/s and an air temperature in excess of ambient conditions of Θ_{jo} = 100 K. Considering the experimentally obtained functions as the correct solution (for example, the experimentally obtained function for temperature is labeled "HS2" in Figures 2-45a and 2-45b), one can determine the mean square root of the error for each simulation and for

both the centerline temperature and velocity. As can be seen in Figures 2-45a and 2-45b, Pr_t values of 0.30, 0.35 and 0.40 give simulated temperature profiles that visually look much closer to the HS2 function than profiles predicted with the other Pr_t values. The root mean squared error for the temperature decay and the velocity decay at z/h>10 are given in Table 2-7. (The errors for velocity and temperature are higher for the other values of Pr_t that are shown on Figures 2-44, 2-45a, and 2-45b.) Since the error for the temperature decay is one order of magnitude less for Pr_t = 0.30, while the error for the velocity is of the same order of magnitude for these turbulent Prandtl numbers, Pr_t = 0.30 was chosen for the rest of the simulations. Table 2-8 summarizes the default Fluent™ parameters, the parameters used for the isothermal studies, and the parameters used in the non-isothermal study.

Figure 2-46 compares the simulated centerline velocity of the 60° blunt die, with an inlet temperature above ambient conditions, to experimental data at distances of z/h > 2 below the die face. Similar to Figure 2-43, the velocity profiles are similar, but the higher Θ_{jo}, the lower the dimensionless velocity far from the die face. Figure 2-47 shows a similar comparison of the simulated centerline temperature decay with experimental measurements. The 60° blunt die was simulated with different inlet air flow rates and different inlet air temperatures. In all cases, good agreement is exhibited between these simulations and the laboratory data from HS2. The CFD simulations are able to successfully reproduce this velocity decay. Since the cases being considered are not isothermal, the centerline temperature decay is also important when considering the ability of the CFD simulation to match laboratory results. The experimental correlation

shown on Figure 2-47 is from HS2; this HS2 equation matched several different inlet air temperature and velocity cases.

2.4.2 Non-isothermal Simulation Results

In section 2.3, z_{max} was introduced as a length scale, which allowed the centerline profiles for different geometries to collapse onto a single curve. Likewise, the temperature decay for all the different dies also scales well with the length scale z_{max}, as seen in Figures 2-48a and 2-48b. The curve fit that describes the dimensionless centerline temperature decay for all the different dies is

$$\Theta_o/\Theta_{jo} = 1.0074*(z/z_{max})^{-0.5537}. \qquad (2\text{-}16)$$

The quantity z_{max} is different for each die. Figure 2-36 shows the relationship between z_{max} and the die angle θ for several simulated die geometries. From Figures 2-48a and b, the jet angle does not change the temperature profile when z_{max} is used for the length scale. Therefore, equation 2-16 can be used to predict the centerline temperature decay for different die geometries.

2.5 Conclusions

The flow field resulting from dual rectangular jets has been predicted using CFD methods. The simulations are validated with laboratory data. Detailed numerical procedures have been established for the simulation of flow under two converging rectangular jets. Without modification of the default parameters, turbulence models such as the k-ε standard model, the k-ε realizable model, and the RSM fail to predict the quantitative characteristics of the flow field. The availability of experimental

measurements for specific conditions made possible the identification of the values of the model parameters that can produce the best results.

The flow field for the blunt die exhibits three regions of development. These three regions of development have also been observed in the case of parallel jets (Nasr and Lai, 1997a). In the first region, the two jets are converging, and each jet has its own identity. The mean velocity exhibits two maxima; each maximum is associated with one of the two jets. The interaction of the two jets is manifested by the generation of high Reynolds stresses in the area that is confined between the die surface and the two jets. Mean flow recirculation is also observed in this area, which results in negative mean air velocity at the centerline. The second region is the merging region in which the two air jets are converging. This region is characterized by a maximum in turbulence kinetic energy and turbulence intensity. The mean velocity still exhibits two maxima, but there is no inner region with recirculation. The third region is a self-similar region where flow behaves as if resulting from a single-plane jet. There is only one maximum of the mean velocity, and this maximum is located at the centerline. The flow field for the sharp die does not exhibit the first region of development, but this field exhibits the other two regions of development (the merging region and the fully combined region).

Using CFD allows better understanding of regions of the flow field that are very difficult to measure in the laboratory, such as the recirculation close to the blunt die surface, the turbulence kinetic energy field, the dissipation of turbulence kinetic energy, etc. Several simulations were conducted using different jet angles for the flush blunt and sharp dies to demonstrate the effect of the jet angle on the flow field. For smaller angles, θ, the mean velocity is generally higher at the centerline for the same air flow rate. This

higher velocity might result in higher polymer fiber speeds, which is desirable. However, the turbulence intensity is often higher for small jet angles, which might be a disadvantage in fiber production. Turbulence fluctuations are produced in the area close to the die surface for the case of a blunt die. For a sharp die, fluctuations exhibit a local maximum within the second region of flow development (the converging region of the two jets). If it is desirable to reduce the fluctuations along the path of the polymer fiber, particularly at the die tip, then a blunt die appears to be a better option. On the other hand, if one desires to increase the mean velocity along this path without increasing the air consumption of the die, then a sharp die is more suitable.

Similar to the flush blunt and sharp dies, the flow field resulting from two rectangular jets with either an inset or outset nose piece configurations have been predicted using CFD. These simulations have also been validated with laboratory data. The numerical procedures were the same for the flush, inset, and outset dies. A number of simulations were conducted using different inset and outset levels, in order to investigate the effect of the nose piece position on the flow properties. As the inset level is increased (i.e., as a becomes more negative), the mean velocity is much higher in the centerline for the same air flow rate. This higher velocity may result in higher polymer fiber speeds, which is desirable. However, the turbulence intensity is also dramatically higher, which might be a disadvantage for melt blowing. In fact, a maximum of turbulence intensity occurs right at the die face, where the constriction is at its smallest and where a polymer fiber might start to vibrate and stick to the die tip. For an outset die, the fluctuations tend to a common profile that occurs when $a > b_o$. If it is desirable to reduce the fluctuations along the path of the polymer fiber, particularly at the die tip, then

an outset die appears to be a better option. In fact, the original patent suggests that a slight outset will help prevent fiber breakage and polymer accumulation on the die (Harding et al., 1974). On the other hand, if one desires to increase the mean velocity along this path without increasing the air consumption of the die, then an inset die is more suitable.

The flow and temperature fields resulting from two non-isothermal, rectangular jets that converge in a blunt and a sharp die configuration have been predicted using CFD. After adjusting the model parameters (similar to the isothermal cases), the CFD results have good agreement with the experimentally measured temperature profiles. The compressibility present in the non-isothermal simulations does not change the centerline velocity profiles close to the die face significantly. However, further away from the die face, the velocity for the non-isothermal simulation is slightly lower.

Using the length scale z_{max} permits the comparison and prediction of the flow and temperature fields from different die configurations. This length scale is useful because it allows for the flow and temperature field characteristics from several different dies to be described by one curve fit. Therefore, if the geometry of the jets is known, the correlations that have been presented can be used to estimate the maximum centerline velocity, the location of this maximum, and the maximum turbulence intensity. For the flush blunt and sharp dies, the location of the z_{max} as a function of θ is provided, and the maximum values of the mean velocity and of the turbulence characteristics as a function of θ are also provided. Similarly, for the inset and outset sharp dies, z_{max} can be predicted based on the placement of the nose piece with respect to the die face, a. The procedure to calculate the mean temperature and the mean velocity along the centerline

can be summarized as follows: (a) calculate z_{max} from Figures 2-36, 2-40a, or 2-40b, depending on the geometry, (b) calculate the maximum velocity from the equations given on Figures 2-37 or 2-41, (c) use the equations on Figures 2-35a, 2-35b, 2-39a, or 2-39b to calculate the mean velocity decay, and (d) use Equation 2-16 to calculate the mean temperature decay.

2.7 Nomenclature

b	jet width at die face, mm
b_o	face width of the die slot, mm
c_1	empirical constant (Equation 2-1)
$C_{\varepsilon 1}$	parameter for the RSM model (Equation 1-4)
$C_{\varepsilon 2}$	parameter for the RSM model (Equation 1-4)
d	width of the die slot (see Figure 2-4), mm
G_{ij}	production of i,j Reynolds stresses due to buoyancy
h	distance between the outside edges of the two jets at the die face, mm
k	turbulent kinetic energy ($1/2\overline{u_i u_i}$), m^2/s^2
l	length of the die, mm
L_x	width of the computational domain in the x direction, mm
L_z	length of the computational domain in the z direction, mm
Pr_t	turbulent Prandtl number, Pr_t=(eddy viscosity)/(eddy thermal diffusivity)
q	turbulence intensity, $100*\left(\overline{u_i^2}\right)^{1/2}/V_{jo}$
Q	air flow rate through both slots, m^3/s
Re	Reynolds number
S	Spreading rate constant

T	temperature, degree K
u_i	velocity fluctuation in the *i*-th direction, m/s
U_i	mean velocity in the *i*-th direction, m/s
$\overline{uw}$	Reynolds stress divided by the fluid density, m^2/s^2
V_{jo}	nominal jet velocity, m/s
V_o	*z*-direction velocity along the symmetry line, m/s
V_z	velocity in the z-direction, m/s
x, y, z	spatial coordinates
$x_{1/2}$	the distance from the centerline where the velocity is equal to half the centerline velocity, m or mm
z_{max}	merging distance below the die face at which the dimensionless mean velocity reaches a maximum

Greek Characters

ε	dissipation rate of turbulent kinetic energy, m^2/s^3
θ	angle between jet and die face, degrees
Θ	excess temperaturethe difference between the air temperature and ambient temperature, K
Θ_{jo}	the difference between the jet air temperature and ambient temperature, K
ρ	density, kg/m^3

2.8 References

Anderson, E. A.; Spall, R. L.; Experimental and Numerical Investigation of Two-Dimensional Parallel Jets, *Journal of Fluids Eng.*, **2001**, *123*, 401-406.

Buntin, R.R.; Keller, J.P.; Harding, J.W. Nonwoven Mats by Melt Blowing. U.S. Patent 3,849,241, Nov. 19, 1974.

Bradbury, L. J. S. The Structure of a Self-Preserving Turbulent Plane Jet. *J. Fluid Mechanics*. **1965**, *23*(1), 31-64.

Dejoan, A.; Leschziner, M. A. Large Eddy Simulation of a Plane Turbulent Wall Jet, *Phys. of Fluids*, **2005**, *17*, 025102: 1-16.

Elbanna, H.; Sabbagh, J. A. Interaction of Two Nonequal Plane Parallel Jets, *AIAA Journal*, **1987**, *25*(1), 12-13.

Fluent User's Guide; Fluent Inc.: Lebanon, NH, 2007.

Gambit Modeling Guide; Fluent Inc.: Lebanon, NH, 2007.

Grinstein, Fernando F., Vortex Dynamics and Entrainment in Rectangular Free Jets, *Journal of Fluid Mechanics*, **2001**, *437*, 69-101.

Gutmark, E.; Wygnanski, I. The Planar Turbulent Jet. *J. Fluid Mech.,* **1976**, *73*, 465-495.

Harding, J.W.; Keller, P.P.; Buntin, R.R. Melt-blowing Die for Producing Nonwoven Mats. U.S. Patent 3,825,380, Jul 23, 1974.

Harpham, A.S.; Shambaugh, R.L Flow Field of Practical Dual Rectangular Jets. *Ind. Eng. Chem. Res.,* **1996**, *35*, 3776-3781.

Harpham, A.S.; Shambaugh, R.L Velocity and Temperature Fields of Dual Rectangular Jets. *Ind. Eng. Chem. Res.,* **1997**, *36*, 3937-3943.

Heskestad, G. Hot-Wire Measurements in a Plane Turbulent Jet. *Journal of App. Mech.* **1965**, *32*, 721-734.

Kalita, K.; Dewan, A.; Dass, A. K. Prediction of Turbulent Plane Jet in Crossflow, *Num. Heat. Trans.,* **2002**, *41*, 101-111.

Krothapalli, A.; Baganoff, D.; Karamcheti, K. Development and Structure of a Rectangular Jet in a Multiple Jet Configuration, *AIAA Journal*, **1980**, *18*(8), 945-948.

Lai, J. C.; Nasr, A.; Two Parallel Plane Jets: Comparison of the Performance of Three Turbulence Models, *Proc. Instn. Mech. Engrs.*, **1998**, *212*(G), 379-391.

Majumdar, B., Shambaugh, R. L. Velocity and Temperature Effects of Annular Jets. *Ind. Eng. Chem. Res*. **1991,** *28*, 5125-5138.

Mohammed, A.; Shambaugh, R.L. Three dimensional flow field of a rectangular array of practical air jets. *Ind. Eng. Chem. Res.,* **1993**, *32*, 976-980.

Narayanan, V.; Seyed-Yagoobi, J.; Page, R.H., An Experimental Study of Fluid Mechanics and Heat Transfer in an Impinging Slot Jet Flow, **2003**, *47*, 1827-1845.

Nasr, A., Lai, J.C.S., Comparison of Flow Characteristics in the Near Field of Two Parallel Plane Jets and an Offset Plane Jet. *Phys. Fluids*, **1997a**, *9*(10), 2919-2931.

Nasr, A., Lai, J.C.S., Two Parallel Plane Jets: Mean Flow and Effects of Acoustic Excitation, *Exp. Fluids*, **1997b**, *22*(3), 251-260.

Obot, N.T.; Graska, M.L.; Trabold, T.A. The near field behavior of round jets at moderate Reynolds numbers. *Can. J. Chem. Eng.* **1984**, *62*, 587.

Obot, N.T.; Trabold, T.A.; Graska, M.L.; Gandhi, F. Velocity and temperature fields in turbulent jets issuing from sharp-edged inlet round nozzles. *Ind. Eng. Chem. Fundam.*, **1986**, *25*, 425.

Pope, S. B. *Turbulent Flows*; Cambridge University Press: Cambridge, U.K., 2000; pp 134-135.

Rajaratnam, N. *Turbulent Jets*; Elsevier: New York, 1976.

Ribault, C. L.; Sarkar, S.; Stanley, S. A. Large Eddy Simulation of a Plane Jet, *Phys. of Fluids*, **1999**, *11*(10), 3069 – 3080.

Ribault, C. L.; Sarkar, S.; Stanley, S. A. Large Eddy Simulation of Evolution of a Passive Scalar in a Plane Jet, *AAIA Journal*, **2001**, *39*(8), 1509-1516.

Schlichting, H. *Boundary-Layer Theory*; 8th ed., McGraw-Hill: New York, p. 179, 1987.

Shambaugh, R. L. A Macroscopic View of the Melt Blowing Process for Producing Microfibers. *Ind. Eng. Chem. Res.* **1988**, *27*(12), 2363-2372.

Stanley, S. A.; Sarkar, S.; Influence of Nozzle Conditions and Discrete Forcing on Turbulent Planar Jets, *AIAA Journal*, **2000**, *38*(9), 1615-1623.

Tate, B.D.; Shambaugh, R.L. Modified Dual Rectangular Jets for Fiber Production. *Ind. Eng. Chem. Res.*, **1998**, *37*, 3772-3779

Uyttendaele, M.A., Shambaugh, R.L. The Flow Field of Annular Jets at Moderate Reynolds Numbers. *Ind. Eng. Chem. Res.*, **1989**, *28*, 1735-1740.

Voke, P.R.; Shian, G.; Leslie, D. Large-Eddy Simulations of Plane Impinging Jets, *Int. Journal for Num. Meth. in Eng.*, **1995**, *38*, 489-507.

Wang, J.; Priestman, G. H.; Wu, D. An Analytical Solution for Incompressible Flow Through Parallel Multiple Jets, *Journal of Fluids Eng. – Trans. of the ASME*, **2001**, *123*(2), 407-410.

Wente, V. A. Manufacture of Superfine Organic Fibers, Report PB111437, NRL-4364, April 15, 1954; US Department of Commerce, Office of Technical Services, Washington DC.

Wente, V. A. Superfine Themoplastic Fibers, *Ind. Eng. Chem.* **1956**, *48*, 1342.

Table 2-1. Simulation parameters for the numerical experiments for blunt and flush dies. The computational time designated as P-IV refers to a 1.7 GHz Pentium IV computer and the computational time designated as 2P-II refers to a dual 800MHz Pentium III computer.

Die type	V_{jo} (m/s)	Number of grid cells	Iterations to convergence	Computational time (hours)
45° blunt	14.13	348142	27165	169 P-IV
50° blunt	15.3	338097	37544	227 P-IV
60° blunt	17.3	339301	27373	166 P-IV
60° blunt	34.6	339301	23683	144P-III
70° blunt	18.77	347246	41167	256 P-IV
45° sharp	14.13	254288	28440	174, 2P-III
50° sharp	17.3	259803	23429	83, 2P-III
60° sharp	17.3	246392	45060	276, 2P-III
70° sharp	17.3	248440	41791	256, 2P-III
70° sharp	34.6	248440	25477	156, 2P-III

Table 2-2. Summary of the problem configuration and the computational requirements for each numerical experiment for the simulation of the inset and outset sharp dies.

Die Type	*a*	Number of cells	Number of iterations	CPU Time (hours)
Inset	$-b_o/4 = -0.1625$ mm	112,000	27,892	18:10
Inset	$-b_o/2 = -0.325$ mm	112,657	28,597	18:30
Inset	$-b_o = -0.65$ mm	113,952	28,337	21:00
Inset	$-5b_o/4 = -0.8125$ mm	112,342	34,020	23:45
Outset	$b_o/4 = 0.1625$ mm	111,418	43,542	29:50
Outset	$b_o/2 = 0.325$ mm	109,789	30,640	21:15
Outset	$b_o = 0.65$ mm	110,011	29,691	20:50
Outset	$5b_o/4 = 0.8125$ mm	109,137	30,173	20:00
Outset	$3b_o/2 = 0.975$ mm	110,581	29,598	21:20

Table 2-3. Results of regression analysis for the dual jet problem with Equation 2-2.

Die type	c_1	**Exponent**	**Method**
60° blunt	1.4	-0.61	Laboratory, HS
60° blunt	1.24	-0.5	HS fit with Equation (2-1)
60° blunt	1.8118	-0.6969	Present CFD work
70° sharp	3.09	-0.635	Laboratory, TS
70° sharp	3.1222	-0.6285	Present CFD work
60° sharp	2.88	-0.532	Laboratory, TS
60° sharp	3.3252	-0.6385	Present CFD work

Table 2-4. Coefficients in Equation (2-7) for the inset and outset die configurations examined in this work.

Die Type	***a***	c_1	***m***	R^2
Inset	$-5b_o/4$ = -0.8125 mm	8.4989	-0.6195	0.9996
Inset	$-b_o$ = -0.65 mm	7.3297	-0.6403	0.999
Inset	$-b_o2$ = -0.325 mm	6.2589	-0.6466	0.999
Inset	$-b_o/4$ = -0.1625 mm	6.0333	-0.6533	0.998
Flush	0 mm	5.5037	-0.6385	0.9996
Outset	$b_o/4$ = 0.1625 mm	5.1988	-0.6232	0.9988
Outset	$b_o/2$ = 0.325 mm	5.4609	-0.6429	0.9967
Outset	b_o = 0.65 mm	5.3653	-0.6418	0.9957
Outset	$5b_o/4$ = 0.8125 mm	5.0143	-0.6206	0.9965
Outset	$3b_o/2$ = 0.975 mm	5.3595	-0.6427	0.9948

Table 2-5. Calculated coefficients for Equation (2-14)

Die Type	***e***	***f***
Blunt-Flush	1.118	0.5681
Sharp-Flush	1.201	0.5799
Sharp-Inset	1.277	0.5590
Sharp-Outset	1.257	0.6394

Table 2-6. Number of Cells, Number of Iterations, and Approximate Running Time

Die Type	**Angle**	**Number of Cells**	**Non-Isothermal Iterations**	**Non-Isothermal Computational Time (hrs)**
Blunt	45	112,909	24,441	31:50:00
Blunt	50	112,770	25,630	33:30:00
Blunt	60	112,514	26,191	35:20:00
Blunt	70	112,386	24,280	26:40:00
Sharp	45	110,187	58,288	62:10:00
Sharp	50	109,931	85,550	71:10:00
Sharp	60	109,675	36,630	39:40:00
Sharp	70	109,547	34,930	35:30:00

Table 2-7. Root Mean Squared (RMS) Error for Velocity and Temperature for Pr_t = 0.30, 0.35, and 0.40

	Pr_t = 0.30			**Pr_t = 0.35**			**Pr_t = 0.40**
	V_{jo}= 23.2 m/s	**V_{jo}= 35 m/s**	**Average RMS Error**	**V_{jo}=23.2 m/s**	**V_{jo}=35 m/s**	**Average RMS Error**	**V_{jo}=23.2 m/s**
Error for V_o/V_{jo}	0.067	0.075	0.071	0.065	0.033	0.049	0.048
Error for Θ_o/Θ_{jo}	0.005	0.006	0.0056	0.014	0.108	0.061	0.047

Table 2-8. Reynolds stress model parameters available in the Fluent™ software, and modifications made to agree with the experimental results

	C_μ	$C_{\varepsilon 1}$	$C_{\varepsilon 2}$	C_{1ps}	C_{2ps}	C'_{1ps}	C'_{2ps}	σ_k	σ_ε	Pr_t	Wall Pr_t
Default	0.09	1.44	1.92	1.8	0.6	0.5	0.3	1	1.3	0.85	0.85
Isothermal	0.09	1.24	2.05	1.8	0.6	0.5	0.3	1	1.3	N/A	N/A
Non-isothermal	0.09	1.30	2.05	1.8	0.6	0.5	0.3	1	1.3	0.3	0.85

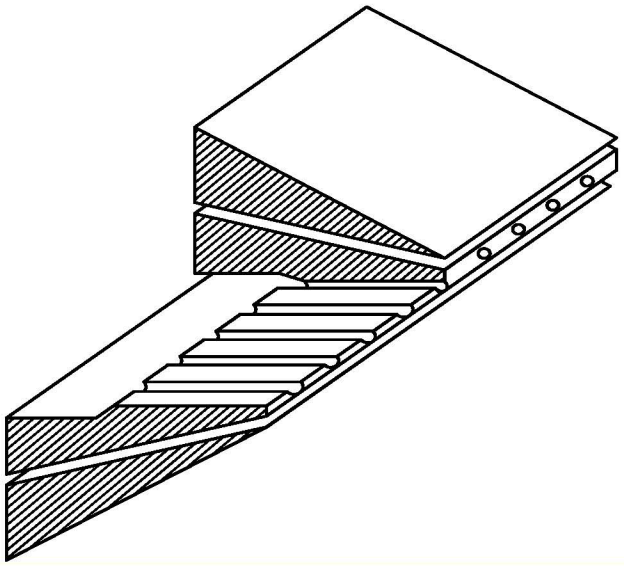

Figure 2-1. Exxon slot melt blowing die with partial cutout

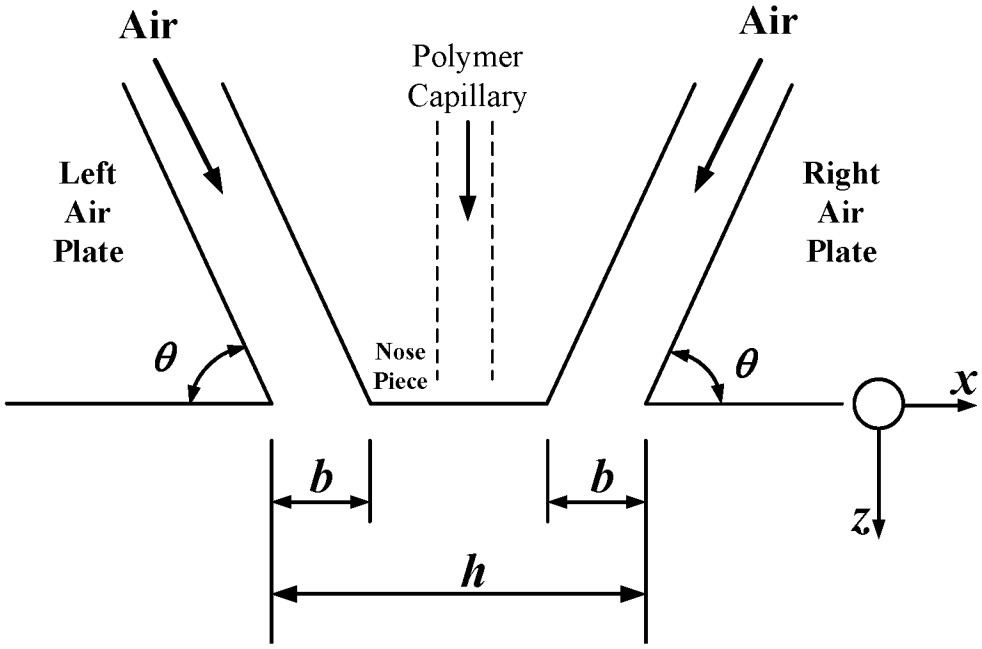

Figure 2-2. Cross Section of Exxon slot melt blowing die

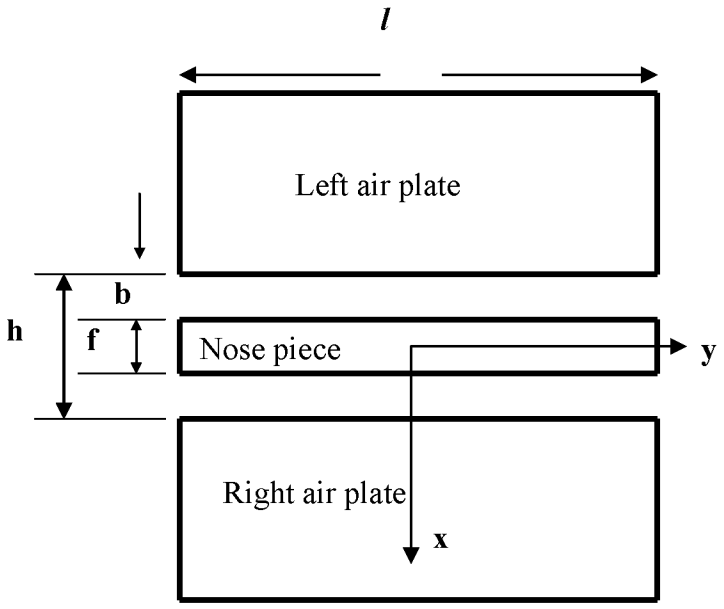

Figure 2-3. Bottom View of Exxon slot melt blowing die

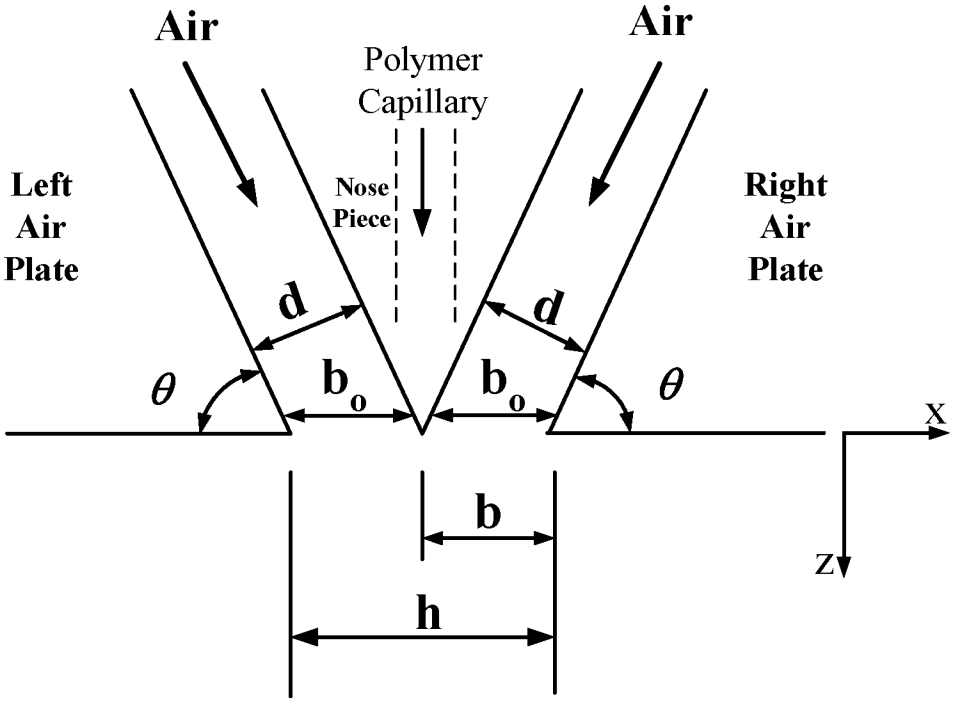

Figure 2-4. Cross section of a sharp slot melt blowing die

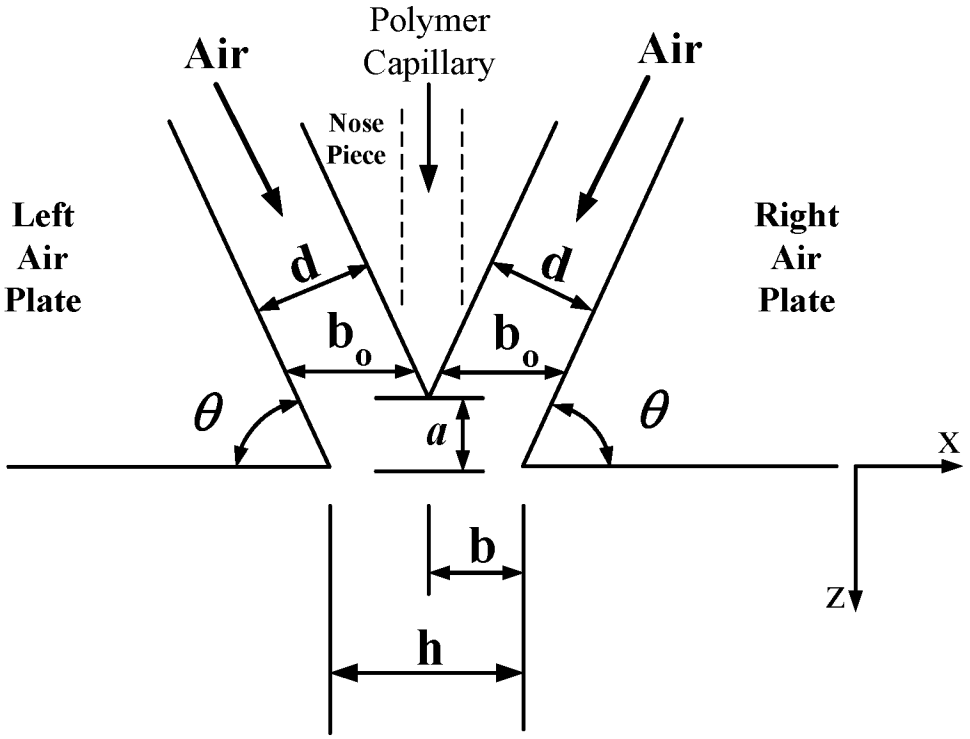

Figure 2-5. Cross section of an inset sharp slot die

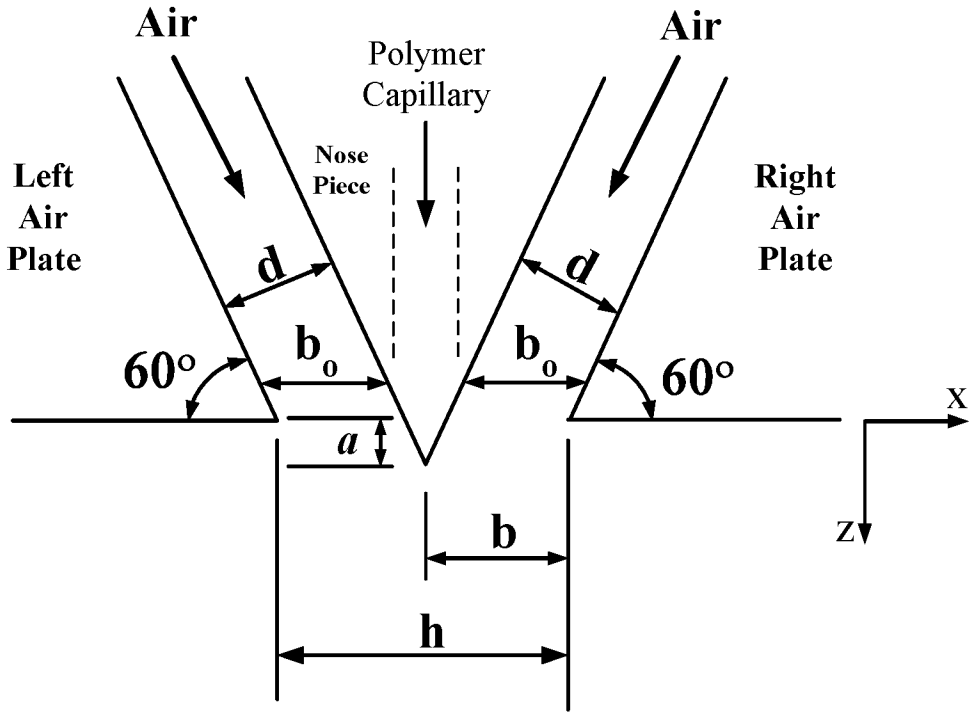

Figure 2-6. Cross section of an outset sharp slot die

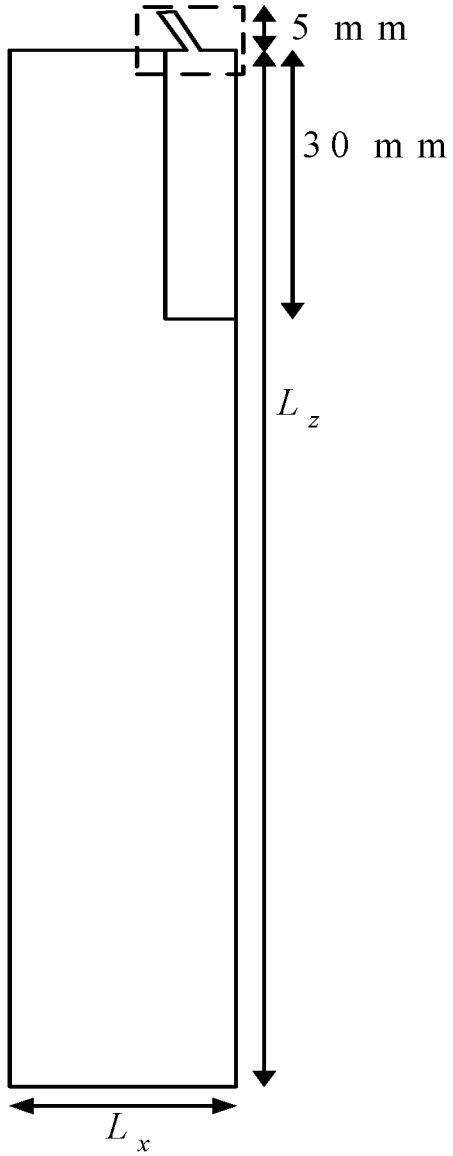

Figure 2-7a. Computational domain for blunt dies and sharp flush dies

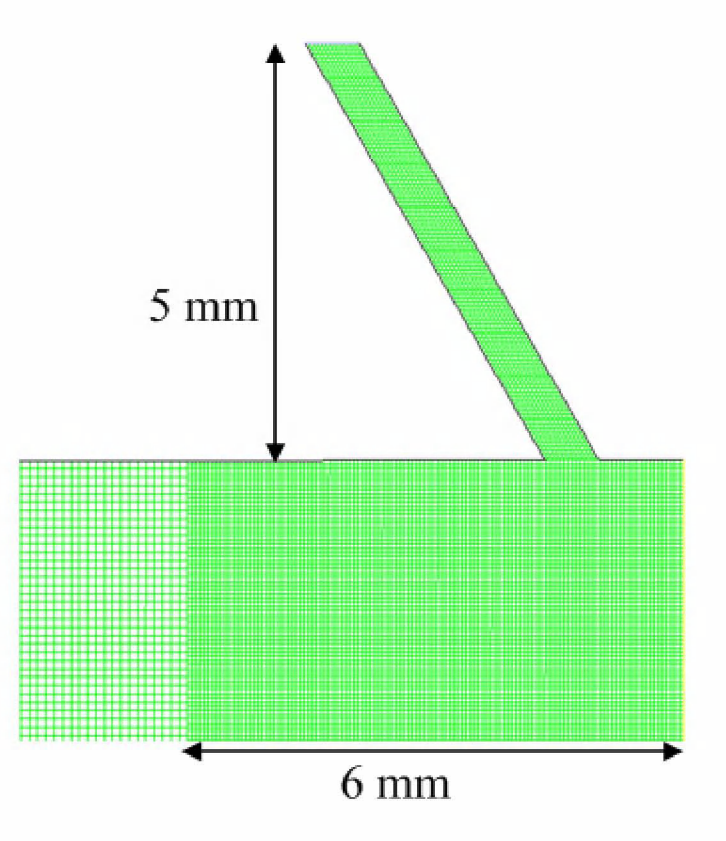

Figure 2-7b. Grid close to the inlet

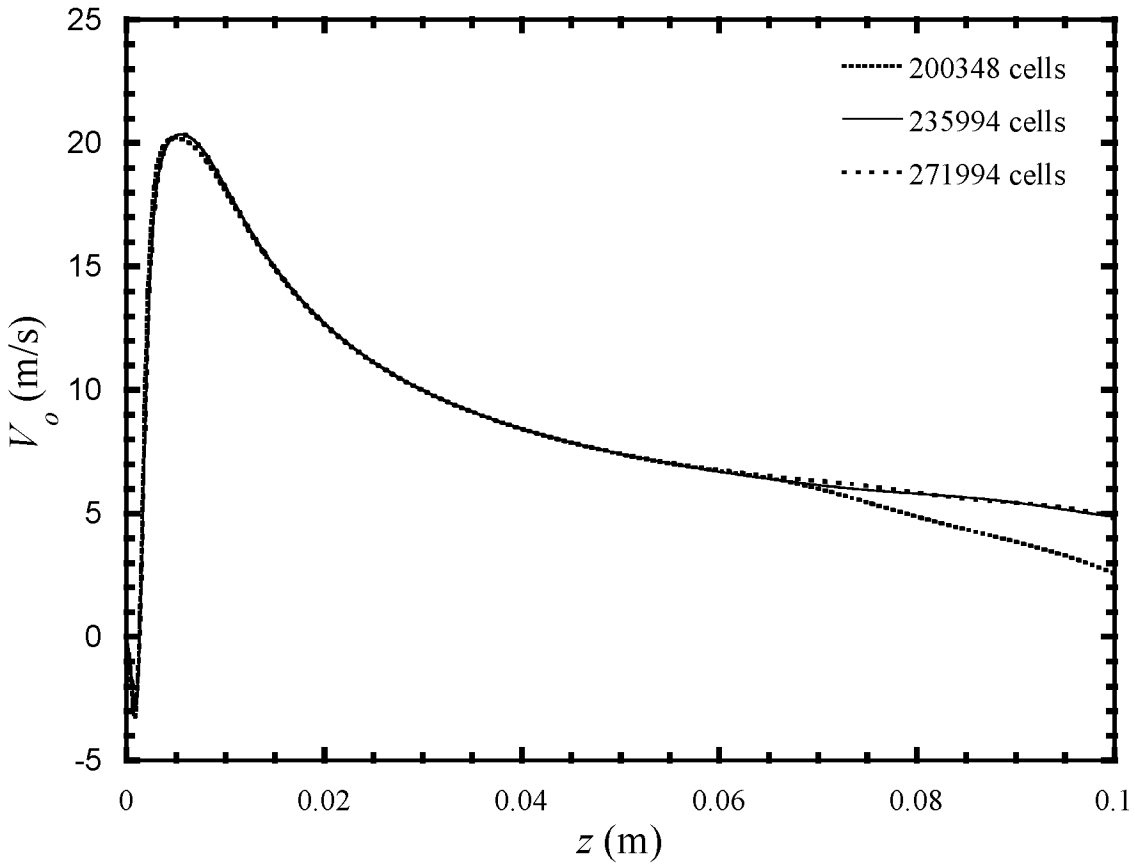

Figure 2-8. Comparison of simulated centerline velocity for blunt die configurations and different grid refinements

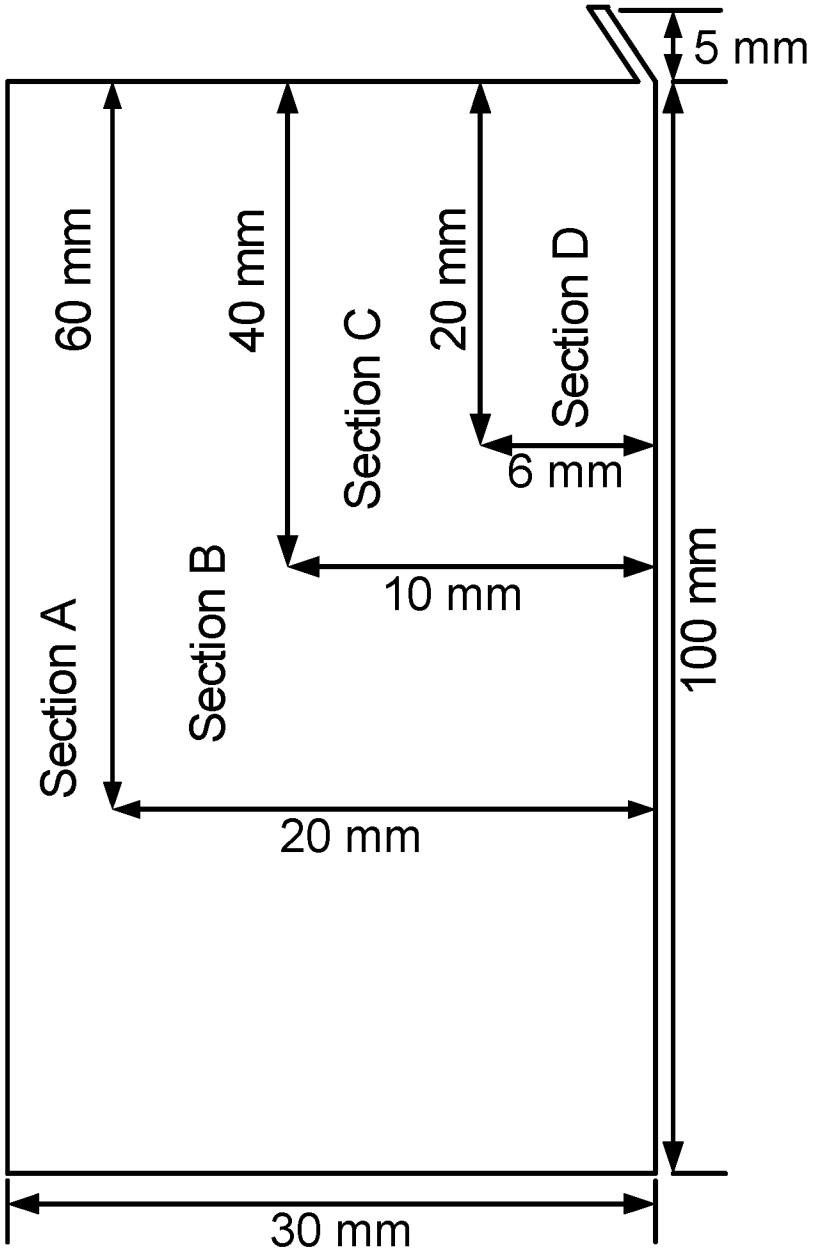

Figure 2-9. Computational domain and grid refinements regions used for inset and outset sharp dies.

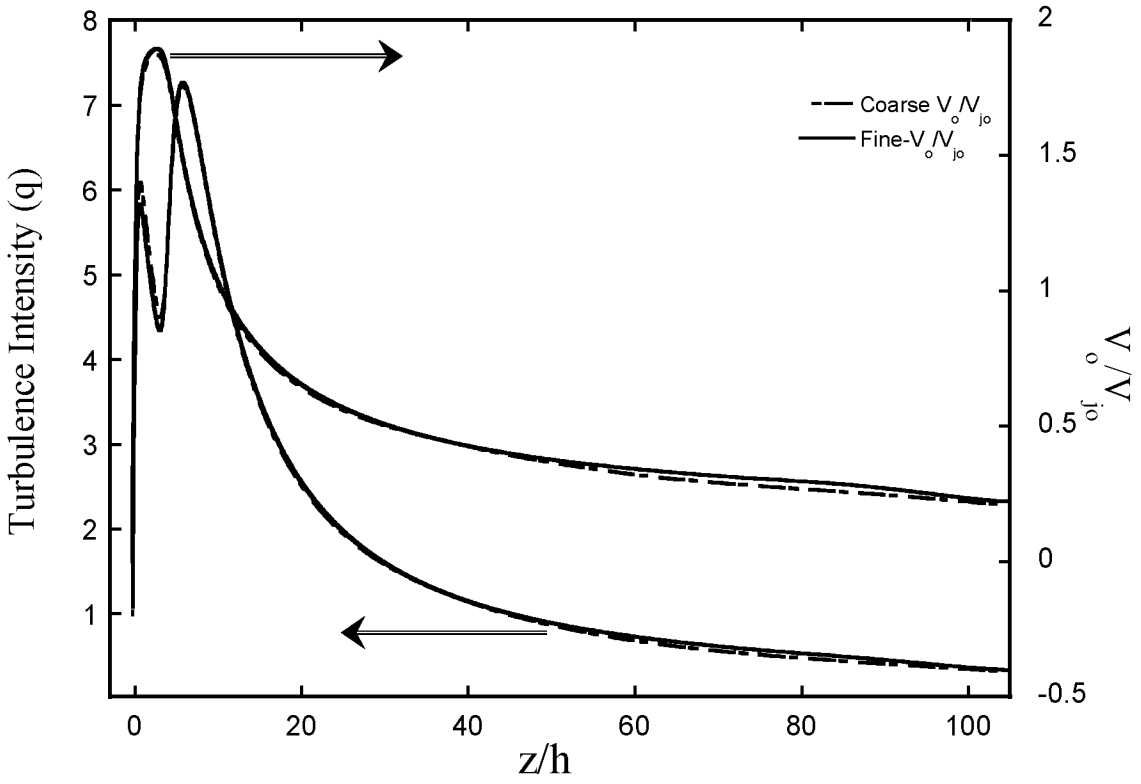

Figure 2-10. Turbulence intensity and velocity decay for different grid resolutions for inset die with $a = -b_o/2$.

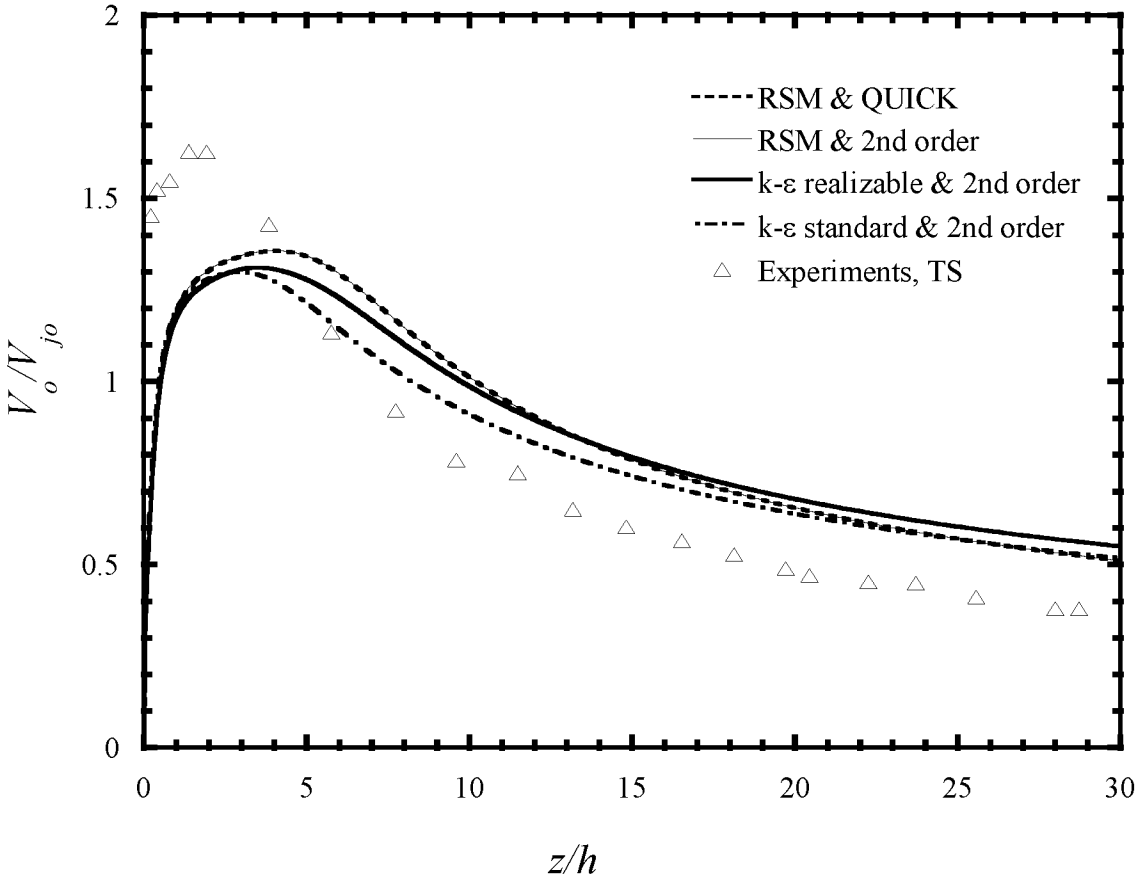

Figure 2-11. Dimensionless *z*-velocity along the centerline for different turbulence models with the experimental results of TS for a 70° sharp die.

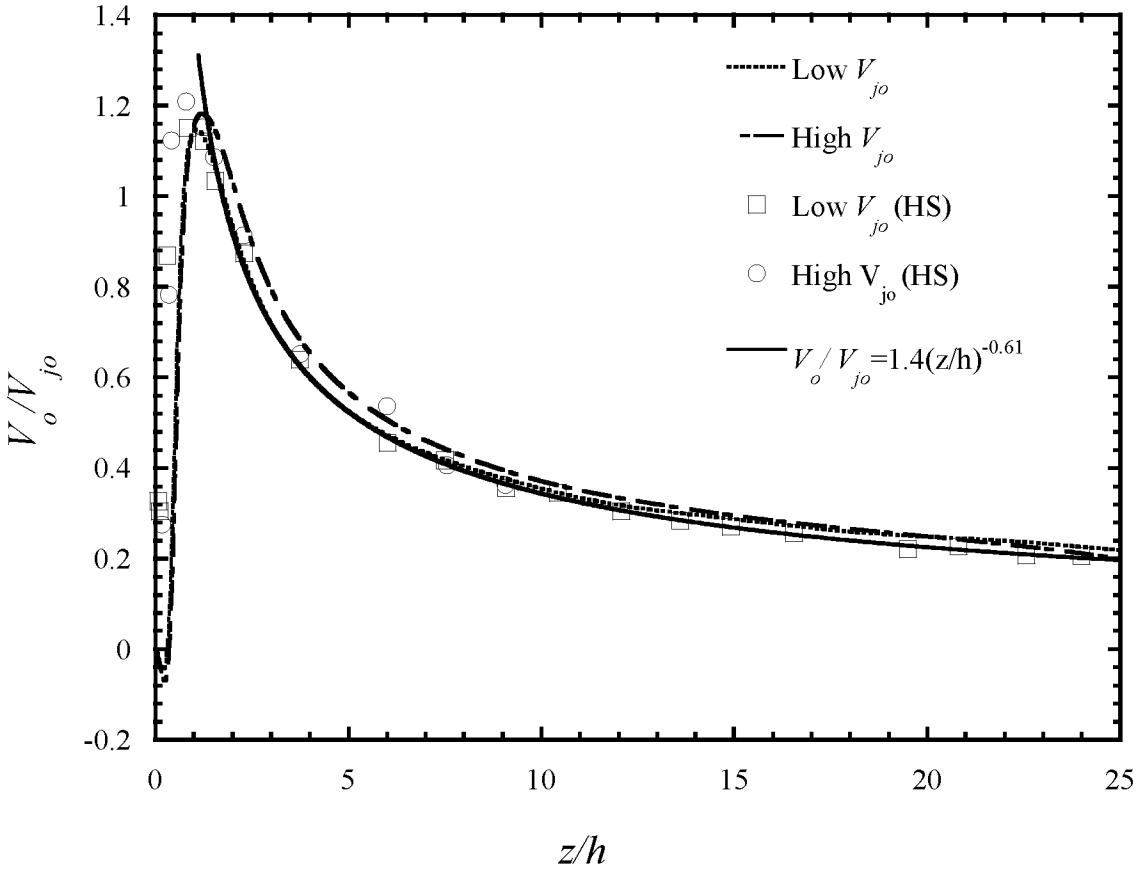

Figure 2-12a. Dimensionless velocity decay along the line of symmetry resulting from the simulation, the empirical decay equations of HS, and the laboratory results for a 60° blunt die geometry. The low V_{jo} is 17.3 m/s and the high V_{jo} is 34.6 m/s.

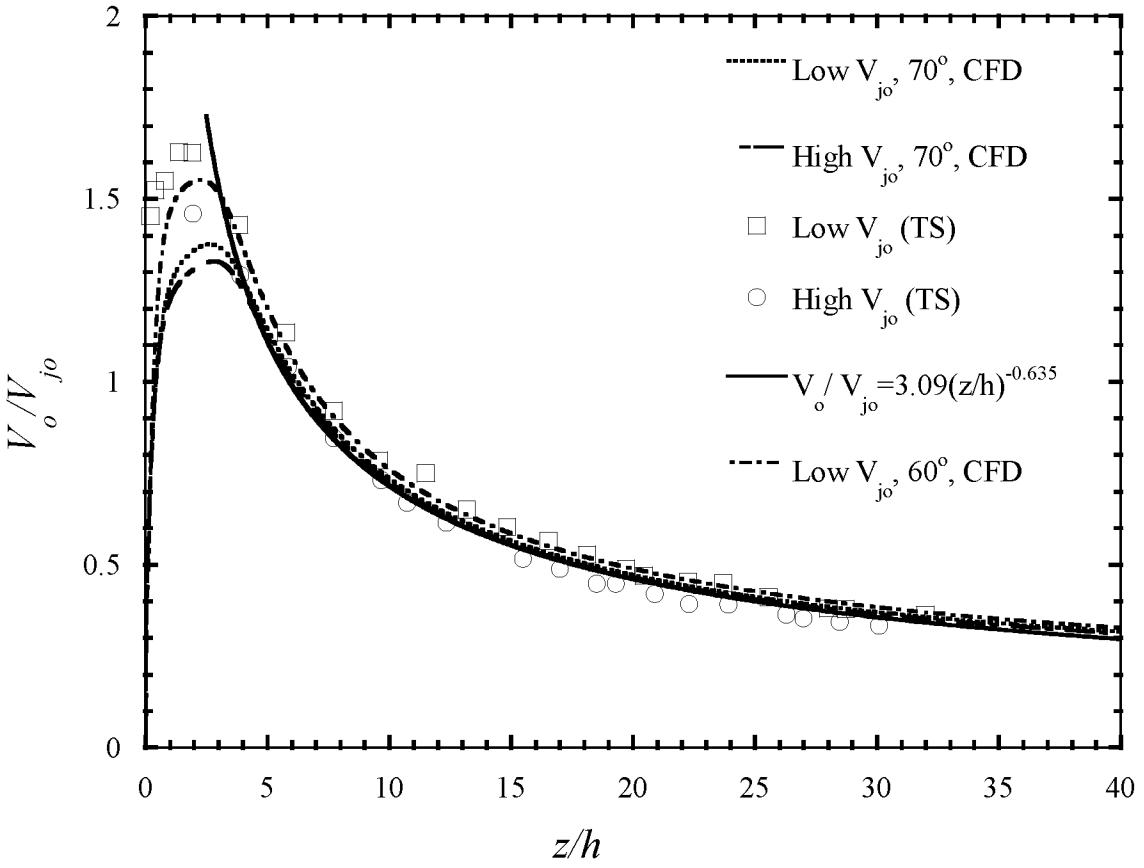

Figure 2-12b. Dimensionless velocity decay along the line of symmetry resulting from the simulation, the empirical decay equations of TS, and the laboratory results for a 70° sharp die geometry. The low V_{jo} is 17.3 m/s and the high V_{jo} is 34.6 m/s.

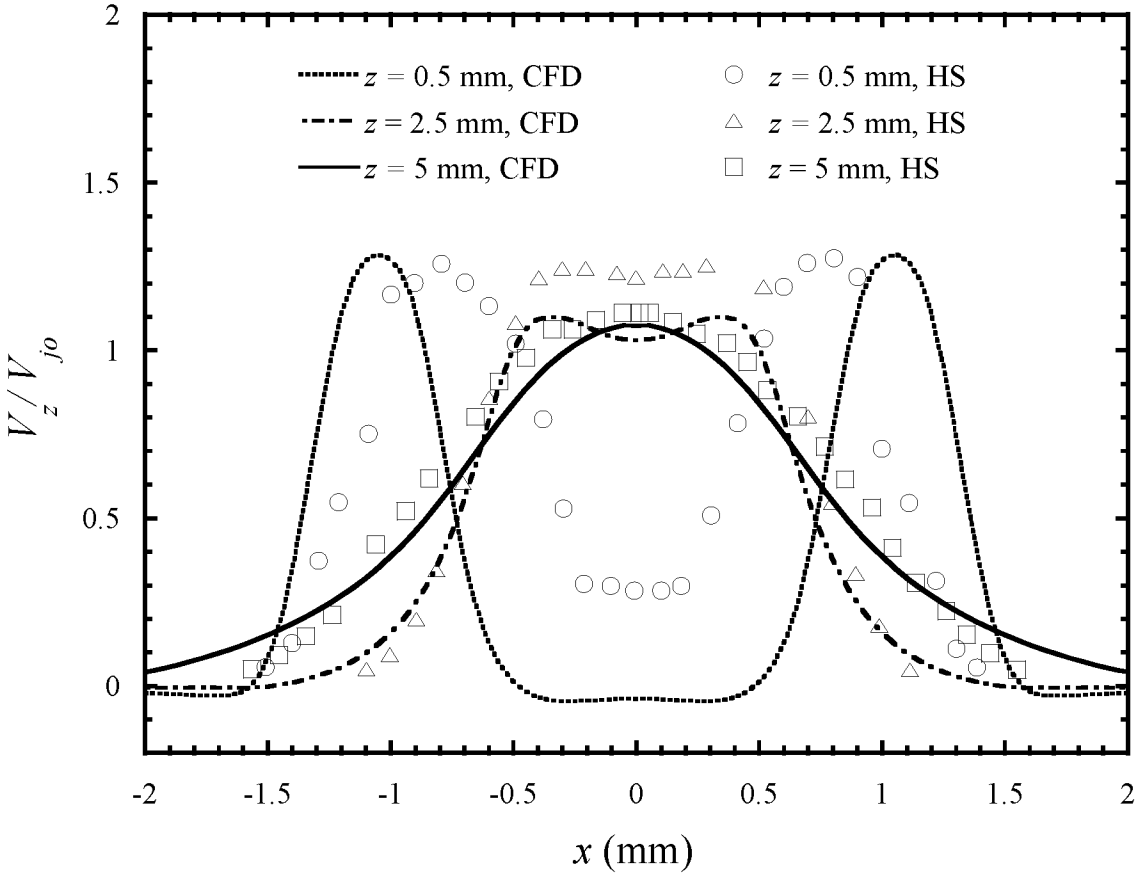

Figure 2-13a. Dimensionless velocity close to the die face; experimental measurements and CFD results for the 60° blunt die geometry.

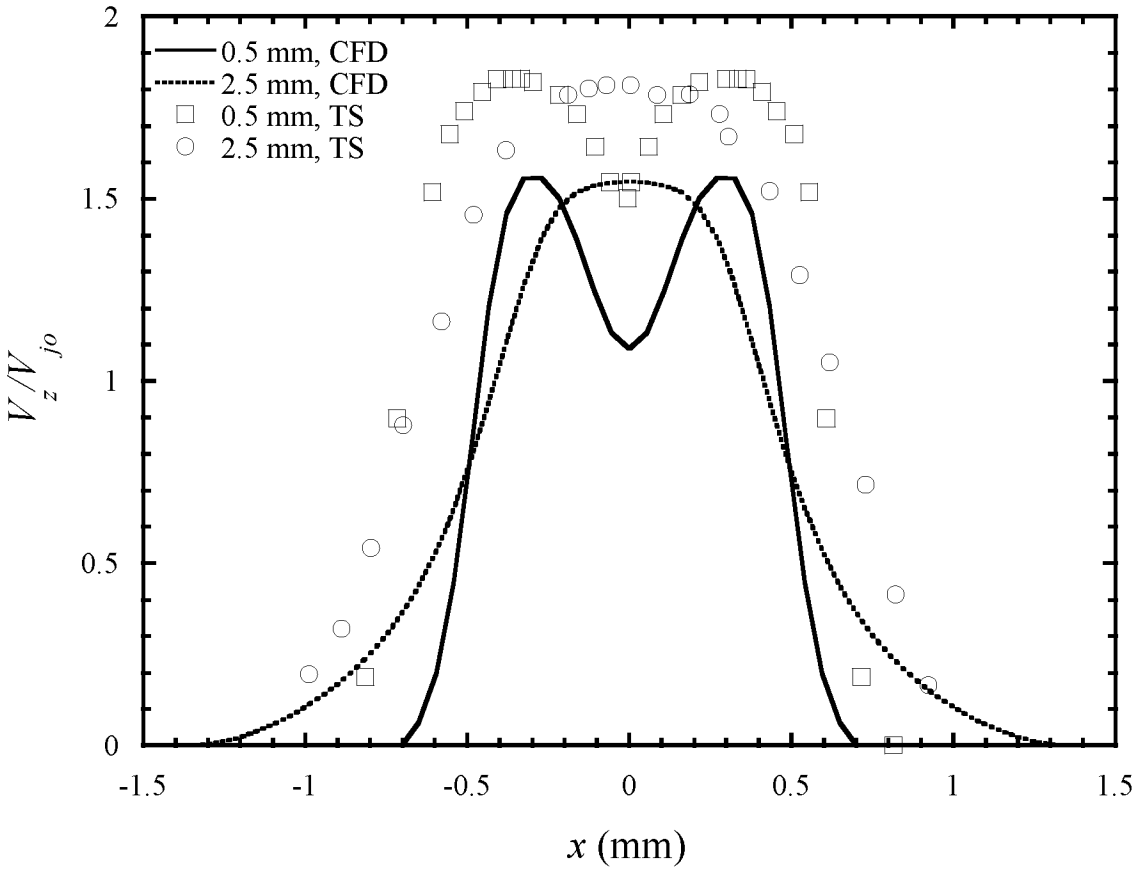

Figure 2-13b. Dimensionless velocity to the die face; experimental measurements and CFD results for the 70° sharp die geometry.

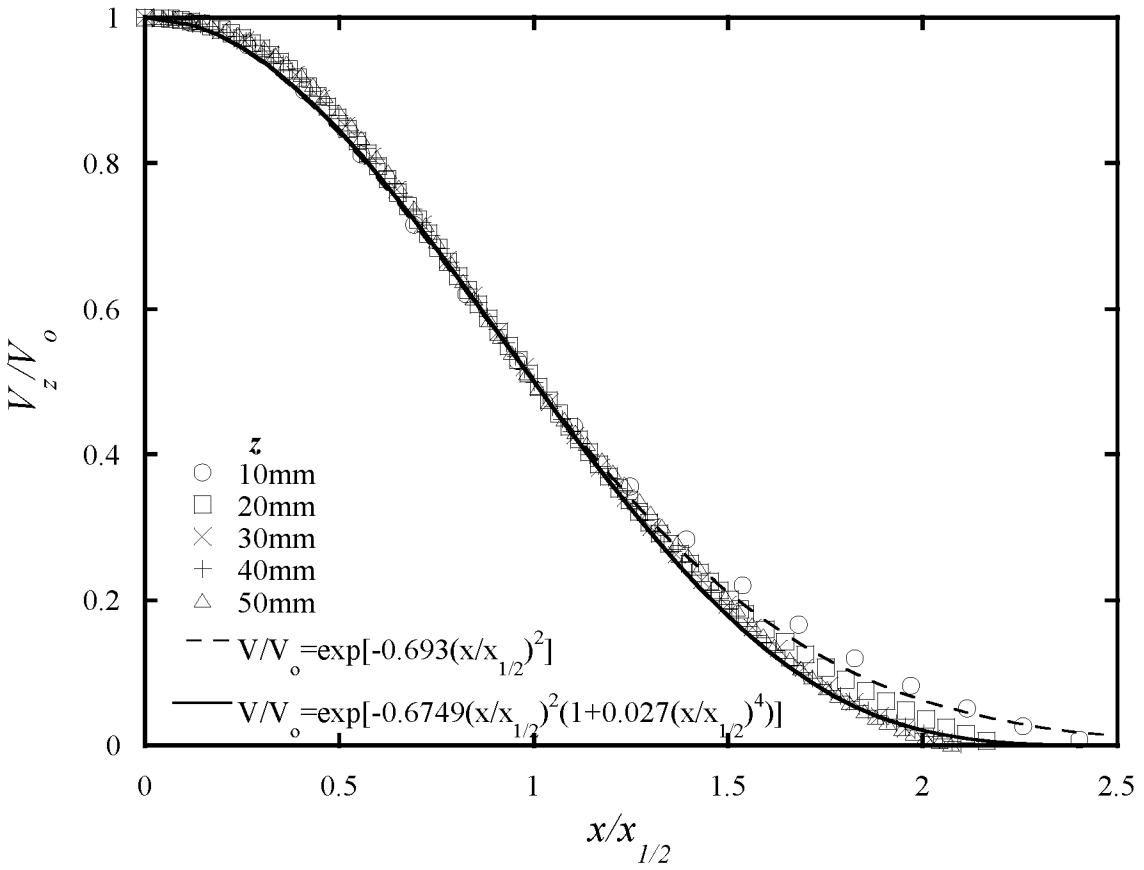

Figure 2-14. Dimensionless velocity profiles within the self-similar region below the die.

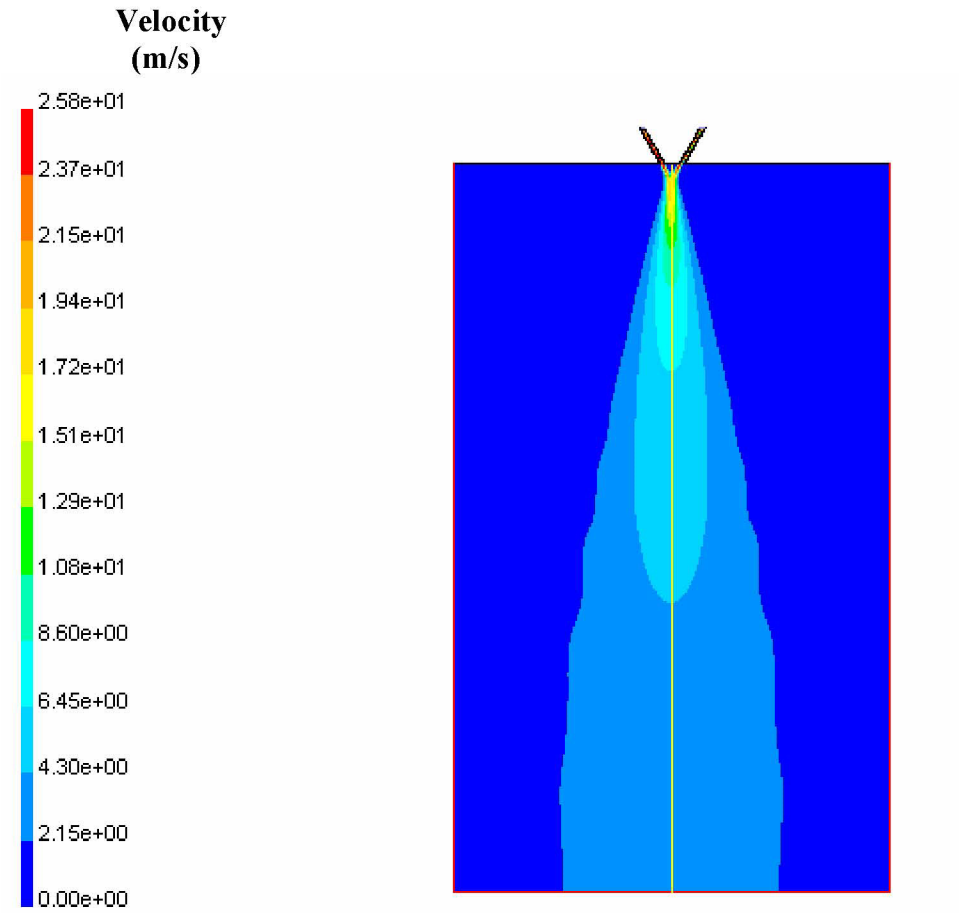

Figure 2-15a. Typical total velocity magnitude (i.e. $|V|$) contours for the flow field resulting from the simulation. The case depicted here is for a 60° blunt die with V_{jo} = 17.3 m/s, RSM, and second-order discretization for the whole computational domain.

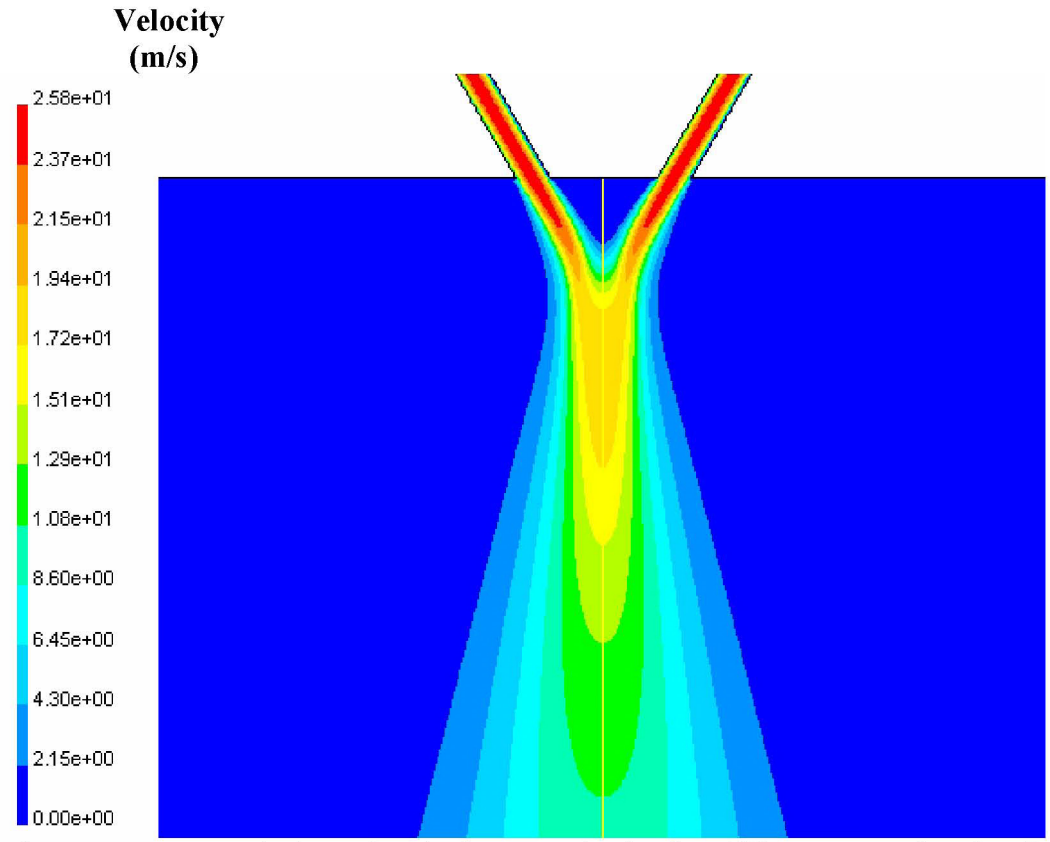

Figure 2-15b. Typical total velocity magnitude (i.e. $|V|$) contours for the flow field resulting from the simulation. The case depicted here is for a 60° blunt die with V_{jo} = 17.3 m/s, RSM, and second-order discretization; this contour plot is close to the die face.

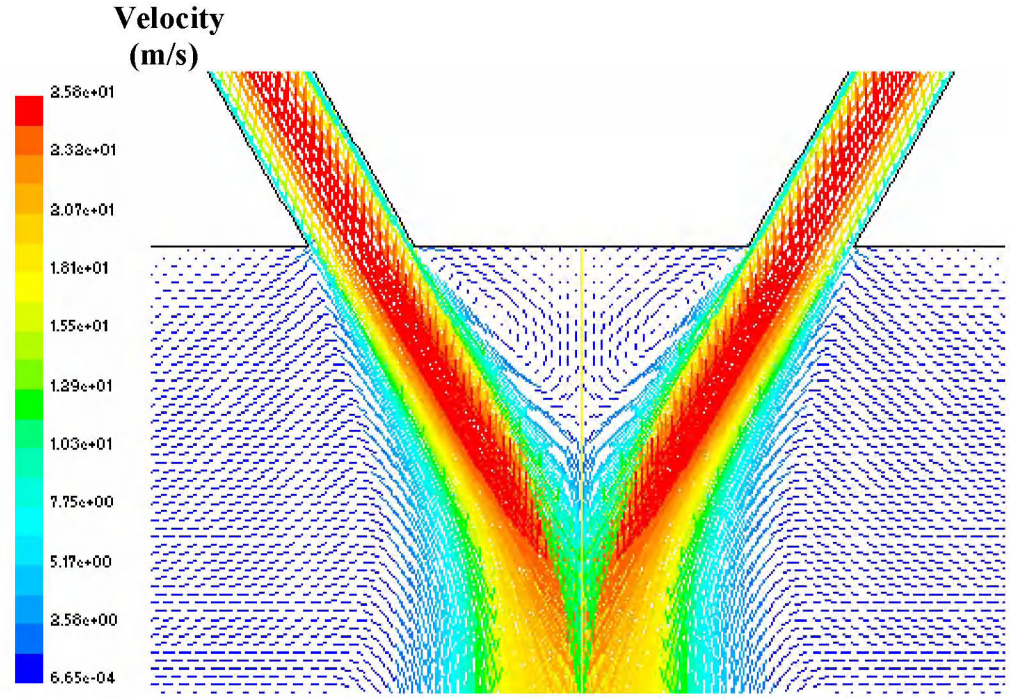

Figure 2-16. Velocity vector field close to the 60° blunt die face. An area of flow recirculation is seen between the two converging jets. The Figure shows an area below the die face that is 8.8 mm wide by 5.3 mm high.

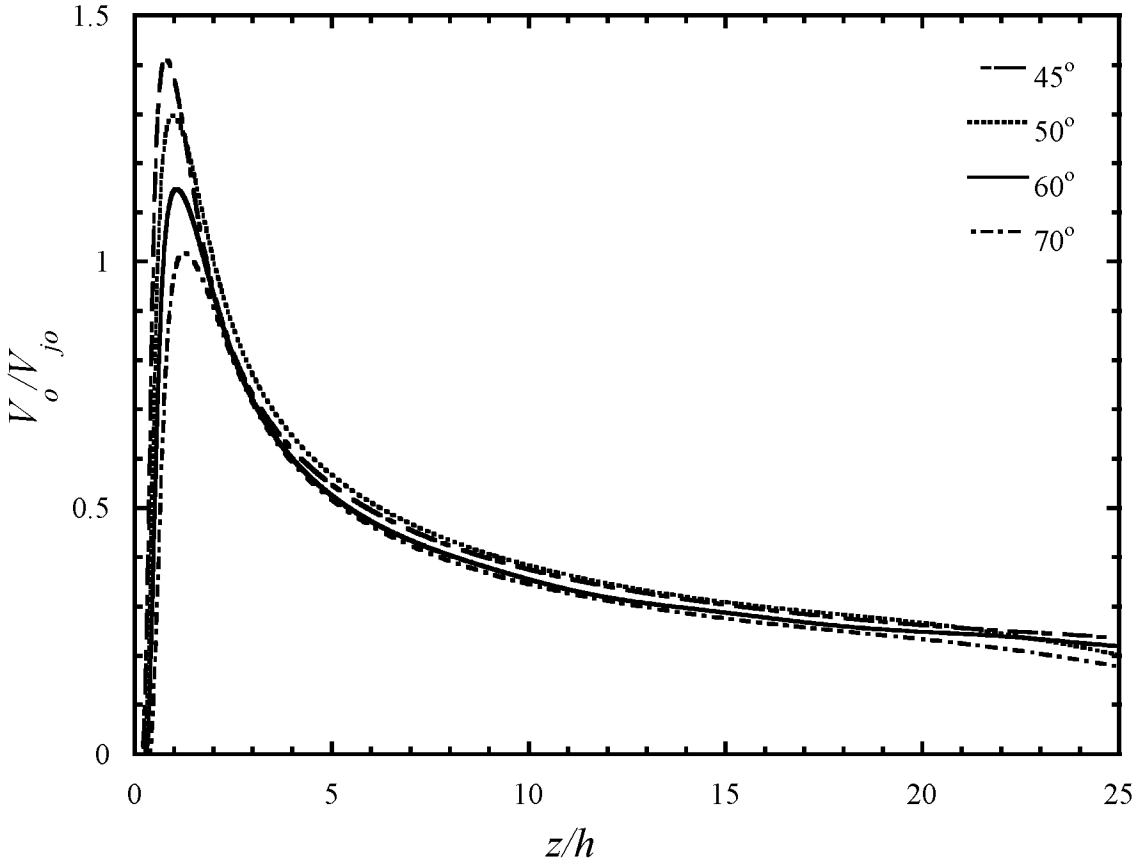

Figure 2-17a. Mean dimensionless velocity along the centerline for different die angles for blunt die configurations.

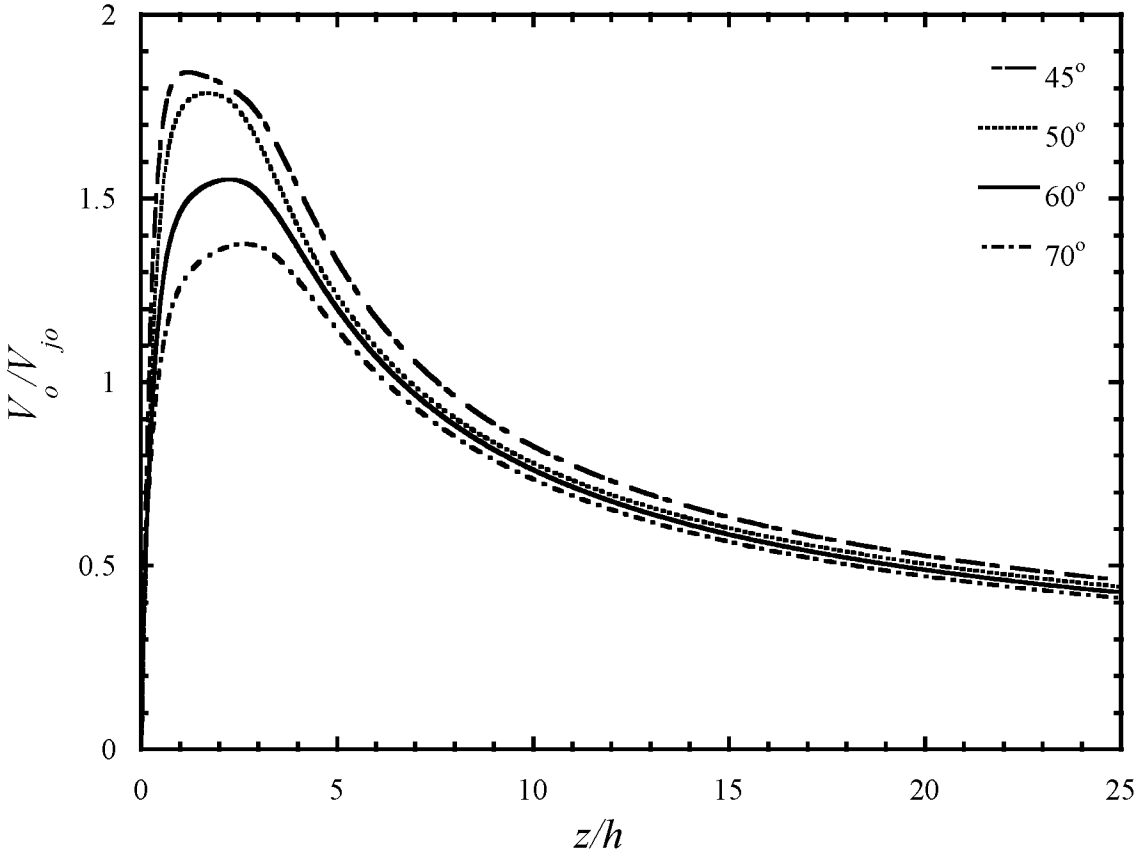

Figure 2-17b. Mean dimensionless velocity along the centerline for different die angles for sharp die configurations.

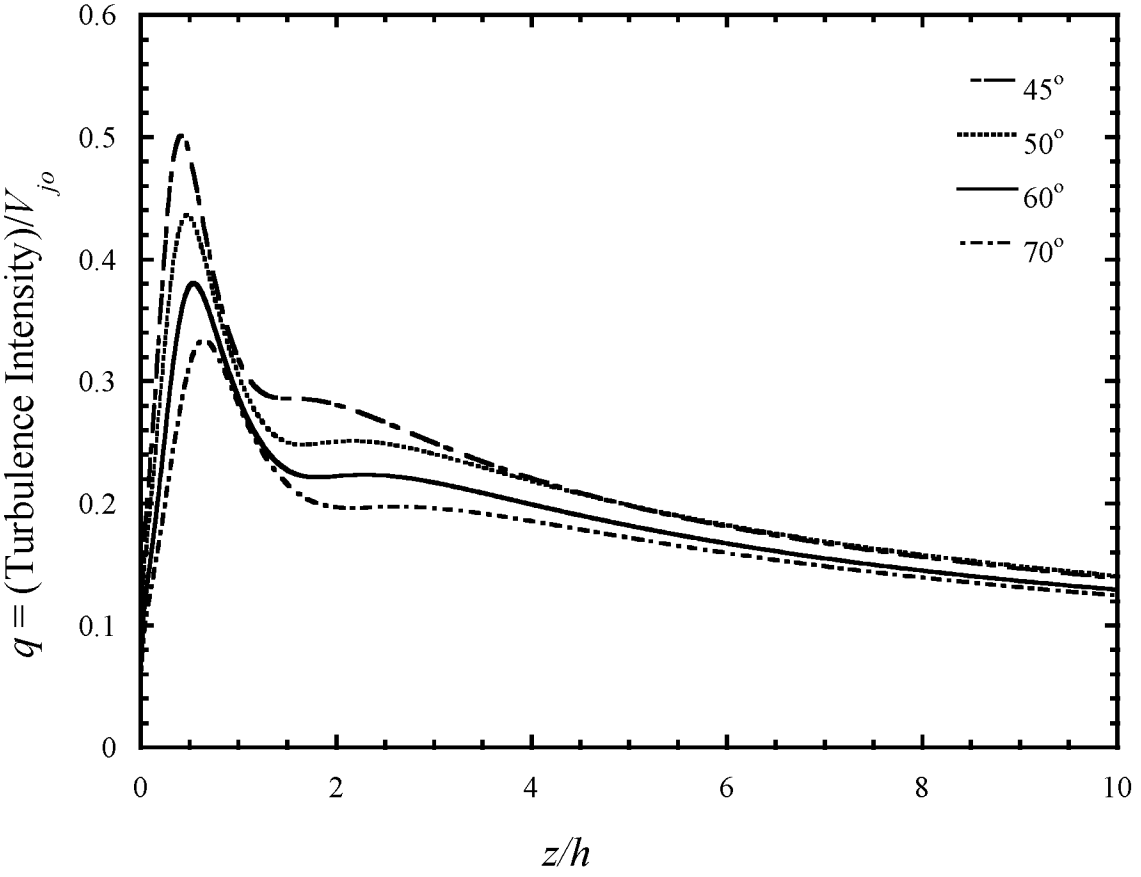

Figure 2-18a. Dimensionless turbulence intensity along the centerline for different die angles for blunt die geometries.

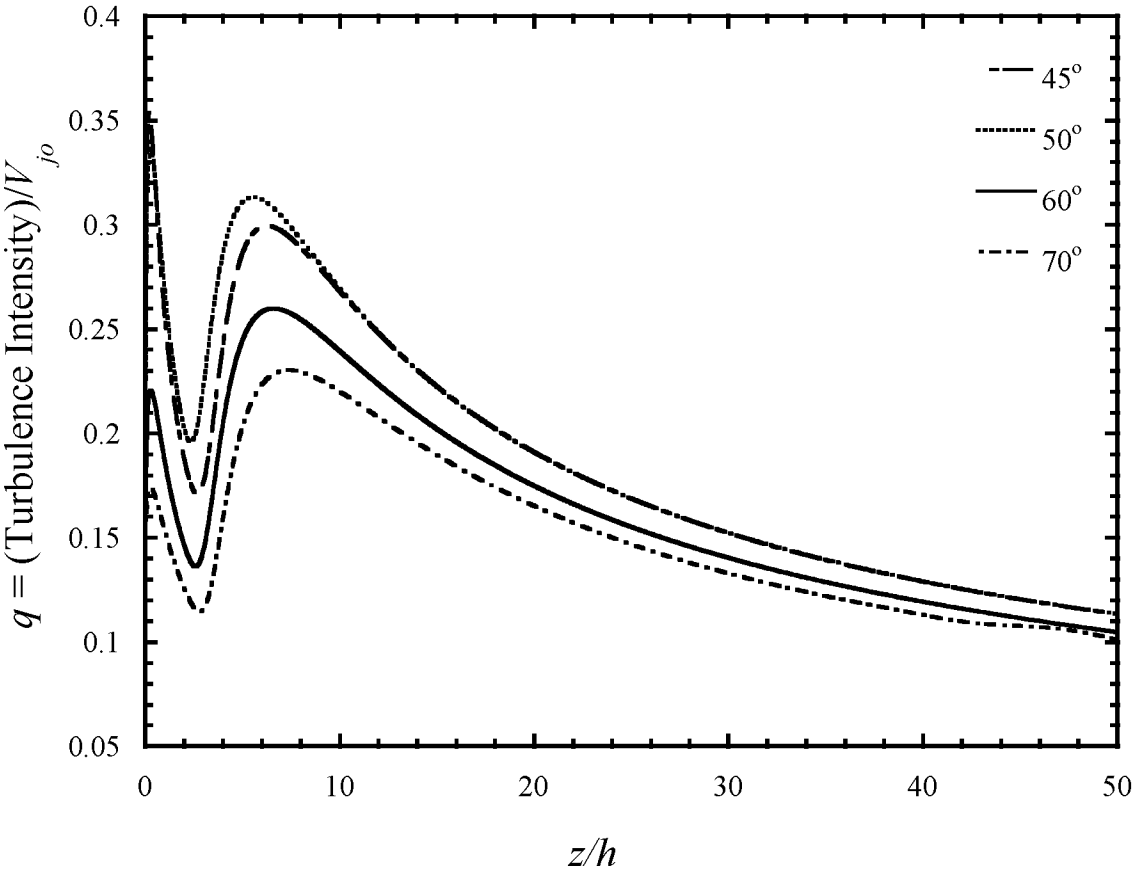

Figure 2-18b. Dimensionless turbulence intensity along the centerline for different die angles for sharp die geometries.

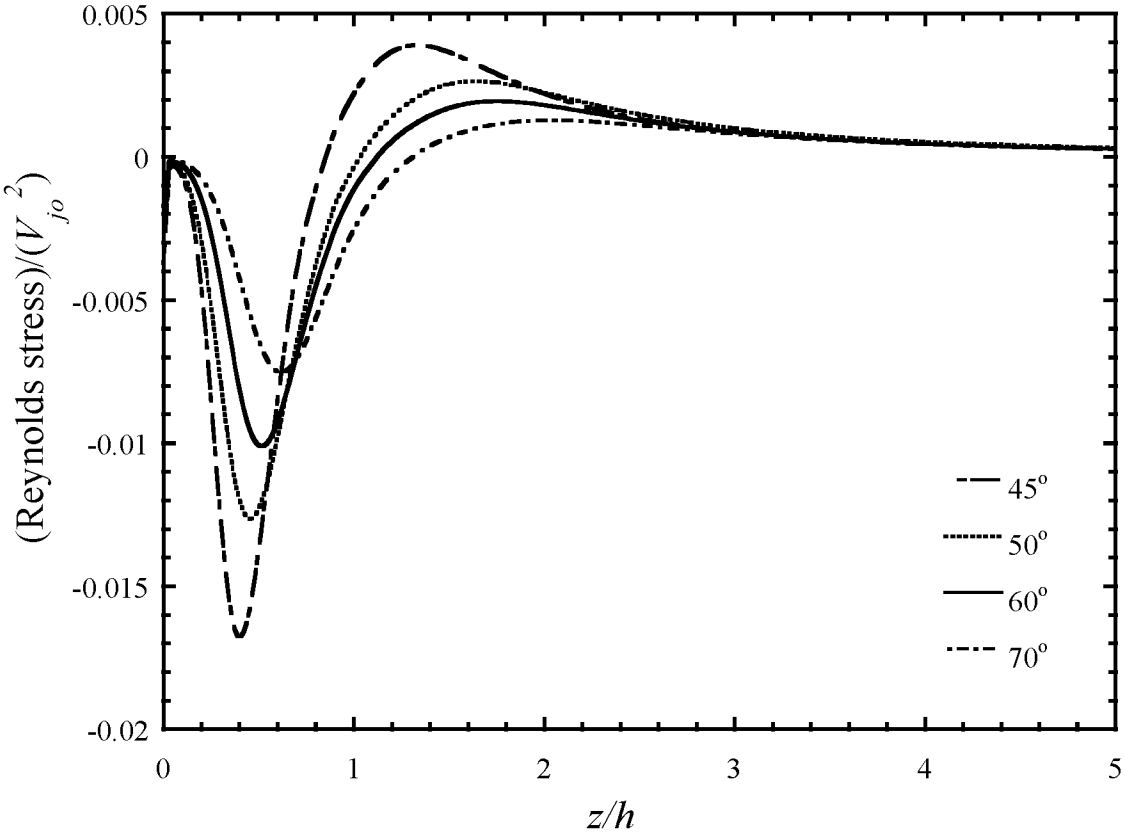

Figure 2-19a. Dimensionless Reynolds stress along the centerline for different die angles for blunt die geometries.

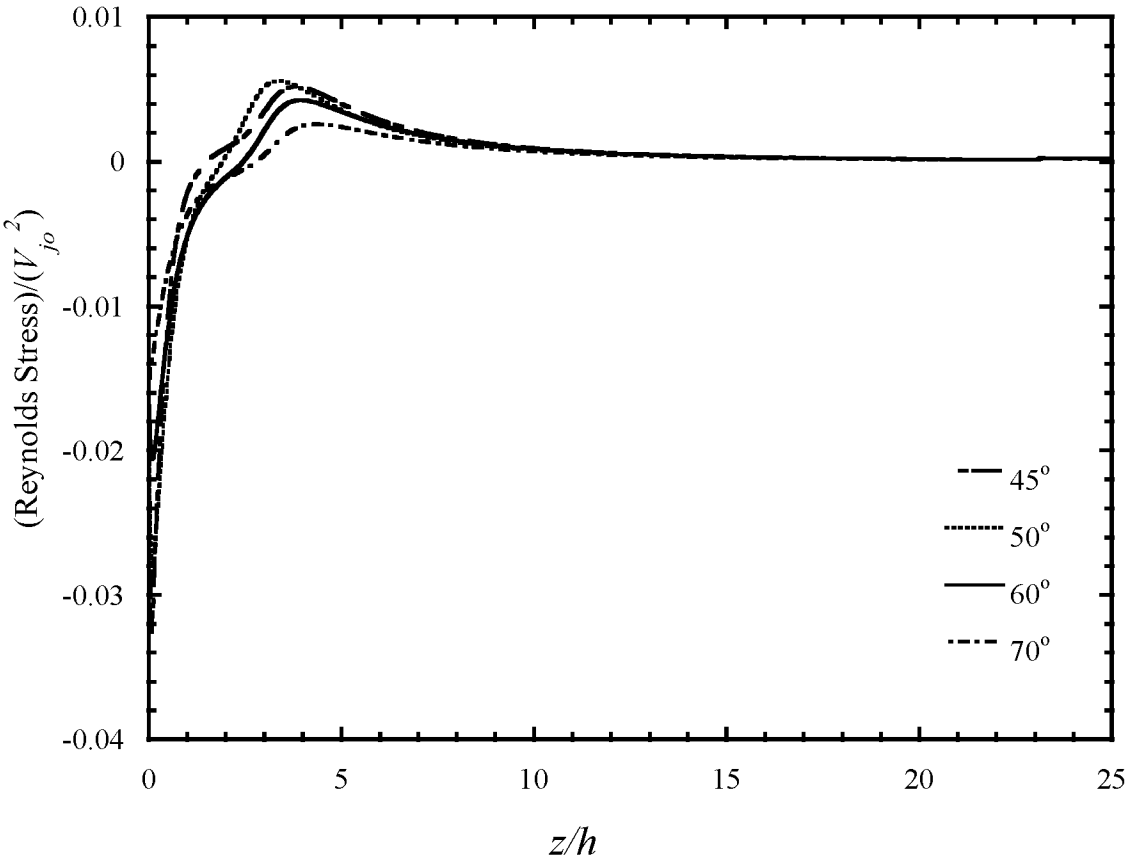

Figure 2-19b. Dimensionless Reynolds stress along the centerline for different die angles for sharp die geometries.

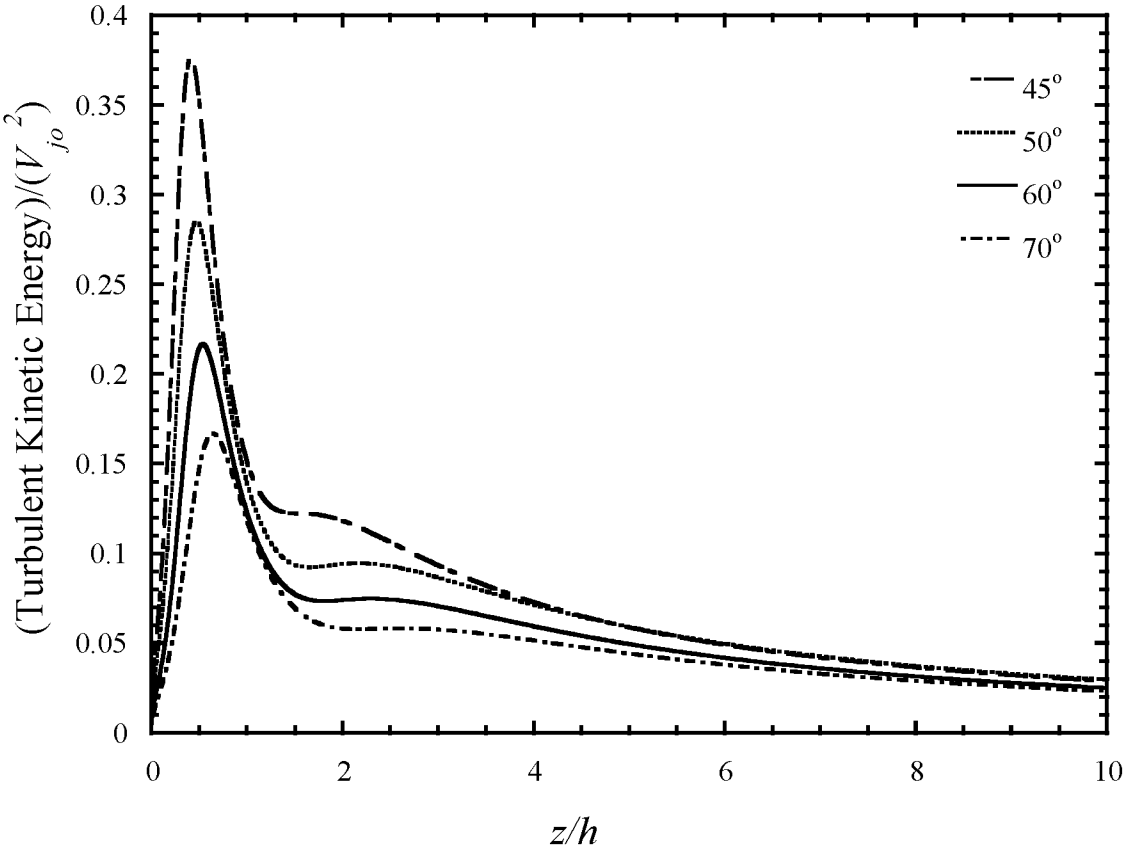

Figure 2-20a. Dimensionless turbulent kinetic energy along the centerline for different die angles for blunt die geometries.

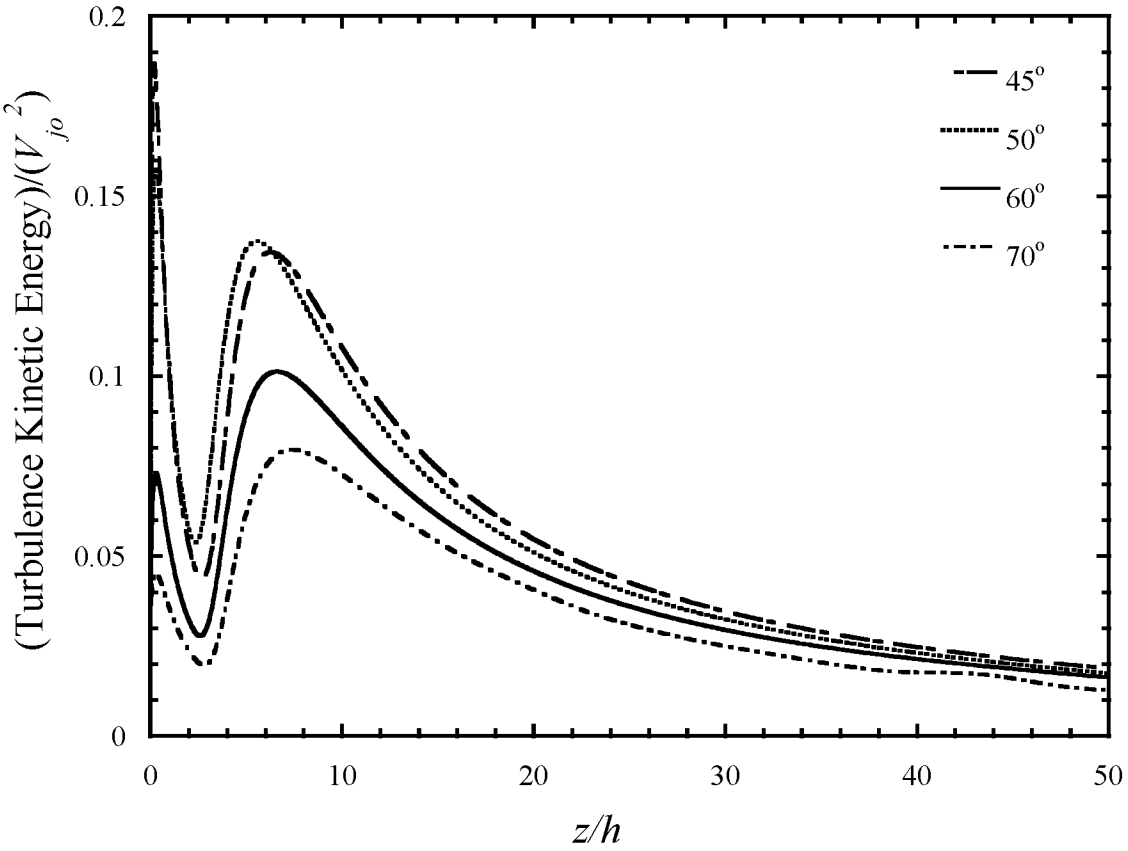

Figure 2-20b. Dimensionless turbulent kinetic energy along the centerline for different die angles for sharp die geometries.

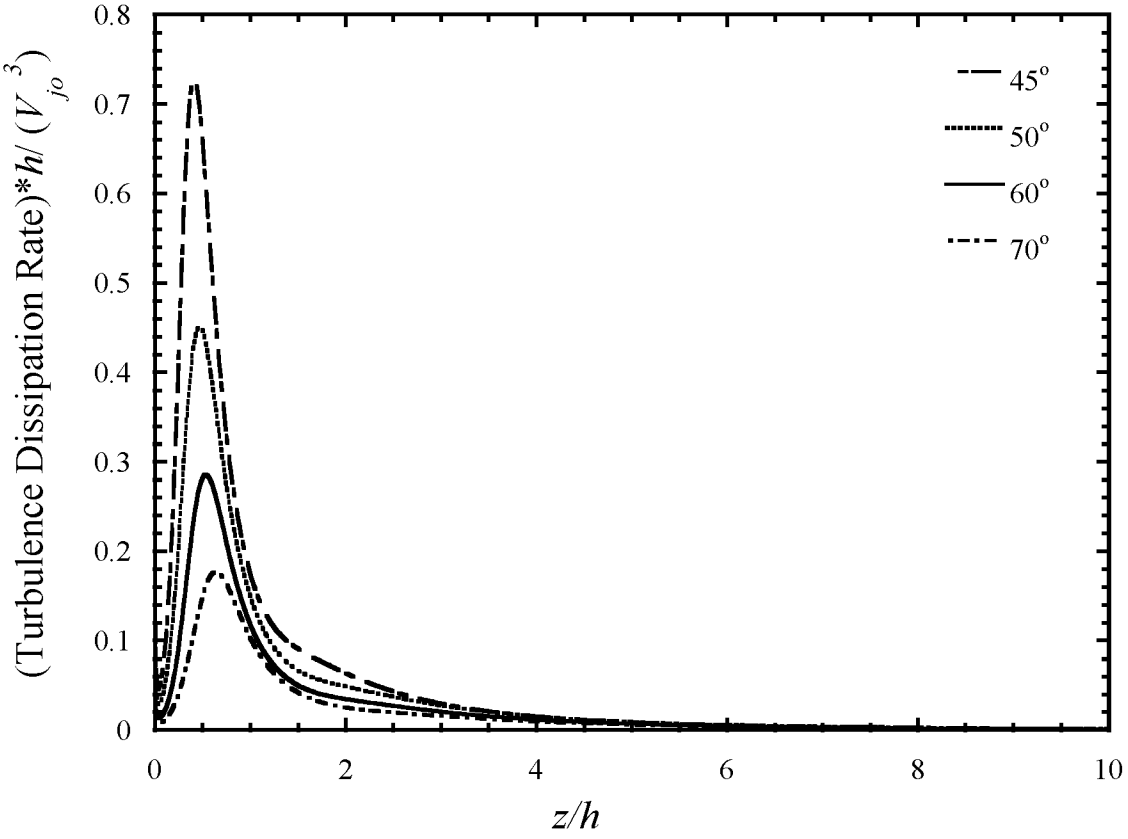

Figure 2-21a. Dimensionless turbulence dissipation rate along the centerline for different die angles for blunt die geometries.

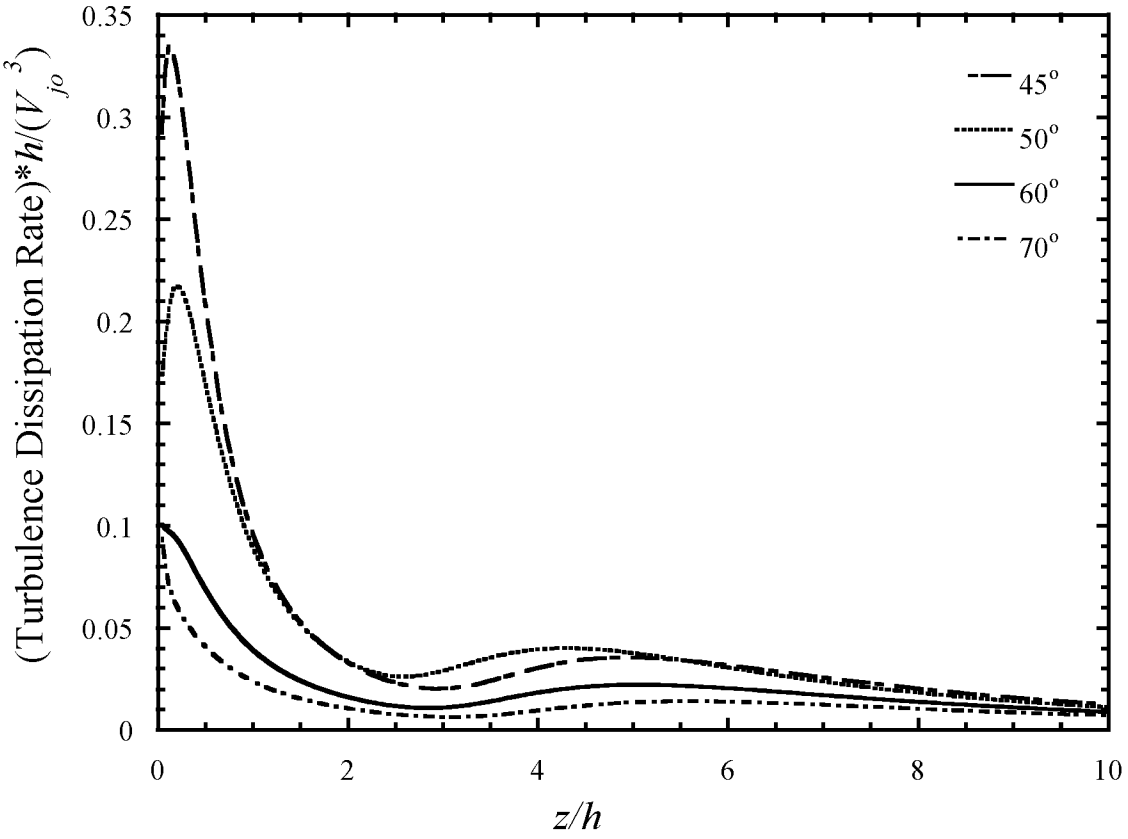

Figure 2-21b. Dimensionless turbulence dissipation rate along the centerline for different die angles for sharp die geometries.

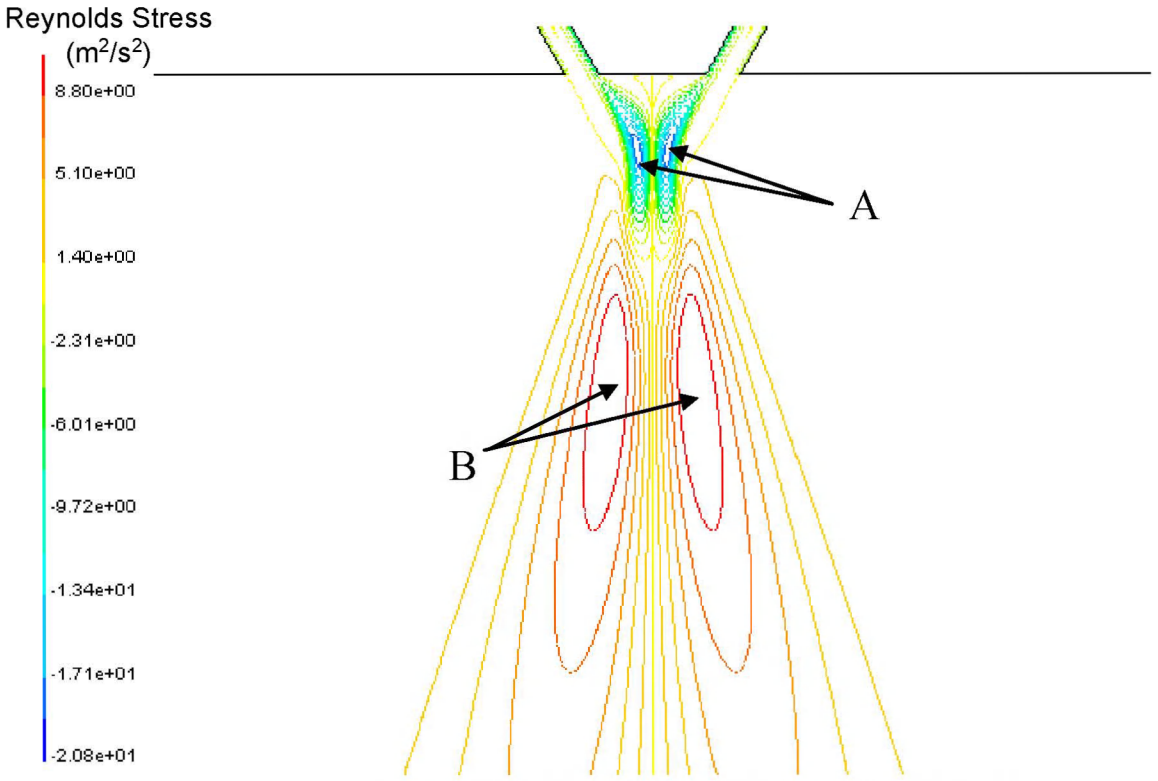

Figure 2-22a. Contours of the Reynolds stress in the flow field close to the die surface for the 60° blunt die with V_{jo} = 17.3 m/s.

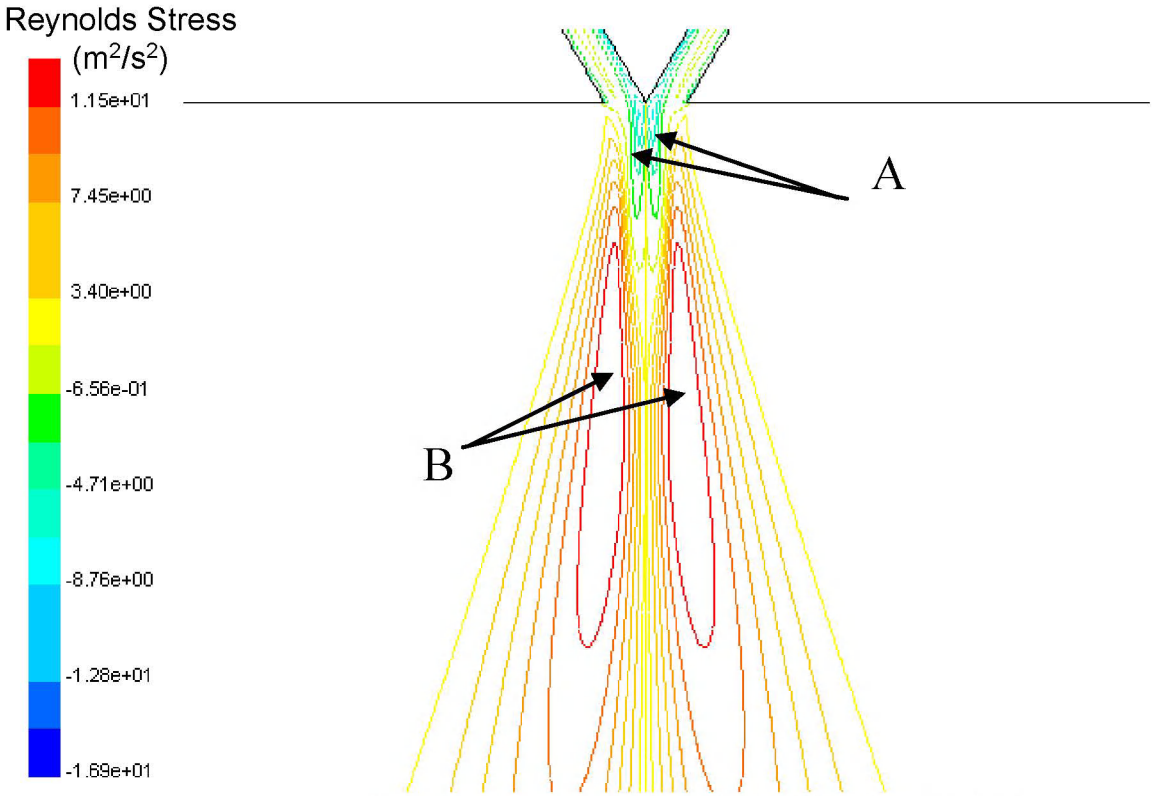

Figure 2-22b. Contours of the Reynolds stress in the flow field close to the die surface for the 60° sharp die with V_{jo} = 17.3 m/s.

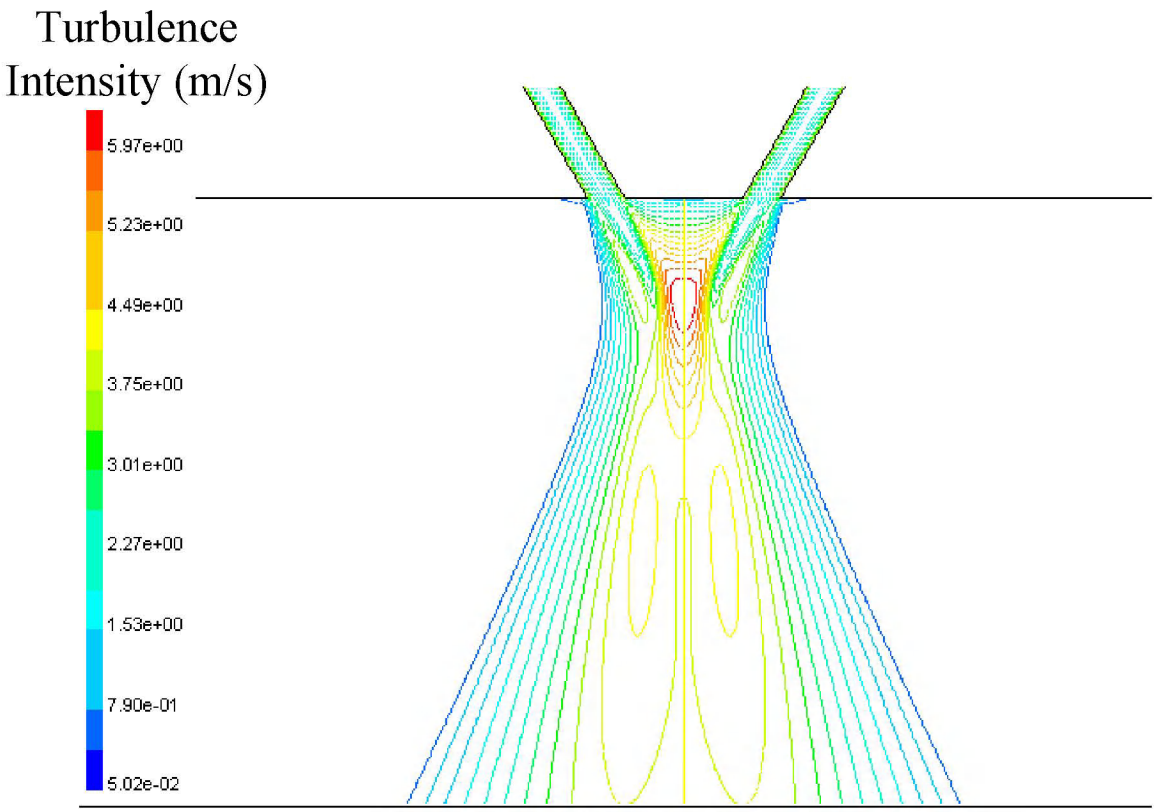

Figure 2-23a. Contours of the turbulence intensity in the flow field close to the die surface for a 60° blunt die with V_{jo} = 17.3 m/s.

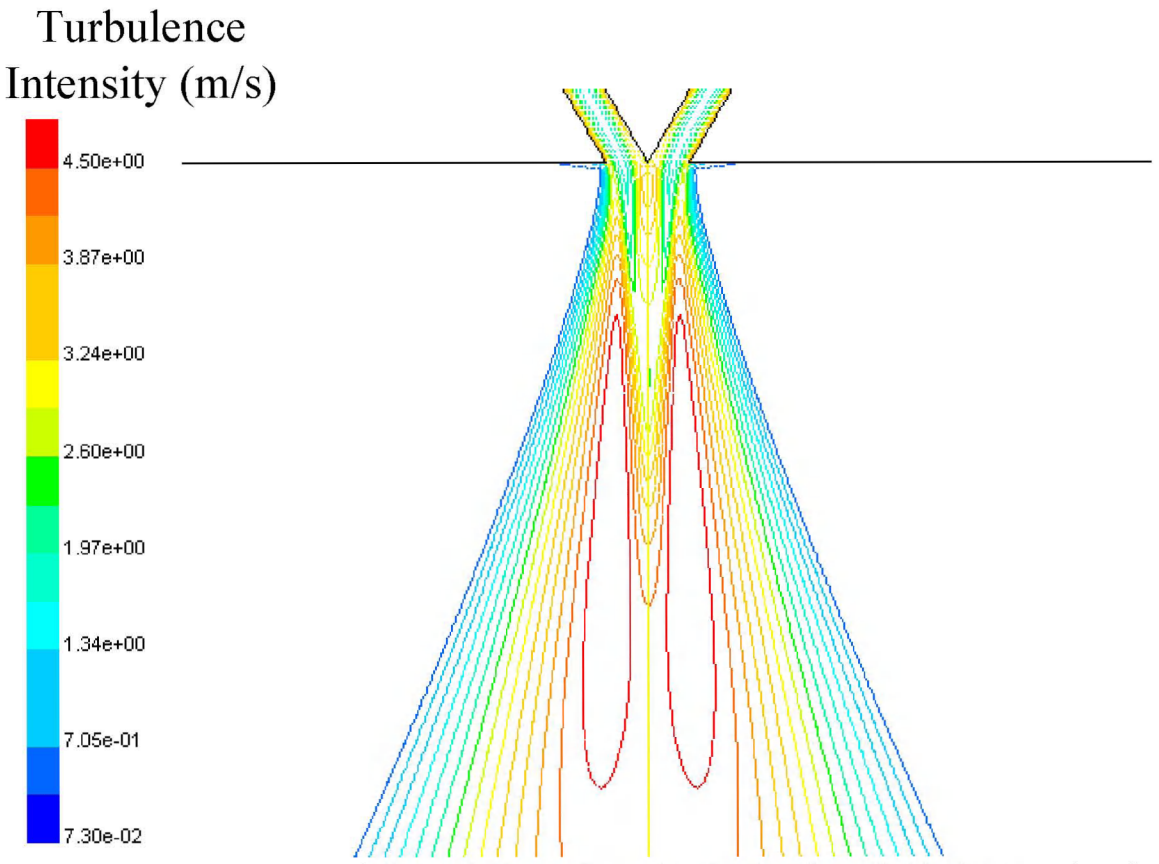

Figure 2-23b. Contours of the turbulence intensity in the flow field close to the die surface for a 60° sharp die with V_{jo} = 17.3 m/s.

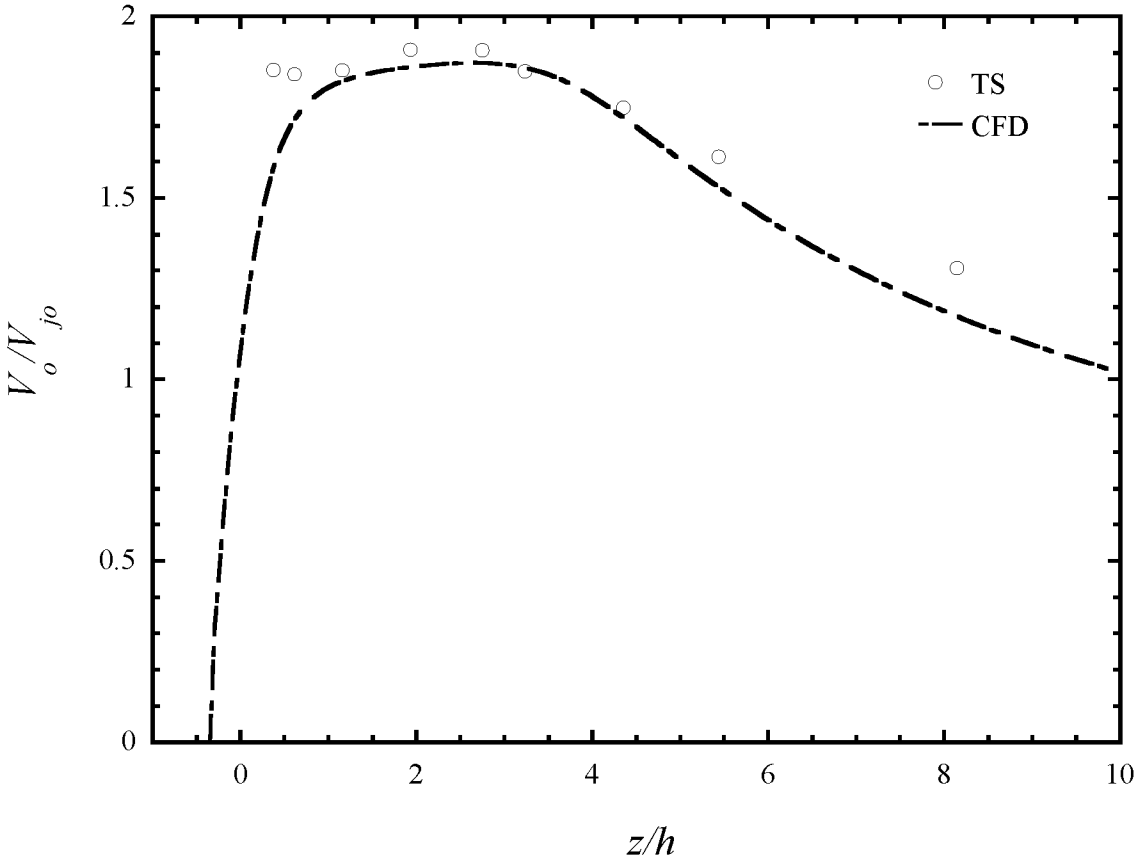

Figure 2-24a. Comparison of CFD results with experiments for dimensionless mean velocity close to the die face.

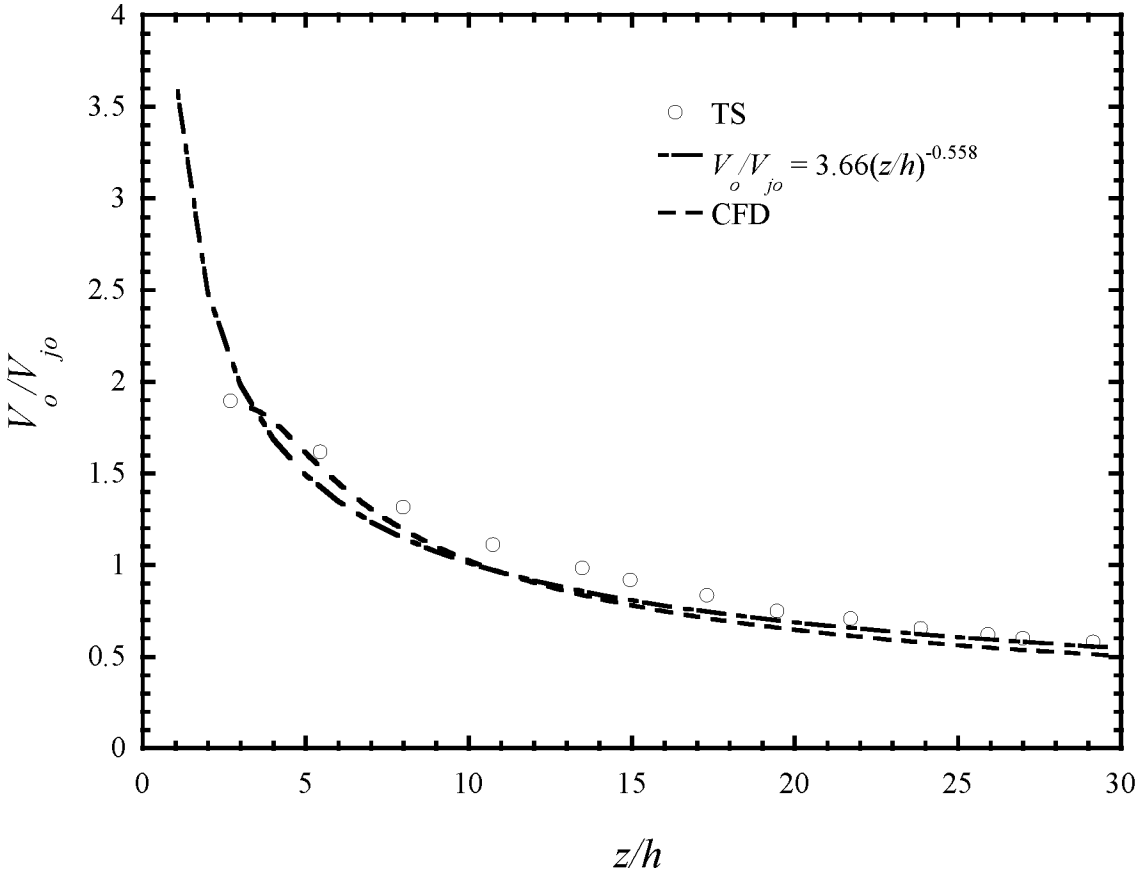

Figure 2-24b. Comparison of CFD results with experiments for the dimensionless mean velocity farther from the die face. The equation $V_o/V_{jo} = 3.66(z/h)^{-0.558}$ is the least squares fit of the experimental data to a power law equation.

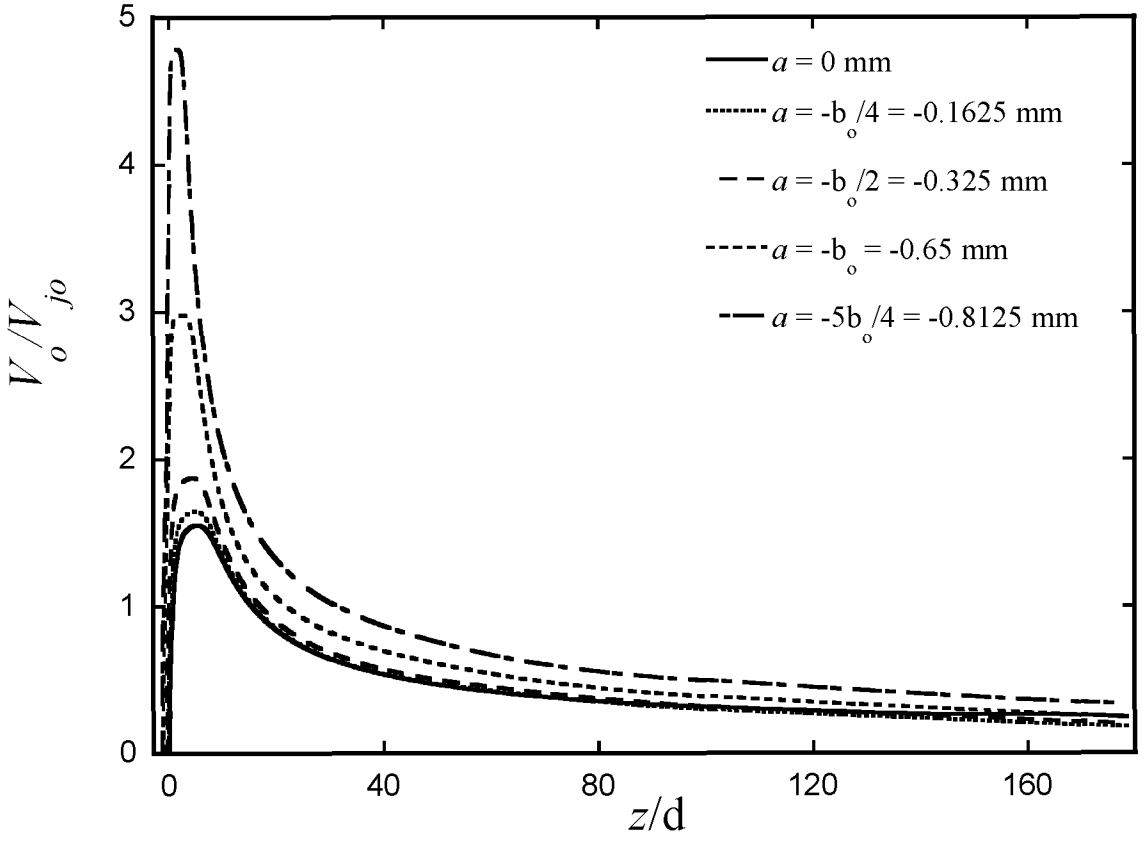

Figure 2-25a. Dimensionless mean centerline velocity for the simulated inset dies.

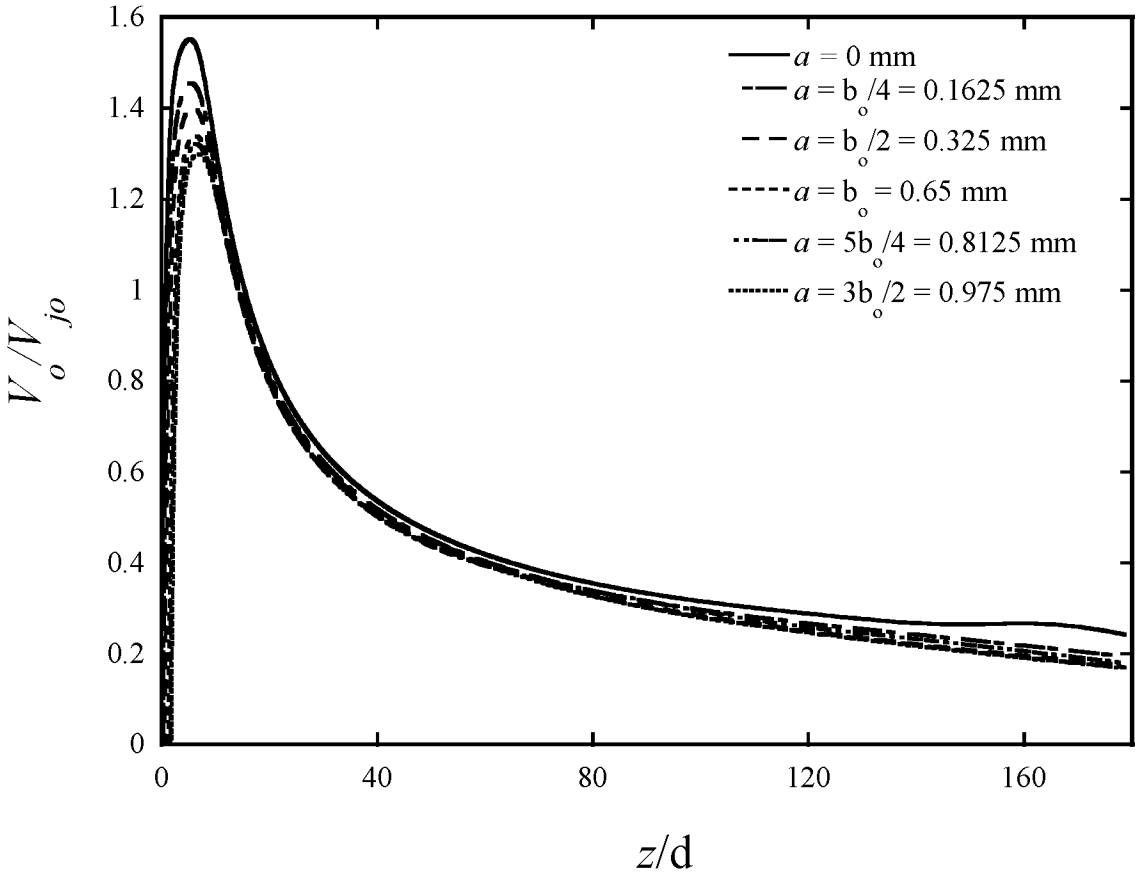

Figure 2-25b. Dimensionless mean centerline velocity for the simulated outset dies.

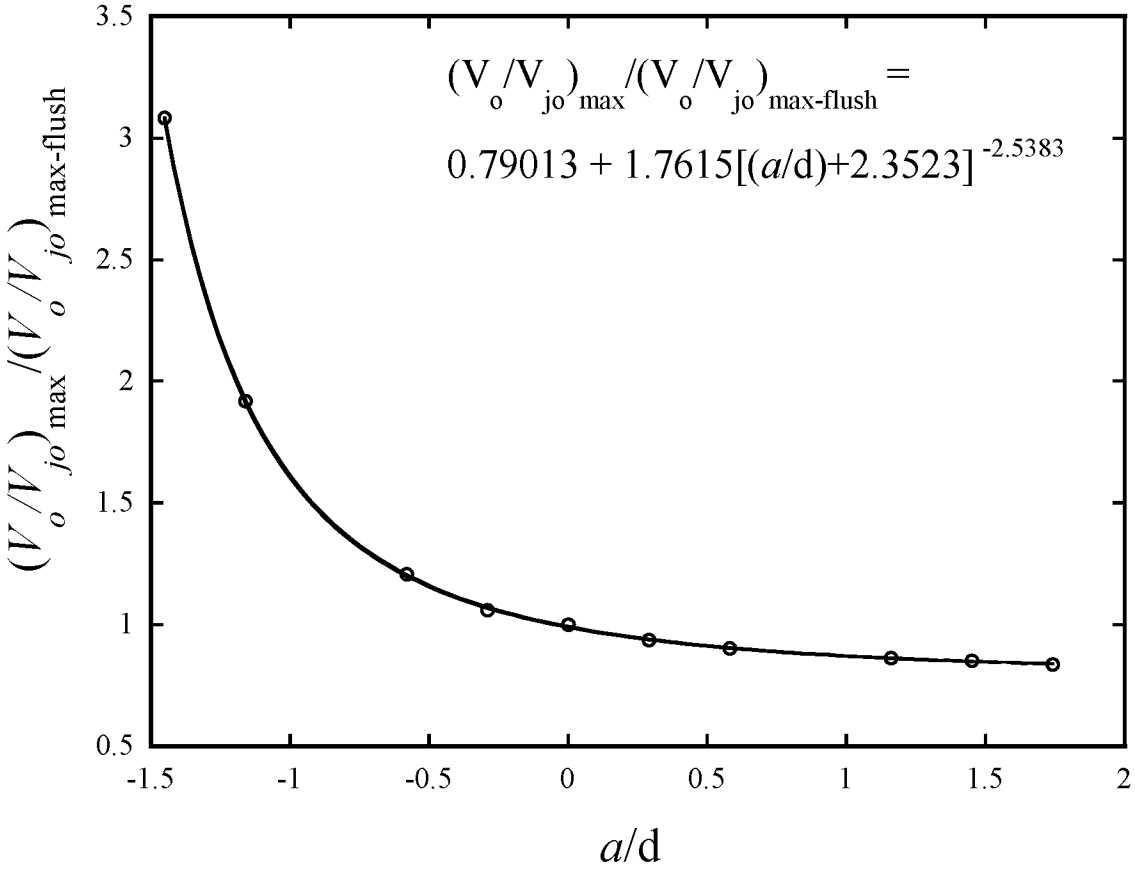

Figure 2-25c. Maximum mean centerline velocity as a function of the die configuration (R = 0.99998 for the equation shown on the graph).

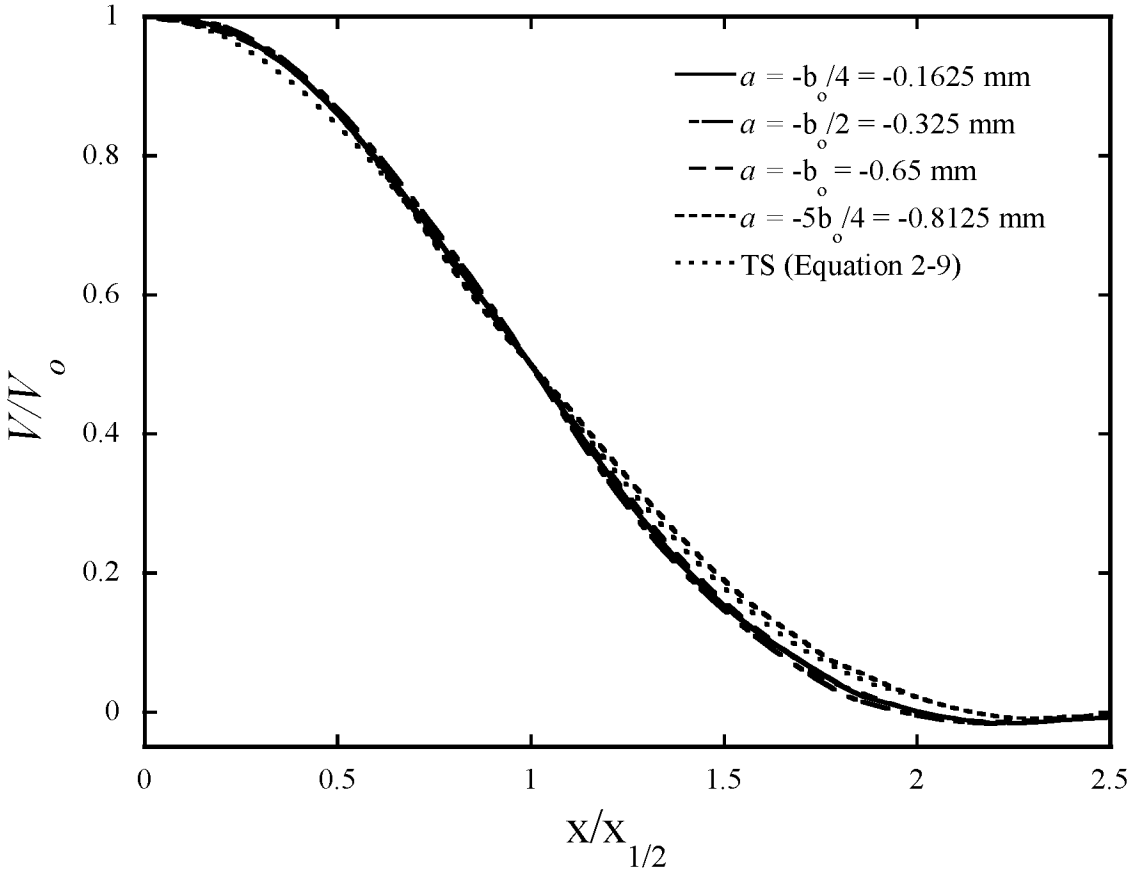

Figure 2-26a. Dimensionless velocity profiles within the self-similar region (z = 50 mm) for the simulated inset dies and the experimental TS flush die.

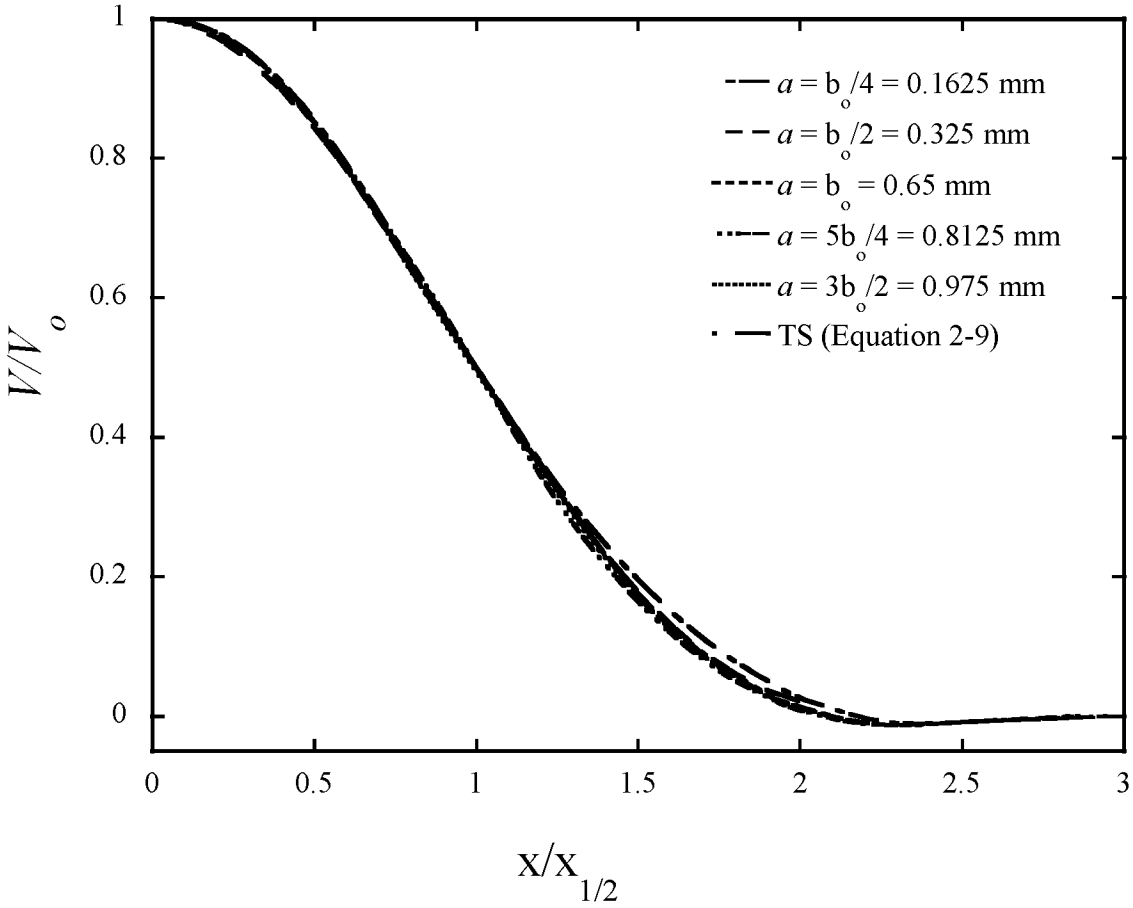

Figure 2-26b. Dimensionless velocity profiles within the self-similar region (z = 50 mm) for the simulated outset dies and the experimental TS flush die.

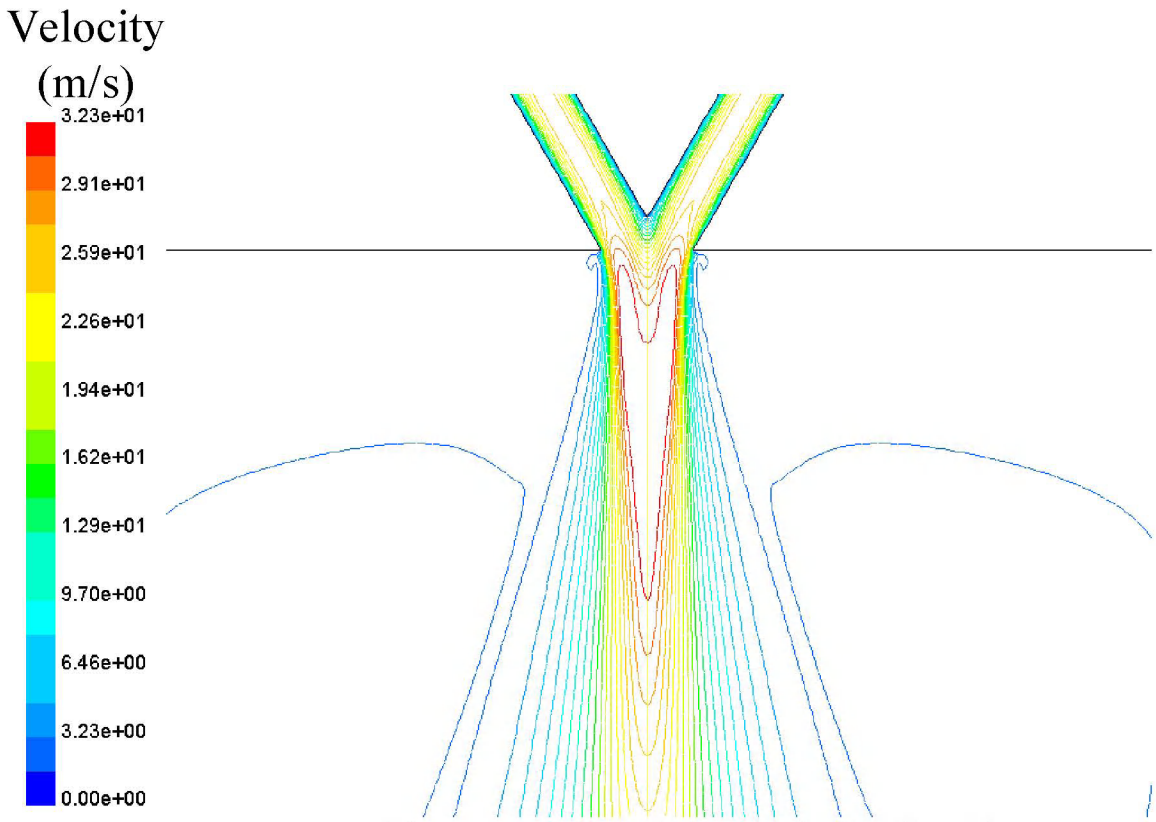

Figure 2-27a. Contour plot of the mean *z*-velocity below the die face for an inset die with $a = -b_o/2$.

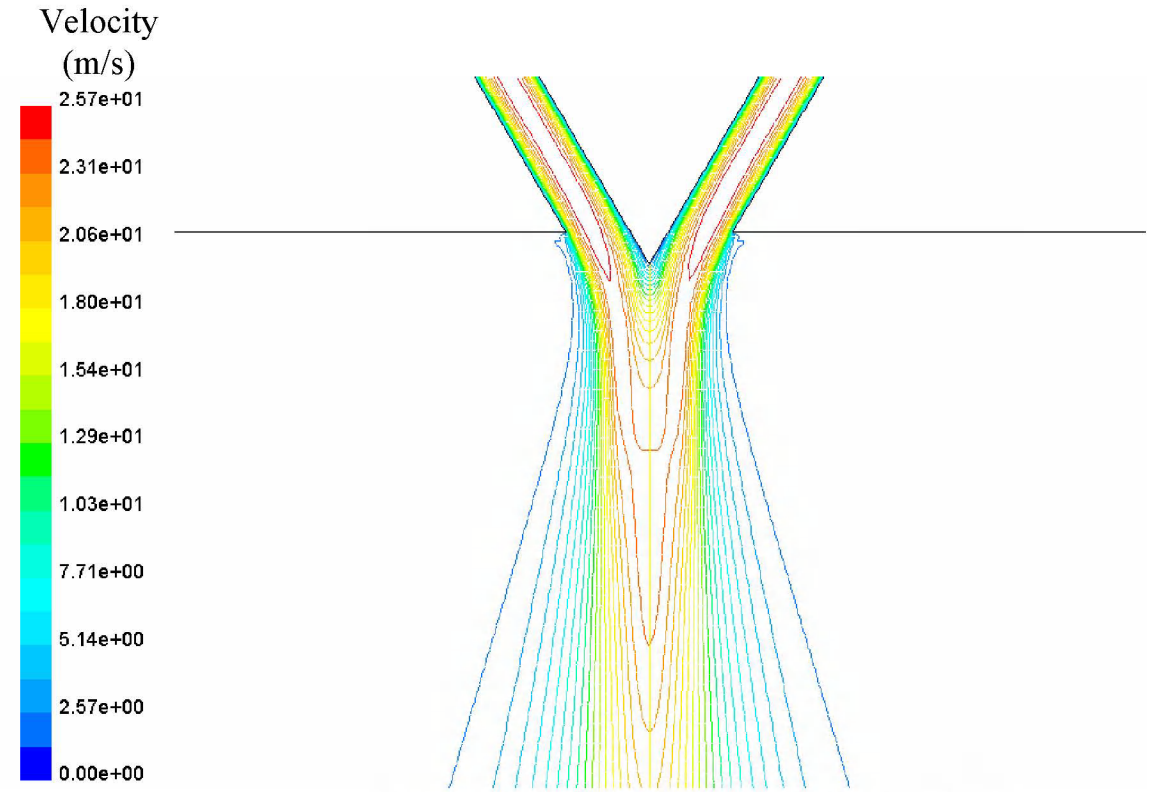

Figure 2-27b. Contour plot of the mean *z*-velocity below the die face for an outset die with $a = b_o/2$.

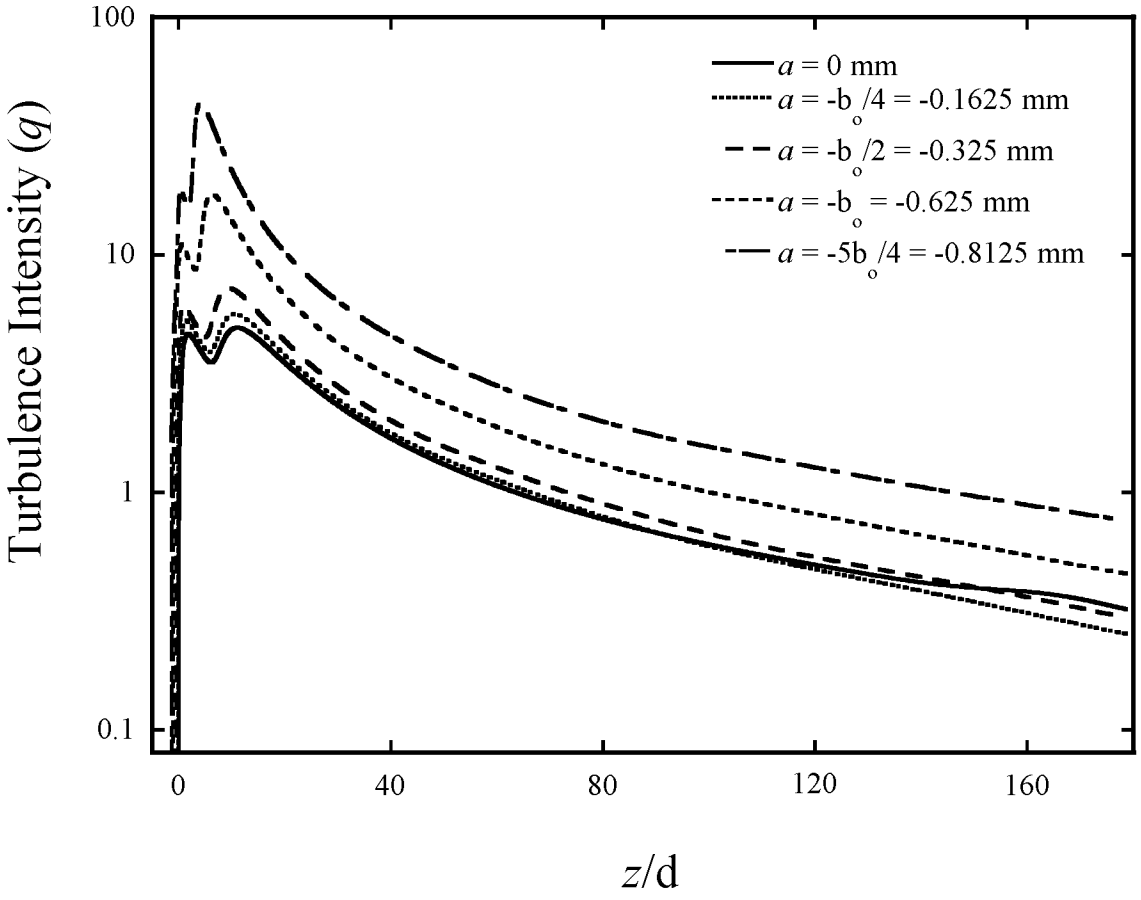

Figure 2-28a. Turbulence intensity along the centerline for inset dies.

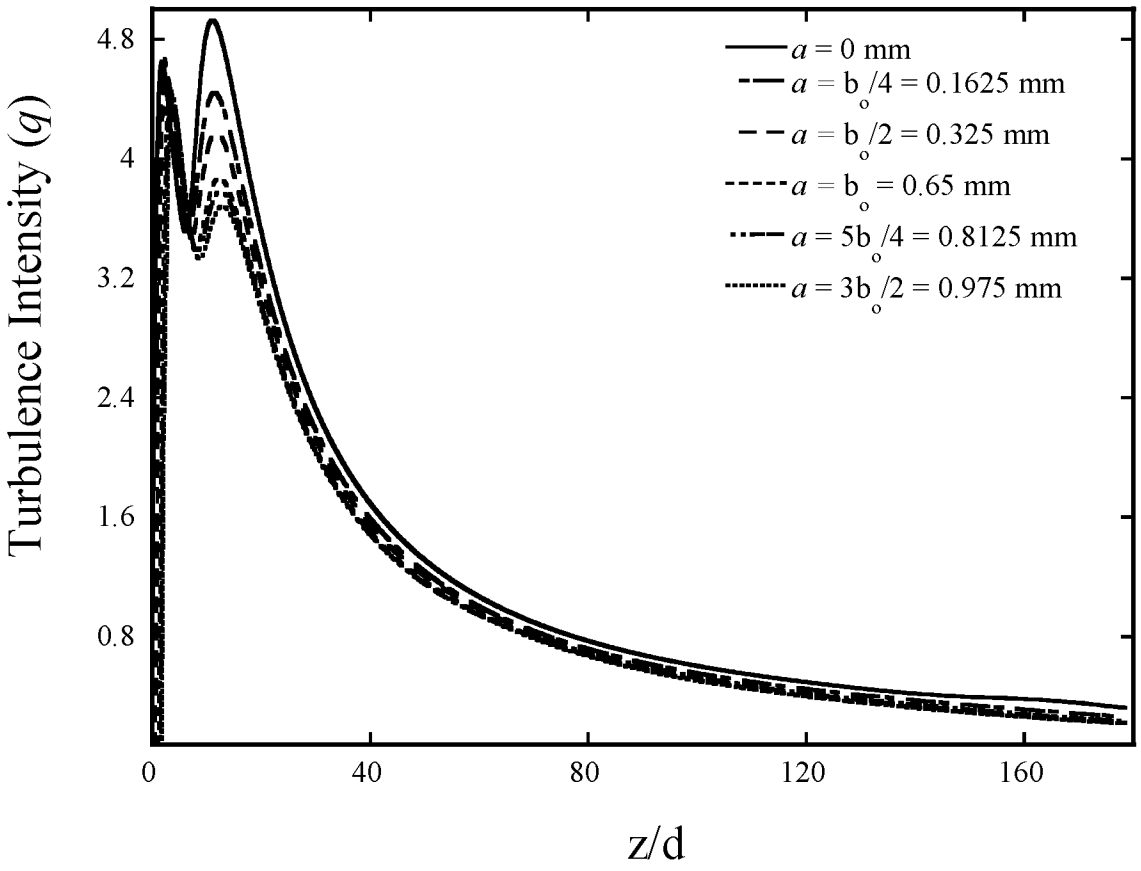

Figure 2-28b. Turbulence intensity along the centerline for outset dies.

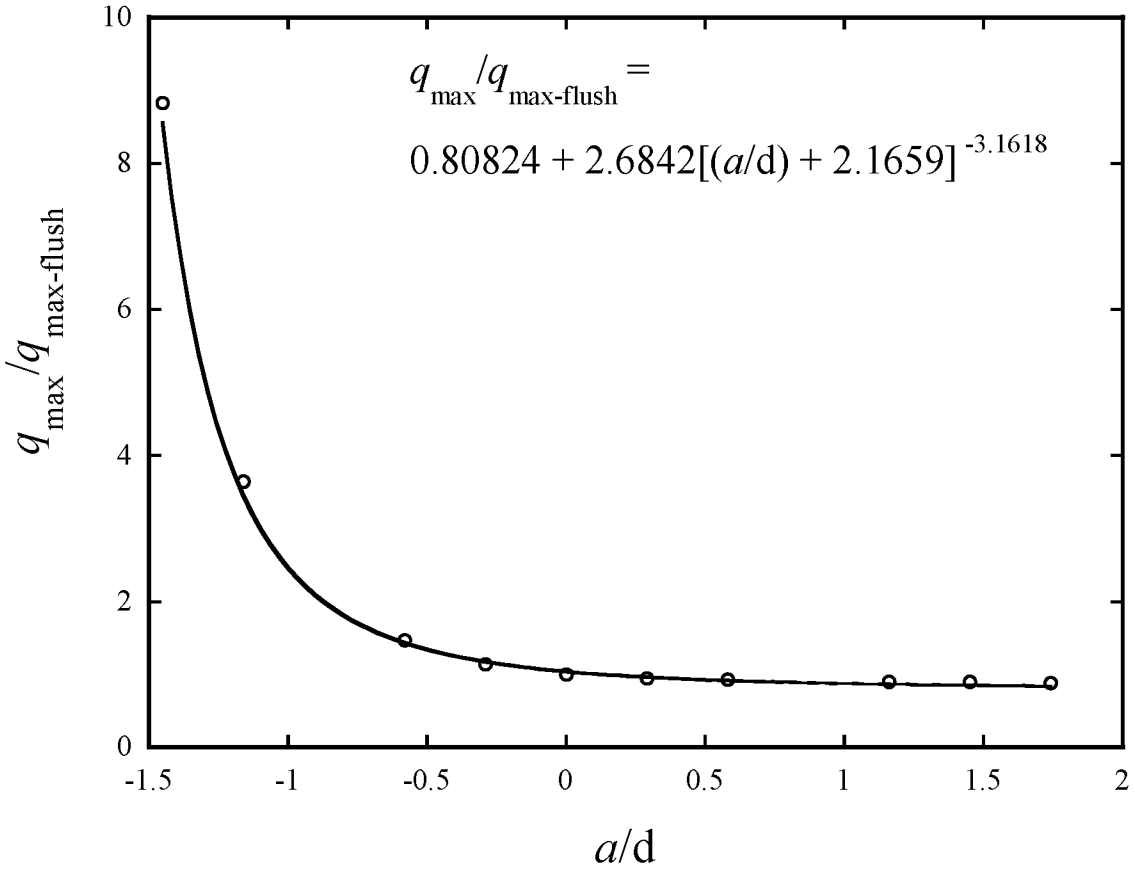

Figure 2-28c. Maximum turbulence intensity as a function of the die configuration (R = 0.99894 for the equation shown on the graph).

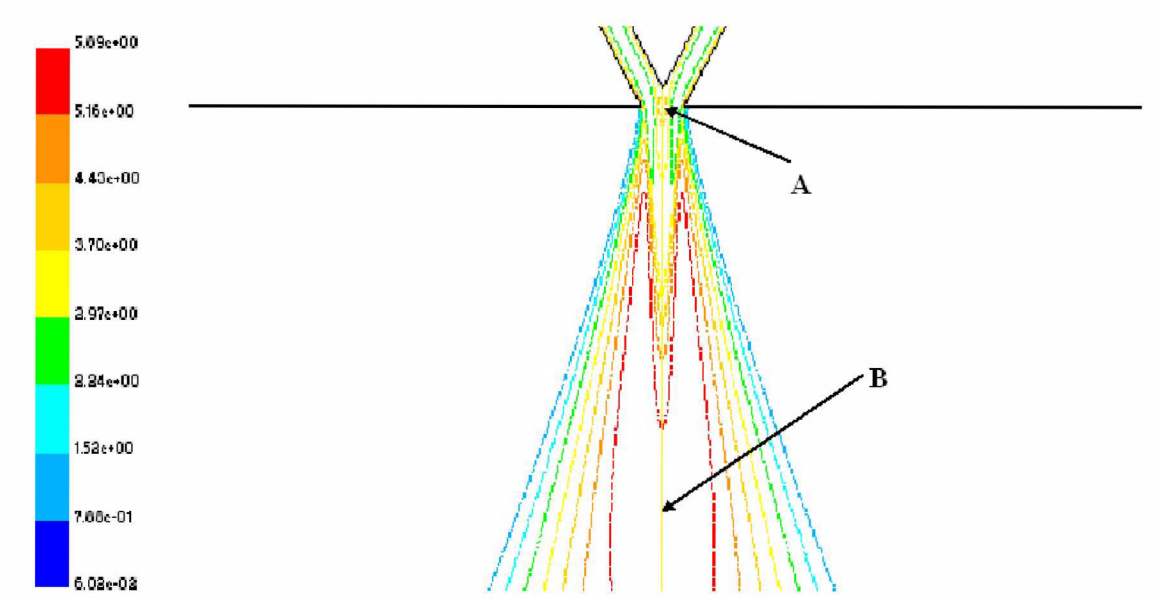

Figure 2-29a. Contour plots of the turbulence intensity below the die face for an inset die with $a = -b_o/2$.

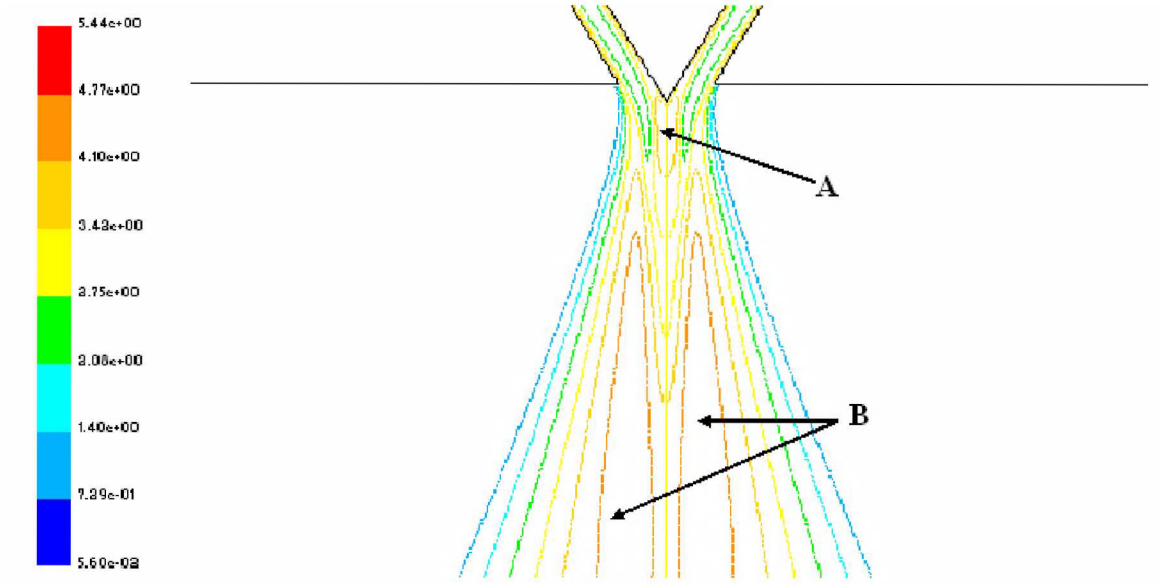

Figure 2-29b. Contour plots of the turbulence intensity below the die face for an outset die with $a = b_o/2$.

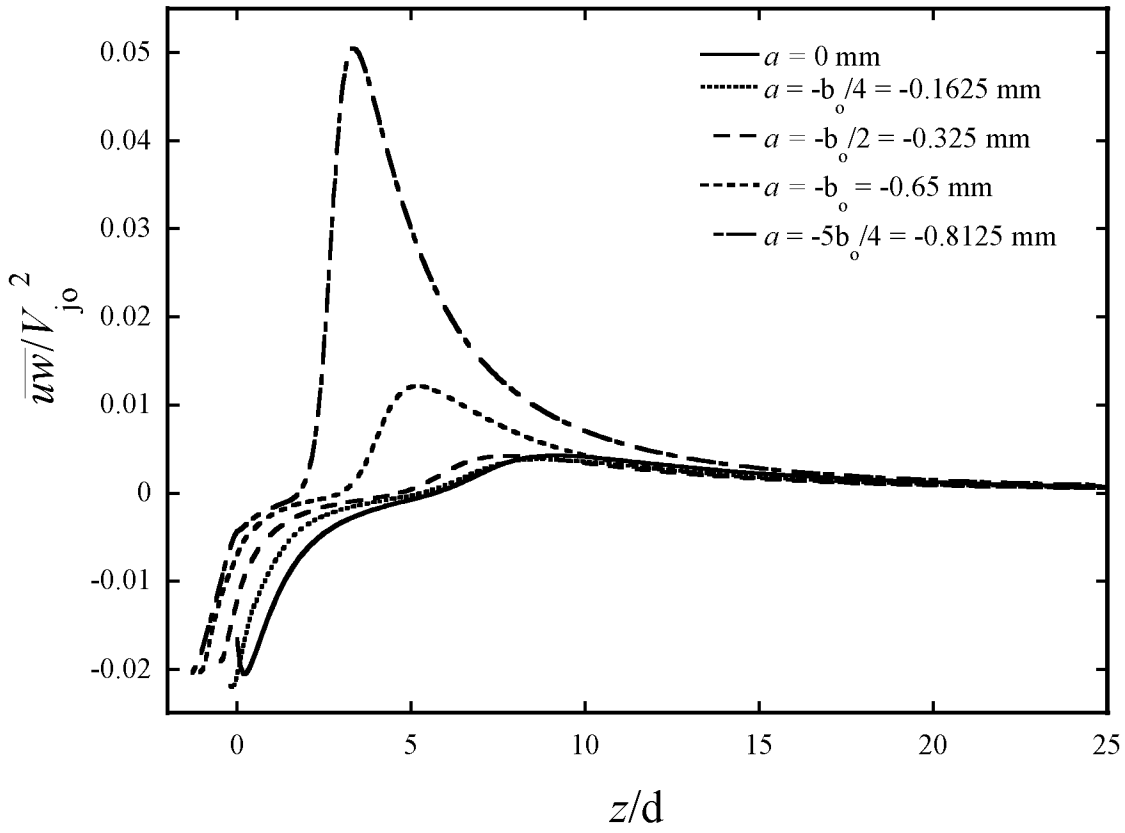

Figure 2-30a. Dimensionless Reynolds stress profiles across the centerline for inset dies.

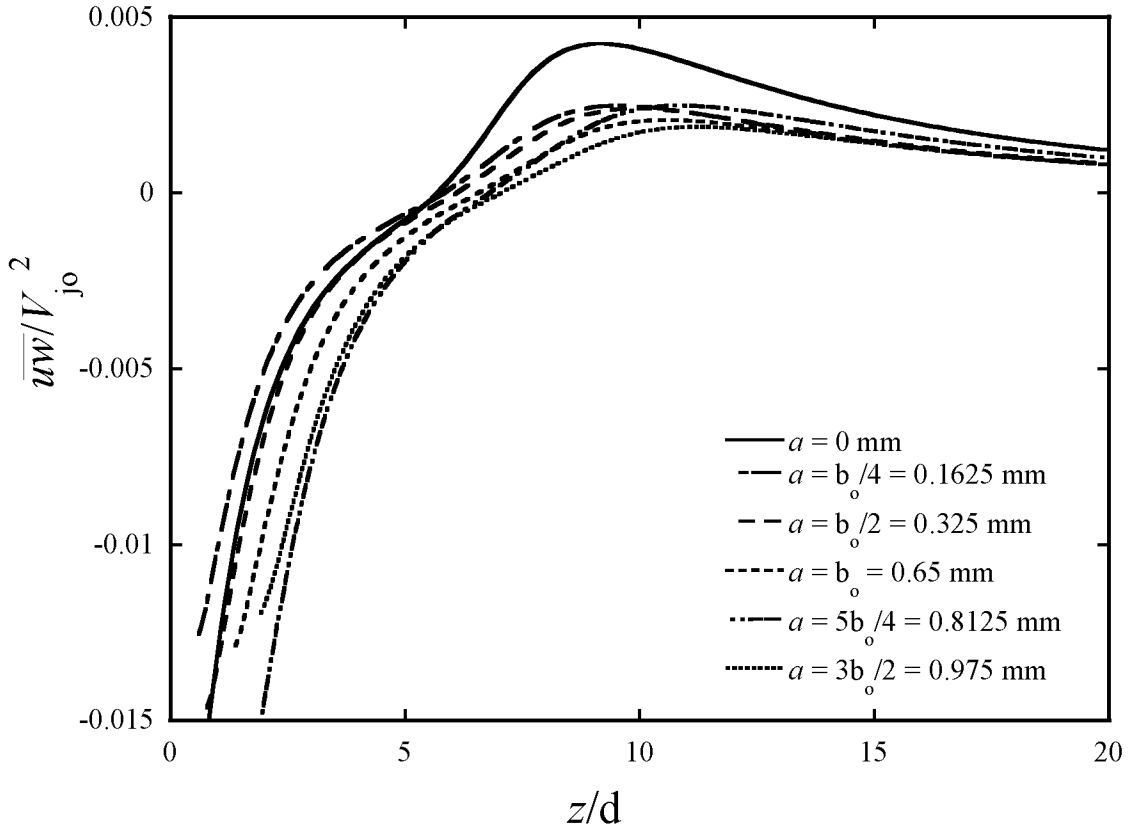

Figure 2-30b. Dimensionless Reynolds stress profiles across the centerline for outset dies.

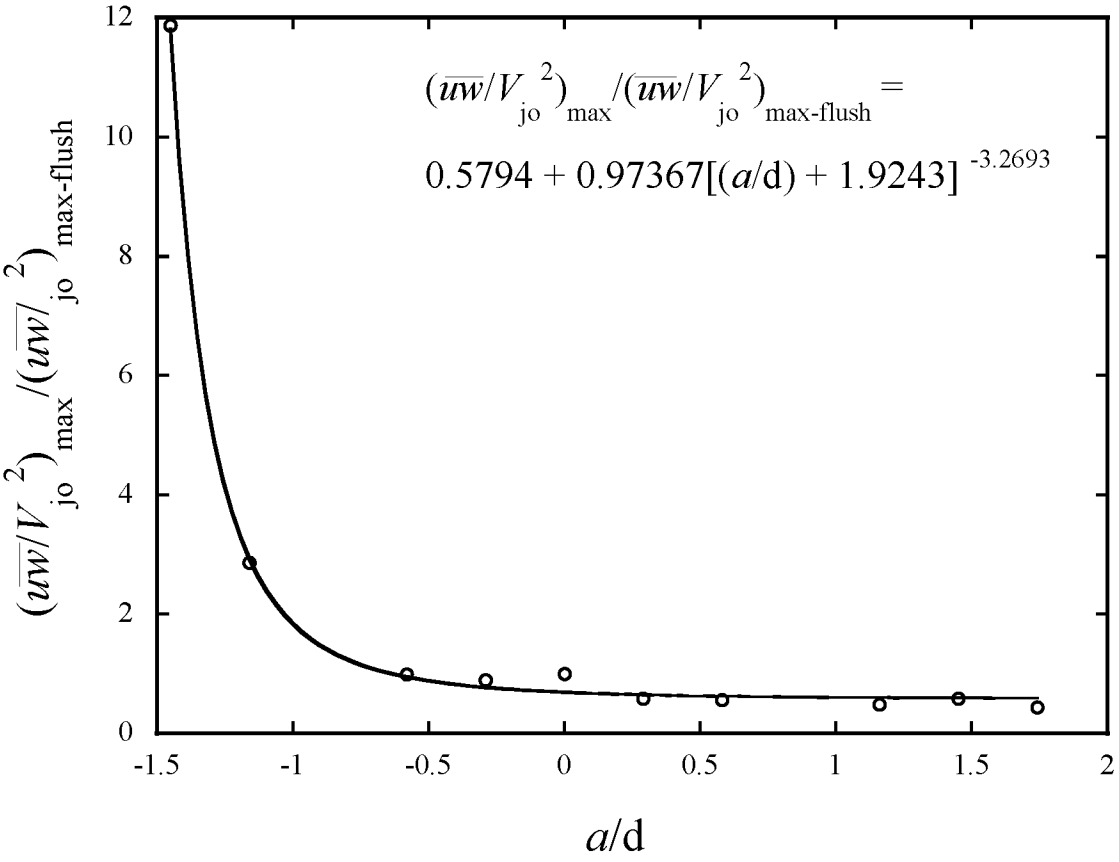

Figure 2-30c. Maximum Reynolds stress as a function of the die configuration (R = 0.99894 for the equation shown on the graph).

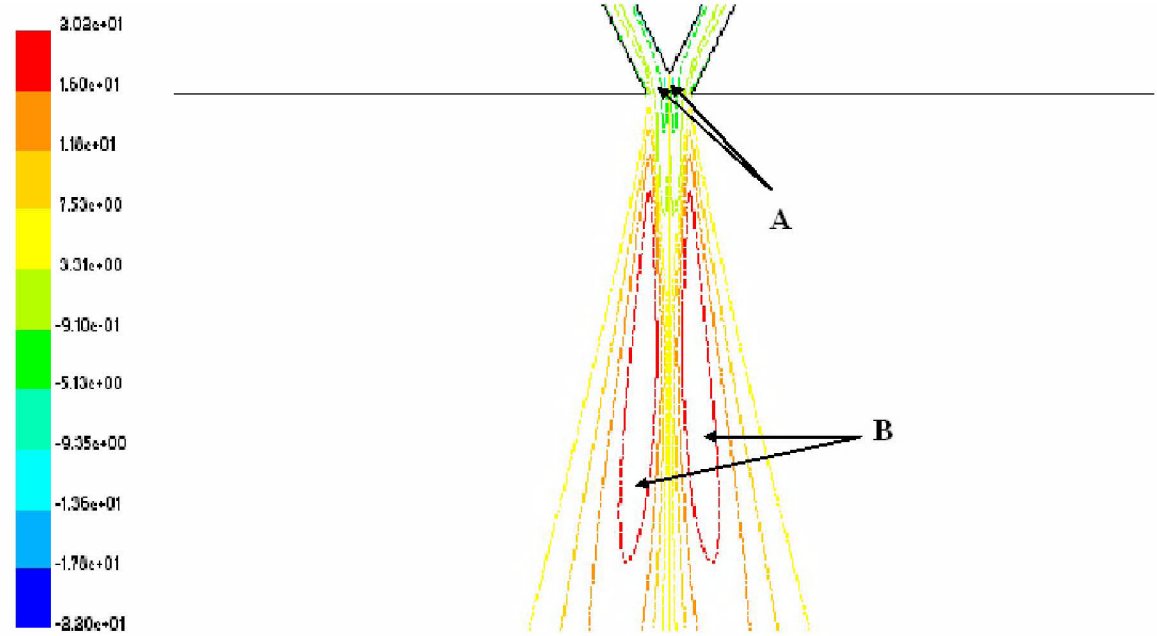

Figure 2-31a. Contour plots of the Reynolds stress below the die face for and inset die with $a = -b_o/2$.

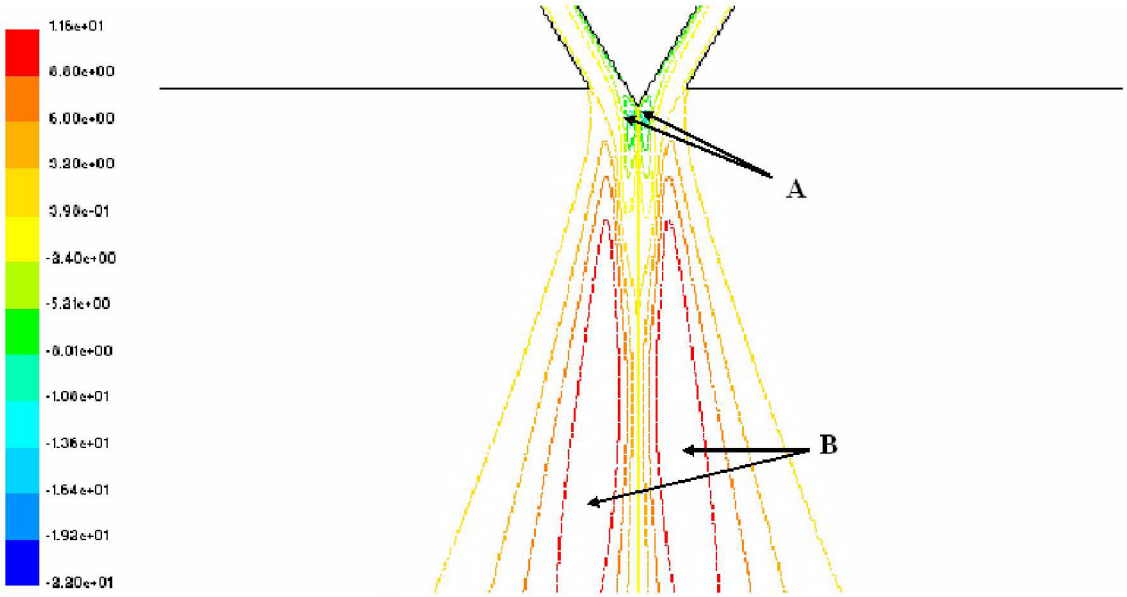

Figure 2-31b. Contour plots of the Reynolds stress below the die face for and outset die with $a = b_o/2$.

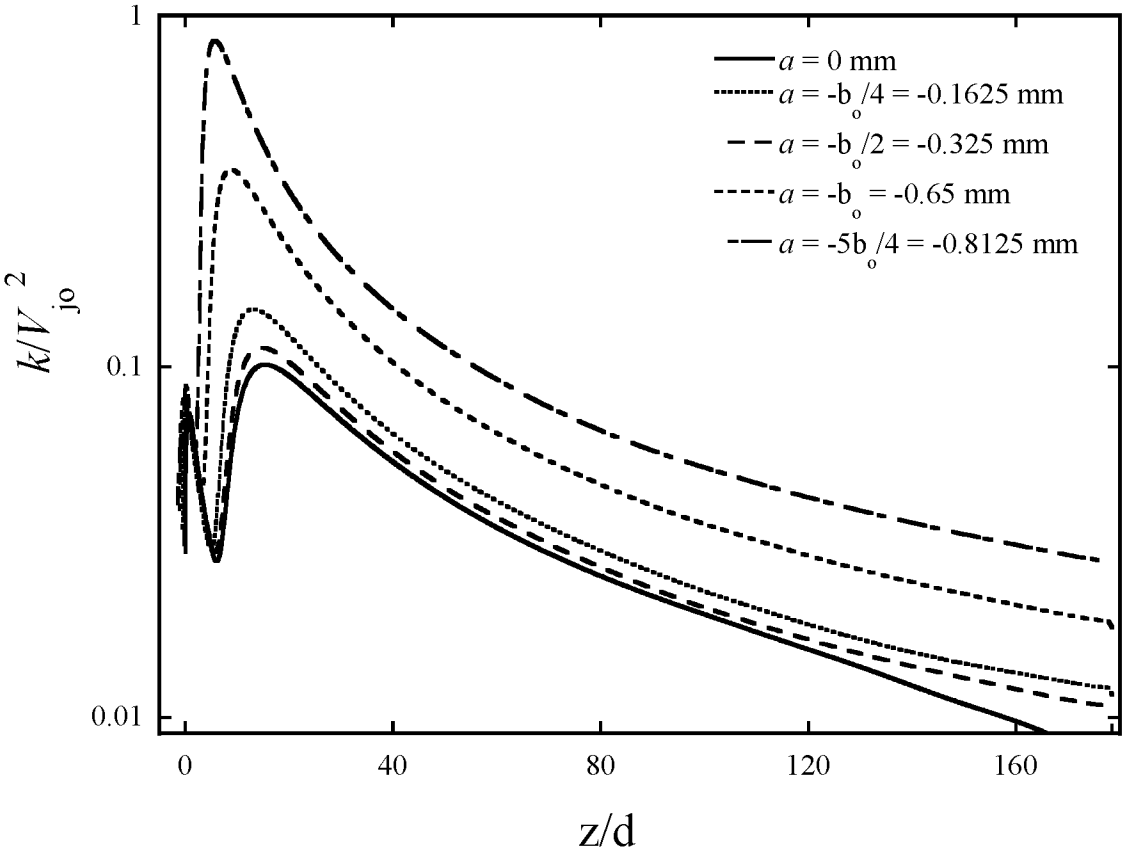

Figure 2-32a. Dimensionless turbulence kinetic energy profiles across the centerline for inset dies.

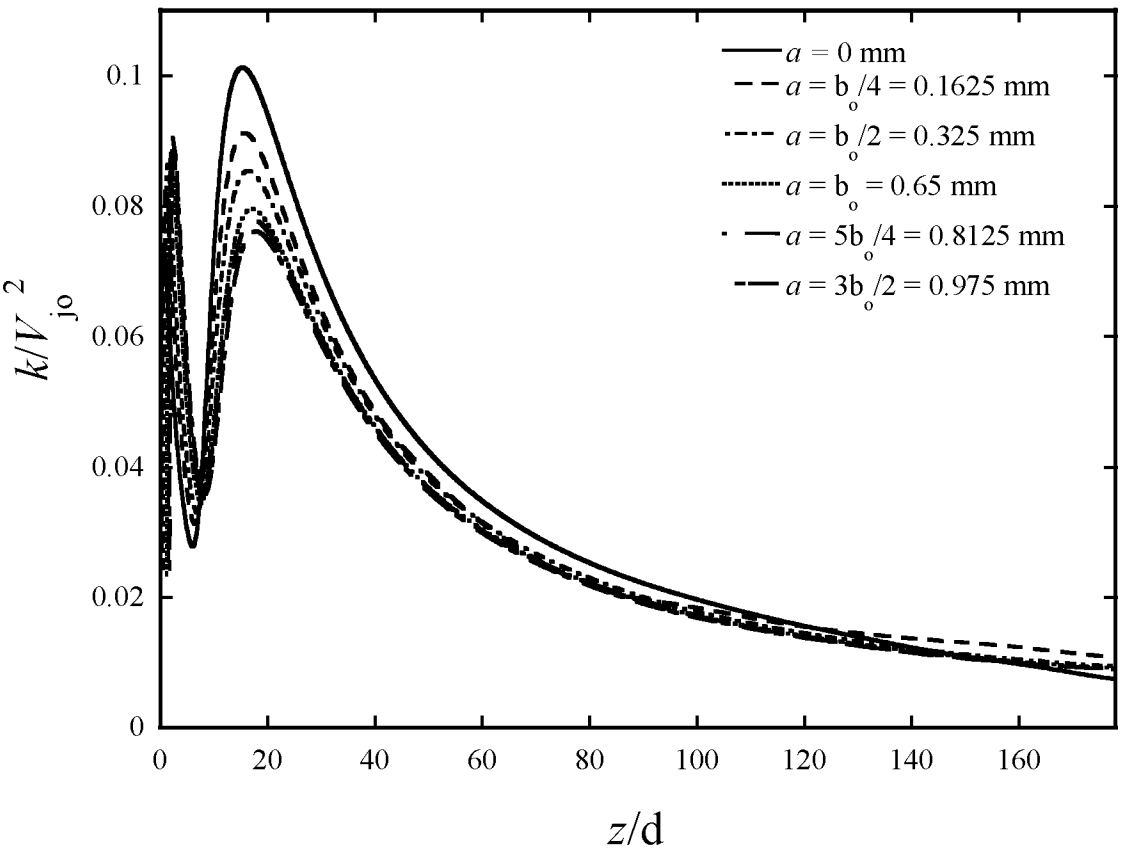

Figure 2-32b. Dimensionless turbulence kinetic energy profiles across the centerline for outset dies.

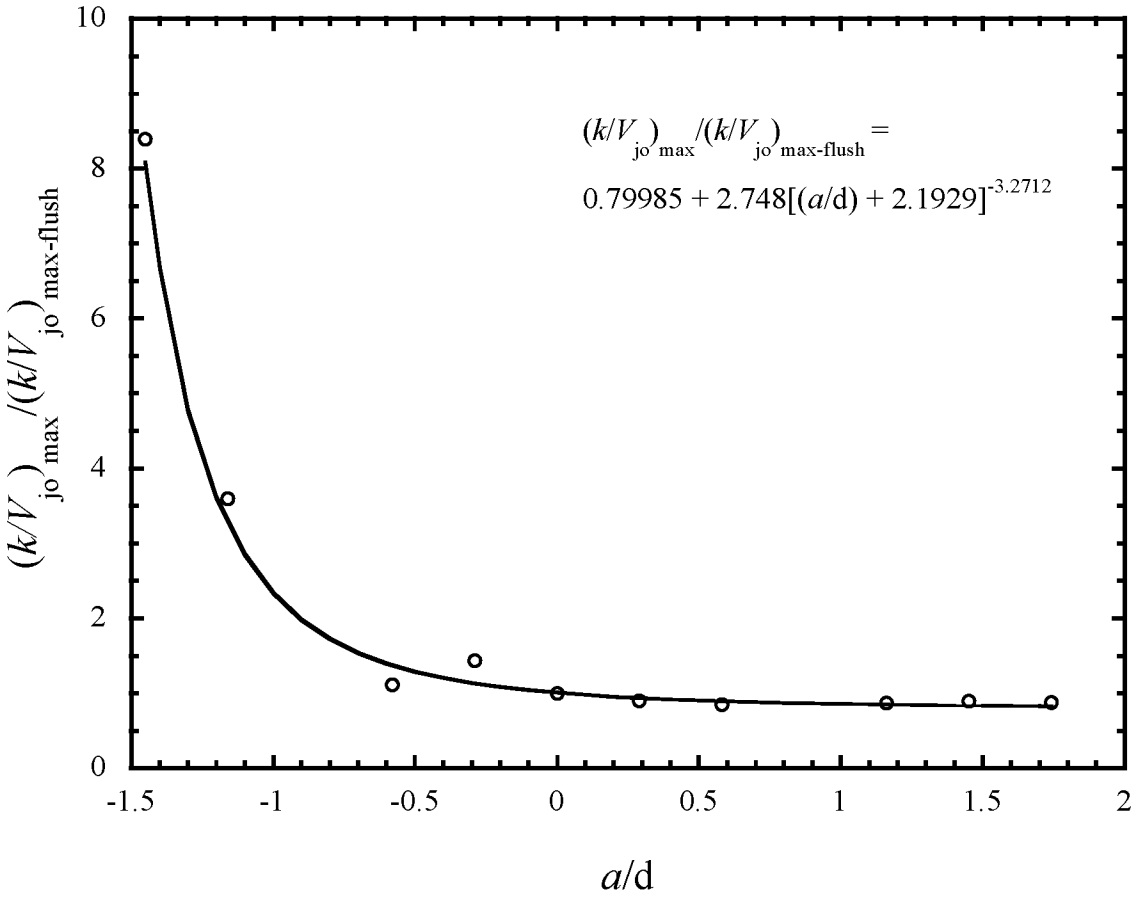

Figure 2-32c. Maximum turbulence kinetic energy as a function of the configuration (R = 0.99647 for the equation shown on the graph).

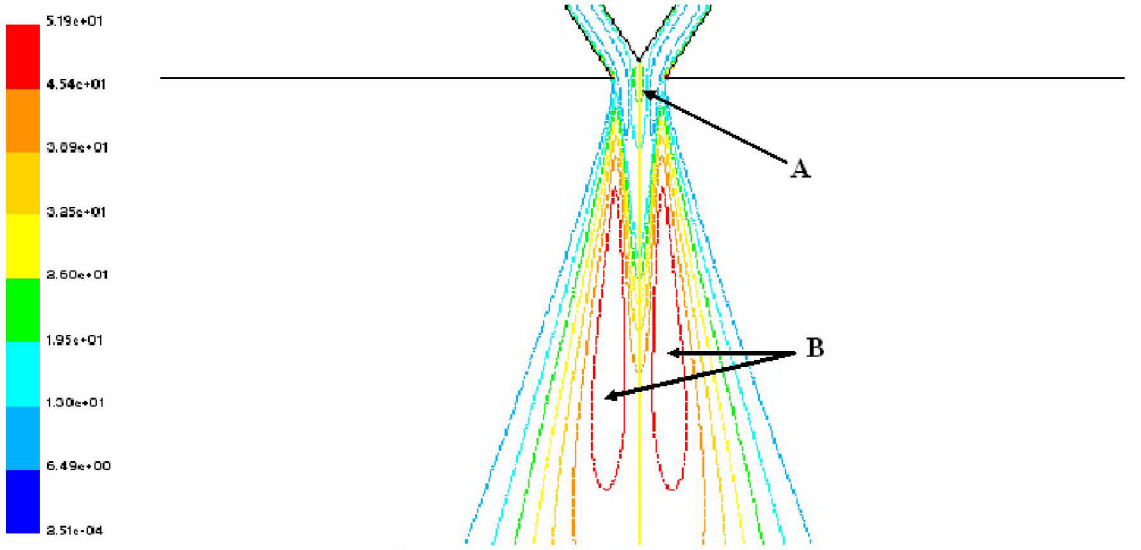

Figure 2-33a. Contour plots of the turbulent kinetic energy below the die face for and inset die with $a = -b_o/2$.

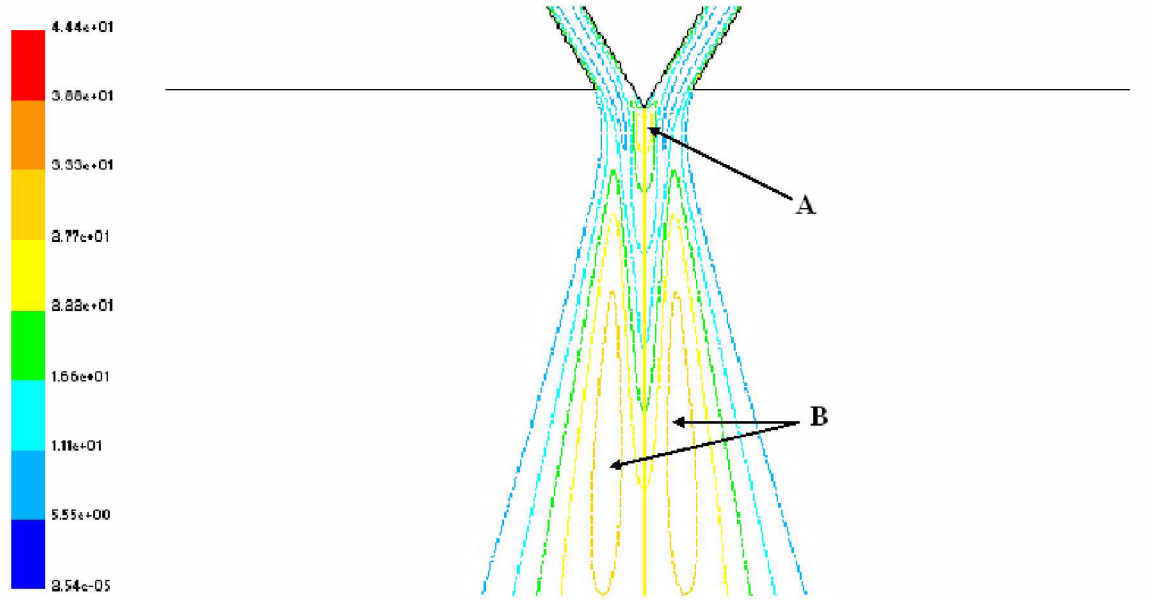

Figure 2-33b. Contour plots of the turbulent kinetic energy below the die face for and outset die with $a = b_o/2$.

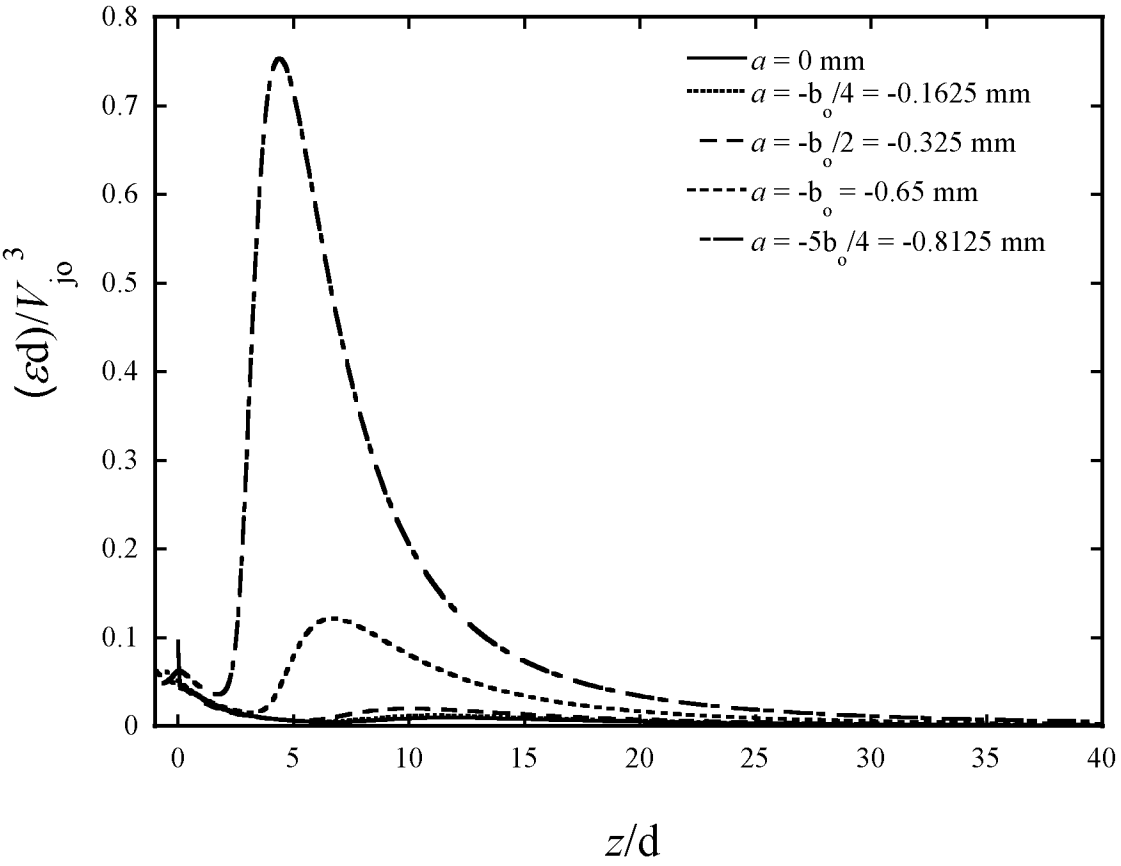

Figure 2-34a. Dimensionless turbulence dissipation rate profiles along across the centerline for inset dies.

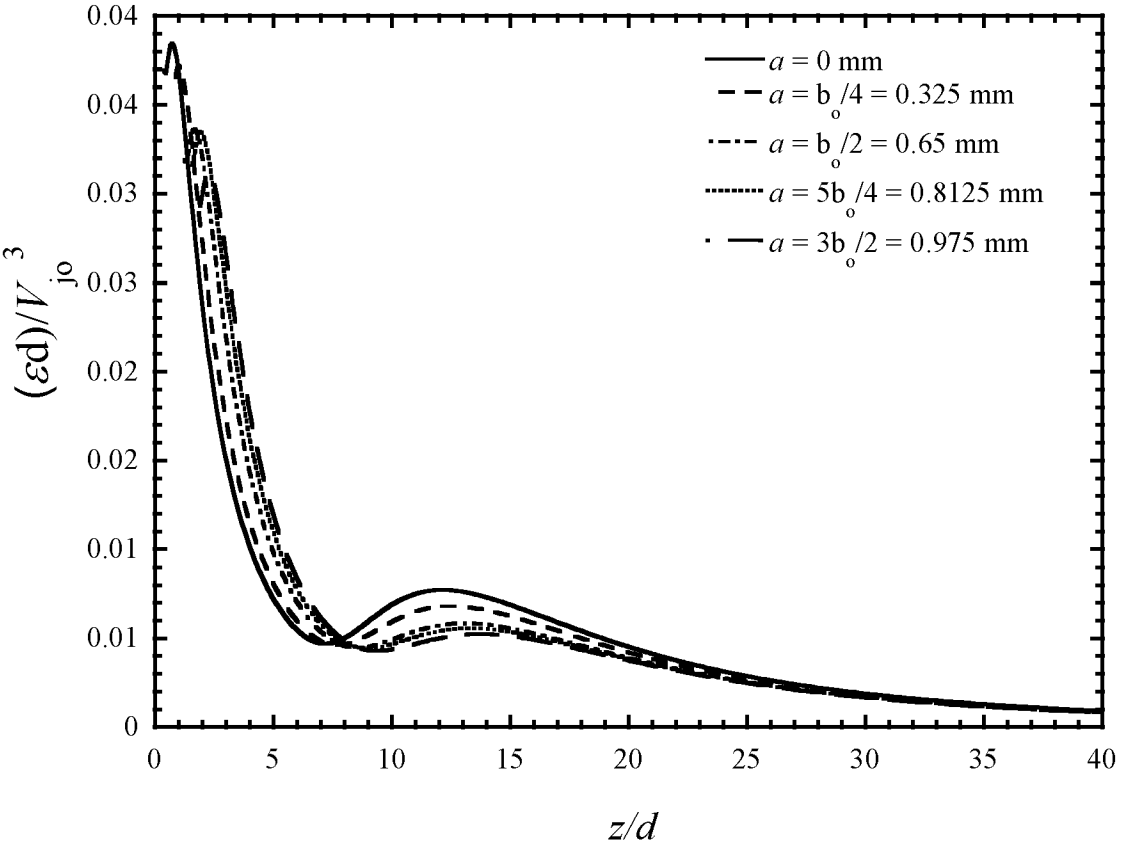

Figure 2-34b. Dimensionless turbulence dissipation rate profiles along across the centerline for outset dies.

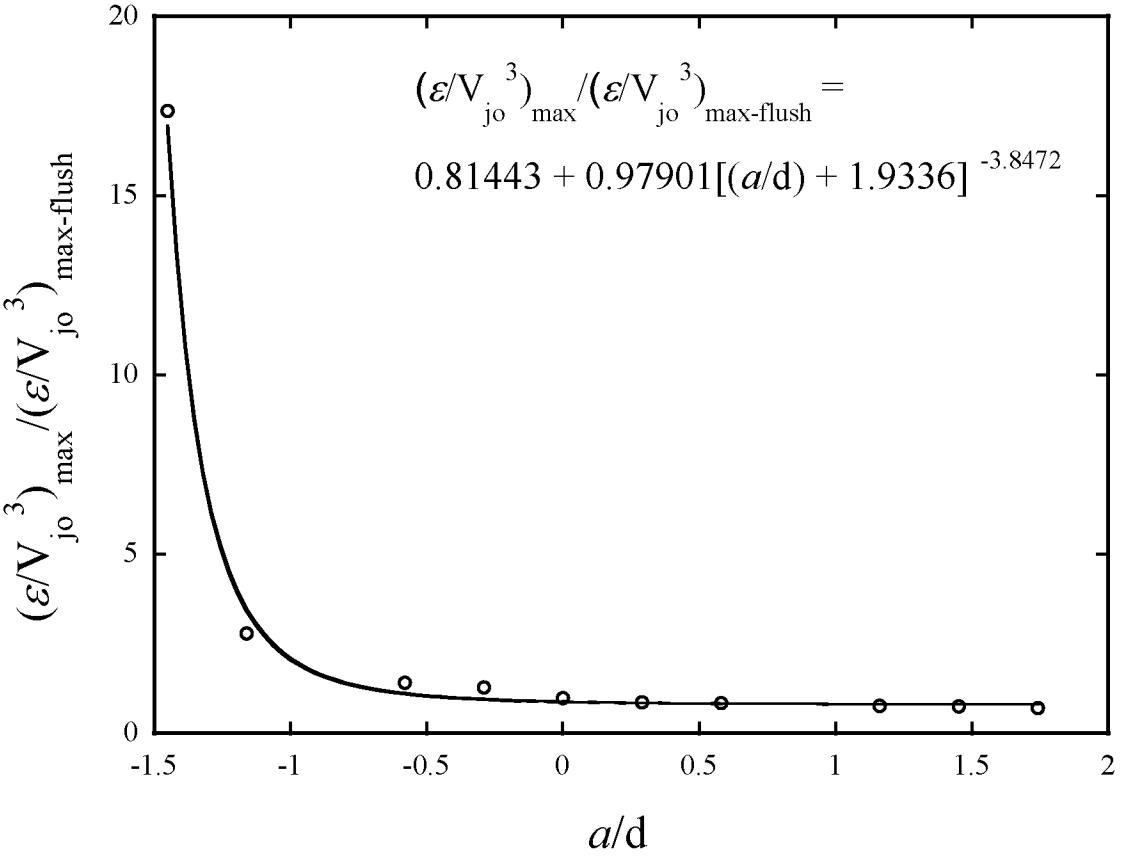

Figure 2-34c. Maximum turbulence dissipation rate as a function of the die configuration (R = 0.99825 for the equation shown on the graph).

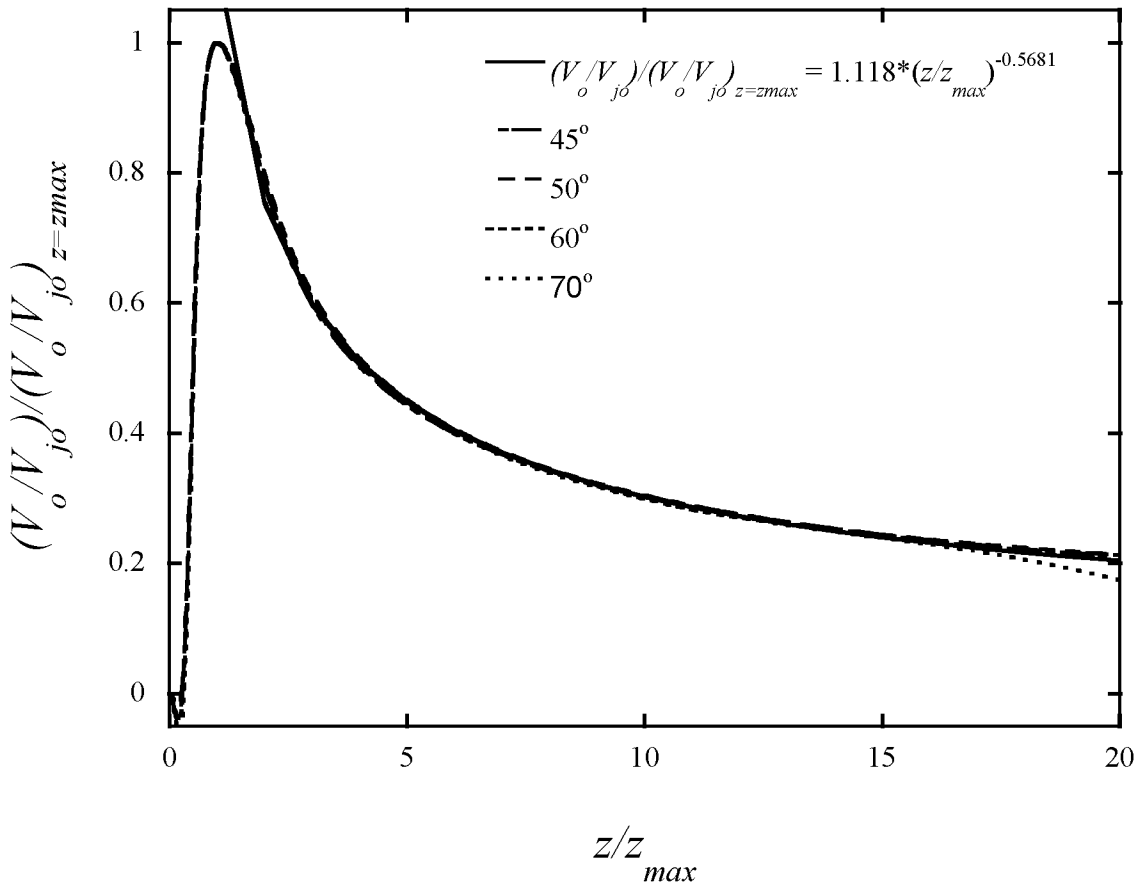

Figure 2-35a. Prediction of dimensionless mean centerline velocity for blunt flush dies (R^2 = 0.9953 for the velocity decay equation shown on the graph).

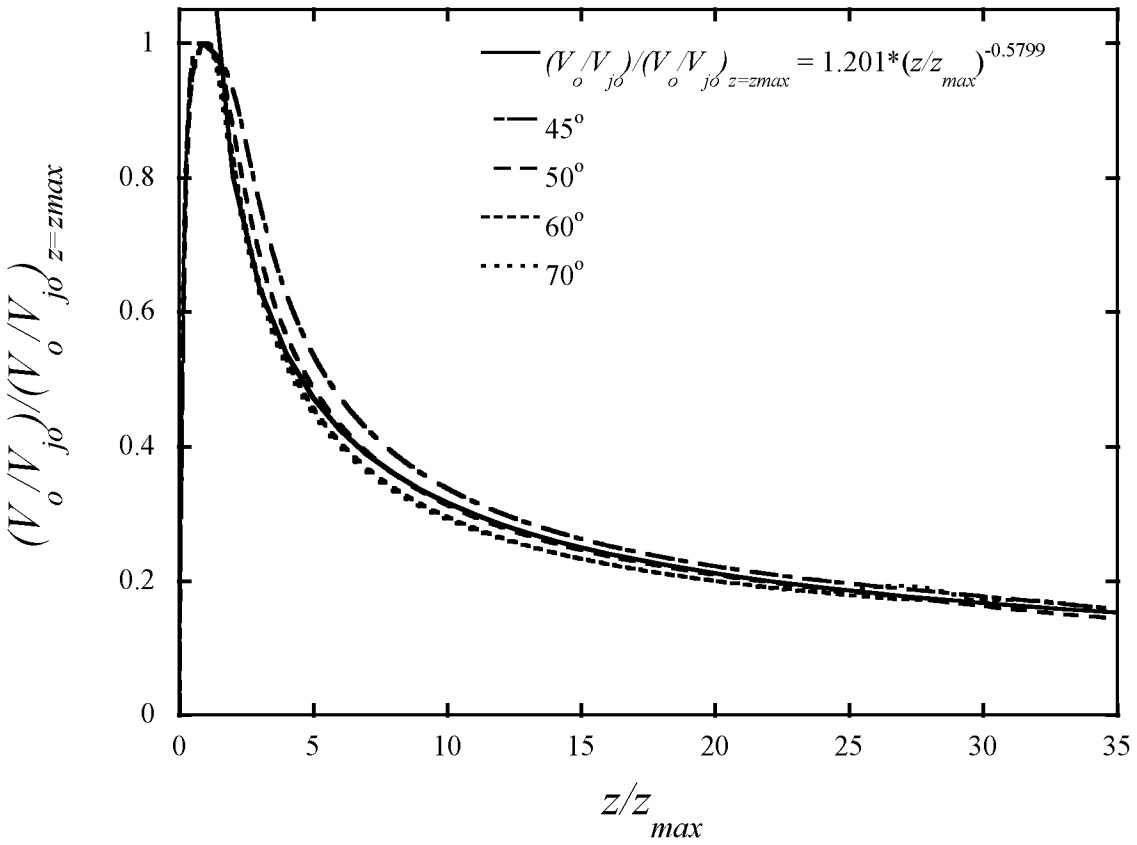

Figure 2-35b. Prediction of dimensionless mean centerline velocity for sharp flush dies ($R^2 = 0.9819$ for the velocity decay equation shown on the graph).

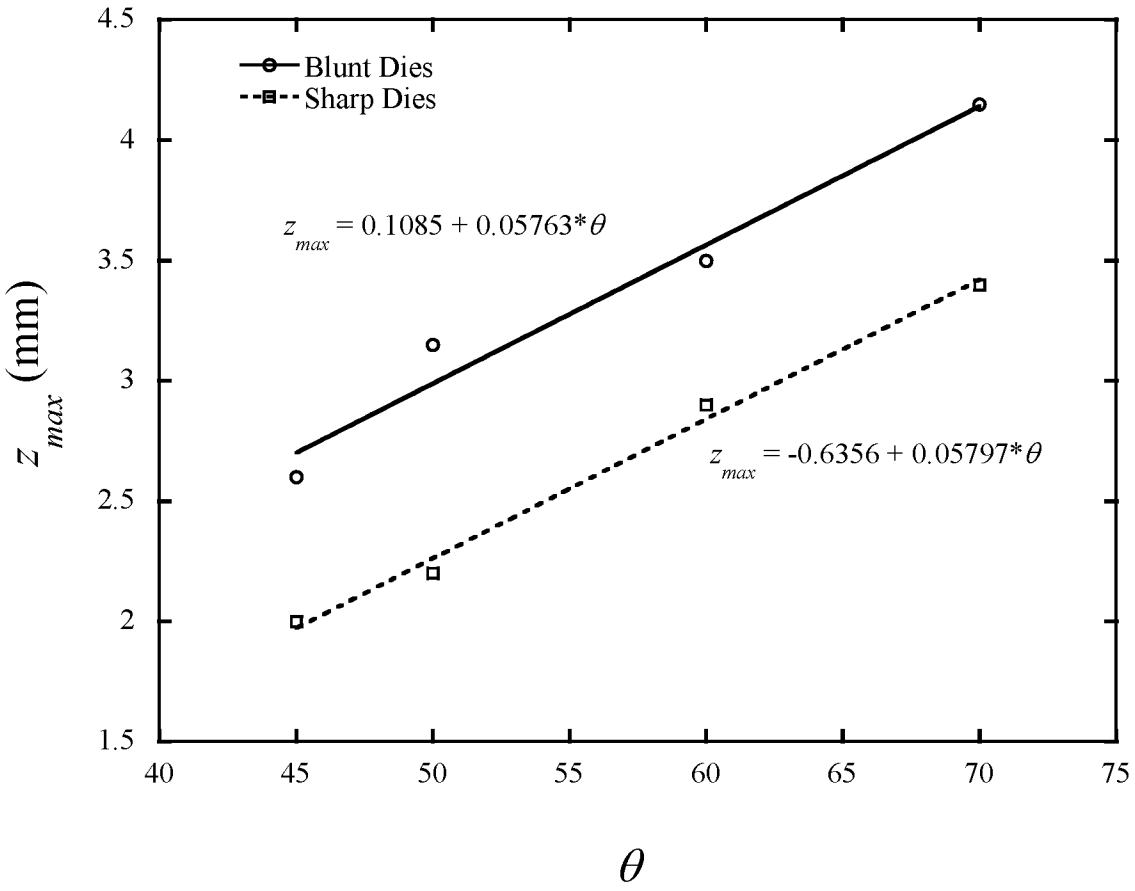

Figure 2-36. Relationship between zmax and q for the blunt flush dies (R^2 = 0.9618 for the curve fit shown on the graph) and sharp dies (R^2 = 0.9932 for the curve fit shown on the graph).

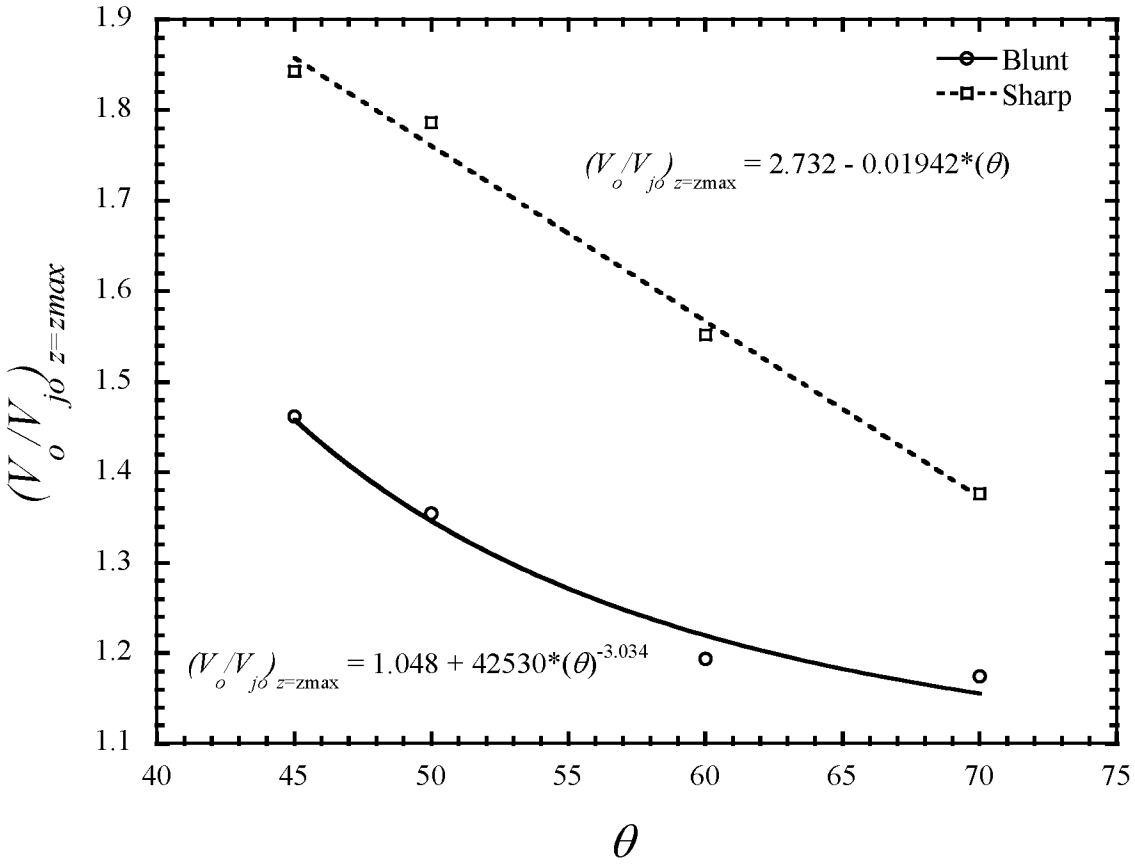

Figure 2-37. Maximum mean centerline velocity as a function of the slot angle of flush blunt dies ($R^2 = 0.9801$ for the equation shown on the graph) and flush sharp dies ($R^2 = 0.9920$ for the equation shown on the graph).

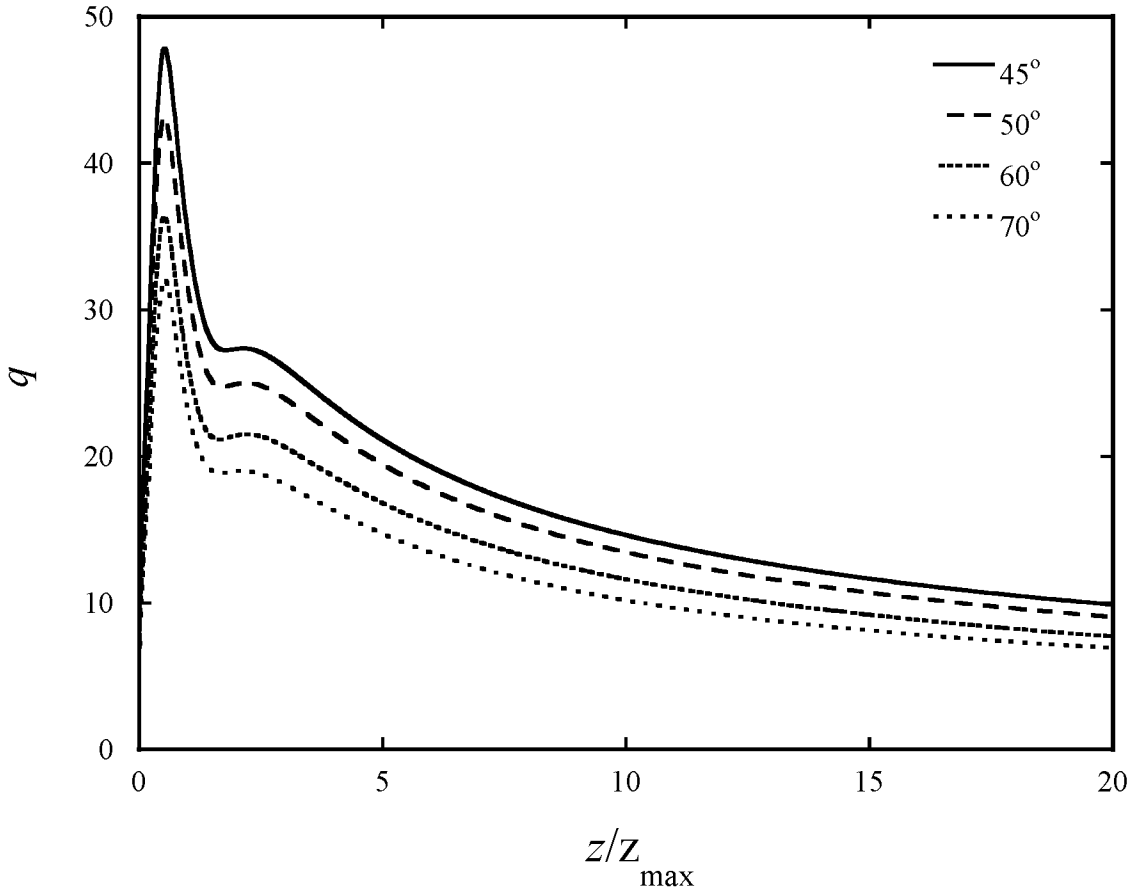

Figure 2-38a. Turbulence intensity along the centerline for blunt flush dies.

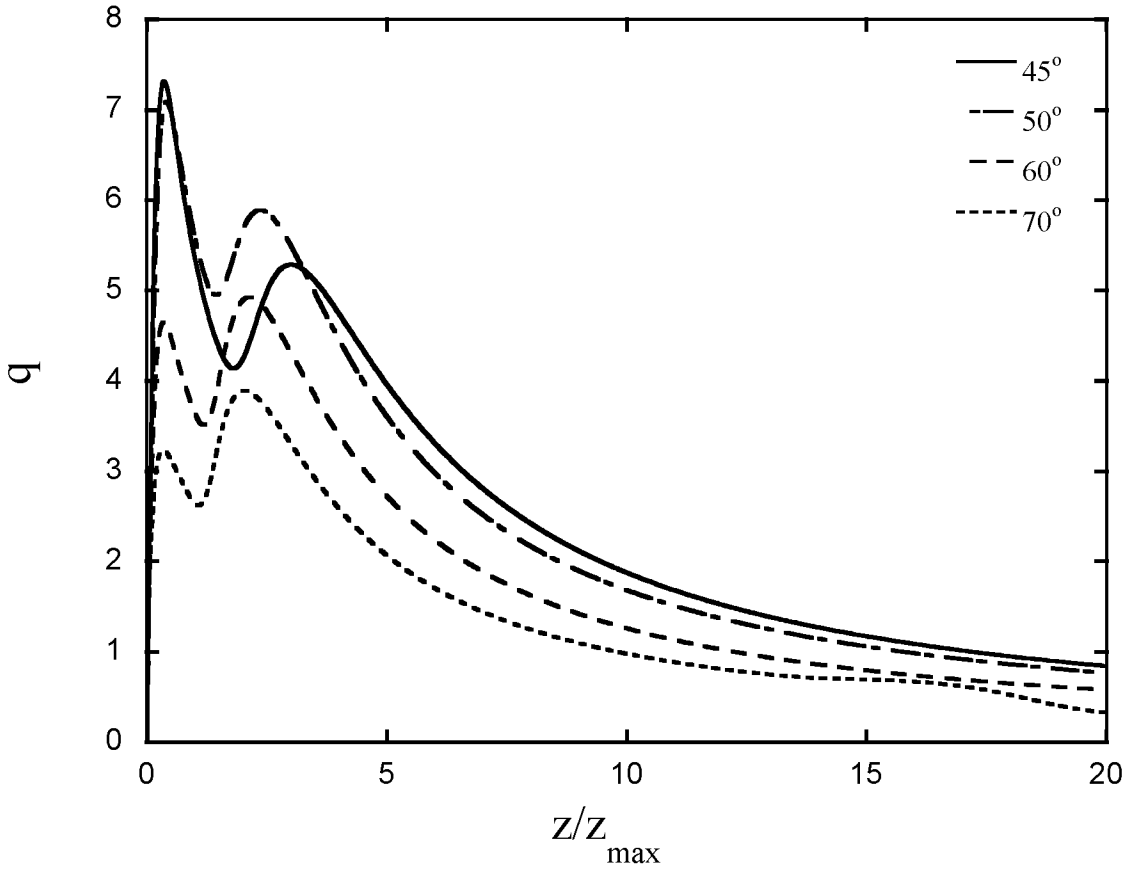

Figure 2-38b. Turbulence intensity along the centerline for sharp flush dies.

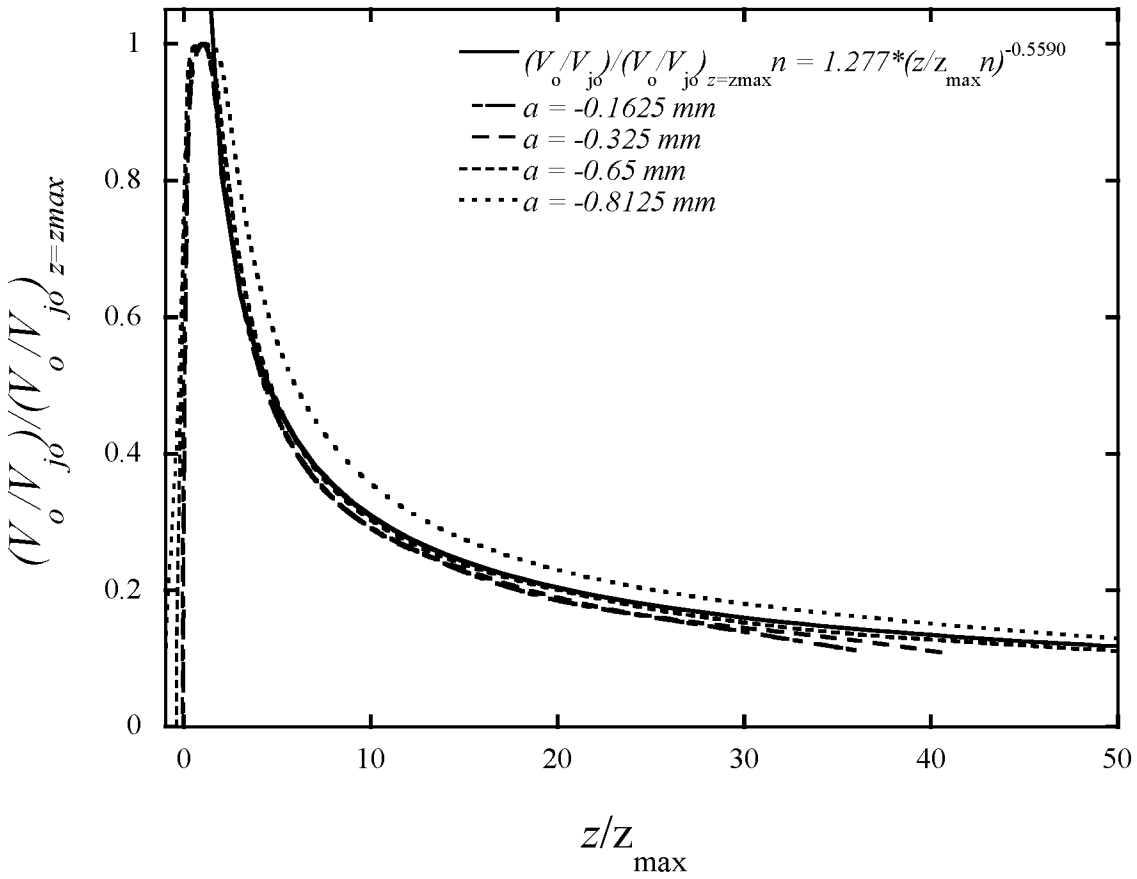

Figure 2-39a. Prediction of dimensionless mean centerline velocity for inset dies (R^2 = 0.9795 for the velocity decay equation shown on the graph).

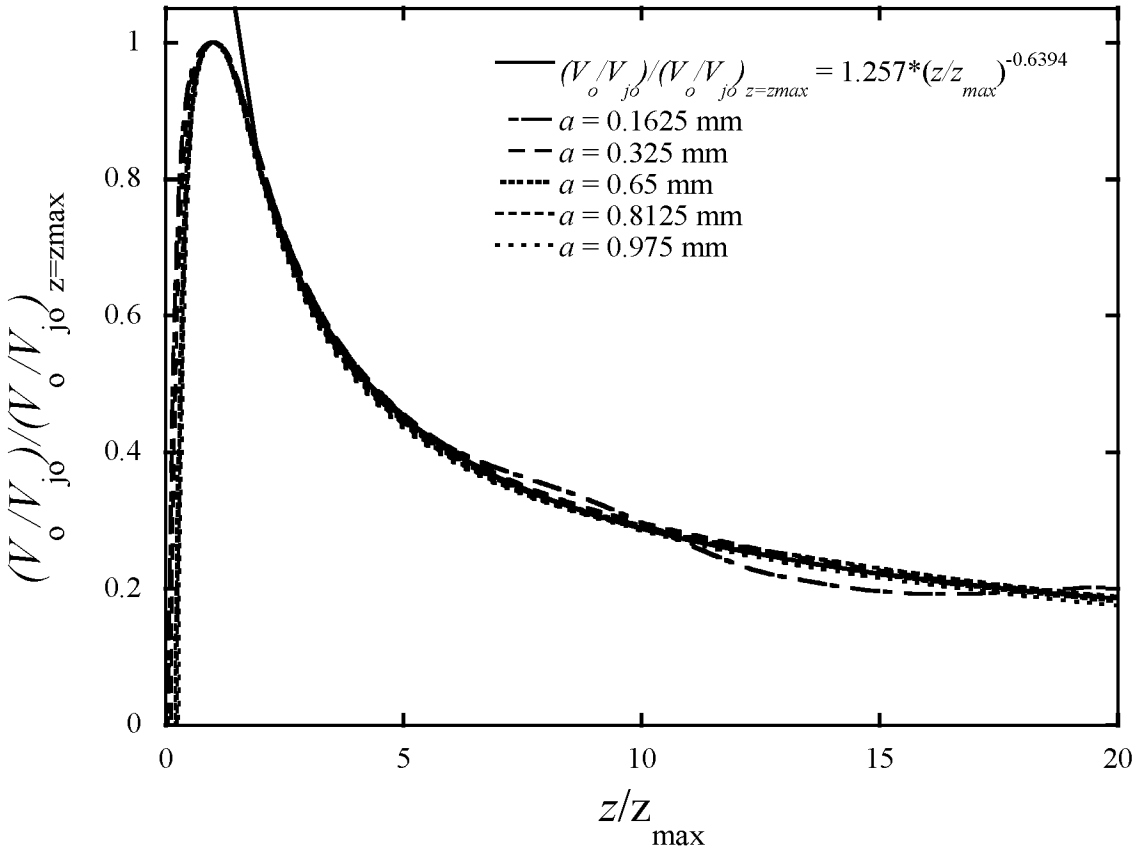

Figure 2-39b. Prediction of dimensionless mean centerline velocity for outset dies (R^2 = 0.9896 for the velocity decay equation shown on the graph).

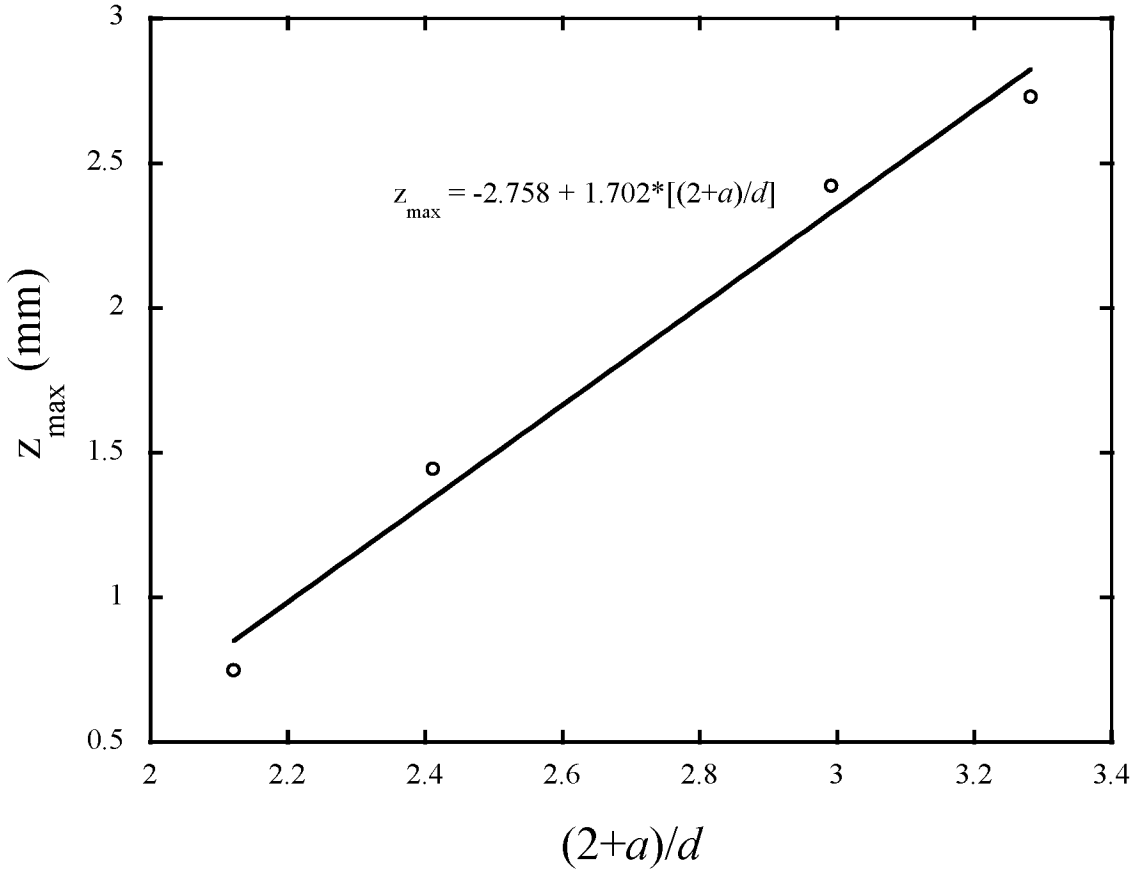

Figure 2-40a. Relationship between z_{max} and (2+*a*)/d for inset dies (R^2 = 0.9847 for the curve fit shown on the graph).

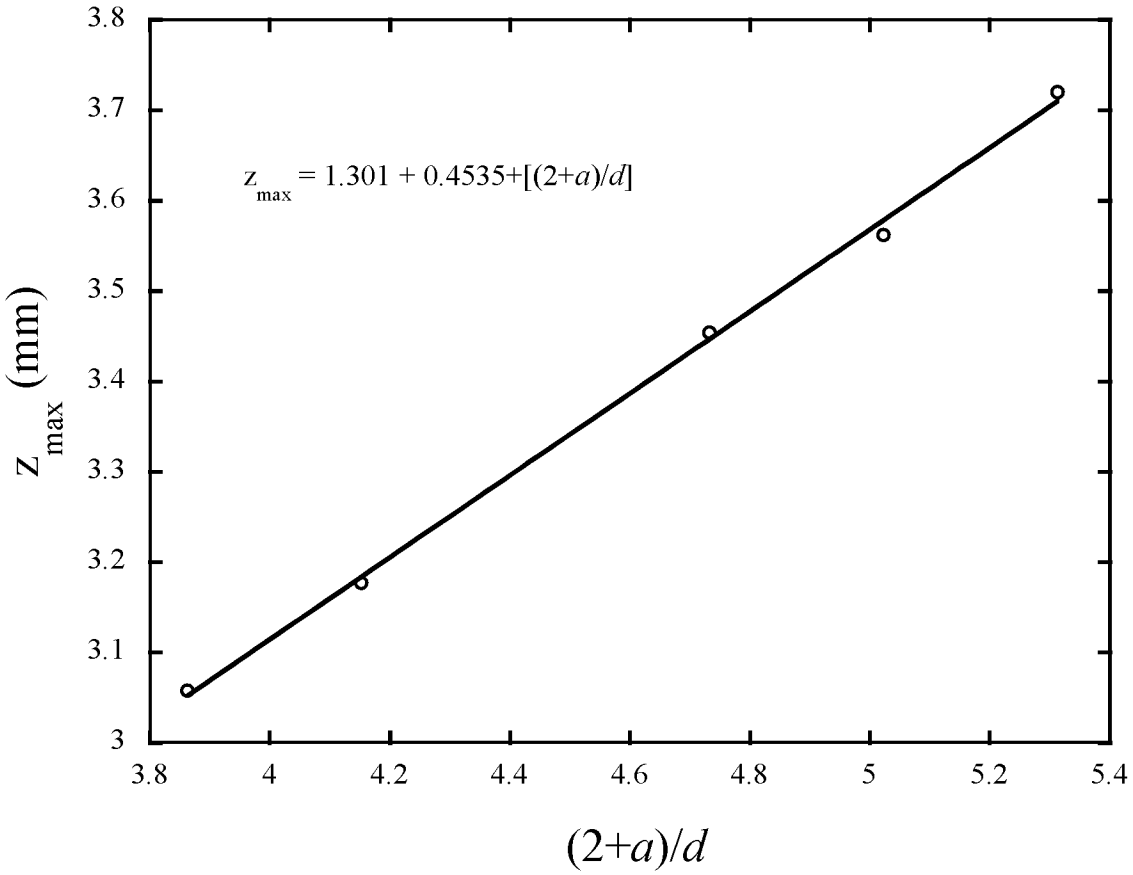

Figure 2-40b. Relationship between z_{max} and (2+*a*)/d for outset dies (R^2 = 0.9982 for the curve fit shown on the graph).

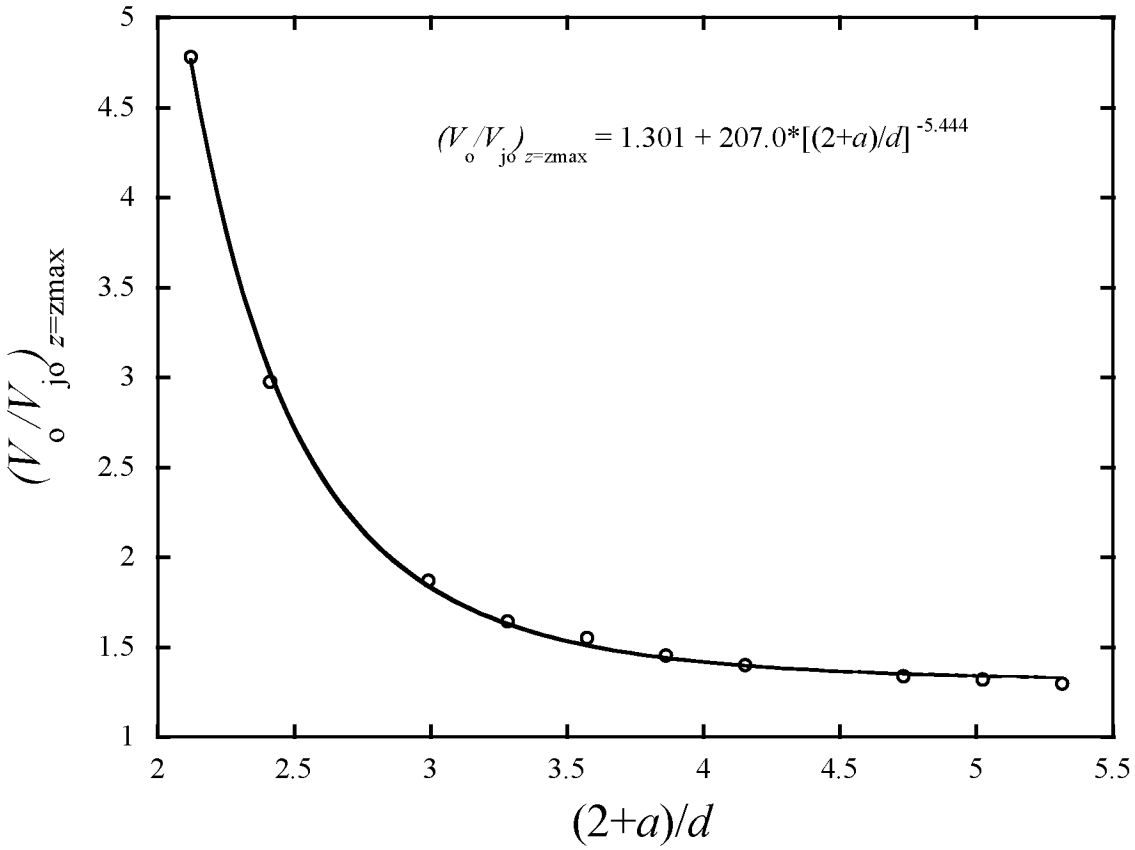

Figure 2-41. Maximum mean centerline velocity as a function of the die configuration for inset, flush, and outset sharp dies ($R^2 = 0.9994$ for the equation shown on the graph).

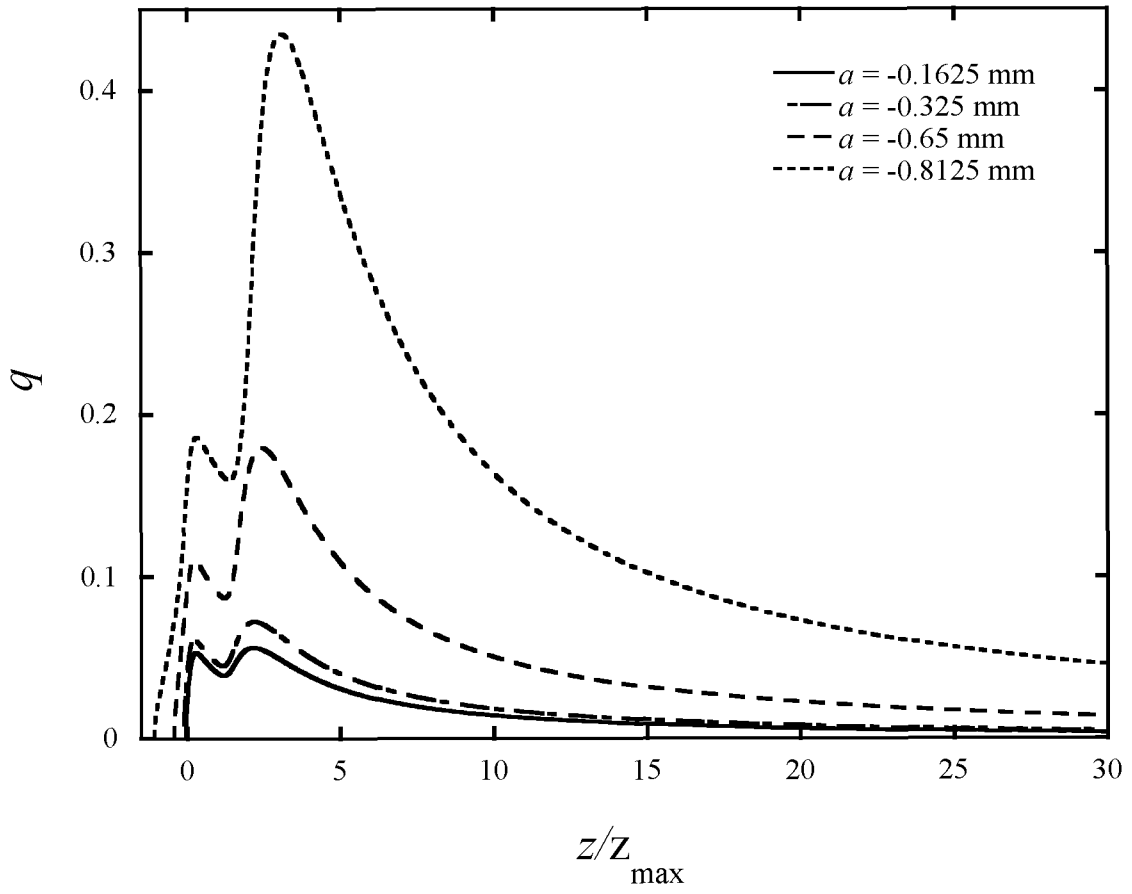

Figure 2-42a. Turbulence intensity along the centerline for inset dies.

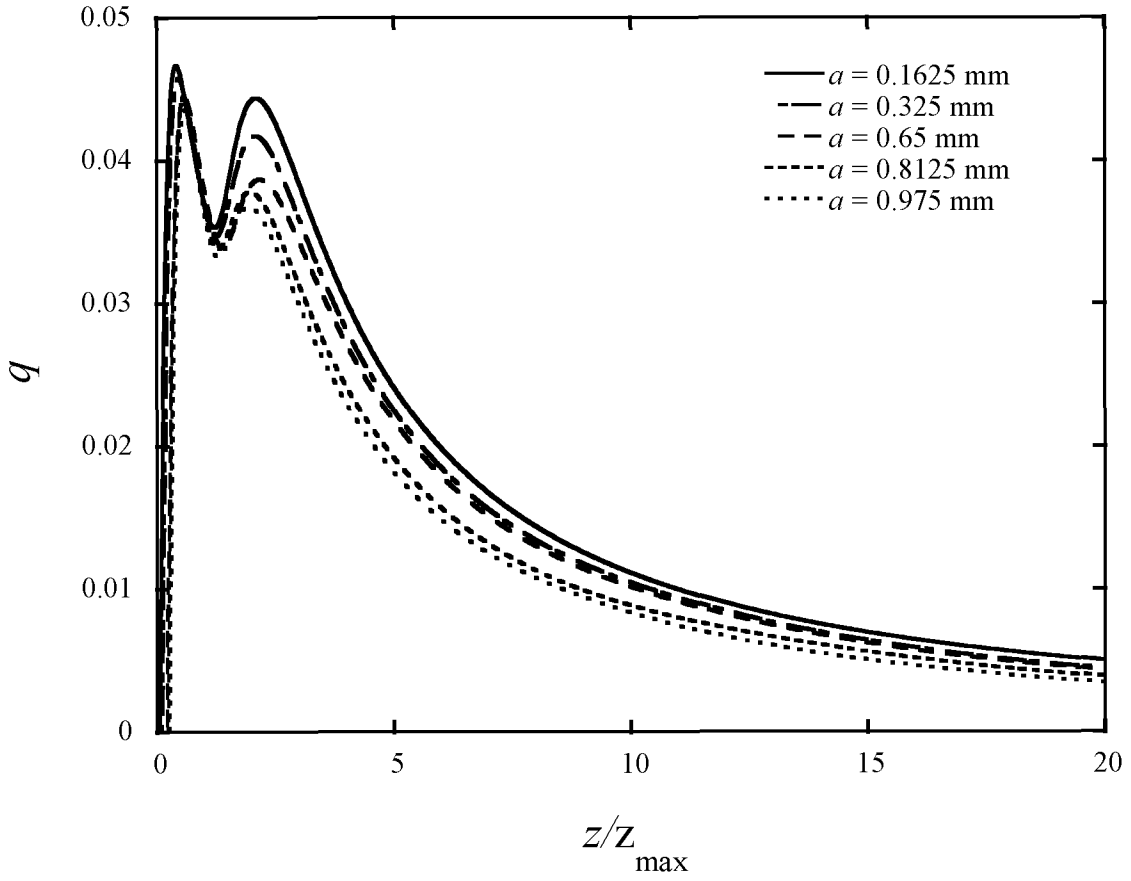

Figure 2-42b. Turbulence intensity along the centerline for outset dies.

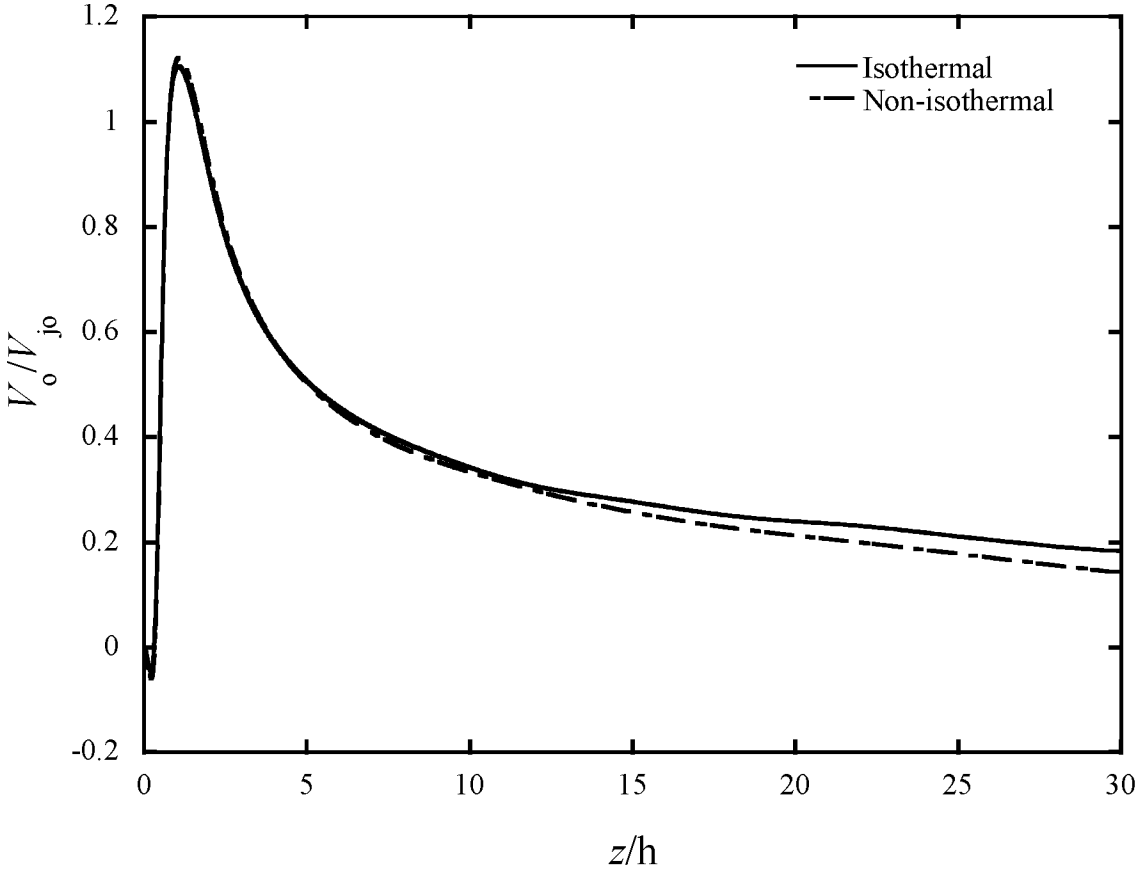

Figure 2-43. Comparison of dimensionless centerline velocity profiles for isothermal and non-isothermal cases. These simulations were conducted for a 60° blunt die.

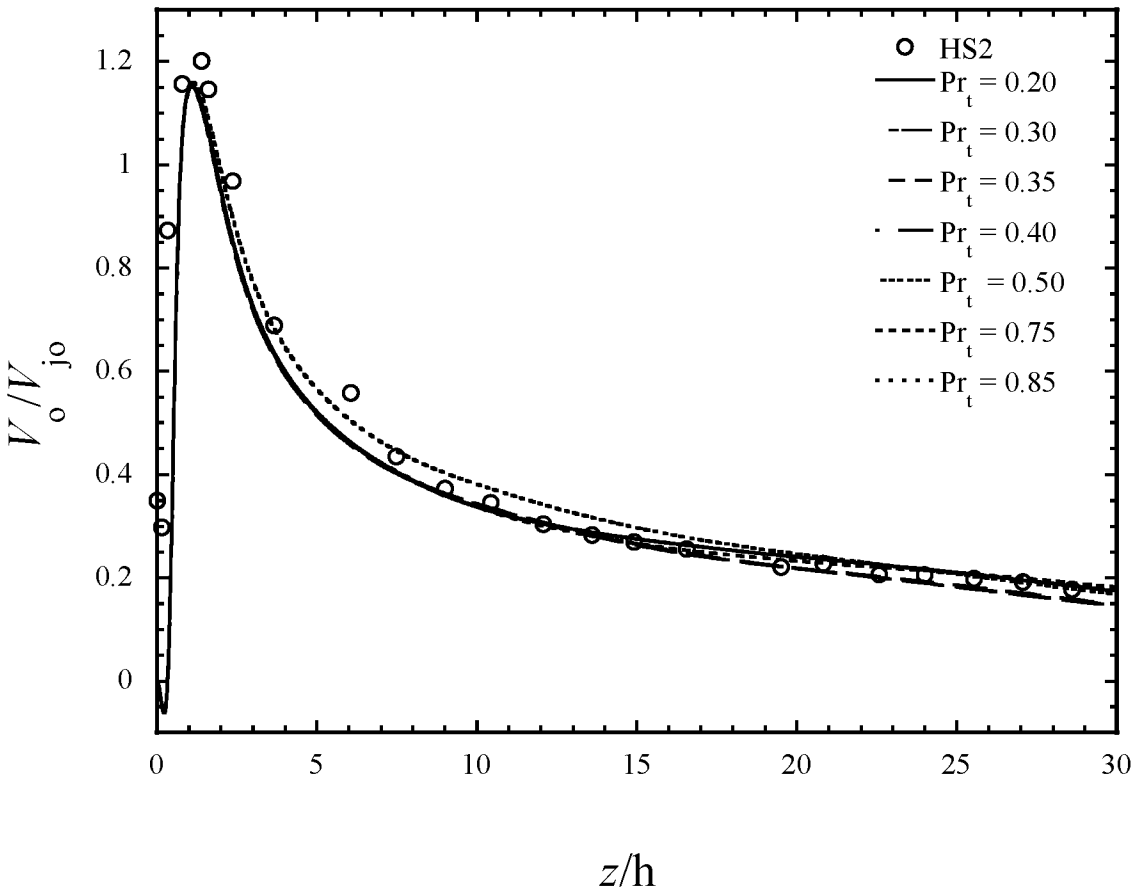

Figure 2-44. Comparison of simulated centerline velocity to experimental data throughout computational domain for 60° blunt die for simulations with different Pr_t values. Θ_{jo} = 100 K for both the simulations and experimental data. The curves shown are simulations run with V_{jo} = 23.2 m/s.

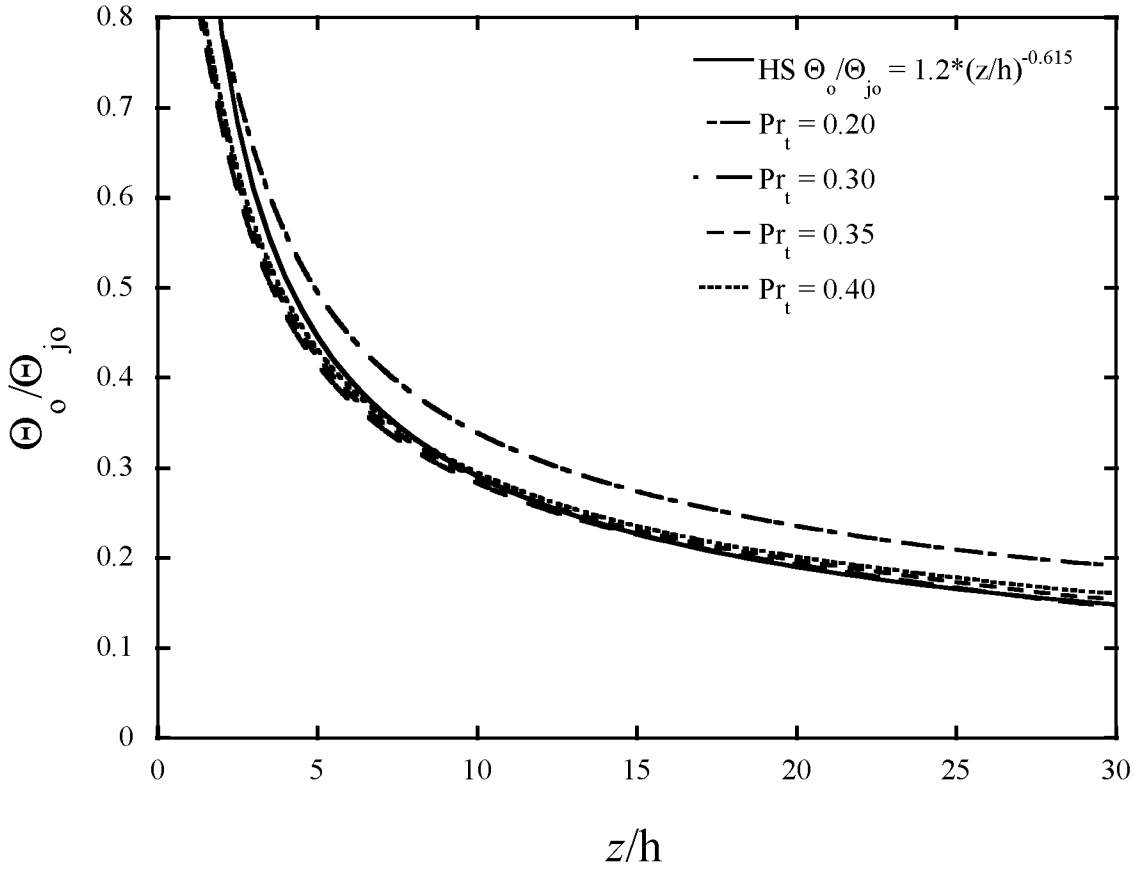

Figure 2-45a. Comparison of simulated centerline temperature decay to an experimental correlation for 60° blunt die for $0.20 \leq Pr_t \leq 0.40$. The simulations were performed with Θ_{jo} = 100K for both the simulations and the experimental fit. The curves shown are the simulations with V_{jo} = 23.2.

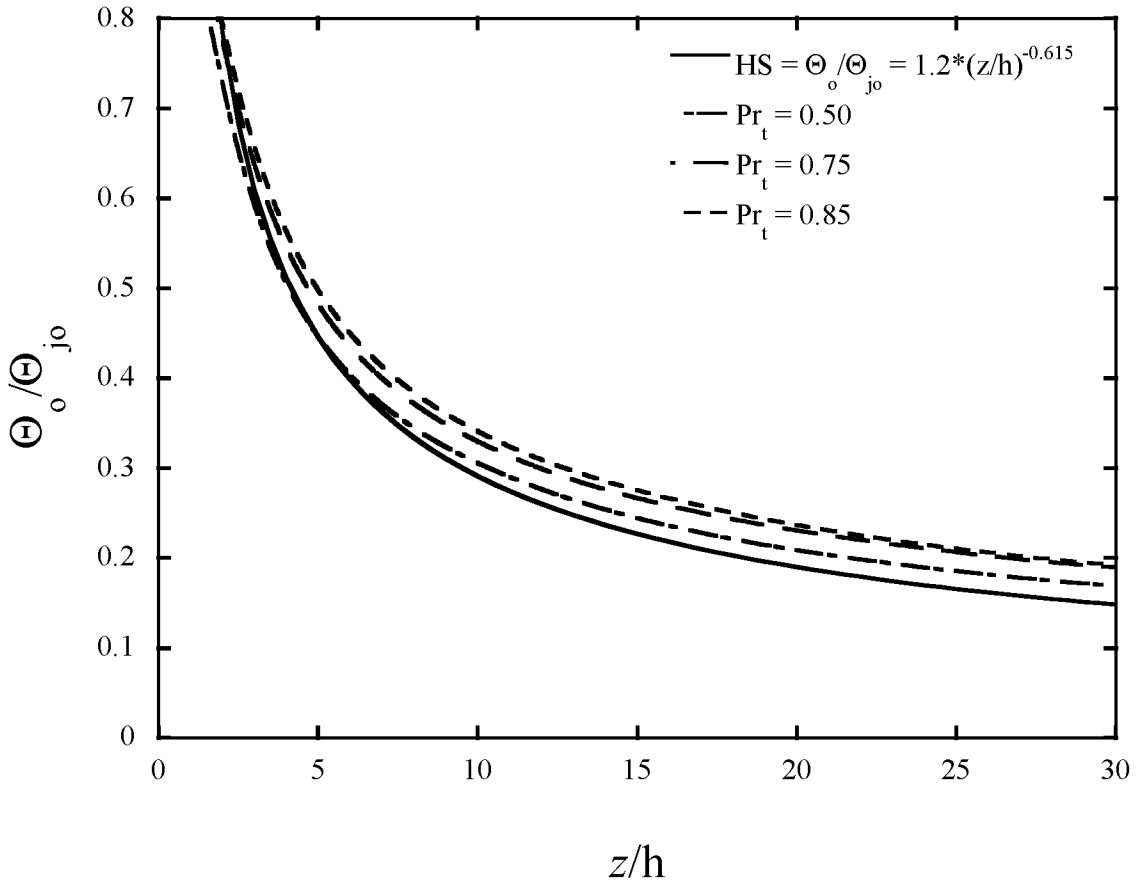

Figure 2-45b. Comparison of simulated centerline temperature decay to an experimental correlation for 60° blunt die for $0.50 \leq Pr_t \leq 0.85$. The simulations were performed with Θ_{jo} = 100K for both the simulations and the experimental fit. The curves shown are the simulations with V_{jo} = 23.2.

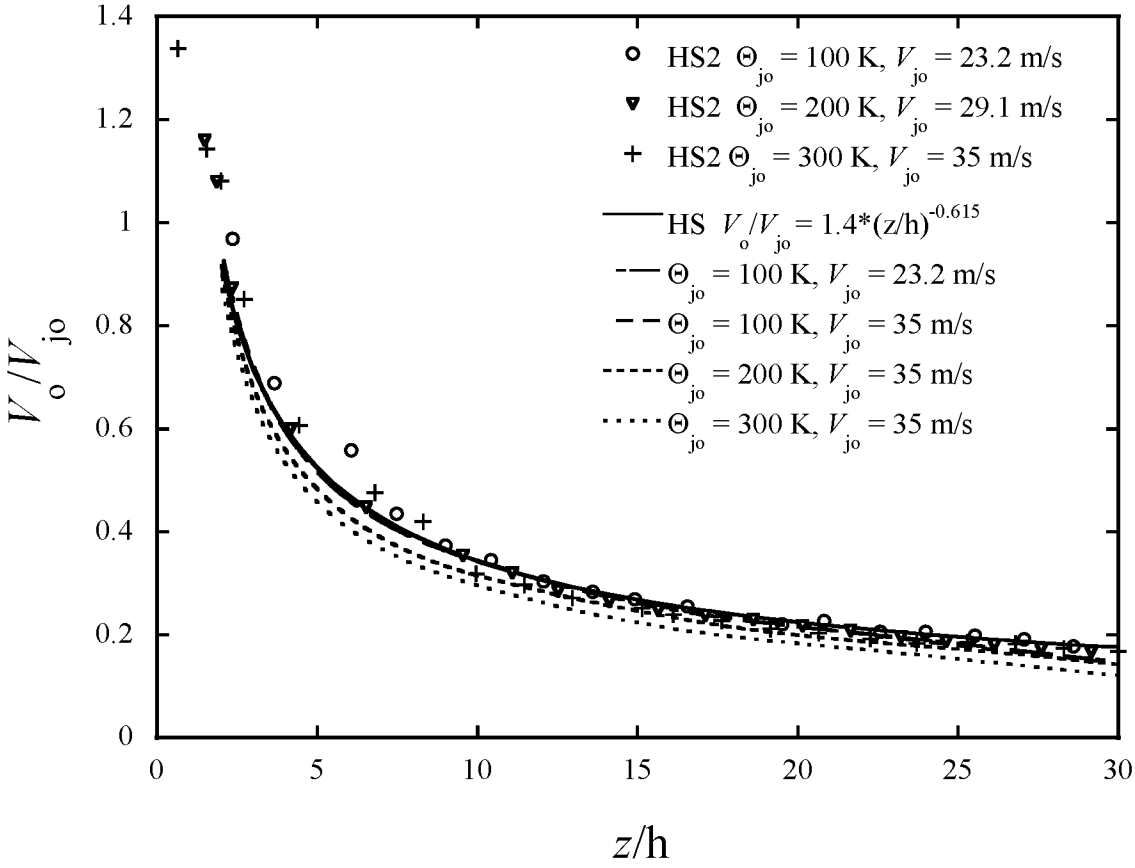

Figure 2-46. Dimensionless centerline velocity as a function of distance below the die face. The simulated curves and the experimental curves are shown for a 60° blunt die with $Pr_t = 0.30$.

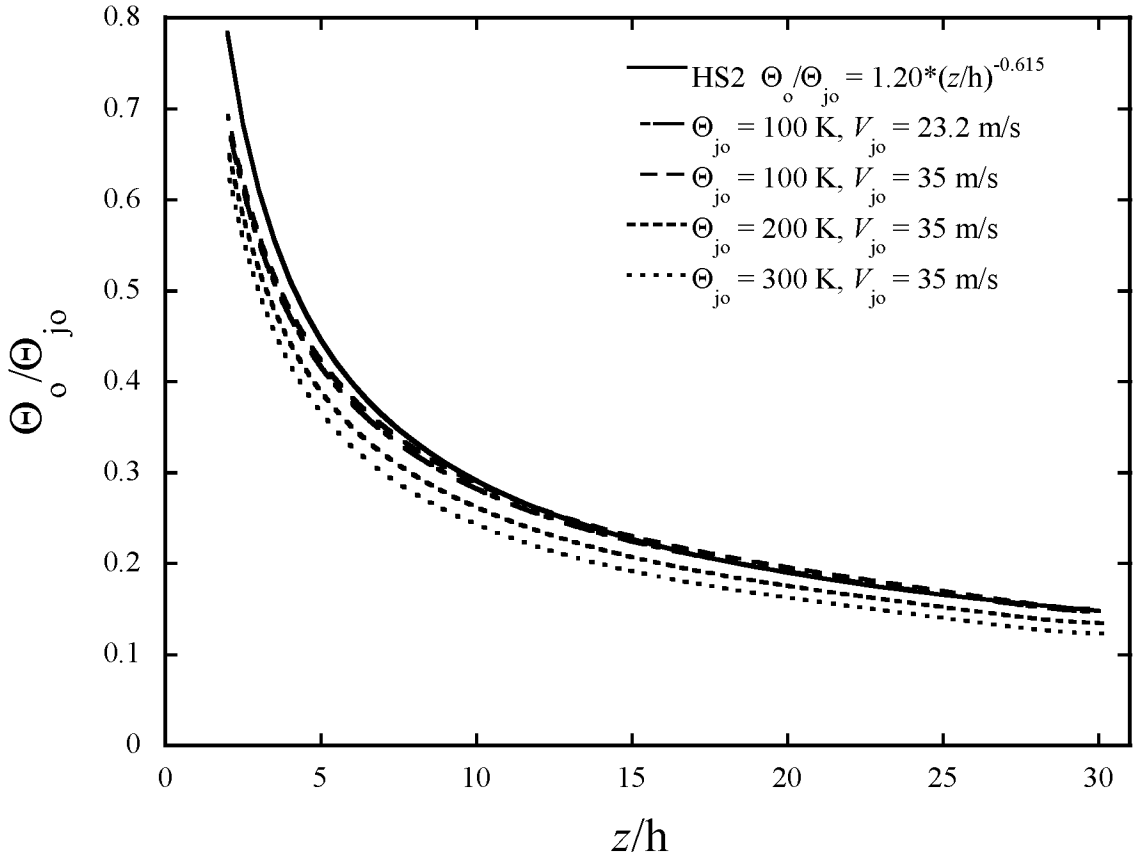

Figure 2-47. Dimensionless centerline temperature as a function of distance below the die face. The simulated curves and the experimental curves are shown for a 60° blunt die with $Pr_t = 0.30$.

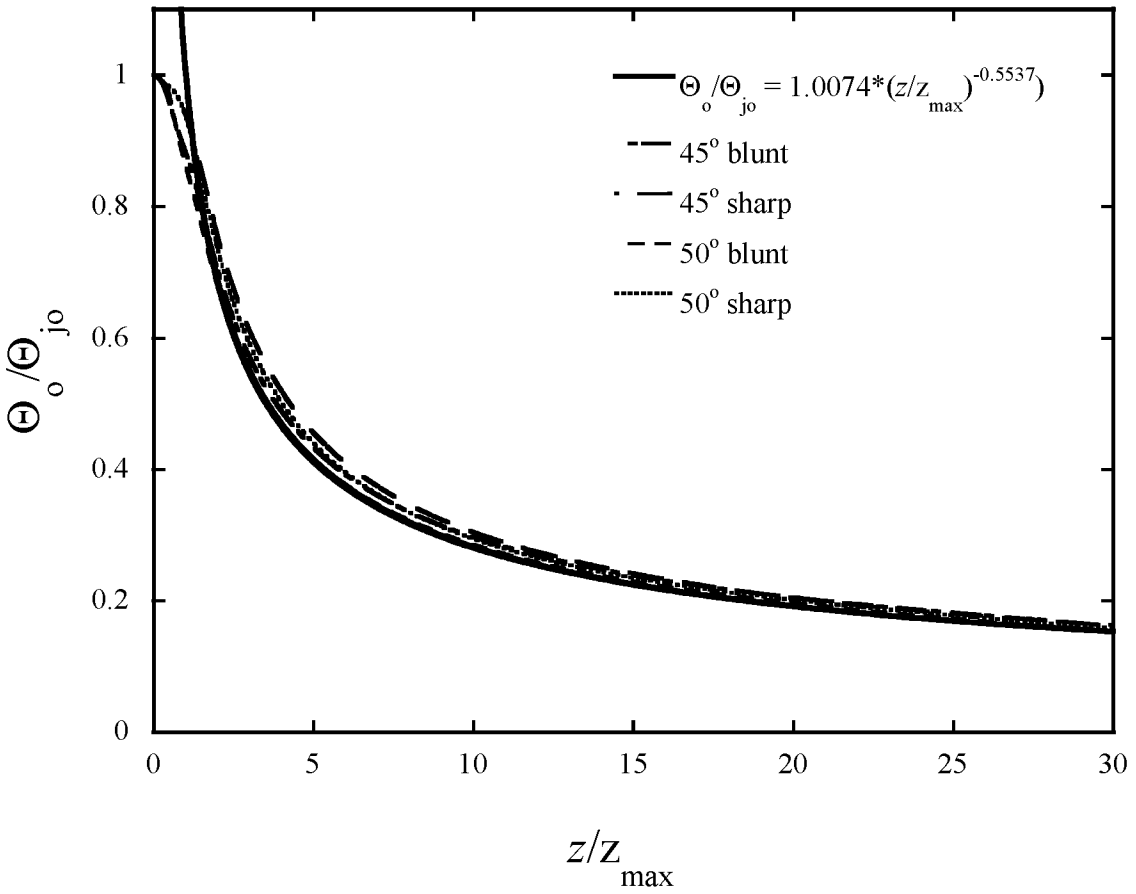

Figure 2-48a. Dimensionless temperature decay for blunt and sharp 45° and 50° dies. The general correlation fitting all temperature decays is $\Theta_o/\Theta_{jo} = 0.0074* (z/z_{max})^{-0.5537}$ with an $R^2 = 0.9831$. The simulations were run for a die with $Pr_t = 0.30$, $\Theta_{jo} = 100$ K, and $V_{jo} = 23.2$ m/s.

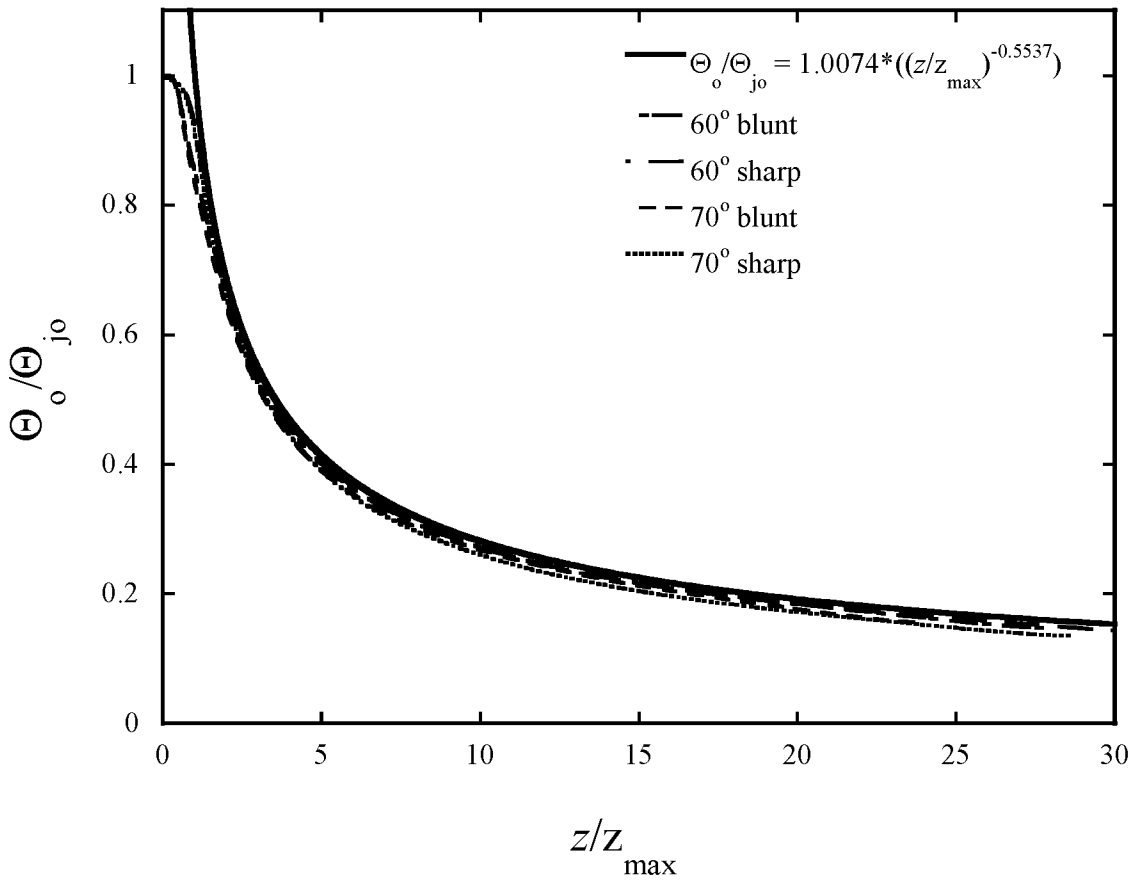

Figure 2-48b. Dimensionless temperature decay for blunt and sharp 60° and 70° dies. The general correlation fitting all temperature decays is $\Theta_o/\Theta_{jo} = 0.0074^* (z/z_{max})^{-0.5537}$ with an $R^2 = 0.9831$. The simulations were run for a die with $Pr_t = 0.30$, $\Theta_{jo} = 100$ K, and $V_{jo} = 23.2$ m/s.

CHAPTER 3: MULTIHOLE MELT BLOWING DIES

Contents of this chapter have been reproduced from the following sources:

Krutka, H. M.; Shambaugh, R. L.; Papavassiliou, D. V. Analysis of Multiple Jets in the Schwarz Melt-Blowing Die Using Computational Fluid Dynamics, *Ind. Eng. Chem. Res.*, **2005**, *44*(23), 8922-8932.

Krutka, H. M.; Shambaugh, R. L.; Papavassiliou, D. V. Analysis of the Temperature Field from Multiple Jets in the Schwarz Melt Blowing Die Using Computational Fluid Dynamics, *Ind. Eng. Chem. Res.*, **2006**, *45*(14), 5098-5109.

3.1 Introduction to Multihole Dies

Melt blowing dies with arrays of annular jets are often referred to as Schwarz dies. The type of Schwarz die discussed in this chapter has an array of 165 annular jets arranged in 55 rows and three columns. This type of melt-blowing die is used in industrial processes for producing nonwoven mats of fibers (Schwarz, 1983). Figure 3-1a is the bottom view of a Schwarz melt blowing die. Figure 3-1b is a closer view of a three by three matrix of jets in the center of a Schwarz die. Figures 3-1a and 3-1b have been adapted from Mohammed and Shambaugh (1993), henceforth referred to as MS, and show the bottom view of a section of such a Schwarz die. In the coordinate system used in Figure 3-1, the air and polymer are traveling from the die face, set at $z = 0$, in the positive z-direction -- which is pointing towards the reader for this figure. (In industrial practice, the z-direction is often facing vertically downward towards the earth.) The polymer exits the die from the capillaries that are located in the center of each orifice/jet assembly (the metal of the capillaries is denoted by cross-hatching). For each capillary, air exits from an approximately annular zone. The inside of each zone is bounded by the 0.635-mm (outside diameter) metal capillary; the outside of each zone is bounded by the

edges of a stack of thin metal plates. The inner diameter of the metal tube that holds the plates (i.e. the outer diameter of the air annulus) has a diameter of 1.016 mm. The plates both provide an outlet for the air and mechanically center the polymer capillaries. Details of the plate assembly are given in MS. In die operation, air is pressurized, heated, and fed to the melt blowing die. As both the air and polymer exit the die face, the high velocity air jet streams impact the molten polymer. The resulting drag force from the air rapidly attenuates the polymer into fine fiber strands (Shambaugh, 1988).

Fluent^{TM} 6.2 was the CFD software package used to simulate the melt-blowing dies. The details concerning the computational domain, grid, and turbulence modeling are discussed in the following subsections. All simulations were completed on a computer with a dual Pentium 4 Xeon, 2.8 GHz processor.

3.1.1 Round and Annular Jet Literature Review

Due to their many practical applications, round air jets (with no polymer involved) have been analyzed in depth (Taylor, 1951, Rajaratnam, 1976 and Schlicting, 1979). Turbulent round jets have been observed to be self similar in the far field (Obot, 1984 and Pope, 2000). They also have a constant spreading rate that relates the distance from the centerline where the velocity is equal to half of the centerline velocity to the distance from the jet nozzle. This spreading rate is defined as follows (Pope, 2000):

$$r_{1/2} = S(z - z_o) \tag{3-1}$$

The spreading rate constant, S, has been measured to be approximately 0.1 (Hussein, 1994).

The centerline velocity decays proportional to the inverse of the distance from the jet nozzle (Pope, 2000). Sforza et al. (1978) used both an experimental and an analytical approach to determine that the mass and enthalpy decay more quickly than the momentum for a round non-isothermal jet. Obot et al. (1986) measured the velocity and temperature field from two heated round jets with different nozzle lengths; during this work, the researchers determined that the shorter nozzle resulted in faster temperature decay due to more rapid entrainment of ambient air. Simulations have been used to model the flow and temperature field from different jet geometries, such as planar jets (Lai, 1998) and round jets (Babu, 2004). Kennedy et al. (2000) used Large Eddy Simulations (LES) to simulate a round two phase jet.

The flow field generated using different jet nozzles, such as annular jets, have been examined experimentally using a Pitot tube (Uyttendaele, 1989). Majumdar and Shambaugh used thermocouples to measure the temperature field from a non-isothermal annular jet (1991). It has been suggested that, in the far field, the effect of an annulus is negligible and an annular jet acts similar to a round jet (Ferdman, 2000). Moore et al. (2004) used CFD to successfully simulate the flow fields from melt blowing dies with single annular jets of various sizes; this research highlighted the effect of different mass flow rates on the flow field characteristics as well as the significant differences between a round jet and an annular jet. In that work, the experimental results from Uyttendaele and Shambaugh (1989) were used to calibrate the CFD model. Kim et al (2000) used hot wire anemometry to measure the flow field from a round jet with an initially asymmetric velocity profile. It was determined that a non-parabolic velocity profile changed the flow in the near field, but that the far field was similar to that of a round jet with a well

developed parabolic profile. Chattopadhyay (2004) completed a numerical investigation to study the heat transfer from impinging annular jets.

In addition, some research has been completed concerning the interactions between multiple round jets. Raghunanthan and Reid (1981) examined the effect on the flow field of changing the number of jets, while keeping the total air flow area the same. Manohar et al. (2004) used both experimental measurements and CFD to investigate the interactions of one round jet with four surrounding round jets. Their study included two cases. One case concerned jets of the same diameter, while the other case involved a large center jet surrounded by smaller jets.

MS measured the isothermal flow field from a Schwarz melt blowing die using a Pitot tube (1993). Later, they measured the non-isothermal flow and temperature fields from the same Schwarz melt blowing die (Mohammed and Shambaugh, 1994). (Henceforth, the 1994 non-isothermal study will be referred to as MS2.) The Schwarz melt-blowing die simulated in this work is composed of an array of inset annular jets. Experimentally, the isothermal flow field under such a Schwarz die has been investigated in MS. However, to the author's knowledge, different jet spacing in an array of jets has not been examined previously. This chapter considers the flow field from different geometries of isothermal Schwarz dies. The contributions of the present work are (a) to examine how relative jet placement alters the air flow field for a Schwarz die, (b) to use CFD to develop empirical correlations that can be used to predict the temperature field of different Schwarz dies, and (c) to investigate the interactions between the flow fields of multiple annular jets.

3.1.2 Computational Domain

Figure 3-1 shows the bottom view of a section of a Schwarz die of the type investigated by MS. The columns of jets in Figures 3-1a and b are parallel to the y-axis, while the rows are parallel to the x-axis. Figure 3-1b shows the location of the origin, which is at the die face at the center jet. The distance between jet centers on two consecutive columns is h_ℓ, while the distance between two jet centers on two consecutive rows is h_w. The hypotenuse of the triangle formed by h_ℓ and h_w is h_h. The dashed lines in Figure 3-1b represent the boundaries of the 3D computational domain used in the simulations. By defining these dashed lines as planes of symmetry, a smaller domain containing only one and a half jet openings was used to simulate the entire die. This domain allows comparison with the experimental work of MS, which focused on an area under a three by three matrix of jets at the center of the die. End effects from the outside rows were neglected by MS, and were also neglected in this computational study.

Figure 3-2a is an xz plane cut through the center of the 3D domain used in the simulations. The width of the domain at the die face is $3/2h_\ell$. The die face is located at $z = 0$. In order to allow for spreading of the outside jet, the domain width increases in the positive z-direction. This increased width results in the bottom of the domain being 2.5625 mm wider than the width at the die face. This width profile was chosen after studying the spreading rate of a singular annular jet. The width of the computational domain is increased so that the outside jet would have space to spread and still remain within the computational domain. The length of the domain, not including the jet, is 30 mm. A close up of the jet (shown surrounded by the dashed lines in Figure 3-2a) is given

in Figure 3-2b; this is representative of the geometry of all the jets in the die. The jet height is 5 mm.

As mentioned previously, there is a stack of five metal plates that center each of the polymer capillaries in the Schwarz die used in the industry. These triangular plates inside the annulus complicate the geometry of the computational domain; an attempt to use this exact geometry led to skewed grid cells, which in turn led to simulations that did not converge. Therefore, the plates were approximated in the computational domain by assuming that the air flowed through an annulus of outside diameter D_o and inside diameter D_i. The outside diameter of the polymer capillary (0.635 mm) was specified as the inside diameter D_i. With the assumption that the triangular plates determined the controlling area for air flow, this area was determined by subtracting $(\pi D_i^2)/4$ from the area of each triangular hole in the plate. This calculation gave $D_o = 0.817$ mm. By using these annular dimensions, the simulation had the same V_{jo} as the experimental studies. Because (in the actual die) the polymer capillary is inset above the die face by 0.254 mm, this inset was also used in the geometry of the simulation.

For the non-isothermal CFD simulations, the inside diameter D_i (the outside boundary of the polymer capillary) was set equal to 0.8766 mm (versus the actual value of 0.635 mm). The outside diameter of the annulus, D_o, was set equal to the experimental value of 1.016 mm. These values for D_i and D_o gave the desired cross-sectional area of 0.207 mm^2, which was the same flow area as in the non-isothermal simulations. By using the D_o and D_i described above, the simulations have the same mass flow rate per hole and the same V_{jo} (nominal face velocity) as in the MS2 experiments.

Similar to the experimental work in MS and MS2, the airflow was examined without the presence of the polymer fiber. The assumption was made that the presence of the fiber would have a negligible effect on the flow and temperature fields. This assumption is examined in depth in Chapters 4 and 5.

3.1.3 Grid for Multihole Dies

The computational domains as well as the corresponding grids were created using Gambit™. The same grids refinements were used for both the isothermal and non-isothermal simulations. The grid for each simulation was composed of tetrahedral cells with 0.15 mm spacing. Once the grids were imported into Fluent™, they were further refined. The area of refinement included the jets (the area above the $z = 0$ in Figure 3-2). Also refined was a box-shaped area from $0 \leq z \leq 2$ mm that is $2D_o$ wide in both the x and y directions and is centered below the jet inlets. After this grid refinement was completed in Fluent™, the entire grid was smoothed to avoid highly skewed grid cells.

Figure 3-3a shows the isothermal centerline z-velocity of three simulations based on the jet spacing of the Schwarz die in MS. Figure 3-3b shows the centerline excess temperature decay for the non-isothermal simulations. All these simulations have the same computational domain size and the same type of cells. However, the simulations have different grid refinements. The coarsest grid has a spacing of 0.2 mm and has been refined three times in Fluent™ to yield 632,782 cells. The next coarsest grid has a spacing of 0.15 mm and has been refined twice in Fluent™ to yield 713,077 cells. The finest grid has a spacing of 0.12 mm and has also been refined twice, resulting in 1,142,708 cells. Since the profiles of the 713,077 and 1,142,708 cells match, 0.15 mm cell spacing with two refinements was used for the grids for the other six simulations

discussed in this work. Table 3-1 presents the number of iterations and time necessary to complete each of the simulations in Figures 3-3a and b.

3.1.4 Multihole Geometries

Six different die geometries will be discussed in this chapter. Case 4 is based on the Schwarz die examined experimentally in MS and MS2. For this simulation, h_w is 2.15 mm, while h_ℓ is 3.25 mm. Case 1 is the array with the smallest spacing between the jets with $h_\ell = h_w = 1.625$ mm. Cases 2 and 3 were created by decreasing both the h_w and h_ℓ distances relative to the base case (Case 4). For Case 2 these distances were decreased by 35%, and for Case 3 the distances were decreased by 25%. Simulations for a case with a decrease in the spacing between the jets by 50% relative to the base case showed that the jets were too close to each other to produce a flow pattern with distinguishable characteristics. Hence, this case is not presented here. Cases 5 and 6 were created by increasing the h_w and h_ℓ distances relative to Case 4. For Case 5 these distances were increased by 25%, and for Case 6 they were increased by 50%. Table 3-2 provides the case numbers with the corresponding values of h_w, h_ℓ, and h_h. Higher case numbers correspond to h_h increases and, therefore, increased inlet spacing between the jets.

3.2 Isothermal CFD Results

For the isothermal simulations the same mass flow rate was used as that given in MS. The air flow to the actual die was 8.27×10^{-3} m^3/s at standard conditions of 21 ^oC and 1 atmosphere pressure. This corresponds to an air loading of 3.62 g/min for each capillary assembly. The simulations were run under isothermal conditions at 21 ^oC. Although the industrial melt-blowing process uses elevated air and die temperatures, the

effect of this temperature difference on the dimensionless velocity flow field is not expected to be significant. Therefore, following the procedure used by the experimentalists, the isothermal simulations were completed first, followed by a second group of simulations with non-isothermal conditions. All the different geometries isothermal simulations have the same jet configuration, the same grid type, and the same refinement. In addition, all the simulations were run using the standard k-ε turbulence model in Fluent^{TM}. The simulations were all required to reach 3×10^{-5} convergence. All the cases were run at isothermal conditions at a temperature of 294 K (the same temperature used in the experiments of MS). The ideal gas model was used to determine the air density.

3.2.1 Comparison to Experiments

In previous work from our laboratory concerning simulations of jets, the Reynolds Stress Model (RSM) has been used. However, the RSM model performs poorly for the 3D simulations discussed in this paper: the simulations failed to converge when the RSM model was used. Since the RSM model is known to perform poorly with tetrahedral cells, such as those used in the multihole grids, this is the probable reason for the failure of RSM. Therefore, the simpler k-ε model was used.

Since the k-ε model was used for the multi-hole simulations in this paper, a 2D simulation of a single annular jet was completed using the k-ε model. The results of this simulation were then compared with both the (RSM) simulation from Moore et al. (2004) (who simulated a single annular jet with RSM) and the data from Uyttendaele and Shambaugh (1989). The comparison revealed that the k-ε model correctly simulated the velocity decay of a singular annular jet. Compared to MS, the simulation over-predicted

the spreading rate of the single annular jet. However, the spreading rate was close to the experimentally measured rate of a round jet (0.106 vs. 0.1).

A well-documented characteristic of jet flow is the entrainment of surrounding air. MS measured the entrainment coefficient from a Schwarz die. This entrainment coefficient is defined as the entrained air mass flow rate at a particular location away from the die divided by the mass flow rate at the die face. The mass flow rate is measured over the area where the velocity is equal to or greater than 10% of the centerline velocity. According to the nomenclature in MS, for the length L of the die, the mass flow rate is defined as follows:

$$\frac{M(z)}{L} = \int_{y=-L/2}^{y=L/2} \int_{x=-\infty}^{x=\infty} \rho(x,y,z)v(x,y,z)dxdy \tag{3-1}$$

Then, the mass flow rate of the air that has been entrained can be defined as

$$\frac{M_e}{L} = \frac{M(z)}{L} - \frac{M_o}{L} \tag{3-2}$$

Finally, the entrainment coefficient can be determined using the following formula:

$$\Psi = \frac{M_e(z)}{M_o} \tag{3-3}$$

Figure 3-4 compares the entrainment coefficient measured by MS to that of Case 4. Close to the die face, the simulation under-predicts the entrainment coefficient, while further away from the die face, good agreement in observed between the CFD and experimental results.

The velocity profiles at different distances from the die were also measured by MS. It was found that the velocity field becomes self similar at far distances from the jet orifices and that one equation can describe the dimensionless velocity profile in the far field. Figure 3-5 compares the velocity profile of Case 4 to the experimental data and the corresponding fit proposed in MS. At all positions below the die face, good agreement is observed between the simulations and the experiments. (Keep in mind that positions below the die face are for $z > 0$ and do not involve internal velocities in the air capillaries).

Figure 3-6a is a three dimensional contour plot of the z-velocity in Case 4 at the position $z = 1.27$ mm. Figure 3-6b is the corresponding plot from MS. In both these plots, one observes that the jets are still distinct, and have not merged together. However, as one moves in the positive z-direction, neighboring jets begin to merge to form, in effect, one jet. This phenomenon can be observed in Figures 3-7a and 3-7b, which are the 3D contour plots for the z-velocity at the position $z = 7.62$ mm for Case 4 and MS, respectively. The outside jets have begun to merge into the center jets, and the distinction between separate jets is becoming less obvious.

3.2.2 Comparison between a Schwarz Die and a Single Annular Die

Based on Baron and Alexander (1951), MS suggested a method of predicting the air flow profiles from the Schwarz die in terms of the velocity profiles from a single annular jet. This method is based on the assumption that the kinetic energy profile under the jets in the Schwarz die can be predicted by calculating the sum of the kinetic energy contributions from all the jets in the array. The following equation was suggested by MS:

$$\frac{\rho V^2}{\rho_{jo} V_{jo}^{\ 2}} = \frac{A_o}{\pi C_m^{\ 2} z^2} \sum_{n=-27}^{n=+27} \sum_{m=-1}^{m=+1} e^{-(a^2/C_m^{\ 2} z^2)} \qquad (3\text{-}4)$$

Thus, the contribution of a jet on the outside column (see Figure 3-1a or 3-1b) to the kinetic energy along the centerline of a jet on the inside column is equal to the kinetic energy of a single jet at the distance of h_ℓ away from, but parallel to, the centerline. To compare the simulated velocity profiles from the Schwarz die to the prediction of equation 3-4, the effect of the jets immediately surrounding the jet under consideration were summed. The effect of jets farther away is negligible. For instance, to predict the kinetic energy profile for the center jet in Figure 3-1b, the surrounding eight jets were considered. Figure 3-8a shows the kinetic energy profile that is predicted by this method for the centerline of the center jet in Figure 3-1b. Clearly, the prediction misses the location of the maximum, as well as the magnitude of the dimensionless kinetic energy throughout the domain.

To test the ability of the prediction method for a jet on the outside column, the five jets immediately surrounding the outside jet were considered. Figure 3-8b shows the simulated centerline dimensionless kinetic energy profile of the outside jet to the predicted profile. Clearly, the prediction method is less accurate for this jet than for the center one. Therefore, the flow field from multiple jets is the result of nonlinear interactions between the individual jets, which can not be described with the summation of profiles from a single jet. The prediction method misses the actual flow field profiles because it does not take into account the entrainment of the outside column of jets by the inside column, as was also pointed out in MS.

Figure 3-9 shows a comparison of the jet centerline velocity profile of a simulated single annular jet with the center and outer jet profiles in the simulated Case 4 (the case

that is based on the experimental geometry of MS). The differences in the velocity profiles are significant. For a jet in the center column of the array, the position where the maximum *z*-velocity occurs has been shifted towards the die face. In addition, the decay in the far field is more gradual. This can be attributed to the contribution of the air from the surrounding jets.

The outside jet dimensionless velocity profile in Figure 3-9 deviates even more strongly from the single jet profile than the center jet. Compared to the center jet, the outside jet exhibits a maximum that is closer to the die face and shows a much sharper decay. The entrainment effect of jets causes the outside jets to be pulled toward the center jet. At some distance from the die face ($z/D_o \approx 7$ on Figure 3-9), the velocity profile under the outside jet actually reaches a minimum, a result that is not present in the profiles of the center jet or the single jet. Even farther from the die face, the velocity (of the outside jet) increases because the velocity field is the result of the merged flow field of the initially separate jets.

3.2.3 Qualitative Flow Field Description

Figure 3-10 is a qualitative diagram of the flow zones created by multiple jets; such a diagram is helpful in understanding the quantitative results of multiple annular jet simulations. Figure 3-10 shows a side view of the flow from two annular jets. At the top of the figure is an outside jet, while a center jet is located at the bottom of the figure. The identification and naming of the zones is based on the jet development regions that are exhibited in single annular jets (Moore, 2004) and parallel plane jets (Lai, 1998). In a multiple jet arrangement, each jet behaves as a single jet in a region close to the jet orifice (Moore, 2004). Both annular jets shown in Figure 3-10 have an *inner recirculation zone*,

which is followed by the *inner converging zone*. The inner recirculation zone ends at the *inner merging point*. Then, the *inner merging zone* begins, where the two distinct velocity maximums come together to form one velocity maximum at the *inner combined point*. The *inner combined zone* begins at the inner combined point. Beyond this position in the flow field, each annular jet exhibits a velocity profile that is similar to that of a round jet. Only a single velocity maximum exists for each of the jets present.

Similar zones are also observed due to the interaction of the separate (outside and center) jets. A *recirculation zone* exists in the area between the two jets. Then there is a *merging point*, which signifies the end of the recirculation zone and the beginning of the *merging zone*. In this merging zone, the velocity maximums of each of the two jets merge together until they reach the *combined point*, also called z_{merge}, where the jets come together to form one jet stream that has only one velocity maximum. The flow field after the combined point is called the *combined zone*.

3.2.4 Comparison between Different Multihole Geometries

Since the fiber properties in the melt blowing process are determined by the air flow field, it is of interest to determine how changing the jet spacing affects this flow field. To test this spacing, six different variations of the multi-hole die were simulated. The inlet mass flow rate of air was set at 3.62 g/min per hole for all simulations, which is the same flow used in the experiments of MS. Figure 3-11a presents the dimensionless *z*-velocity along the center jet centerline for all six simulations. The location of the velocity maximum is similar for all the cases, but the magnitude of the maximum varies slightly with the different cases. The difference between the cases becomes much more apparent farther away from the die. Beyond $z/D_o \geq 15$, the value of h_h has an important

effect on the flow field. The dimensionless z-velocity decreases as h_h increases (see Table 3-2 for h_h values). Simply put, the closer the two jets are to each other, the more quickly (in terms of distance from the die face) the outside jet contributes to the flow field of the inside jet, and vice versa. Since Case 1 is not a scaled version of Case 4, its velocity profile has a different shape than the profiles of the other simulations.

Figure 3-11b shows the dimensionless z-velocity profile along the halfline. The halfline is the vertical (z-direction) line that passes through the x-position located halfway between the centers of the inside and outside columns of jets. Since the domains are different in size for each simulation, the halfline x-position will depend on the case. (However, the x-position will be at $h_\ell/2$ for all cases.) In comparison to the centerline velocity profiles (Figure 3-11a), the halfline velocity profiles have a broader a range of values. Also, the halfline velocity profiles have minima that are located much farther from the die than the location of the minima for the centerline profiles. In addition, the maximums of the halfline velocity profiles occur farther from the die face than the maximums of the centerline profiles. For the halfline profiles, as h_h increases, the positions of the maxima and minima move away from the die face (for the centerline velocity, this effect is much smaller). Like the centerline velocity profiles, the halfline velocity profiles are higher for geometries with lower values of h_h.

Figure 3-11c presents the dimensionless z-velocity along the outside jet centerline for all six simulations. The maximums are clustered together at nearly the same position. However, the magnitude of the maximums increases as h_h increases, because the outside jets are less entrained toward the center jet for higher h_h values. Farther away from the

die face, the magnitude of the dimensionless z-velocity profile decreases for the higher h_h values (where the jet inlets are farther apart).

One of the goals of our research is to provide predictive correlations for the velocity flow field from Schwarz dies. Previously, the dimensionless velocity decay for a single jet was successfully described using an empirical equation of the following form (Moore, 2004; Schlicting, 1979):

$$\frac{V}{V_{jo}} = a * (z/D_o)^b \tag{3-5}$$

However, the multi-hole die is sufficiently different (and more complex) than single jet dies that equation 3-5 cannot adequately model the velocity decay. The decay profiles in Figure 3-11a appear to exhibit power law behavior near the die as the profiles go through maximums. Farther away from the die, the velocity profiles appear to decay linearly. This behavior suggested that an equation of the following form might fit the data:

$$\frac{V}{V_{jo}} = a + b * (z/D_o) + \frac{c}{(z/D_o)^2} \tag{3-6}$$

Equation 3-6 has three empirical constants: a, b, and c. Equation 3-6 provides a good empirical fit for the velocity decay for the six different simulations. For each of the cases, Table 3-3 lists the R-value for the equation, the starting z/D_o, and the constants a, b, and c. Figures 3-12a, b, and c compare the velocity decay simulation with the correlation of equation 3-6 for cases 1, 4, and 6. As can be seen, the three-constant equation 3-6 does a good job of matching profiles produced by a fairly complex simulation.

Figure 3-13a compares the z-velocity profile as a function of dimensionless x for y = 0 at a distance of z = 2 mm under the die face. Since this y location is very close to the die face, there are two distinct jet profiles at this position. For each profile, the starting peak at x = 0 corresponds to the center jet, while the peak at $x/h_\ell \approx 1$ corresponds to the outside jet (compare Figure 3-10). For the different cases, observe that the location of the maximum of the outside jet moves closer to the center jet as h_h becomes smaller. Even at a position this close to the die face, the center column of jets has begun to entrain the outside column of jets inwards. For single jets, a plot like Figure 3-13a would typically use $x_{1/2}$ as a length scale, but $x_{1/2}$ cannot be clearly defined when maxima from two jets coexist. Hence, the plot uses h_ℓ as the appropriate length scale.

Figure 3-13b shows the z-velocity profiles along the x-direction at y = 0 and z = 5 mm. In this plot the two jets in Case 1 have already combined to form one jet. For the other cases, the shift of the locations of the outside jet maximums is much stronger than that shown for z = 2 mm (see Figure 3-13a). For both Figure 3-13a and Figure 3-13b, smaller h_ℓ results in a stronger pull of the outside jets toward the center jets.

Figure 13c shows the z-velocity profiles at y = 0 and z = 10 mm – a position much farther away from the die face. In this plot, most of the outside jets have been entrained by the center jets to form one jet maximum. The Case 5 and Case 6 profiles still show distinct outside jets, but these outside jets have clearly moved towards the center of the domain when compared to their position in Figure 3-13b. Figure 3-13d shows the z-velocity profiles at a cut in the x-direction located at y = 0 and z = 20 mm. At this position, the inside and outside jets have combined for all cases. Because the jets have all

combined, $x_{1/2}$ was used as the appropriate length scale in Figure 3-13d. Figure 3-13d shows that all cases have a self-similar *z*-velocity profile.

To further illustrate the effect of increasing h_h on the merging of the two jets, Figures 3-14a, 3-14b, and 3-14c show the *z*-velocity contour plots for Cases 1, 4, and 6, respectively. In Figure 3-14a, the outside jets quickly bend towards the center jet, leading to a single jet profile close to the die face. The *z*-velocity contour plot for Case 4 is similar, but shows that the increased distance between the jets has a clear effect on the velocity profiles. The outside jets bend toward the center jet at a distance farther below the die than those observed in Case 1. Finally, Figure 3-14c shows the *z*-velocity contours for Case 6, which has the largest value of h_h. Clearly, the outside jets are able to remain distinct for a longer distance below the die than in the other cases.

In addition to the velocity profiles, the turbulence in the flow field is important in the melt blowing process. Figure 3-15 shows the turbulence intensity along the centerline of the center jet. The turbulence intensity q is a measure of the magnitude of the velocity fluctuations and is defined as the ratio (expressed as a percentage) of the root mean square of the velocity fluctuations to inlet velocity V_{jo}. The maximum turbulence intensity occurs in the region of inset above the die face. Since this area is the same for all cases, it is expected that for all cases this maximum would occur at the same position and would have the same magnitude. As Figure 3-15 shows, this is indeed the case, and q reaches nearly 25% for all cases. Throughout the rest of the domain, the turbulence intensity profiles do not differ enough to warrant concern about the effect of turbulence intensity on the operability of industrial dies run at conditions matching any of our six simulated cases.

A relationship can be derived between h_h and the position z_{merge}, where the two jets (center and outside) have merged together. This relationship is shown in Figure 3-16. The farther away the jets are from each other at the die face, the farther below the die face they merge together. The position z_{merge} is defined as the point where the velocity profile along a cut in the x-direction, and at a location of $y = 0$, will not show an inflection point due to the outside jet. Within the range of geometries simulated, the effect of h_h and z_{merge} can be fit with the following linear equation (R = 0.997):

$$z_{merge} = -0.692 + 2.22 * h_h \qquad (3\text{-}7)$$

In an additional simulation (not one of the six cases listed in Table 1), h_w and h_ℓ in the base case (Case 4) were reduced by 50%. The flow field in this simulation did not agree with equation 3-7. Apparently, with these values of h_w and h_ℓ, the two jets are too close to have distinguishable characteristics in the flow field. Hence, Equation 3-7 should not be extrapolated beyond the dimensions of the six die geometries (cases) discussed in this chapter.

In the far field, the spreading rate of a round die has been found to be linear. Spreading rate S is defined as the slope of the linear fit of $x_{1/2}$ versus z-position. Experimentally, S for a round jet was been found to be between 0.102 and 0.094 (Hussein, 1994). Their experimental results can be fairly closely matched by a simulation. A two-dimensional single inset annular jet, with the same dimensions as the multi-hole jets described previously, gives a spreading rate of 0.106 when simulated with the k-ε turbulence model with the default parameters. Figure 3-17 shows the spreading rate of the center jet in the multi-hole die as a function of h_h. (For this plot, the slope of the linear fit of $x_{1/2}$ versus z-position was determined for z distances larger than z_{merge} for

all simulated cases.) Since the h_w and h_t from Case 1 are the same, the jets in this case are allowed to spread symmetrically, which may explain a higher spreading rate for this case (the S value of 0.064 corresponds to this case). Although the value of the spreading rate does not seem to depend on h_h, it is important to observe that the spreading rate experienced by the center jets of the multi-hole die is lower than the spreading rate of a single annular jet. Specifically, the simulated spreading rate of the annular multiple jets is about half of that for a single annular jet.

3.3 Non-Isothermal Simulation Results

In the industrial melt blowing process, air is heated and pressurized before it is fed to the melt blowing die. At the die exit, the air jets contact the molten polymer, and the resulting drag force elongates the fiber. The polymer fiber properties are directly affected by the air temperature and flow fields. In turn, the characteristics of these fields are determined by the melt blowing die configuration.

The experimental work in MS2 (1994) reported an air flow rate of $2.01*10^{-3}$ m^3/s for the 165 hole die (at the standard conditions of 21 ^oC and 1 atm pressure). This corresponds to a mass flow rate of 0.895 g/min per orifice. After this flow rate was measured in the experiments, it was heated. The excess temperature, Θ, is the difference between the temperature at any location and the ambient temperature of 21^oC. For the non-isothermal simulations, an excess temperature of 155^oC was selected (Θ_{jo} = 155 ^oC); this value was one of the temperatures used in the experiments of MS2. Enabling the energy equation was necessary to simulate the air temperature field (see equation 1-10). The same jet configurations, listed in Table 3-2, used for the isothermal simulations were also used to study the temperature field. Holding all but one of the simulation parameters

constant for all of the different cases allowed for the investigation of the effect of the jet spacing on the temperature field.

3.3.1 Comparison to Experiments

It is of particular interest to examine the temperature field along the centerline ($x = 0$ and $y = 0$); this line approximates where the polymer fiber spends most of its time during the attenuation process. This temperature field has a profound effect on the final fiber properties. MS2 measured the temperature decay along the centerline of a Schwarz die. Figure 3-18 shows the temperature decay measured by MS2 and the simulated temperature decay of Case 4; Case 4 has the same jet spacing as was used in the experiments of MS2. Although the CFD domain length is not long enough to include all of the experimentally-measured points, there is good agreement between the simulation and the experiment.

The temperature profiles at different distances from the die face were also measured by MS2. Within the region examined in the experiments, the temperature field was found to be self-similar. Figure 3-19 shows that good agreement was achieved between MS2 experiments and the simulated Case 4 at 5.08, 7.62, and 25.4 mm below the die face.

Figure 3-20a is a three dimensional contour plot of the excess temperature for the simulation of Case 4 at $z = 2.54$ mm. Figure 3-20b is the corresponding contour plot from the averaged experimental values in MS2. Comparison of these two figures shows that there is good agreement between simulation and experiment. Both figures show that, at 2.54 mm below the die face, the maxima in the excess temperature from the outside column jets are barely distinguishable. Also, similar to the velocity profile examined in

the isothermal simulations, the temperature profile reveals the entrainment of the jets on the outside column by the jets on the inside column. Figures 3-21a and 3-21b further illustrate this observation. These figures show the temperature contours at z = 5.08 mm below the die face for Case 4 and the averaged MS2 experiments, respectively. By z = 5.08 mm, only a single maximum in the temperature profile is observed, indicating that the temperature fields resulting from the individual jets have merged together.

3.3.2 Comparison between a Schwarz Die and a Single Annular Die

Figure 3-22 presents the excess temperature decay for two simulations. One simulation is that of a single annular jet with the same geometry as each of the jets in the multihole Schwarz die. The second simulation is that of Case 4, which has the same geometry as the experimental MS2 die. For the Case 4 simulation, the center jet centerline is directly under the jet at x = 0 and extends in the positive z-direction. The results of these two simulations show that the interactions between the multiple jets in the array lead to a very different centerline excess temperature profile when compared with that of a single annular jet. The excess temperature profile along the centerline of the center jet is significantly higher than that of the annular jet acting alone. This may be attributed to the higher temperature of the air entrained by the inside jets in the array when compared to the air entrained by the single annular jet. A single annular jet acting alone entrains air at ambient conditions.

There is also a significant difference in the excess temperature profile generated by the single annular jet and the profile on the centerline of a jet on the outside column of the array. Note that the centerline of the outside jet is defined to be at $x = h_b$, and extends in the positive z-direction. The outside jet centerline does not coincide with the location

of the velocity maximum or the location of the maximum temperature value produced by the jet. The location of the temperature maximum is not at a constant x-position due to the entrainment caused by the jets in the center column. The excess temperature along the centerline of a jet on the outside column reaches a minimum that is not observed in the center jet of the array or the single annular jet. The interactions between the jets in the Schwarz die are complex, and these interactions lead to a temperature field that can not be easily predicted by examining the temperature field under a single annular jet.

Figure 3-22 also shows that the centerline temperature profiles under the inside and outside jets are very different from each other; as well as being different from the profile from a single annular jet acting alone. Similarly, Figure 3-9 shows that the velocity profiles under the center jet and the outside jet are very different from each other, regardless of whether the flow field is isothermal or not. This is an important observation for the process of melt blowing, since it is optimal that each polymer stream encounters a similar velocity and temperature field. Otherwise, fiber properties such as fiber diameter and strength, which depend on the flow conditions generated by the melt blowing die, will not be the same for all of the fibers.

3.3.3 Comparison between Different Multihole Geometries

Since the polymer properties are affected by the temperature field from a melt blowing die, it is of interest to examine how changing the orifice spacing in the Schwarz die affects the temperature field. Figure 3-23a presents the simulated excess temperature along the centerline of the jet in the center column for the six different Schwarz melt blowing dies. The orifice spacing (i.e., the value of h_h) has an important effect on the temperature decay. Cases 1 and 6 represent the die geometries with the smallest and

largest values of h_h, respectively. These two simulations also represent two extremes in the shape of the center jet centerline temperature decay profile. Case 1 has a higher excess temperature close to the die face, but then the excess temperature decreases rapidly until it is less than the excess temperature of Case 6. This can be explained by considering the effect of the jet spacing on the temperature field. The jets in Case 1 are very close to each other, which leads to the inside and outside columns of jets merging together very close to the die face (see also Figure 3-26a). After the inside and outside columns of jets have merged together and a single maximum in the temperature field is formed, the resulting single jet entrains air at ambient conditions that lead to rapid cooling. Case 6 represents the other extreme, where the air jets are spaced farther apart. Close to the die face, the air being entrained is between the jet air temperature and ambient air temperature, so the temperature decreases quickly in this region of the flow field (see Figure 3-26c). Then, the inside column of jets begins to entrain the outside column of jets. Since the air from the outside column of jets is also heated, the center jets entrain heated air, which explains the slowing of the temperature decay for this case. The excess temperature profiles for Cases 2-5 fall between the two extremes of Cases 1 and 6.

Figure 3-23b presents the excess temperature decay along the halfline, which is a line located at an x-position halfway between the centerlines of the center and outside columns of jets. Since the domain size is different in each of the cases (due to the different jet spacing), the halfline is at a different x-location for each case, but is always at a position of $h_\ell/2$ between the centerlines of the jets on the inside and outside columns. Similar to the center jet centerline, the excess temperature decay along the halfline shows a large range of values for the different cases. The explanation given for the shape of the

excess temperature profile under the center jet applies also for the profiles along the halfline. There appears to be a local minimum at the temperature profile at small z/D_o followed with a local maximum for the cases where the jet spacing is large. The reason for this profile shape is that the outside jet is entrained by the inside jet, and the location below the die face where this entrainment takes place becomes larger as the spacing between the jets increases. (See below the discussion related to Figure 3-25.) Therefore, along the halfline the temperature is higher for the cases where the jets are closer together, but the temperature decreases rapidly because, once the inside and outside jets merge, the air being entrained is at ambient temperature. The cases where the jets are farther apart have lower temperatures close to the die face (along the halfline), but when the inside jet begins to entrain the outside jet, the rate of temperature decay is slowed.

The excess temperature along the centerline of the outside jet is shown in Figure 3-23c. In comparison with the excess temperature along the center jet centerline (Figure 3-23a) and the halfline (Figure 3-23b), the shapes of these profiles are more similar for all the cases. The outside jet is entrained towards the inside jet at small distances below the die face, resulting in temperature reduction directly below the jet. After the inside and outside jets merge, the combined jet starts to spread, and the temperature increases again along the centerline below the outside jet. As distance from the die face increases, the excess temperature profile becomes self-similar, as seen in Figure 3-19.

One goal of this work is to provide predictive correlations for the temperature field from different melt blowing die geometries. For a single annular jet, the temperature decay can be described using an equation of the following form (Majumdar, 1991):

$$\Theta_{jo}/\Theta_o = a + b(z/D_o)(\rho_\infty/\rho_{jo})^{1/2} \qquad (3\text{-}8)$$

However, the centerline excess temperature decay from an array of jets cannot be described accurately using equation 3-8. Hence, the following equation form was selected to describe the temperature decay within the range of the computational domain for all cases:

$$\Theta_o/\Theta_{jo} = a + b(z/D_o)^2 + \frac{c}{(z/D_o)^{1/2}} \qquad (3\text{-}9)$$

This empirical fit was used to describe the temperature decay for the different simulated Schwarz dies because close to the die face the temperature decay behaves as an inverse square root (the third term on the right side of equation 3-9), while farther from the die face the temperature decay can be represented more accurately using a squared z/D_o term (the second term in equation 3-9). For the six cases simulated, Table 3-4 lists the three empirical constants (*a*, *b*, and *c)* as well as the R^2 value. Figures 3-24a, b, and c show the fit of equation 3-9 compared to the simulated excess temperature decay for Cases 1, 4, and 6, respectively. As seen in these figures, this equation is a good empirical fit for the temperature decay. Similarly, equation 3-9 also provides good fits for Cases 2, 3, and 5 (these figures are not shown).

The section concerning the isothermal simulations discusses how the velocity maxima from each jet in the Schwarz die emerge from the individual orifices and are clearly distinguishable. It also describes that the outside column of jets is entrained by the inside column of jets. At a sufficient distance from the die face, the entrainment results in a merging of the jets, and then the maxima from the different jets combine to form a single maximum. The same trend is observed in the temperature field for the

simulations discussed in this paper. Figure 3-25a is a comparison of the dimensionless temperature at the $y = 0$ plane at a distance of $z = 0.5$ mm below the jets. Since this position is very close to the heated die face, the peaks in the temperature are less distinct than those observed in the velocity field for the isothermal simulations. At this position from the die face, the temperature profiles from all the cases show a local minimum, indicating that the excess temperature maxima from the inside and outside jets have not completely merged. Usually, in a graph like Figure 3-25a, the abscissa value would be non-dimensionalized by dividing the x-position value by the position value where the excess temperature reaches half of its centerline value, $t_{1/2}$. However, in this situation, where two temperature maxima are observed (one due to the center jet and one due to the outside jet), $t_{1/2}$ is not defined. For this reason, in Figure 3-25a the x-position is non-dimensionalized using h_ℓ, the distance between the columns of jets.

Figure 3-25b shows the excess temperature profile at $y = 0$ and $z = 2$ mm. By this position below the die face, the separate temperature jet profiles from Cases 1, 2, and 3 have merged together and only a single peak is observed. The peak from the outside jet in Case 4 no longer occurs at $x/h_\ell = 1$ because the inside jet has begun to entrain the outside jet. The outside jet peaks from Cases 4, 5, and 6 are distinct, but are lower than those under the center jet. This can be attributed to the entrainment of air at ambient temperatures by the outside jet, while the inside jet is entraining the heated air from the outside jet. This process is also manifested by the presence of local minima in the temperature below the jet centerline for the outside jets (Figure 3-23c) or below the half-point between the jets (Figure 3-23b).

Figure 3-25c is a comparison of the excess temperature profiles at $y = 0$ and $z =$ 10 mm. At this distance from the die face, the normalized temperature does not show a peak due to the outside jet. Since the only maximum in the profiles occurs at the centerline of the center jet, $t_{1/2}$ is defined and is the appropriate length scale to non-dimensionalize x. Figures 3-25a, b, and c show that, as h_h increases, the distance required for the separate excess temperature peaks to merge together also increases.

The excess temperature contour plots on the $y = 0$ plane for Cases 1, 4, and 6 are presented in Figures 3-26a, b, and c, respectively. Because the temperature of the two jets merges together close to the die face for Case 1, which has the smallest value of h_h, it is difficult to distinguish an independent temperature profile resulting from each individual jet. The contours of excess temperature for Case 4 show that the jets are distinct close to the die face, but then merge together at larger z values. The effect of the entrainment is observed because the outside jets are bending toward the center jet. Case 6 shows that the effect of the entrainment is decreased as h_h increases: the outside jets in Case 6 do not bend as significantly as the outside jets in Case 4.

The parameter t_{merge} can be introduced in order to characterize the temperature profile resulting from the interactions of multiple annular jets. The value of t_{merge} is defined as the z-position at which there is no local minimum in the excess temperature profile when looking at the profile in the x-direction (as in Figures 3-25a, b, and c). In other words, t_{merge} is the distance below the die face where the excess temperature profiles of the two jets merge completely. Figure 3-27 shows the position t_{merge} for the six different jet configurations. The distance for the outside and inside jets to merge together

increases as the orifice spacing increases. The relationship between t_{merge} and h_h, both in mm, can be described by the following equation ($R^2 = 0.9962$):

$$t_{merge} = 0.231 * h_h^{1.803} \quad (3\text{-}10)$$

MS2 suggested that the temperature spreading rate from a Schwarz die can be described by the following equation (with $t_{1/2}$ and z in mm):

$$t_{1/2} = d_2 * z \quad (3\text{-}11)$$

Note that d_2 is an empirical constant that describes the linear relationship between $t_{1/2}$ (the distance from the centerline where the excess temperature is equal to half of the centerline excess temperature) and z (distance below the die face). Figure 3-28 shows the relationship between d_2 and h_h for each of the six cases. The value of d_2 for the six simulated cases shown in Figure 3-28 ranges between 0.07 and 0.14. Experimentally, MS2 measured a value of $d_2 = 0.2466$ for Case 4. The difference between this experimental value and the simulated spreading rate can be attributed to the length of the computational domain. The temperature spreading rate from MS2 included measurements to $z > 60$ mm, while the computational domain used for the simulated Case 4 ended at $z = 30$ mm. Examination of the temperature half-width plot from MS2 shows that using just the data from $z < 30$ mm would result in a lower temperature spreading rate.

The values of d_2 in Figure 3-28 for the different cases simulated show a minimum for Case 4, which is the geometry of a melt blowing die that has been used industrially. The interactions between the multiple jets lead to this complicated relationship between d_2 and h_h. Cases 1, 2, and 3 have jets that are closer together than the base case, Case 4. This may lead to the temperature fields acting more like the result of a single jet than an

array of jets, since the temperature maximums from the different jets merge together closer to the die face and then the temperature field spreads as if only one jet were present. The simulation cases where the jets are farther apart than those in the base case (Cases 5 and 6) show spreading rates that are also higher than that of the base case. This behavior can be attributed to the fact that the jets are farther apart, so the outside jets do not affect the spreading of the inside jets as much. Therefore, the temperature profile from the center jet in these cases is allowed to spread more freely.

Heating the air in the melt blowing process requires energy. The optimal melt blowing die will use less energy to produce the polymer fibers. Therefore, a lower temperature spreading rate is desired so that the hot air will remain close to the fiber, as opposed to dissipating quickly. The temperature spreading rate reaches a minimum at the h_h of Case 4.

3.4 Conclusions

When compared to a typical single-row, Exxon die (Harpham, 1996), a multiple-row Schwarz die has the ability to produce more fibers per die length. However, there are differences in the air field experienced by polymer exiting the center holes versus polymer exiting the outside holes (for a 3-row die). In a multi-row die, the outside jets are entrained towards the inside jets, resulting in a decrease in the spreading rate of the inside column of jets compared to the spreading rate of a single round jet. Six different multi-hole die geometries were simulated in this paper, and the flow and temperature fields of these different geometries show significant variations from each other. The isothermal and non-isothermal simulations were studied using separate groups of simulations.

The isothermal simulations were used to study the air flow field. The larger the spacing between the jets, the larger the distance (below the die face) required for the jets to merge. Within the range of geometries examined, the equations presented in this work allow for the prediction of the dimensionless velocity profiles under the center jet as well as the position where the jets merge together (one can apply Equation 3-6 for distances beyond the merging distance given in Equation 3-7). Consideration of the turbulence intensity showed that all of the die geometries examined in this paper exhibit similar levels of turbulent velocity fluctuations. Hence, for the geometries considered in our work, the choice of die could be based on the mean velocity requirements. Past work determined that, as expected, high air velocities along the threadline path are desirable for producing maximum polymer attenuation (Marla, 2003). Since the turbulence fluctuations were similar for all simulated cases, then our work suggests that the higher velocity cases that resulted when h_h was smaller (e.g., Case 2) would give better conditions for the melt-blowing process. However, there is probably a value of h_h below which this benefit is counterbalanced by the excessive entrainment of the outer column jet towards the center column jet. In this case, the fibers from the outer and the center jet columns might become entangled. It appears that this critical value of h_h is approached when the distance between two jets becomes similar to the jet diameter D_o (e.g., Case 1).

Similar to the velocity flow fields, the temperature fields from the jets on the outside column of the die are entrained by the jets on the inside column. The distance required for the temperatures profiles from two jets to merge increases as the jet spacing is increased. Empirical correlations were developed to predict t_{merge} (the location where the temperature profiles merge together), the excess temperature decay under the center

column of jets, and the temperature spreading rate. However, these predictive correlations are only applicable within the range of the melt blowing dies simulated. Of the six cases simulated, the temperature spreading rate of the jets is a minimum for Case 4, the case which corresponds to the geometry of the actual Schwarz die that was experimentally tested by MS2.

3.5 Nomenclature

a	constant in low z/D_o decay equation
b	constant in low z/D_o decay equation
c	constant in high z/D_o decay equation
d	constant in high z/D_o decay equation
d_2	constant in temperature spreading rate equation (Equation 3-11)
A_o	discharge area of a single orifice, mm
C_m	spreading coefficient for momentum transfer (Equation 3-4)
D_o	outer diameter of annular orifice, mm
D_i	inner diameter of annular orifice, mm
h_h	Hypotenuse of triangle formed by h_ℓ and h_w, mm
h_ℓ	Distance between jet centers on neighboring rows, mm
h_w	Distance between jet centers on neighboring columns, mm
k	turbulent kinetic energy, $(1/2\overline{u_i u_i})$, m^2/s^2
L	length of the die, mm
M_e	mass flow rate of entrained air, kg/s
M_o	mass flow rate of air through jet orifice, kg/s
$M(z)$	mass flow rate per length L of the jet, kg/s

q	turbulence intensity, $100 * \left(\left(\overline{u_i^2} \right)^{1/2} / V_{jo} \right)$, (% of $\underline{V_{jo}}$)
Q_{air}	volumetric flow rate through a single, approximately-annular air orifice, m^3 /s
r1/2	for a round jet, the distance from the centerline where the velocity is equal to half the centerline velocity, mm
S	momentum spreading rate constant
$t_{1/2}$	distance from the centerline where the excess temperature is half of the centerline excess temperature, mm
t_{merge}	distance from the die where the *z*-velocity shows no inflection point due to two separate jets, mm
U_i	mean velocity in the ith direction, m/s
u_i	velocity fluctuation in the ith direction, m/s
V	velocity in the *z*-direction, m/s
V_{jo}	nominal discharge *z*-velocity defined as (Q_{air}/A_o), m/s
V_o	center jet centerline *z*-velocity, m/s
x, y, z	spatial coordinates, mm or m
$x_{1/2}$	distance from centerline where the *z*-velocity is half the magnitude of the centerline *z*-velocity, mm
z_o	virtual origin for spreading rate equation, mm
z_{merge}	distance from the die where the *z*-velocity shows no inflection point due to two separate jets, mm

Greek characters

ε	dissipation rate of turbulent kinetic energy, m^2/s^3
Θ	excess temperaturethe difference between the air temperature and ambient temperature, K

Θ_{jo} the difference between the jet air temperature and ambient temperature, K

ρ density, kg/m^3

ρ_{jo} discharge density, kg/m^3

Ψ entrainment coefficient (Equation 3-3)

3.6 References

Babu, P.C.; Mahesh, K. Upstream Entrainment in Numerical Simulations of Spatially Evolving Round Jets. *Phys. Fluids*, **2004**, *16*(10), 3699-3705.

Baron, T.; Alexander, L.G. Momentum, Mass, and Heat Transfer in Free Jets, *Chem. Eng. Prog.*, **1951**, *47*(4), 181.

Chattopadhyay, Himadri, Numerical Investigations of Heat Transfer from Impinging Annular Jet, *International Journal of Heat and Mass Transfer*, **2004**, *47*, 3197-3201.

Ferdman, E.; Otugen, M.V., Kim, S. Effect of Initial Velocity Profile on the Development of Round Jets, *Journal of Propulsion and Power*, **2000**, *16*(4), 676- 686.

Fluent User's Guide; Fluent Inc.: Lebanon, NH, 2007.

Gambit Modeling Guide; Fluent Inc.: Lebanon, NH, 2007.

Harpham, A.S.; Shambaugh, R.L. Flow Field of Practical Dual Rectangular Jets. *Ind. Eng. Chem. Res.*, **1996**, *35*, 3776-3781.

Hussein, H. J.;Capp, S.; George, W. K. Velocity Measurements in a High-Reynolds-Number, Momentum-Conserving, Axisymmetric, Turbulent Jet, *J. Fluid Mech.*, **1994**, *258*, 31-75.

Kennedy, I.M.; Santangelo, P.J.; Kollmann, W. Measurements and LES Modeling of Dispersion in a Turbulent Two Phase Round Jet. *Adv. Turb. III*, Proc. Eighth European Turbulence Conference, Barcelona, 2000.

Kim, K.H.; Kim, B.W.; Kim, S.W. Turbulent Flow Field Structure of Initially Asymmetric Jets. *KSME Int. J.*, **2000**, *14*(2), 1386-1395.

Krothapalli, A. Development and Structure of a Rectangular Jet in a Multiple Jet Configuration, *AIAA*, **1980**, *18*(8), 945-948.

Lai, J. C.; Nasr, A.; Two Parallel Plane Jets: Comparison of the Performance of Three Turbulence Models, *Proc. Instn. Mech. Engrs.*, **1998**, *212*(G), 379-391.

Majumdar, B.; Shambaugh, R.L. Velocity and Temperature Fields of Annular Jets. *Ind. Eng. Chem. Res.*, **1991**, *30*(6), 1300-1306.

Manohar, C. H.; Isaac T.; Sundararajan, T.; Ramjee, V.; Kumar, S. Sasi, A Numerical Investigation of the Interactions Between a Non-uniform Planar Array of Incompressible Free Jets, *Int. J. Numer. Meth. Fluids.*, **2004**, *44*, 431-446.

Marla, V.T.; Shambaugh, R.L. Three-Dimensional Model of the Melt Blowing Process. *Ind. Eng. Chem.* **2003,** *42*(26), 6993-7005.

Mohammed, A.; Shambaugh, R.L. Three-Dimensional Flow Field of a Rectangular Array of Practical Air Jets, *Ind. Eng. Chem. Res.*, **1993**, *32* (5), 976-980.

Mohammed, A.; Shambaugh, R.L. Three-Dimensional Temperature Field of a Rectangular Array of Practical Air Jets, *Ind. Eng. Chem. Res.*, **1994,** *33*(3), 730-735.

Moore, E.M.; Shambaugh, R.L.; Papavassiliou D.V.; Analysis of Isothermal Annular Jets: Comparison of CFD and Experimental Data, *J. Appl. Polym. Sci.*, **2004**, *94*(3), 909-922.

Obot, N.T.; Graska, M.L.; Trabold, T.A. The near field behavior of round jets at moderate Reynolds numbers. *Can. J. Chem. Eng.* **1984**, *62*, 587.

Obot, N.T.; Trabold, T.A.; Graska, M.L.; Gandhi, F. Velocity and temperature fields in turbulent jets issuing from sharp-edged inlet round nozzles. *Ind. Eng. Chem. Fundam.*, **1986**, *25*, 425.

Pope, S. B. *Turbulent Flows*; Cambridge University Press: Cambridge, U.K., 2000; pp 134-135.

Raghunathan, S.; Reid I.M., A Study of Multiple Jets, *AIAA*, **1981**, *19*(1), 124-127.

Rajaratnam, N. *Turbulent Jets*; Elsevier: New York, 1976.

Schlichting, H. *Boundary-Layer Theory*; 8th ed., McGraw-Hill: New York, p. 179, 1987.

Schwarz, E.C.A. Apparatus and Process for Melt-Blowing a Fiberforming Thermoplastic Polymer and Product Produced Thereby, U.S. Patent 4,380,570, **1983**.

Sforza, P.M.; Moons, R.F. Mass, Momentum, and Energy Transport in Turbulent Free Jets. *J. Heat Mass Trans*, **1978**, 371-384.

Shambaugh, R. L. A Macroscopic View of the Melt Blowing Process for Producing Microfibers. *Ind. Eng. Chem. Res.* **1988**, *27*(12), 2363-2372.

Taylor, J.F.; Grimmett, H.L.; Comings, E.W.; Isothermal Free Jets of Air Mixing with Air. *Chem. Eng. Proc.* **1951**, *17*(4), 175-180.

Uyttendaele, M.A.; Shambaugh, R.L. The Flow Field of Annular Jets at Moderate Reynolds Numbers. *Ind. Eng. Chem. Res.*, **1989**, *28*, 1735-1740.

Table 3-1. Grid Independence Time Requirements

# of Cells	Iterations	Time (hr:min)
632,782	3,555	16:10
713,077	3,307	17:30
1,142,708	5,148	43:40

Table 3-2. Multihole Die Geometries

Case	h_w (mm)	h_t (mm)	h_h (mm)
1	1.625	1.625	2.298
2	1.3975	2.1125	2.533
3	1.6125	2.4375	2.923
4	2.15	3.25	3.897
5	2.6875	4.0625	4.871
6	3.225	4.875	5.845

Table 3-3. Centerline Velocity Decay Equation Constants (see Equation 3-6)

Case	h_h (mm)	z/Do>	*a*	*b*	*c*	R
1	2.298	1.5	0.315	-0.00457	0.677	0.989
2	2.533	2	0.261	-0.00169	1.03	0.992
3	2.923	3	0.227	-0.00104	1.70	0.991
4	3.897	4	0.172	-0.00291	3.98	0.997
5	4.871	4	0.149	-0.000436	5.46	0.991
6	5.845	4	0.152	-0.00119	5.89	0.984

Table 3-4. Empirical Constants for Equation 3-9

Case	*a*	*b*	*c*	R^2
1	0.357	-3.871E-04	1.174	0.990
2	0.667	-4.655E-04	0.540	0.996
3	0.642	-3.241E-04	0.485	0.999
4	0.485	-1.062E-04	0.678	0.999
5	0.390	-4.591E-05	0.766	0.999
6	0.329	-1.734E-05	0.824	0.999

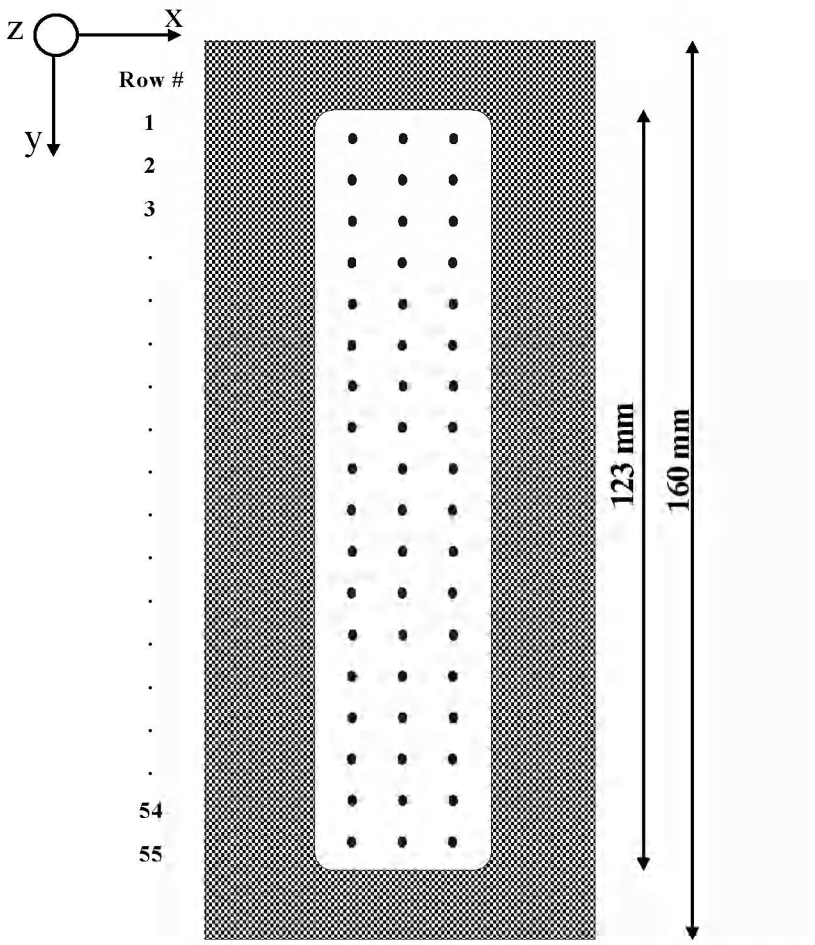

Figure 3-1a. View of the face of the Schwarz melt blowing die. Each black circle represents a capillary/air jet configuration. The Schwarz die has an array of 165 jets in 55 rows (the die in the figure has been reduced in size for purposes of illustration.) The *z*-direction is perpendicular to the plane of the die face, and the origin is at the center orifice.

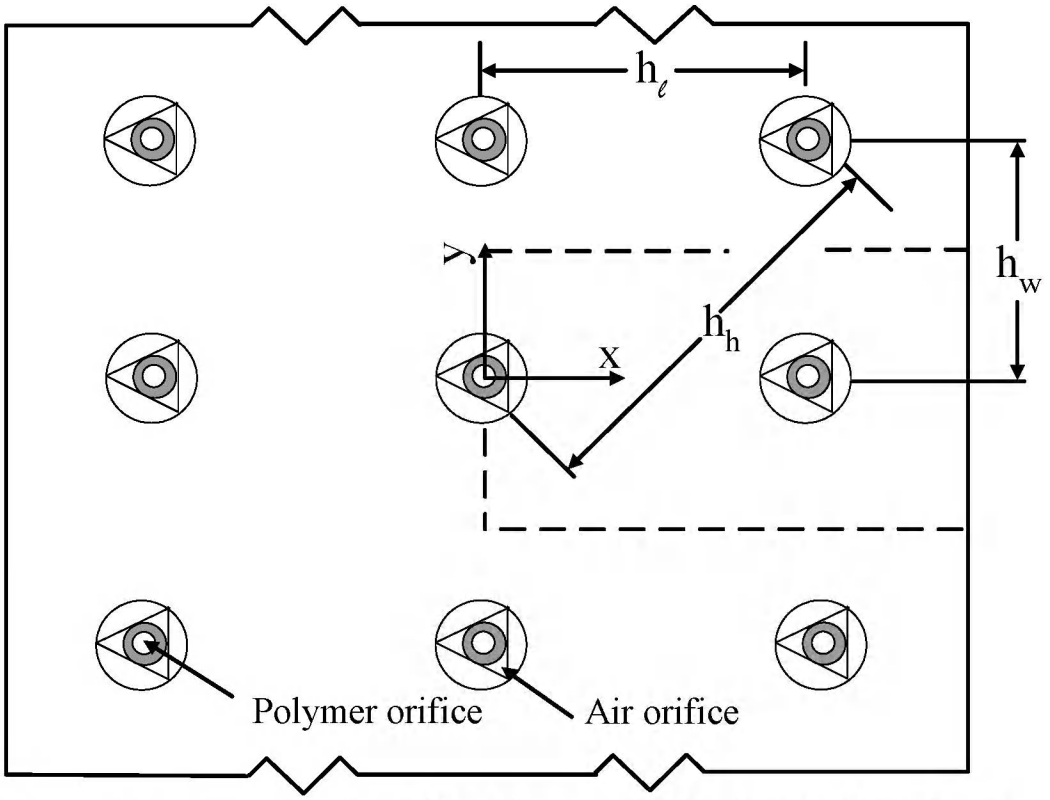

Figure 3-1b. View of the face of the Schwarz melt blowing die. This view shows only 9 holes; the full die has 165 jets in three columns (see Figure 3-1a). The origin of the coordinate system is at the center of the center hole. The *z*-direction is perpendicular to the plane of the die face.

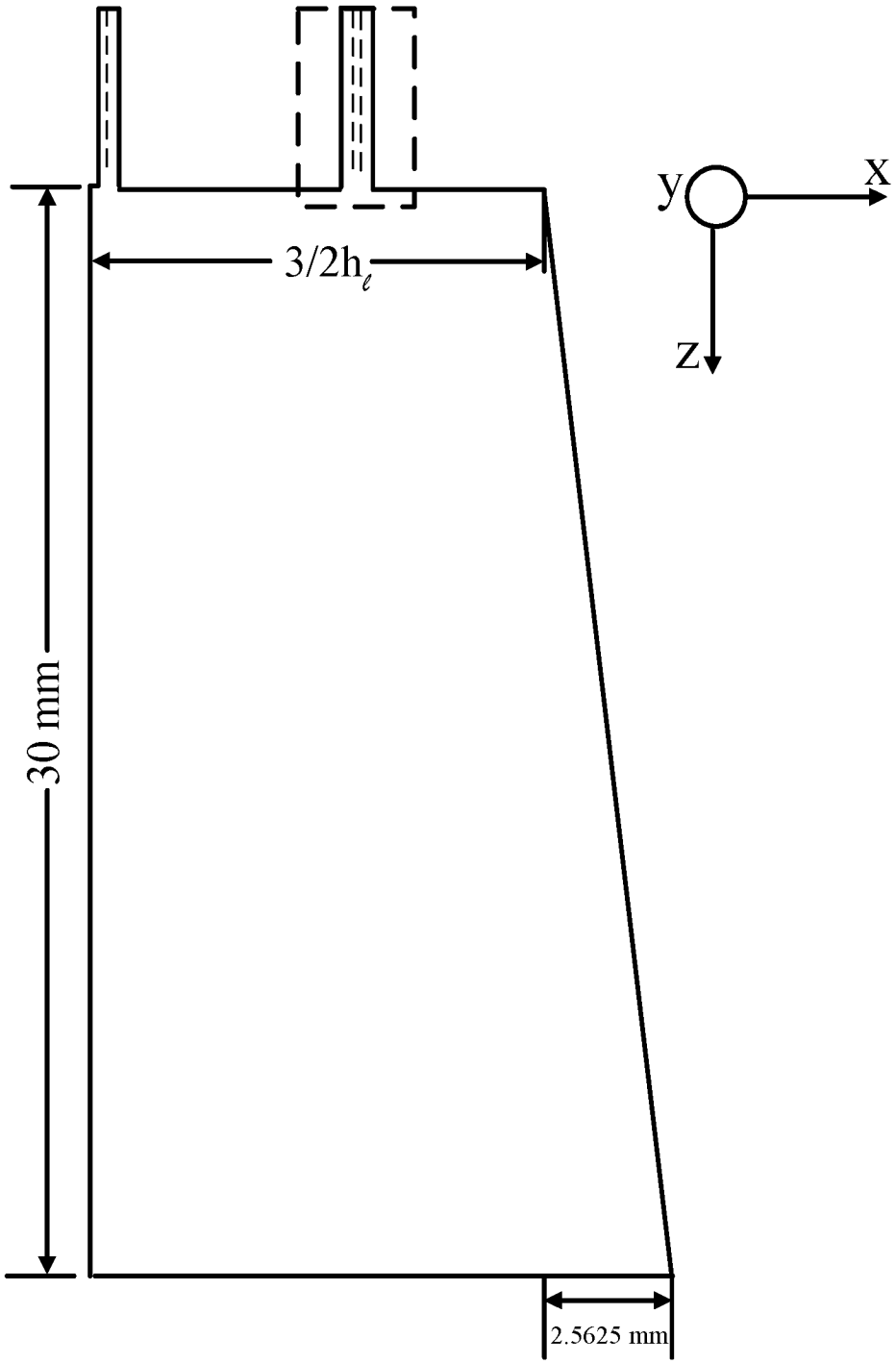

Figure 3-2a. Geometry of the side view of the entire computational domain used in the simulations (shown at the n used in the simulations (shown at the $y = 0$ plane).

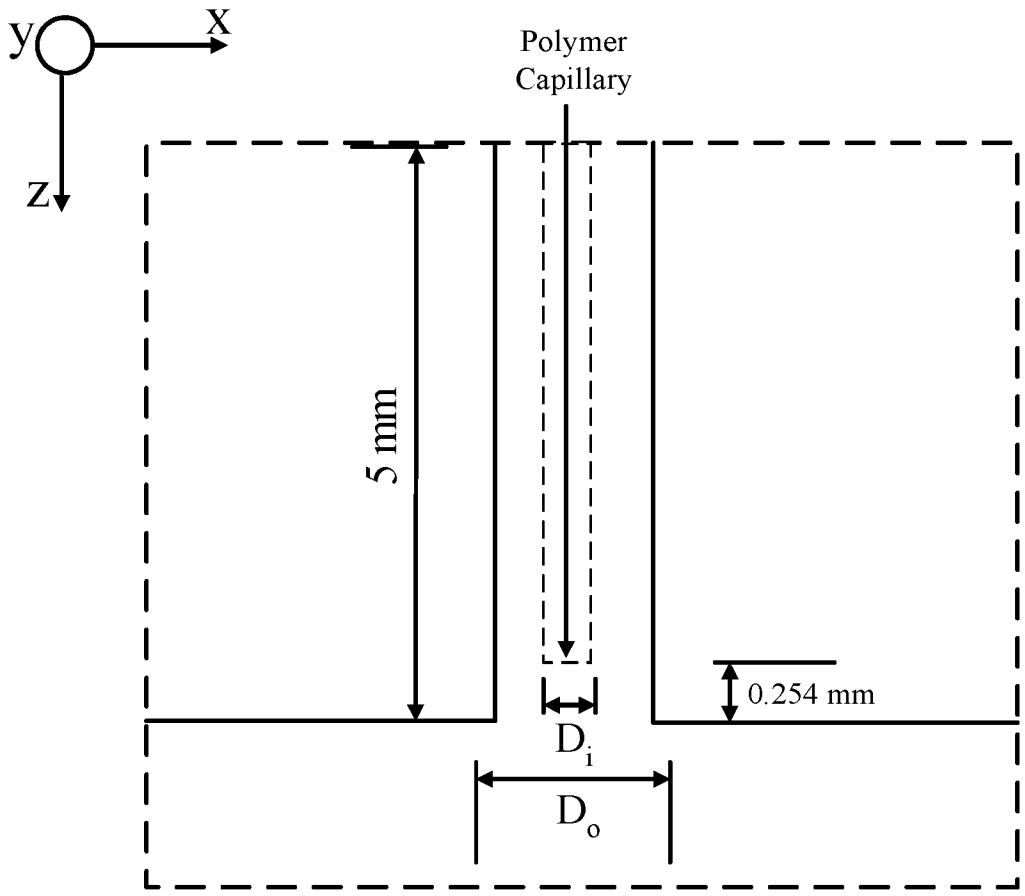

Figure 3-2b. A close up of the view of the jet shown surrounded by the dashed lines in Figure 3-2a.

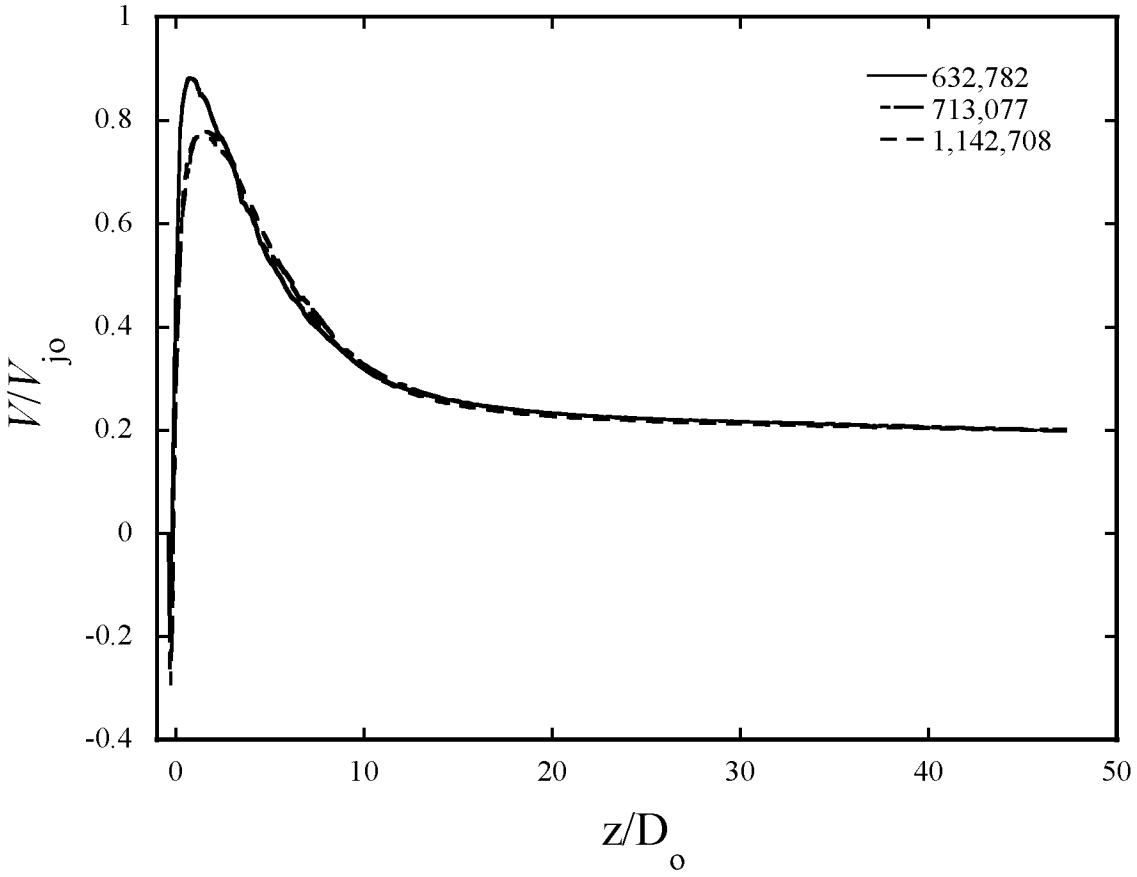

Figure 3-3a. Dimensionless z-velocity at $x = 0$ and $y = 0$ for simulations run under the same conditions, but with different grid refinement.

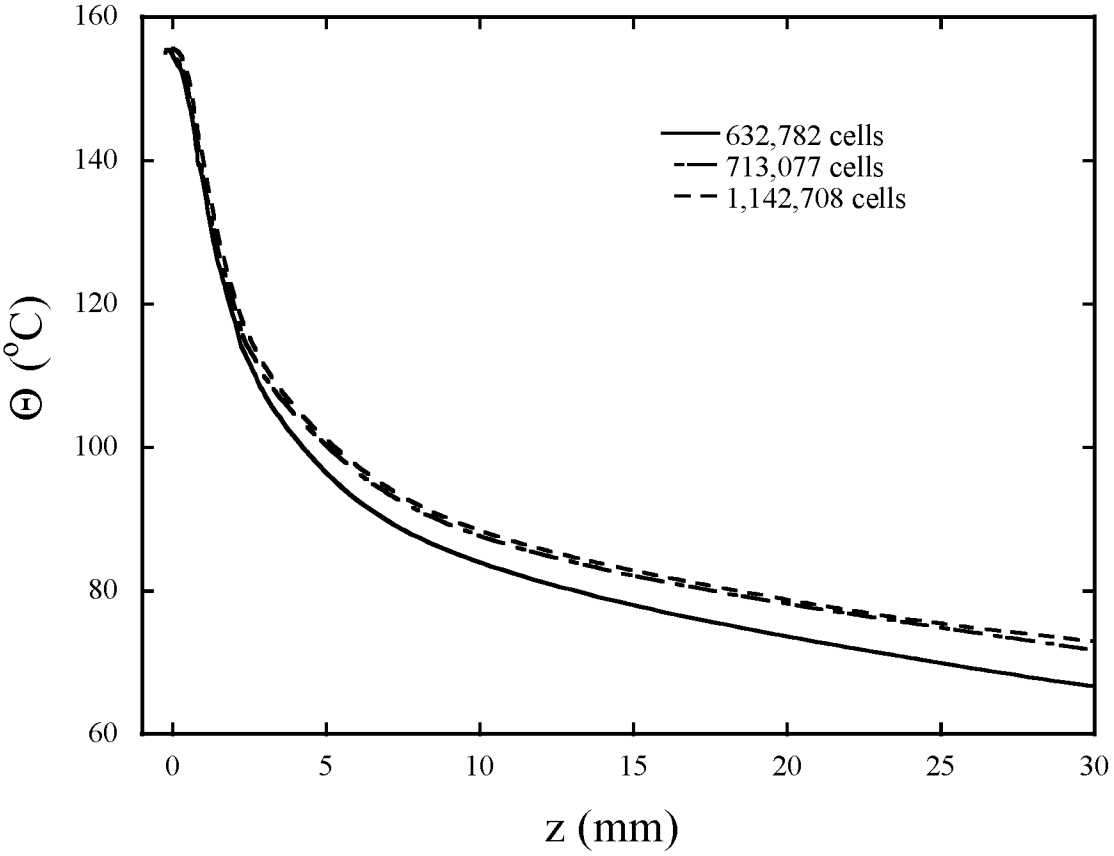

Figure 3-3b. Centerline excess temperature at z-velocity at $x = 0$ and $y = 0$ for simulations run under the same conditions, but with different grid refinement.

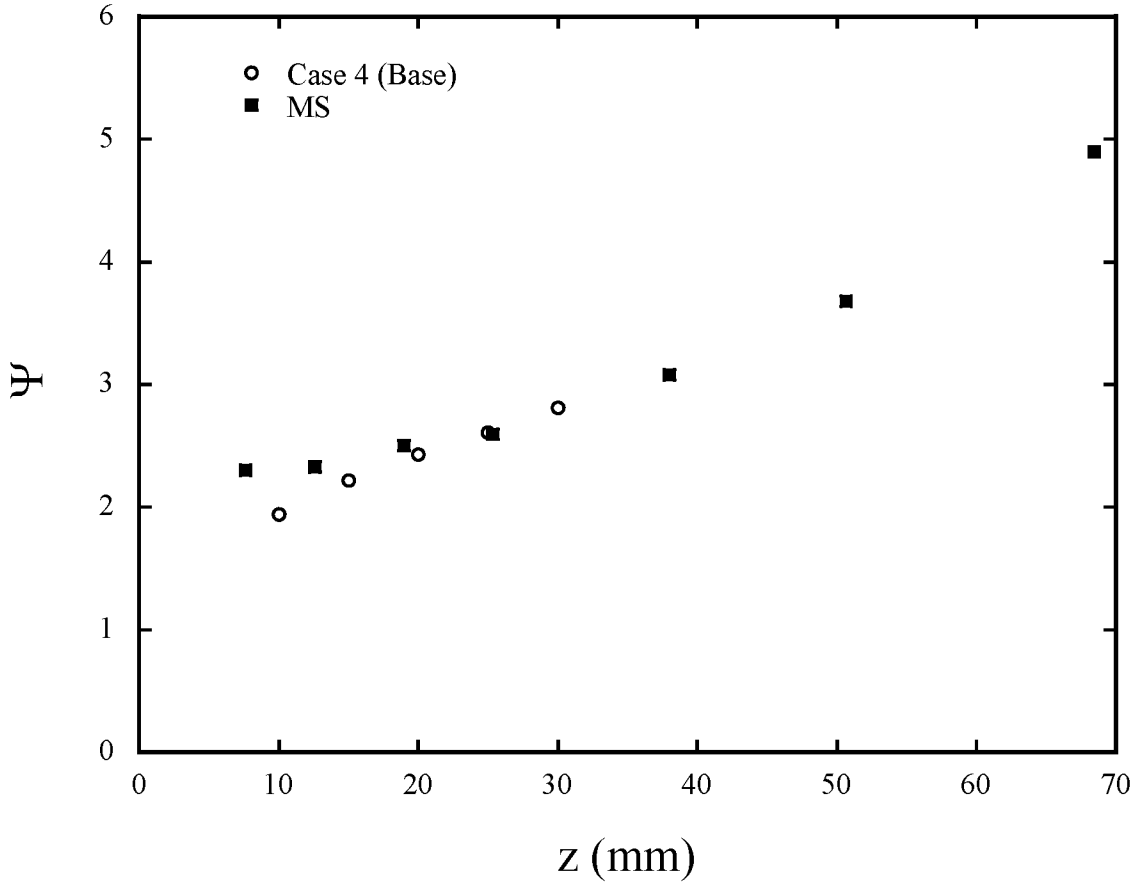

Figure 3-4. Entrainment coefficient for Case 4 compared with the experimentally determined coefficient from MS.

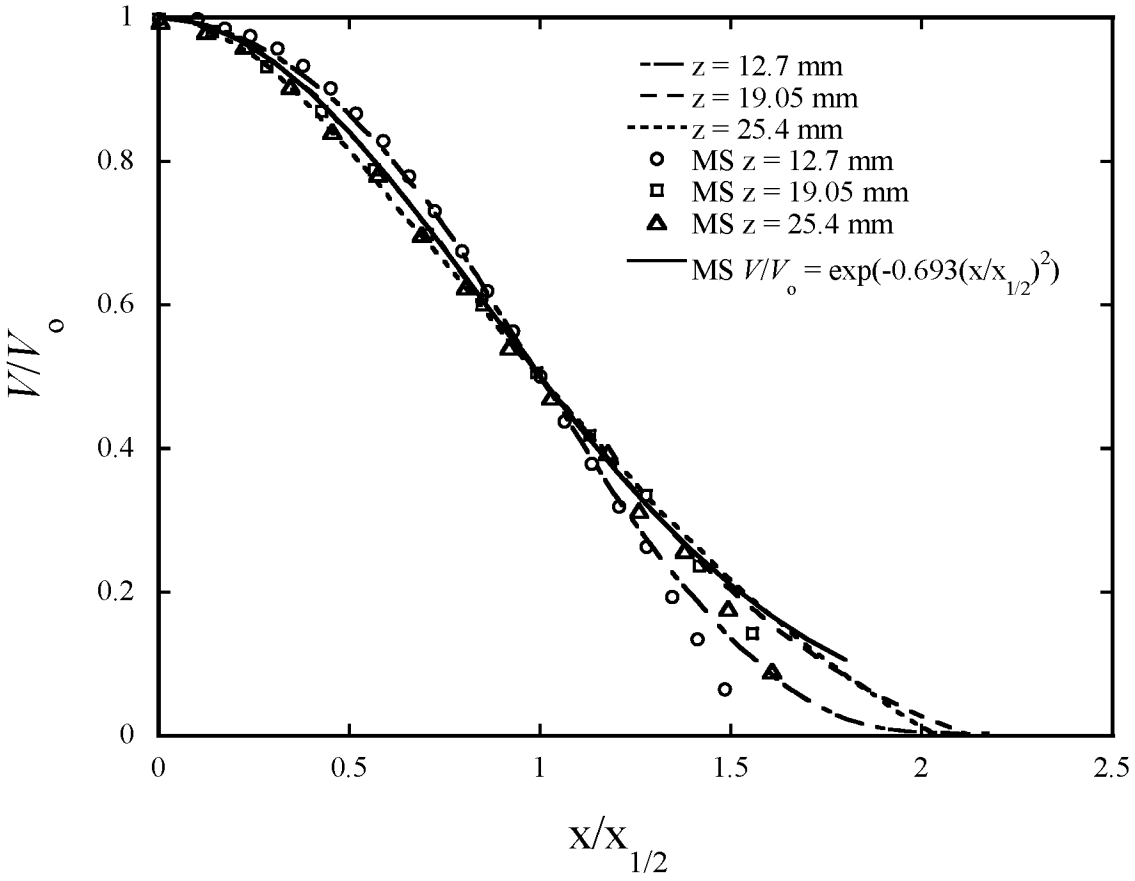

Figure 3-5. The profiles of z-velocity at $y = 0$ and different z positions below the die. The simulations for Case 4 are compared to the experimental data of MS. Also on the figure is the exponential fit equation proposed by MS.

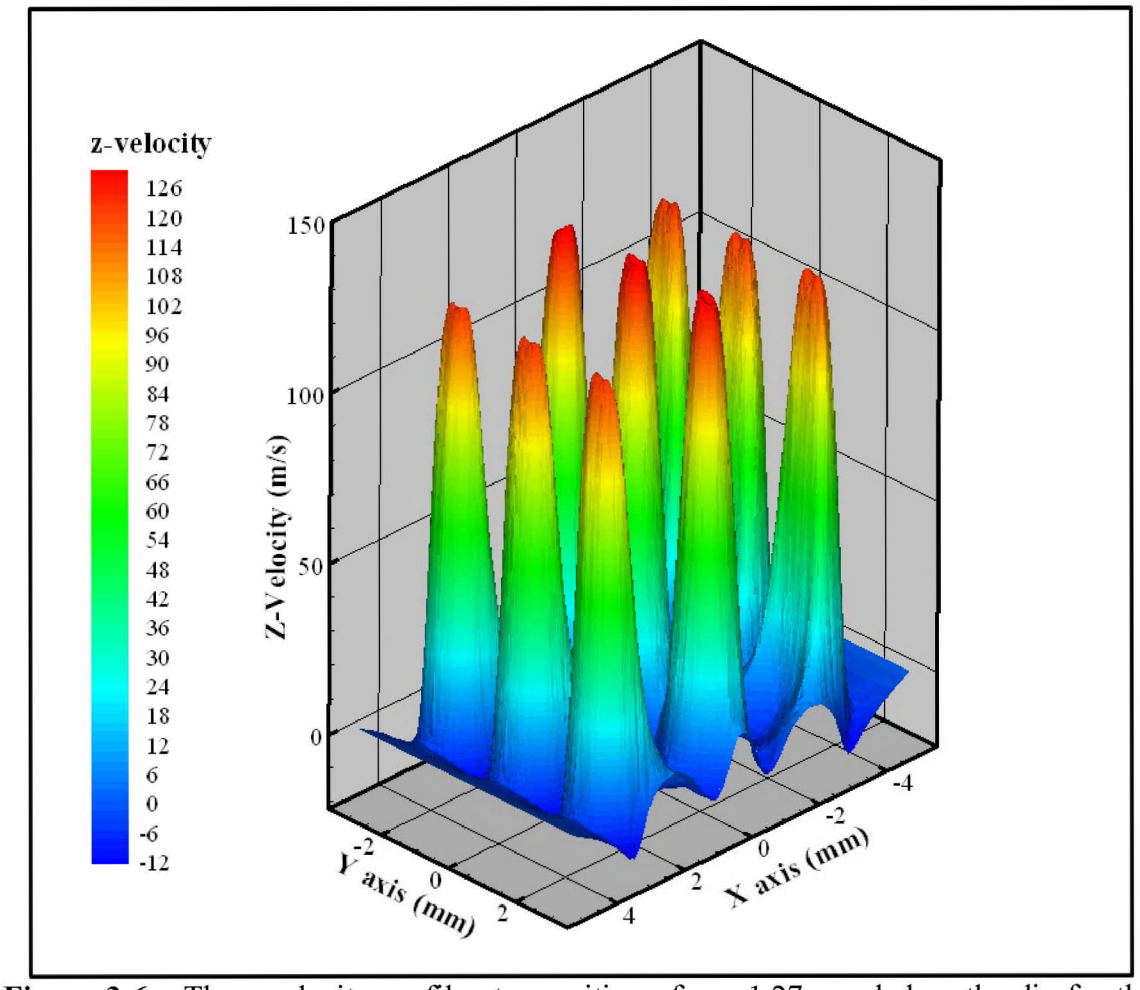

Figure 3-6a. The *z*-velocity profile at a position of z = 1.27 mm below the die for the Case 4 simulation.

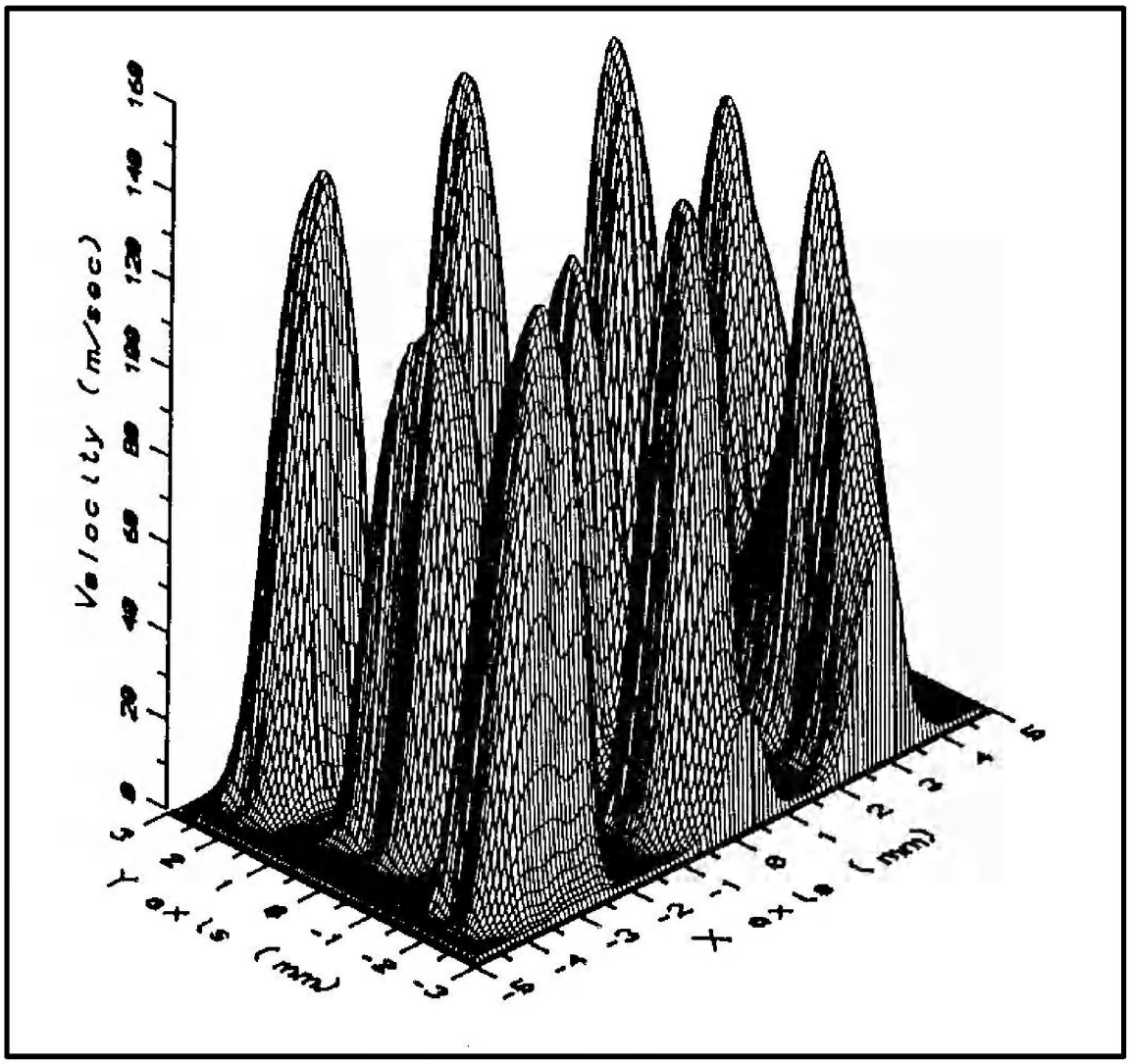

Figure 3-6b. The z-velocity profile at a position of z = 1.27 mm below the die for the MS experimental data.

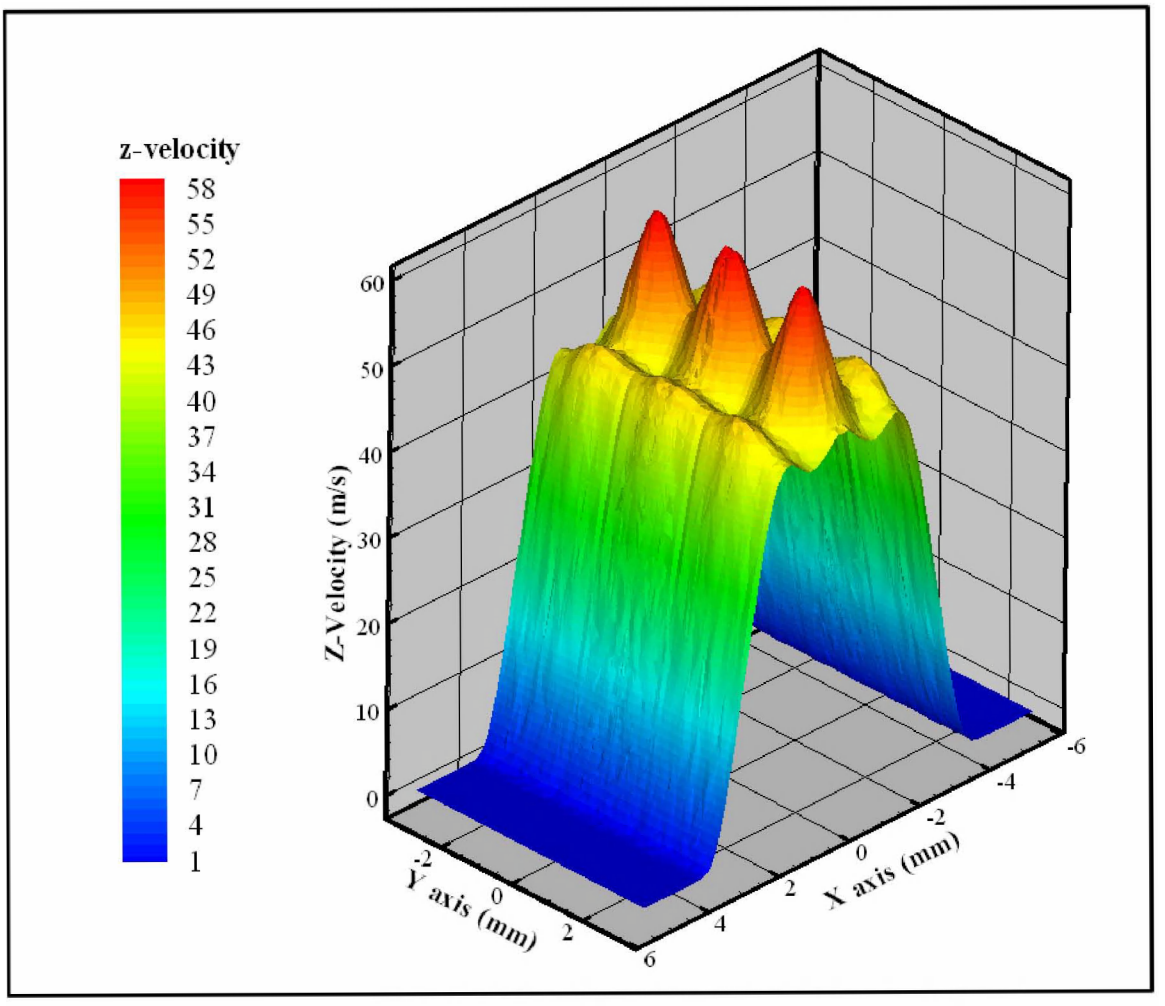

Figure 3-7a. The *z*-velocity profile at a position of z = 7.62 mm below the die for the Case 4 simulation.

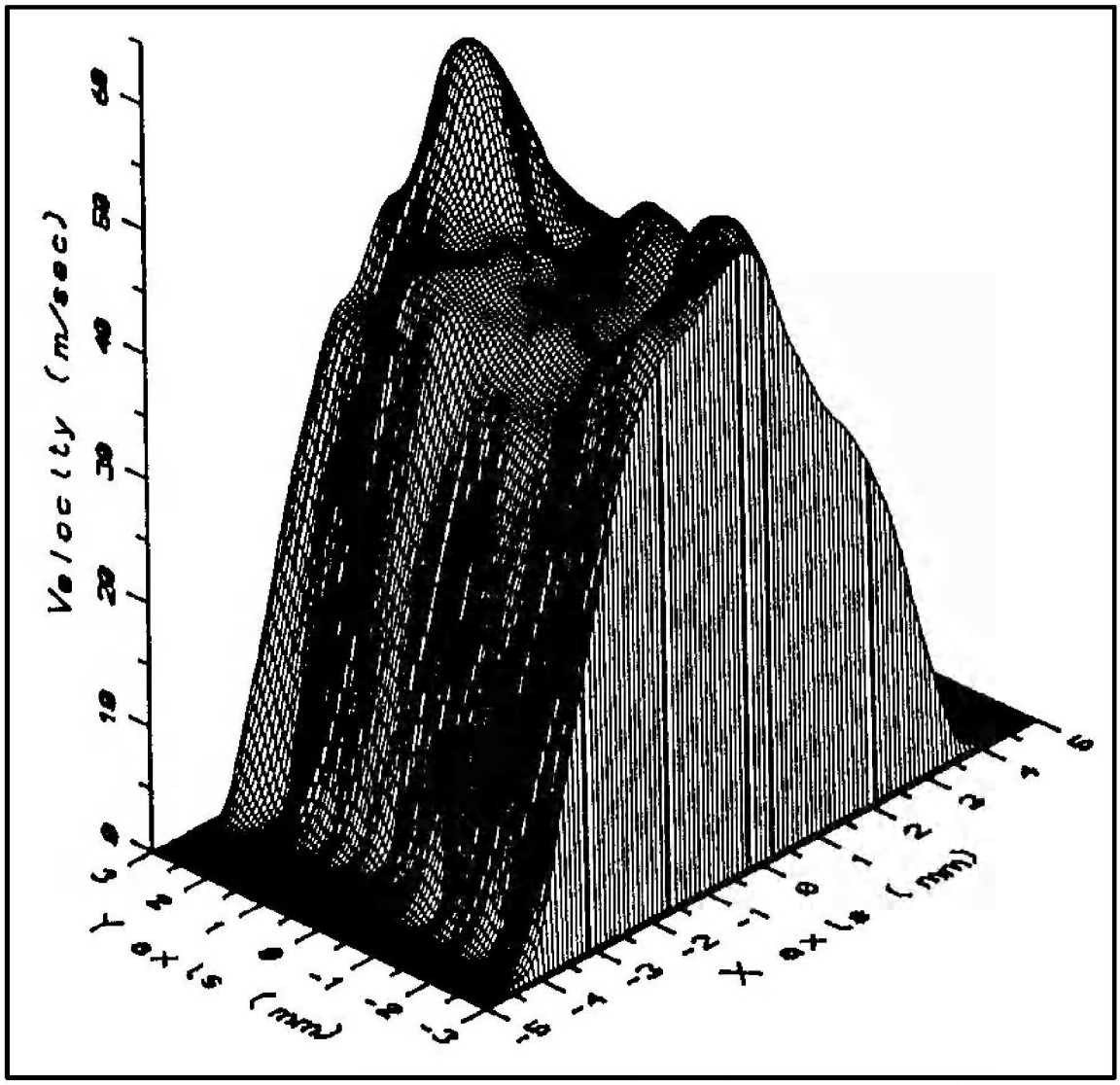

Figure 3-7b. The z-velocity profile at a position of z = 7.62 mm below the die for the MS experimental data.

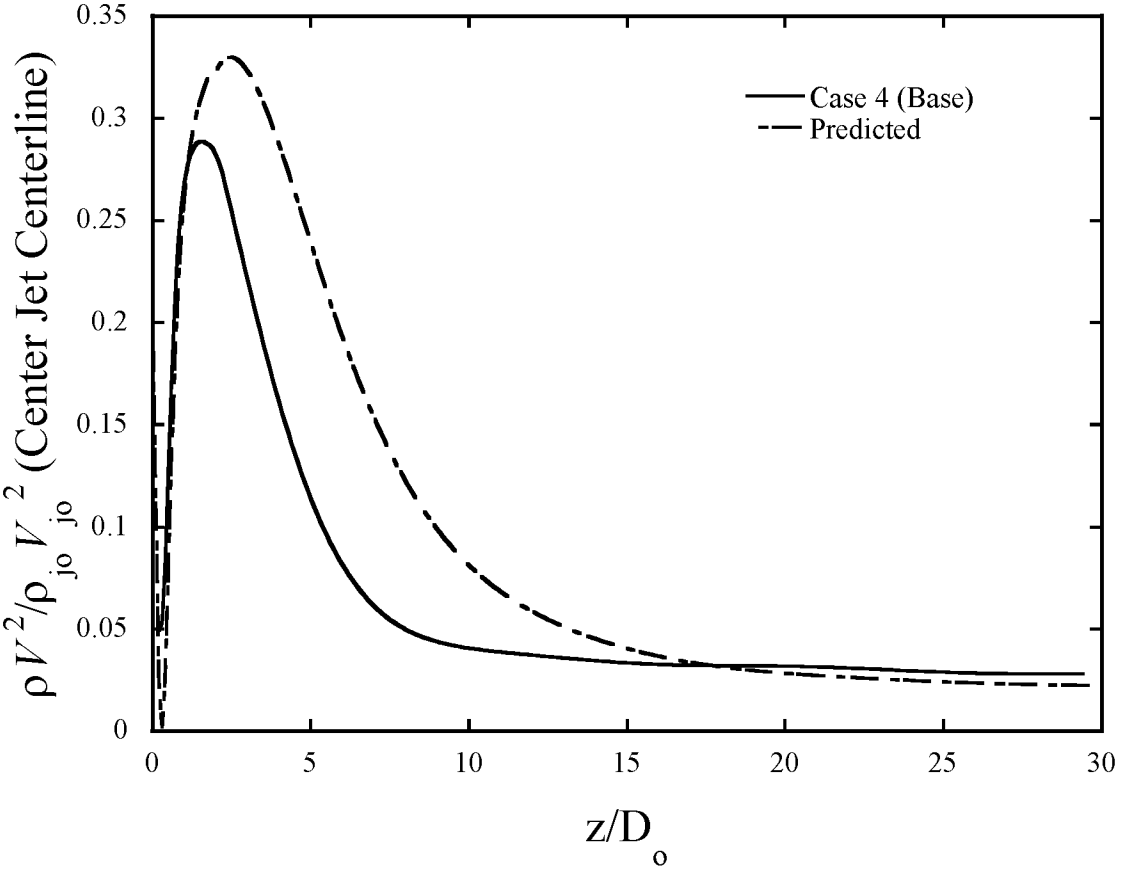

Figure 3-8a. Comparison between the Case 4 and predicted axial velocity profile for the centerline of the center jet. The predictions, which are based on the work of MS, are a derivation of the work of Baron and Alexander (1951).

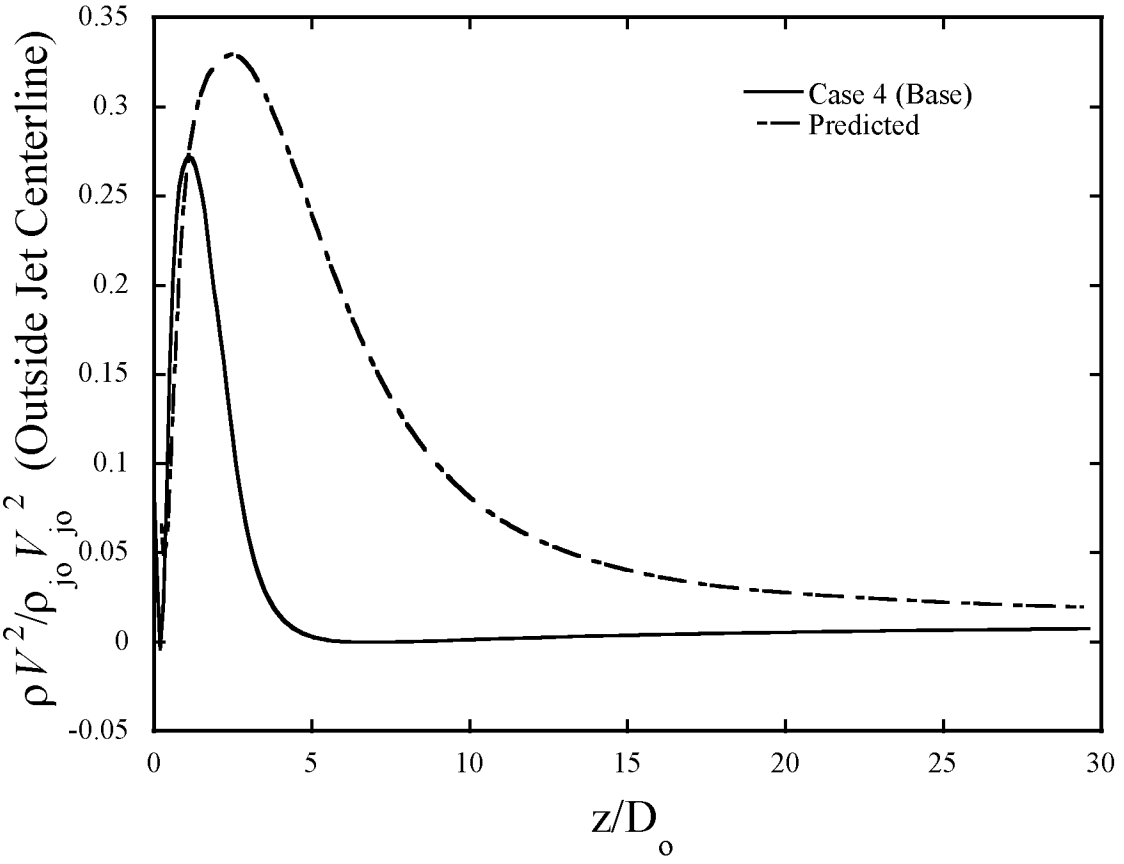

Figure 3-8b. Comparison between the Case 4 and predicted axial velocity profile for the centerline of the outside jet. The predictions, which are based on the work of MS, are a derivation of the work of Baron and Alexander (1951).

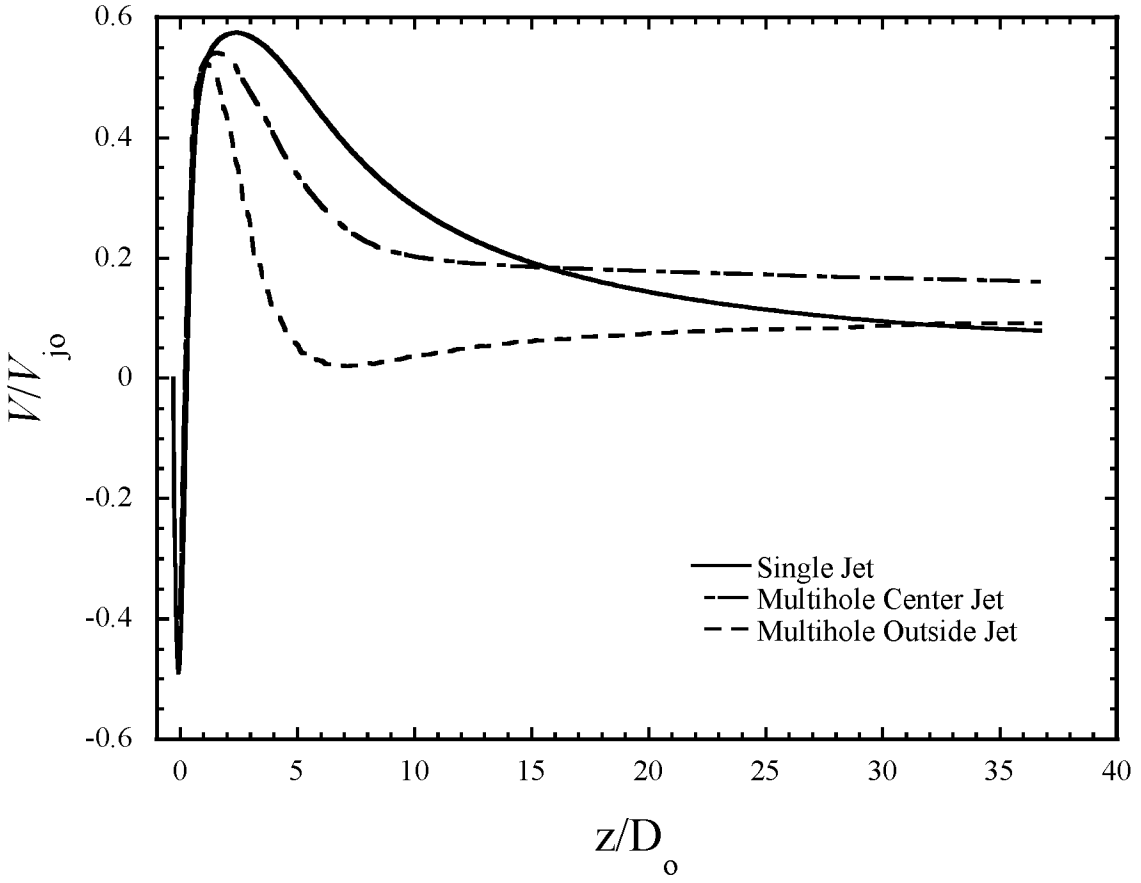

Figure 3-9. A comparison of the jet centerline velocity profile at $x = 0$ and $y = 0$ for a simulated single annular jet with the center and outer jet profiles in the simulated Case 4.

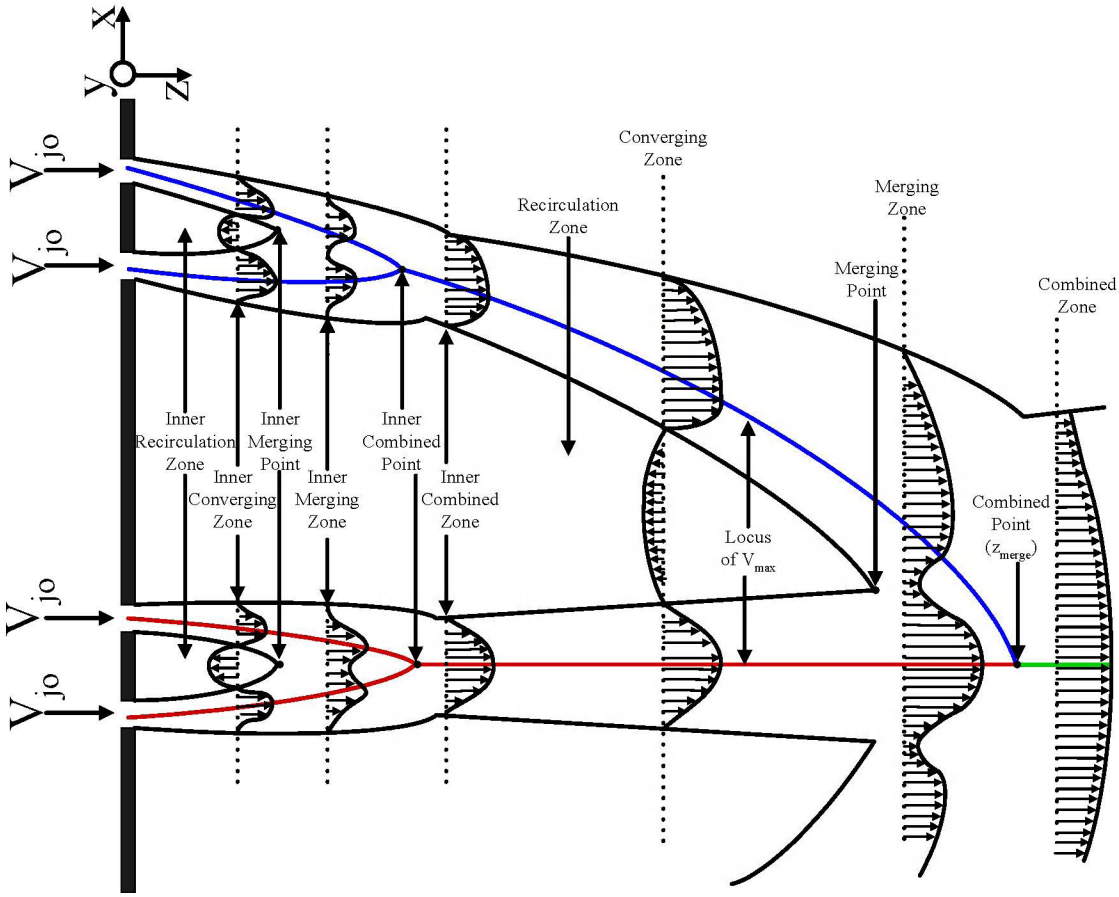

Figure 3-10. A qualitative diagram of the flow zones created by multiple jets. This diagram shows a side view (*x*-*z* plane) of the flow from two annular jets in a Schwarz die configuration. At the top of the figure is an outside jet, while a center jet is located at the bottom of the figure. This diagram was adapted from Moore et al. (2004) and Lai and Nasr (1998).

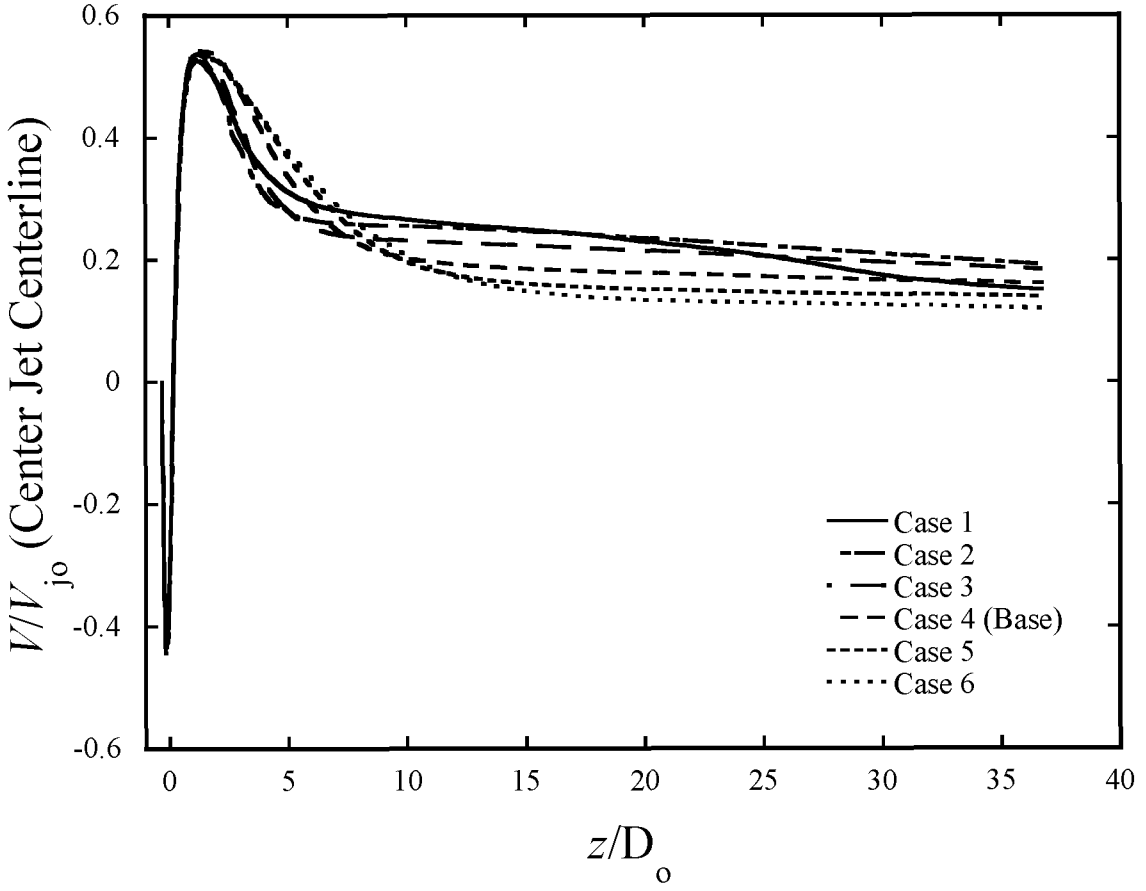

Figure 3-11a. The dimensionless z-velocity, for all six simulations for the centerline of the center jet where $x = 0$ and $y = 0$.

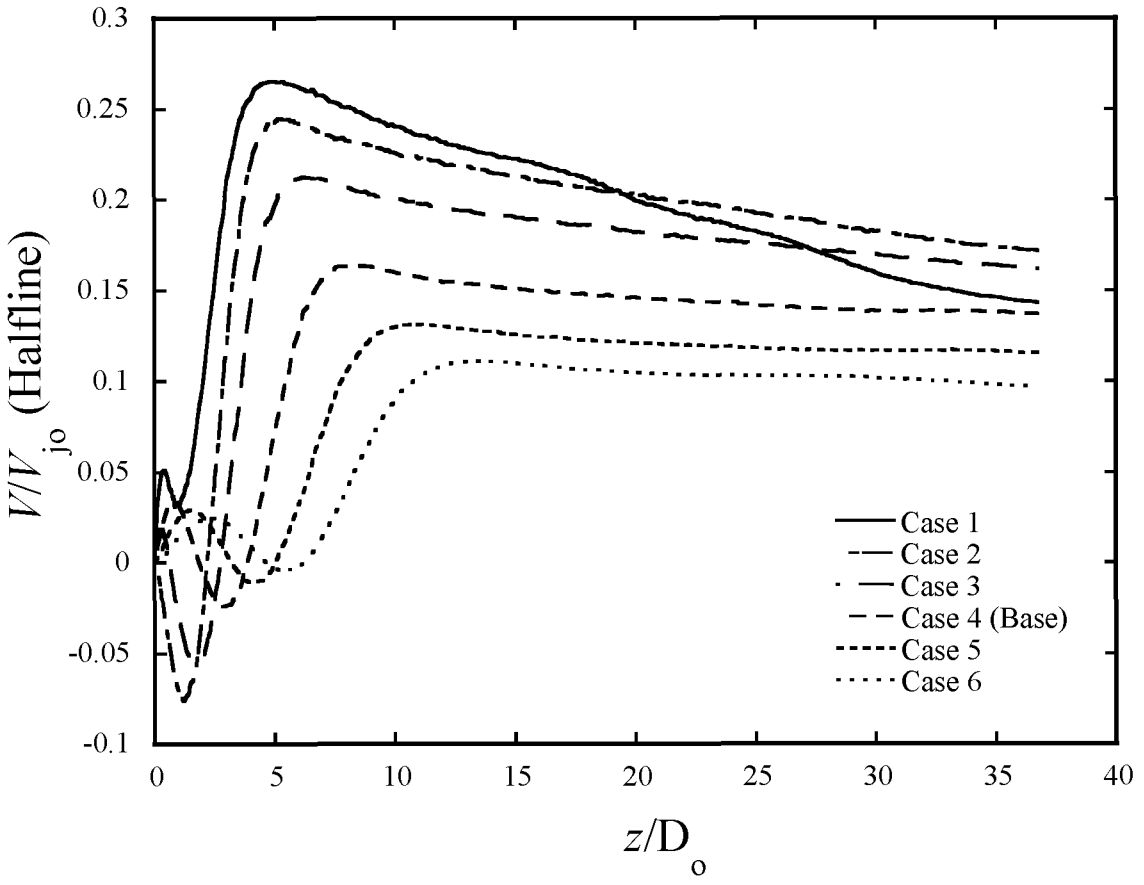

Figure 3-11b. The dimensionless z-velocity, for all six simulations compared for a line halfway between the center and outside jets where $y = 0$ and $x = h_\ell/2$.

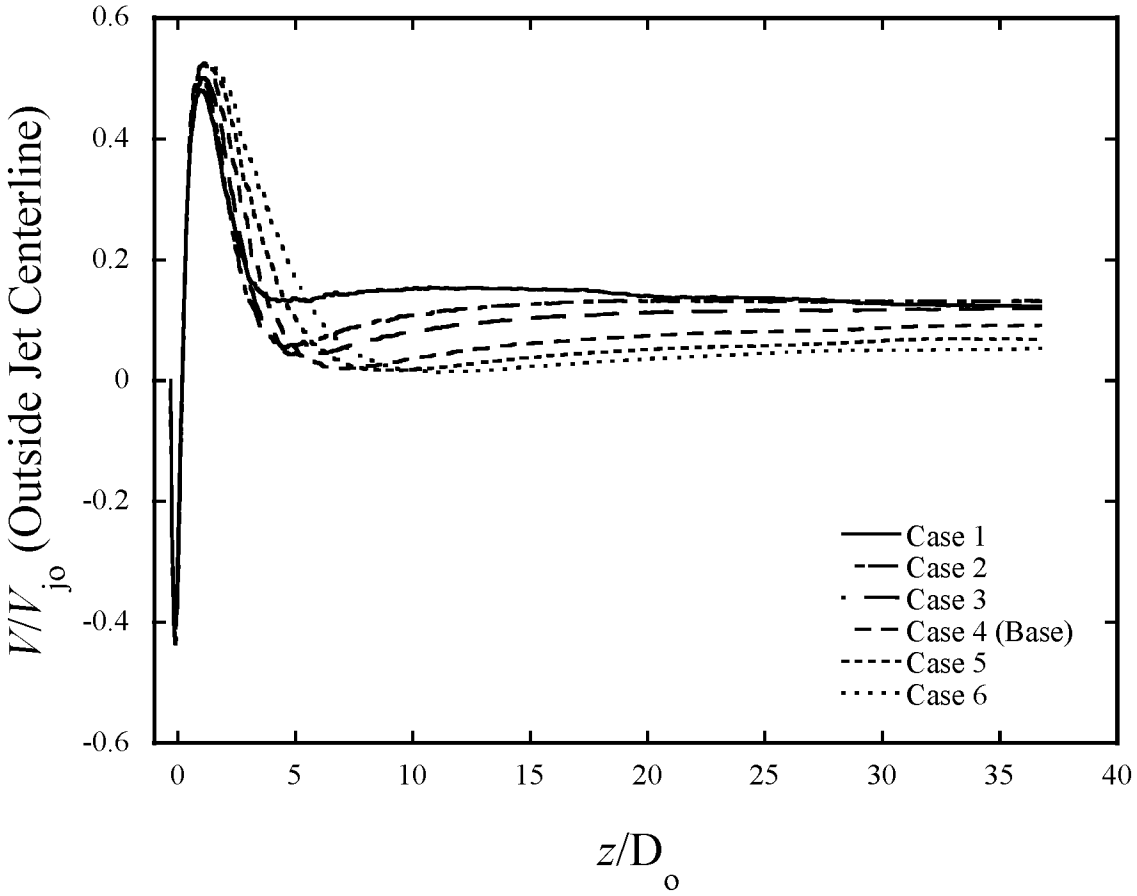

Figure 3-11c. The dimensionless z-velocity, for all six simulations, compared for the centerline of the outside jet where $y = 0$ and $x = h_e$.

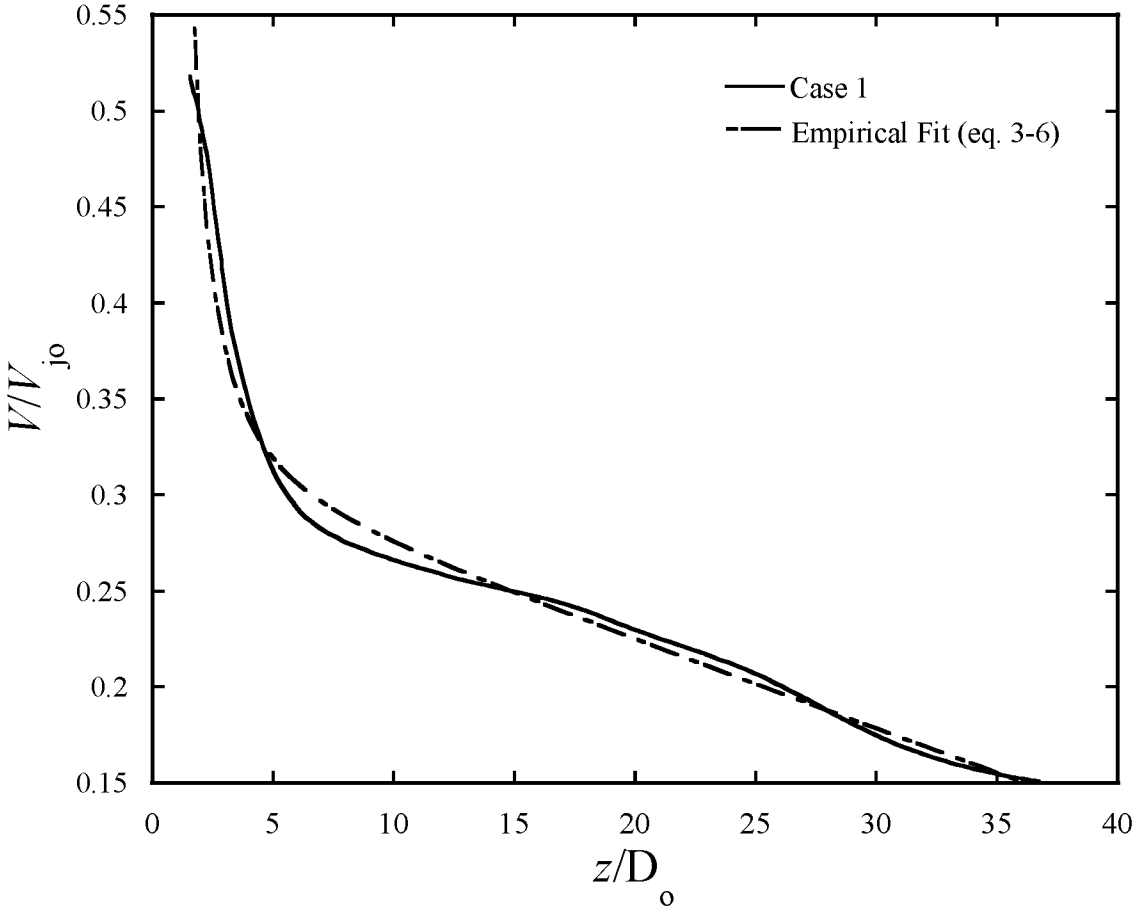

Figure 3-12a. Simulation velocity decay at $x = 0$ and $y = 0$ compared with the correlation for Case 1. The correlation is equation 3-6 with the constants listed in Table 3-3.

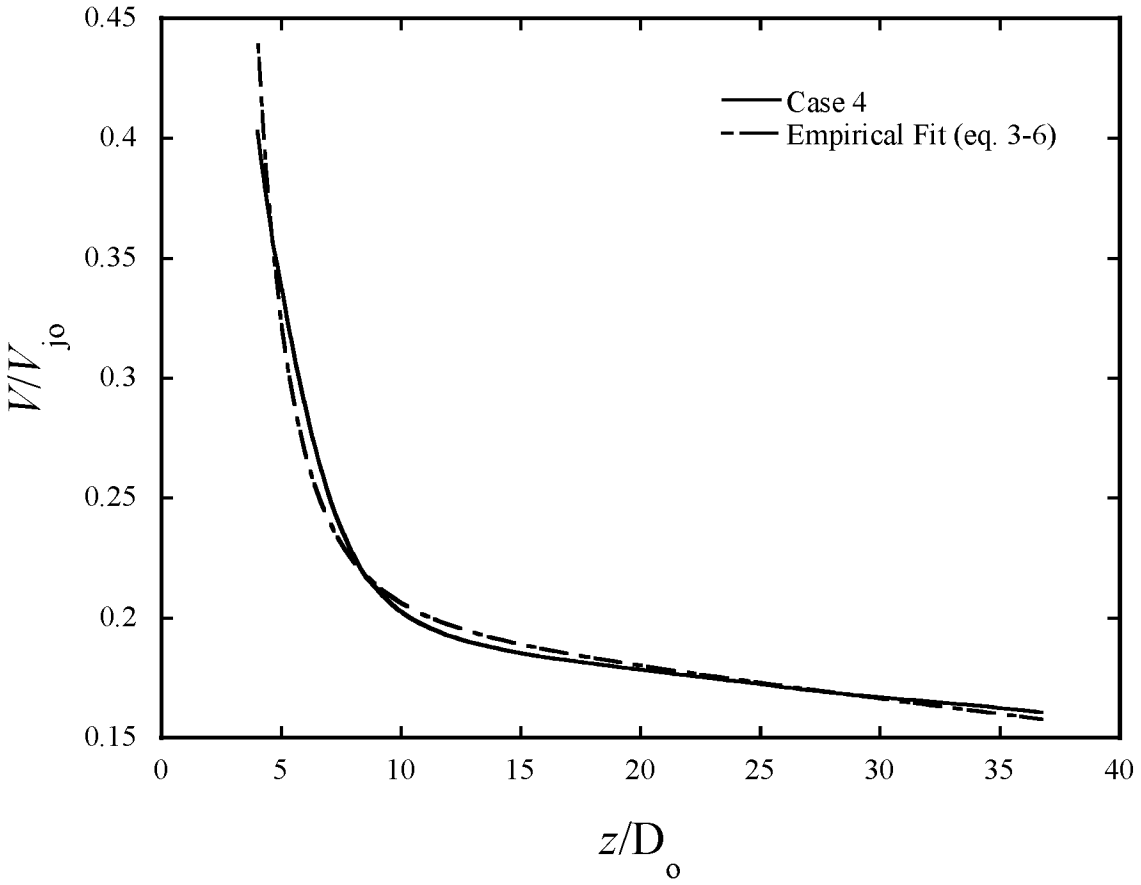

Figure 3-12b. Simulation velocity decay at $x = 0$ and $y = 0$ compared with the correlation for Case 4. The correlation is equation 3-6 with the constants listed in Table 3-3.

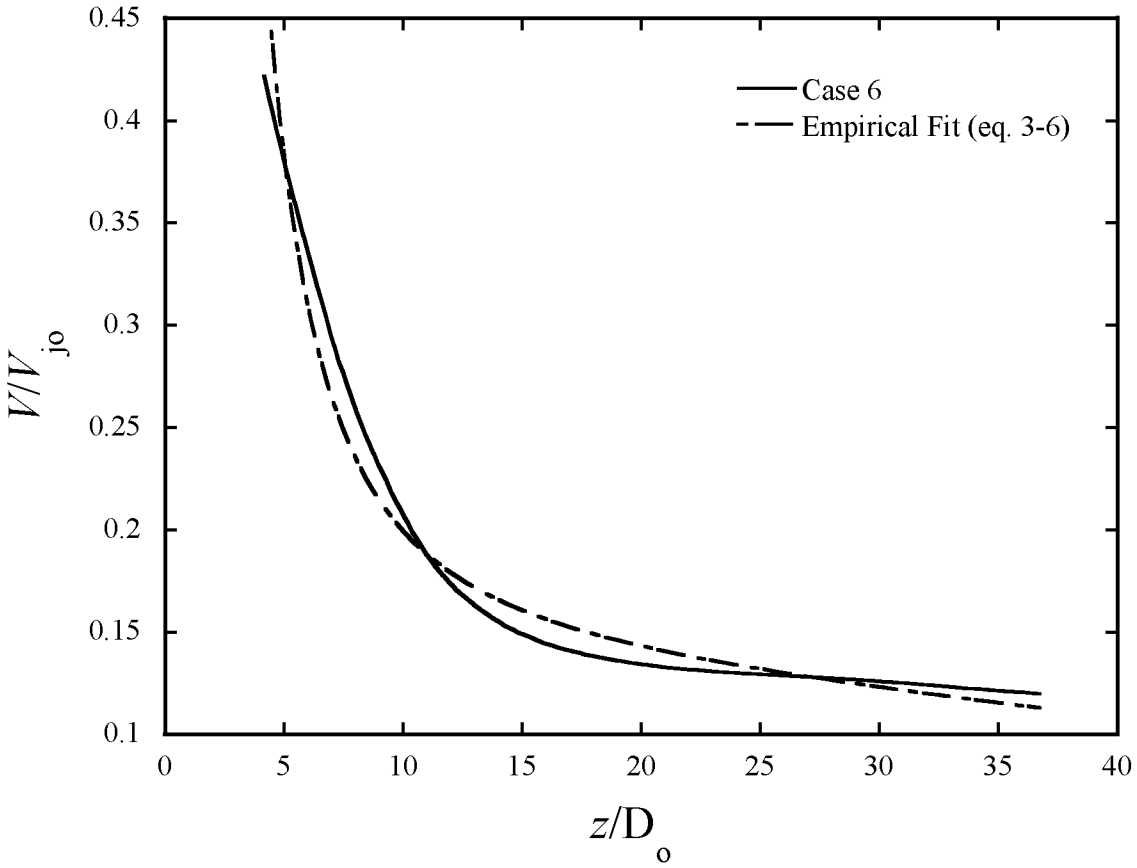

Figure 3-12c. Simulation velocity decay at $x = 0$ and $y = 0$ compared with the correlation for Case 6. The correlation is equation 3-6 with the constants listed in Table 3-3.

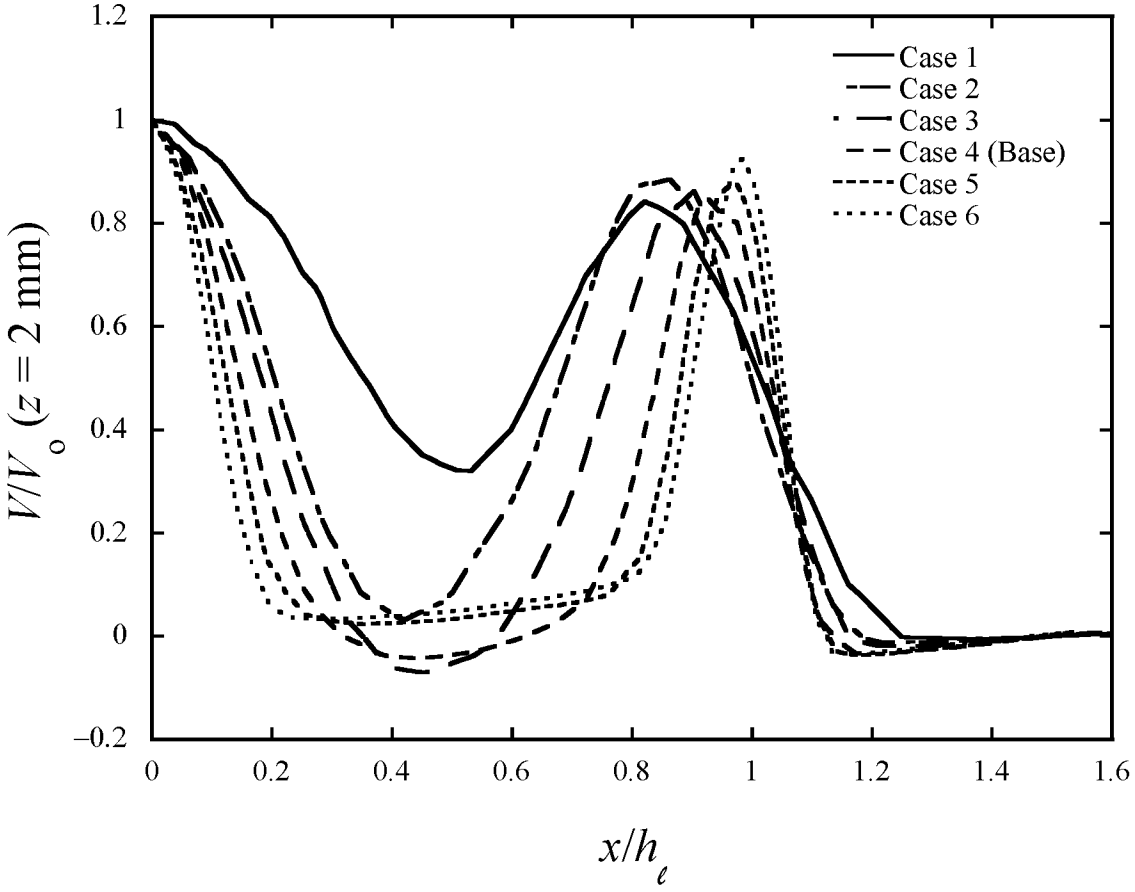

Figure 3-13a. Comparison of the z-velocity profiles of all simulations at z = 2 mm. All profiles are shown for the y = 0 plane.

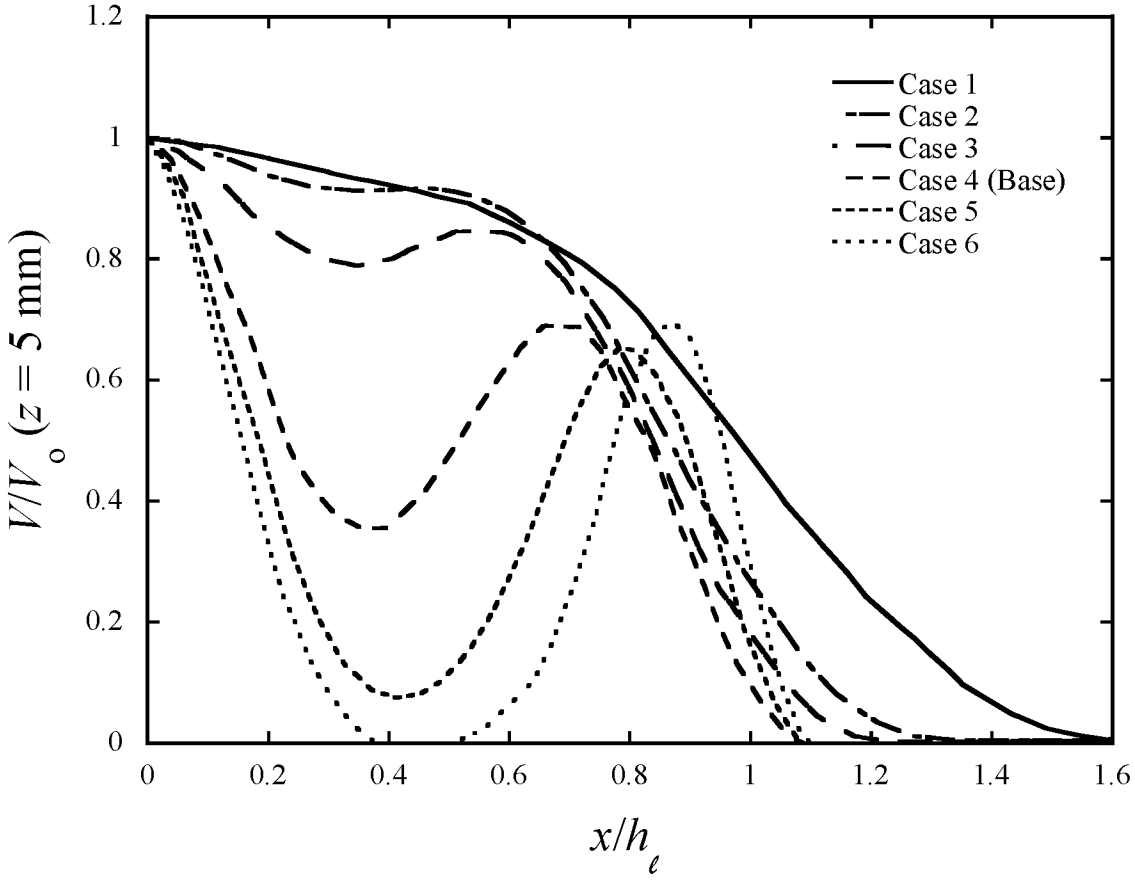

Figure 3-13b. Comparison of the z-velocity profiles of all simulations at and z = 5 mm. All profiles are shown for the y = 0 plane.

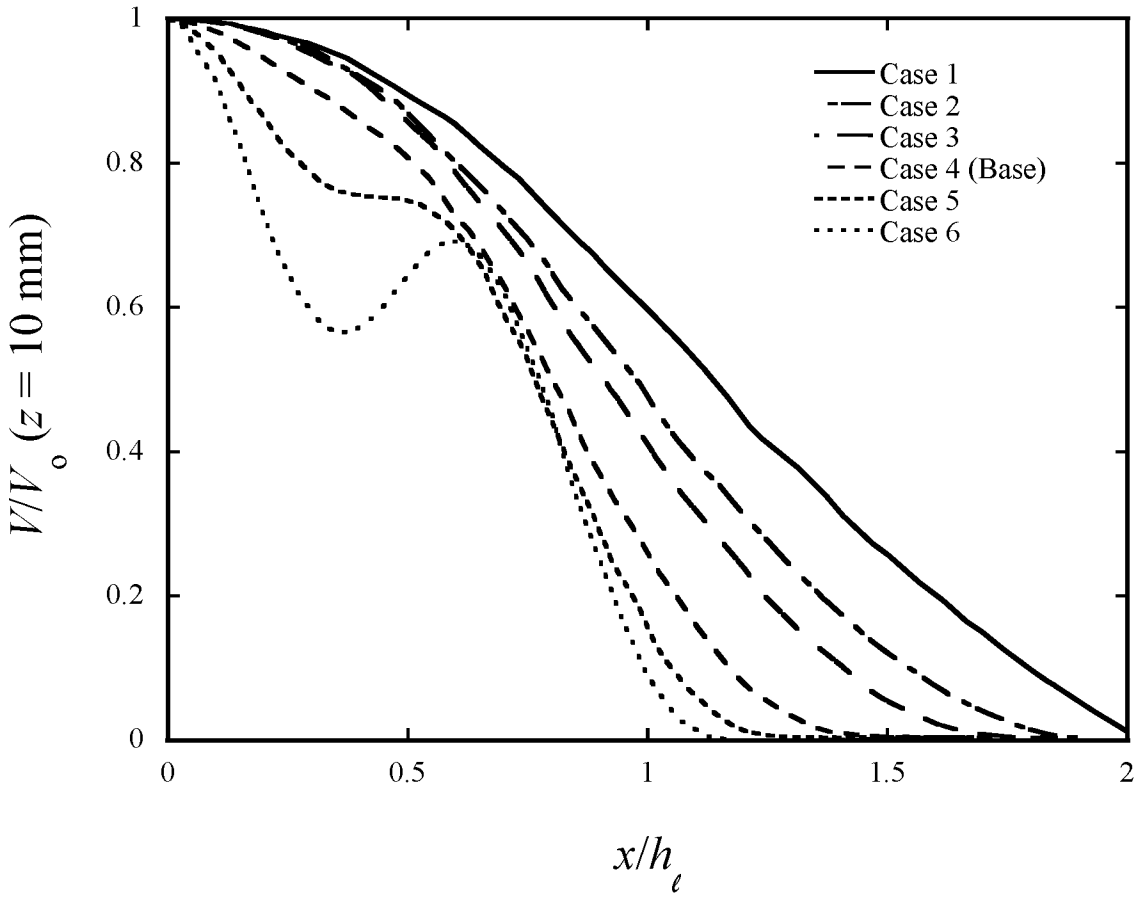

Figure 3-13c. Comparison of the z-velocity profiles of all simulations at z = 10 mm. All profiles are shown for the y = 0 plane.

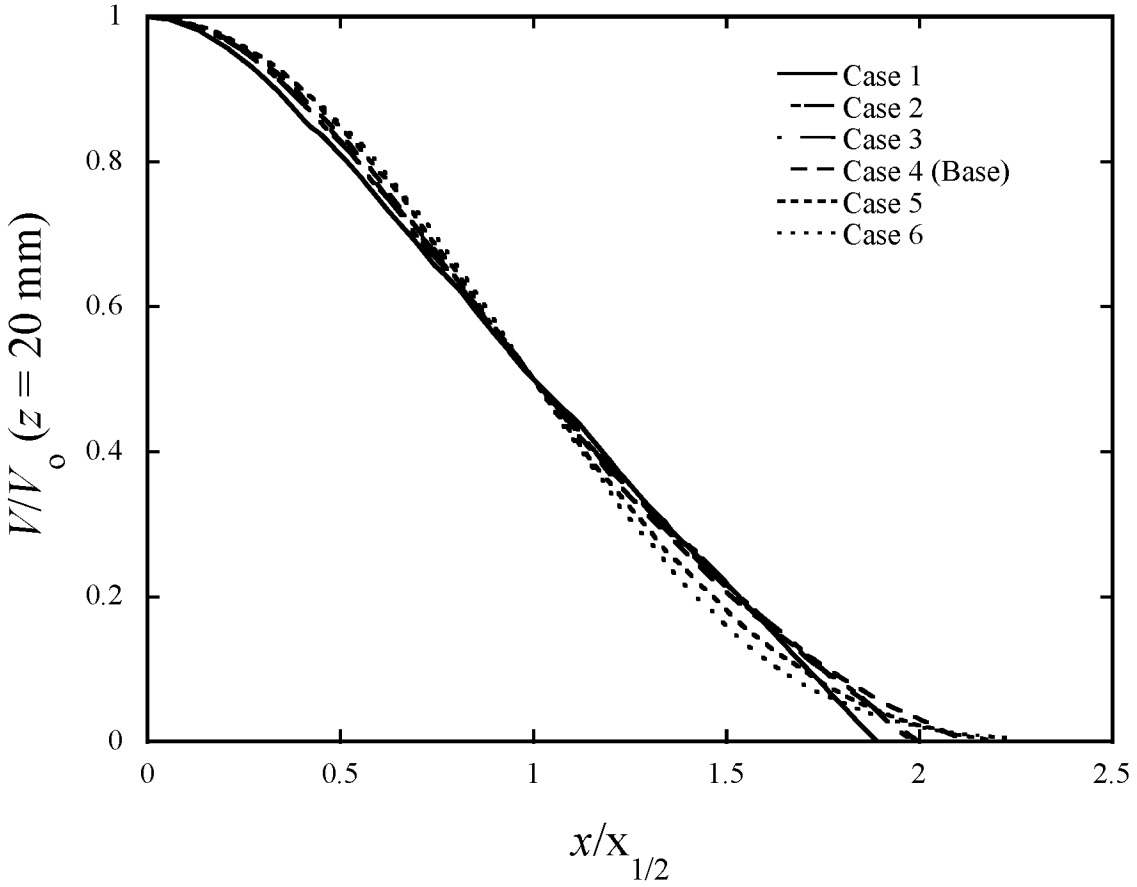

Figure 3-13d. Comparison of the *z*-velocity profiles of all simulations at $z = 20$ mm. All profiles are shown for the $y = 0$ plane.

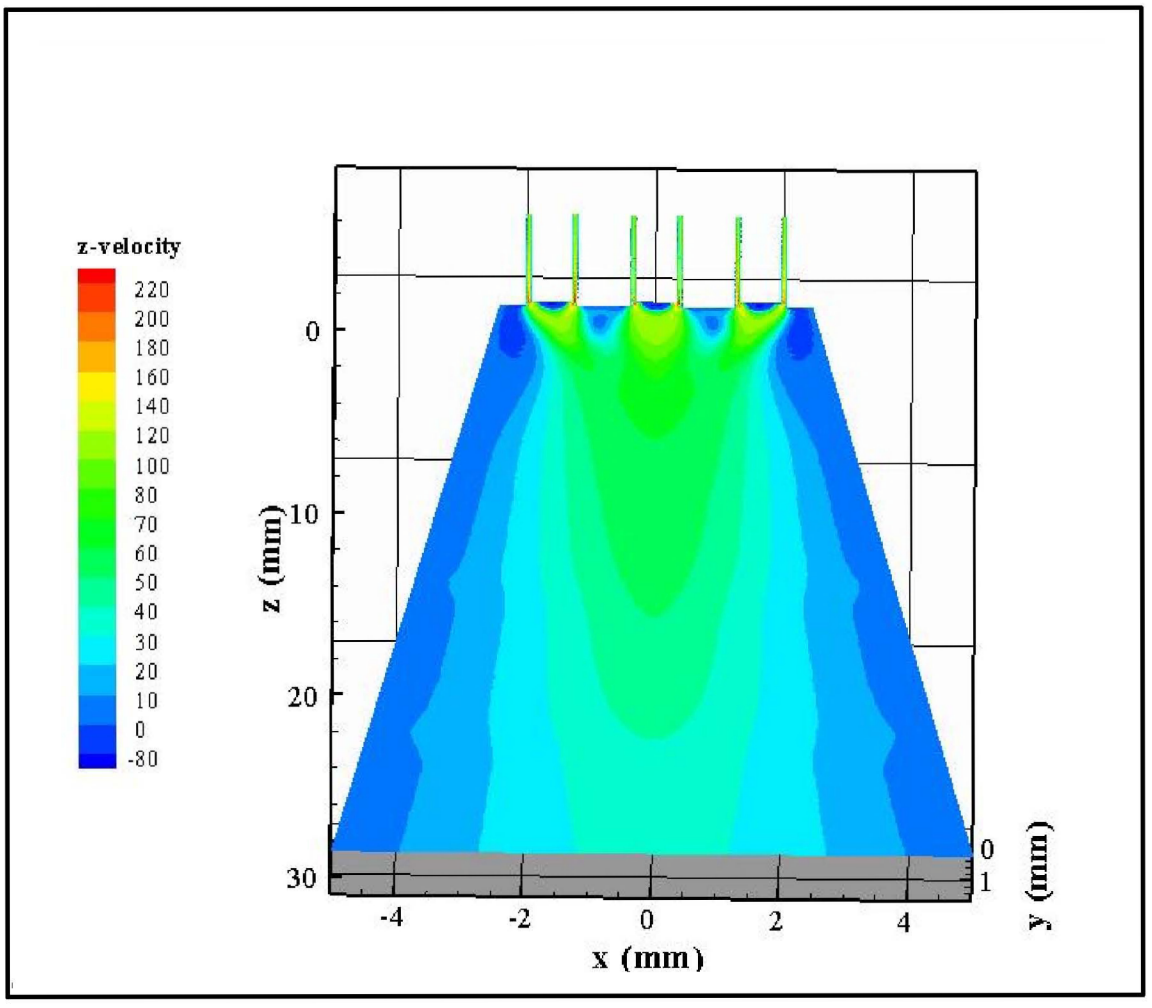

Figure 3-14a. Contour plot of z-velocity for Case 1. All contours are shown for the $y = 0$ plane.

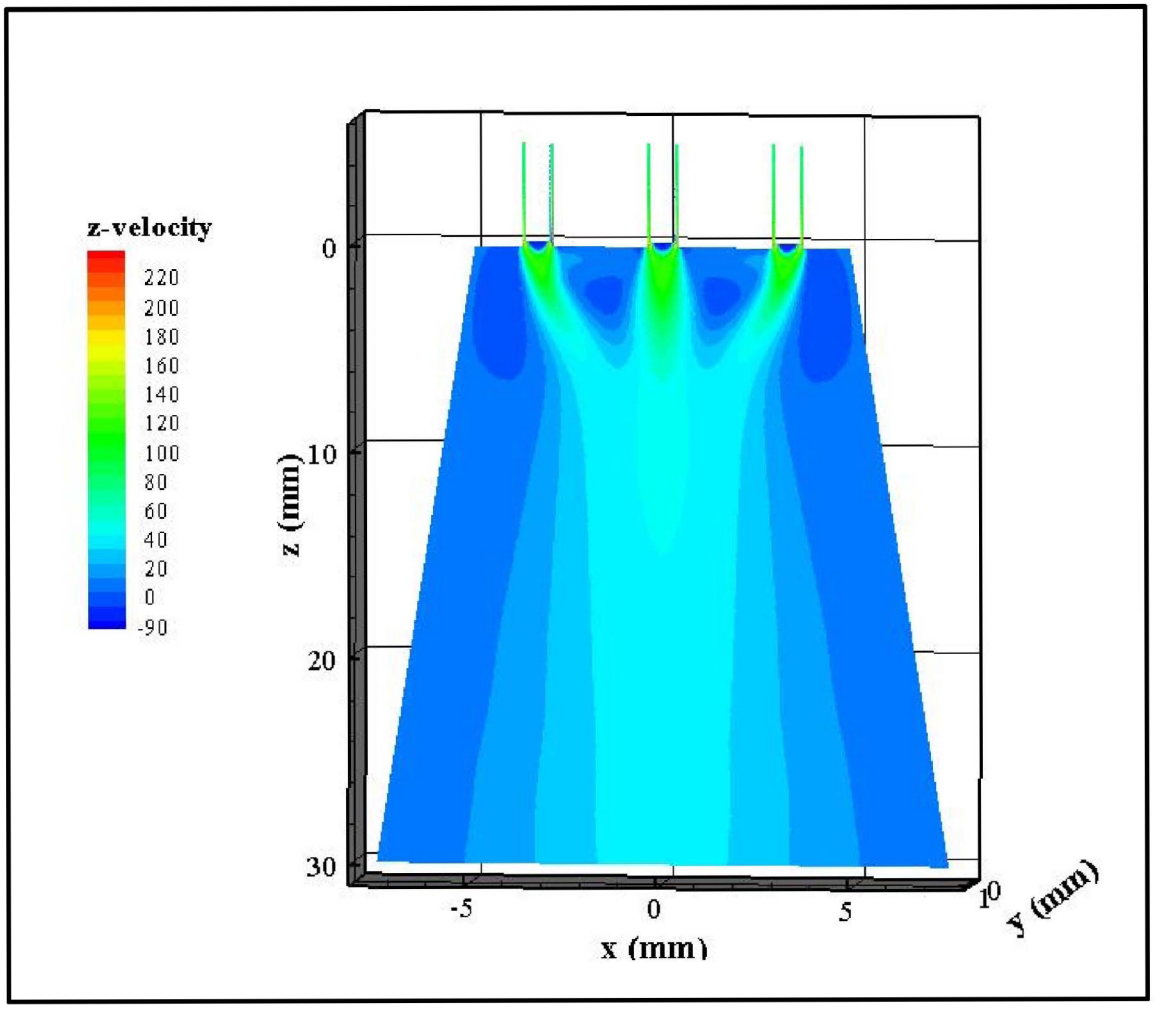

Figure 3-14b. Contour plot of *z*-velocity for Case 4. All contours are shown for the $y = 0$ plane.

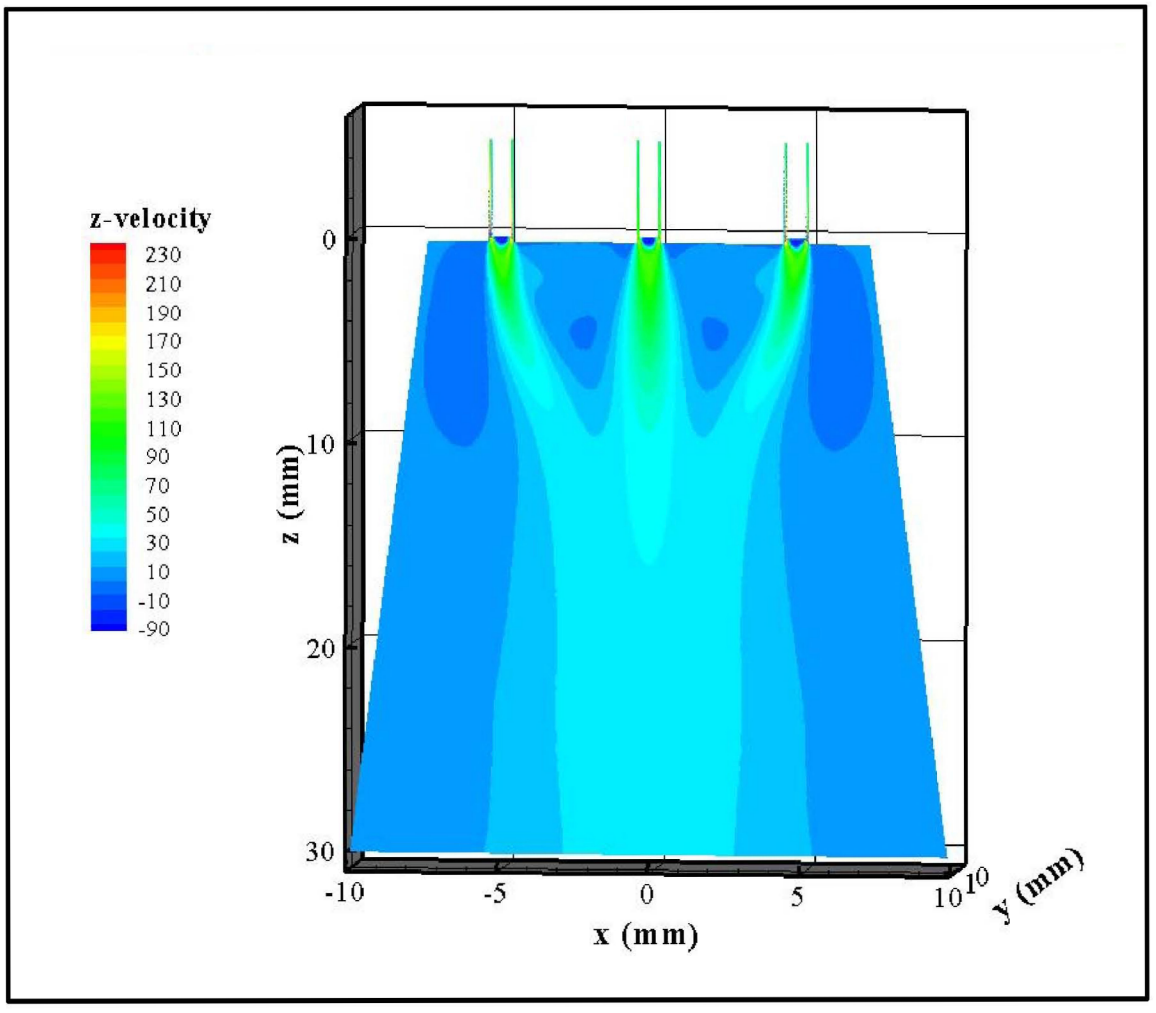

Figure 3-14c. Contour plot of z-velocity for Case 6. All contours are shown for the $y = 0$ plane.

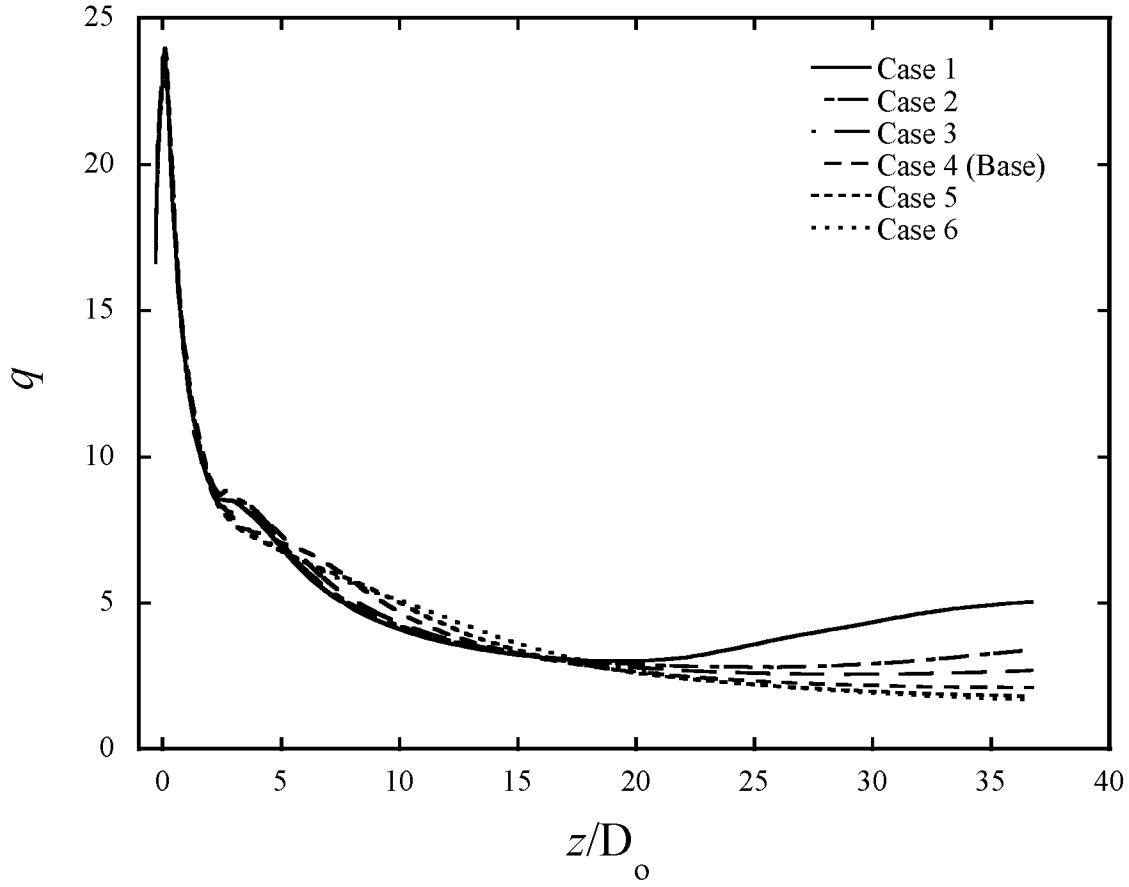

Figure 3-15. Center jet centerline turbulence intensity for all simulations.

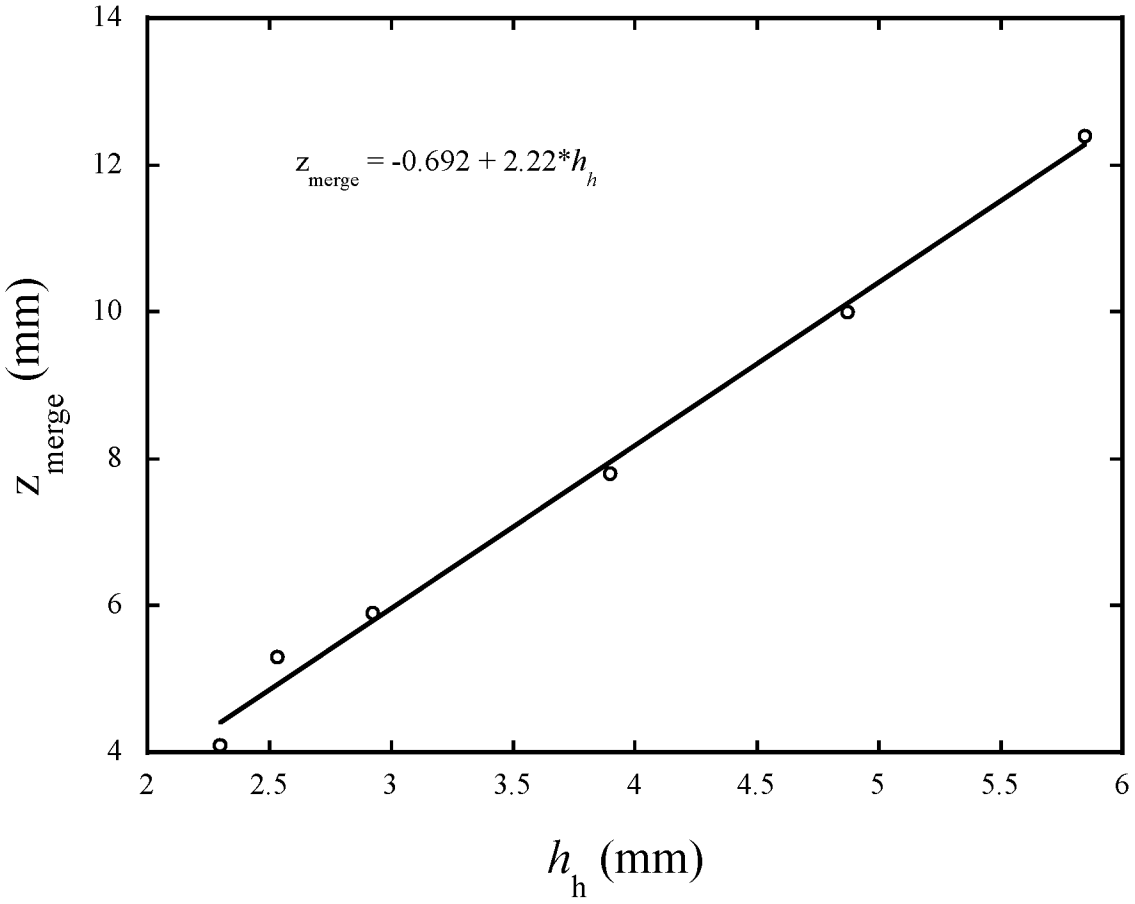

Figure 3-16. The location of z_{merge} as a function of h_h for all cases.

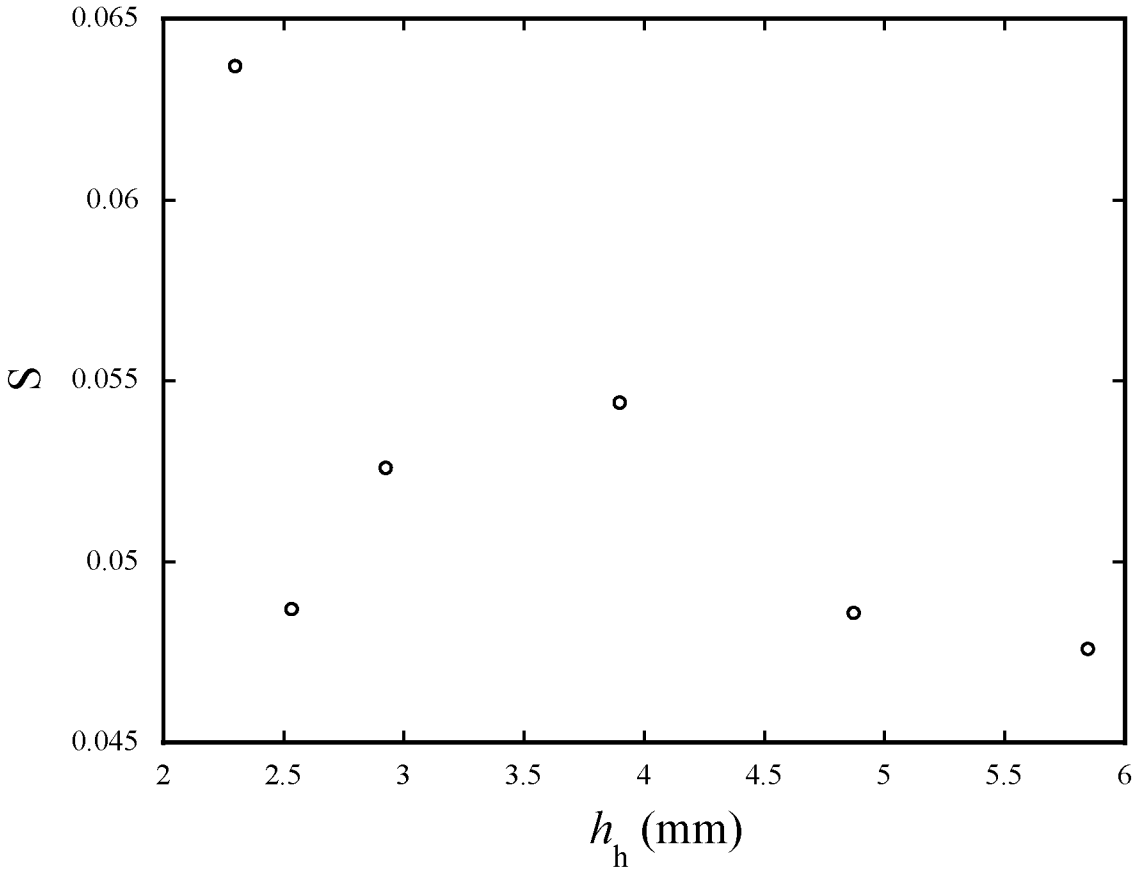

Figure 3-17. The spreading rate of the center jets in the multi-hole die as a function of h_h.

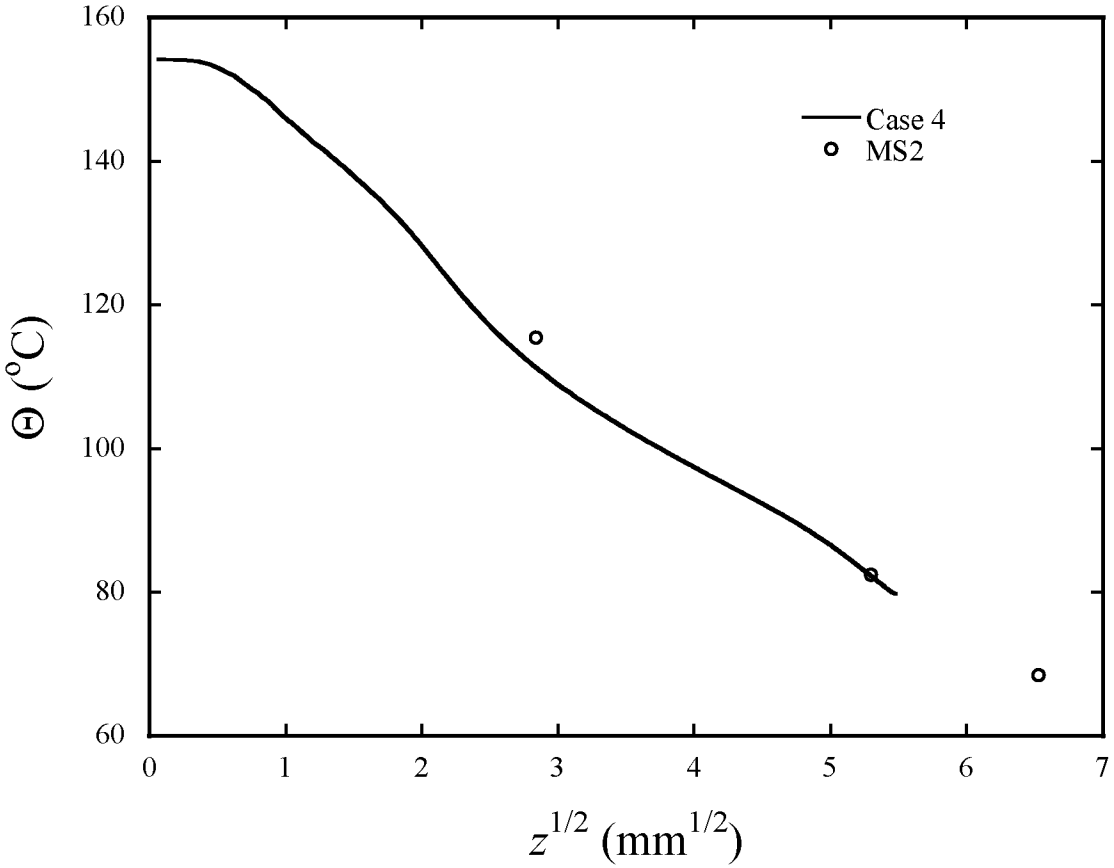

Figure 3-18. The centerline excess temperature decay from Case 4 simulation compared with the experimental data of MS2.

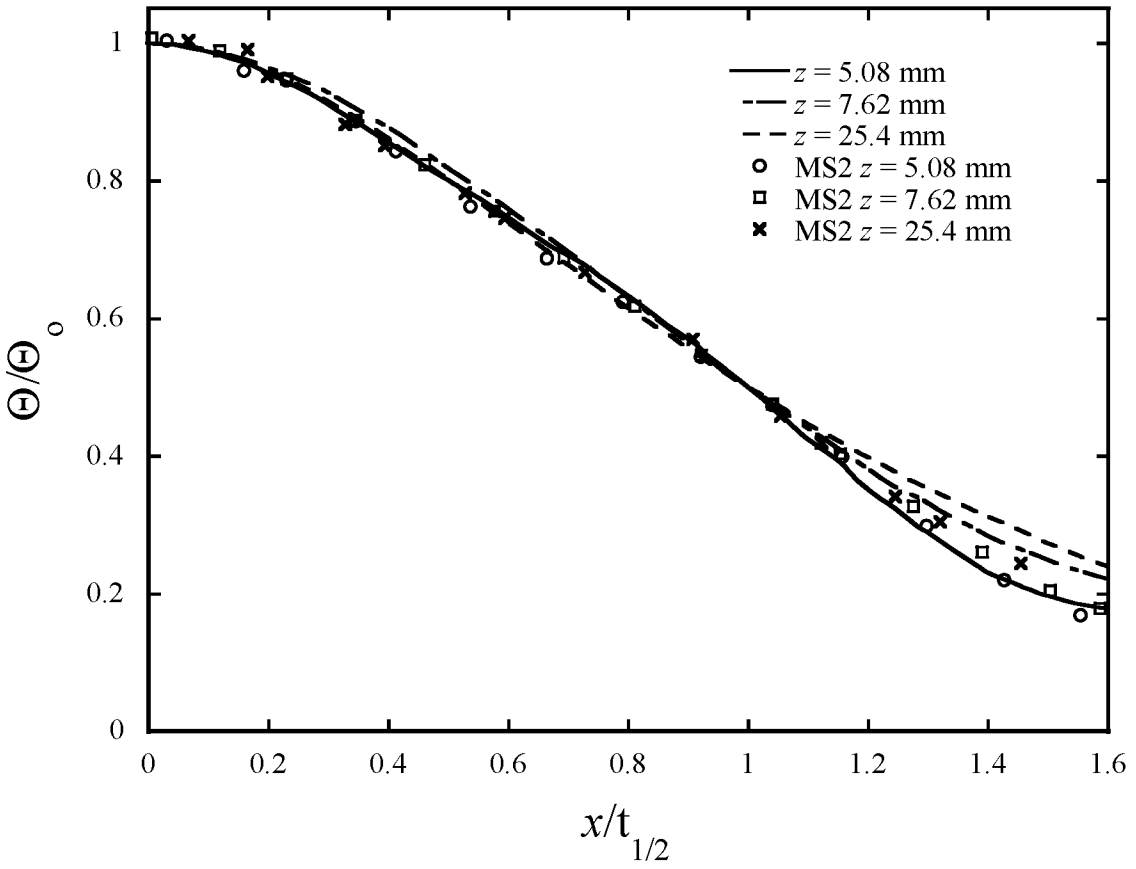

Figure 3-19. Comparison of Case 4 and MS2 excess temperature profiles on the $y = 0$ plane.

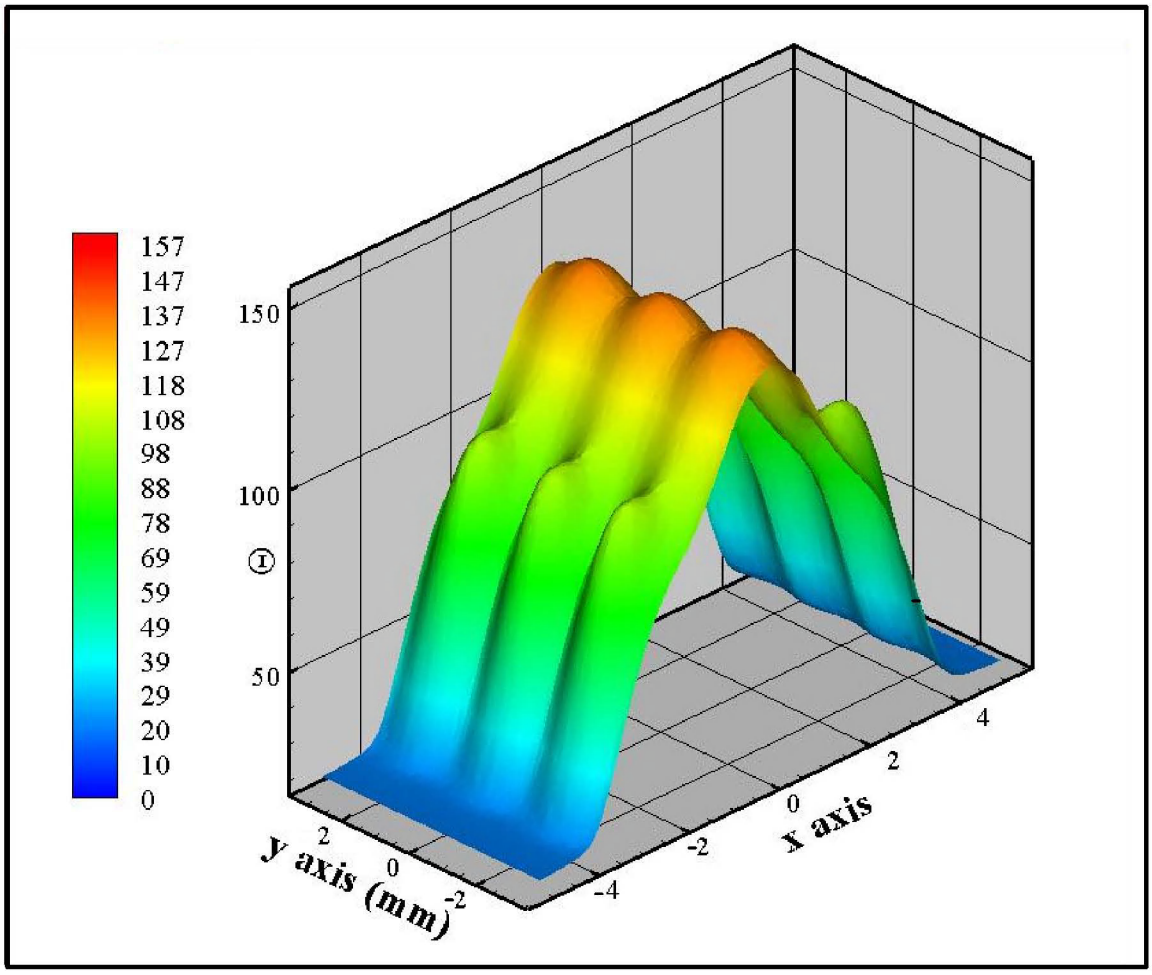

Figure 3-20a. Excess temperature profile at a position of z = 2.54 mm below the die for Case 4.

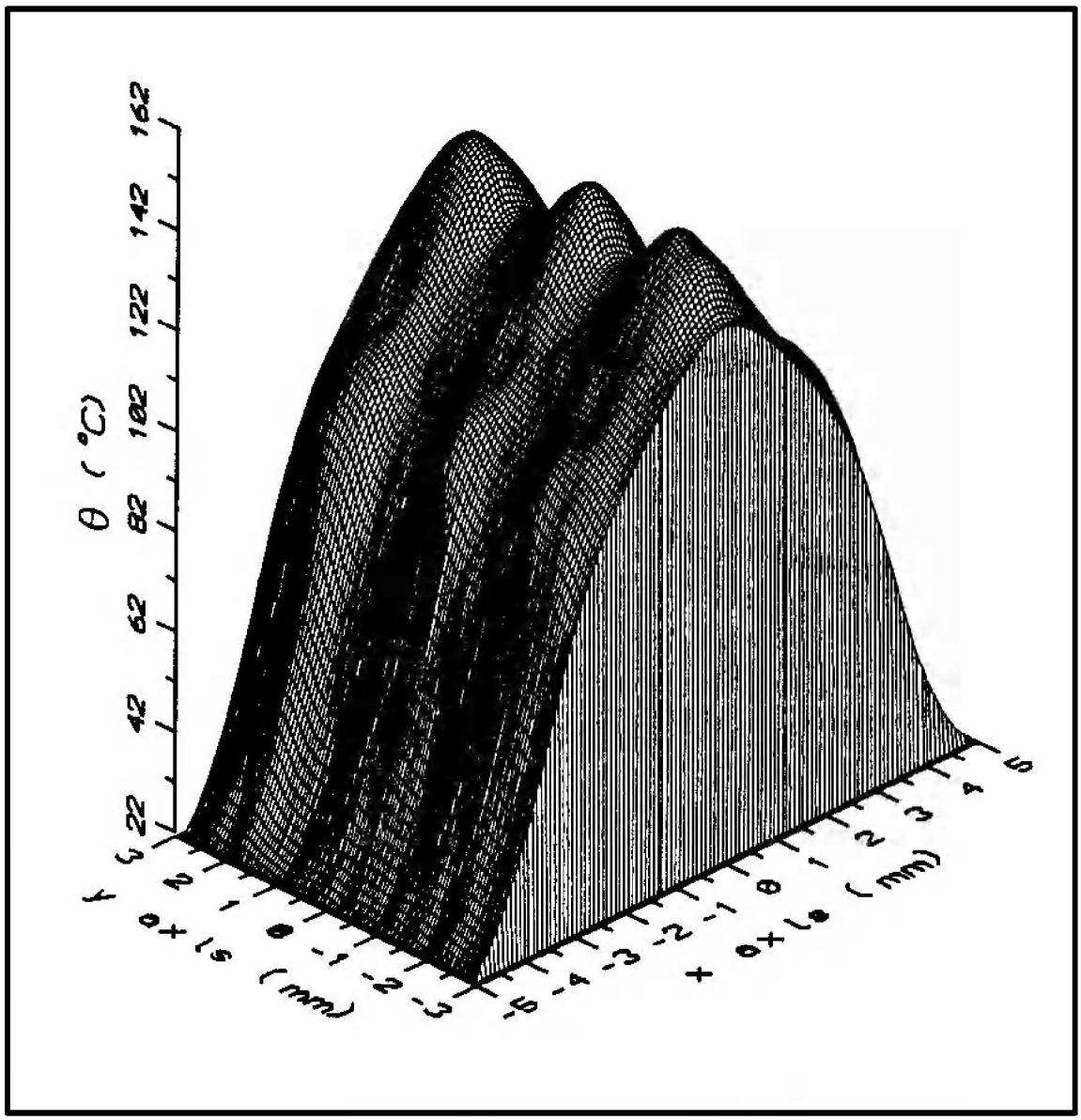

Figure 3-20b. Excess temperature profile at a position of z = 2.54 mm below the die for the averaged MS2 experiments.

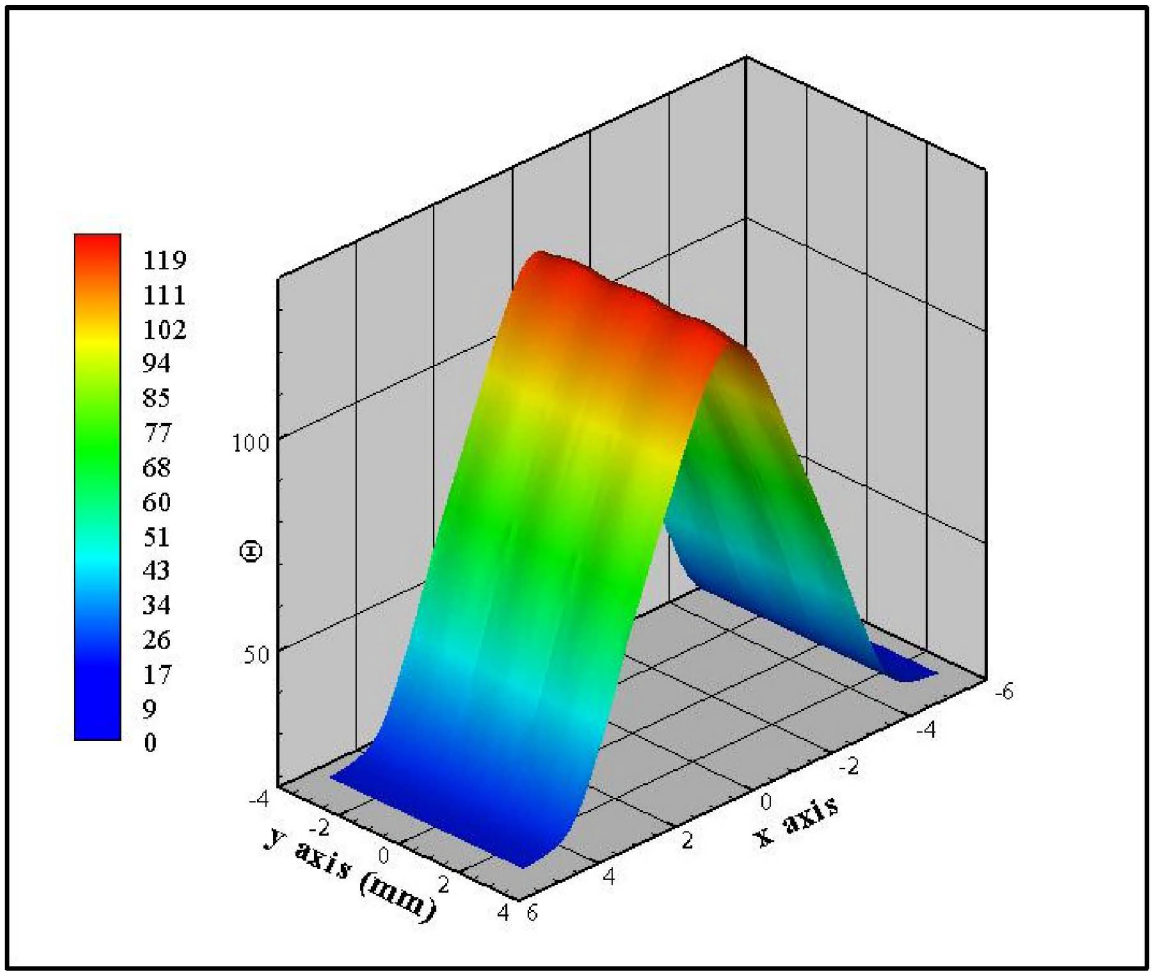

Figure 3-21a. Comparison of the temperature profiles at a position of z = 5.08 mm below the die for Case 4.

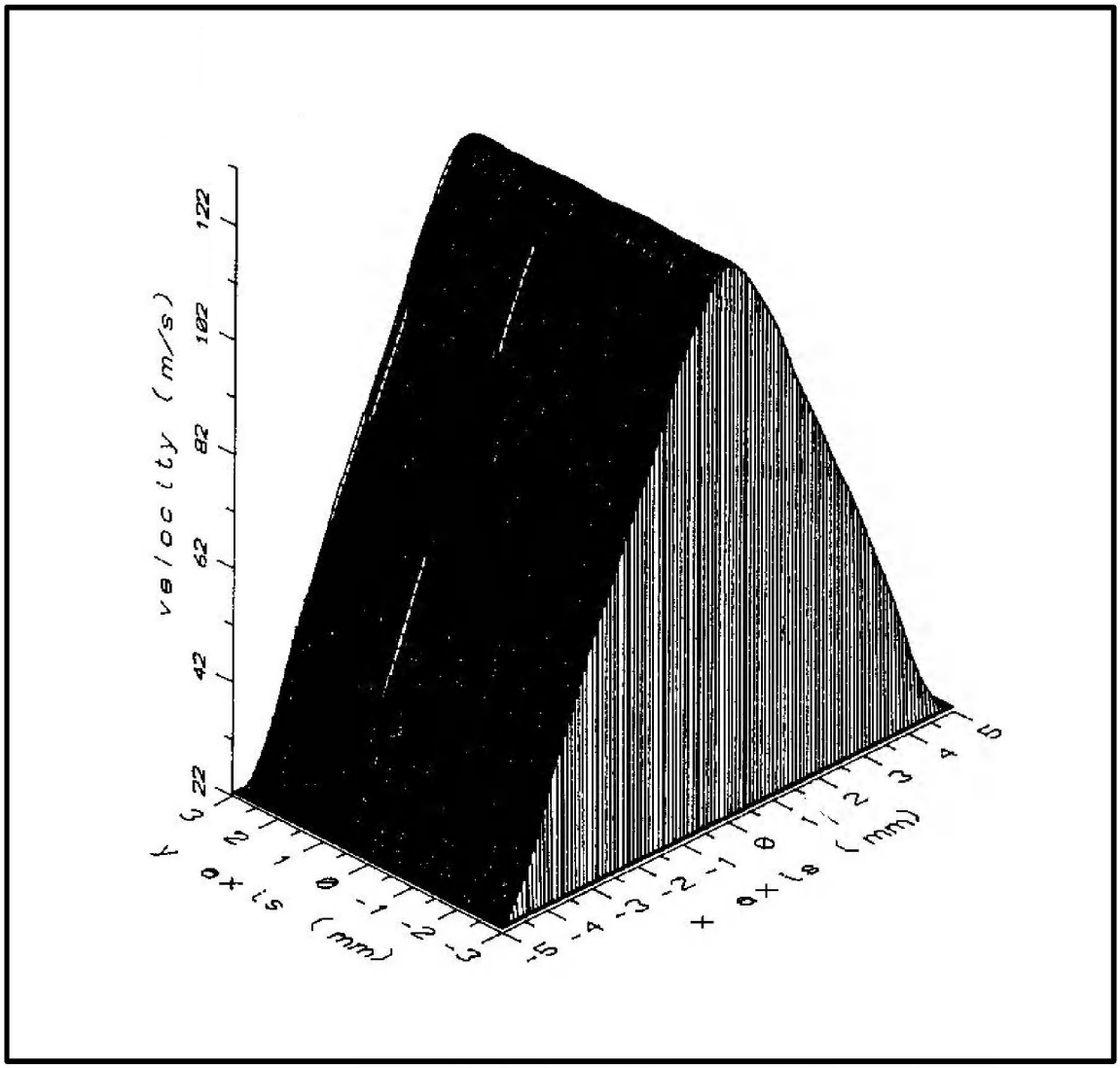

Figure 3-21b. Comparison of the temperature profiles at a position of z = 5.08 mm below the die for the averaged MS2 experiments.

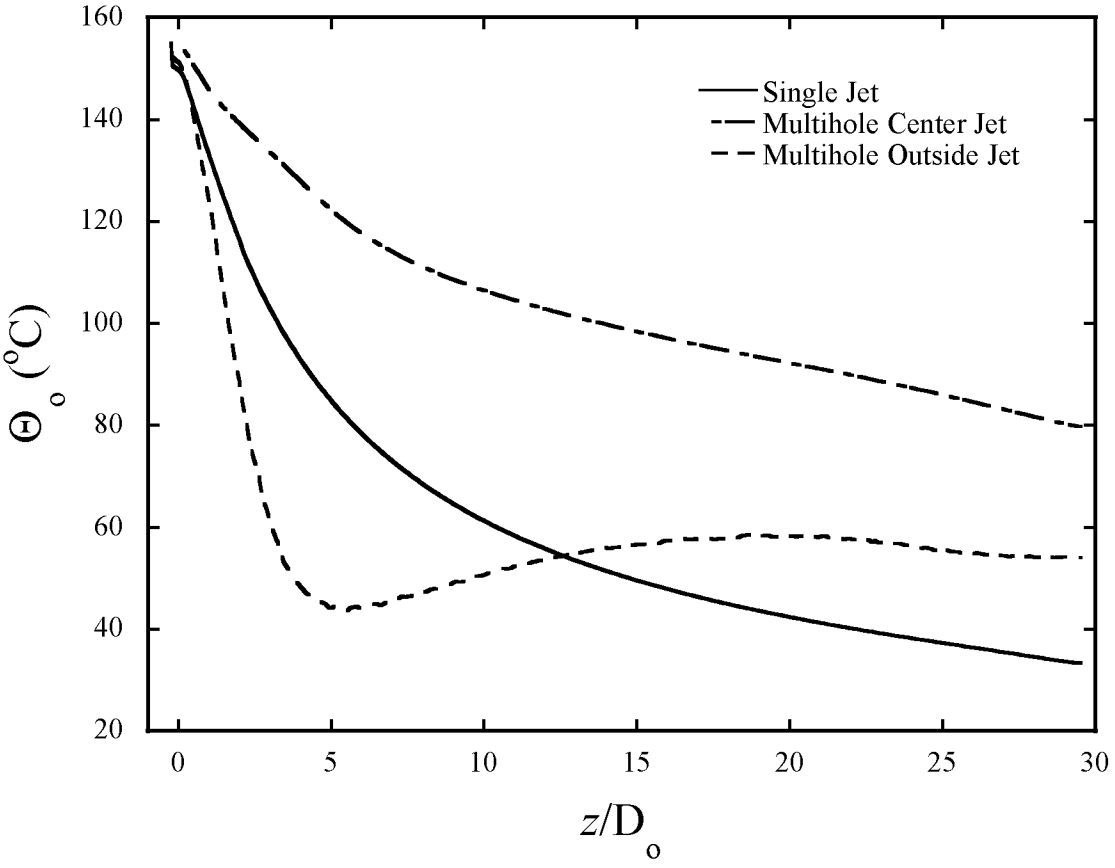

Figure 3-22. Comparison between the centerline temperature profiles for a single annular jet and the center and outside jet from Case 4.

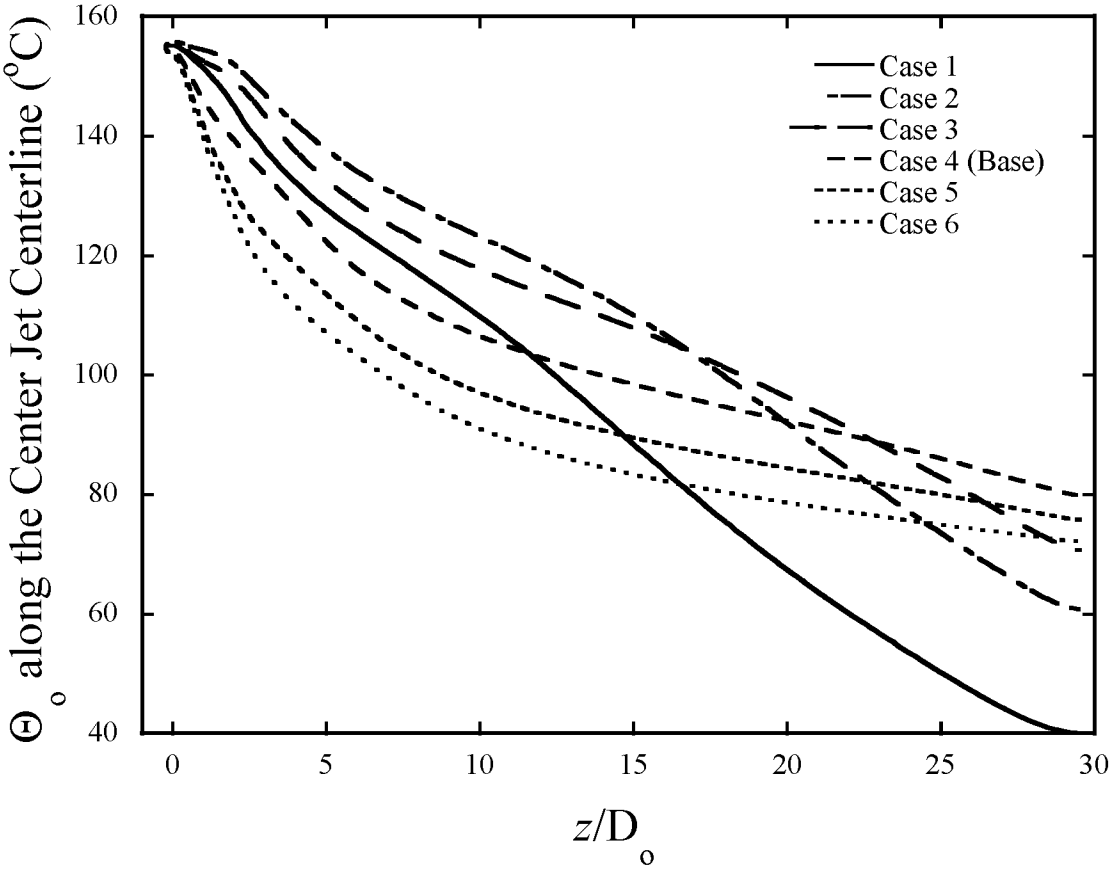

Figure 3-23a. Comparison of temperature profiles of all simulations at the centerline of the center jet.

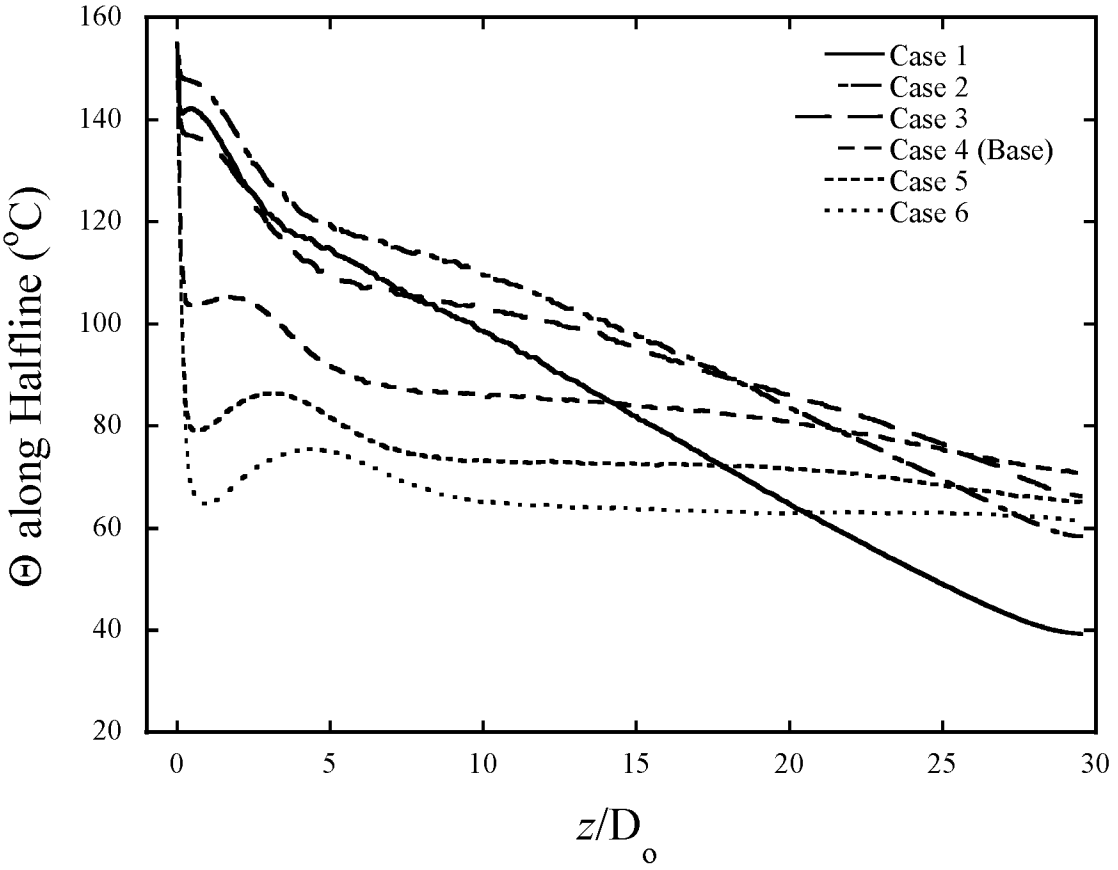

Figure 3-23b. Comparison of temperature profiles of all simulations at a line halfway between the center and outside jets.

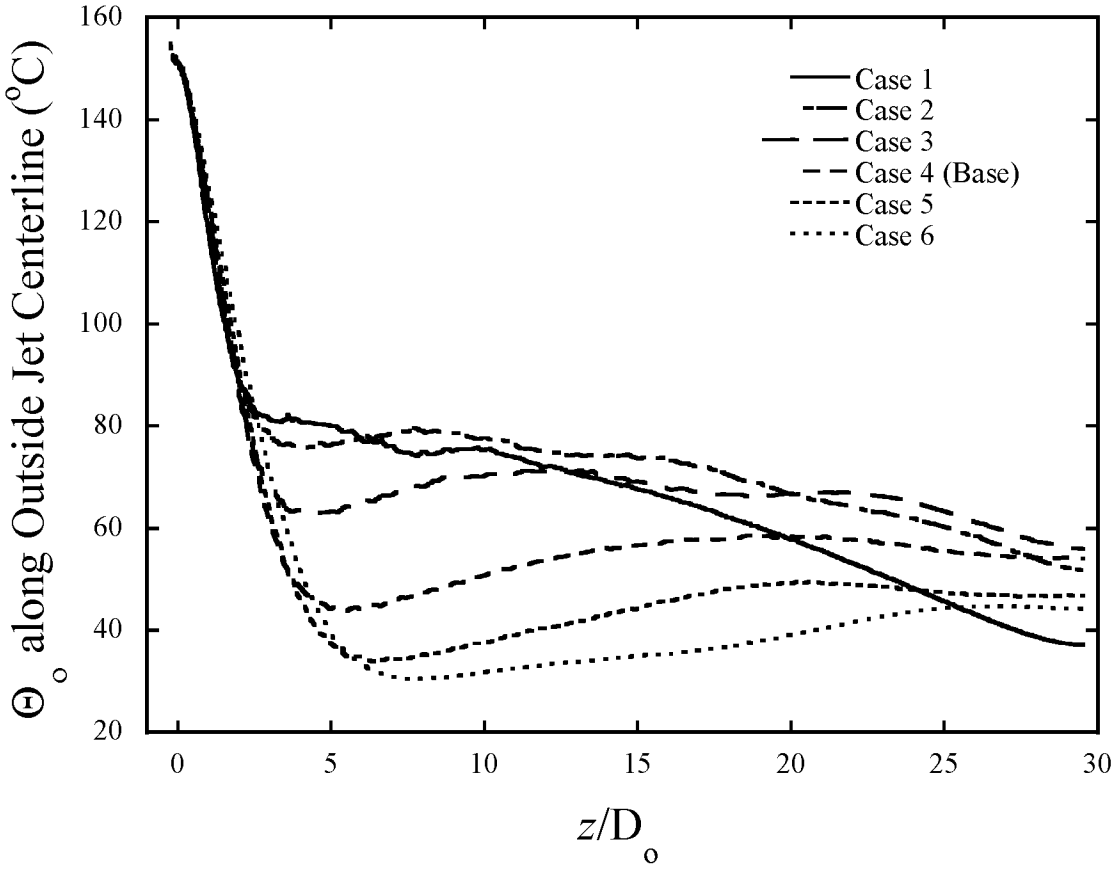

Figure 3-23c. Comparison of temperature profiles of all simulations at the centerline of the outside jet.

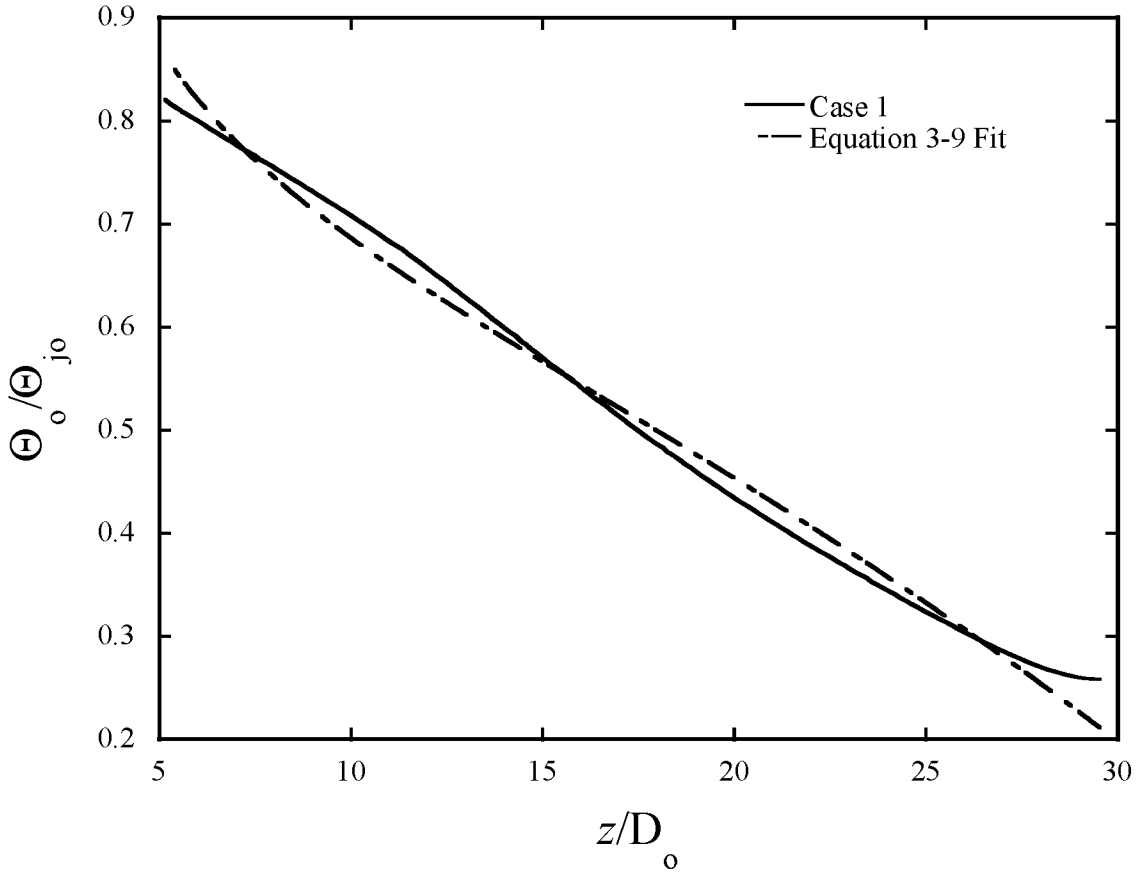

Figure 3-24a. Comparison of empirical predictive correlation to the simulation results of the temperature decay for Case 1. The correlation is given by equation 3-9 with the corresponding constants given in Table 3-4.

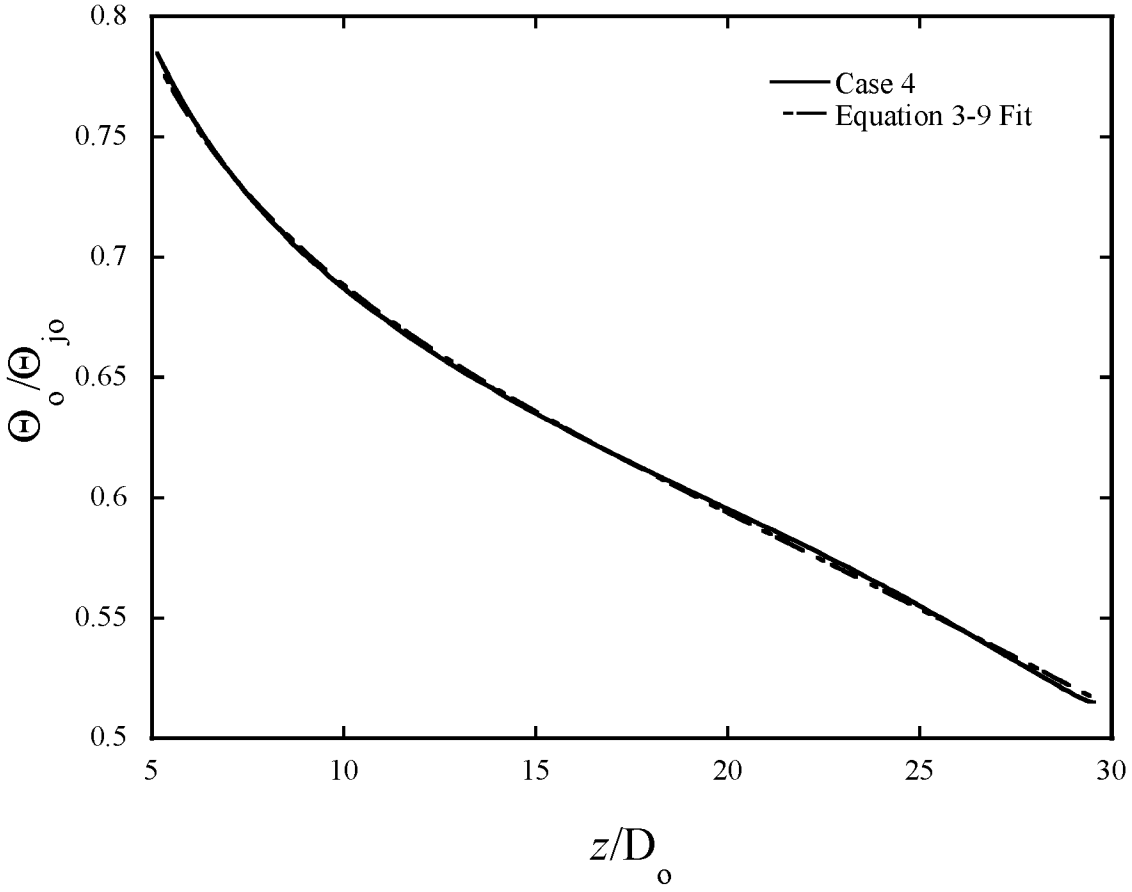

Figure 3-24b. Comparison of empirical predictive correlation to the simulation results of the temperature decay for Case 4. The correlation is given by equation 3-9 with the corresponding constants given in Table 3-4.

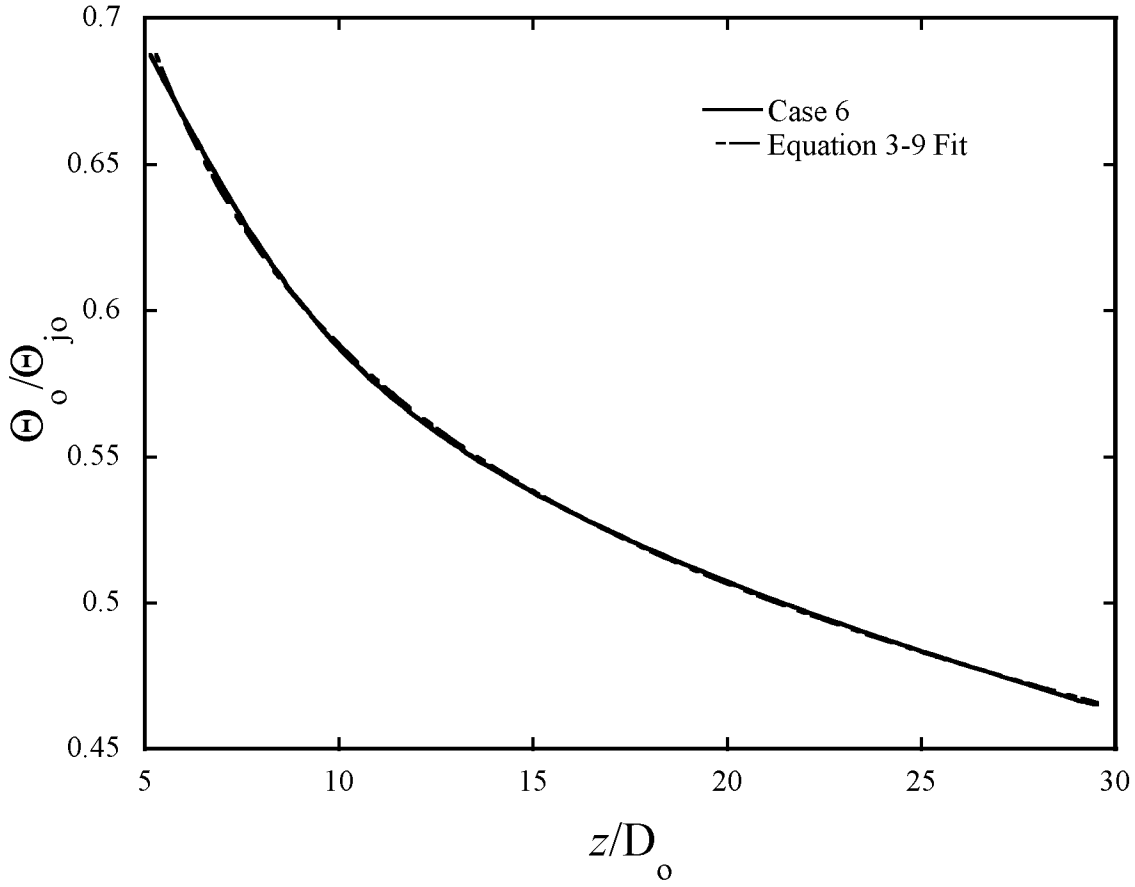

Figure 3-24c. Comparison of empirical predictive correlation to the simulation results of the temperature decay for Case 6. The correlation is given by equation 3-9 with the corresponding constants given in Table 3-4.

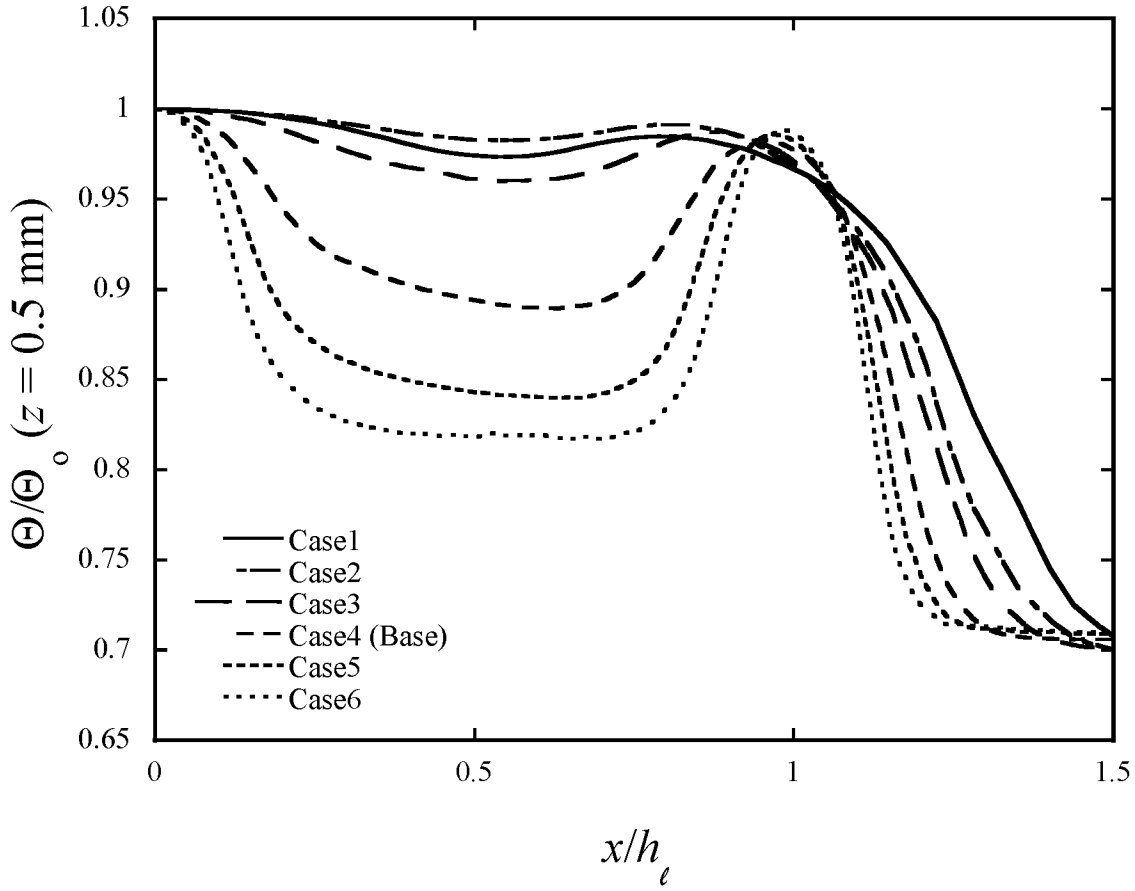

Figure 3-25a. Comparison of the temperature profiles of all simulations at z = 0.5 mm. These profiles are for the y = 0 plane.

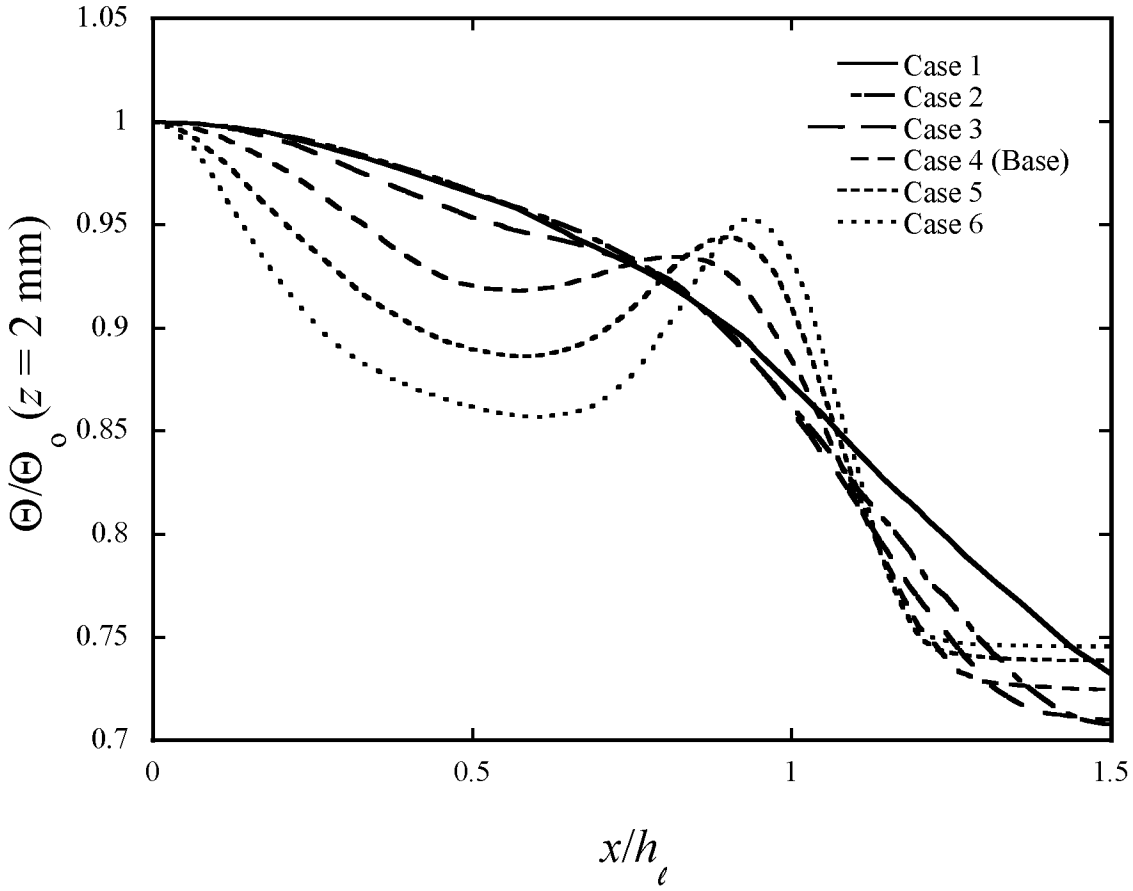

Figure 3-25b. Comparison of the temperature profiles of all simulations at z = 2 mm. These profiles are for the y = 0 plane.

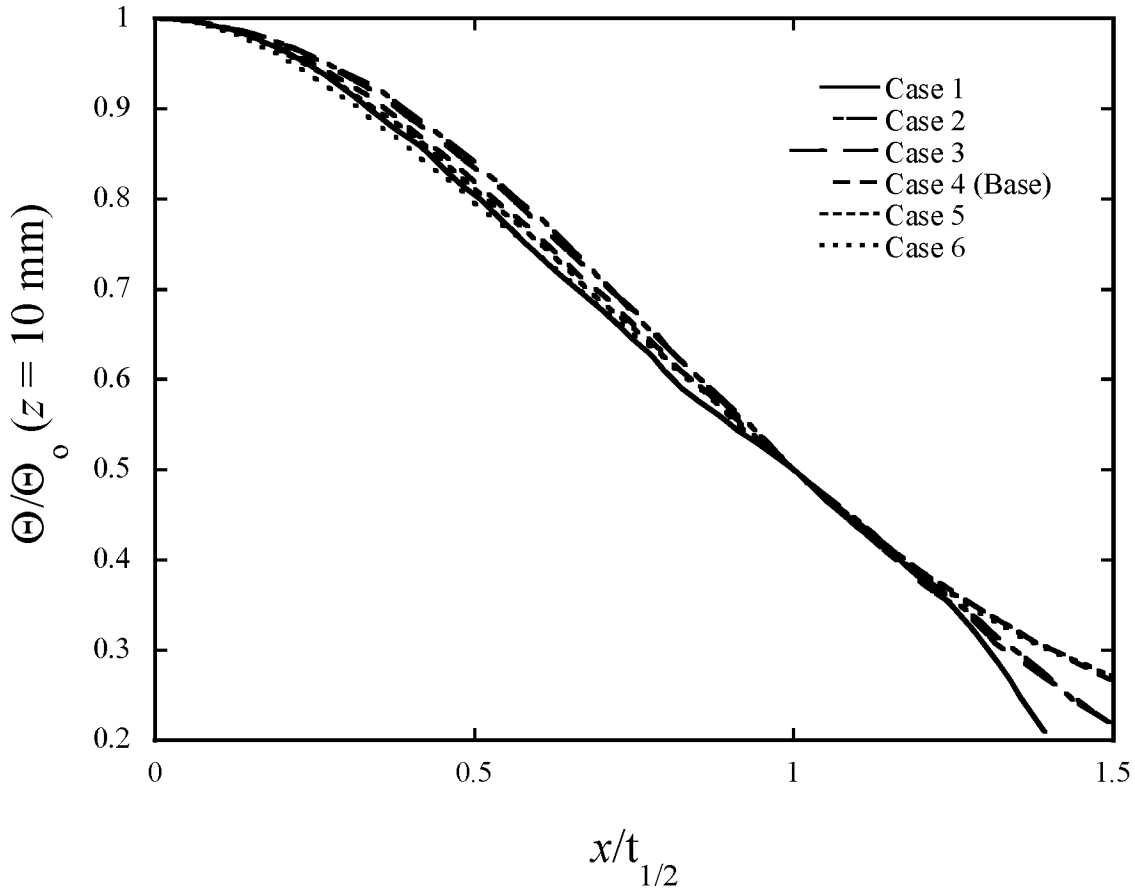

Figure 3-25c. Comparison of the temperature profiles of all simulations at z = 10 mm. These profiles are for the y = 0 plane.

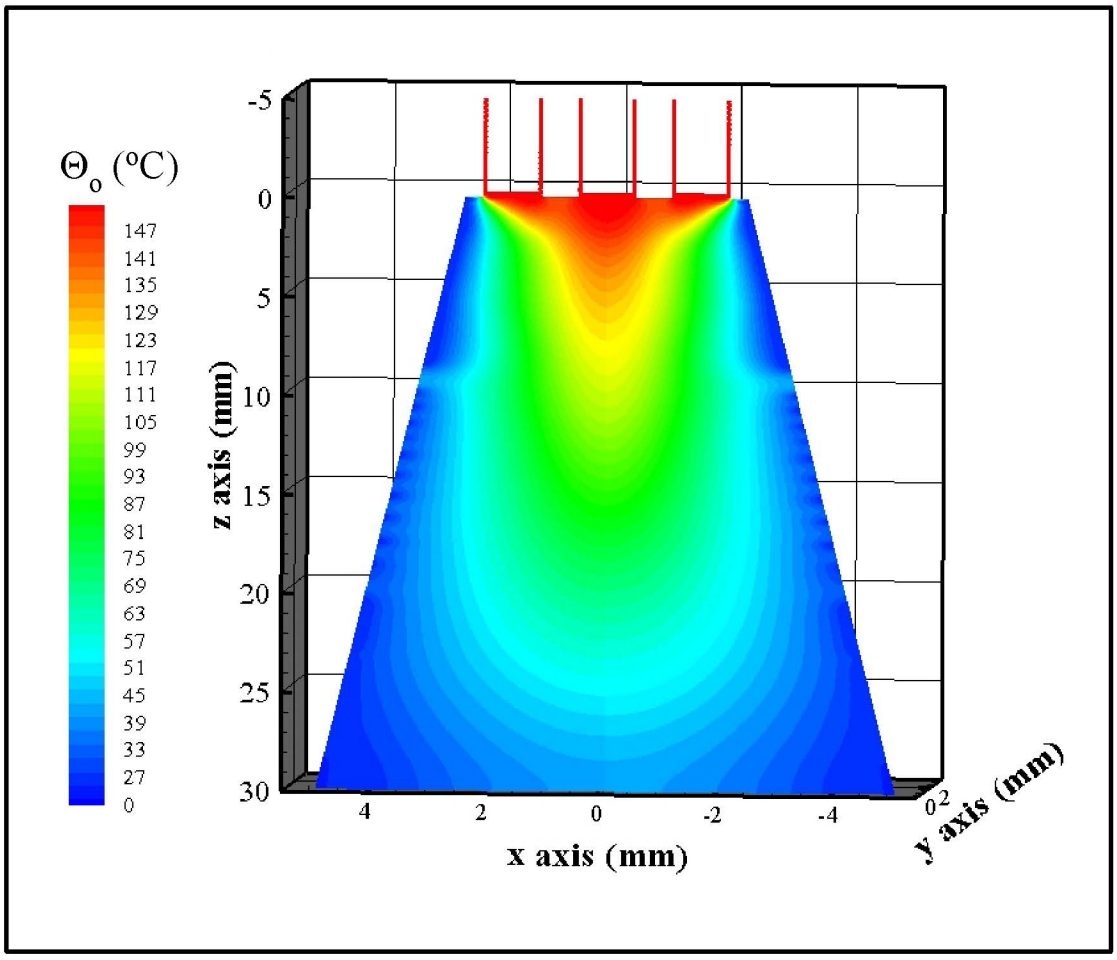

Figure 3-26a. Contour plot of excess temperature for Case 1. These contours are for the $y = 0$ plane.

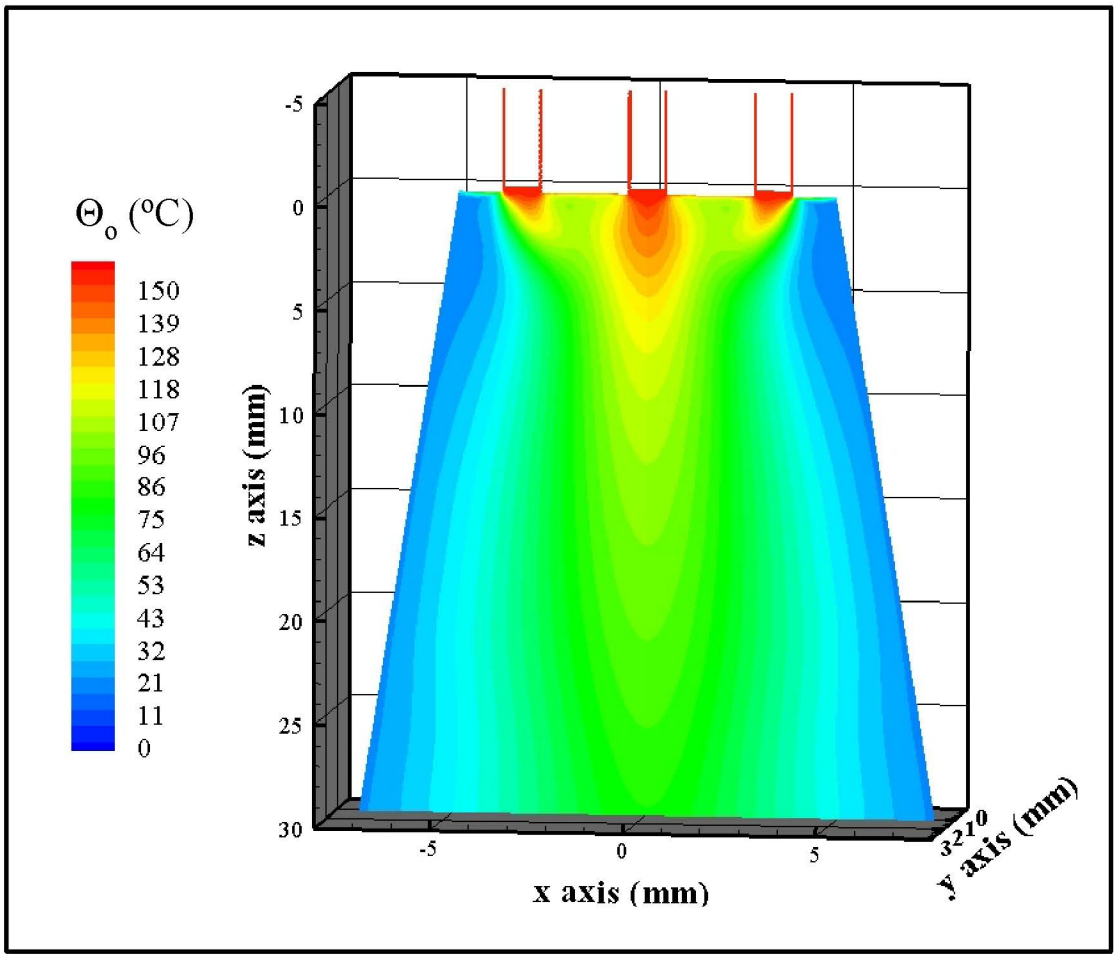

Figure 3-26b. Contour plot of excess temperature for Case 4. These contours are for the $y = 0$ plane.

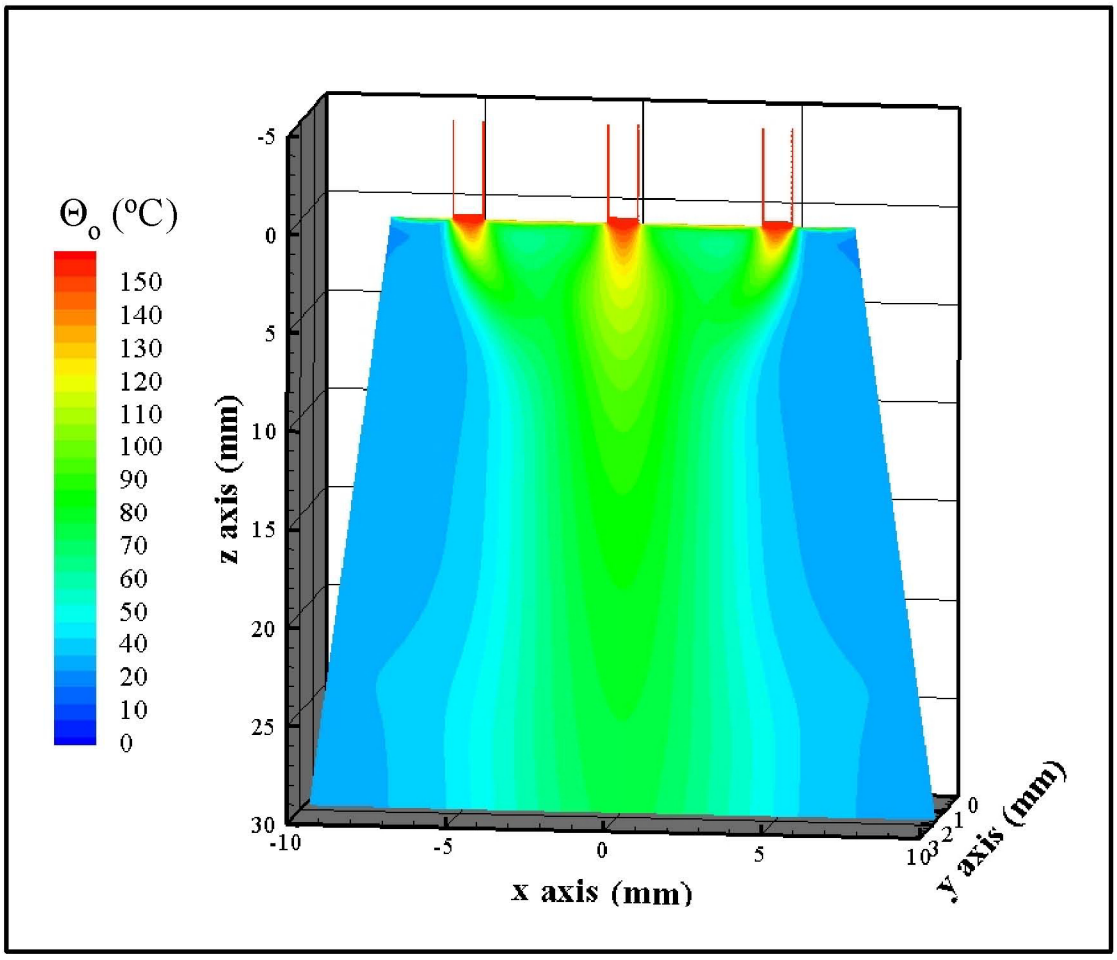

Figure 3-26c. Contour plot of excess temperature for Case 6. These contours are for the $y = 0$ plane.

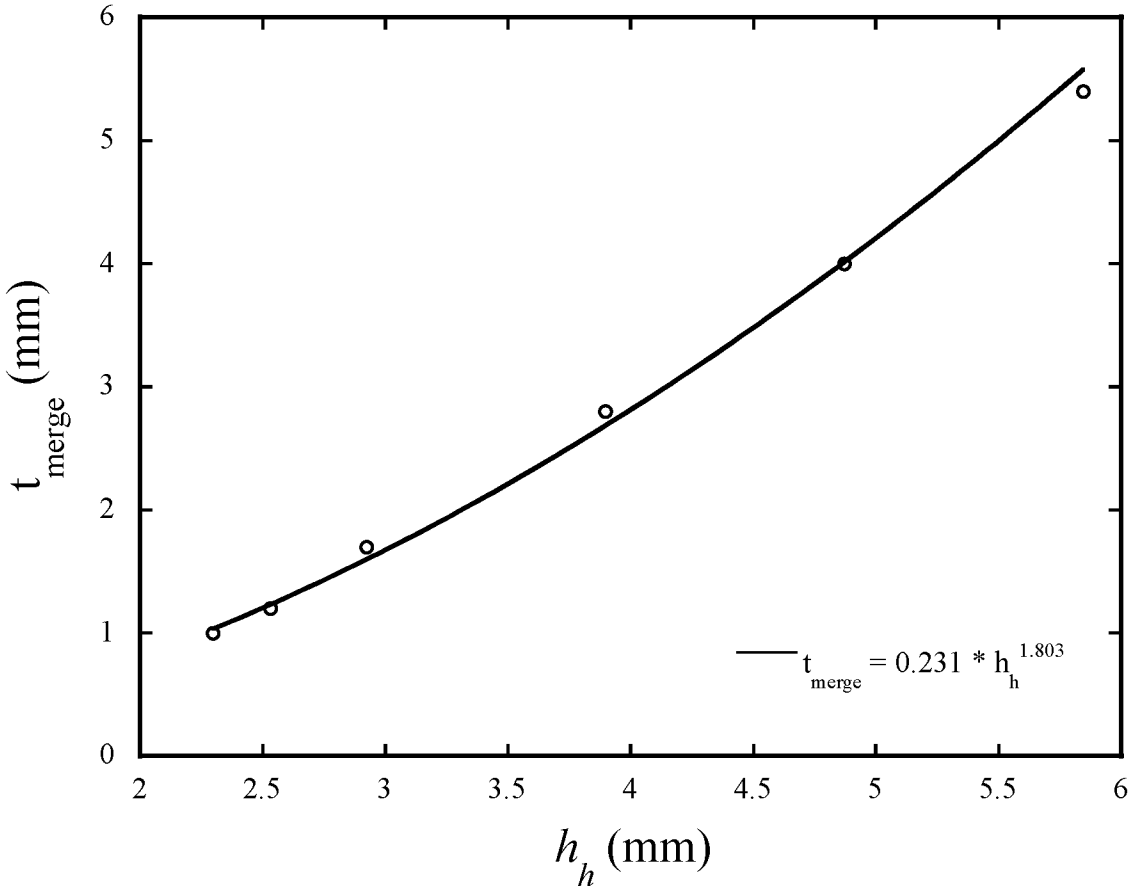

Figure 3-27. Position along the *z*-axis at which the temperature maximums of the two jets merge. The fit for these points is given by equation 3-10.

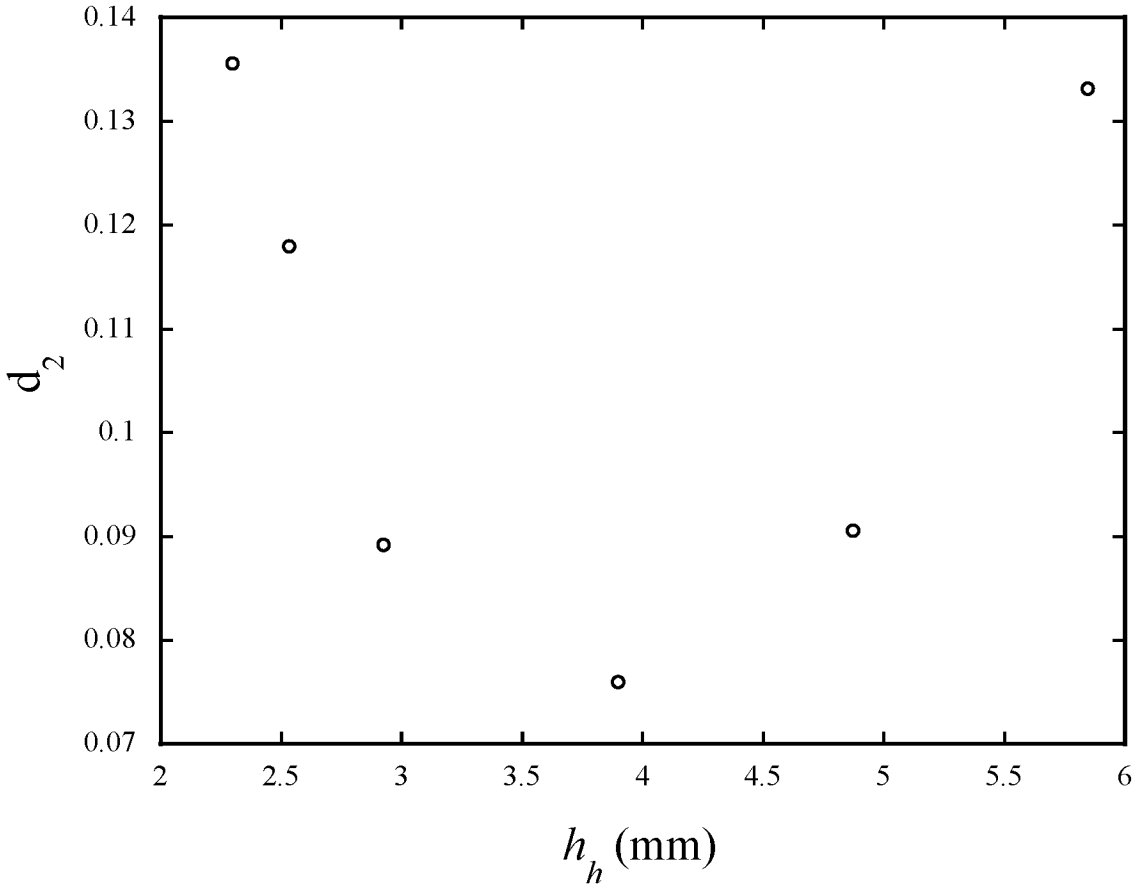

Figure 3-28. The temperature spreading rate of the jets versus h_h. The fit for these points is given by equation 3-11.

CHAPTER 4: SWIRL MELT BLOWING DIE

4.1 Introduction to Swirl Melt Blowing Dies

The swirl melt blowing die is a relatively new and innovative invention. In chapters 2 and 3, slot and multihole melt blowing dies were discussed. Their purpose is fast and efficient attenuation of molten polymer fibers (Shambaugh, 1988). However, the swirl melt blowing die was developed with a different goal. The swirl melt blowing die consists of six round air jets surrounding a polymer capillary; it is designed to cause a helical lay down pattern that is often desirable for the melt blowing of adhesives (Zieker et al., 1988). These adhesives are used in the production of disposable diapers, cardboard boxes, automobile upholstery, etc.

4.1.1 Literature Review

An in depth literature review of round jets can be found in section 3.1. Therefore, only the swirl die literature will be discussed. Because the swirl die is new compared to other melt blowing dies, the literature discussing it is much less extensive. Marla et al. (2006) used a swirl nozzle to create both solid and hollow fibers. They examined the effect of the air flow rate, polymer flow rate, and temperatures of both on the swirl frequency, fiber diameter and swirl lay down pattern (Marla et al., 2006). Like other melt blowing dies, the swirl die must be able to operate continuously during production (Allen and Fetcko, 1997). Marla et al. (2006) were concerned with the polymer side of the swirl die. Others, have researched the lay down pattern and the bond strength from a swirl die (Saidman, 2003; Saidman, 2002). To the knowledge of the author, the air flow field from the swirl melt blowing die has not been researched in depth.

4.1.2 Swirl Die Geometry

Figure 4-1a shows the cross sectional view of the swirl die that was used for on-line measurements in Marla et al. (2006) (also used in the experiments and simulations in this chapter). From the point of view in Figure 4-1a, the swirl die looks similar to a blunt slot die with an outset nose piece (see chapter 2). However, instead of rectangular jets, the air flows through six distinct round jets. The nose piece, which contains the polymer capillary, extends below the die face. Figure 4-1b is the bottom view of a swirl melt blowing die. The six round air jets surrounding a polymer capillary are visible. The air jets have an angle, α, with respect to the die face (similar to the slot dies in chapter 2), as well as a twist angle, ϕ. The twist angle is responsible for the angular velocity in the flow field. For the die geometry discussed in this chapter, $\alpha = 60^{o}$ and $\phi = 10^{o}$. The twist angle causes a component of the air velocity vector to be tangential to the adhesive. This tangential velocity, in the θ-direction, is the driving force for the desired helical lay down pattern. The air jets have a diameter of 0.46 mm, while the center-to-center distance between opposite air jets is 4.19 mm (Zieker et al., 1988). The polymer capillary also has a diameter of 0.46 mm. This is the area through which the adhesive is extruded. The polymer capillary is surrounded by a conical nose piece, which extends 1.84 mm below the die face ($z = 0$). At the tip of the nose piece, its diameter is 0.61 mm; at the die face it is 2.74 mm (Zieker et al., 1988).

Figure 4-2 is a photograph of a molten fiber from a swirl melt blowing die. This picture was taken using high speed photography by Marla et al. (2006). From this view, the swirling motion of the fiber can be observed. While Marla et al. (2006) measured the fiber characteristics of this melt blowing die, this chapter discusses the air side. Similar

to experimentalists who measured the isothermal air flow of slot (Harpham and Shambaugh, 1996), annular (Majumdar and Shambaugh, 1991), and multihole (Mohammed and Shambaugh, 1993) dies, the air without the presence of any polymer was measured. Then, these experiments were used to validate CFD simulations. In this chapter, both experimental measurements and CFD simulations of the isothermal air flow from a swirl melt blowing die are discussed.

4.2 Experimental Setup

The experimental setup is the same as that used by Moore (2004). A Pitot tube was used to measure the pressure of the air at different locations in the flow field. The inner diameter of the Pitot tube was 0.4 mm, while the outer diameter was 0.7 mm. The Pitot tube position was controlled using a traverse, which allowed movement in 3D. The scale on the traverse system readings was refined to take readings with 0.025 mm accuracy. The Pitot tube was connected to one of two Dwyer pressure gauges. One had a scale with a range of -0.5 in H_2O to 3 in H_2O, while the readings on the other ranged from -0.1 in H_2O to 7 in H_2O. Since the gauge with the smaller range had better refinement, the broad-range gauge was only used when the measured pressure was too high for the smaller range gauge. The flow rate of the air was kept steady at 5.9 slpm, and the air was not heated. This mass flow rate resulted in a jet z-velocity, V_{jo}, of 90 m/s.

The following equation was used to convert the measured pressure readings into air velocities (Moore, 2004; Uyttendaele and Shambaugh, 1989; Chue, 1975):

$$V = \sqrt{\frac{2\gamma}{\gamma - 1} \frac{P_o}{\frac{MW \cdot P_o}{R_{ig} \cdot (T + 273.15)}} \left[\left(\frac{P}{P_o} \right)^{\frac{\gamma - 1}{\gamma}} - 1 \right]} \tag{4-1}$$

The Pitot tube tip was aimed in the negative z-direction, which allowed for the z-component of the air velocity to be measured in the flow field. The z-velocity was measured on the centerline ($r = 0$). Since the nose piece of the swirl die extended below the die face, all measurements are for $z > 2$ mm. The diameter of the nose piece and the Pitot tube are of the same scale, which led to large errors in measurements taken close to the nose piece. Figure 4-4 shows the experimental results for the centerline z-velocity. Close to the die face, the centerline profile may have significant error. The error in measurements was partly due to the Pitot tube interfering with the flow. In addition, if a recirculation area was present (similar to the blunt slot die in chapter 2 and the annular jets in chapter 3), the Pitot tube is not capable of accurately measuring this flow (due to geometric limitations). The centerline velocity at positions close to $z = 1.84$ mm (the tip of the nose piece) was expected to be low because of the presence of the wall (which does not allow slip), but high velocities were measured. The observed minimum in the centerline velocity also was also measured by Moore (2004), who used an experimental setup very similar to the one used in this work. It is believed that the accuracy of the experimental measurements increase with increasing z-position. Another experimental method, such as hot wire anemometry, may offer improved experimental results.

4.3 CFD Simulations

The computational fluid dynamics software package used to complete all the simulations discussed in this chapter was Fluent^{TM} 6.2 (Fluent, 2007). The determination of the geometry of the computational domain, the generation of the computational grid, and the turbulence modeling are discussed in detail in the following sections.

4.3.1 Computational Domain

Figure 4-5a shows a side view of the computational domain. The domain extends 50 mm below the die face, which is at $z = 0$. The jet height is 3.3 mm. At the die face, the domain width is $r = 5$ mm. In order to capture the jet spreading, the domain widens with increasing z-position. At $z = 50$ mm, the domain is 20 mm wide in the r-direction. Since the swirl die contains six evenly spaced jets, it is necessary to include only one of these jets in the computational domain by using rotational periodicity as a boundary condition. The domain (without the jet) was created in an rz-plane (at $\theta = 0$). Then, this plane was rotated 60° in the θ-direction to create a volume and the jet was added. This represents 1/6 of the actual swirl die. Using periodic conditions on the two outside boundaries (the one at $\theta = 0^{\circ}$ is shown in Figure 4-5a) accounted for the effect of the other jets during simulations. Modeling only one jet greatly reduced the computational time. The bottom and side boundaries were pressure outlets. The jet boundary condition was a mass inlet, while the die face, including the nose piece and jet walls, were set as no-slip walls.

4.3.2 Grid for Swirl Dies

The computational domain shown in Figure 4-5a has a round air jet as well as a round nose piece. Therefore, close to these regions, it was not possible to generate a grid using only hexahedral cells. (Any attempt either failed or lead to highly skewed cells.) However, using tetrahedral cells throughout the computational domain would result in a much greater number of cells, as well as longer computational times. Therefore, the domain was divided up into three sections (designated by A, B, and C on Figure 4-4a). Section A included the air jet and the nose piece and the domain up to $r = 3$ mm and $z = 3$

mm. In section A, the cells were tetrahedral and had a cell size spacing of 0.1 mm. Sections B and C contained hexahedral cells with cell edge length of 0.25 mm and 0.40 mm, respectively. In total, this grid contained 559,430 cells. Figure 5-4b shows the grid at the die face. To ensure grid independence, several simulations were completed with different grid refinements. Figure 6 shows the centerline velocity for three cases with the following number of cells: 202,946, 559,430 (described above), and 1,155,852. The case with 202,946 does not match the other two cases, but the case with 559,430 and 1,155,852 agree well.

4.3.3 Turbulence Modeling

For other types of melt blowing dies, both the RSM and k-ε model have resulted in good agreement with experimental measurements (see chapters 2 and 3). For the multihole annular die, the RSM had difficulty converging, which was likely due to the tetrahedral cells that were also necessary in the swirl die simulations. Because the swirl die is different and more complex than the previously discussed geometries, it is of interest to study the effect of the turbulence model on the simulation results.

As expected, the RSM had difficulty converging. However, some of these simulations were able to converge. Table 1 lists all the models that achieved convergence for simulations of the air flow from the swirl melt blowing die. The results from the different turbulence models, as well as the different turbulence parameters $C_{\varepsilon 1}$ and $C_{\varepsilon 2}$ (see eq. 1-4), led to significant differences between simulation results. Since too many results were available to present in a single plot, Figure 4-7 shows only selected results. Clearly, the simulation results show significant variations from each other, both close to the die face, as well as in the far field. A higher value of $C_{\varepsilon 2}$ led to a more rapid

dissipation of turbulence, which led to a higher velocity decay; this trend was also observed in the slot die simulations. The RSM would not converge for $C_{\varepsilon 1}$ = 1.24 and $C_{\varepsilon 2}$ =2.05, but did converge for $C_{\varepsilon 1}$ = 1.34 and $C_{\varepsilon 2}$ =2.05.

4.3.4 Comparison to Experiments

In the previous chapters, experimental results were used to validate the simulations. Figure 4-8a compares the centerline velocity for the experiments and simulation results. Close to the die face, the centerline velocity maximum measured by the experiment was lower than all simulations. However, this is in the region where the Pitot tube was likely interfering with the flow field. Farther from the die face, the experimental results fell in between the centerline velocity predicted by the simulations. No simulation matched the experimental measurements well.

For the slot dies, z_{max} (the distance below the die face where the centerline velocity reaches a maximum) was determined to be an appropriate length scale. In addition V_{max}, the magnitude of the centerline velocity maximum, was used to nondimensionalize the velocity. Figure 4-8b shows the centerline velocity of the experiments and three simulations with different models and/or model parameters using z_{max} and V_{max} to nondimensionalize the z-position and z-velocity, respectively. Using these velocity and length scales, the k-ε model with $C_{\varepsilon 1}$ = 1.24 and $C_{\varepsilon 2}$ = 2.05 (used for the slot die simulations) was closest to experimental results. Because of the uncertainties in the experiments, another method of validating the turbulence model was necessary.

4.3.5 Comparison to Theory

Baron and Alexander (1951) proposed the following formula to predict axially directed momentum flux from a point source:

$$\frac{\rho V^2}{\rho_{jo} V_{jo}^{\ 2}} = \frac{A_o}{\pi C_m^{\ 2} z^2} e^{\left(\frac{r}{C_m z}\right)^2} \qquad (4\text{-}2)$$

This equation only accounts for a single point source; the total momentum flux was calculated by summing the contribution of all the individual jets. For the case of the swirl die, the right hand term should be multiplied by 6 (since there are 6 jets and they are all equidistant from the centerline). The empirical constant, C_m, was determined to be 0.075. For the multihole die, Mohammed and Shambaugh[15] found that $C_m = 0.2733$. It is expected that the value of the constant C_m for a multihole annular die would be different from that of a point source because the multihole die consists of 165 annular jets that eventually merge together. The interactions between the jets were significant (see chapter 3). In addition, in the far field the multihole die created a flow field that resembled that of a single rectangular jet more than that of a single annular or round jet. For the swirl melt blowing die, the interactions are also important. However, the six round jets are converging (see Figure 4-1a). Therefore, it is reasonable to expect that a merging point will exist in the flow field and that, after this merging point, the flow field will be similar to that of a single round jet, and equation 4-2 will be applicable.

Baron and Alexander (1951) developed equation 4-2 for a point source. There are six air jets in the swirl die. Therefore, when calculating the value of C_m for the swirl die, only the far field ($z \geq 30$ mm) was used. Table 4-2 lists the different values of C_m from Baron and Alexander (1951), experiments, and simulations. For the experimental results,

C_m was calculated to be 0.11, which differs from the empirical value for a round jet that was reported to be 0.075 (Baron and Alexander, 1951), by 32%. In the far field, the simulation completed using k-ε and $C_{\varepsilon 1}$ = 1.24 and $C_{\varepsilon 2}$ = 2.05 (the constants developed for the slot dies) resulted in centerline velocity that was closest to that of the experiments. Using this turbulence model and parameters resulted in a C_m value of 0.076, which is only 1.3% different from the Baron and Alexander (1951) value. Therefore, based on this analysis, the k-ε model with parameters $C_{\varepsilon 1}$ = 1.24 and $C_{\varepsilon 2}$ = 2.05 appears to be the most accurate model for simulating the flow field from a swirl melt blowing die.

4.3.6 Angular Velocity

The swirl melt blowing die is used to deposit an adhesive in a controlled pattern (Ziecker et al., 1988). Therefore, the angular velocity is of interest. Figure 4-9 shows the contours of the θ-velocity at positions of $\theta = 0^o$ (periodic boundary in simulations and half way between two jets) and $\theta = 30^o$ (immediately under the jet and halfway between periodic boundaries in the computational domain) at $z \geq 10$ mm. These contour plots show that the greatest angular velocity is in the jet, as well as the area close to the die face and nose piece. After this z-position, the θ-velocity is small. From these contours, it can be concluded that the helical motion of the fiber occurs due to the velocities close to the die face. It also appears that the two locations of $\theta = 0^o$ and 30° have different profiles of θ-velocity. If a larger or smaller helical pattern was desired, it would be of interest to study how the air jet geometry affects this θ-velocity.

4.4 Conclusions

Swirl melt blowing dies, which are designed to deposit adhesive in a helical pattern, have been studied both experimentally and computationally. The experiments were completed under isothermal conditions. The centerline *z*-velocity was measured. The Pitot tube interfered with the air flow close to the die face, which led to large error. In addition, the presence of a recirculation area may be present, which can not be measured using the Pitot tube. The CFD simulation results using a *k*-ε model with $C_{\varepsilon 1}$ = 1.24 and $C_{\varepsilon 2}$ =2.05 were similar to the experiments in the far field, but did not match them at $z < 40$ mm. Because the experimental results were questionable, the theoretical equation developed by Baron and Alexander (1951) was used to evaluate the accuracy of the simulation results. This equation was developed for a point source, and was found to accurately predict the decay of a round jet. It was proposed that in the far field this equation was applicable, because the flow from a swirl die became similar to that of a round jet. The values of an empirically derived constant for the Baron and Alexander (1951) experiment and the simulation result matched within 2%. Contour plots of the angular velocity supported the hypothesis that the flow in the far field was similar to that of a round jet because most of the angular velocity occurred close to the die face.

4.5 Nomenclature

A,B,C	labels for different grid refinement (Figure 4-4a)
C_p, C_v	heat capacity of air at constant pressure and volume, respectively
C_m	empirical constant for calculating momentum flux (eq. 4-2)
MW	molecular weight of air, g/mol
P	pressure measured by Pitot tube, in H_2O

P_o ambient pressure, in H_2O

R_{ig} ideal gas constant (8.3413 J/mol K)

T temperature, ^oC or ^oF

V air velocity in the z-direction

V_{max} maximum centerline velocity, m/s

V_θ air velocity in the θ-direction

r, z spatial coordinates

z_{max} distance from the die face of the maximum centerline velocity occurs, mm

Greek Characters

α die angle (Figure 4-1a)

ϕ twist angle (Figure 4-1b)

γ specific heat ratio, ($\gamma = C_p/C_v$)

θ spatial coordinate

4.6 References

Allen, M.; Fetcko, J. Method of Continuously Forming and Applying a Hot Melt Adhesive. U.S. Patent 5,605,720, **1997**.

Baron, T.; Alexander, L.G. Momentum, Mass, and Heat Transfer in Free Jets, *Chem. Eng. Prog.*, **1951**, *47*(4), 181.

Chue, S.H. Pressure Probes for Fluid Measurement. *Prog. Aerospace Sci.* **1975**, *16*(2), 147-223.

Fluent User's Guide; Fluent Inc.: Lebanon, NH, 2007.

Harpham, A.S.; Shambaugh, R.L Flow Field of Practical Dual Rectangular Jets. *Ind. Eng. Chem. Res.*, **1996**, *35*, 3776-3781.

Majumdar, B., Shambaugh, R. L. Velocity and Temperature Effects of Annular Jets. *Ind. Eng. Chem. Res.* **1991,** *28*, 5125-5138.

Marla, V.T.; Shambaugh, R.L.; Papavassiliou D.V. Using Swirl Dies to Spin Solid and Hollow Fibers, *Ind. Eng. Chem. Res.*, **2006**, 2331-2340.

Mohammed, A.; Shambaugh, R.L. Three-Dimensional Flow Field of a Rectangular Array of Practical Air Jets, *Ind. Eng. Chem. Res.*, **1993**, *32* (5), 976-980.

Moore, E.M. Experimental and Computational Analysis of the Aerodynamics of Melt Blowing Dies. PhD Thesis, University of Oklahoma, 2004.

Saidman, L. *Hitting the Target: Accurate Adhesive Application at Increasing Line Speeds*; Proceedings of International Nonwovens Technical Conference, Baltimore, MD, Sept. 15-18, 2003.

Saidman, L. Rules for Optimized Bonding: Advancements in Fiber Application Technology Minimize Waste and Refine Product Features. *Adhes. Age*, **2002**, *45*, 24-28.

Shambaugh, R. L. A Macroscopic View of the Melt Blowing Process for Producing Microfibers. *Ind. Eng. Chem. Res.* **1988**, *27*(12), 2363-2372.

Uyttendaele, M.A.; Shambaugh, R.L. The Flow Field of Annular Jets at Moderate Reynolds Numbers. *Ind. Eng. Chem. Res.*, **1989**, *28*(11), 1735-1740.

Ziecker, R.A.; Boger, B. J.; Lewis, D.N. Adhesive Spray Gun and Nozzle Attachment. U.S. Patent 4,785,996, **1988**.

Table 4-1: List of models and the modifications made to simulate the swirl die air flow.

Model	$C_{\varepsilon 1}$	$C_{\varepsilon 2}$	**Notes**
k-ε	1.44	1.92	
k-ε	1.24	2.05	Constants used for slot dies
k-ε RNG	1.42	1.68	Default for k-ε RNG
k-ε Realizable	N/A	1.9	Default for k-ε Realizable
RSM	1.24	2.05	Constants used for slot dies
RSM	1.44	1.92	Default
RSM	1.44	1.82	Constants used by Moore[10] for annular jet
RSM	1.44	2.05	
RSM	1.44	2.10	
RSM	1.54	1.92	
RSM	1.64	1.92	
RSM	1.54	2.05	

Table 4-2: Values of C_m

Source	C_m
Baron and Alexander (1951)	0.075
Experiments	0.11
Simulation (k-ε, $C_{\varepsilon 1}$ = 1.24, $C_{\varepsilon 2}$ = 2.05)	0.076

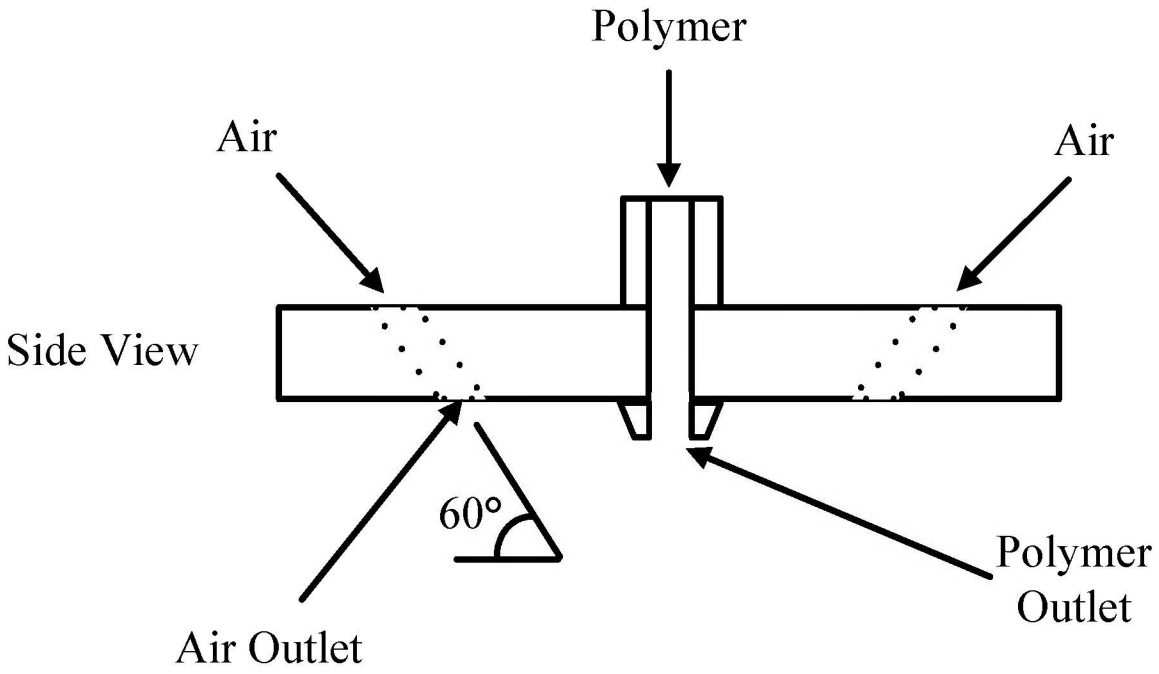

Figure 4-1a. Cross section of a swirl nozzle.

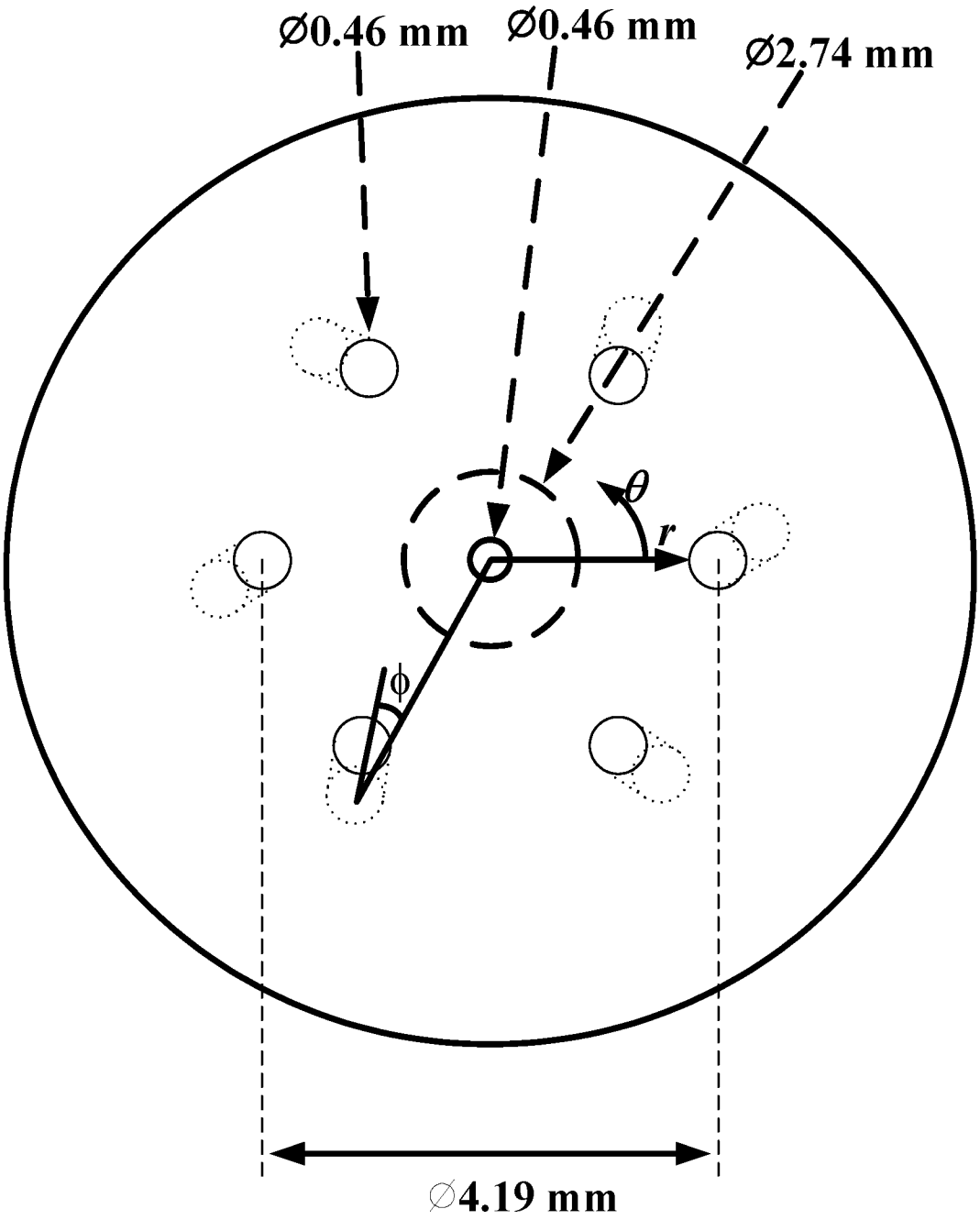

Figure 4-1b. Bottom view of a swirl melt blowing die.

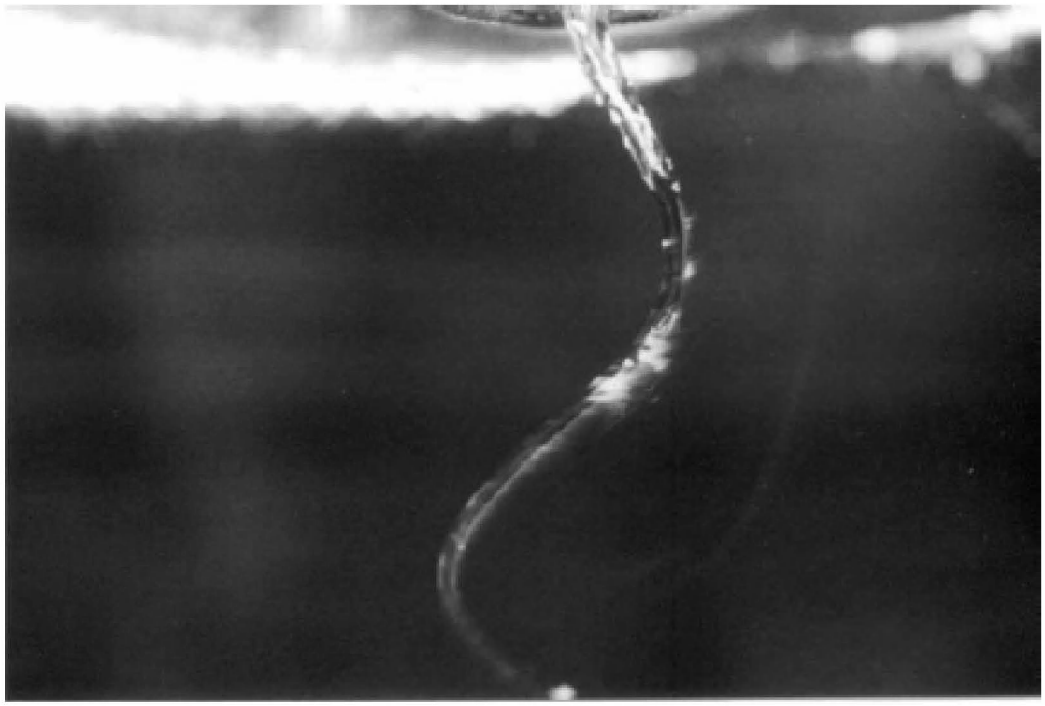

Figure 4-2. Molten polymer from a swirl die. This picture was taken by Marla et al. (2006) using high speed photography.

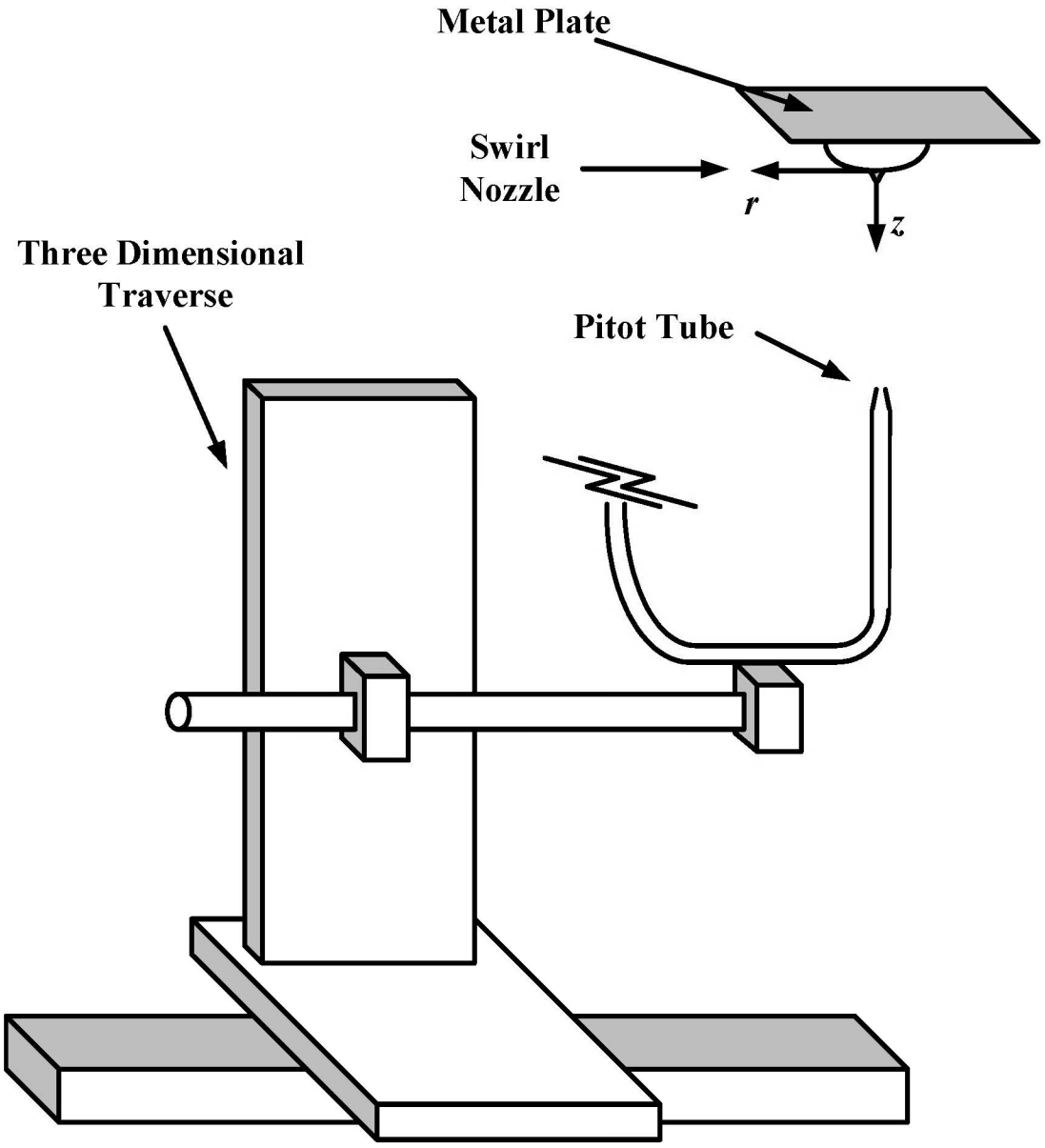

Figure 4-3. Experimental setup for measurement of air flow. Figure adapted from Moore.[10]

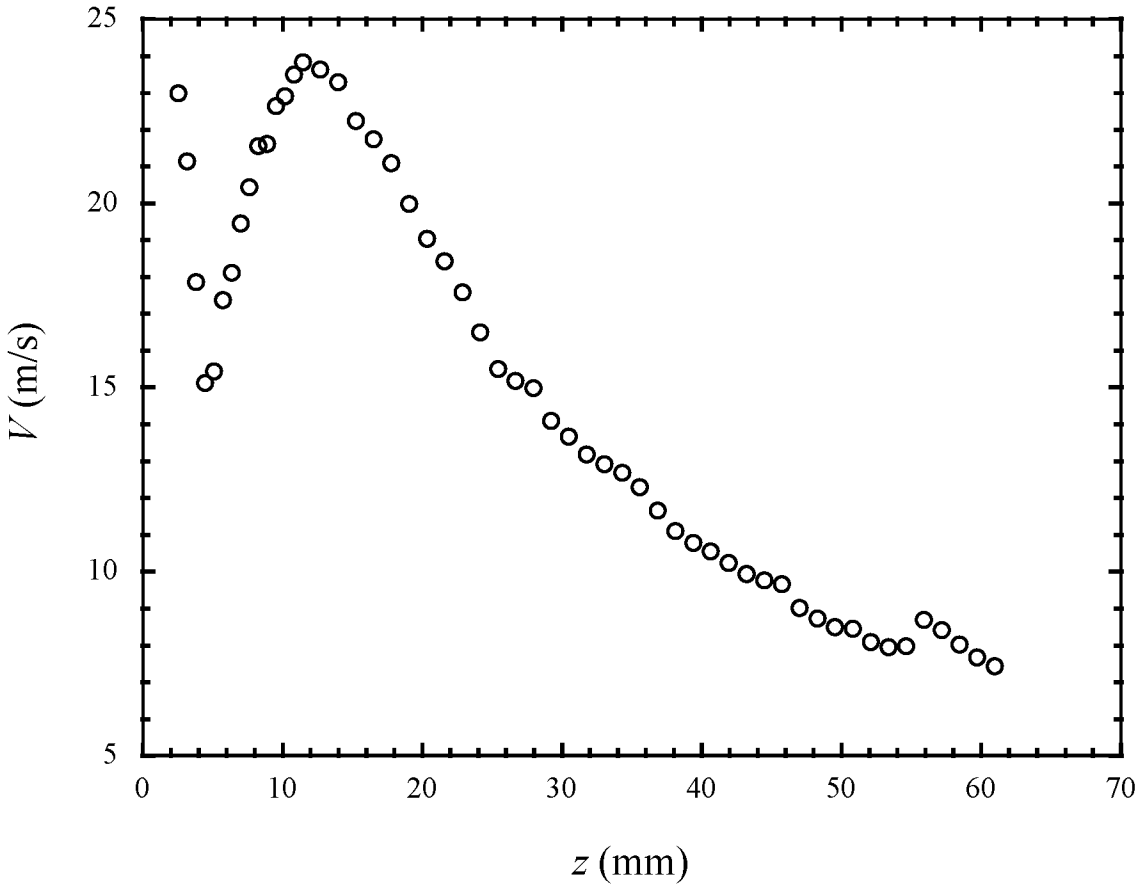

Figure 4-4. Experimental measurements of air-velocity on centerline.

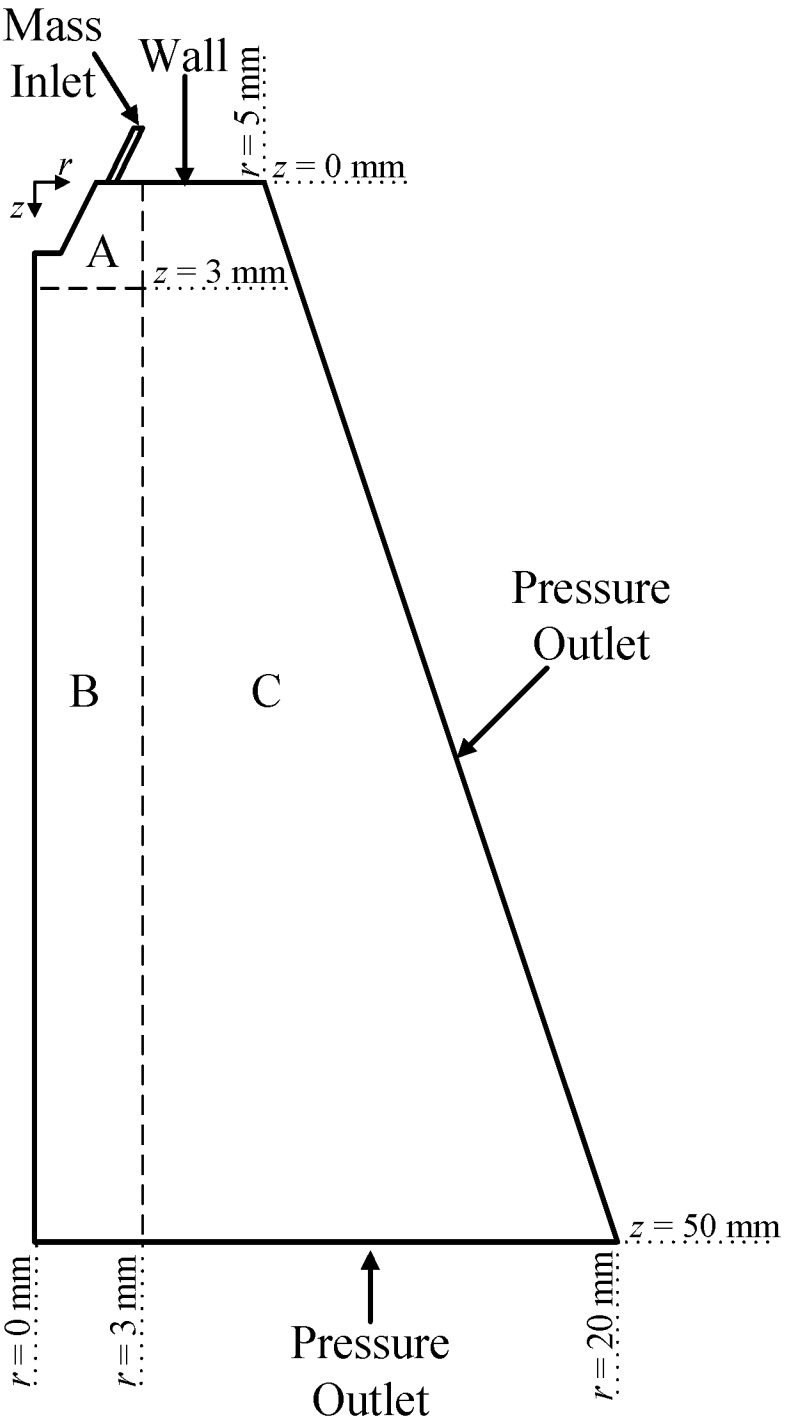

Figure 4-5a. The computational domain at $\theta = 0^{o}$. The letters A, B, and C designate the different areas of grid refinement.

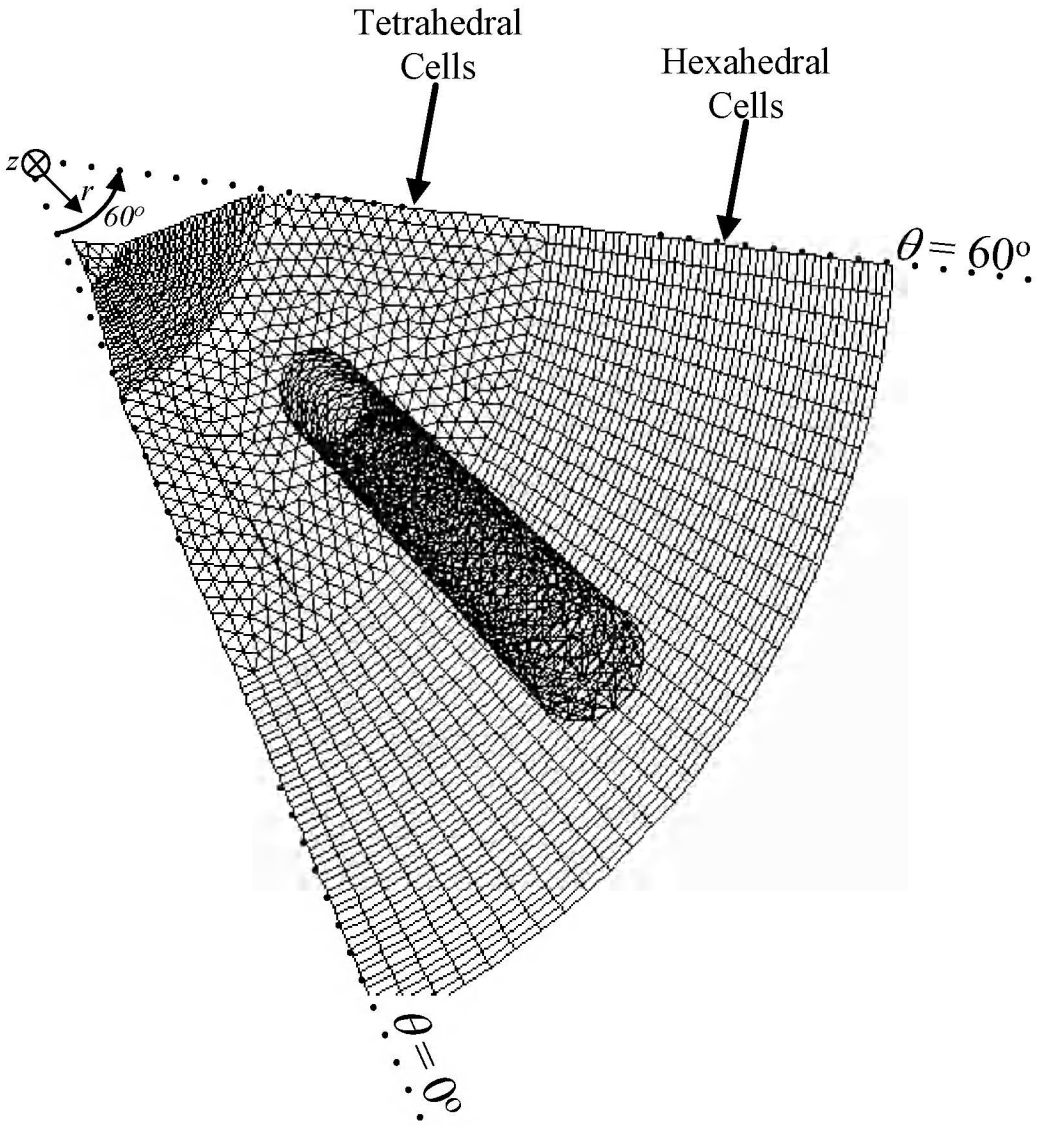

Figure 4-5b. Top view of the die face in the computational domain, both tetrahedral and hexahedral cells are used in this domain.

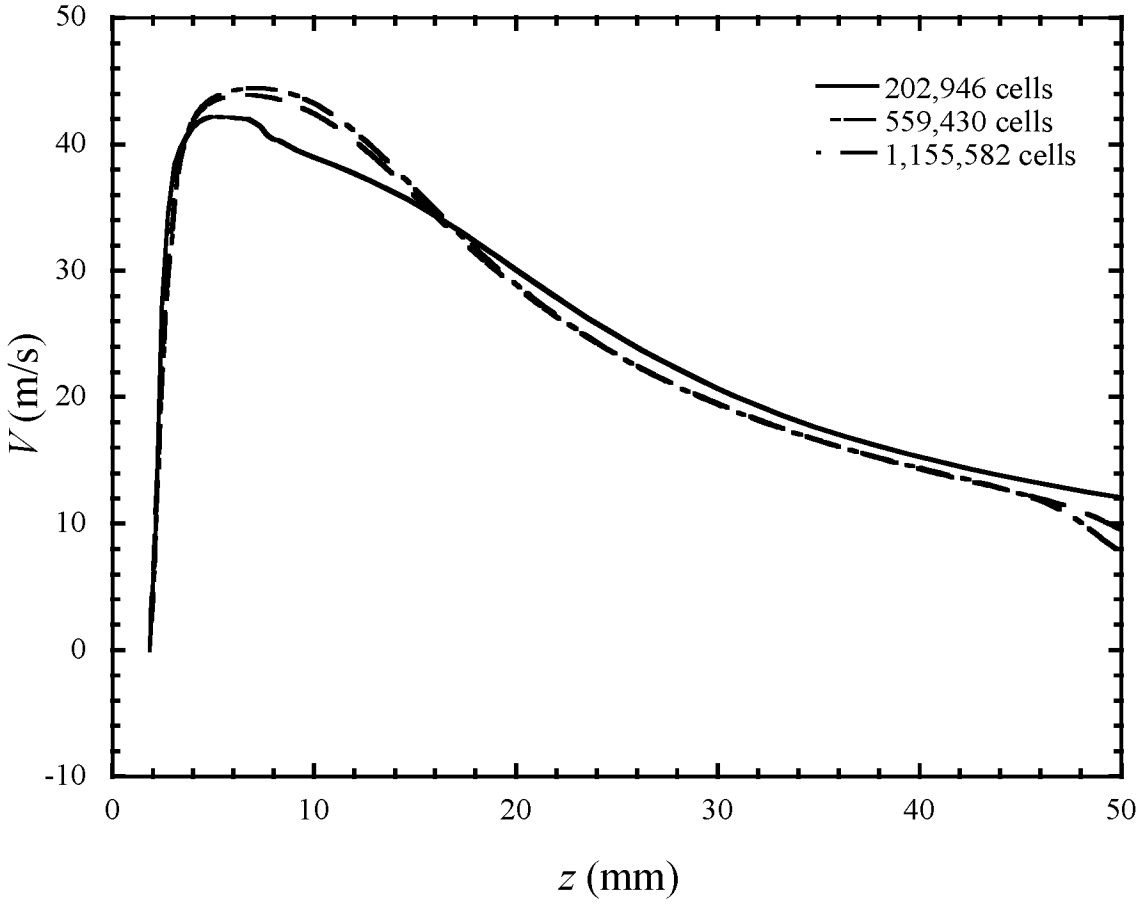

Figure 4-6. Comparison of centerline velocity for different grid refinements.

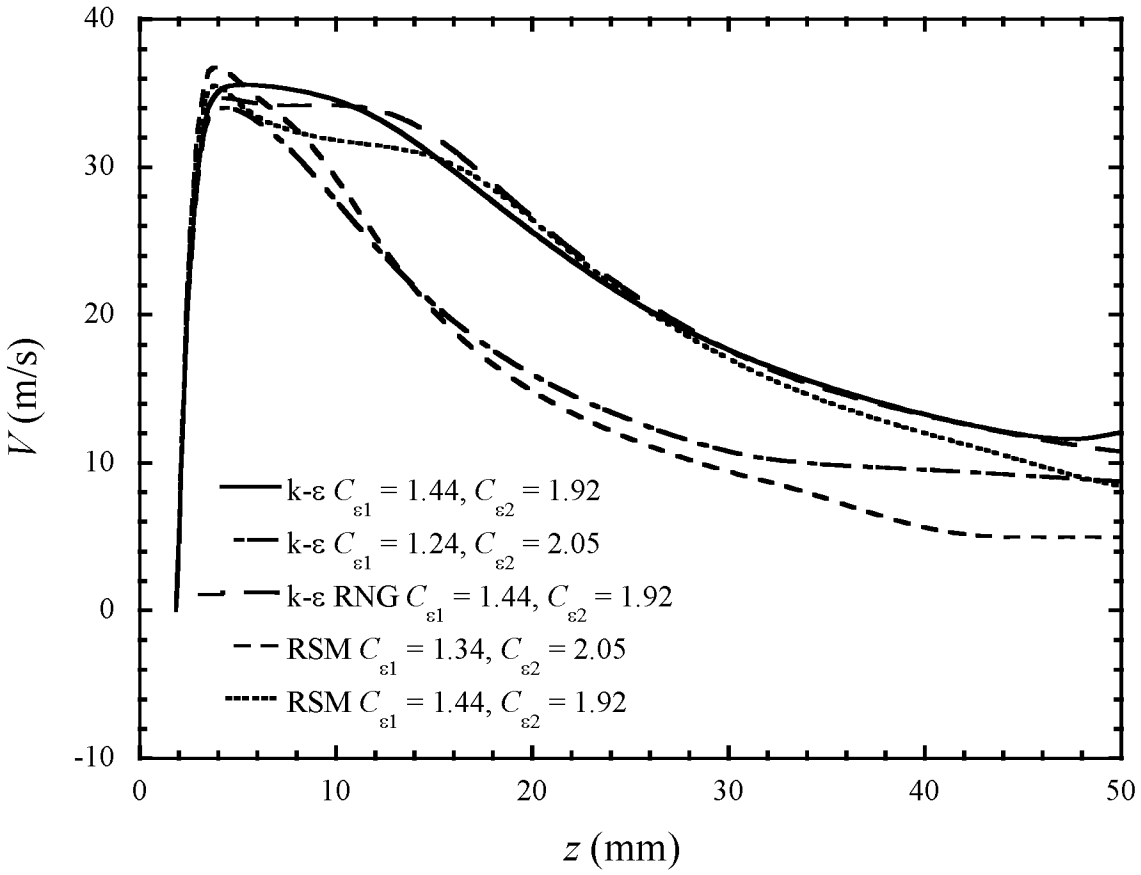

Figure 4-7. Comparison of the z-velocity on the centerline as predicted by different turbulence models. Table 4-1 contains the list of all models and modifications for simulations of the swirl melt blowing die.

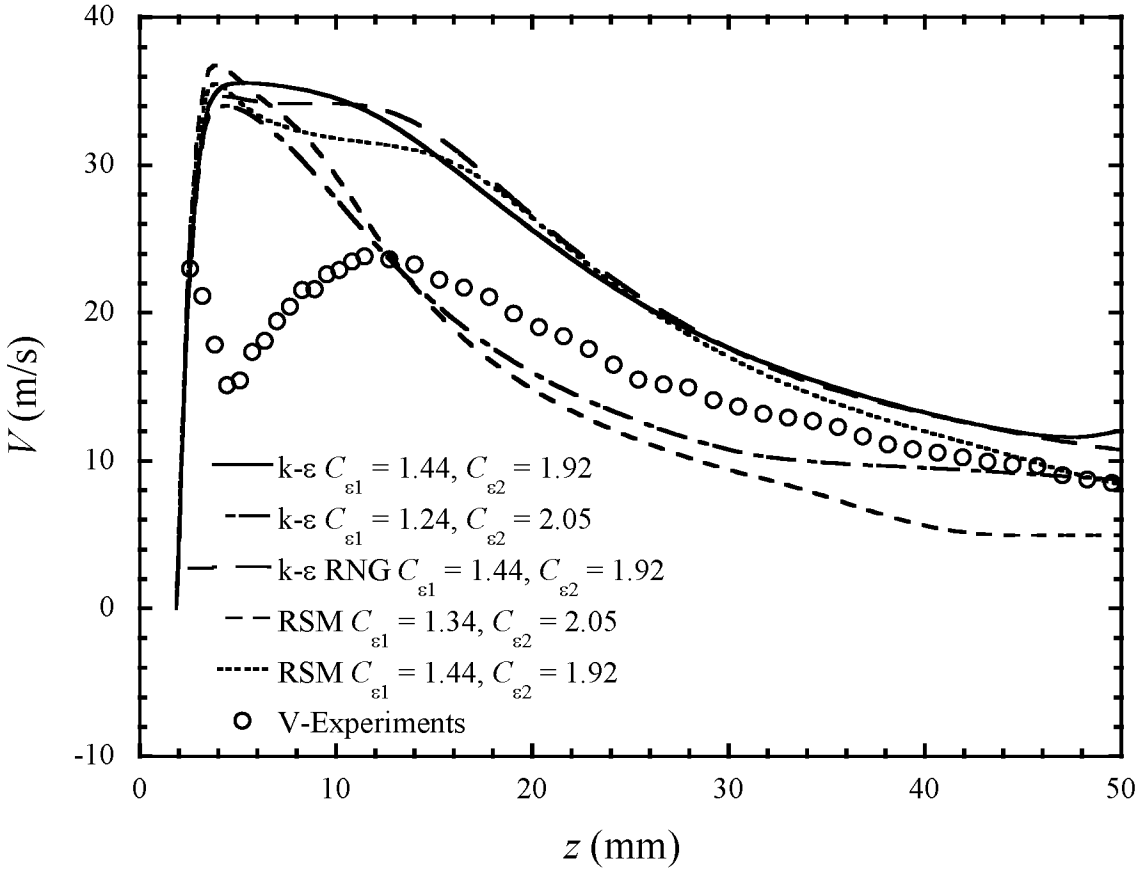

Figure 4-8a. Comparison of simulations with different turbulence models to experimental measurements.

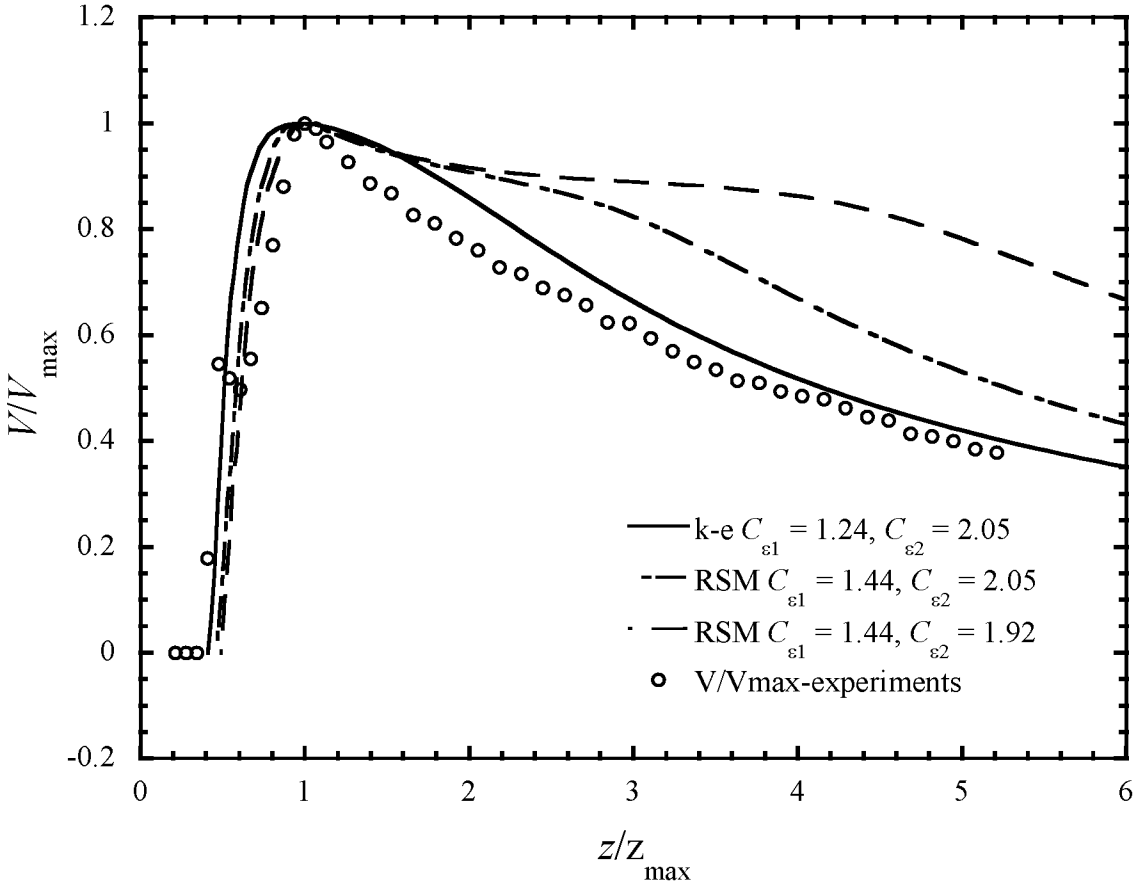

Figure 4-8b. Comparison of the centerline velocity from three simulations with different turbulence model and/or parameters and experimental results. V_{max} and z_{max} are used to non-dimensionalize velocity and z-position, respectively.

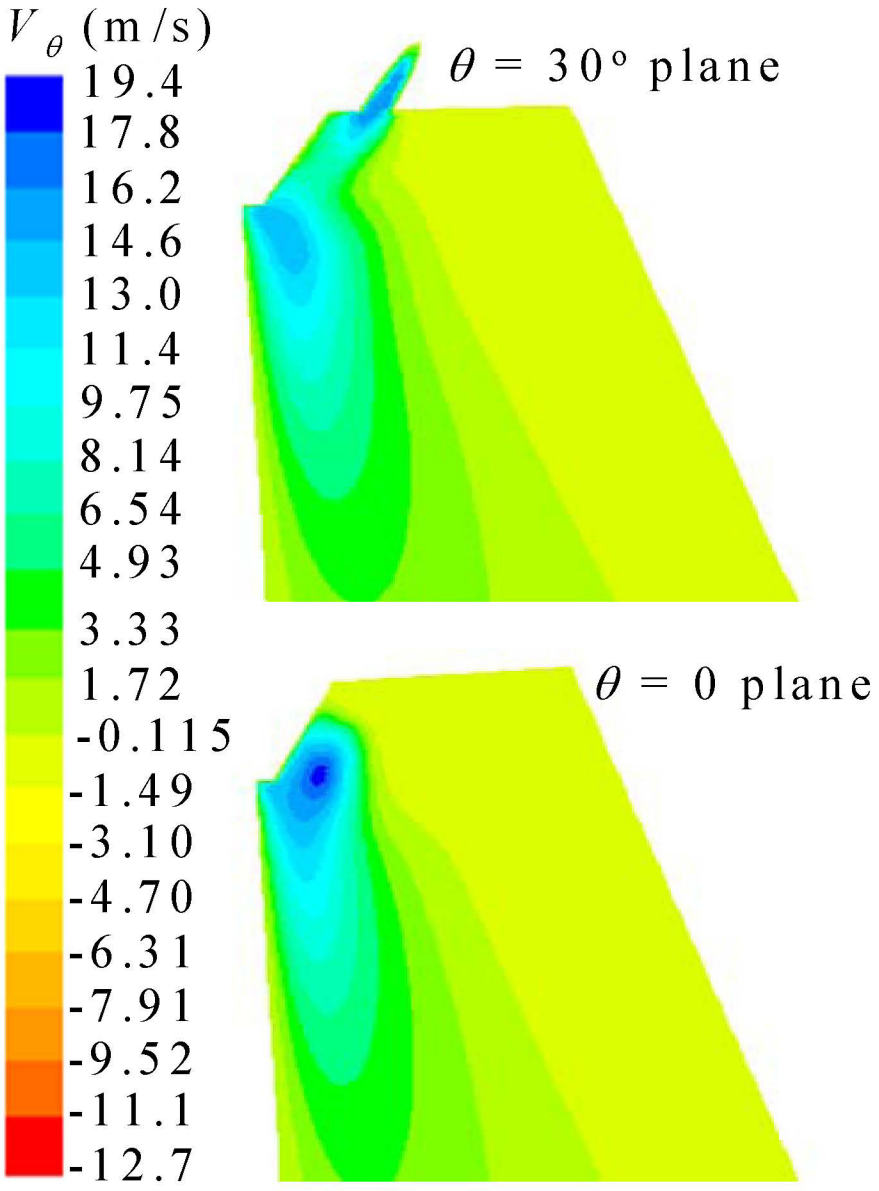

Figure 4-9. Contours of θ-velocity at $\theta = 30^{\circ}$ and at $\theta = 0^{\circ}$ (the periodic boundary). This figure is for $z \leq 10$ mm.

CHAPTER 5: EFFECT OF A FIBER ON AIR FLOW

Contents of this chapter have been reproduced from the following sources:

Krutka, H. M.; Shambaugh, R. L.; Papavassiliou, D. V. Effects of the Polymer Fiber on the Flow Field from an Annular Melt Blowing Die, *Ind. Eng. Chem. Res.*, **2007**, *46*(2), 655-666. Copyright Am. Chem. Soc. 2007.

5.1 Introduction

As stated in previous chapters, the experimental measurements of air flow from melt blowing dies were made without any polymer flow, due to the complications involved with testing the air flow and temperature field with a fiber present. However, CFD is well suited to examine the fiber-air interactions without the same restrictions. The goals of this work are to (a) examine how the air flow field changes with the inclusion of a fiber, (b) investigate how the flow field is affected by changing polymer or air flow rates, and (c) calculate the air drag force on the polymer fiber.

Fiber inclusive simulations have been completed for both a slot die (see Chapter 2 for complete description of a slot die) and an annular jet, similar to those used in Schwarz melt blowing dies (see Chapter 3 for description of a Schwarz die). Although the fiber vibrates during melt blowing, the CFD simulations discussed in this chapter had a fiber moving along the centerline without oscillations, representing the time averaged polymer. Both the slot die and the annular die simulations were conducted at non-isothermal conditions, using the ideal gas law to determine the air density.

5.1.1 Literature Review

Both slot ("Exxon") dies and multiple rows of annular jets are used commercially in the melt-blowing process to attenuate molten polymers (see Chapters 2 and 3).

Experimentally, it is difficult to study the air flow field while the polymer is present. Since the polymer sticks to any invasive device used to measure the air field, the use of pitot tubes and hot wire anemometers are ruled out. Noninvasive techniques – e.g., LDV (laser Doppler velocimetry) – can be used to give measurements of the polymer motion (Hietel, 2005). However, seeding is required to measure air motion with an LDV. Seeding problems include the creation/injection of the seeds, collision of the seeds with the fiber, agglomeration of the seeds with each other, and the separation of the LDV signals of the seeds from the signal of the fiber. Breesee et al. (2003) used high speed photography to take online measurements of the fiber velocity, but in order to measure the air flow rate, they stopped the polymer flow and measured the air without the presence of a fiber. Because of these experimental difficulties, CFD simulations are ideal to explore the flow field of slot and annular melt blowing dies with inclusion of polymer fibers.

For the air-side of a melt blowing slot die, previous work has shown that CFD can be used to successfully reproduce experimental measurements of the air flow (see previous chapters). Moore et al. (2004) used CFD to simulate a single annular jet with air only and found good agreement with experiments. Much research has also been completed in order to more fully understand the fiber side of melt blowing. For instance, several researchers have used both experiments and theoretical analysis to determine a method of predicting the stress on the fiber due to the air. Matsui (1976) proposed the following relationship:

$$C_f = \beta^* Re_{DP}^{-n} \tag{5-1}$$

The Reynolds number in equation 5-1 is defined as follows:

$$Re_{DP} = \rho_a v_{a,eff,PAR} d_f / \mu_a \quad (5\text{-}2)$$

To calculate this drag force, the air and polymer velocities are examined separately (either computationally or experimentally). The Reynolds number defined in equation 5-2 is based on $V_{a,eff,PAR}$, which is the difference between the air and the fiber velocities in the stream wise direction. Re_{DP} is used to find C_f in equation 5-1, and then this C_f is used to find F_{PAR}, which is the force due to air drag. An implicit assumption in these calculations is that the air flow is the same whether the polymer is present or not. At low spinning speeds (300 - 1,000 m/min) flow rates, β = 0.37, while at higher flow rates (1,000 – 6,000 m/min), β = 0.78 instead of 0.37 (Matsui, 1976). However, n was experimentally determined to be 0.61 for both high and low spinning speeds. Majumdar and Shambaugh (1990) used filaments of different lengths and diameters and found that their drag coefficient matched the Matsui correlation with β = 0.78 and n = 0.61. Miller (2004) numerically solved the equations relating to the aerodynamic drag for melt spinning. Since the fiber in melt blowing is oscillating, Ju and Shambaugh (1994) measured the air drag on filaments oblique to the angle of the air flow.

Different models have been used to simulate the fiber properties and movement during the melt blowing process. For a blunt slot melt blowing die (see Chapter 2) Wang et al. (2005) used a model of spheres and weightless springs to simulate the movement of a fiber during melt blowing. The interactions between air and a fiber have been examined for melt spinning, where the final fiber velocity is determined by the take up roll (Hietel, 2005). For melt blowing, theoretical models have been developed to predict the polymer diameter as a function of position below the die. This modeling has been done for both solid (Uyttendaele, 1990; Rao, 1993; Marla 2003) and hollow fibers

(Marla, 2006). Uyttendaele (1990) first developed a model in 1-D, and found that using either a Newtonian viscosity or a Phan-Thien viscosity resulted in very similar predictions of final fiber diameters, which both compared well with experiments. Then Rao and Shambaugh (1993) extend this model to include 2-D, in order to predict the oscillations in the melt blowing process. Finally, Marla and Shambaugh (2003) extended this model into 3D so that it was able to fully simulate the fiber during the melt blowing process. The air velocity and temperature profiles from the simulations described in Chapter 2 were input into the model, and based on these flow profiles, initial air flow rate, and polymer flow rate, the rheological model predicted fiber temperature, speed, diameter, frequency of vibration, and amplitude of vibration (Marla, 2003). However, the interactions between the air and the fiber as they occur in the melt blowing process have been studied in much less detail. In this chapter, fiber inclusive simulations will be discussed for both the slot melt blowing die as well as the annular melt blowing die. Due to the geometry of these two cases, the annular die can be represented using an axisymmetric computational domain, and is therefore a simpler simulation, while the slot die must be simulated in 3D. Therefore, the annular die results will be given first, followed by the discussion for the slot die.

5.2 Effect of Fiber on Air Flow for an Annular Die

The computational fluid dynamics software package used to complete all the simulations discussed in section 5.2 was Fluent^{TM} 6.1. The determination of the geometry of the computational domain, the generation of the computational grid, and the turbulence modeling are discussed in detail in the following sections.

5.2.1 Air and Polymer Flow Rates for Simulations

Results from ten simulations with different air and polymer flow rates are discussed in section 5.2. The air and polymer flow rates for each of these simulations are given in Table 5-1. Cases 1, 5, 7, and 9 do not include a polymer (Q = 0). The computational domain geometry and grids for these cases are based on Moore et al (2004). Cases 1, 5, 7, and 9 are used to compare air only flow to flow with both air and a polymer fiber. For the simulations that included a fiber, it was necessary to know the diameter as a function of the position below the die in order to construct the computational domain. For Cases 2, 4, 8, and 10, the fiber diameters were based on the modeling results of Marla and Shambaugh (2003). For Case 3, the diameter was generated using a linear interpolation between the diameters of Cases 2 and 4. The diameter used in Case 6 was based on a least squares fit to the experimental results of Uyttendaele and Shambaugh (1989). Results from Cases 7-10 were only used in the study of the air drag force.

5.2.2 Computational Domain

In order to incorporate the moving polymer in the simulations, the fiber diameter and speed, as functions of distance from the die face, must be known. The diameter is used to set the shape and position of the boundary that represents the fiber edge in the computational domain. The velocity of the fiber is input into the simulation to set the speed at which the fiber edge boundary moves. The polymer diameter was determined using either the model of Marla and Shambaugh (2003) or the experimental work of Uyttendaele and Shambaugh (1989). For the simulations, the fiber edge velocity was determined using a material balance over the polymer, since the mass flow rate of the

polymer is constant, while the diameter of the fiber, found from the aforementioned publications, is changing as the fiber moves away from the die face.

Figure 5-1 shows a cross-sectional cut of a standard annular die. In actual operation during melt blowing, polymer is forced through the center capillary and exits at the die face. Air also exits the die face; the air discharges through an annular space that encircles the exiting polymer. The impact of the hot air upon the polymer stream causes the polymer to rapidly attenuate to a fine fiber. All the simulations discussed in this paper were completed with an annular die of the configuration shown in Figure 5-1. For these simulations, the outer and inner diameter dimensions were D_o = 2.37 mm and D_i = 1.3 mm, respectively. The polymer capillary had a diameter of 0.76 mm. An annular die with these same dimensions was called Die A in the experiments of Majumdar and Shambaugh (1991) and in the computational work of Moore et al (2004).

Figure 5-2 shows the computational domain, including the regions of different grid refinement. The cylindrical coordinates r and z are shown on this figure. The origin of these coordinates is located at the exact center of the die face (at the center of the polymer discharge capillary – compare Figure 5-1). The curved left side of the domain corresponds to the surface of the polymer fiber. The 5 mm jet at the top of the domain allows modeling of air flow through the annulus. Although the domain in Figure 5-2 was based on the work of Moore et al. (2004), the domain in this work was different due to the inclusion of the polymer. Similar to Moore et al., the flow field was assumed to be axisymmetric and a 2D computational domain was implemented. The length of the computational domain extended 70 mm below the die face. At the die face, the width of the domain was 5 mm. However, at z = 70 mm, the width of the domain was 20 mm.

Expanding the width of the computational domain was important in order to ensure that the spreading jet remains within the domain boundaries. The most important difference between the computational domains used in this work and those in Moore et al.was that the boundary at the left (see Figure 5-2) is not designated as an axis of symmetry, but is used to represent the moving polymer fiber. Note that the axis of symmetry ($r = 0$) is not included in the computational domain.

5.2.3 Grid Generation

There are four different sections of the grid, each having computational cells of a different size (see Figure 5-2). Section A, where the quadrilateral cells have sides with lengths of 0.1 mm, is the coarsest part of the grid. The grid in section B is finer than in section A; here, the cells have side lengths of 0.05 mm. Section C_1 includes the portion of the computational domain immediately under the jet nozzle, and section C_2 is the area next to the polymer, but farther away from the die face than section D. Both C_1 and C_2 are composed of quadrilateral cells that have a side length of 0.025 mm. Finally, section D is the finest part of the grid. This area is close to the die face, and is immediately next to the location where the polymer exits the die face and where fiber attenuation is very rapid. In this section, the length of the quadrilateral cells is ~0.0125 mm (due to the shape of the polymer, the cells close to the die face in this section are somewhat smaller than the cells farther away from the die). Note that sections C_1 and B lie directly below the annular air discharge area. The computational domains and grids were constructed using Gambit, and the grids were refined after they were imported into Fluent™. The coordinate origin is outside the domain; it is located at the center of the polymer stream (at $z = 0$ on the axisymmetric line).

As stated above, the curved boundary on the left side of the computational domain (as seen in Figure 5-2) corresponds to the edge of the polymer fiber. The position and velocity of this boundary depend on the melt-blowing conditions, such as the air and polymer flow rate. Figure 5-3a shows the radii of the polymer fibers as a function of distance from the die face for cases 2, 3, 4, and 6. Also shown in Figure 5-3a is a horizontal solid line that represents the polymer edge (polymer-air interface) if the polymer radius is approximated to be constant at 0.25 mm (i.e., if the polymer fiber was a cylinder). In each of the simulations, the fiber radius, which represents the fiber edge, corresponds to the position of the left boundary of the computational domain.

Figure 5-3b shows the velocity of the polymer edge boundary in the simulations. These velocities were calculated by performing a mass balance over the fibers, using the fiber diameters measured by Uyttendaele and Shambaugh (1989) or modeled by Marla and Shambaugh (2003). As the ratio of the air flow rate to the polymer flow rate is decreased, the velocity of the fiber also decreases. A horizontal solid line with a constant velocity of 5 m/s is also included on the figure; this line corresponds to the situation where the polymer fiber is treated as a cylinder.

For a position close to the polymer fiber (r = 0.4 mm), the dimensionless axial air velocities for case 1 (air only) and case 4 (Q = 0.658 cm^3/min) are presented in Figure 5-3c. The profiles along the r = 0.4 mm line were used instead of the centerline, r = 0, because the fiber is present on the centerline (i.e., r = 0 is not within the computational domain). The value of 0.4 mm was determined on the basis of the criterion that (a) this line should be between the polymer capillary and D_i and (b) this line is within the computational domain (i.e., the fiber radius is smaller than 0.4 mm). Also shown on the

figure is the speed at which the edge of the fiber is moving for case 4. The differences in the air velocity profiles between these different cases show that the presence of the polymer affects the air flow field.

Figure 5-4 shows the dimensionless z velocity along the r = 0.4 mm line for different simulations that were conducted with the same computational domain, but with different grid resolutions. The different grid resolutions were compared for the case 4 fiber radius and velocity. In addition to the dimensionless axial velocity, Figure 5-4 also shows the turbulence intensity as a function of dimensionless distance below the die face. The smallest number of cells examined was 72,534; the most was 483,702. Clearly, the grid with 72,534 cells misses both the axial velocity and turbulence intensity in the near field. All of the simulations agree in the far field, where $z/D_o > 9$. The simulations with 121,137 and 290,136 cells agree very well with each other, as well as with the 483,702 cell grid. However, there is a slight variation between the 483,702 cell grid and the others. The average percent difference between the axial velocity profiles along r = 0.4 mm for the 483,702 and 121,137 cell simulations was only 1.41%.

The simulations discussed in the following sections of this paper (see Table 5-1 for details) were completed using grids with the same cell size as the 121,137-celled grid for case 4 (the arrangement shown in Figure 5-2). This grid size showed good agreement with the finer grids but required significantly less computational time. For the simulations shown in Figure 5-4, Table 5-2 gives the number of iterations necessary to reach 10^{-5} convergence as well as the computational time required on a single processor of a dual Pentium 4 Xeon, 2.8-GHz computer. Observe that using a grid of 121,137 cells

required about an order of magnitude less time than either of the two simulations that contained more cells.

5.2.4 Incorporation of Fibers in the Simulation

Figure 5-5 shows an axial velocity comparison at r = 0.4 mm for three different simulations. The first simulation is Case 1 (Q = 0 cm^3/min and V_{jo} = 110.26 m/s). The second simulation is Case 4 (Q = 0.658 cm^3/min and V_{jo} = 110.26 m/s); the fiber diameter and speed for Case 4 are based on the model of Marla and Shambaugh (2003) (see Figures 5-3a and b). The third simulation was completed assuming that the fiber edge can be represented by a cylinder moving at 5 m/s, which is the average speed of the polymer in case 4. For this simulation, the left boundary of the computational domain was fixed at R = 0.25 mm.

Near the die, the axial velocity for case 4 along the r = 0.4 mm line is similar to that of case 1; however, for $z/D_o > 1$, the axial velocity profile for case 1 is greater than case 4. This is expected because close to the die face, the fiber (which is present in case 4) is moving more slowly than the surrounding air and, thus, exerts a decelerating drag force upon the air. For the simulation with constant fiber diameter, the air stream is slowed at positions near the die, because near the die, the air velocity is > 5 m/s. However, the location of the maximum air velocity for the simulation with the cylinder is shifted significantly from where the maximums occur for either case 1 or case 4 (the maximums occur at approximately the same position for cases 1 and 4). Farther from the die, approximating the fiber with a cylinder causes the air velocity to be faster than the velocities in either case 1 or case 4. The two overall conclusions from Figure 5-5 are that (a) the polymer stream can, indeed, perturb the air field close to the fiber, and (b) using a

constant velocity cylinder to represent a polymer in the simulations does not lead to an accurate simulation of the actual flow field.

5.2.5 Turbulence Modeling

Moore et al. (2004) showed that the ideal gas equation accurately represents the compressibility observed in experimentally measured flow fields with the same conditions as the present simulations. In all simulations presented in this paper, the ideal gas equation was used to model the air density. The inlet static air temperature of the simulations was 648 K; this temperature was based on conditions used in the modeling work of Marla and Shambaugh (2003) as well as the experiments of Uyttendaele and Shambaugh (1989).

According to previous studies (see Chapter 2), the Reynolds stress model (RSM) can be used to accurately predict the air flow field from melt-blowing dies. Therefore, the RSM was used with the parameter modifications suggested by Moore et al. (2004) to model the flow field. (See Chapter 2 for the description and equations for the RSM.) The default values suggested in the Fluent^{TM} software for the parameters appearing in equation 1-4 are $C_{\varepsilon 1} = 1.44$, and $C_{\varepsilon 2} = 1.92$. For the prediction of both the mean velocity decay and the jet spreading rate, Moore et al. (2004) compared their simulations with experiments. On the basis of these comparisons, Moore et al. (2004) suggested that the use of $C_{\varepsilon 2} = 1.82$, instead of its default value of 1.92, provided more accurate results. Therefore, this modified $C_{\varepsilon 2}$ was also used in the simulations discussed in this paper. The enhanced wall treatment option was also enabled during the simulations listed in Table 5-1.

To decrease the computational time involved with each simulation, the residuals of the viscous model equations were made to converge to 10^{-4} for a constant density, isothermal flow, then the temperature at the boundary conditions was changed, and the density was calculated on the basis of the ideal gas law. Under these new conditions, the CFD software iterated until the residuals reached 10^{-5}, except for the energy equation residual, which was required to reach 10^{-6}.

5.2.6 Effects of the Polymer on the Mean Flow Field

When no polymer is present, the development of the air flow field downstream from an annular jet has been found to exhibit three major zones (Moore, 2004). The first zone is the converging zone, which is close to the orifice and centered on the jet axis. In this zone, the air jet stream is still annular in shape. In addition, fluid recirculation occurs where air is traveling in the opposite direction from the main axial path of the jet. The next zone is the merging zone, where a transition occurs between the converging zone and the fully developed zone. The dominant characteristics of the merging zone are the lack of flow recirculation and the presence of peak mean velocities at radial locations away from the centerline. The third region is the well developed region. In this zone, the velocity maximum is along the centerline, and the mean velocity is decaying.

Figure 5-6a shows a velocity vector plot of the recirculation area, which occurs very close to the die face for the case 1 (air only) annular jet. Figure 5-6b shows the corresponding recirculation area for the case 4 simulation. An inlet air velocity of 110.26 m/s was used for both simulations. Significant differences are observed in this recirculation area. For case 1, the recirculation area is much wider and extends farther away from the die face. In addition, the center of the recirculation area is close to $z = 0.4$

mm for the simulation that includes the polymer, whereas the air-only simulation has a center near $z = 0.65$ mm. This recirculation area retards polymer attenuation, since close to the die face the fiber is in contact with air that is moving in the opposite direction. Since the magnitudes of the recirculation velocity vectors are smaller for case 4 than for case 1, the presence of the fiber actually improves the air flow field with respect to enhancing fiber attenuation during melt blowing.

The merging point of an annular jet is the point that marks the end of the converging zone and the beginning of the merging zone. It is defined as the distance below the die face where the maximum axial velocity first occurs on the jet centerline. For the simulations that included the polymer, the maximum axial air velocity cannot occur on the centerline at any point, so there is no merging point. We define r_{max} as the radial position of the maximum axial air velocity (this definition is appropriate for situations both with and without the presence of a fiber). Figure 5-7 compares the dimensionless position (r_{max}/D_o) of the maximum axial velocity for cases 1 and 4. The points for the two cases nearly coincide for $z/D_o \leq 2$; hence, in this range, the effect of the polymer on the position of the maximum axial velocity is small. Beyond $z/D_o = 2$, the two flow fields exhibit differences. The case 1 simulation shows a merging point near $z/D_o = 2.5$. For the case 4 (fiber-inclusive) simulation, the r_{max}/D_o reaches a near-constant value of ~0.13 for $z/D_o > 3$.

Figure 5-8 shows the dimensionless mean axial velocity along the $r = 0.4$ mm line. Close to the die, the differences among cases 1, 2, 3, and 4 are small; however, for positions close to the die, cases 5 and 6 differ from the other four cases (because cases 5 and 6 have lower air flow rates). Farther from the die (for $z/D_o > 12$), the axial velocity

profiles for cases 2-5 fall onto the same curve. In this same region, case 1 velocities are above cases 2-5 velocities, and case 6 velocities are below cases 2-5 velocities. For the dimensionless axial velocity profile at r = 0.4 mm, the air velocity has a stronger effect than the polymer flow rate (compare cases 6 and 4 that have the same polymer flow rate but different V_{jo}).

Figure 5-9a and b shows the dimensionless velocity decay at r = 0.4 mm for the different simulations using z/D_o as a dimensionless length. Figure 5-9a shows that the same empirical fit can be used to describe the dimensionless velocity decay of cases 2, 3, and 4, whereas case 1 and case 6 each require their own fits. Case 1 shows a slightly sharper decay than the cases that include the fibers with the same V_{jo} (cases 2-4). In Figure 5-9a, correlations of the following form were used to predict the velocity decay.

$$V_{az}/V_{jo} = a*(z/D_o)^{-b} \qquad (5\text{-}3)$$

The values of constants a and b, as well as the R^2 values, for each of the simulations are given in Table 5-3.

Figure 5-9b compares the velocity decay profiles at r = 0.4 mm for the different cases, but uses $V_{az}/V_{az\text{-}max}$ versus z/D_o as the dimensionless variables, where $V_{az\text{-}max}$ is the maximum axial velocity along the r = 0.4 mm line. When this dimensionless velocity is used, the decay profiles for the simulations in which polymer is present (cases 2, 3, 4 and 6) can be described by the same empirical fit. Similarly, cases 1 and 5 can be approximated by a single empirical fit. The decay equations using $V_{az\text{-}max}$ to nondimensionalize V_{az} have the same form as equation 5-3, and the values of constants a' and b', as well as the corresponding R^2 values, are given in Table 5-4. It appears that $V_{az\text{-}max}$ is more appropriate than V_{jo} as a velocity length scale.

On the basis of previous work (see Chapter 2), the position z_{max} could be used as a length scale. However, in the case in which a polymer is present, z_{max} is difficult to predict a priori. One would need to generate data for many different cases of air and polymer flow rates and then develop a correlation for the prediction of z_{max}. To complete this task with the simulation methodology discussed in this work, one would also need to know the fiber speed and diameter for all cases. To avoid these difficulties, D_o was used as a length scale. D_o is known from the geometry of the die, and z/D_o was used as the dimensionless length coordinate in this work.

The jet entrainment of ambient air throughout the computational domain can also be used to compare the simulated air flow fields with and without the presence of the fiber. The following equation provides the total mass flow rate per length of the jet in axisymmetric cylindrical coordinates.

$$M(z) = \int_0^z \int_{R_1}^{R_2} \rho_a (r,\theta,z) V_{ax}(r,\theta,z) 2\pi r \, dr \, dz \tag{5-4}$$

For the air-only simulations, $R_1 = 0$, but for the polymer inclusive simulations, R_1 was the fiber radius. The width of the domain in the r direction, R_2, is the same for all the simulations. The mass flow rate of the entrained air is calculated by subtracting the jet discharge flow rate from the total mass flow rate at any z location. Mathematically, this entrained mass rate can be expressed as

$$M_e = M(z) - M_o \tag{5-5}$$

Then the entrainment coefficient can be determined using the following equation:

$$\Psi = \frac{M_e(z)}{M_o} \tag{5-6}$$

Figure 5-10 shows the entrainment coefficient throughout the computational domain for cases 1 and 4. The entrainment coefficient is not changed significantly by the presence of a fiber. The largest difference in the entrainment coefficient for cases 1 and 4 occurs close to the die face, although this difference is only 2.41% at z = 10 mm. Since the entrainment coefficient is a useful quantity when examining the entire flow field, the small change in this number shows that the presence of the fiber does not have a large impact on the overall flow field.

5.2.7 Fluctuating Velocity Field

Figure 5-11 shows the turbulence intensity as a percentage of V_{jo} along the r = 0.4 mm line for cases 1-6. The presence of the fiber has a dampening effect on the velocity fluctuations of the flow field. Among cases with the same air flow rate, increasing the polymer flow rate decreases the turbulence intensity along the r = 0.4 mm line. This can be attributed to the application of a no-slip boundary condition on the polymer-air interface. The result is to have zero fluctuations at the air-fiber interface. Since the r = 0.4 mm line is close to this interface, the presence of this boundary limits the turbulent fluctuations. The presence of the fiber makes the air flow less turbulent near the fiber, which enhances the process of melt blowing (since turbulence wastes attenuation energy and causes random fiber motion).

The maximums of the turbulence intensity of cases 1-4 occur at approximately the same z/D_o position of 1.6 mm. This location is indicated on the axial velocity contour plots for case 1 and case 4 in Figure 5-12a and b, respectively. The turbulence intensity at z = 1.6 mm for all the cases is given in Figure 5-13a. In addition, the line r = 0.4 mm has been included on this plot. In Figure 5-13a, the turbulence intensity profiles for cases

1-4 are different close to the centerline and become more similar until they fall on the same curve after $r/D_o = 0.4$; however, the case 5 and case 6 turbulence intensity profiles are different from each other at large r/D_o values (farther away from the fiber). Again, it is observed that, compared to the polymer flow rate, the air velocity has a more important effect on the air velocity and turbulence profiles. Examining the turbulence intensity along the line $z = 1.6$ mm demonstrates that the majority of the effects caused by the presence of the fiber occur near the fiber edge.

Figure 5-13b presents the turbulence intensity and axial velocity for case 4 at $z = 1.6$ mm below the die. A maximum in velocity corresponds to a minimum in turbulence intensity. This is expected, since the production of turbulence (the third term on the right-hand side of equation 1-7) is almost zero when the mean velocity slope is almost zero, and production increases as the mean velocity slope increases. Moore et al. (2004) also observed that the maximum in axial velocity corresponds to a minimum in turbulent kinetic energy.

Figure 5-14 presents the $\overline{uw}$ Reynolds stresses along the line $r = 0.4$ mm for the different cases. The $\overline{uw}$ profile for case 6 shows a minimum that is located at a different position and is much smaller in magnitude than the minimums for the other cases (i.e., the minimum for case 6 is higher than the minimums for the other cases). This behavior is caused by the combination of a low flow rate of air with high polymer flow rate. However, close to the die face, there are differences in the magnitude of the Reynolds stresses for all the cases. For the same V_{jo}, the simulations without fiber exhibited a $\overline{uw}$ minimum of significantly larger magnitude than the cases that included a fiber. This

further supports the observation that the presence of the fiber leads to a decrease in the turbulence close to the fiber edge.

Figure 5-15 is a comparison of the turbulent kinetic energy of the flow fields along the line r = 0.4 mm. Along this line, case 1 has a higher turbulent kinetic energy than cases 2, 3, and 4; similarly, case 5 has a higher turbulent kinetic energy than case 6. The difference in the magnitude of the turbulent kinetic energy between cases 5 and 6 was greater than the difference between case 1 and cases 2, 3, and 4. Case 1 exhibited a higher maximum than the simulations that included the polymers; this is related to the dampening effect that the polymer flow has on the turbulent fluctuations. For the same air flow rate, the magnitude of the turbulent kinetic energy profiles consistently decreased as the polymer flow rate increased. Similar to the results for the other turbulent quantities, the presence of the polymer decreased the turbulent kinetic energy in the air flow field.

Figure 5-16 shows the nondimensionalized turbulence dissipation rate for the different cases at r = 0.4 mm in the region close to the die face, where most of the turbulence dissipation occurs. Once again, the presence of the fiber decreases the turbulence in the flow field, since turbulence dissipation was higher for the simulations when a fiber was included in the flow field. Case 1 has a lower turbulence dissipation rate than cases 2, 3, and 4. This is to be expected, since examination of other turbulence characteristics showed that turbulence was dampened by the presence of a fiber. At distances farther from the die face, the turbulence dissipation profiles of all the cases became more similar. After a maximum, the dissipation of turbulence decreased as the position from the die face increased.

5.2.8 Stresses on the Fiber Edge

Figure 5-17 shows the wall shear stress on the polymer surface. The wall shear stress in the coordinate system being used is defined by the following equation:

$$\tau_w = \rho\nu\left(\frac{\partial V_{az}}{\partial r}\right)_{r=R(z)} \tag{5-6}$$

Case 2, which was the fiber-inclusive simulation with the lowest polymer flow rate, shows the highest wall shear stress. The simulation with the highest ratio of polymer-to-air flow rate, case 6, shows the lowest wall shear stress. These results seem reasonable, since the lower air flow rate means that the difference in velocity between the air and fiber is less. It appears that a polymer-to-air flow ratio similar to that for case 2 (i.e., Q = 0.329 cm^3/min and V_{jo} = 110.26 m/s) leads to shear stresses on the polymer fiber that are almost twice as large as the shear stresses for the base case (case 4). As evidenced by Figure 5-3a, these high stresses result in smaller fiber diameters. The fiber attenuation depends on the air drag force exerted on the polymer fiber. Matsui (1976) developed an empirical relation for the friction factor at the interface between the air and fiber (see Equation 5-1). Marla and Shambaugh (2006) described the drag force on the fiber using the following equation:

$$F_{PAR} = C_f(1/2)\rho_a v_{a,eff,PAR}{}^2 \pi d_f L_f \tag{5-7}$$

To calculate this drag force, the air and polymer velocities are examined separately (either computationally or experimentally). The Reynolds number defined in equation 5-2 is based on $V_{a,eff,PAR}$, which is the difference between the air and the fiber velocities in the stream wise direction. Re_{DP} is used to find C_f in equation 5-1, and then this C_f is used to find F_{PAR}, which is the force due to air drag. An implicit assumption in these calculations is that the air flow is the same whether the polymer is present or not. For

instance, the centerline velocity of the air in case 1 and the fiber velocity in case 2, 3, or 4 can be used to calculate $V_{a,eff,PAR}$, then this $V_{a,eff,PAR}$ can be used in equation 5-2 to determine Re_{DP}, and both values can be used in equation 5-7 to find F_{PAR}. One of the advantages of using CFD is that the drag force due to air on the fiber can be found directly from the simulation. Table 5-5 shows the percent difference in the drag force when calculated using equations 5-1, 5-2, and 5-7 versus the drag force calculated by the simulations.

Cases 7-10 were included to provide additional data to assess the value of β. The value of $\beta = 0.78$ has been suggested for the application of melt-blowing (Matsui, 1976). This value was determined experimentally on the basis of the assumption that a fiber does not significantly affect the air flow (for the calculations of $V_{a,eff,PAR}$). However, $V_{a,eff,PAR}$ is not the true velocity of the air near the polymer. In addition, the velocity of the air close to the polymer is affected more significantly by V_{jo} (not Q), so $V_{a,eff,PAR}$ is V_{jo}-dependent, which leads to the conclusion that the value of β should be investigated for different air flow conditions. If the appropriate values of β are used, the calculated drag force can match the drag force calculated with the Fluent^{TM} simulation. Table 5-6 shows the values of β that must be used in equation 5-1 to calculate an air drag force that is within 1% of the simulation results.

5.2.9 Jet Spreading Rate

Figure 5-18 shows the spreading rates of the simulated jets. For cases 2, 3, 4, and 6, the maximum axial velocity does not occur at the centerline. Therefore, to compare the spreading rate for these jets to that for cases 1 and 5 (in which the maximum velocity occurs on the centerline in the far field), the jet half width was calculated as the

difference between the location where the mean velocity is one-half of the maximum, $r_{1/2}$, minus the location at which the velocity exhibits a maximum, r_{max}. The spreading rates for cases 1 and 5 are similar to each other and are lower than for the cases that included the polymer. The spreading rates can be fit to a linear equation of the following form:

$$\frac{(r_{1/2} - r_{max})}{D_o} = c * (z/D_o) + d \qquad (5\text{-}8)$$

The constants c and d can be found in Table 5-7 for each of the cases.

5.3 Effect of Fiber on Air Flow for a Slot Melt Blowing Die

The computational fluid dynamics software package used to complete all the simulations discussed in section 5.3 was Fluent™ 6.2. The determination of the geometry of the computational domain, the generation of the computational grid, and the turbulence modeling are discussed in detail in the following sections.

5.3.1 Computational Domain

For simulations of an Exxon slot die without the presence of a fiber, the geometry is statistically 2D (see chapter 2). However, the inclusion of a fiber required a 3D simulation. The computational domain and grid were created in Gambit™. To determine the diameter, velocity, and temperature of the fiber as a function of distance from the die, the model developed by Marla and Shambaugh (2003) was used. Then, the predicted fiber diameter was used as a boundary condition for the CFD simulation. The velocity and temperature of the fiber, which vary with position, were specified for the CFD simulations with *User Defined Functions* (UDF). All the simulations discussed in section 5.3 were run for the die type show in Figure 5-19a. The jet width at the die face, b, was 0.65 mm. The distance between the outside edges of both jets, h, was 3.32 mm.

For all simulations, the angle between the die face and the jets, θ, was 60°. A melt blowing die with this configuration has been studied experimentally by Harpham and Shambaugh (1996; 1997).

Seven different simulations are discussed in section 5.3. The difference between the cases is in the air and/or polymer flow rates. The momentum flux ratio which is defined as follows (Schetz and Padhye, 1977):

$$\overline{q} = \frac{\rho_{f,die} V_{f,die}^{\ 2}}{\rho_{a,die} V_{jo}^{\ 2}} \tag{5-9}$$

can be used to distinguish the simulation cases. The cases are named with increasing momentum flux ratio. All cases are listed in Table 5-8. Case A is the only simulation that does not include a fiber ($m_f = 0$), and is used to compare the results of an air-only simulation to those simulations that include a fiber. Cases A, C, D, E, and F have the same air flow rates as experiments completed by Harpham and Shambaugh (1997) (the experiments were completed without the presence of a fiber).

5.3.2 Grid Generation

Figure 5-19b shows the computational domain for all slot jet fiber inclusive simulations. This domain extends 50 mm below the die face, in the z-direction, not including the air jet, which extends 5 mm above the die face. The width of the domain is 15 mm in the x-direction. The $y = 0$ plane is at the center of the domain. The width of the domain in the y-direction is 0.7257 mm, in order to create a domain with a spacing of 35 polymer capillaries per inch. Although the simulation can not be completed in 2D, due to the presence of the fiber, using symmetry for the boundary condition on the left side of the domain ($x = 0$) allows for the computational domain to be reduced. In

previous CFD simulations, the grid has been refined in Fluent™ in order to reduce the size of the cells in the area of most interest (see chapter 2). This was attempted with this geometry also, but a sharp change in the cell size close to the fiber created discontinuities in the simulation results, as well as instability during the simulations. It is desirable to have smaller cells in the area of most interest, which is the area close to the die face and close to the fiber, without rapid changes in the cell size. In order to accomplish this, the average cell spacing was specified on each edge in the domain with a successive ratio (the fraction of cell edge length increased) between consecutive cells. Next, the faces and domain volume were meshed using quadrilateral cells. Figure 5-19c shows a close up of the section of the computational domain that includes the jet, fiber, and die face. Periodic boundary conditions were used on the front and back of the domain, in order to simulate the flow around polymer fibers in the center of the die, where end effects are negligible. The fiber (with a diameter that changes with z-position) was represented using a round half-cylinder wall with a no-slip surface. Symmetry was used in order to negate the inclusion of both slot jets. The boundary condition for the air entrance into the jet was a mass inlet. Because the simulation was non-isothermal and several different air flow rates were simulated, compressibility is could not be neglected, and the mass inlet is the appropriate choice for this boundary (as opposed to a velocity inlet boundary that was used for 2D isothermal simulations in chapter 2). The die face was represented as a no-slip wall.

Several different simulations were run at different grid refinements in order to determine the cell size necessary to achieve grid independence. Figure 3 shows the dimensionless velocity at the $y = L_c/2$, $x = 0$, centerline for three different grids. Table 5-

9 gives the number of cells, the number of iterations necessary, and the computational time when the simulation was run using four Dell Pentium 4 Xeon64 processors in parallel. (Note that the simulation using the finest grid refinement did not converge to 10^{-5} as did the other two simulations, but was stopped after it achieved $5x10^{-5}$ convergence). For the grid with 653,090 cells, the symmetry (left boundary) and side pressure outlet (right boundary) were split up into five sections. These sections had increasingly large cell with increasing z-position. The quadrilateral cells close to the die face were the smallest, with an edge length of 0.10 mm. The largest cells, at the bottom of the domain, had an edge length of 0.22 mm. For the 1,023,162 cell simulation, the edges of the computational domain were specified using an average cell size of 0.08 mm with a successive ratio of 1.002. The cells closest to the die face had an edge length of 0.04 mm, while the cells at the bottom of the domain (far from the areas of interest and high gradients) had cells with a side length of 0.14 mm. Although this is a wide range of cell spacings, the change in the cell size is gradual, which is important for the simulation results and stability. Finally, the finest grid had 2,640,102 quadrilateral cells. This grid contained the cells with an edge length close to 0.03 mm close to the die face, but 0.14 mm far from the die face. In addition, these cells were also smaller in the y-direction.

Figure 5-20 shows that all three simulations resulted in a centerline velocity with a maximum close to $z/h \sim 1$. However, the maximum reached for the 653,090 celled case was slightly lower than the other two cases. Therefore, the grid with 1,023,162 was used for all simulations. Figure 5-19b shows this computational domain and the edges labeled according to the cell size. Sides with the label "A" have an average cell edge length of 0.08 mm with a successive ratio of 1.002. The walls and inlet of the air jets are labeled

"B", these sides have cells with 0.08 mm spacing. The sides labeled "C" have cells with 0.12 spacing. These cell sizes were used for all the simulations listed in Table 5-8.

5.3.3 Turbulence Modeling

The non-isothermal simulations of the slot die (in chapter 2) have shown that the ideal gas equation can accurately represent the compressibility in non-isothermal simulations and simulations with high air flow rates, similar to those discussed in this paper. Therefore, for all simulations listed in Table 5-8, the ideal gas equation was used to model the air density. All simulations were run with an inlet air temperature of 330 °C (the inlet excess temperature was Θ_{jo} = 309 °C). The inlet polymer temperature was 295 °C. These temperatures were based on the experiments by Harpham and Shambaugh (1997) and the modeling work of Marla et al. (2006). RSM was used for the turbulence modeling with modification of the empirical parameters $C_{\varepsilon 1}$ and $C_{\varepsilon 2}$, which were set at 1.24 and 2.05, respectively (see eq. 1-4).

In order to decrease the amount of computational time required and increase the stability of the simulations, isothermal conditions with constant air density were applied until the residuals of the model equations reached 10^{-4}. Then, the density was determined using the ideal gas equation, and the appropriate temperature was applied at the boundaries. After these changes, the simulations were run until the residuals reached 10^{-5} convergence, except for the energy equation, which was required to reach 10^{-6} convergence.

5.3.4 Results from the Rheological Model

For cases B-G the radius of the polymer capillary was 475 μm. Therefore, this was the diameter of the polymer at the die face. However, the air flow quickly creates a high drag force on the fiber, rapidly reducing the diameter in a matter of microseconds. This process was modeled using the software written by Marla and Shambaugh (2006). Figure 5-21a shows the radius of the fibers predicted by the model. As expected, the higher the momentum flux ratio, the larger the fiber diameter. In addition, the model predicts, within the range of values tested, that the momentum flux ratio, not the air flow rate, determines the fiber diameter. This is based on the fact that cases C and D, which have the same momentum flux ratio, but different air and polymer flow rates, have similar diameters. In addition, cases E and G, which also have the same momentum flux ratio, have similar diameters.

Figure 5-21b shows the velocity of the fibers, as predicted by the Marla-Shambaugh model (2006). The fibers with smaller diameters are traveling at higher velocities. The radii of the fibers were used to construct the computational domain with the corresponding flow rates for the CFD simulations of the air velocity. In addition, the fiber velocities were read into the simulation through a *UDF* and the wall representing the fiber was set as a moving wall. Since this is not a time dependent simulation, the mean flow of the air and polymer were modeled. In reality, the fiber position would be oscillating due to the air turbulence.

5.3.5 Effects of the Polymer on the Mean Flow Field

Without a fiber present, dual rectangular jets have been found to exhibit three regions of development (Nasr and Lai, 1997). For a complete description of all three regions, see section 2.5. In the first region the jets are separate and a maximum velocity is present due to each individual jet. For the blunt melt blowing die, a recirculation area is present between the two jets (see chapter 2). The recirculation area in the first region of flow is not beneficial for melt blowing, because the negative centerline velocity creates a drag force towards the die face, instead of a drag force in the direction of flow. Cases D-F had much weaker recirculation areas when compared to that present in the case A simulation. (These cases were compared because they all had the same V_{jo}.)

When a fiber is not present, the third region of the flow field is characterized by the maximum velocity occurring on the centerline. For a slot die, if a fiber is present, the maximum air velocity can not occur along the centerline (although this maximum will still occur on the centerline between the fibers). The location of the maximum velocity, x_{max} on the $y = 0$ plane, for case A (air only) and for cases D, E, and F, which all have the same nominal air velocity as case A, are shown in Figure 5-22. These locations were determined by examining the velocity on lines beginning at the fiber edge (at $y = 0$ and a constant z-position) to find the distance from $x = 0$ where the maximum velocity occurred. Close to the die face, the location of the maximum velocity is governed by the location of the air jet. All simulations in Figure 5-22 show that the maxima move closer to the centerline, and all simulations are similar until $z < 2$ mm. At $z > 3$, the maximum for case A is located on the centerline; while the maxima for cases D-F are near $x = 0.3$ mm. The location of the maximum for cases D-F appears to be the same for same for all

cases and constant. However, when the simulation results for the entire computational domain are closely examined, there is a slight spreading rate of x_{max}. At positions of $z >$ 10 mm, a constant spreading of x_{max} for cases B-G can be described by the following equation (with both x_{max} and z in mm):

$$x_{max} = S'*z \tag{5-10}$$

For all cases $S' \approx 0.005$. Also, for all cases $x_{max} < 1$ mm throughout the entire 50 mm computational domain.

The first goal stated in this chapter is to investigate how the presence of a fiber affects the air flow field. Since the fiber moves along the centerline ($x = 0$) in melt blowing, this is an area of interest. Figure 5-23 shows the dimensionless centerline velocity for case A (no fiber) and at two different y-locations for case D. The first centerline location for case D is halfway between two fibers (represented by the periodic boundary in the simulations). Since the stress on the fiber is determined by the gradients close to the fiber, it is also of interest to look at the maximum velocity close to the fiber. The velocity at the points with $y = 0$ (center of the domain) and $x = x_{max}$ is plotted on Figure 5-23. Although the position of x_{max} is difficult to measure experimentally, CFD allows fast and simple determination of x_{max}. As shown in Figure 5-22, the maximum velocity does not occur along the centerline at $y = 0$ due to the presence of the fiber. The velocity profiles for case A and both positions for case D show significant differences. The case D profile at $y = L_c/2$ has the highest maximum, which can be attributed to the fact that space available for the air flow is reduced due to the presence of the fibers. The case D profile at $y = 0$ has the lowest maximum because the movement of the fiber, which is slower than the air, reduces the air velocity. The $x = x_{max}$ position is very close

to the fiber, and the difference between the air velocity and the fiber speed results in the attenuating drag force. This velocity gradient is of interest because this is the air velocity that the fiber "feels", and it plays a critical role in the mechanism of the melt blowing process. Figure 5-23 shows that the velocity profiles of the air are non-uniform, and are altered due to the presence of a fiber.

Figure 5-24 shows the z-velocity contours for case F, and helps to illustrate the development of the flow field with the inclusion of a fiber. At z = 1 mm the two bands representing the highest air speeds show that the velocity maxima are determined by the location of the jet (also see Figure 5-22); the two jets have not merged together. The second contour is at z = 2.5 mm below the die face. The two jets have merged together as much as possible with the fiber between them; the maximum air velocity occurs on either side of the fiber at $y = 0$. A strong attenuating force is present at this location (see Figure 5-28), but the force on the fiber is not uniform due the non-uniform velocity profiles. The next contour, at z = 5 mm, shows that the air velocity maxima are now located halfway between the fibers, at $y = \pm L_c/2$. This is the location of the velocity maxima for the computational domain beyond this point, as is also shown in the final contour plot at z = 10 mm. Figure 5-24 shows the development of the velocity field when a fiber is included, and that the velocity gradients around the fiber are not uniform.

Figure 5-25a shows the dimensionless centerline velocity profiles halfway between two fibers, at $y = L_c/2$. The location and magnitude of the velocity maxima for cases B-G are similar, but are different from that of case A (air only simulation). The air is being squeezed by the presence of the fiber close to the die face (where the diameter is the greatest), which leads to higher air velocity. The velocity for case G decays more

rapidly than for the other cases. This is the case with the lowest air flow rate; the slow moving polymer is creating a slowing drag force on the air flow. Far from the die, the velocity decays of cases B-F are close to each other. Figure 5-25b shows the dimensionless velocity on the y = 0 plane for all cases. For cases B-G, this velocity occurs at $x = x_{max}$. When compared to the air velocities close to the fiber, the air only simulation reaches a higher maximum because it is not being slowed by a fiber (which is moving slowly close to the die face). It has been shown that the velocity decay from a single planar jet can be described using the following equation:

$$V_o = c_1 V_{jo} z^{-1/2} \tag{5-11}$$

where c_1 is an empirical constant (Pope, 2000). Harpham and Shambaugh (1996) measured the centerline velocity decay for a blunt slot die and developed the following correlation:

$$V_o = 1.4 V_{jo} * z^{-0.610} \tag{5-12}$$

Although the profiles for cases B-G in Figure 5-25b are not directly on the centerline, a power law correlation similar to equations 5-11 and 5-12 can be used to describe the decay for these cases for $z > 10$ mm. Table 5-10 gives the values of c_1 for all cases that included a fiber; they range from 1.2613 to 0.9938. In general, the value of this constant decreases as the momentum flux ratio increases. The exponent for cases B-G is also given in Table 5-10. In theory, this exponent for a single planar jet is -0.5 (equation 5). The value of the exponent for cases B-G range between -0.5813 to -0.5007. These exponents are between the theoretical value for a single plane jet and the experimentally measured decay for a blunt melt blowing die when no fiber is present. Averaging the best fit constants and exponents for cases B-G, results in the following equation:

$$V_o = 1.123 * V_{jo} z^{-0.5378} \quad (5\text{-}13)$$

The R^2 value for equation 7 for cases B-G is 0.9835. Therefore, this equation can be used to predict the velocity decay at $y = 0$, $x = x_{max}$, which is the velocity that is closest to the fiber, and is responsible for the fiber attenuation. The trendline of equation 5-13 is included on Figure 5-25b.

5.3.6 Fluctuating Flow Field

Figure 5-26a shows the turbulence intensity, q, along the periodic centerline, as a percentage of V_{jo}, for all simulations in Table 5-8. Case A, which does not include a fiber, has the highest turbulence intensity maximum (although the location of this maximum is the same for all simulations). Throughout the entire computational domain, case A has higher turbulence intensity. Therefore, even at the centerline location farthest from the fibers, the turbulence intensity is dampened significantly. In addition, examination of cases B-G reveals that in the far field (where the largest differences in turbulence intensity profile occur), a higher momentum flux ratio leads to lower turbulence intensity.

Figure 5-26b shows the contour plots of turbulence intensity for cases A and F at the positions of $z = 1.2$ mm and $z = 10$ mm below the die face. The location of $z = 1.2$ mm is shown because it is the distance from the die face where all cases exhibit a maximum (see Figure 5-26a). For case A at $z = 1.2$ mm the turbulence intensity is clearly the highest at the center of the domain. Turbulence intensity for case F is also at a maximum on the centerline halfway between the fibers, where there is the least effect from the dampening presence of the fiber. However, it is clear that even at the location of maximum turbulence intensity, case F has smaller velocity fluctuations than case A.

At z = 10 mm, which was chosen because the flow field is self-similar, the turbulence intensity remains the highest along the centerline for case A. However, for case F the turbulence intensity is dampened, and is not on the centerline.

Figure 5-27 shows the dimensionless turbulence dissipation rate for cases A-G at $y = L_c/2$. All of the cases exhibit local maxima near $z/h \approx 0.3$ mm. However, case A has the lowest peak at this point. Because the rate of turbulence dissipation is higher for the cases that include a fiber, they have less turbulent flow fields. Similar to the results for the annular air jet, the velocity fluctuations are decreased due to the presence of a fiber, while the dissipation of turbulence is increased by the fiber. This is because the fiber provides a solid boundary in an area of the flow field where the fluctuations were high in the air-only case. This solid wall has a no-slip boundary, which leads to zero fluctuations on the solid and small fluctuations close to this boundary. For optimal melt blowing, the air would act only to create a drag force on the fiber; since turbulence fluctuations do not help to attenuate the fiber, they are a waste of energy, and minimizing these fluctuations is beneficial.

5.3.7 Stress on Fiber Edge

The wall shear stress on the fiber is a result of the difference between the air and fiber speeds. The wall shear stress is defined in equation 5-6. Figure 5-28 shows the wall shear stress on the surface of the fiber as reported from the simulations. Since the velocity flow field surrounding the fibers is not uniform (see Figure 5-24), the wall shear stress at the same z-position, but different radial locations of the fiber is also different. Figure 5-28 shows the averaged wall shear stress at different distances below the die face. The average wall shear stress changes depending on both the initial air velocity as well as

the polymer flow rate, since the stress is related to the difference in the velocity of the air and fiber. The wall shear stress from case B has the highest maximum, because it has the largest difference between the air and fiber speed. Cases D-F all have the same air flow rates, so the difference in the shear stress for these cases can be explained by the different fiber speeds. Out of these three cases, case F has the largest polymer flow rate, which leads to the lowest fiber speed. Therefore, case F has a higher wall shear stress maximum, while case D (with the lowest polymer flow rate out of these cases) shows a higher wall shear stress maximum compared to cases E and F. Finally, case G, with the lowest air flow rate, has the lowest wall shear stress maximum.

As mentioned previously, the wall shear stress is not constant at each z-location. In order to quantify the variance in the wall shear stress at any given z-position, Table 5-11 gives the maximum coefficient of variation (the standard deviation at each z-position divided by the average wall shear stress at that position) for each of the cases. In addition, the average coefficient of variation for the wall shear stress is also provided. Because of the amount that wall shear stress varies, the fiber oscillations that occur during melt blowing are important. They serve to ensure that one side of the fiber does not "feel" a greater drag force than another side.

The experiments of Majumdar and Shambaugh (1990) as well as the modeling work of Marla and Shambaugh (2006) are based on the assumption that the air flow field is not changed by the presence of a fiber. Therefore, they measured the air and fiber velocities separately to calculate $V_{a,eff,PAR}$. Using CFD, this assumption can be tested, since the CFD package reports the wall shear stress. The centerline velocity from case A (air only) was used with the fiber speed from cases D, E, and F (same V_{jo} as case A) to

calculate $V_{a,eff,PAR}$. Then equations 5-1, 5-2, 5-6 and 5-7 were used to determine the wall shear stress, which is the drag force divided by the fiber surface area. Table 5-12 compares the calculated wall shear stress using this methodology with the wall shear stress calculated by the simulations. As the momentum flux ratio increases, the percent difference also increases. This suggests that equations 5-1, 5-2, 5-6 and 5-7 work better when the fiber flow rate is lower. As mentioned above, the value of $\beta = 0.78$ was determined experimentally. Table 5-12 gives the value of β that is necessary for the calculated and CFD reported wall shear stresses to be the same, called β'. As the momentum flux ratio increases, the value of β' also increases.

5.3.8 Jet Spreading Rate

The spreading rate for a slot jet can be described as follows (Pope, 2000):

$$x_{1/2}/h = S(z/h) + A \tag{5-14}$$

where $x_{1/2}$ is the distance from the centerline where the air velocity is equal to half the centerline velocity. The constant A is related to the virtual origin of the jet. For a blunt, slot melt blowing die, Harpham and Shambaugh (1996) measured $S = 0.118$.

When a fiber is present at the center of the domain, the following equation must be used to calculate the spreading rate, since $x_{max} \neq 0$:

$$\frac{(x_{1/2} - x_{max})}{h} = S(z/h) + B \tag{5-15}$$

Table 5-13 gives the spreading rates for all cases at two positions. The first is halfway between the fiber capillaries at $y = L_c/2$, which is calculated using equation 5-14. The second position is at $y = 0$, where the fiber is present. For this position, equation 5-15

must be used to determine the spreading rate. For all cases, the spreading rate at $y = L_c/2$ is higher than at $y = 0$.

5.3.9 Temperature Field

In order to more closely model industrial melt blowing conditions, all simulations discussed in this paper were completed at non-isothermal conditions. The initial excess temperature of the air, Θ_{jo}, was 309 °C, while the initial temperature of the fiber was 295 °C. The air being entrained by the jet through the pressure outlet boundaries was 21 °C. Figure 5-29a shows the excess temperature at $y = L_c/2$ for all cases. Case A (air only) has the most rapid temperature decay. This is because the fiber present in cases B-G is hot and releases heat to the air. The temperature depends on the momentum flux ratio. The simulation with the highest momentum flux ratio, case G, also exhibits the highest temperature because the fiber is larger and can heat more of the air, which is moving more slowly for this case.

The mean velocity, fluctuations, and spreading rate have been discussed in the previous sections at both $y = 0$ and $y = L_c/2$. Figure 12b shows the contour plots of the excess temperature at z = 1 mm and z = 2.5 mm. At these positions, as well as throughout the computational domain, the excess temperature field is does not change significantly between different y-positions. Therefore, correlations for temperature decay at $y = L_c/2$ will also apply at y = 0, $x = x_{max}$. Experimental (Harpham and Shambaugh, 1997) and computational (see chapter 2) studies have shown that the temperature from a non-isothermal jet decays as follows:

$$\Theta/\Theta_{jo} = c^*(z/h)^d \qquad (15)$$

For cases A-G the excess temperature decay constants for $z \geq 5$ mm are given in Table 5-14. Harpham and Shambaugh (1997) experimentally measured c and d to be 1.2 and -0.615, respectively. As the momentum flux ratio increased, the decay exponent, d, decreased in magnitude because the fiber releases more heat to the air and therefore, slows the excess temperature decay.

5.4 Conclusions

Computational fluid dynamics is a useful tool that allows for the fast and efficient examination of the interactions between a fiber and turbulent air flow. These interactions are very important during the melt-blowing process. Both a single annular die, and an Exxon slot die were simulated with the inclusion of a fiber. Using simulations with several fiber flow rates and diameter profiles, it was found that the presence of the fiber has a significant effect on the air flow field close to the fiber edge for both geometries.

For the annular simulations, close to the die face the presence of the fiber decreases the maximum velocity reached by the axial air flow. Velocity profiles along the line $r = 0.4$ mm, which is close to the edge of the fiber, show significant differences between the cases in which the polymer is present and when it is not. If V_{max} is used to make the axial velocity dimensionless, the decay for the flow fields without fibers falls onto the same curve. The velocity decay for the flow fields that include fibers collapses onto a different curve. The fiber also has a dampening effect on the turbulence in the air flow field. Stress due to air drag on the fiber is greater when the ratio of air flow rate to polymer flow rate is increased. The spreading rate of the annular jet is increased by the

presence of a fiber. A comparison of entrainment coefficients shows that, over a much larger area, the presence of the polymer has little effect on the overall flow field.

For the slot die simulations, the maximum of the centerline velocity of the air is slightly increased relative to over the air only case at a position halfway between two fibers, $y = L_c/2$. The decay of the maximum air velocity, at $y = 0$, for all cases can be modeled with a single curve for all fiber-inclusive simulations. The simulation results showed the air profile to be non-uniform, so the drag force depends on the radial position on the fiber edge. The turbulence intensity is dampened by the presence of a fiber, while the dissipation of turbulence is increased. Lower turbulence intensity means lower velocity fluctuation which allows for higher air velocities to be used, and thus the presence of the fiber actually improves air conditions for the process of melt blowing. The jet spreading rate is increased by the presence of a fiber, and the spreading rate halfway between fibers is higher than the spreading rate at $y = 0$. As the momentum flux ratio increases, the rate of the excess temperature decay of the air is decreased.

The present work, using CFD to investigate the fiber-air interactions during the melt-blowing process, can open numerous areas of research with industrial impact. For example, simulations could be used to determine how the size, shape, and angle of the air jet (or jets) can alter the stress on the fiber and, thus, affect the diameter and strength of the fiber. These simulations could be done for annular dies, slot dies, swirl dies, or any other geometry. In addition to the air jet geometry, the melt-blowing conditions could also be altered. For example, all the simulations discussed herein were performed for an air temperature of 648 K (a temperature based on actual experimental conditions); however, it would be of interest to examine how changing the air temperature alters the

stress on the fiber and, thus, the final diameter and strength of the fiber. Such studies could determine an optimal temperature for the melt-blowing process.

5.5 Nomenclature

a, b	coefficients for the air velocity decay when the decay is made dimensionless with the nominal discharge velocity (equation 5-3)
a', b'	coefficients that characterize the air velocity decay when the decay is made dimensionless using the maximum air velocity
A, B, C	domain edges to indicate different cell spacing (see Figure 5-19a)
A	constant in slot die spreading rate equation (equation 5-14)
b	jet slot width at die face, mm
c, d	coefficients that characterize the jet spreading rate (equation 5-8)
$C_{\varepsilon 1}$, $C_{\varepsilon 2}$	parameters for the dissipation equation in the RSM model
C_{f}	drag coefficient
d_{f}	fiber diameter, μm or mm
D_{c}	diameter of polymer capillary, mm
D_{i}	inner diameter of annular orifice, mm
D_{o}	outer diameter of annular orifice, mm
h	distance from the beginning of one air jet to the end of the next air jet, mm
k	turbulent kinetic energy, $(1/2\overline{u_i u_i})$, $\mathrm{m^2/s^2}$
L	length of air annulus, mm
L_{c}	domain width in y-direction, mm
m_{a}	mass flow rate of air, g/min
m_{f}	mass flow rate of polymer, g/min

M_e	mass flow rate of entrained air, kg/s
M_o	mass flow rate of air through jet orifice, kg/s
$M(z)$	mass flow rate per length L of the jet, kg/s
N	exponent used to calculate drag coefficients (equation 5-1)
q	turbulence intensity, $100*\left(\overline{u_i^2}\right)^{1/2}/V_{jo}$
$\overline{q}$	momentum flux ratio (equation 5-9)
Q	polymer flow rate, cm^3/min
Q_{air}	air flow rate, slpm
r	spatial coordinate, mm
Re_{DP}	Reynolds number of air based on fiber diameter
R^2	coefficient of determination for the evaluation of regression analysis
R(z)	fiber radius as a function of z, mm
$r_{1/2}$	distance from centerline where mean velocity is half the magnitude of the maximum velocity, mm
r_{max}	distance from centerline where mean velocity is maximum, mm
S	momentum spreading rate (Equation 5-14 and 5-15)
S'	spreading rate of x_{max} (Equation 5-10)
u_i	velocity fluctuations, m/s
$v_{a,eff,PAR}$	the difference between the fiber and air velocity parallel to the filament axis, m/s
V_{az}	air velocity in the z-direction, m/s
$V_{az\text{-}max}$	maximum air velocity in the z-direction along the r = 0.4mm line, m/s
V_{fz}	fiber velocity (also, the velocity of the left boundary in Fig. 2) in the z-direction, m/s

V_{jo} nominal discharge velocity defined as the volumetric air flow divided by the area available for flow, m/s

x, y, z spatial coordinates, mm

z_{max} merging distance below the die face at which the dimensionless mean velocity reaches a maximum

Greek Characters

β coefficient in Matsui's correlation for the drag coefficient (equation 5-1)

ε dissipation rate of turbulent kinetic energy, m^2/s^3

μ viscosity, kg/(m•s)

μ_a air viscosity, kg/(m•s)

π trigonometric pi, π=3.1415926

ρ_a air density, kg/m^3

ρ_f polymer density, kg/m^3

θ spatial coordinate, radians

θ angle between slot jets and the die face, radians

Θ excess air temperature defined as the difference between the ambient temperature and the air jet temperature, °C

Θ_{jo} initial air excess temperature, °C

τ_w wall shear stress, Pa

Ψ entrainment coefficient

5.6 References

Breese, Randall R., Ko, Wen-Chien, Fiber Formation During Melt Blowing, *International Nonwovens Journal*, **2003**, 21-28.

Fluent User's Guide; Fluent Inc.: Lebanon, NH, 2007.

Gambit Modeling Guide; Fluent Inc.: Lebanon, NH, 2007.

Harpham, A.S.; Shambaugh, R.L Flow Field of Practical Dual Rectangular Jets. *Ind. Eng. Chem. Res.,* **1996**, *35*, 3776-3781.

Harpham, A.S.; Shambaugh, R.L Velocity and Temperature Fields of Dual Rectangular Jets. *Ind. Eng. Chem. Res.,* **1997**, *36*, 3937-3943.

Hietel, D,; Marheineke, N., Modeling and Numerical Simulation of Fiber Dynamics. *Proc. Appl. Math. Mech.* **2005**, *5*, 667-670.

Ju, Y. D., Shambaugh, R. L., Air Drag on Fine Filaments at Oblique and Normal Angles to the Air Stream, *Polymer Engineering and Science*, **1994**, *34* (12), 958-964.

Majumdar, B.; Shambaugh, R. L. Air Drag on Filaments in the Melt Blowing Process. *J. Rheol.* **1990**, *34* (4), 591-601.

Majumdar, B., Shambaugh, R. L. Velocity and Temperature Effects of Annular Jets. *Ind. Eng. Chem. Res.* **1991,** *28*, 5125-5138.

Marla, V.T.; Shambaugh, R.L. Three-Dimensional Model of the Melt-Blowing Process. *Ind. Eng. Chem. Res.*, **2003**, *42* (6), 6993-7005.

Marla, V.; Shambaugh, R.L.; Papavassiliou, D.V., Modeling the Melt Blowing of Hollow Fibers. *Ind. Eng. Chem. Res.,* **2006**, *45*(1), 407-415.

Matsui, M., Air Drag on a Continuous Filament in Melt Spinning. *Trans. Soc. Rheol.* **1976**, *20* (3), 465-473.

Miller, C., Effect of Filament Drawdown on Aerodynamic Drag and Heat Transfer in Fiber Spinning. *AICHE Journal*, **2004**, *50* (5), 898-905.

Moore, E.M., Shambaugh, R.L., Papavassiliou, D.V. Analysis of Isothermal Annular Jets: Comparison of Computational Fluid Dynamics and Experimental Data, *Journal of Applied Polymer Science*, **2004**, *94*, 909-922.

Pope, S. B. *Turbulent Flows*; Cambridge University Press: Cambridge, U.K., 2000; pp 134-135.

Rao, R. S.; Shambaugh, R. L. Vibration and Stability in the Melt Blowing Process. *Ind. Eng. Chem. Res.* **1993**, *32*(12), 3100-3111.

Schetz, J.A.; Padhye, A. Penetration and Breakup of Liquids in Subsonic Airstreams. *AIAA Journal*, **1977**, *15*(10), 1385-1390.

Uyttendaele, M.A., Shambaugh, R.L. The Flow Field of Annular Jets at Moderate Reynolds Numbers. *Ind. Eng. Chem. Res.*, **1989**, *28*, 1735-1740.

Uyttendaele, M. A. J.; Shambaugh, R. L. Melt Blowing: General Equation Development and Experimental Verification. *AIChE J.* **1990**, *36*(2), 175-186.

Wang, K.; Ke, Q. Computational Simulation of the Fiber Movement in the Melt-Blowing Process, *Ind. Eng. Chem. Res.*, **2005**, *44*(11), 3912-3917.

Wang, K.; Ke, Q. Empirical Formulas for Distributions of Air Velocity/Temperature Along the Spinline of a Dual Slot Die. *Polymer Eng. Sci.*, *45*(8), **2005**, 1092-1097.

Table 5-1: Polymer Flow Rates and Initial Air Velocities Used in the Annular Jet Simulations

	Q (cm^3/min)	V_o (m/s)
Case 1	0	110.26
Case 2	0.329	110.26
Case 3	0.4935	110.26
Case 4	0.658	110.26
Case 5	0	57.93
Case 6	0.658	57.93
Case 7	0	150.00
Case 8	0.658	150.00
Case 9	0	200.00
Case 10	0.658	200.00

Table 5-2: Grid and Computational Requirements for the Simulations in Figure 5-4

Number of Grid Cells	Number of Iterations	CPU Time
72,534	6,878	3:10
121,137	7,510	6:50
290,136	16,946	57:30
483,702	19,603	115:30

Table 5-3: Velocity Decay Constants when V_{jo} is used to Nondimensionalize the Velocity (as Defined in Equation 5-3)

Applicable Cases	a	b	R^2
1	4.176	-0.953	0.996
2, 3, 4	3.288	-0.902	0.998
6	1.536	-0.801	0.999

Table 5-4: Velocity Decay Constants when $V_{az\text{-}max}$ is used to Nondimensionalize (as defined in Equation 5-3)

Applicable Cases	a'	b'	R^2
1, 5	3.579	-0.902	0.985
2, 3, 4, 6	3.115	-0.922	0.984

Table 5-5: Percent Difference Between Calculated Drag Force and Value from Simulations

Cases	% Difference
1, 2	16.36
1, 3	18.75
1, 4	23.12
5, 6	45.88
7, 8	2.72
8, 9	1.76

Table 5-6: β Values for Calculated Drag Force To Be Within 1% of the Simulation Results

Cases	n	β
1, 2	0.61	0.93
1, 3	0.61	0.96
1, 4	0.61	1.01
5, 6	0.61	1.44
7, 8	0.61	0.80
9, 10	0.61	0.79

Table 5-7: Spreading Rate Constants for Equation 5-8

	c	d
Case 1	0.0675	0.0901
Case 2	0.0818	0.134
Case 3	0.0891	0.0267
Case 4	0.0919	-0.0398
Case 5	0.0670	0.308
Case 6	0.0808	0.354

Table 5-8: Polymer Flow Rates and Initial Air Velocities Used in the Slot Jet Simulations

Case	m_f (g/min)	$V_{f\text{-}die}$ (m/s)	Q_{air} (slpm)	m_a (g/min)	$V_{a\text{-}die}$ (m/s)	Momentum Flux Ratio ($\bar{q}$)
A	0	0	100	120	33.7	N/A
B	0.55	0.058	300	360	101.1	4.87e-4
C	0.55	0.058	200	240	67.4	1.09e-3
D	0.275	0.0289	100	120	33.7	1.09e-3
E	0.55	0.058	100	120	33.7	4.38e-3
F	1.1	0.1156	100	120	33.7	1.74e-2
G	0.55	0.058	50	60	16.85	1.74e-2

Table 5-9: Simulation Grid and the Computational Requirements for the Simulations Shown in Figure 5-20

Number of Grid Cells	Number of Iterations	Computation Time (hrs)
653,090	15,177	15
1,023,162	18,736	29
2,640,102	48,000	195

Table 5-10: Velocity Decay Constants for $y = 0$, $x = x_{max}$ starting at $z > 10$mm

Case	*a*	*b*	R^2
B	1.2613	-0.5813	0.9979
C	1.201	-0.5516	0.9989
D	1.201	-0.5434	0.9993
E	1.0243	-0.509	0.9975
F	1.0566	-0.5007	0.9993
G	0.9938	-0.5405	0.9985

Table 5-11: Wall Shear Stress Deviation

Case	Maximum Coefficient of Variation	Average Coefficient of Variation
B	0.562	0.117
C	0.572	0.098
D	0.520	0.119
E	0.542	0.116
F	0.711	0.102
G	0.517	0.087

Table 5-12: Comparison of Calculated Drag Force and Simulation Results

Cases	Percent Difference	β'
A,D	5.47	0.825
A,E	18.66	0.956
A,F	34.25	1.186

Table 5-13: Spreading Rates for $z \geq 30$ mm

Case	$S_{y=0,\, x=xmax}$	$S_{y=Lc/2}$
A	N/A	0.1091
B	0.0922	0.1357
C	0.1096	0.1159
D	0.1296	0.1398
E	0.1295	0.1407
F	0.1197	0.1449
G	0.1255	0.1369

Table 5-14: Excess Temperature Decay Constants for at $z \geq 5$ mm

Case	*c*	*d*	R^2
A	0.9961	-0.5911	0.9831

B	1.1053	-0.4715	0.9987
C	1.0937	-0.4566	0.9959
D	1.0085	-0.3735	0.9994
E	1.0185	-0.3630	0.9992
F	1.0196	-0.3374	0.9989
G	0.9981	-0.2882	0.9956

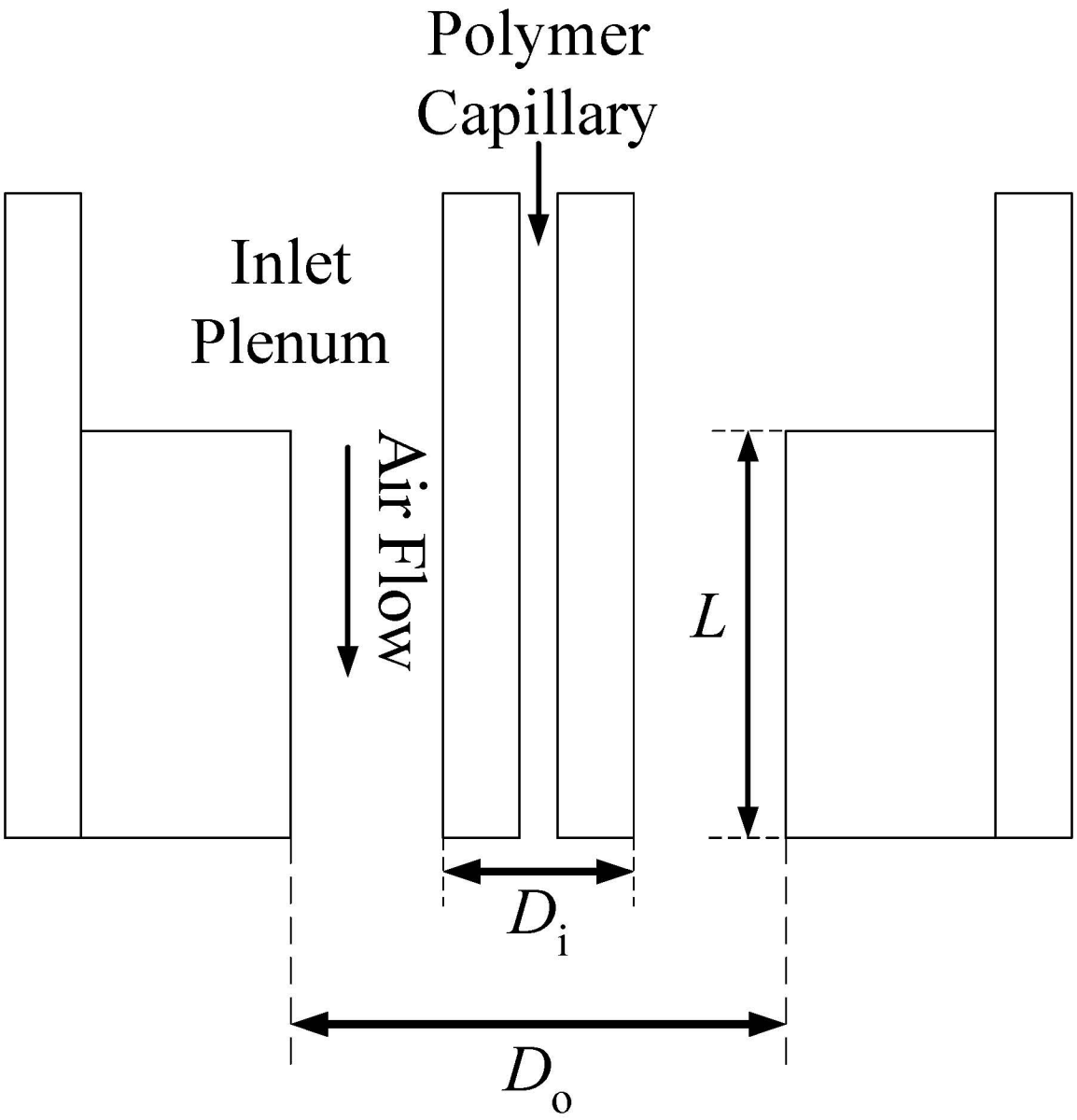

Figure 5-1. Cross-sectional view of an annular melt-blowing die.

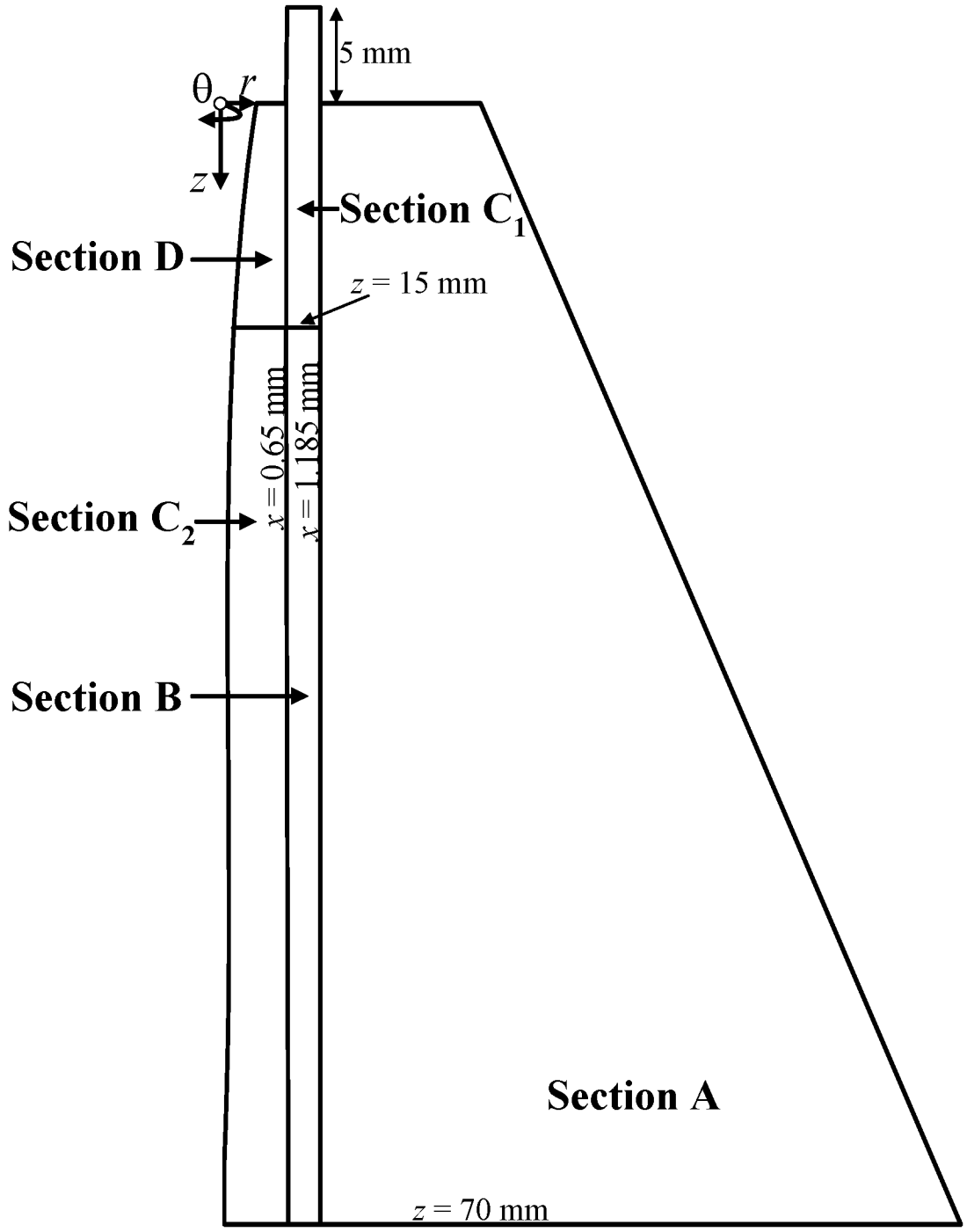

Figure 5-2. Computational domain and grid refinement regions. In section A, the outermost region, the length of the sides of the quadrilateral cells is 0.1 mm. Sections B, C_1 and C_2, and D have, respectively, cell sides of 0.05, 0.025, and 0.0125 mm. The curved left side of the domain corresponds to the surface of the polymer fiber.

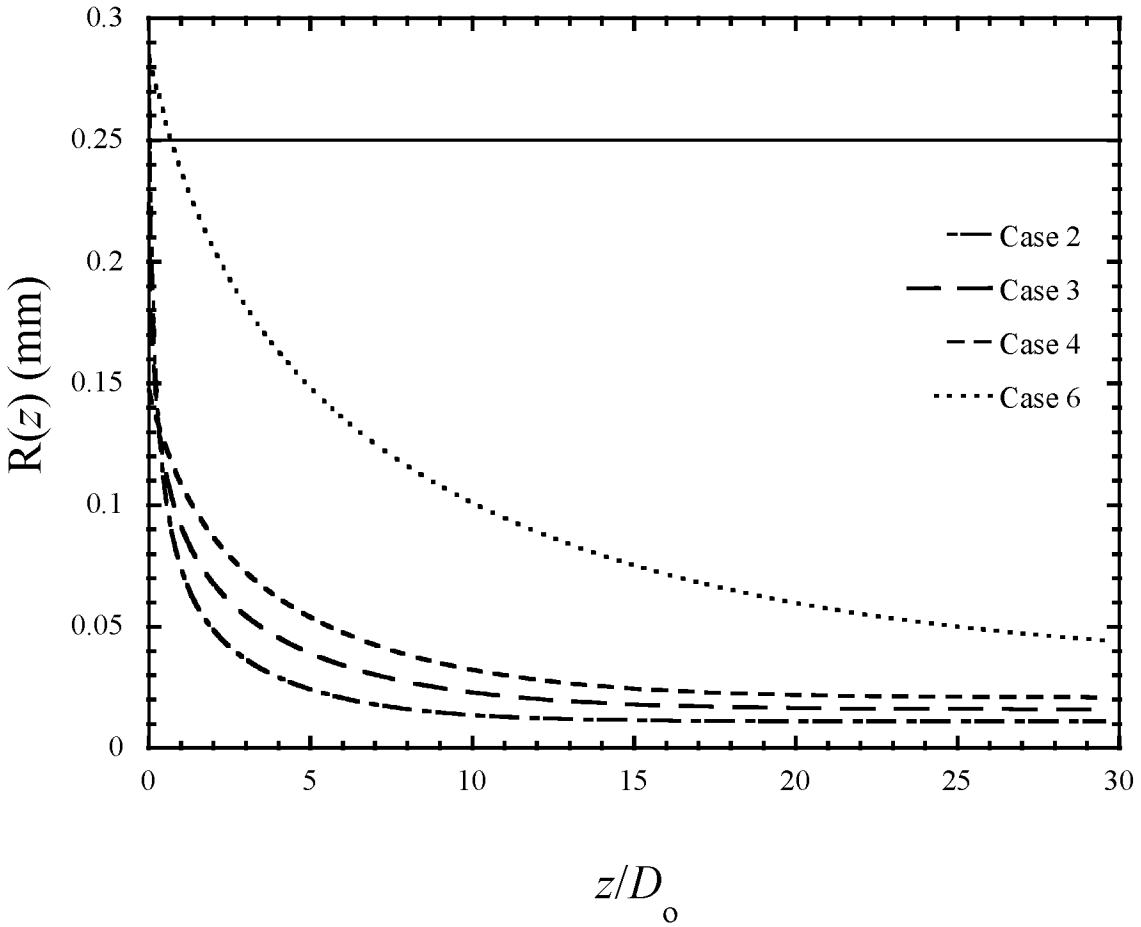

Figure 5-3a. The fiber radius as a function of position below the die. The fiber radius establishes the left boundary of the computational domain seen in Figure 5-2. The horizontal solid line designates the radius of a cylinder with diameter equal to 5 mm and constant velocity $V_{fz} = 5$ m/s.

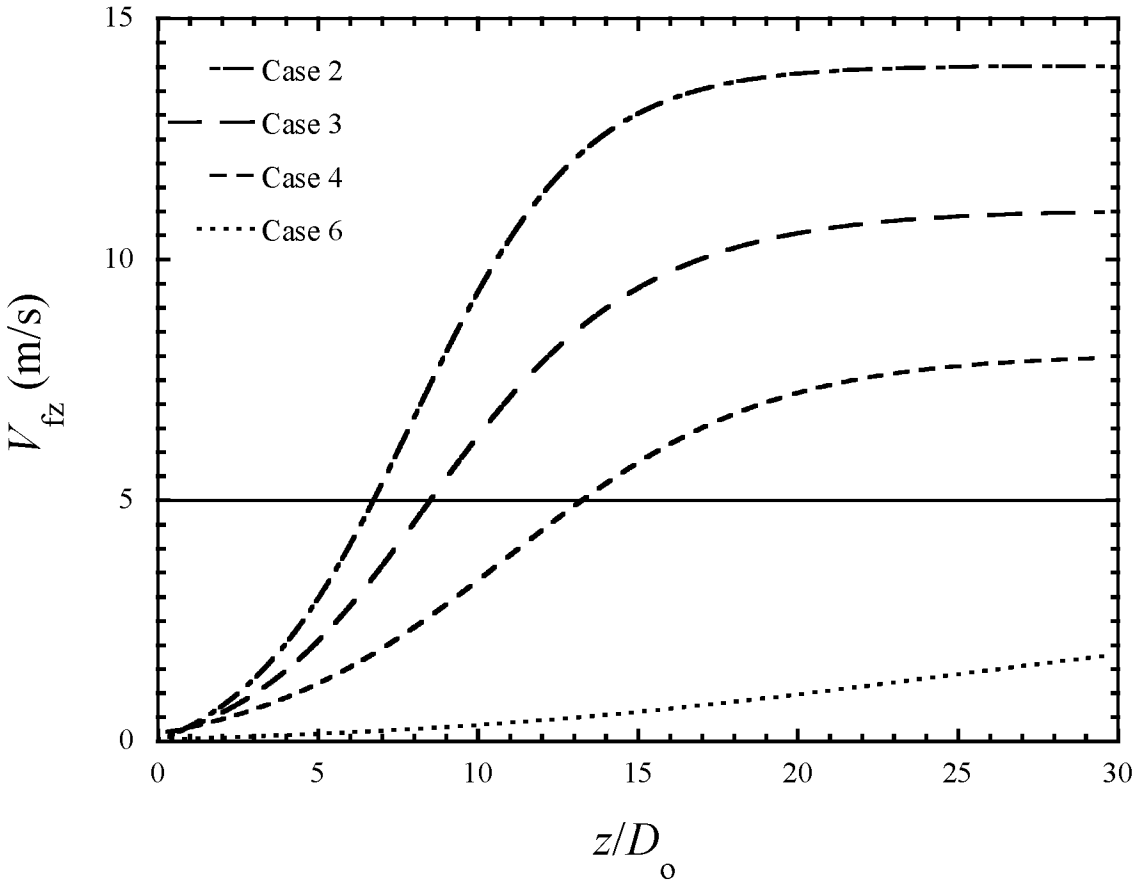

Figure 5-3b. The fiber radius as a function of position below the die. The horizontal solid line designates the velocity of a cylinder with diameter equal to 5 mm and constant velocity $V_{fz} = 5$ m/s.

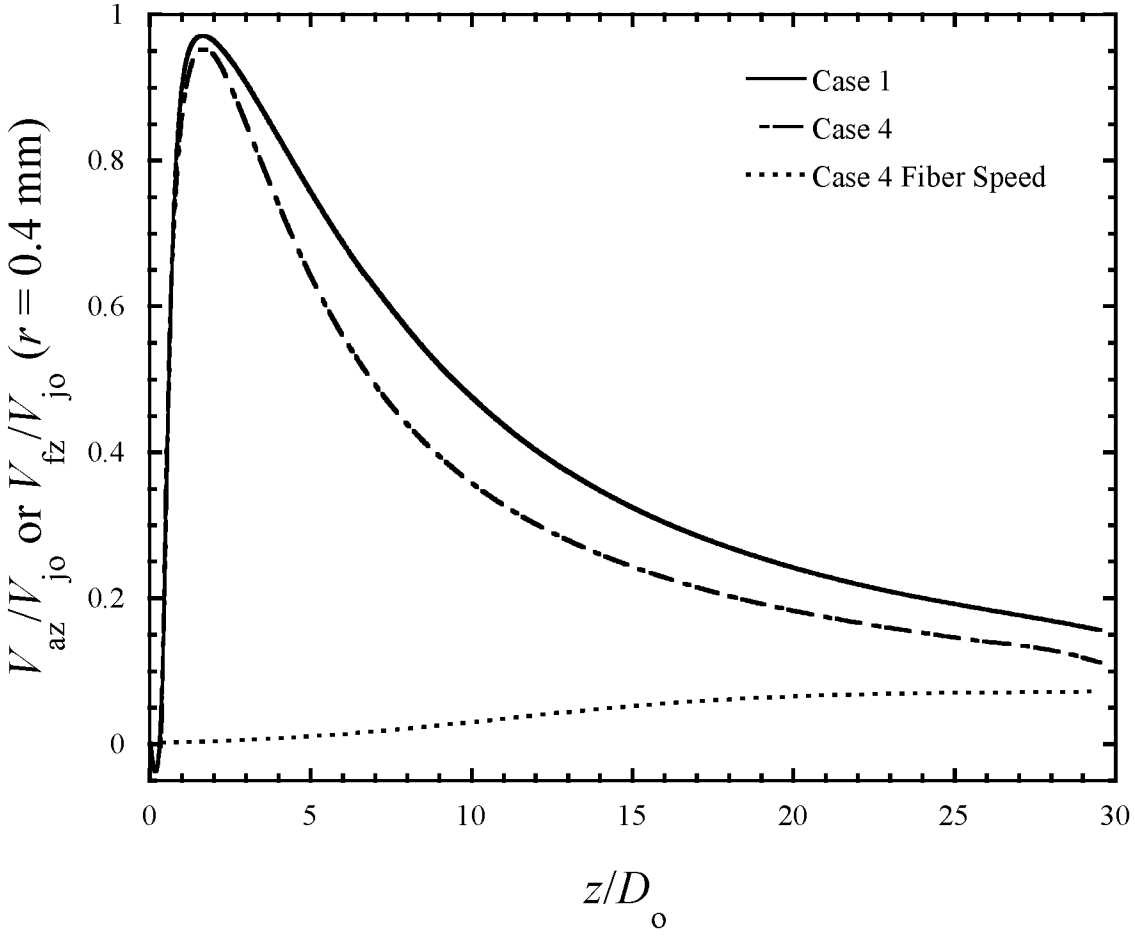

Figure 5-3c. The fiber velocity for Case 4 compared with the axial air velocity at r = 0.4 mm for Case 1 and Case 4.

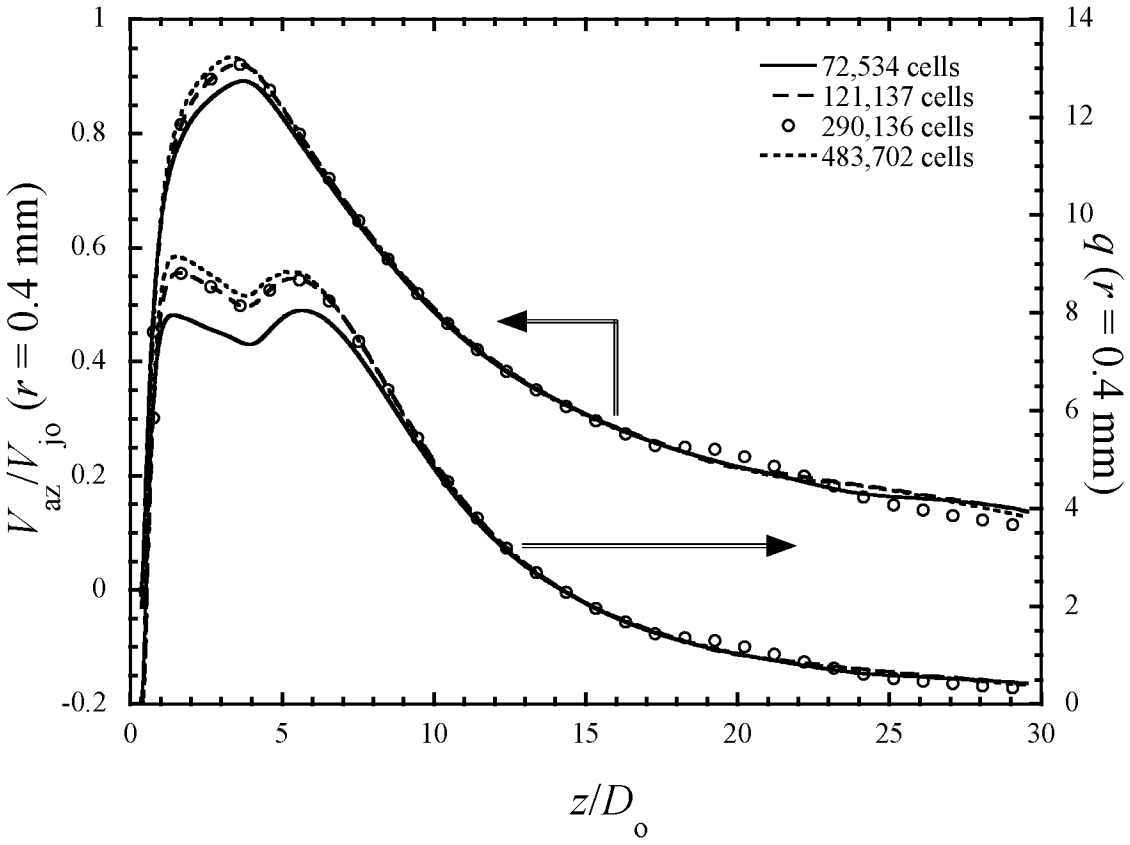

Figure 5-4. The dimensionless axial velocity and turbulence intensity for simulations run under the same (case 4) conditions but with different grid refinements.

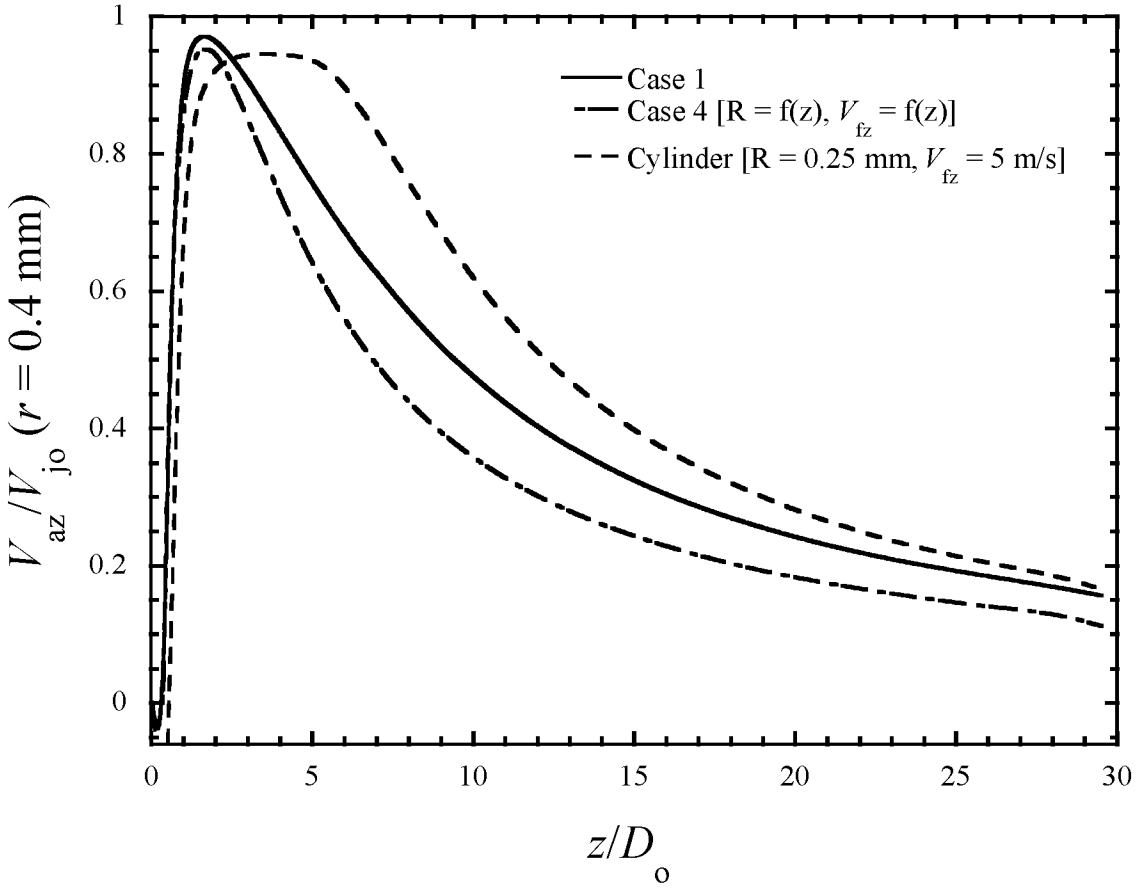

Figure 5-5. Comparison of axial velocity at r = 0.4 mm for cases 1 and 4 and a cylinder with a radius of 0.25 mm. Case 4 is based on the model by Marla and Shambaugh (2003).

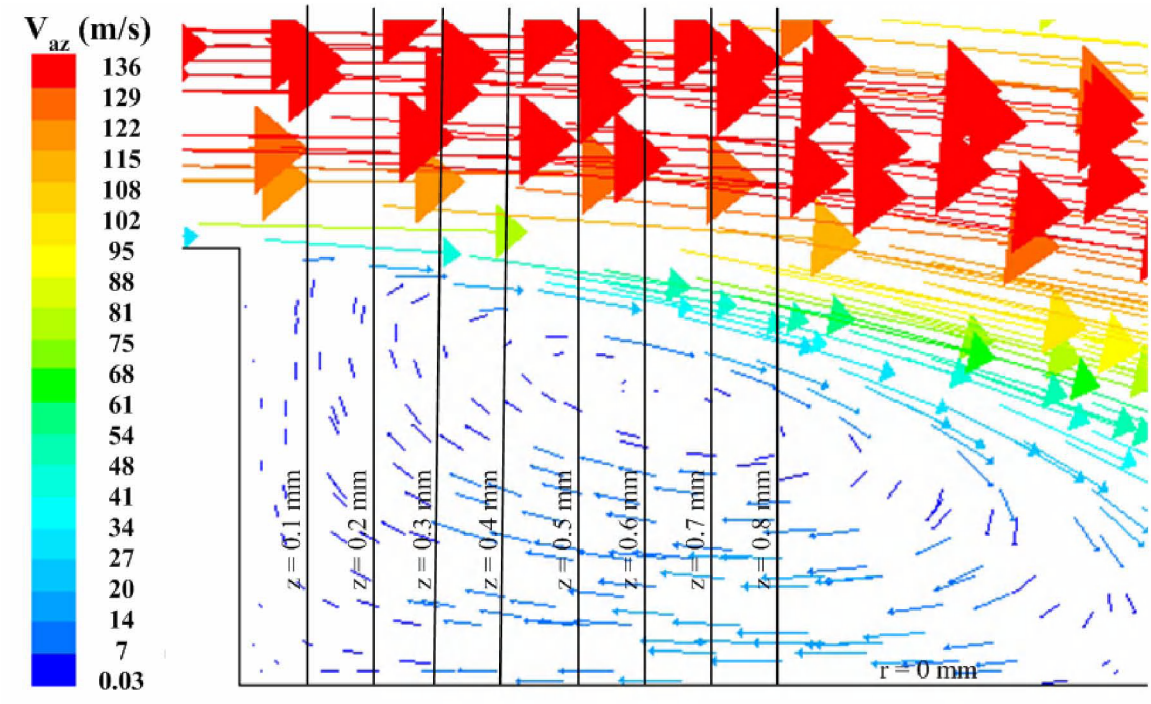

Figure 5-6a. Axial velocity vector plot in the recirculation area for case 1.

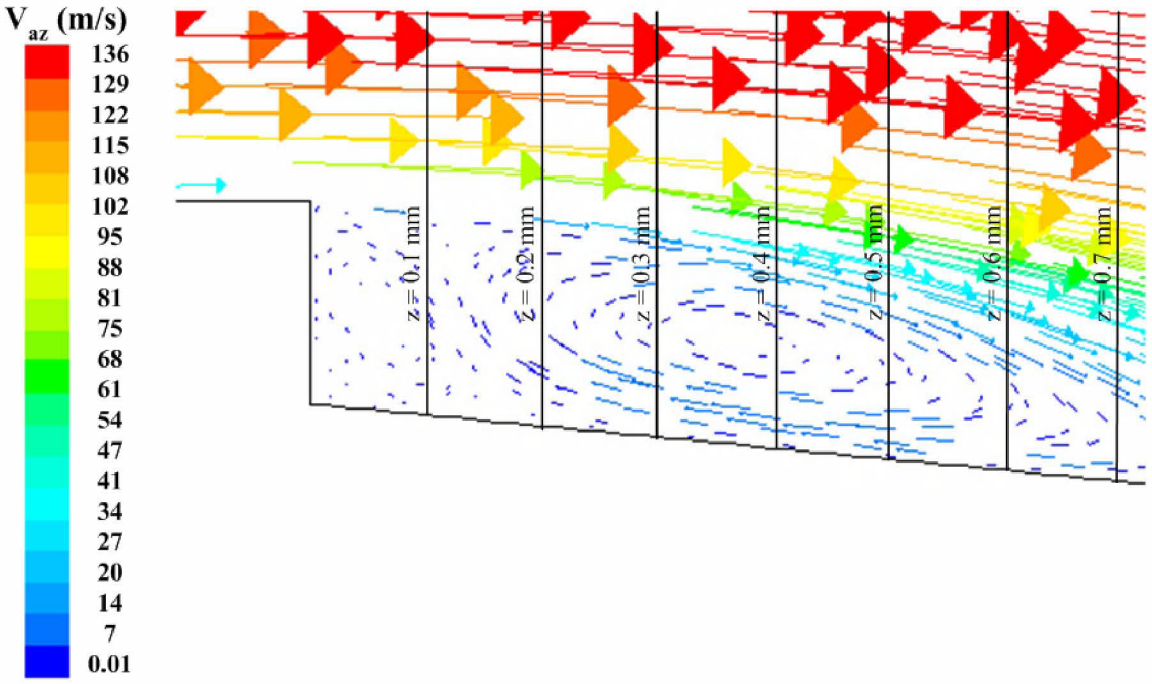

Figure 5-6b. Axial velocity vector plot in the recirculation area for case 4.

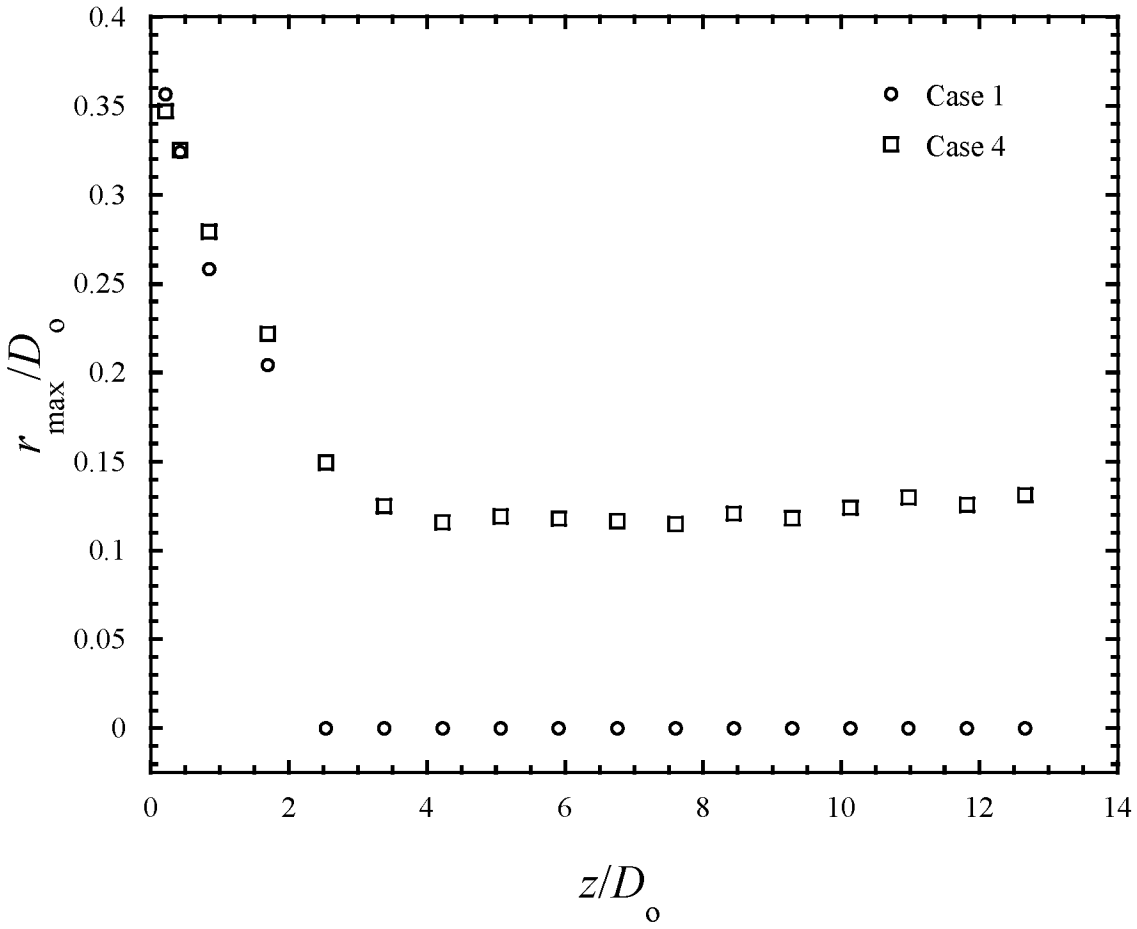

Figure 5-7. Comparison of the position of maximum axial velocity for cases 1 and 4.

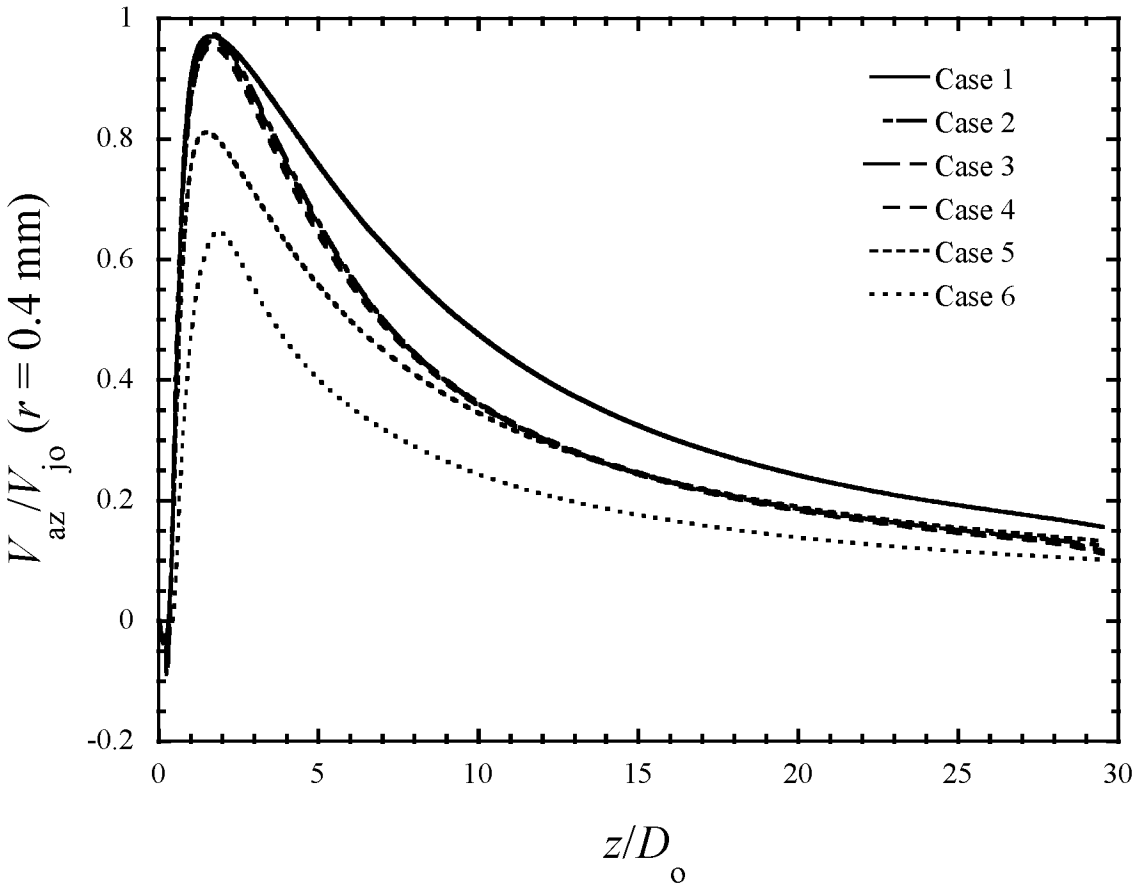

Figure 5-8. Comparison of axial velocity at r = 0.4 mm for all simulations.

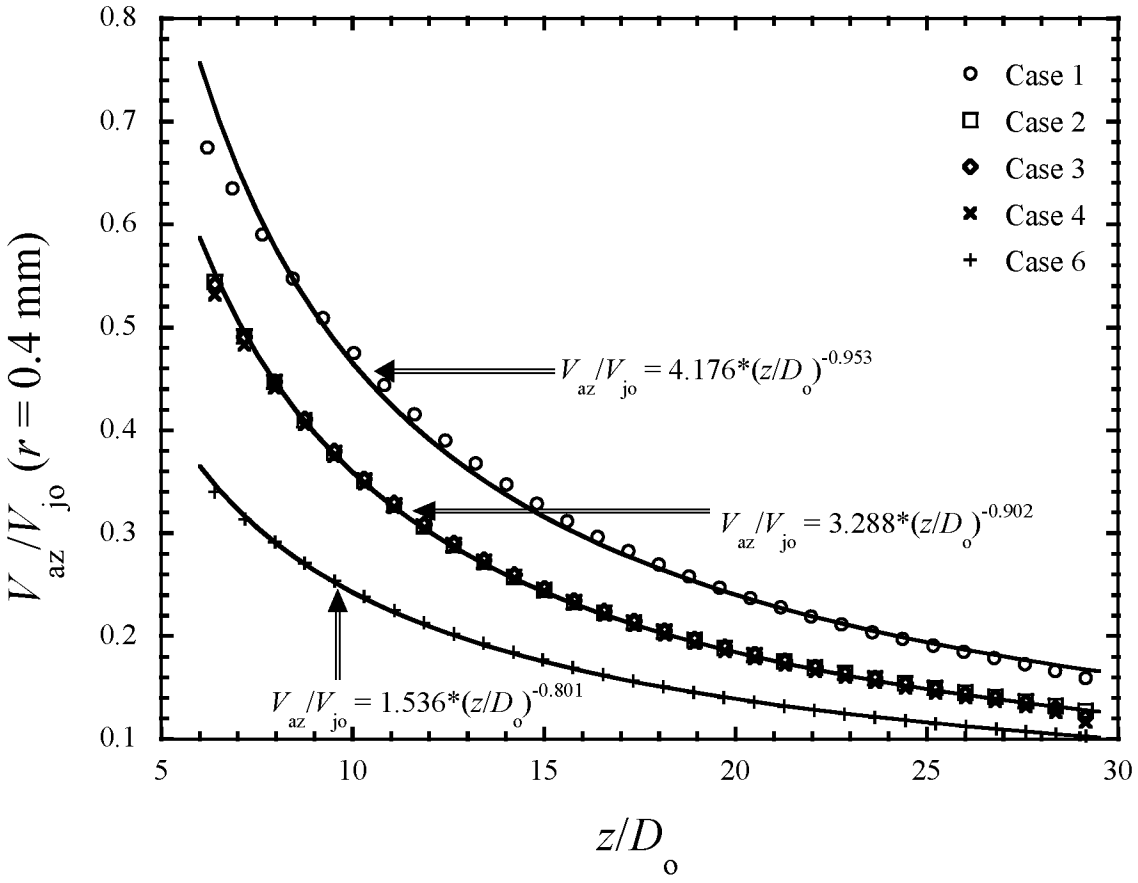

Figure 5-9a. Comparison of axial velocity decay at r = 0.4 mm. V_{jo} was used to nondimensionalize V_{az}. The fit for case 1 is $V_{az}/V_{jo} = 4.176*(z/D_o)^{-0.953}$ (R^2 = 0.996), the fit for the case 2, 3, and 4 simulations is $V_{az}/V_{jo} = 3.288*(z/D_o)^{-0.902}$ (R^2 = 0.998), and the fit for case 6 is $V_{az}/V_{jo} = 1.536*(z/D_o)^{-0.801}$ (R^2 = 0.999).

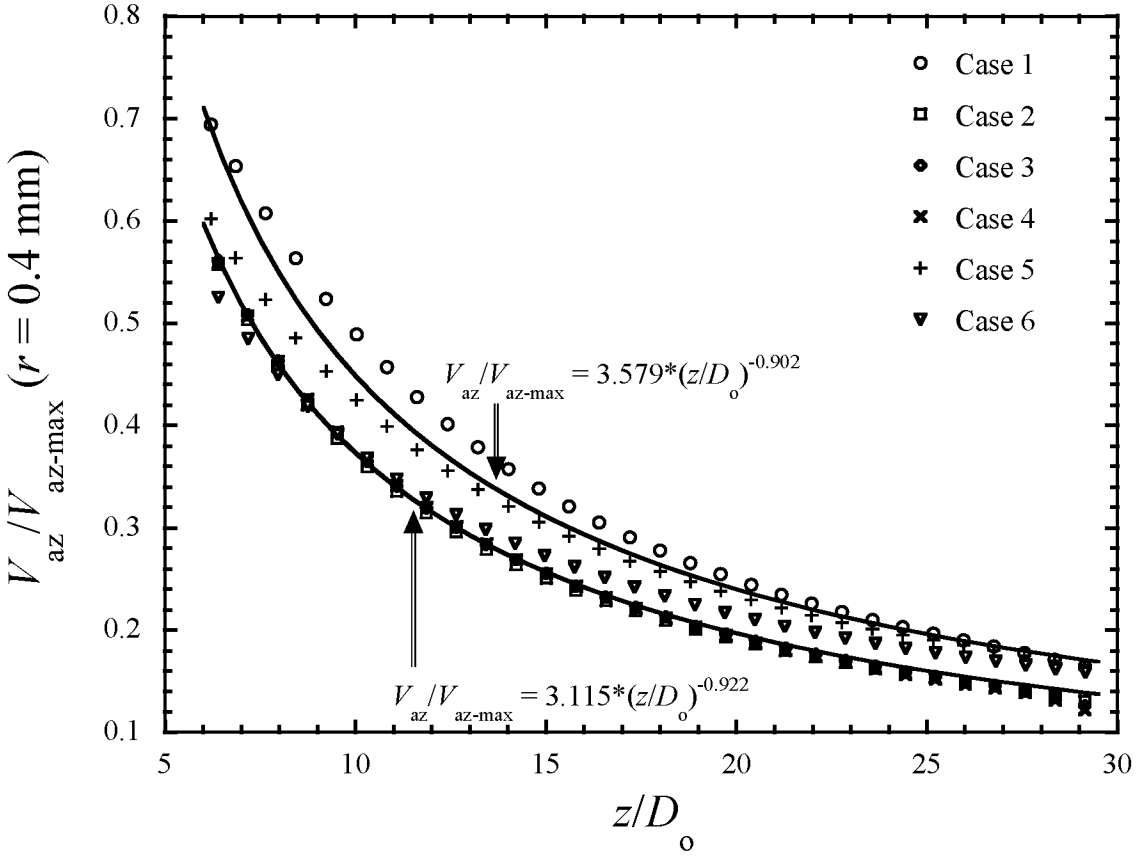

Figure 5-9b. Comparison of axial velocity decay at r = 0.4 mm. $V_{az\text{-}max}$, rather than V_{jo}, was used to nondimensionalize the ordinate. The fit for the simulations without polymer is $V_{az}/V_{az\text{-}max} = 3.115*(z/D_o)^{-0.922}$ (R^2 = 0.985), the fit for the simulations that include the polymer is $V_{az}/V_{az\text{-}max} = 3.579*(z/D_o)^{-0.902}$ (R^2 = 0.984).

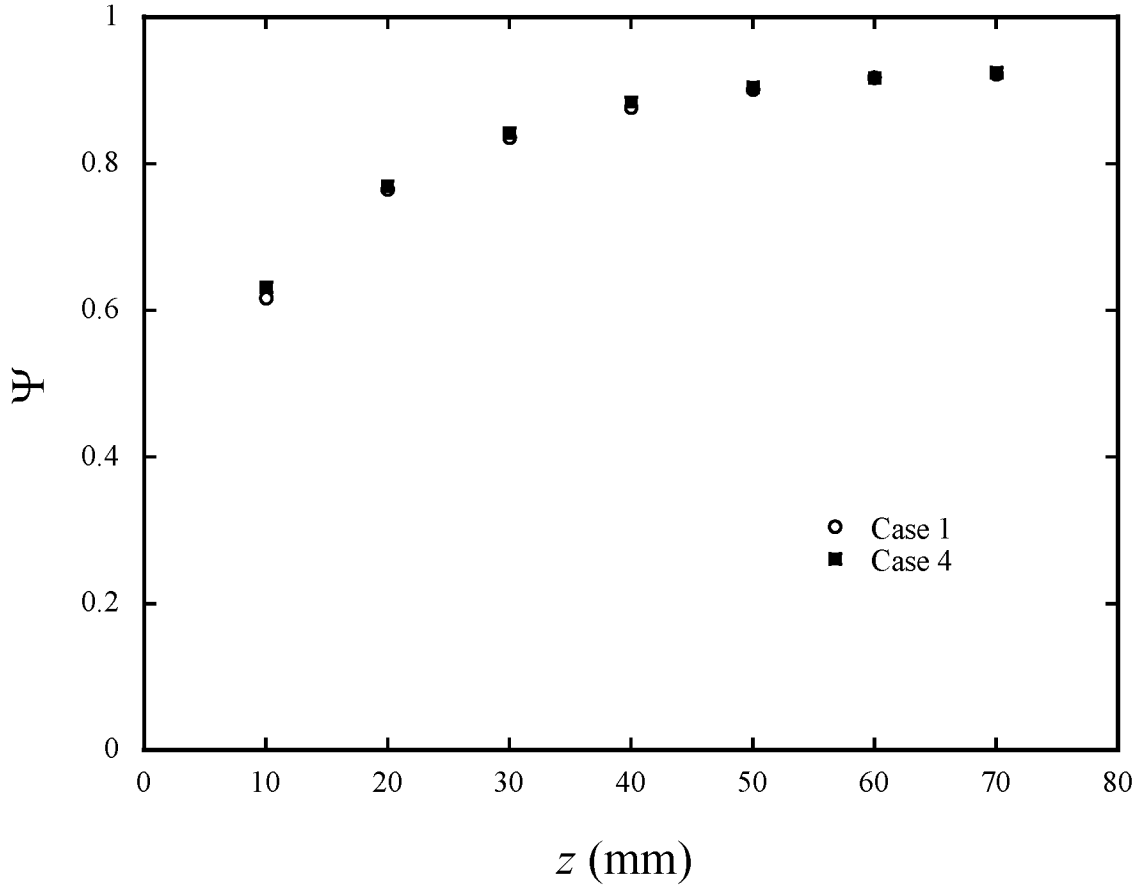

Figure 5-10. Comparison of the entrainment coefficients for cases 1 and 4.

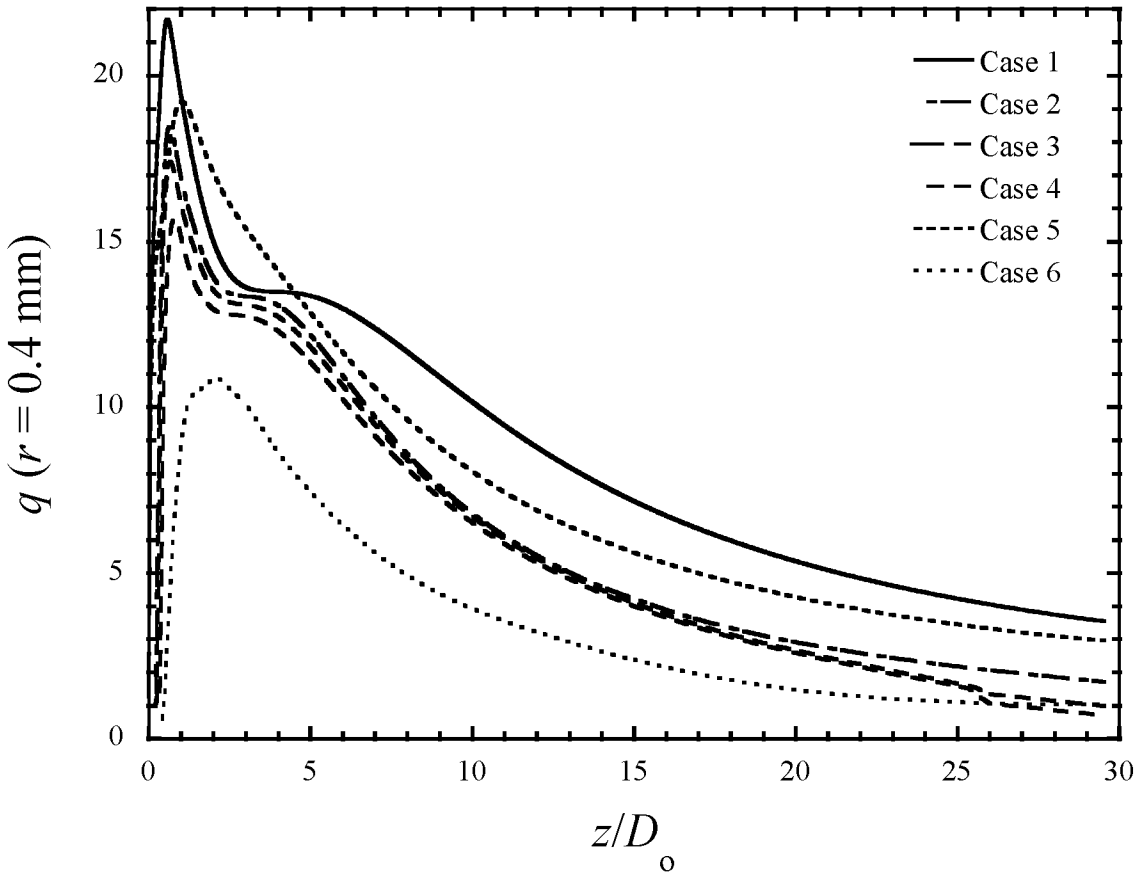

Figure 5-11. Comparison of the turbulence intensity of cases 1-6 at r = 0.4 mm.

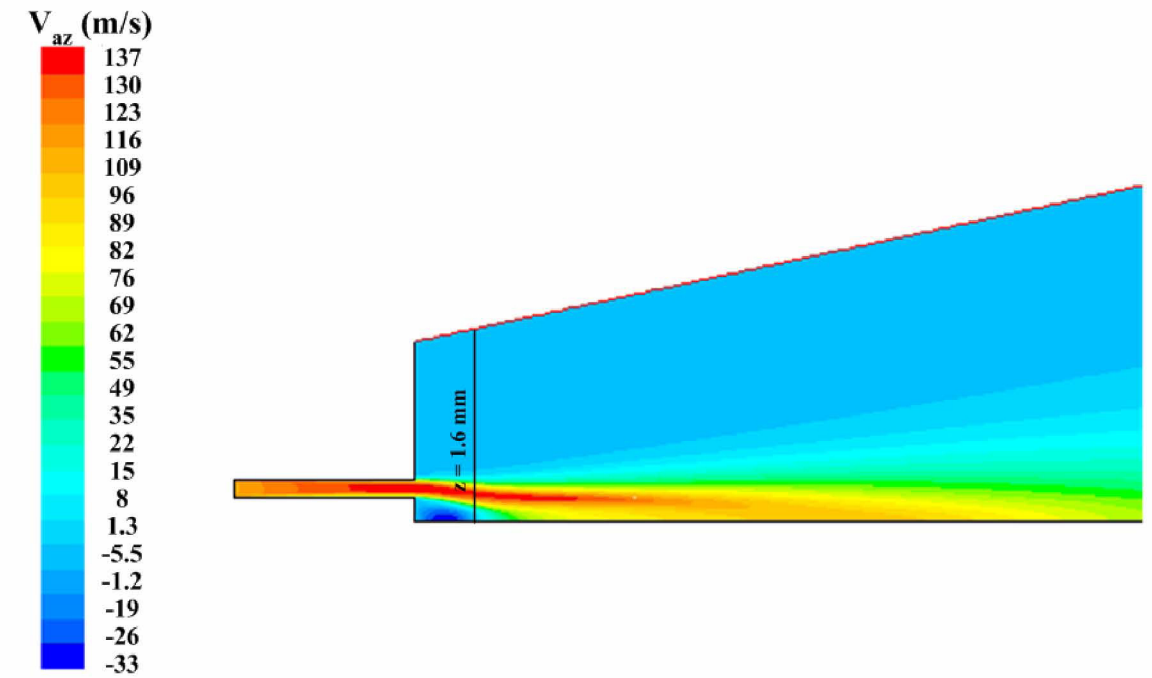

Figure 5-12a. The axial velocity contour plots showing the z = 1.6 mm line for case 1.

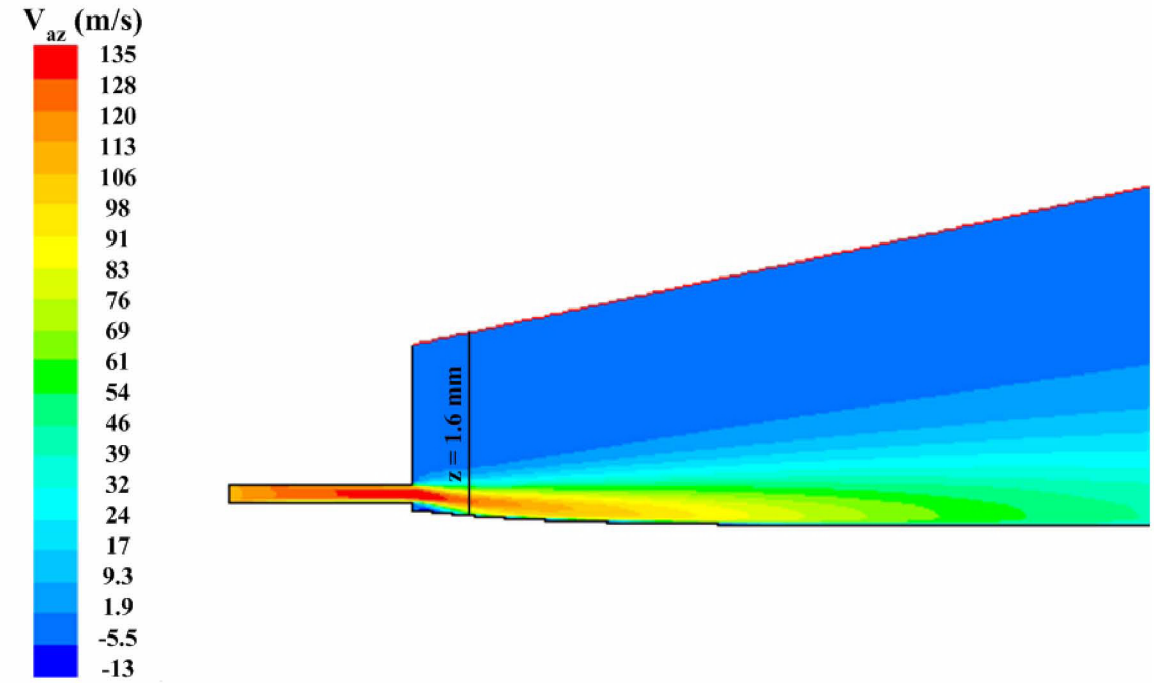

Figure 5-12b. The axial velocity contour plots showing the z = 1.6 mm line for case 4.

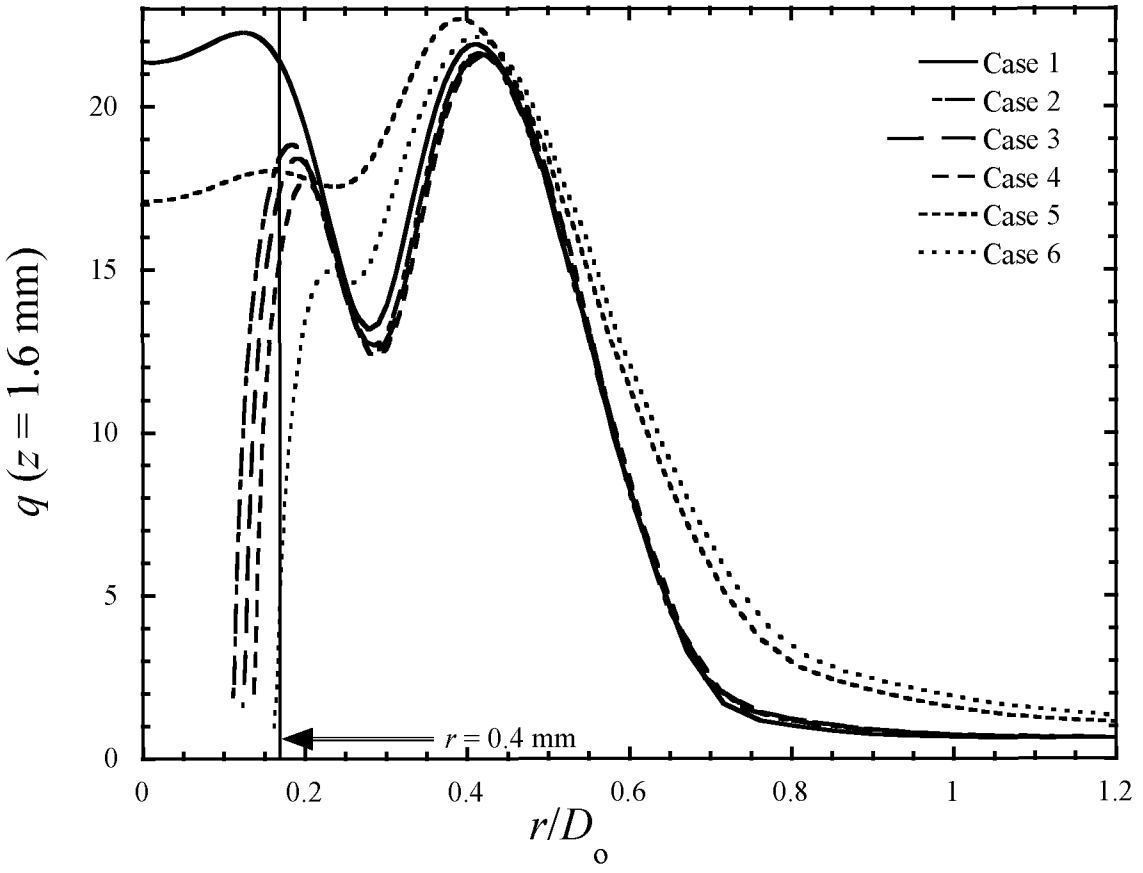

Figure 5-13a. The turbulence intensity profiles for all simulations. The profiles are for z = 1.6 mm.

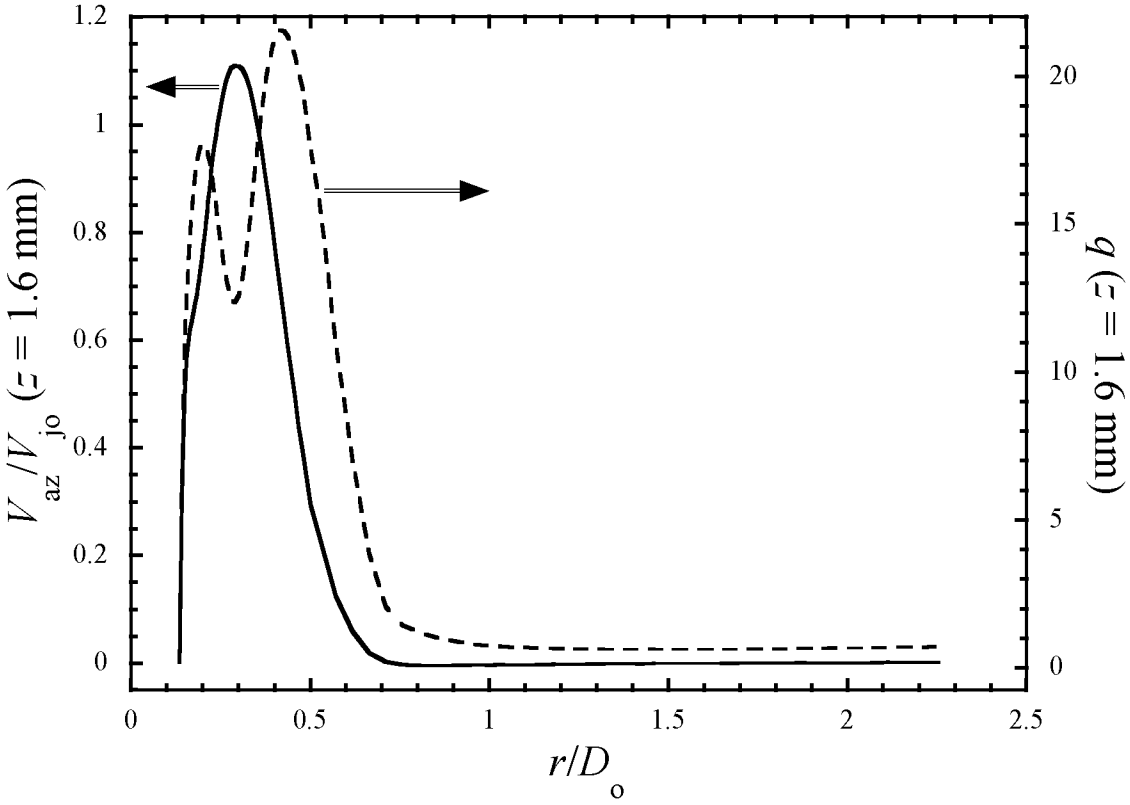

Figure 5-13b. A comparison at z = 1.6 mm between the turbulence intensity and the axial velocity for case 4.

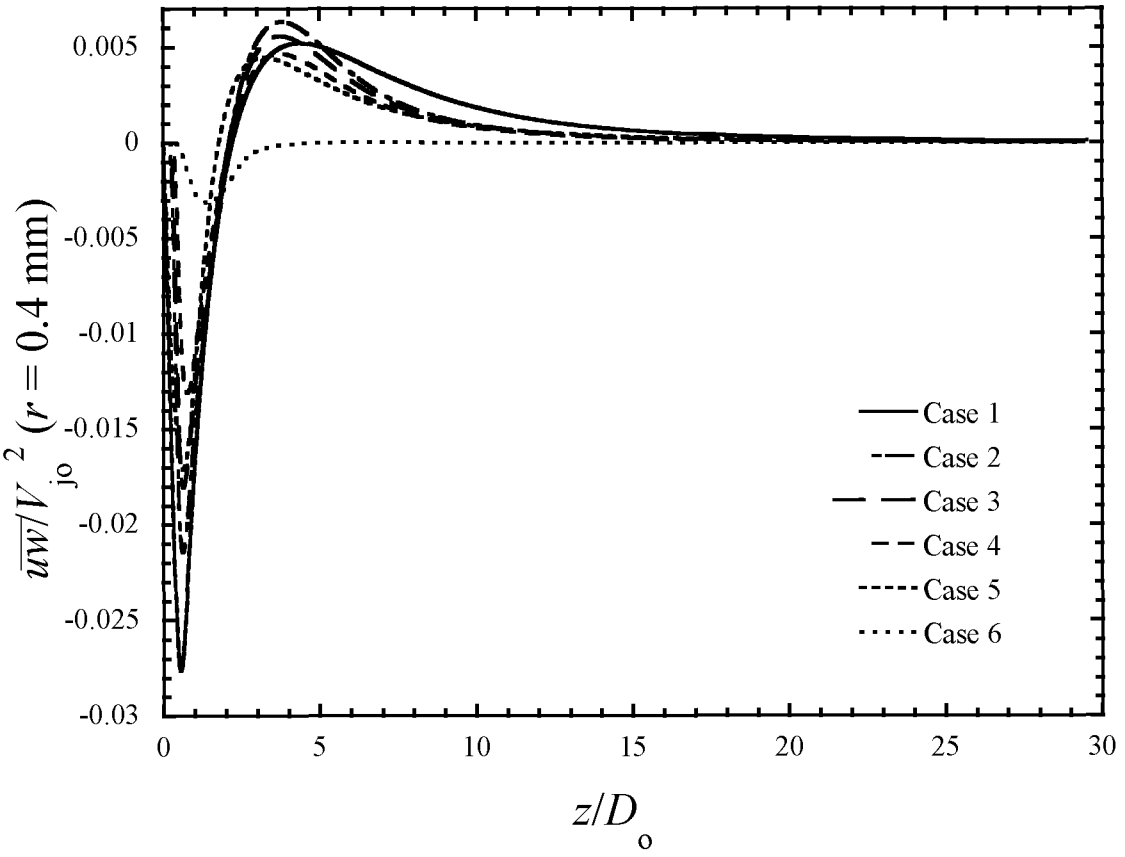

Figure 5-14. Comparison of $\overline{uw}$ Reynolds stresses of cases 1-6 at r = 0.4 mm.

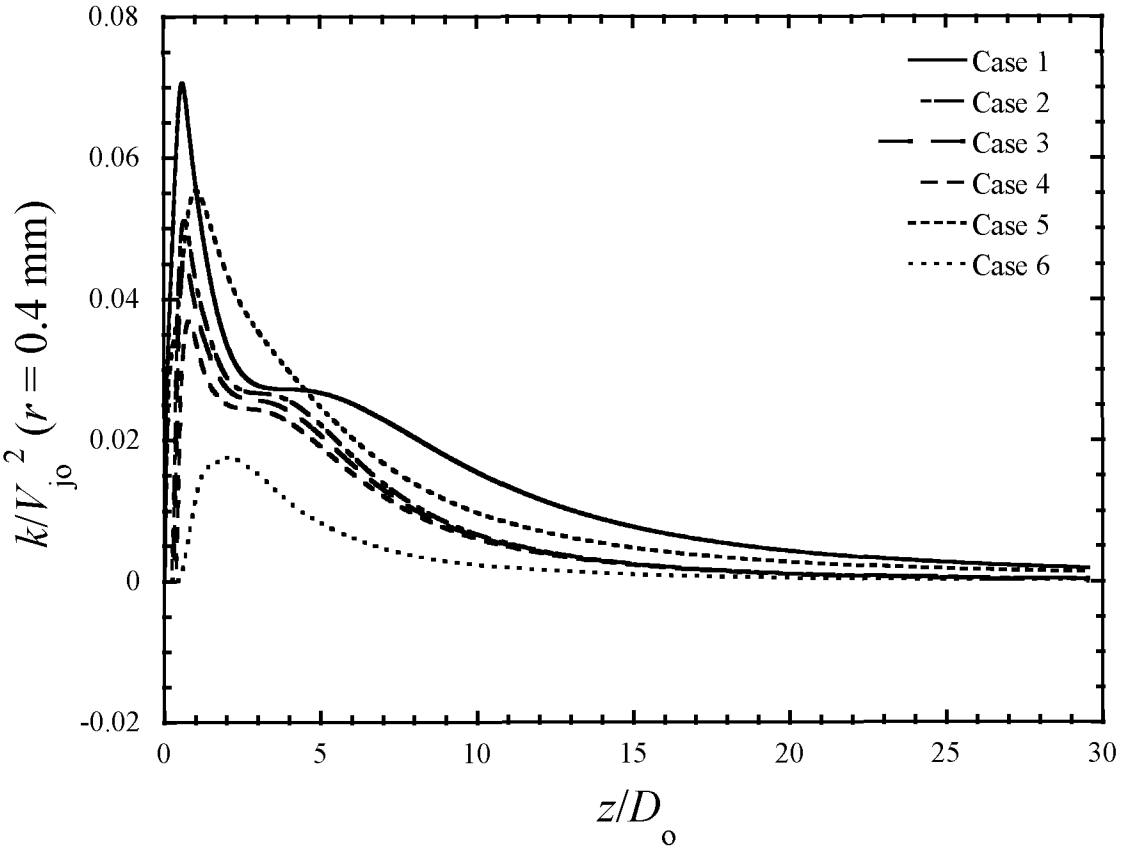

Figure 5-15. Comparison of turbulence kinetic energy of cases 1-6 at r = 0.4 mm.

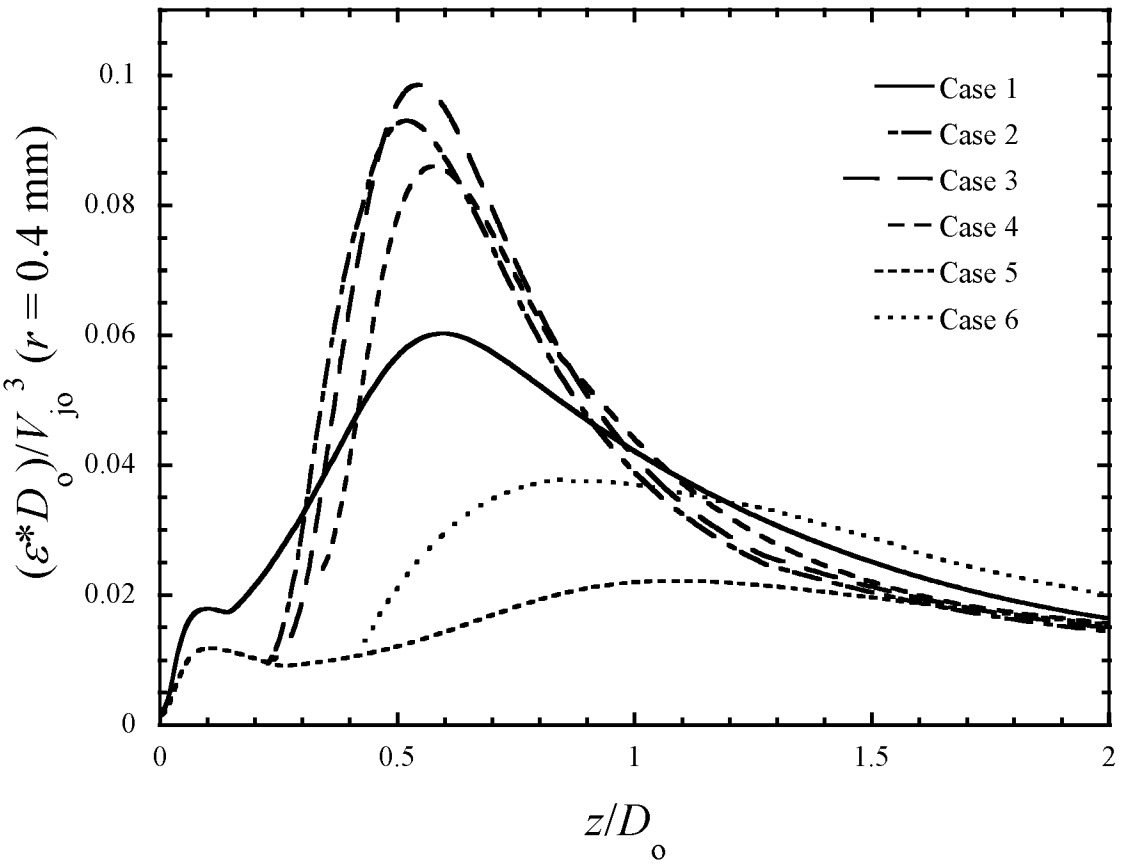

Figure 5-16. Comparison of turbulence dissipation rate of cases 1-6 at r = 0.4 mm.

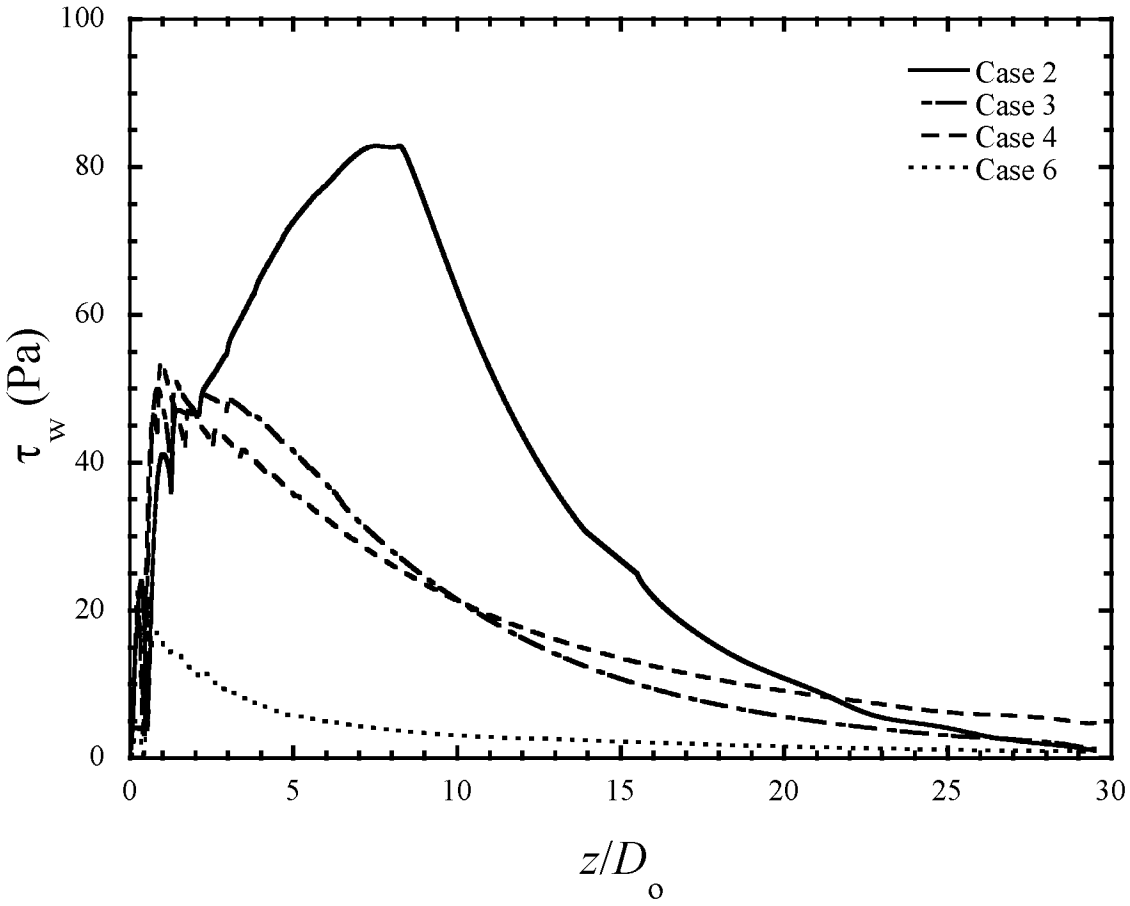

Figure 5-17. Wall shear stress comparison at the polymer edge for cases 2,3,4, and 6.

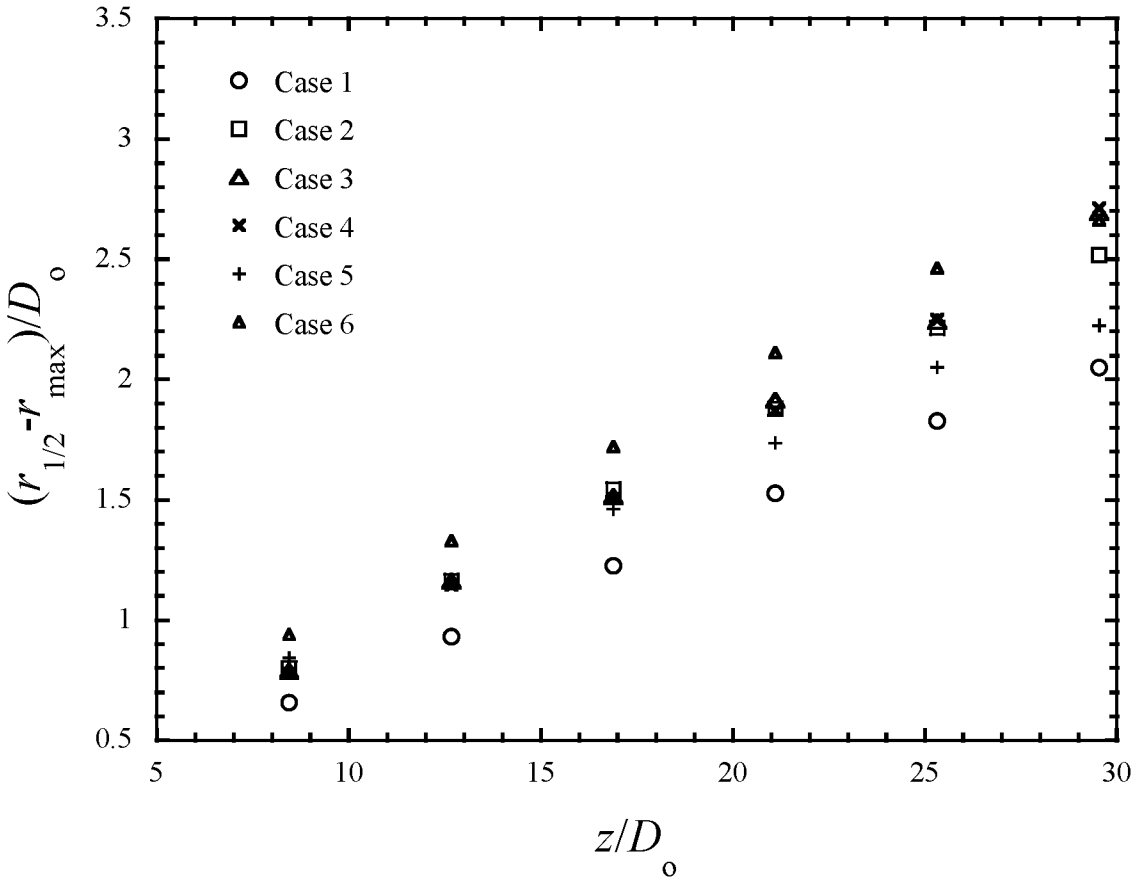

Figure 5-18. Spreading rate comparison for cases 1-6.

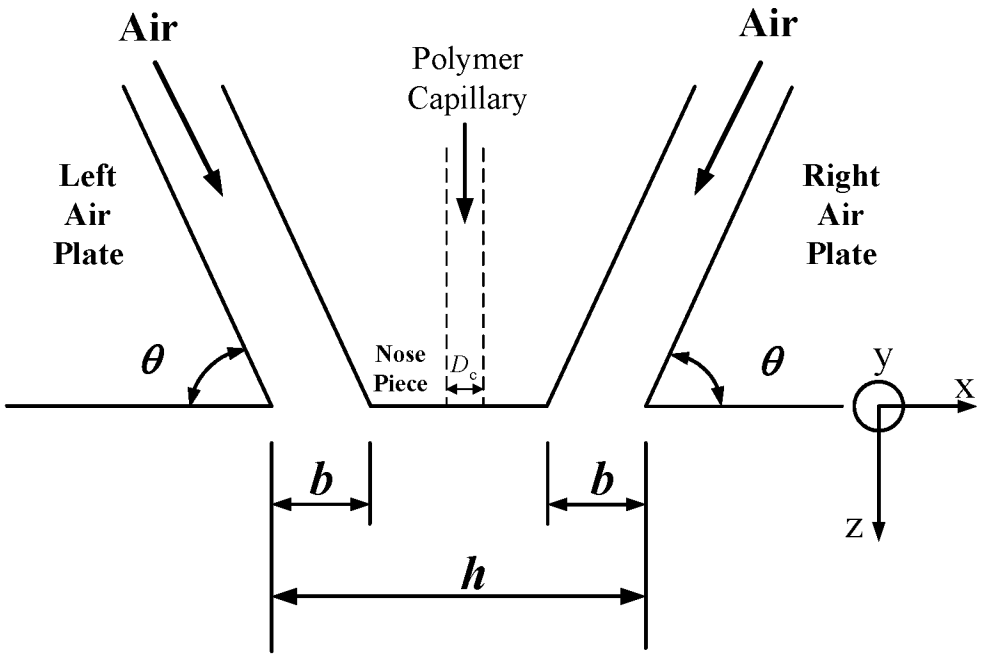

Figure 5-19a. Geometry for an Exxon slot melt blowing die from a cross-sectional view.

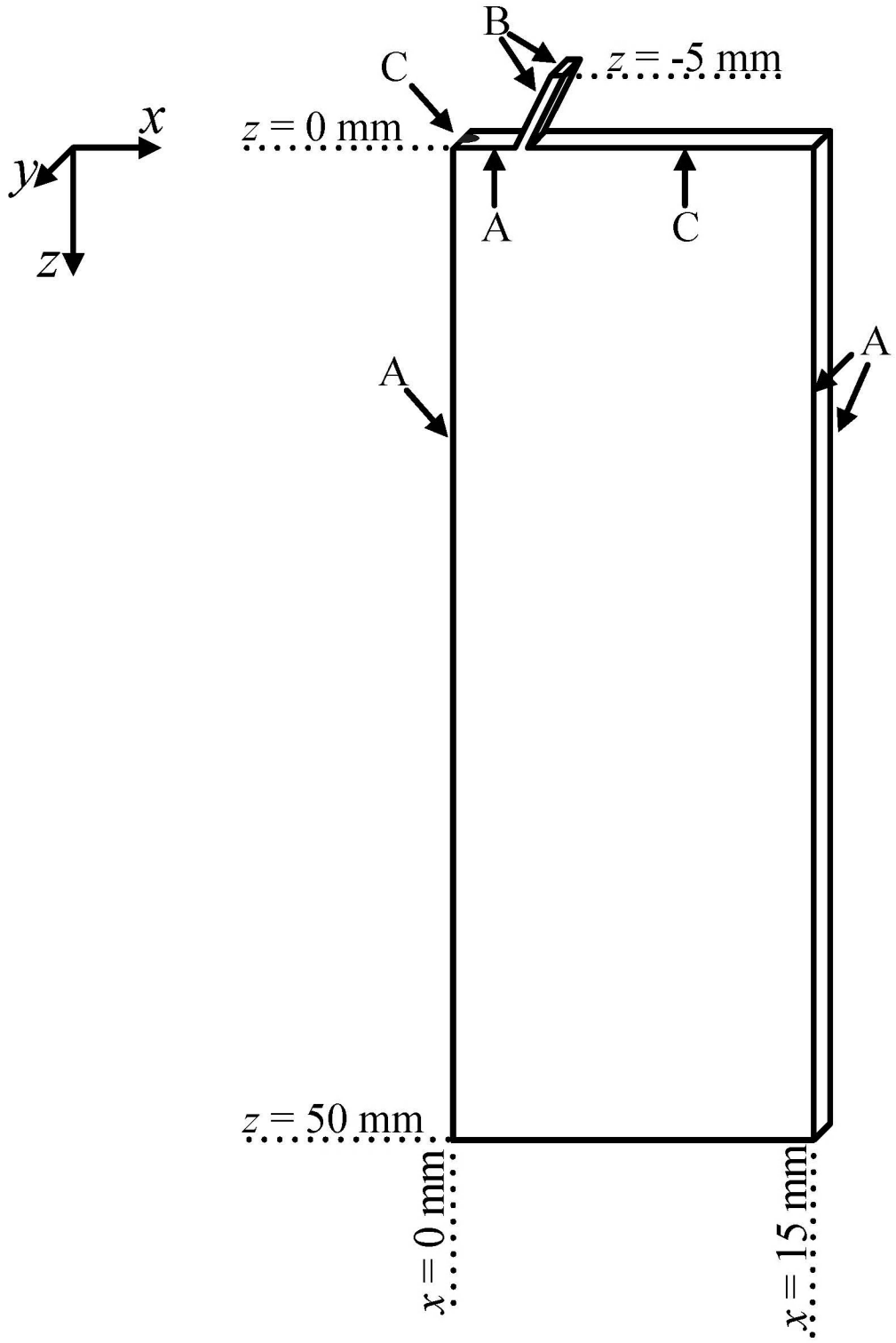

Figure 5-19b. The computational domain used in the simulations.

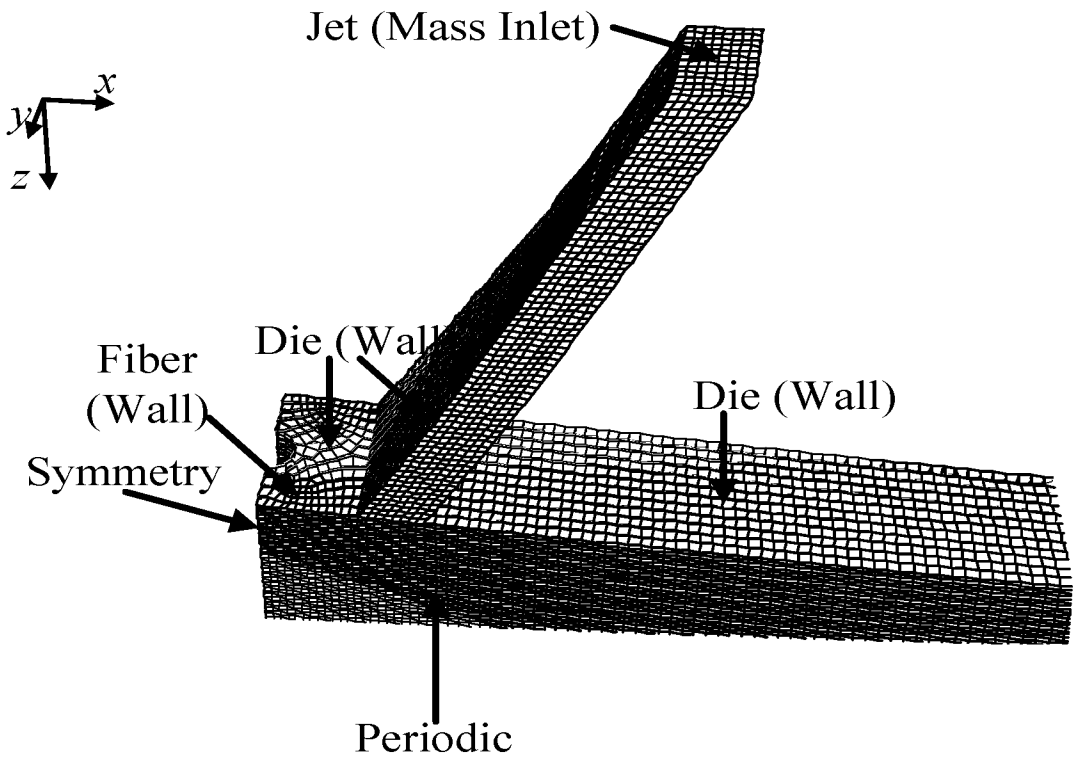

Figure 5-19c. A close up of the area of interest, including the boundary conditions.

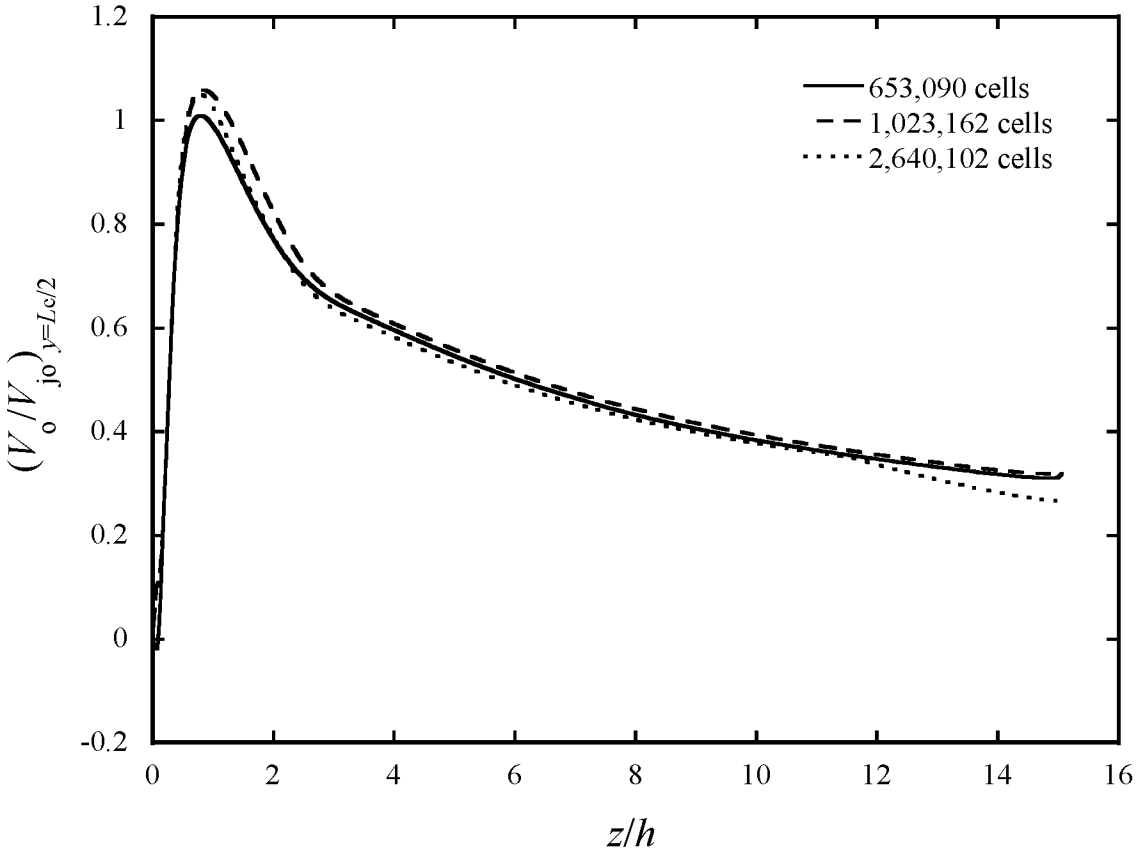

Figure 5-20. Centerline velocity at $y = L_c/2$ for different grid resolutions. These simulations all correspond to $V_{jo} = 33.7$ m/s, $m_f = 0.55$ g/min.

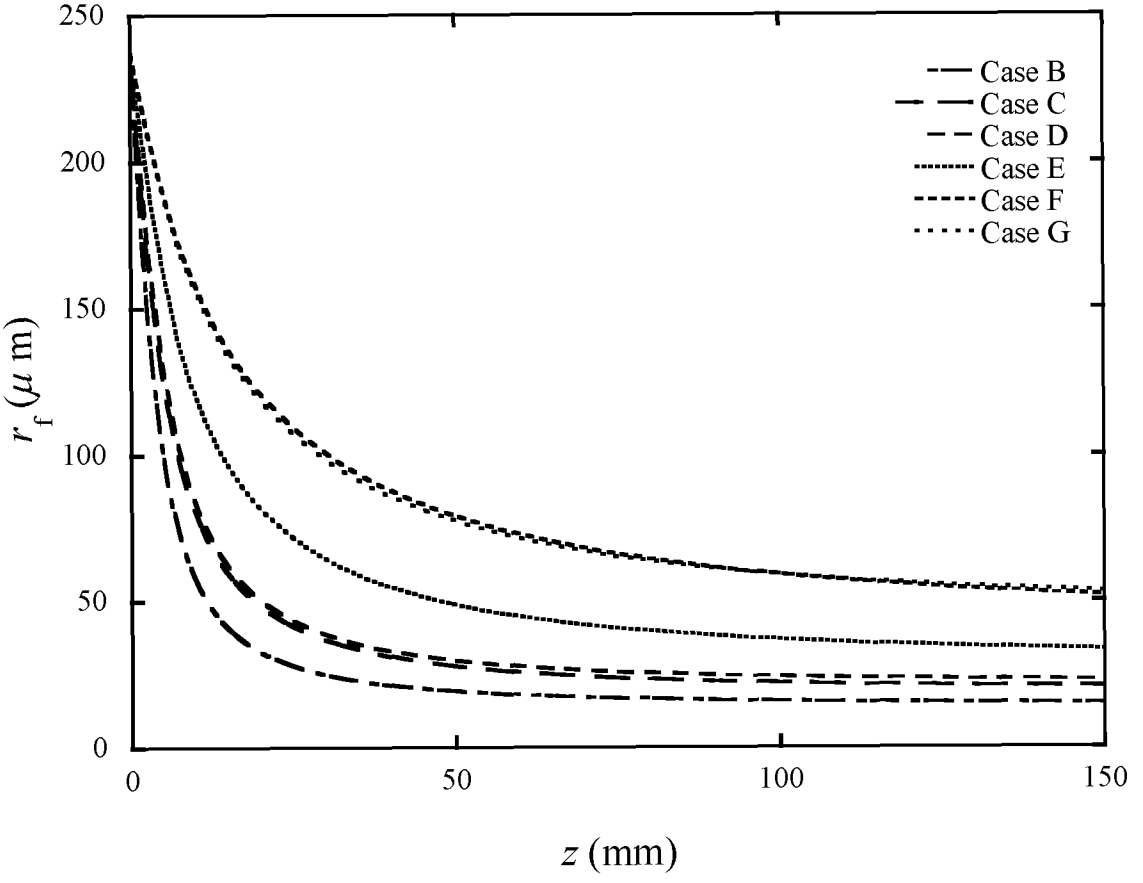

Figure 5-21a. The predictions of the rheological model for fiber radii.

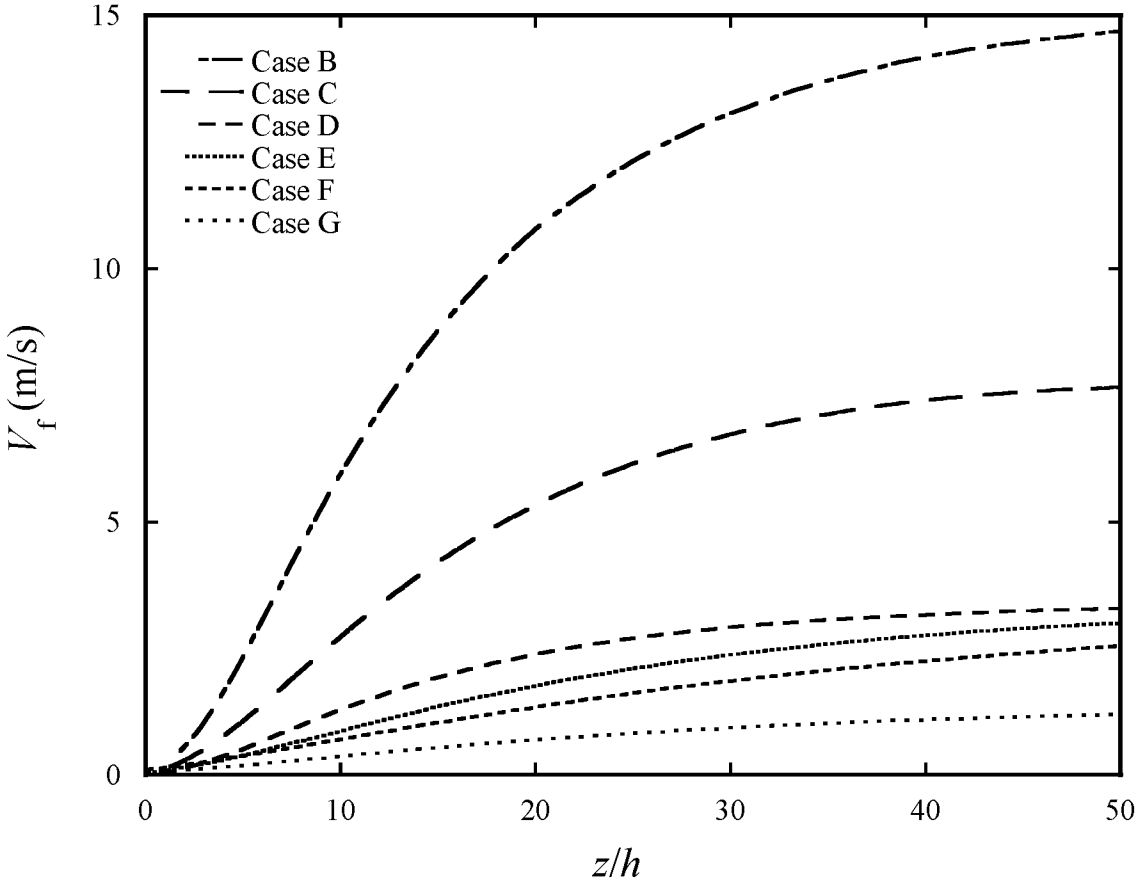

Figure 5-21b. The predictions of the rheological model for fiber *z*-velocity.

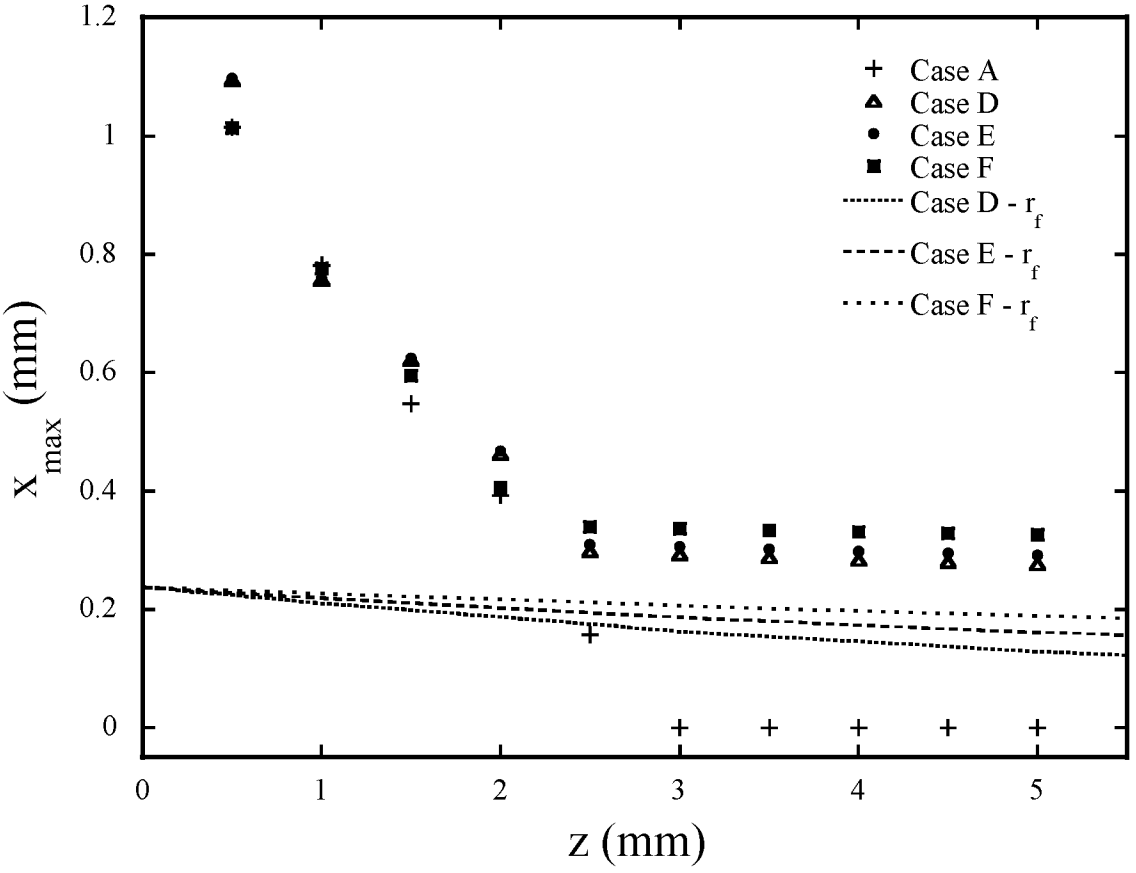

Figure 5-22. The location of the maximum air velocity at different *z*-positions for cases A, D, E and F on the $y = 0$ plane. Also included are the fiber radii for cases D, E and F.

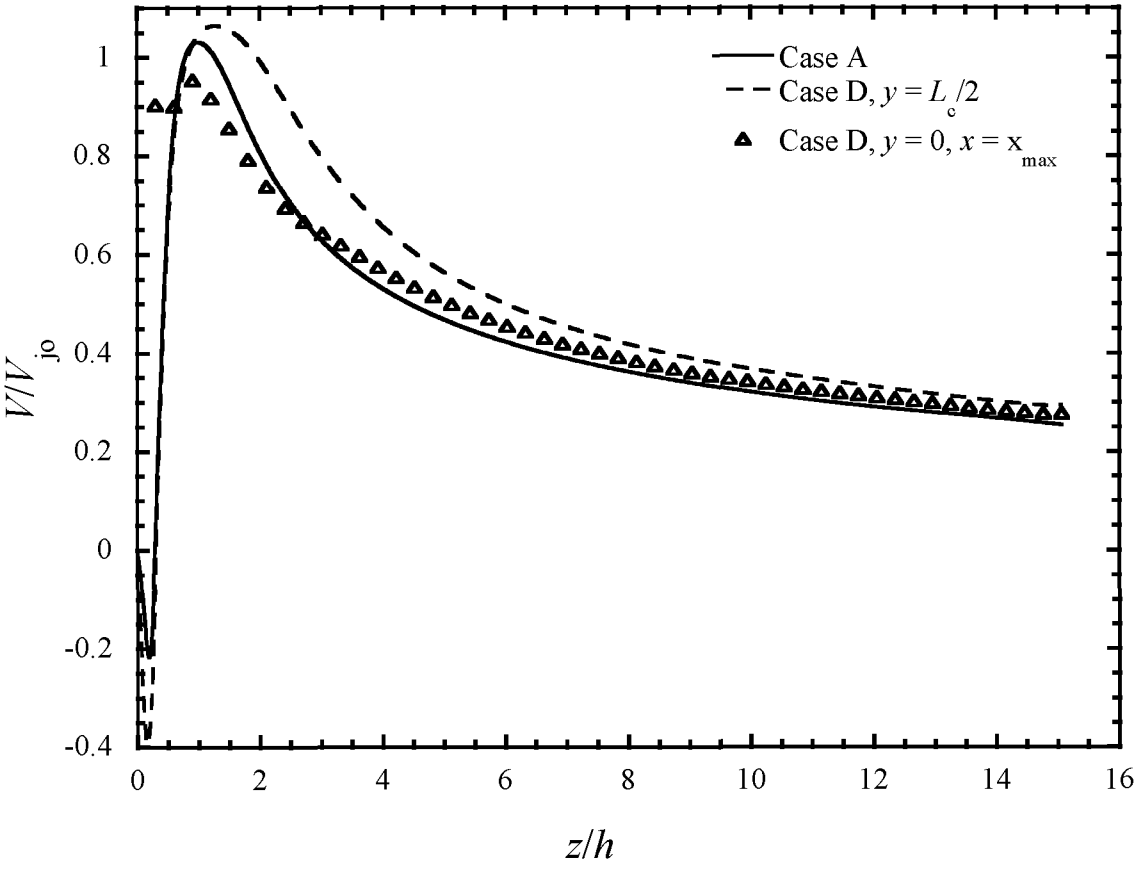

Figure 5-23. Dimensionless velocity for the centerline of case A and at $y = L_c/2$ and $y = 0$ for case D.

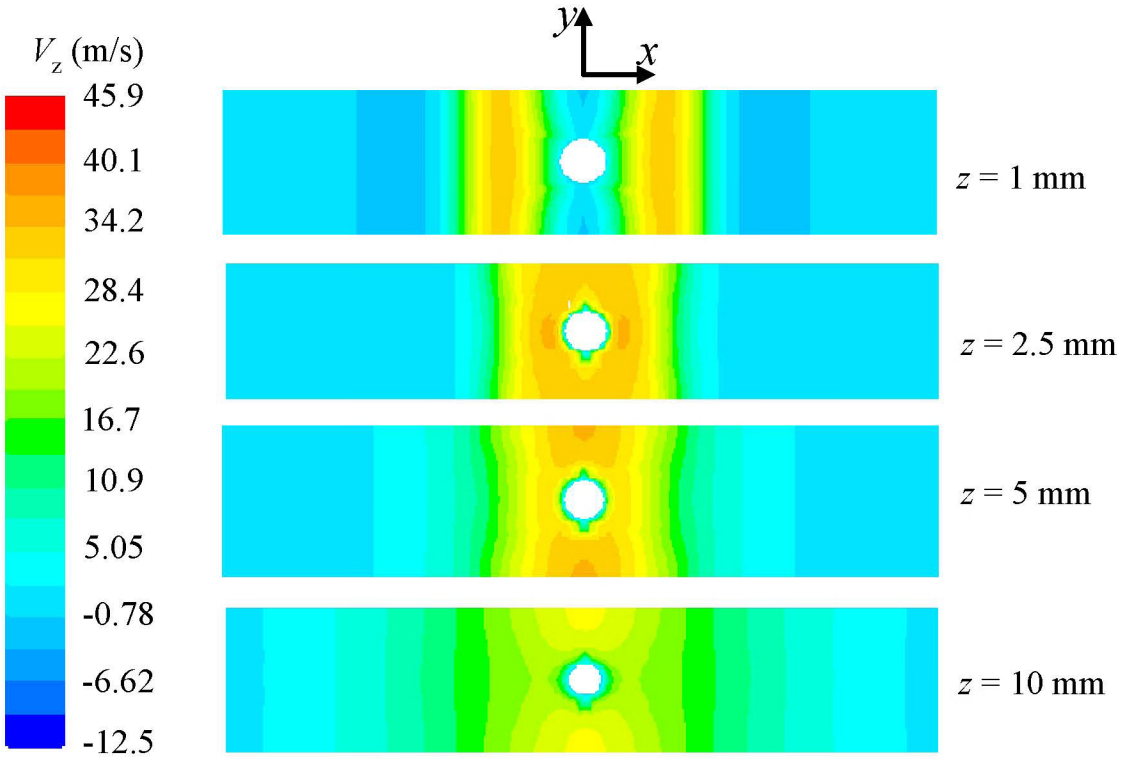

Figure 5-24. Contour plots of *z*-velocity for case D at z = 1, 2.5, 5, and 10 mm below the die face.

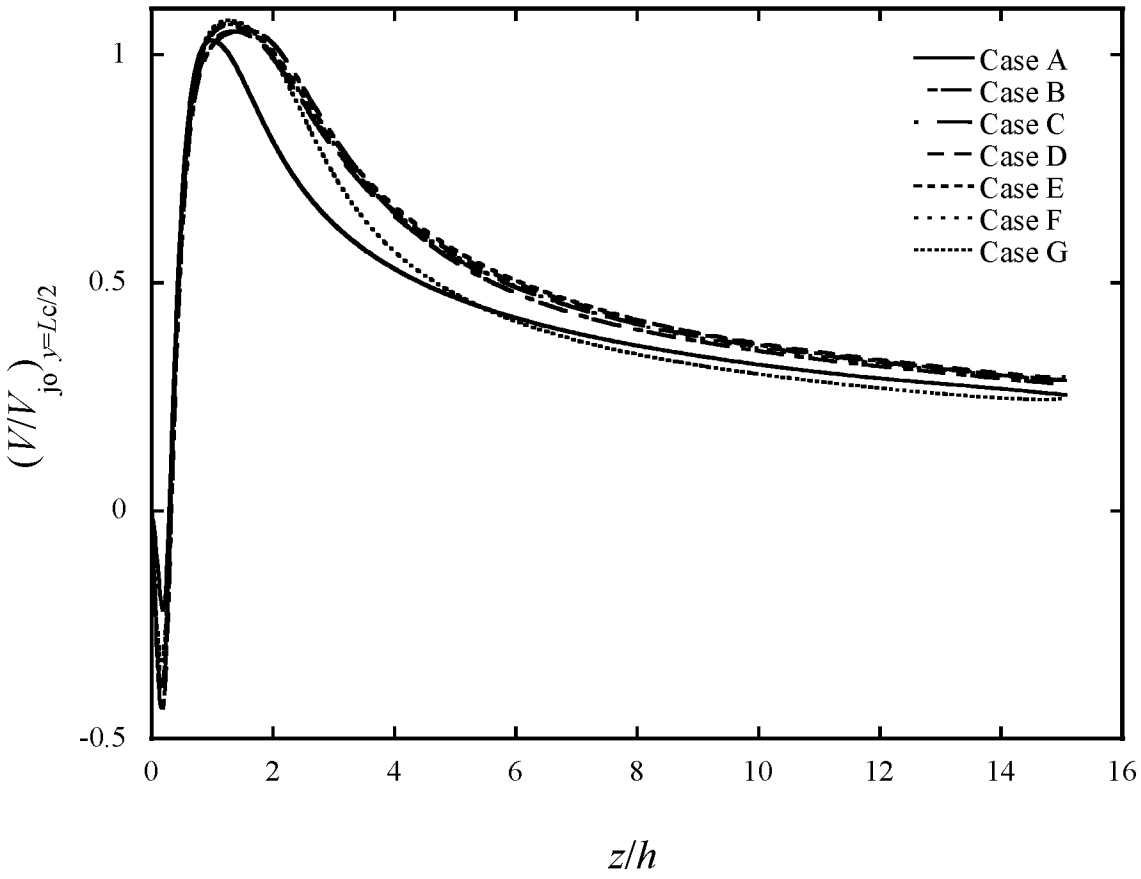

Figure 5-25a. Dimensionless centerline velocity for all cases at $y = L_c/2$.

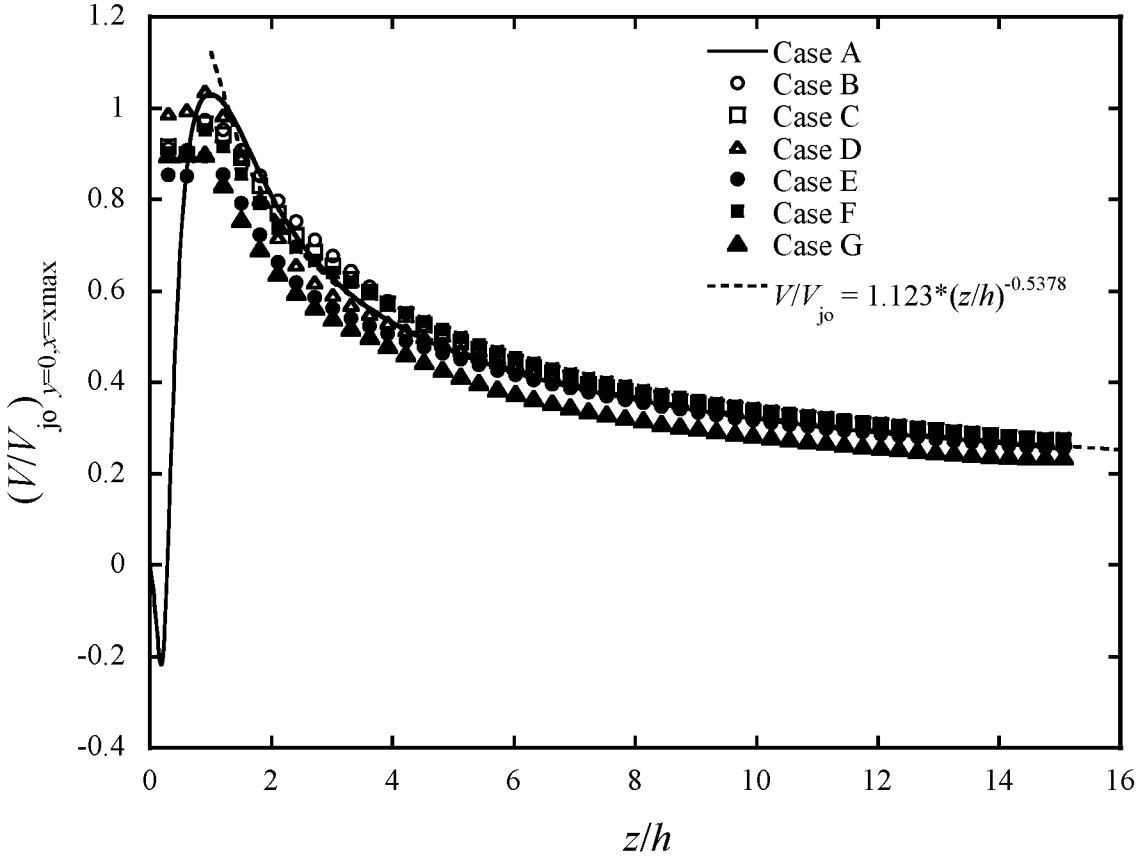

Figure 5-25b. Dimensionless centerline velocity for all cases at $y = 0$, $x = x_{max.}$ The $R^2 = 0.9835$ for the fit shown on the figure.

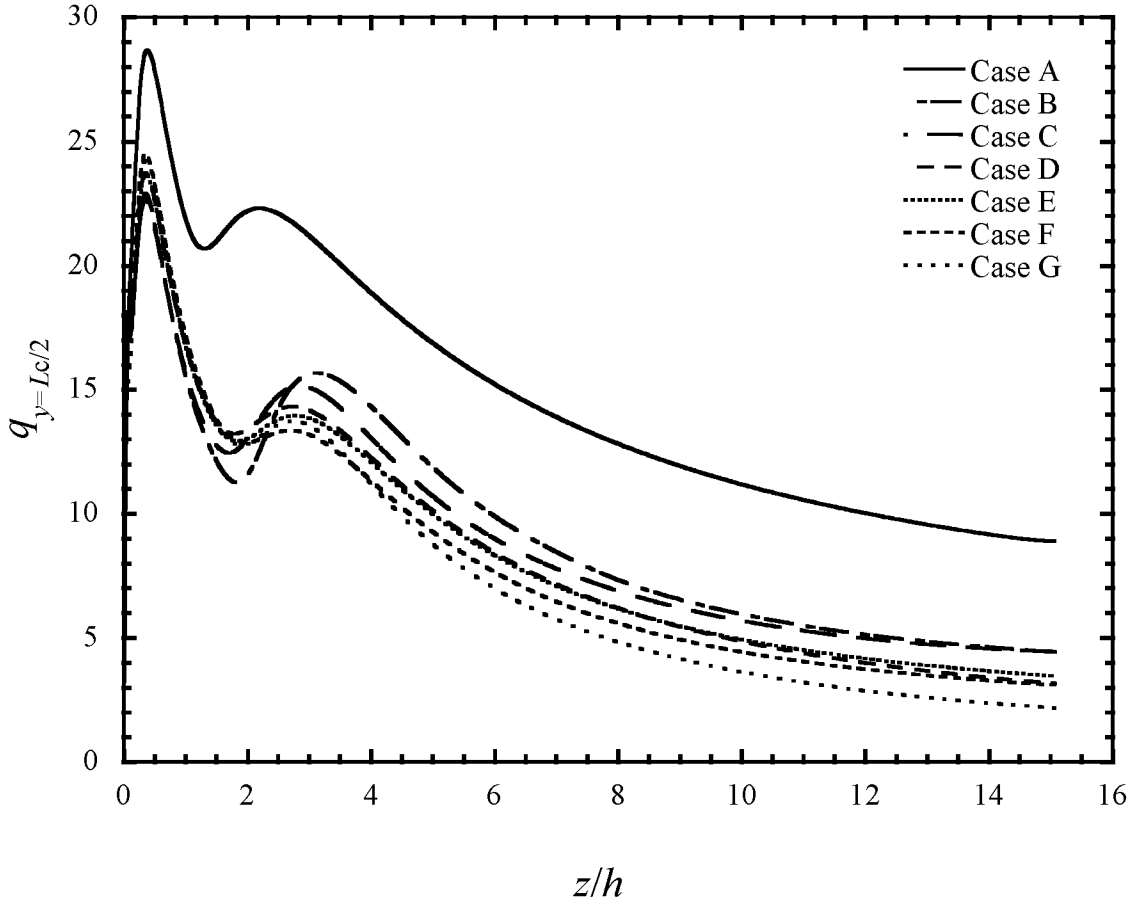

Figure 5-26a. Turbulence intensity as a percentage of V_{jo} on the centerline at $y = L_c/2$ for all cases.

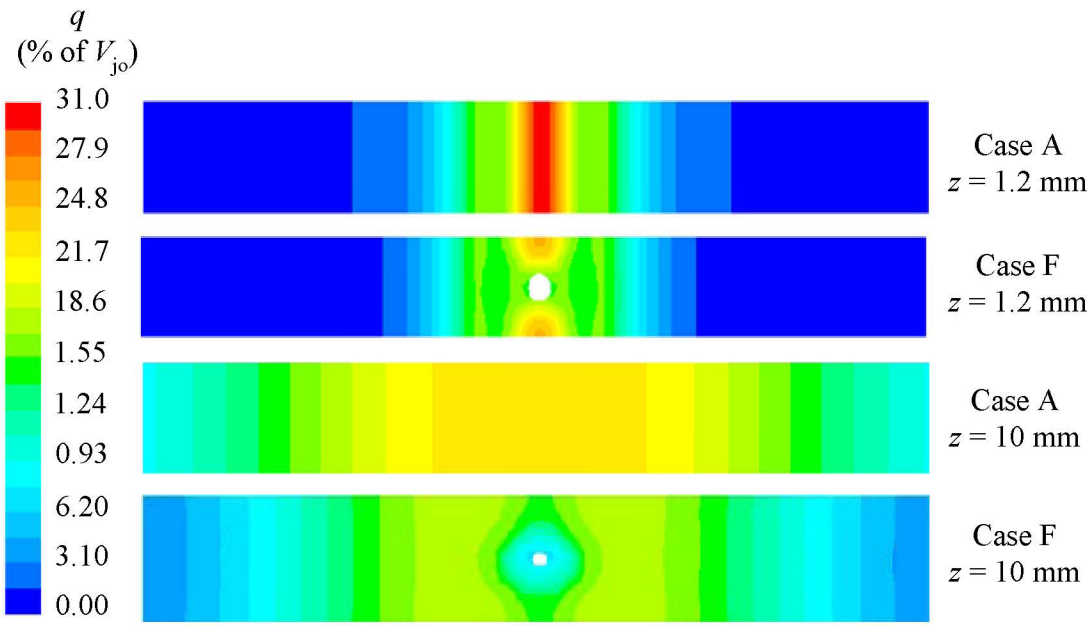

Figure 5-26b. Contour plots of turbulence intensity as a percentage of V_{jo} at *xy*-planes located at $z = 1.2$ mm and $z = 10$ mm for cases A and F.

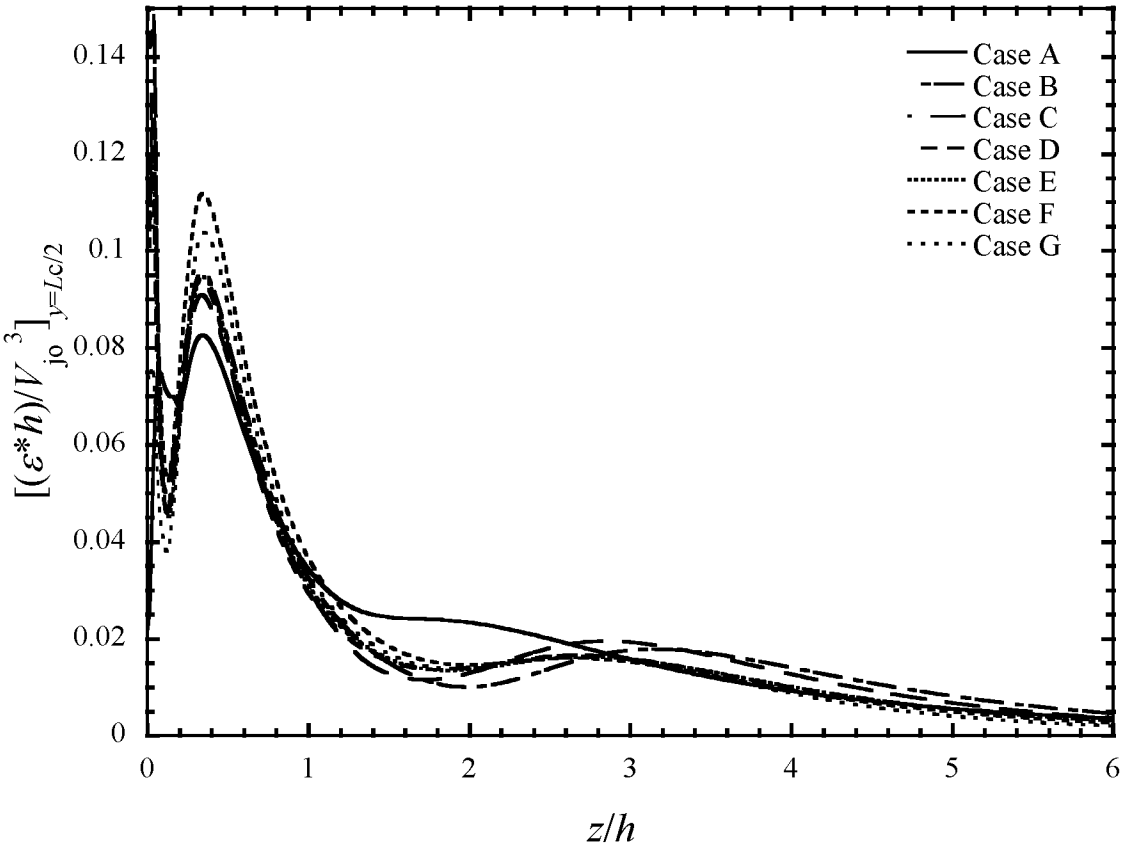

Figure 5-27. The dimensionless turbulence dissipation rate for all cases on the centerline at $y = L_c/2$.

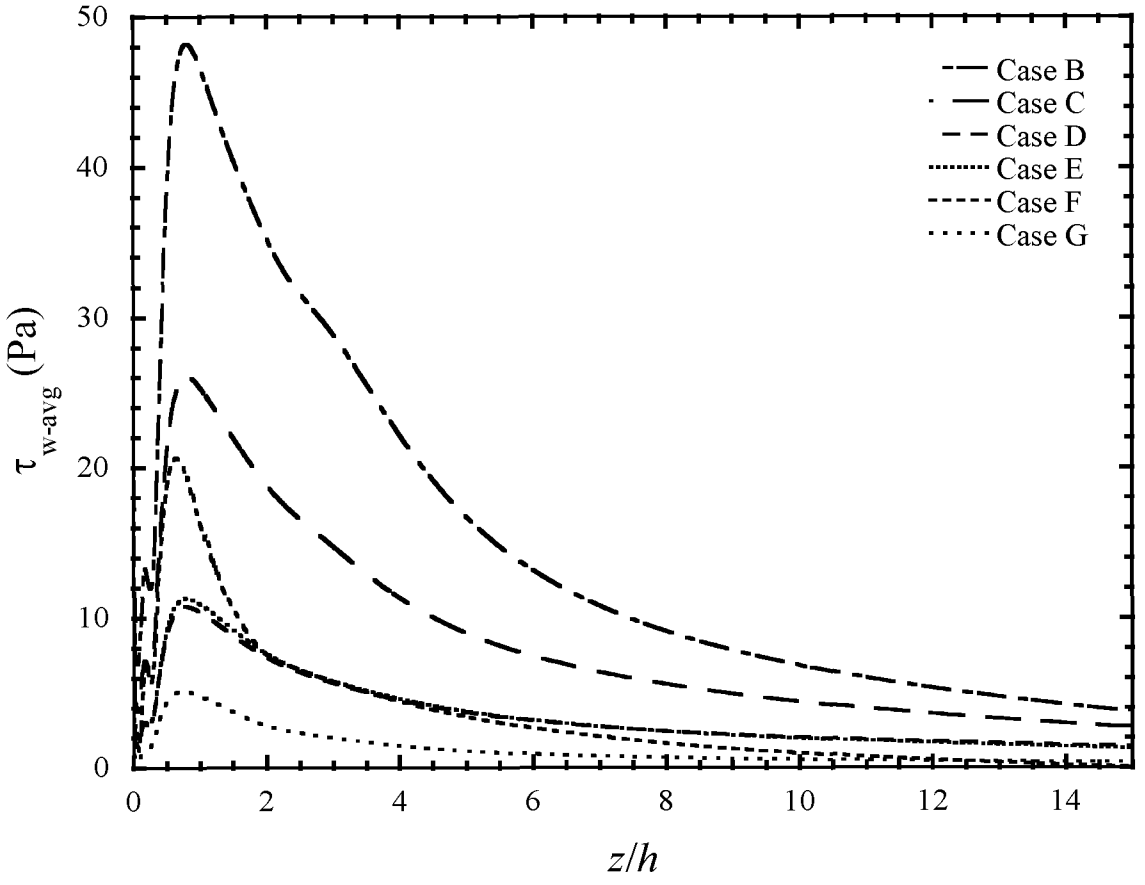

Figure 5-28. The averaged wall shear stress on the fiber edge for cases B-G.

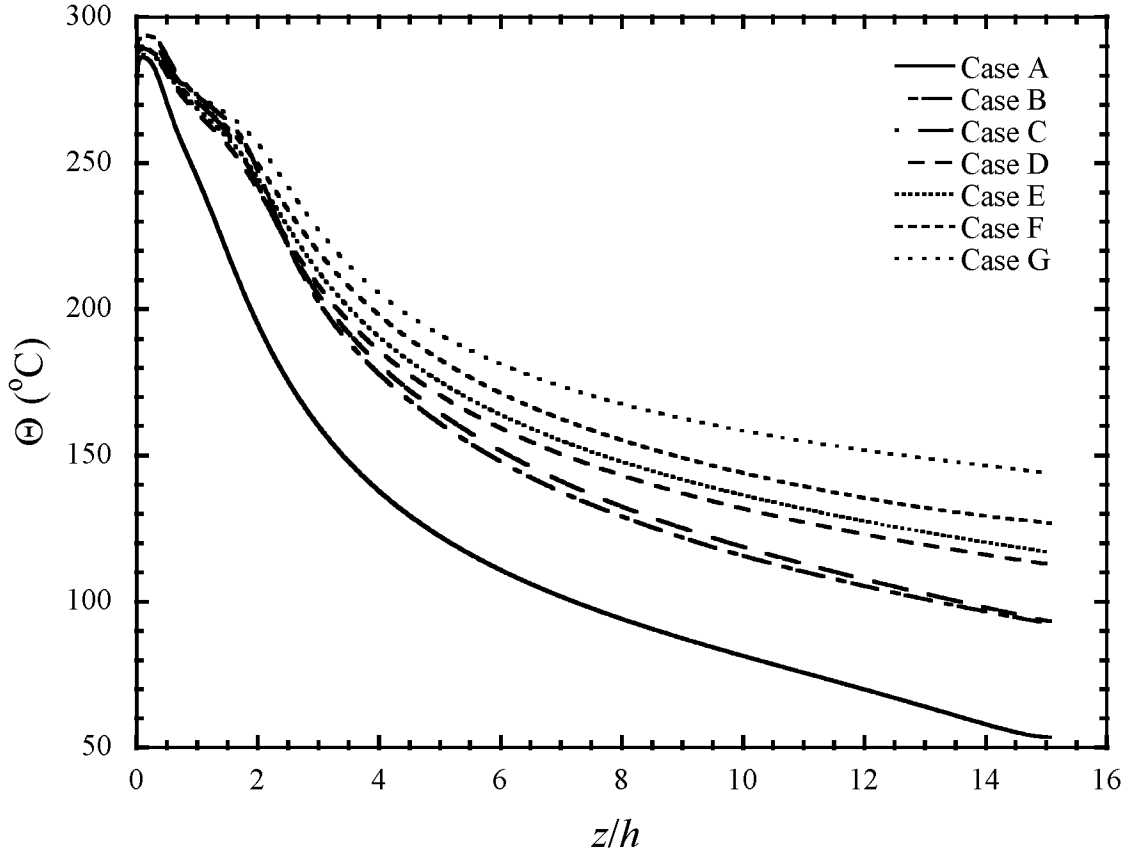

Figure 5-29a. The excess temperature decay on the centerline at $y = L_c/2$ for all cases.

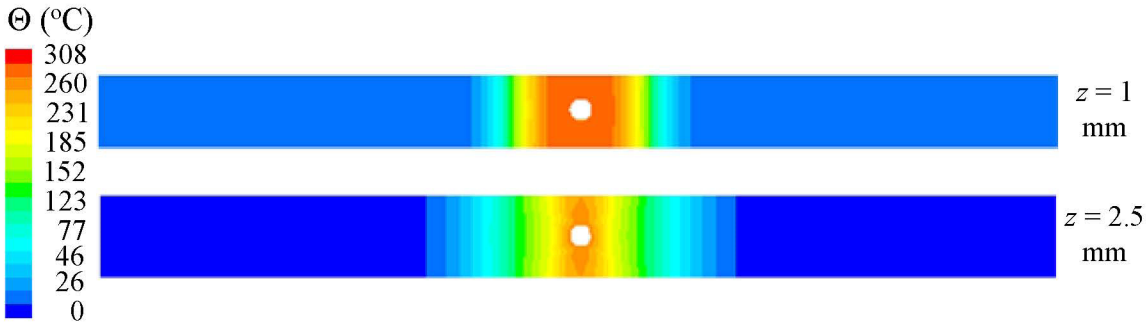

Figure 5-29b. Contour plot of the excess temperature for case F at z = 1 mm and z = 2.5 mm.

CHAPTER 6: CONCLUSIONS

This chapter contains a summary of conclusions as well as recommended future work for the material discussed in Chapters 1-5. Each previous chapter contains a complete conclusion section. Please refer to the respective chapters for more detailed conclusions.

6.1 Conclusions

Melt blowing is the industrial process of converting round polymer pellets into long, thin fibers with diameters on the order of microns (Shambaugh, 1988). The driving force for the attenuation of the fiber is drag created by the difference in the speed of the fast moving air flow and the polymer. Three different types of melt blowing dies were studied. The Exxon slot melt blowing die contained two rectangular air jets (Buntin et al., 1974). The Schwarz multihole die contained 165 annular air jets (Schwarz, 1983). The swirl melt blowing die was designed to deposit adhesive in a controlled pattern (Zeiker et al., 1988), and consisted of six round air jets.

For the slot melt blowing die, the velocity and temperature fields of the air, without the presence of a fiber, have been studied experimentally (Harpham and Shambaugh, 1996; Harpham and Shambaugh, 1997). These experimental studies were used to determine the best turbulence model for computational fluid dynamics (CFD) simulations using the software Fluent^{TM} (Fluent^{TM}, 2002). Variations of the k-ε model, as well as the Reynolds Stress Model (RSM) were used to simulate the air flow from 60° blunt and 70° sharp slot melt blowing dies. The RSM was found to agree with the experimental results with the empirical constants $C_{\varepsilon 1} = 1.24$ and $C_{\varepsilon 2} = 2.05$ (see eq. 1-4).

Using the RSM with these constants, the air flow from different jet configurations was simulated and compared. It was determined that smaller jet angles with respect to the die face led to higher centerline velocities, but also led to higher turbulence intensity in the flow field. The effect of the nose piece location was also studied. For different cases, the nose piece was either recessed above (inset dies) or extended below (outset dies) the die face. The more inset a die, the higher the centerline velocity close to the drag face. In addition, the turbulence intensity was also increased as the nose piece is inset. The location of z_{max} was defined as the distance from the die face where the highest centerline velocity occured. Correlations (depending on jet geometry) were developed to predict z_{max}, maximum centerline velocity, velocity decay, and temperature decay (for non-isothermal cases).

The multiple row Schwarz die studied consisted of 165 annular jets in three columns and 55 rows. Each annular air jet surrounded a polymer capillary. Six different dies were simulated, each with a different spacing between the jets. Due to tetrahedral cells in theses simulations, the RSM model would not converge, so the k-ε turbulence model was used. Good agreement was observed between the CFD simulations and experimental measurements (Mohammed and Shambaugh, 1993; Mohammed and Shambaugh, 1994). It was determined that for all cases, the air flow under the outside column of jets is different than that under the inside column. The outside jets were pulled inward by the center jets due to entrainment. The larger the distance between the jets, the farther below the die face the two jets merged together. Correlations were developed to predict the location of the merging point, as well as the centerline velocity decay beyond the merging point. The turbulence in the flow field did not vary significantly between

cases. Similar to the velocity profiles, the distance below the die face where the temperature maximum from the distinct jets merged together increased with increased jet spacing.

Experimental measurements for the mean air velocity on the centerline of a swirl die were taken using a Pitot tube. These experiments were completed under isothermal conditions. The Pitot tube interfered with the flow close to the die face. Simulations of the air flow were completed using several different turbulence models. The RSM would not converge with $C_{\varepsilon 1} = 1.24$ and $C_{\varepsilon 2} = 2.05$, which was likely due to the tetrahedral cells in the jet. The k-ε model did reach convergence using these constants, and was the model closest to predicting the centerline velocity measurements in the far field ($z > 40$ mm). Because of the error in the experiments, an equation developed by Baron and Alexander[10] was used to analyze the simulation results. The k-ε model with $C_{\varepsilon 1} = 1.24$ and $C_{\varepsilon 2} = 2.05$ agreed to empirical parameters found by Baron and Alexander (1951) within 2%. Using contour plots, it was determined that the angular velocity is non-uniform close to the die face and that this component of the velocity is small far from the jets.

For the experiments and simulations discussed until this point, the presence of the fiber in the flow field was neglected and the assumption was made that the air flow is not altered significantly by the presence of a fiber. In order to test this assumption, an axisymmetric simulation of a single annular jet with a fiber, as well as a 3D simulation of a slot die with a fiber were completed. For the single annular jet, the simulations revealed that the presence of the fiber decreased the recirculation area close to the die face. The turbulence in the air field around the annular jet was decreased by the presence of the fiber. For the slot die simulations, the maximum of the centerline velocity of the

air was slightly increased relative to the air only case at a position halfway between two fibers. The simulation results showed the air profile to be non-uniform, so the drag force depended on radial position on the fiber edge. Similar to the annular jet, the presence of the fiber dampened the turbulence in the flow field.

6.2 Major Contributions

There are several major contributions of this research to the field of melt blowing. One of the most important are the values of the empirical constants in the dissipation equation (eq. 1-4) $C_{\varepsilon 1}$ and $C_{\varepsilon 2}$ (1.24 and 2.05, respectively), which are optimized to model the air flow in melt blowing. These led to good matches with the experimentally measured air velocity on the centerline, which is the area of most interest for melt blowing. Using the simulation conditioned described in this research, the flow from different melt blowing die configurations can be simulated quickly and efficiently. In addition, the boundary conditions, turbulence model, discretization, and convergence criteria described in this dissertation can be used for future simulations.

For different types of melt blowing dies, empirical correlations were developed to predict centerline velocity decay, maximum in centerline velocity, and distance from the die face where the maximum centerline velocity occurs. These correlations were based on the die geometry, and give important information about the air flow in melt blowing (within the range of geometries simulated) without the need for additional simulations or experiments. Due to the lack of a wide range of experimental geometries, CFD was ideal for determining such empirical correlations.

An important step in the modeling of the air flow for melt blowing was the inclusion of a polymer fiber, which was discussed for both an annular jet and a slot die in

chapter 5. The main goal of this work was to quantify the effect of the fiber on the air flow, since this can not be measured experimentally (or at least poses great difficulty). The only differences in the flow field were observed close to the fiber. The question arises, then, whether it is worth the computational effort to include the fiber in the simulations. Although there were differences between air only and fiber inclusive results, if the purpose of simulations is to compare the air flow for different die configurations, then the important information for comparison (much of which is qualitative) can be gained from simulations without a fiber.

6.3 Recommended Future Work

The measurements and CFD of the air flow from a swirl die was discussed in chapter 4. The swirl die is new, relative to the other types of melt blowing dies. Much more stands to be learned about both the air and polymer flow from the swirl die. For the experimental measurements of the air, it is suspected that the Pitot tube interfered with the flow, so it would be beneficial to use a different experimental method. The k-ε model with the suggested modifications (see chapter 2), can be used to model the turbulent air flow from the swirl die. Since this die is new, different jet configurations should be simulated in order to determine the effect of the angle with respect to the die face and the twist angle on the air flow field. There is potential to optimize this die. In addition, the rheological model could be used to determine the lay down pattern for the swirl die. If successful, the air and fiber side could be used in conjunction (as described in the previous paragraph) to learn about, and possible optimize, this complex interaction.

6.4 Nomenclature

$C_{\varepsilon 1}$	parameter for the k-ε model
$C_{\varepsilon 2}$	parameter for the k-ε model
z	spatial coordinate, mm
z_{max}	distance from the die where the highest centerline velocity occurs, mm

6.5 References

Baron, T.; Alexander, L.G. Momentum, Mass, and Heat Transfer in Free Jets, *Chem. Eng. Prog.*, **1951**, *47*(4), 181.

Buntin, R. R.; Keller, J. P.; Harding, J. W.; Nonwoven Mats by Melt Blowing. U.S. Patent 3,849,241, Nov. 19, 1974.

Fluent User's Guide; Fluent Inc.: Lebanon, NH, 2007.

Harpham, A.S.; Shambaugh, R.L Flow Field of Practical Dual Rectangular Jets. *Ind. Eng. Chem. Res.*, **1996**, *35*, 3776-3781.

Harpham, A.S.; Shambaugh, R.L Velocity and Temperature Fields of Dual Rectangular Jets. *Ind. Eng. Chem. Res.*, **1997**, *36*, 3937-3943.

Marla, V.T.; Shambaugh, R.L. Three-Dimensional Model of the Melt-Blowing Process. *Ind. Eng. Chem. Res.*, **2003**, *42* (6), 6993-7005.

Mohammed, A.; Shambaugh, R.L. Three-Dimensional Flow Field of a Rectangular Array of Practical Air Jets, *Ind. Eng. Chem. Res.*, **1993**, *32* (5), 976-980.

Mohammed, A.; Shambaugh, R.L. Three-Dimensional Temperature Field of a Rectangular Array of Practical Air Jets, *Ind. Eng. Chem. Res.*, **1994,** *33*(3), 730-735.

Rao, R. S.; Shambaugh, R. L. Vibration and Stability in the Melt Blowing Process. *Ind. Eng. Chem. Res.* **1993**, *32*(12), 3100-3111.

Shambaugh, R. L. A Macroscopic View of the Melt Blowing Process for Producing Microfibers. *Ind. Eng. Chem. Res.* **1988**, *27*(12), 2363-2372.

Schwarz, E. C. A. Apparatus and Process for Melt-Blowing a Fiberforming Thermoplastic Polymer and Product Produced Thereby. U.S. Patent 4,380,570, 1983.

Uyttendaele, M. A. J.; Shambaugh, R. L. Melt Blowing: General Equation Development and Experimental Verification. *AIChE J.* **1990**, *36*(2), 175-186.

Zieker, R. A.; Boger, B. B.; Smyrna, L. Adhesive Spray Gun and Nozzle Attachment. U.S. Patent 4,785,966, November 22, 1988.